

Lecture Notes in Mechanical Engineering

Hemant B. Mehta

Manish K. Rathod

Rufat Abiev

Müslüm Arıcı *Editors*

Recent Advances in Thermal Sciences and Engineering


Select Proceedings of ICAFFTS 2021

 Springer

Lecture Notes in Mechanical Engineering


Series Editors

Fakher Chaari, National School of Engineers, University of Sfax, Sfax, Tunisia

Francesco Gherardini , Dipartimento di Ingegneria “Enzo Ferrari”, Università di Modena e Reggio Emilia, Modena, Italy

Vitalii Ivanov, Department of Manufacturing Engineering, Machines and Tools, Sumy State University, Sumy, Ukraine

Editorial Board

Francisco Cavas-Martínez , Departamento de Estructuras, Construcción y Expresión Gráfica Universidad Politécnica de Cartagena, Cartagena, Murcia, Spain

Francesca di Mare, Institute of Energy Technology, Ruhr-Universität Bochum, Bochum, Nordrhein-Westfalen, Germany

Mohamed Haddar, National School of Engineers of Sfax (ENIS), Sfax, Tunisia

Young W. Kwon, Department of Manufacturing Engineering and Aerospace Engineering, Graduate School of Engineering and Applied Science, Monterey, CA, USA

Justyna Trojanowska, Poznan University of Technology, Poznan, Poland

Lecture Notes in Mechanical Engineering (LNME) publishes the latest developments in Mechanical Engineering—quickly, informally and with high quality. Original research reported in proceedings and post-proceedings represents the core of LNME. Volumes published in LNME embrace all aspects, subfields and new challenges of mechanical engineering.

To submit a proposal or request further information, please contact the Springer Editor of your location: **Europe, USA, Africa:** Leontina Di Cecco at Leontina.dicecco@springer.com **China:** Ella Zhang at ella.zhang@springer.com **India:** Priya Vyas at priya.vyas@springer.com **Rest of Asia, Australia, New Zealand:** Swati Meherishi at swati.meherishi@springer.com Topics in the series include:

- Engineering Design
- Machinery and Machine Elements
- Mechanical Structures and Stress Analysis
- Automotive Engineering
- Engine Technology
- Aerospace Technology and Astronautics
- Nanotechnology and Microengineering
- Control, Robotics, Mechatronics
- MEMS
- Theoretical and Applied Mechanics
- Dynamical Systems, Control
- Fluid Mechanics
- Engineering Thermodynamics, Heat and Mass Transfer
- Manufacturing
- Precision Engineering, Instrumentation, Measurement
- Materials Engineering
- Tribology and Surface Technology

Indexed by SCOPUS and EI Compendex.

All books published in the series are submitted for consideration in Web of Science. To submit a proposal for a monograph, please check our Springer Tracts in Mechanical Engineering at <https://link.springer.com/bookseries/11693>

Hemant B. Mehta · Manish K. Rathod ·
Rufat Abiev · Müslüm Arıcı
Editors

Recent Advances in Thermal Sciences and Engineering

Select Proceedings of ICAFFTS 2021

 Springer

Editors

Hemant B. Mehta
Department of Mechanical Engineering
S. V. National Institute of Technology
Surat, India

Manish K. Rathod
Department of Mechanical Engineering
S. V. National Institute of Technology
Surat, India

Rufat Abiev
Department of Optimization of Chemical
and Biotechnological Equipment
Saint Petersburg State Institute
of Technology
Saint Petersburg, Russia

Müslüm Arıcı
Department of Mechanical Engineering
Kocaeli University
Kocaeli, Türkiye

ISSN 2195-4356

ISSN 2195-4364 (electronic)

Lecture Notes in Mechanical Engineering

ISBN 978-981-19-7213-3

ISBN 978-981-19-7214-0 (eBook)

<https://doi.org/10.1007/978-981-19-7214-0>

© The Editor(s) (if applicable) and The Author(s), under exclusive license to Springer Nature Singapore Pte Ltd. 2023

This work is subject to copyright. All rights are solely and exclusively licensed by the Publisher, whether the whole or part of the material is concerned, specifically the rights of translation, reprinting, reuse of illustrations, recitation, broadcasting, reproduction on microfilms or in any other physical way, and transmission or information storage and retrieval, electronic adaptation, computer software, or by similar or dissimilar methodology now known or hereafter developed.

The use of general descriptive names, registered names, trademarks, service marks, etc. in this publication does not imply, even in the absence of a specific statement, that such names are exempt from the relevant protective laws and regulations and therefore free for general use.

The publisher, the authors, and the editors are safe to assume that the advice and information in this book are believed to be true and accurate at the date of publication. Neither the publisher nor the authors or the editors give a warranty, expressed or implied, with respect to the material contained herein or for any errors or omissions that may have been made. The publisher remains neutral with regard to jurisdictional claims in published maps and institutional affiliations.

This Springer imprint is published by the registered company Springer Nature Singapore Pte Ltd. The registered company address is: 152 Beach Road, #21-01/04 Gateway East, Singapore 189721, Singapore

Contents

Experimental Investigation on Passive Direct Methanol Fuel Cell with Dissimilar Current Collector Materials	1
N. V. Raghavaiah and G. Naga Srinivasulu	
Performance Comparison of Different Geometries of Thermal Energy Storage Unit for Solar Cooker	15
B. C. Anilkumar, Ranjith Maniyeri, and S. Anish	
Automobile Air Conditioning Loads Modelling Using Heat Balance Method	27
Vanita Wagh and A. D. Parekh	
Computational Modelling of Bioheat Transfer for Hyperthermia Using Finite Difference Method	45
Tarun Hegde and Ranjith Maniyeri	
Application of Phase Change Material in Electronic Heat Dissipation: State-Of-The-Art	59
Kapil Kalra and Amit Arora	
Experimental Study of Integrated Solar Dryer with and Without Reversed Absorber and Reflector	71
Vijay R. Khawale, Bhojraj N. Kale, and Sandeep Lutade	
An Overview on Composites Used in Phase Change Materials for Battery Thermal Management System	87
Nishi Mehta, Shivam Prajapati, and Shulabh R. Yadav	
Effect of Semi-cylindrical Protrusions on Thermal Behaviour of SPHE	99
Darshilkumar N. Chhatrodiya, Kuldeep Parmar, Jay Chavda, Yash Kalola, and Vipul M. Patel	
Thermal Analysis for Solar Water Heater by Implementing Fins	113
Rushil Patel, Harshal Sonawane, Yogesh Mane, and Mandar Lele	

Emission Analysis Through Numerical Simulation of Three-Way Catalytic Converter with Thermal Energy Storage	125
Sanket S. Keer, Gargee Pise, and M. R. Nandgaonkar	
Optimization of 3D Plate Fin Heat Sinks Through Analytical Modelling	139
Niyaj Shikalgar, Pushkar Chitale, and S. N. Sapali	
Comparative Energy Analysis of R1234yf and R134a Refrigerants	151
Vanita Wagh and A. D. Parekh	
Recent Trends in Artificial Intelligence-Inspired Electronic Thermal management—A Review	165
Aviral Chharia, Nishi Mehta, Shivam Gupta, and Shivam Prajapati	
Investigation on Heat Transfer Performance of Nanofluids	177
Shankar Durgam and Ganesh Kadam	
A Comprehensive Review on Nano-additives for the Enrichment of Diesel and Biodiesel Blends for Engine Applications	187
Gandhi Pullagura, Srinivas Vadapalli, V. V. S. Prasad, Venkateswarlu Velisala, Kodanda Rama Rao Chebattina, and Abdul Razack Mohammad	
Convective-Radiative Heat Transfer in a Rotating Cubic Cavity with a Local Heat Source	207
S. A. Mikhailenko and M. A. Sheremet	
Performance Analysis of IC Engine Using Parabolic Fin	215
Ruchika Dnyaneshwar Lande, Onkar Pravinrao Ajegaonkar, Swapnil Suresh Nikam, Yogesh Mane, and Mandar M. Lele	
Numerical Study on Operating Temperature of PV and PV-PCM Systems	227
Deepak Kumar Sharma, Manish K. Rathod, and Purnanand V. Bhale	
Aluminum Oxide as Potential Additives to N-Butanol-Diesel Blends on Emission and Performance Characteristics of the Diesel Engine	241
Gandhi Pullagura, Srinivas Vadapalli, V. V. S. Prasad, Suryanarayana Varma Datla, Arhun Jaya Sai Makkena, Ashok Srinivas Reddy Chilla, Venkateswarlu Velisala, and Kodanda Rama Rao Chebattina	
Analytical Study of Thermal Stresses Generated in a Carbon Fiber-Reinforced Wheel Hub	257
Prasanna Kadambi, Bikash Prasad, Pranay Luniya, Parth Kulkarni, Sandip T. Chavan, and Yogesh G. Mane	

Estimation of Emissivity of the Surface Using Jaya Algorithm 265
 Sanil Shah and Ajit Kumar Parwani

Development of an Empirical Model for the Prediction of Thermoelectric Behavior of Lithium Iron Phosphate Pouch Cell Under Different Discharge Rates 273
 Indraneel Naik, Pravin Nemade, and Milankumar Nandgaonkar

Application of Artificial Neural Network to Predict Effective Thermal Conductivity of Porous Foam Structure 285
 Vipul M. Patel, Harsh Kumar, and Kuldeep Singh

Numerical Analysis of Heat Transfer Enhancement of Heat Sink Using Different Phase Changing Materials for Electronic Cooling Application 299
 K. Naga Ramesh, M. Manoj Sai, K. Vineeth Goud, K. Raghavendra, S. Amruth, and T. Karthikeya Sharma

Performance Analysis of Active Cooling System in Lithium-Ion Batteries Using Dual Potential Multi-Scale Multi-Dimensional Battery Model Approach in Extreme Environment 311
 Ashima Verma and Dibakar Rakshit

Numerical Investigation on Characteristics of Methane Combustion 321
 Keyur Kadia, Nikhil A. Baraiya, and R. D. Shah

Computational Heat Transfer Analysis of Perforated Annular Fin with Highly Conductive Insert Under Forced Convection 333
 S. Lakshmanan and M. Venkatesan

Membrane Electrode Assembly Material for DMFC-A Review 345
 Seema S. Munjewar, Arunendra K. Tiwari, and Rohan Pande

Thermal Management of Lithium-Ion Battery Pack with Liquid Cooling: A Computational Investigation 357
 Shankar Durgam and Vikrant Mahesh Deshmukh

Heat Transfer Characteristics of a Two-Phase Closed Vertical Thermosyphon: An Experimental Study 371
 Aalekh Srivastava, Manish K. Rathod, and Naresh Yarramsetty

Application of Inverse Heat Transfer Technique in Thin Slab Continuous Casting for Estimating the Interfacial Boundary Heat Flux 385
 Ananda S. Vaka, Pedduri Jayakrishna, Saurav Chakraborty, Suvankar Ganguly, and Prabal Talukdar

Heat Transfer Enhancement of Fin and Tube Heat Exchanger Using Ribs	399
Vaidant Rathore, Atharva A. Lokhande, Yogesh G. Mane, and Mandar M. Lele	
Effect of Dilution on Lean Blow-Off Limit of Methane Combustion	409
Keyur Kadia, Nikhil A. Baraiya, and R. D. Shah	
Experimental Investigation on the Performance of Solar Stills with Vent Holes and Hybrid Nano PCM	421
M. Padmanaban, S. Suresh, and P. Kalidoss	
Performance Characterization of Domestic Liquefied Petroleum Gas Cookstove	437
Kishan Dash and Sikata Samantaray	
Improvement in the Electric Vehicle Battery Performance Using Phase Change Material	447
Jay R. Patel and Manish K. Rathod	
Effect of Dilution on Emission from Methane Combustion	459
Keyur Kadia, Nikhil A. Baraiya, and R. D. Shah	
Energy and Exergetic Analysis of Thermal Transport in Latent Heat Thermal Energy Storage Systems Impregnated with Metal Foam	473
Varun Joshi, Jay R. Patel, and Manish K. Rathod	
Numerical Investigation on Finned Latent Heat Storage Unit	485
Nitish Gupta and Manish K. Rathod	
Material Recovery from End-of-Life Solar Photovoltaic Module Through Thermal and Chemical Processes	499
Aparna Singh, Ahmed Ali Kabir, Sachin Gupta, Jyotsna Singh, and R. B. Singh	
Effect Analysis of Heat Extraction on the Performance of the TAE	513
S. R. Solanki, A. B. Desai, and H. B. Mehta	

About the Editors

Dr. Hemant B. Mehta is currently an associate professor at the Department of Mechanical Engineering, National Institute of Technology Surat, Gujarat. He obtained his B.E. (Mechanical), M.Tech. (Turbomachines) and Ph.D. from the National Institute of Technology, Surat, Gujarat. His major areas of research interests include two-phase flow induced heat transfer in micro and minichannels, active and passive thermal management using microchannel heat sink, heat pipe and its variants and nanofluids, CFD analysis of thermal systems, radiative heat transfer and thermoacoustic engine/refrigerator. He has published more than 50 articles at national and international levels and he has been granted five design patents. He completed two research projects of Rs. 35 lakhs. He is a Fellow of Institution of Engineers and a life member of Indian Society of Heat and Mass Transfer.

Dr. Manish K. Rathod is currently an assistant professor at the Department of Mechanical Engineering, National Institute of Technology (SVNIT), Surat, India. He obtained his B.E. (Mechanical) and M.E. (Thermal Sciences) from M S University of Baroda and Ph.D. from SVNIT Surat. His area of interest is thermal energy storage using phase change material (PCM), Thermal management by PCM, Passive cooling in buildings, Energy and exergy analysis of thermal systems, Heat exchangers design and its augmentation. He has more than 70 journal/conference publications of the nation and international repute and 4 design patents in the field of his research. He was awarded Outstanding Scientist in Mechanical Engineering by the 4th Venus International Research Awards. He has published a book chapter entitled “Thermal Stability of Phase Change Material” in a book named Phase Change Materials and Their Applications.

Prof. Dr. Sc. Rufat Abiev is a Professor and Head in the Department of Optimization of Chemical and Biotechnological Equipment, Saint Petersburg State Institute of Technology (Technical University), Saint Petersburg, Russia. His research interest lies in Process Intensification, Microreactors, Process Simulation, Bubbles and Droplets break up, Heat- and Mass Transfer intensification, Pulsations for chemical engineering. Rufat Abiev has more than 450 publications, 6 books, 5 chapters

in a *New Handbook of Chemist and Technologist* (in Russian), 2 chapters in handbooks (*Process Analysis, Design, and Intensification in Microfluidics and Chemical Engineering*, Hershey, PA: IGI Global, USA, 2019; *Transport Processes at Fluidic Interfaces*, Springer-Verlag, Germany, 2017), more than 100 papers in peer-reviewed international and Russian journals and more than 90 patents. Several patents are implemented in the industry.

Prof. Müslüm Arıcı is a faculty member in Thermodynamics and Heat Technique Division of Mechanical Engineering Department of Kocaeli University, Turkey. He completed Diploma Course at von Karman Institute, Belgium in 2007. He received Ph.D. degree from Kocaeli University in 2010. He worked in Fluid Mechanics Research Group, University of Zaragoza, Spain in 2014 and 2016–2017 as a visiting professor. He has co-authored of more than 100 papers in refereed journal papers and presented numerous research papers in international conferences. He has been invited to as an invited speaker in several international conferences and workshops held in Croatia, Algeria, Ukraine, China, and Kazakhstan. He has served as a guest editor and has been in the editorial board of several international journals. His fields of interest are Numerical Heat Transfer, Computational Fluid Dynamics, Nanofluids, Solar Energy, Energy Efficient Buildings and Thermal Management by Phase Change Materials.

Experimental Investigation on Passive Direct Methanol Fuel Cell with Dissimilar Current Collector Materials



N. V. Raghavaiah and G. Naga Srinivasulu

Abstract Experimental investigation is carried out on passive direct methanol fuel cell, to study with the selected combination of different anode and cathode current collectors which have high electrical and thermal conductivity together with corrosion resistance compatibility properties. These collectors are fabricated with an opening ratio of 45.3% on Stainless Steel Grade-316L, Nickel-201 and brass (70% Cu-30% Zn) and experimented at 5 M concentration of methanol solution. Polarisation curves and maximum power density curves have been drawn with the experimental results for performance comparison using Ni-SS, Ni-Brass, SS-Ni and SS-brass anode and cathode combinations of current collectors. Comparative studies for maximum power and current densities are investigated and represented on bar charts for identifying the better combination of anode and cathode materials. Performance of cell is found best with the combination using Nickel-201 as anode and brass as cathode. With this combination, the maximum power density developed is 7.157 mW cm^{-2} , and the maximum current density produced is 65.6 mA cm^{-2} at 5 M concentration.

Keywords Passive direct methanol fuel cell · Current collector · Corrosion resistance material · Electrical conductivity · Thermal conductivity · Nickel · Stainless steel · Brass

Nomenclature

CC	Current collector
CD	Current density
MEA	Membrane electrode assembly
Ni	Nickel
PD	Power density

N. V. Raghavaiah (✉) · G. N. Srinivasulu
National Institute of Technology, Warangal, Telangana State, India
e-mail: nvraghavaiah@student.nitw.ac.in

PTFE	Polytetrafluoroethylene
pDMFC	Passive direct methanol fuel cell
SS	Stainless Steel

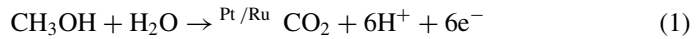
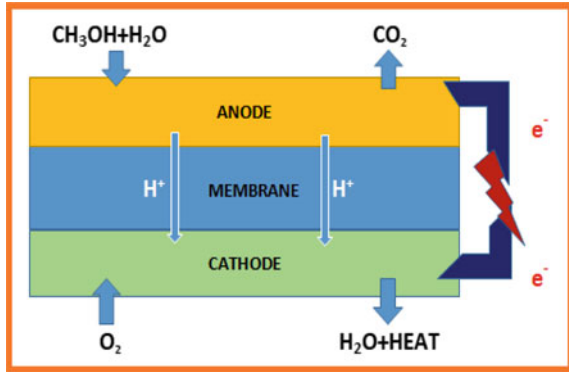
1 Introduction

With increase in societal demand for electricity every year across the globe, fuel cell technology is evolving out as one of the protuberant energy resources among the accessible alternative energy resources in place of fossil fuels which are going to be lost within next few decades. Fuel cells are similar to conversion devices like a battery; it converts the chemical energy of reactants into electricity leaving other reaction compounds as by-products [1]. However, fuel cell differs from a battery in that as long as the fuel and oxygen are supplied, it produces electric power continuously. Out of the other well-known fuel cells classified based on proton conducting membrane electrolyte, polymer exchange electrolyte membrane-based cell working with direct liquid feed methanol as fuel and air as an oxidant emerges out as an electric power source for the applications [2] of portable electronic appliances like mobile phones, laptops, tape recorders, Walkman, toys, computers, cell phones, emergency lights, including material handling equipment like forklifts, cargo loaders, etc., and also for space application systems [3]. As a fuel, liquid methanol is relatively inexpensive and easily available and has more specific energy density, quick refuelling and good transportation and better storage facility. Further, fuel cell characteristics are ultimately affected by significant aspects such as choice and make use of suitable materials and its novel designing. These fuel cells facilitate to operate at low temperatures and pressures without additional liquid electrolyte requirement [4]. pDMFC can also be operated at ambient pressure and temperatures conditions. It has other advantages like clean by-products, extremely no/low emission of oxides of nitrogen and sulphur, operates quietly, not having any moving parts and extra fuel processing to meet demand requirement and high energy. Compact cell design of pDMFC makes it easy to handle. Schematic representation of passive direct methanol fuel cell is represented in Fig. 1.

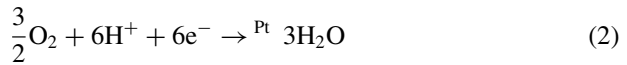
To have better reaction kinetics, pDMFC makes use of ruthenium and platinum as catalyst on the anodic side of the membrane to break the chemical bonds in the methane water solution to form carbon dioxide, hydrogen ions (protons) and free electrons as shown in Eq. (1). In the cell, the liberated electrons flow from the anodic side of the cell through an external circuit to the cathodic side, and the protons are transported through the proton conducting electrolyte membrane. At the cathode, the electrons and hydrogen ions react with oxidant to form water as shown in Eq. (2). The liberated heat of reaction is mostly released to surroundings through cathode side current collector. Overall chemical reaction of the cell is shown in Eq. (3).

Anode End Reaction:

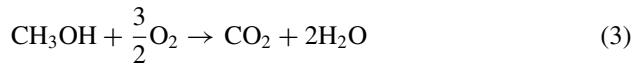
Fig. 1 Schematic representation of passive direct methanol fuel cell



Cathode End Reaction:



Overall Fuel Cell Reaction:



2 Literature Survey

Passive direct methanol fuel cell is getting importance across the globe as an electrical power source due to high-energy density of fuel. Among the fuel cell components, current collector material properties and their compatibility in water–methanol solution are influencing cell durability, performance and effectiveness.

Braz et al. [5] has studied the optimization process of passive direct methanol fuel cell with various current collector materials. It is indicated that to ascertain DMFC commercially, an optimum balance between its price, competence and durability should be achieved. Current collectors are accountable for about 70–80% of the system weight, and different current collector materials were tested to balance price and weight reduction. Performance of the fuel cell and its duration were identified using polarisation measurements. A serious novelty of this study is the use of an innovative identification and quantification of performance. The utmost power density of 5.23 mW cm^{-2} was achieved using Titanium as anode current collector and Stainless Steel as cathode current collector at a methanol concentration of 7 M.

The durability tests showed a lifetime about 200 h and a reduction in efficiency of fuel cell by 41% from original value.

Tabbi et al. [6], in their investigation, identified that the automobile industry is encouraging the use of metals as current collector plates as metals having small thickness and weight as well as good conductivity both thermally and electrically. Using stainless steel would reduce the cost, but non-coated SS from investigation still has some challenge with surface-insulating layer of chromium oxide (Cr_2O_3).

Seema et al. [7] has made comprehensive review on recent material development of passive direct methanol fuel cell and emphasis on the performance activity, cost, durability and stability aspects. Each component with their material development along with basic desirable characteristics is reported in this paper. This paper has also reviewed all possible materials of passive DMFC component, which might make the passive DMFC compact and feasible energy source in future.

Mallick et al. [8] in their study on critical review of current collectors for passive direct methanol fuel cells has emphasis on the important aspects such as profile of the current collectors including materials of construction of the current collectors. A number of current collectors of passive DMFC have been selected and reviewed thoroughly. However, very less research works have been found concerning to decrease in the weight of the current collectors as the current collector majorly contributes on the total weight of pDMFC and affects the gravimetric energy density of the fuel cell.

3 Objective

After going through the literature study, it is inferred that the materials of the current collectors influence the performance of the pDMFC. Required properties of the current collector materials are high electrical conductivity at operating zone, thermal conductivity to optimise and to maintain the thermal stability of cell during operation and high corrosion resistance having compatibility in dilute methanol environment. After considering the desirable properties of the bipolar plates, this experimental study has been taken up to identify the better current collector materials combination among Nickel-201, brass and SS-316L current collectors in anode–cathode ends.

4 Problem Description

Current collectors of passive direct methanol fuel cell play as a key component, and the performance of the fuel cell depends on its material of construction, dimensions and novel design with shape factors. The weight of the current collectors contributes almost 3/4 of the total weight of the cell [9]. Hence, the gravitational power density is significantly affected by the selection of current collector materials and its design aspects.

The required characteristics of materials [10] of the current collectors in pDMFC are as follows:

1. Good electrical conductivity or very low electrical resistivity at operating zone of the direct liquid feed methanol cell [11].
2. High thermal conductivity to optimise and to maintain the thermal stability of cell during operation [12].
3. Desirable mechanical properties like high tensile strength and flexural rigidity of materials [13].
4. Better fabrication and machinability processes of materials [14].
5. Corrosion resistance in methanol environment at various concentrations and wide range of operating temperatures [15].
6. Longer durability and life [16].
7. Low density of materials [17].
8. Easily available at cheaper cost [18].
9. Less contact resistance with the diffusion layers [19].
10. Even distributing and transport area of reactants [20].

The functions of the anode and cathode side current collectors are relatively different; however, they have some of the common aspects like uniform spreading of chemical reactants, maintaining cell structure support, disposal of reaction by products and providing the electrical connectivity with adjacent cells in case of stacking of cells. At the anode, current collector allows the passage of transporting methanol solution and carbon dioxide. Further it collects the electric current from MEA, whereas the cathodic end current collector provides transportation of water, collects the current from cathodic end diffusion layer and receives the oxidant from ambient air.

Details of the materials compositions are given in Table 1 [21], and properties of the materials are provided in Table 2.

5 Experimental Set-Up

To evaluate performance of passive DMFC with the combination of Nickel-201, brass and SS-316L current collectors, a single direct methanol fuel cell fixture is selected. For carrying out this experimental testing, different anode and cathode current collector materials, fabricated with 2.00 (± 0.02) mm thickness sheets, are used. The circular openings of 100 numbers, in 10 by 10 matrix pattern, are made using 3.8-mm diameter drill. Fabrication drawing detail of the current collector is shown in Fig. 2.

Nafion-117 solid electrolyte is used as permeable membrane in membrane electrode assembly. The anode catalyst layer (ACL) is made up of Pt-Ru (1:1)/C with a catalyst loading of 4 mgcm⁻², and on cathode catalyst layer (CCL), it is made up of Pt/C with a catalyst loading of 2 mg cm⁻². To prevent methanol solution and oxidant leakages, PTFE sealing gaskets are provided in between current collectors

Table 1 Material composition

Composition, Element	Material (% by weight)		
	Stainless steel-316L	Nickel-201	Brass
Carbon, C	0.03 max	0.02 max	–
Manganese, Mn	2.0 max	0.35 max	–
Silicon, Si	0.75 max	0.35 max	–
Phosphorus, P	0.045 max	–	–
Sulphur, S	0.03 max	0.01 max	–
Chromium, Cr	16–18	–	–
Nickel, Ni	10–14	99.00 min	~ 0.05
Copper, Cu	–	0.25 max	65–70
Zinc, Zn	–	–	35–30
Nitrogen, N	0.1 max	–	–
Iron, Fe	Balance	0.40 max	~ 0.4

Table 2 Properties of materials

Material of construction	Maximum corrosion rate in pure methanol, (mm/year)	Density of material, (kg/m^3)	Electrical resistivity of material at 20°C, ($\text{X}10^{-7} \Omega\text{m}$)
SS-316L	0.5	7900	7.4
Ni-201	0.05	8890	0.68
Brass	1.25	8500	0.62

and MEA components of the cell. The fabricated active area of the cell is 5.0 cm × 5.0 cm. Methanol solution with 5 M concentration has been prepared to use in this experiment. The required clamping of the cell assembly is made using M8 fasteners, and uniform tightening of the bolts is ensured using a torque wrench which is pre-set at 5Nm value. The experimental set-up of the DMFC is shown in Fig. 3.

6 Experimental Methodology

To evaluate performance of passive DMFC with the combination of Nickel-201, brass and SS-316L current collectors, four set-ups of anode and cathode combinations as referred in Table 3 with single direct methanol fuel cell fixture are chosen. As brass is getting reacted with dilute methanol with the formation of metal methoxides, the use of brass as current collector material in anode side is not considered. As Ni and SS material are performed better at 5 M, experiments have been carried out at this concentration of methanol solution.

Fig. 2 Fabrication drawing detail of current collector

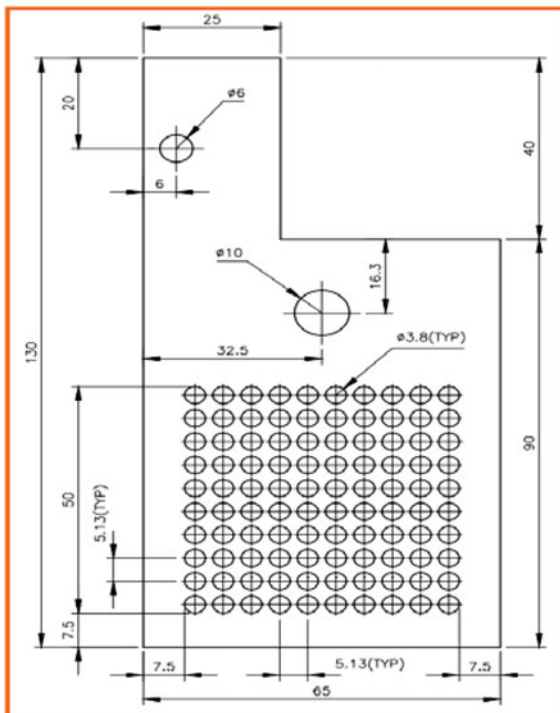


Fig. 3 Experimental set-up of passive DMFC



Table 3 Experimental set-up

Set-up	Anode	Cathode
I	Nickel-201	Stainless steel, Gr 316L
II	Nickel-201	Brass (70/30)
III	Stainless steel, Gr 316L	Nickel-201
IV	Stainless steel, Gr 316L	Brass (70/30)

While performing the experiment, the first set of voltage and current readings has been taken by varying current characteristic conditions using Nickel-201/SS-316L (set-up-I) materials as current collectors at 5 M methanol concentration. This experiment further repeated with the other mentioned set-up-II, Nickel-brass; set-III Stainless Steel-Nickel and with set-up-IV Stainless Steel-brass current collectors, and corresponding voltage and current characteristics have been noted. Total experiment has been repeated thrice at this 5 M concentration methanol solution to get repeatability and consistency in the readings. Mean value of the three readings of observations corresponding to current–voltage is taken for analysis of the cell characteristics.

7 Experimental Results and Analysis

7.1 Polarisation and Power Density Characteristics

In the experimental set-up-I, Nickel-201 material as anode and SS316L as cathode current collector have been used. Cell is tested with 5 M methanol solution concentration at ambient conditions. In this experiment, the highest power density recorded is 6.720 mW cm^{-2} at current density of 32.0 mA cm^{-2} . During testing, the maximum current density that recorded is 62.4 mA cm^{-2} at 5 M methanol concentration.

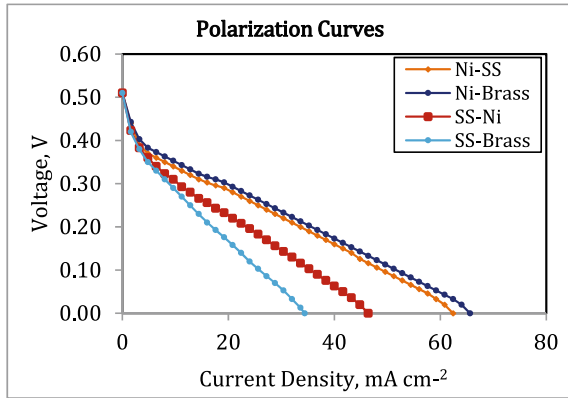
In the experimental set-up-II, Nickel-201 material as anode and brass as cathode current collector have been used. Cell is tested with 5 M methanol solution concentration at ambient conditions. In this experiment, the maximum power density recorded is 7.157 mW cm^{-2} at a current density of 33.6 mA cm^{-2} . During testing, the maximum current density recorded is 65.6 mA cm^{-2} at 5 M methanol concentration.

In the experimental set-up-III, SS316L material as anode and Nickel-201 as cathode current collector have been used. Cell is tested with 5 M methanol solution concentration under ambient conditions. In this experiment, the peak power density recorded is 4.704 mW cm^{-2} at a current density of 24.0 mA cm^{-2} . During testing at the same 5 M methanol concentration, the largest current density recorded is 46.4 mA cm^{-2} .

In the experimental set-up-IV, SS316L material as anode and brass as cathode current collector have been used. Cell is tested with 5 M methanol solution concentration in ambient conditions. In this experiment, the highest power density recorded is 3.397 mW cm^{-2} at a current density of 17.6 mA cm^{-2} . During testing, the maximum current density recorded is 34.4 mA cm^{-2} at 5 M methanol concentration.

Polarisation curves (voltage–current density characteristics) of the four set-ups of pDMFC configuration are plotted as shown in Fig. 4. Initially when current density is zero, the cell generated voltage is maximum (open circuit voltage), and as the current density increases, the cell voltage decreases to zero. From Fig. 4, Nickel-brass combination as anode and cathode is performing better with the highest current density as revealed in polarisation characteristics.

Fig. 4 Voltage–current density characteristics



Power density curves (power density versus current density characteristics) of these four set-ups of pDMFC configuration are plotted as shown in Fig. 5. Power density of the cell increases from zero to a maximum value, and further, it decreases to zero with increase in the current density. Nickel-brass combination as anode and cathode is performing better with maximum power density as revealed from the drawn characteristics.

The combined voltage and power density superimposed characteristics against the current density are plotted as shown in Fig. 6.

Fig. 5 Power density characteristics

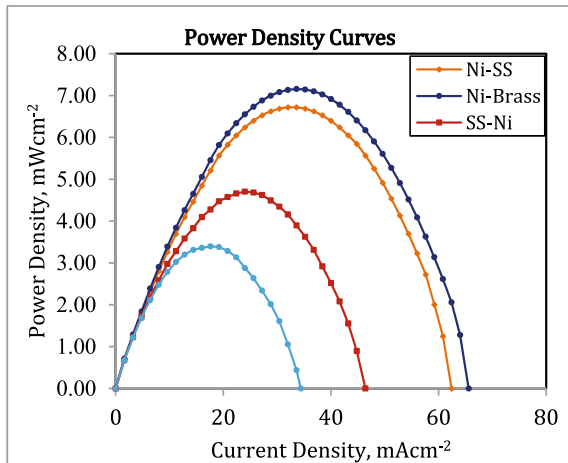
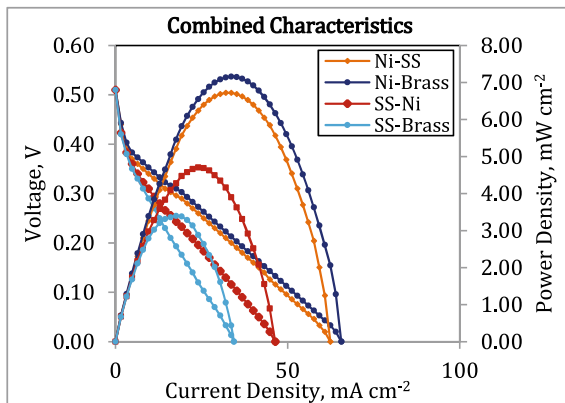


Fig. 6 Voltage and power density superimposed curves



7.2 Comparison of Maximum Power Density and Maximum Current Density

Results of the four set-ups with current collectors against current density and power density are taken for analysis. Bar charts of current collectors' combinations as anode–cathode materials versus maximum power density produced (refer to Fig. 7) and current density (ref to Fig. 8) are drawn. Anode–cathode combination of Nickel-brass showed better current density and power density among these four set-ups, and SS-brass combination showed the least performance. Better performance of Nickel is due to higher conductivity and higher resistance to methanol solution, whereas brass has superior conductivity but lack of compatibility with methanol solution. For short-term applications, Ni-brass combination is satisfactory, but for long-term applications, Ni-SS is better, as Nickel and SS materials have better compatibility in methanol environment compared to brass.

8 Conclusions

In the commercialisation process of the passive direct methanol fuel cell (pDMFC), market demands for efficient systems with optimisation of components performance with respect to durability and effectiveness. The desirable qualities of the current collector materials are excellent electrical conductivity and high thermal conductivity to optimise and to maintain the thermal stability of cell during operation and high corrosion resistance with compatibility in dilute methanol environment. These aspects are experimentally investigated with the combination of anode and cathode current collectors, fabricated with an opening ratio of 45.3% with combination set-ups, set-up-I, Nickel-Stainless steel; set-up-II, Nickel-brass; set-up-III

Fig. 7 Maximum power density versus anode–cathode materials

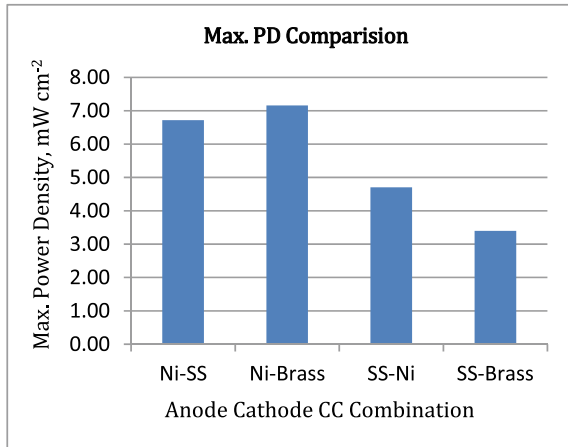
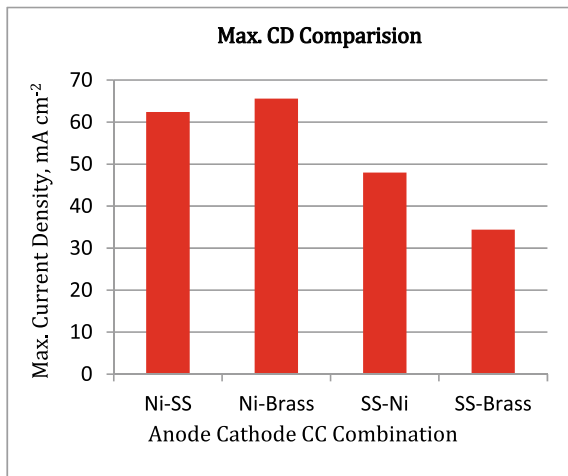


Fig. 8 Maximum current density versus anode–cathode materials



Stainless Steel-Nickel and with set-up-IV Stainless Steel-brass materials. The anode–cathode combination of set-up-II, Nickel-brass showed the best current density (46.4 mA cm⁻²) and power density (7.157 mW cm⁻²), and set-up-IV, SS-brass combination showed the least performance with current density (34.4 mA cm⁻²) and power density (3.397 mW cm⁻²). Superior performance of Nickel is due to good electrical conductivity and better corrosion resistance to dilute methanol solution, whereas brass has the best electrical conductivity among the selected materials but suffers lack of compatibility with methanol solution. For short-term durations, Ni-brass combination performance is found satisfactory, but for long-term applications Ni/SS-316L is better as these materials have excellent compatibility and corrosion resistance in methanol environment compared to brass. In future investigations, materials that are

suitable in dilute methanol environment either bare or with electrical conducting coatings may be used with combination of current collectors.

References

- O'Hayre R, Cha S-W, Colella W, Prinz FB (2016) Fuel cell fundamentals, 3rd edn. John Wiley & Sons Inc., New Jersey
- Raghavaiah NV, Naga Srinivasulu G, HariPrasad I (2020) Review of challenges in direct methanol fuel cell and contemporary status. *Res Appl Thermal Eng* 3(2):1–8. <https://doi.org/10.5281/zenodo.3989515>
- Kamarudin SK, Achmad F, Daud WRW (2009) Overview on the application of direct methanol fuel cell (DMFC) for portable electronic devices. Published by Elsevier Ltd., International Association for Hydrogen Energy. <https://doi.org/10.1016/j.ijhydene.2009.06.013>
- Boni M, Srinivasa Rao S, Naga Srinivasulu G (2020) Performance evaluation of an air breathing–direct methanol fuel cell with different cathode current collectors with liquid electrolyte layer. *Asia-Pac J Chem Eng* 2020:2465. <https://doi.org/10.1002/apj.2465>
- Braz BA, Oliveira VB, Pinto AMFR (2020) Optimization of a passive direct methanol fuel cell with different current collector materials. *Energy* 208:118394
- Wilberforce T, Ijaodola O, Ogungbemi E, El Hassan Z, Thompson J (2018) Effect of bipolar plate materials on performance of fuel cells. Module in Mater Sci Mater Eng. <https://doi.org/10.1016/B978-0-12-803581-8.11272-X>
- Munjewar SS, Thombre SB, Mallick RK (2017) A comprehensive review on recent material development of passive direct methanol fuel cell, *Ionics* vol 23, pp 1–18
- Mallick RK, Thombre SB, Shrivastava NK (2015) A critical review of the current collector for passive direct methanol fuel cells. *J Power Sources* 285:510–529
- Yuan W, Tang Y, Yang X, Liu B, Wan Z (2012) Structural diversity and orientation dependence of a liquid-fed passive air-breathing direct methanol fuel cell. *Int J Hydrogen Energ* 37:9298–9313
- Raghavaiah NV (2019) Overview of pressure vessel design using ASME boiler and pressure vessel code section viii division-1 and division- 2. *Int J Res Eng Sci Manage* 2(6):525–526
- YangaW M, ChoubC SK (2007) Shua 2007, Effect of current-collector structure on performance of passive micro direct methanol fuel cell. *J Power Sources* 164(2):549–554. <https://doi.org/10.1016/j.jpowsour.2006.11.014>
- Dohle H, Mergel J, Stolten D (2002) [2002], Heat and power management of a direct-methanol-fuel-cell (DMFC) system. *J Power Sources* 111(2):268–282
- Huang J, Baird DG, McGrath JE (2005) Development of fuel cell bipolar plates from graphite filled wet-lay thermoplastic composite materials. *J Power Sources* 150:110–119. <https://doi.org/10.1016/j.jpowsour.2005.02.074>
- Abraham BG, Chetty R (2021) Design and fabrication of a quick-fit architecture air breathing direct methanol fuel cell. *Int J Hydrogen Energ* 46(9), pp 6845–6856
- Song SQ, Liang ZX, Zhou WJ, Sun GQ, Xin Q, Stergiopoulos V, Tsiakaras P (2005) Direct methanol fuel cells: The effect of electrode fabrication procedure on MEAs structural properties and cell performance. *J Power Sources* 145(2):495–501. <https://doi.org/10.1016/j.jpowsour.2005.02.069>
- Cha H-C, Chen C-Y, Shiu J-Y (2009) Investigation on the durability of direct methanol fuel cells. *J Power Sources* 192(2):451–456. <https://doi.org/10.1016/j.jpowsour.2009.03.028>
- Kuan Y-D, Lee S-M, Sung M-F (2014) Development of a direct methanol fuel cell with lightweight disc type current collectors. *Energies* 7:3136–3147. <https://doi.org/10.3390/en7053136>
- Sgroi M, Zedde F, Barbera O, Stassi A, Sebastián D, Lufrano F, Schuster M (2016) Cost analysis of direct methanol fuel cell stacks for mass production. *Energies* 9(12):1008. <https://doi.org/10.3390/en9121008>

19. Braz BA, Oliveira VB, Pinto AM (2020) Experimental evaluation of the effect of the anode diffusion layer properties on the performance of a passive direct methanol fuel cell. *Energies*13:5198. <https://doi.org/10.3390/en13195198>
20. Shrivastava NK, Harris TA (2017) Direct methanol fuel cells. *encyclopedia of sustainable technologies*, pp 343–357. <https://doi.org/10.1016/b978-0-12-409548-9.10121-6>
21. Properties of Some Metals and Alloys (2021) Nickel Institute, [https://nickelinstitute.org/media/1771/propertiesofsomemetals and alloys_297_pdf](https://nickelinstitute.org/media/1771/propertiesofsomemetals%20and%20alloys_297.pdf).

Performance Comparison of Different Geometries of Thermal Energy Storage Unit for Solar Cooker



B. C. Anilkumar, Ranjith Maniyeri, and S. Anish

Abstract Many researchers have been interested in solar energy as an unlimited energy resource over the last few decades due to its vast range of applications, including household cooking. The present work aims to design, optimize, fabricate, and test different geometries of thermal energy storage (TES) units for solar cooker (SC) using paraffin wax as the phase change material (PCM). The optimum amount of PCM necessary for different geometries (cylindrical, square, and hexagonal) of TES units surrounding the cooking vessel is computed using a computational approach. The TES units developed in this study have the provisions for filling the PCM on all sides, including the lid, enhancing the heat transfer to the cooking load. The performance comparison of different TES units is carried by conducting the indoor test. The experimental findings show that after 6 h, all geometries of TES units maintain the temperature of the cooking load at the melting point of PCM. However, cylindrical-shaped TES unit performs best in comparison with hexagonal and square. A cylindrical box solar cooker performance test is also carried out with an optimized cooking vessel surrounded by the PCM-filled TES unit and lid.

Keywords Cylindrical box solar cooker · Thermal energy storage unit · Phase change material · Cooking pot

Nomenclature

T_{mp} Melting temperature of PCM
 M_{pcm} Mass of PCM
 U Overall heat transfer coefficient

B. C. Anilkumar · R. Maniyeri (✉) · S. Anish
Department of Mechanical Engineering, National Institute of Technology Karnataka (NITK),
Surathkal, Mangalore, Karnataka 575025, India
e-mail: mrانji1@nitk.edu.in

S. Anish
e-mail: anish@nitk.edu.in

Greek Symbol

λ Latent heat of fusion of PCM

1 Introduction

Renewable energy systems, particularly solar cookers (SCs), are viable for meeting global cooking needs. SC converts the insolation into useful thermal energy for cooking. Solar energy has become more prominent in the present worldwide debate on energy and the environment. Today, growing awareness for the benefits of renewable energy and increasing prices of fossil fuels drive the SC market. Many modifications were made to SCs over the last four to five decades across the world [4, 5]. In a recent study, we examined the effects of various box shapes on solar cooker performance by using numerical analysis, including rectangular, trapezoidal, cylindrical, and frustums of cones [3].

The evening or night cooking is possible with the provision of the heat storage facility in SCs. Thermal energy can be stored in the SC as sensible or latent heat. Generally used sensible heat storage materials (SHSMs) in SCs are sand [13], engine oil [10], and carbon [15]. In our recent study [1], we experimentally investigated the effects of the optimum mixture of SHSMs such as sand, iron grits, brick powder, and charcoal on the performance of solar box cooker (SBC). In the latent heat storage (LHS) units, energy stored during a phase change is used for cooking. Generally, phase change materials (PCMs) are used to store heat energy in the latent form. The cooking pot incorporated with the LHS system contains two concentric cylindrical vessels made of aluminium or steel with an annular cavity filled with PCM (Fig. 1). The PCMs contained in the cooking vessel are heated and solidified by the SBC or concentrated/indirect SCs. Recently, several review papers [12, 17] are reported on the developments of SCs incorporated with PCMs. Nkhonjera et al. [11] reviewed the heat storage units, materials, and performance of SCs included with thermal energy storage (TES) units. They recommended that the shape and heat transfer properties of TES units need be optimized.

In general, the TES units surrounding the cooking vessel were filled with PCM along the lateral side [6–9, 16, 18]. In the present work, we aim to introduce a new design of the TES unit that includes the facility for filling the PCM at the bottom part of the cooking pot and on the lid. This will enhance the cooking performance as heat is transferred to the load through all sides of the pot. Therefore, the primary objective of this research is to design and develop the TES units of different geometries incorporated with the cooking pot. The present study also compares the cylindrical, square, and hexagonal geometry of TES units by conducting the indoor test. Another goal of this research is to conduct outdoor tests to evaluate the performance of the improved TES unit with the cylindrical box solar cooker (CBSC). The optimum

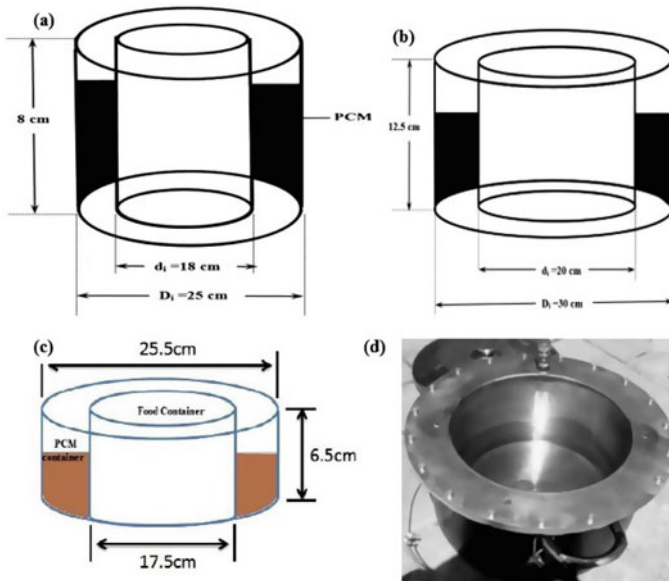


Fig. 1 Schematic of TES units for solar cooker **a** Buddhi et al. [7] **b** Sharma et al. [16] **c** Vigneswaran et al. [18] **d** Photo of TES unit [8]

mass of PCM and dimensions for the different geometries of TES units are found following our recently developed computational procedure [2].

2 Methodology

Latent Heat Storage Medium: Paraffin wax can reach a wide range of temperatures, thus making it a useful heat storage material in several applications. Paraffin wax is considered as good heat storage material because of its fast-charging properties and high latent heat of fusion. Furthermore, they are non-corrosive, compatible with many materials, chemically stable, non-toxic, and do not segregate. In general, the paraffin wax used as PCM is of technical grade. This grade of paraffin wax is also cost effective, feasible, and widely used. However, they also present some disadvantages, such as low thermal conductivity, more significant volume changes between the solid and liquid phases, and the possibility of flammability.

The solid–liquid phase transition temperature should be around 100 °C or higher for practical cooking. Paraffin wax is available in different fusion temperatures. The melting temperature and latent heat of fusion of paraffin wax tested in SCs by Saxena et al. [14], Yuksel et al. [19], and Lecuona et al. [8] are, respectively, 41–44 °C, 58–60 °C, 100 °C and 250 kJ/kg, 189 kJ/kg, and 140 kJ/kg. Paraffin wax shows a decrease

Table 1 Thermo-physical parameters of commercial-grade paraffin wax

Properties		
Melting temperature (°C)		55–60
Latent heat of fusion (kJ/kg)		220
Density (kg/m ³)	Solid	818
	Liquid	760
Specific heat (kJ/kg °C)	Solid	2.95
	Liquid	2.51
Thermal conductivity (W/m°C)		Liquid 0.22

in latent heat of fusion with increasing melting temperature. In the present work, we used paraffin wax with fusion temperature of 55–60 °C and latent heat of 220 kJ/kg.

Design of TES Unit: The TES units of cylindrical, hexagonal, and square geometries are designed using the previously developed computational procedure [Anilkumar et al. 2021]. The dimension of the TES container depends on the properties of the heat storage material to be used, and the time for the evening or night cooking is required. The thermo-physical parameters of commercial-grade paraffin wax, which is employed as the PCM for heat storage in all geometries, are given in Table 1. For maintaining the temperature of the cooking vessel at PCM's melting point for a specific duration of time, latent heat rejected by the PCM and energy loss from the container should be equal. This is expressed by the equation [13]

$$M_{pcm}\lambda = U(T_{mp} - T_a)t \quad (1)$$

The procedure to be followed in the design of TES unit is as follows: [3]

Step 1: Initially guess the temperatures of PCM, the inner and outer surface of the TES unit, and ambient air.

Step 2: Compute air and PCM's thermal properties (Pr , k , and ν) at the corresponding mean temperature.

Step 3: Calculate the Nusselt number and convective heat transfer coefficient at the inner and outer surface of the TES unit using analytical correlations.

Step 4: Guess the dimension of the TES unit of each geometry.

Step 5: Compute U-value for each geometry of the heat storage container.

Step 6: Compute the mass of PCM required using Eq. (1).

Step 7: Update the dimension of the TES unit.

Step 8: Compare the updated and previous dimension value and repeat the step 5 to 7 until it converges.

Step 9: Update the temperature at the inner and outer surfaces of the TES unit.

Step 10: Compare the updated and previous temperature values and repeat the step 2 to 9 until it converges.

The mass of paraffin wax required and dimensions of heat storage containers of different geometries surrounding the cooking vessel of diameter 16 cm and height

Table 2 Dimensions of different geometries of TES units and required mass of PCM

Geometry	Dimension of TES container (cm)	Mass of PCM (kg)		
		Lateral side	Bottom side + Lid	Total
Cylindrical	18.7	1.01	0.416	1.426
Hexagonal	10.7	1.32	0.452	1.772
Square	17.5	1.44	0.464	1.904

18 cm are given in Table 2. The optimum mass of PCM required for 6 h is found to be maximum for square followed by hexagonal and minimum for the cylindrical geometry. Therefore, a cylindrical-shaped TES unit is considered the optimum geometry as it uses the minimum mass of PCM for maintaining a constant temperature for a specific duration of time.

Fabrication of TES Unit: The TES units of cylindrical, hexagonal, and square geometries (Fig. 2) are fabricated using a stainless steel sheet of 1 mm thickness. The sheet is cut into the required shapes and dimensions by using the automatic CNC machine. Bending and rolling works are carried out using hydraulic press brake bending and rolling machines, respectively. Then the parts are joined by spot/resistance welding at different locations to form the required geometry. Afterwards, the joints are entirely welded by the tungsten inert gas (TIG) welding process. Finally, the grinding process is carried out for the smooth and consistent appearance of the welded parts. Two holes are drilled on the vertical surface of the container facing in the opposite direction for inserting PCM into the cavity. The PCM can be filled in the annular cavity between the inner pot and outer TES container on the lateral side and at the bottom. The lid for all the geometries of TES units is fabricated with provisions for filling the PCM. For this, two holes are provided at the top of the lid in opposite directions.

The designed quantity of PCM should be filled into the TES unit to expand and solidify completely in each cycle. The TES unit is first kept vertically and partially placed in hot water during PCM filling. PCM is filled through one of the provisions at the top. At the same time, the other provision on the opposite side was kept open for the escape of air during filling. After filling at the hole level, one of them is closed, and the container is kept in a horizontal position. Then the PCM is filled, and another provision is also closed. The lid is also filled with PCM by following the same procedure. During the complete filling procedure, PCM is maintained in the liquid state by keeping the TES unit in a hot water bath.

Performance Test: The performance comparison of different geometries of TES units is carried by conducting indoor and outdoor experiments. The indoor test is performed to validate the computational approach used to design the TES containers of all geometries, whereas the outdoor experiment is performed by testing the optimized TES container charged with CBSC.

Indoor test. The experimental set-up for the indoor test is shown in Fig. 3. The temperature of cooking pot surfaces and water is measured by using the K-type

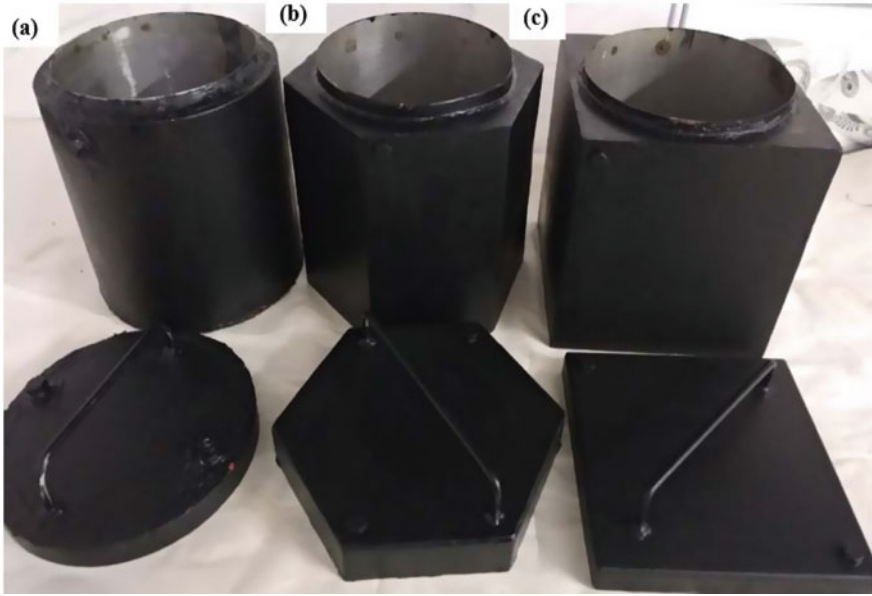
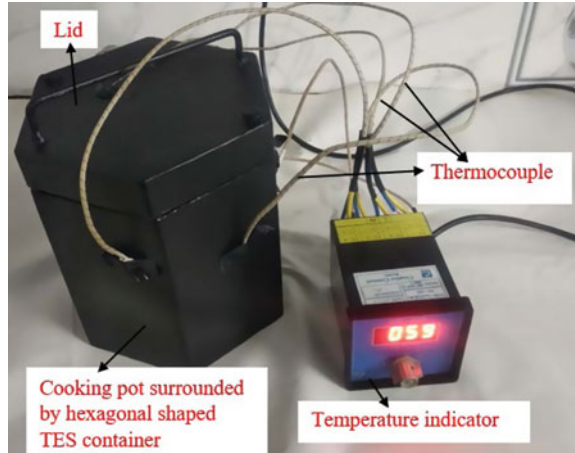


Fig. 2 Cooking pot with TES unit and lid of different geometry **a** cylindrical, **b** hexagonal, and **c** square

thermocouple and an indicator. The container is tested with water for the performance study. Initially, water is heated up to 100 °C and is poured into the vessel fully. Again, water in the vessel is replaced with newly boiled water. Before changing the water, the temperature of the previous water in the container is measured. Also, the temperatures of all the surfaces of the vessel are measured. This process is continued until all the surface temperature reaches the melting temperature of PCM and remains constant after that. This ensures that all PCMs in the container are melted. After PCM gets melted fully, water in the vessel is made empty, and again water at a temperature above the melting point of PCM is filled in the vessel and the lid is closed. The temperature at each surface of the vessel is measured in equal intervals of time. After six hours, the water temperature in the pot is measured and compared with the expected value.

Outdoor test. The performance test of the TES unit with optimum geometry is conducted by charging with CSBC (Fig. 4). The CSBC used in the present work consists of a mild steel cylindrical box with external and internal diameters 53 cm and 43 cm, respectively, and height 30 cm. A double glazed cover is provided at the top of the cooker to form the greenhouse effect, allowing solar radiation to pass into the cavity but preventing it from escaping. Since the glazing is opaque to longer wavelength radiation such as infrared waves emitted by the absorber plate, heat radiation will be trapped inside the cooker. The annular gap between the outer and inner cylinders is insulated with 5-cm-thick glass wool to reduce heat loss to the environment. The circular absorber plate made up of aluminium having a diameter

Fig. 3 Experimental set-up (indoor test)



of 43 cm and thickness of 2 mm painted with black is fixed at the base of the inner cavity of the cooker. The glass wool insulation of 5 cm thickness is also provided below the absorber plate to reduce the heat loss through the bottom surface. A small door is provided on the lateral surface of the cooker. A K-type thermocouple and an indicator are used to measure the required temperatures.

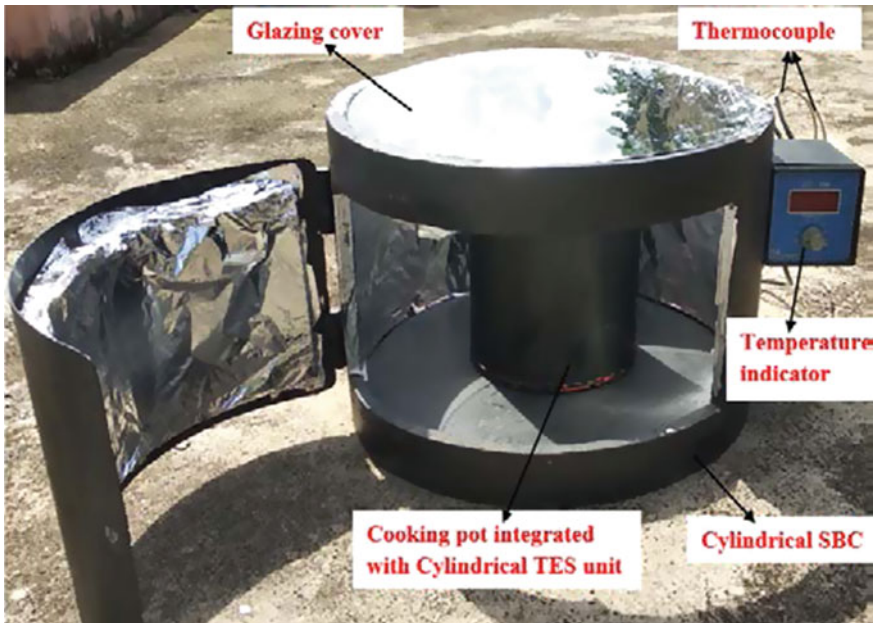


Fig. 4 Experimental set-up (outdoor test)

3 Results and Discussion

Initial Set-up: The cooking pot is filled with water that is hotter than the melting point of paraffin wax. To ensure the complete melting of paraffin wax, the poured water is replaced two to three times with fresh hot water. The temperature of the replacement (prior) water and the time is recorded. The temperature of the replaced and pouring water is the same during the first set. Initially, the cooking pot is filled with water at 91 °C. After 15 min, the water temperature has dropped to 68 °C. The water temperature drops to 66 °C on the third replacement. This means that the paraffin wax absorbs heat from the hot water. The water temperature increases to 76 °C during the fourth replacement, indicating that the paraffin wax melts fully and heat absorption diminishes. Figure 5 depicts the temperature variation of replaced water during the initial heating of the cooking pot integrated with cylindrical, square, and hexagonal TES units.

Indoor Test: Water at a temperature more than the melting point of paraffin wax is filled in the cooking pot and is covered with the lid. Every 30 min, the surface temperature is recorded. The temperature of the water is also monitored after 6, 7, and 8 h. The surface temperature of the cylindrical TES unit is increased from 43 °C to 62 °C after 45 min. At the same time, the lid temperature rises from 38 °C to the maximum of 56 °C after 1 h and 15 min. Figures 6–8 illustrate the variation in surface and lid temperatures of cylindrical, square, and hexagonal TES units. For the square-shaped TES unit, temperatures are measured at the four side faces denoted as surface 1, 2, 3, and 4, as depicted in Fig. 7. Similarly, for the hexagonal geometry, all the six side faces are considered for the temperature measurement denoted by surface 1, 2, 3, 4, 5, and 6, as shown in Fig. 8. The side faces for square and hexagonal geometry of TES units exhibit nearly equal temperatures at every time. The temperature of the surface and lid falls in small units after 1 h and 45 min

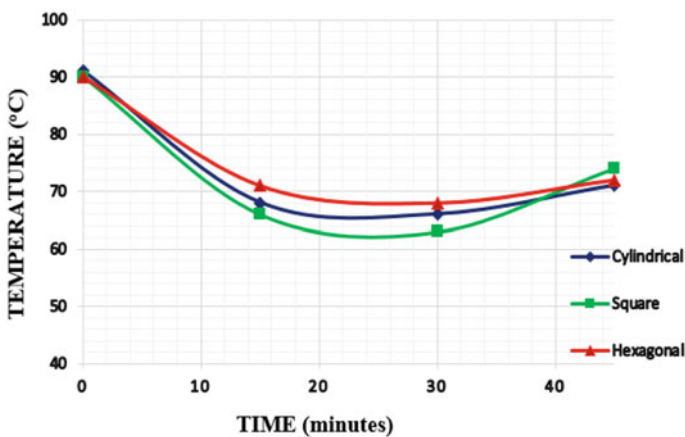


Fig. 5 Variation of temperature of replaced water during initial set-up

from the start of the test. This shows that paraffin wax maintains nearly constant temperature during the phase change. Figure 9 shows the water temperature variation for cylindrical, square, and hexagonal TES units. All of the TES units maintain the water temperature at 59 °C after 6 h of testing. However, compared to cylindrical and hexagonal TES units, square geometry exhibits a slight decrease in water temperature. For cylindrical, hexagonal, and square TES units, the water temperature on the second day (after 24 h) is 46 °C, 44 °C, and 41 °C, respectively. This shows that the heat loss across the cylindrical geometry is lower than other forms due to the small surface area-to-volume ratio.

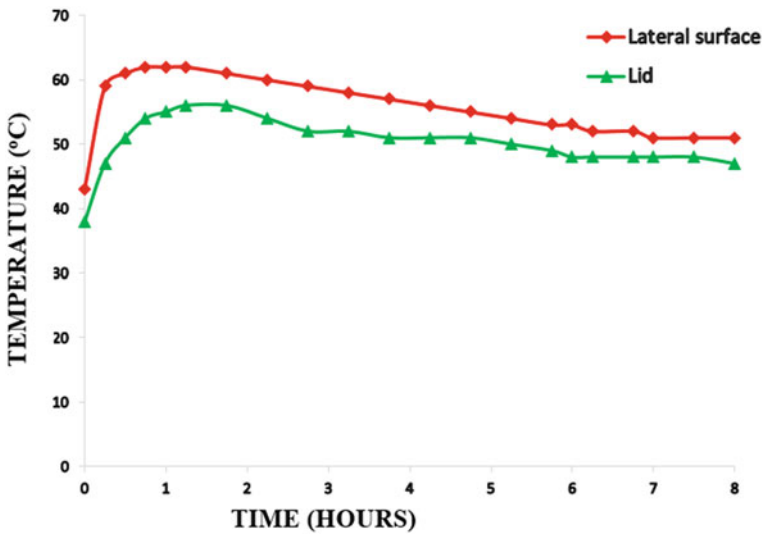


Fig. 6 Variation of surface temperatures of cylindrical TES unit with time

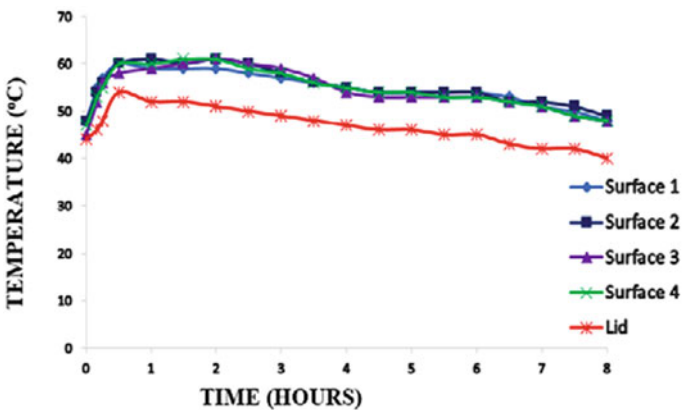


Fig. 7 Variation of surface temperatures of square TES unit with time

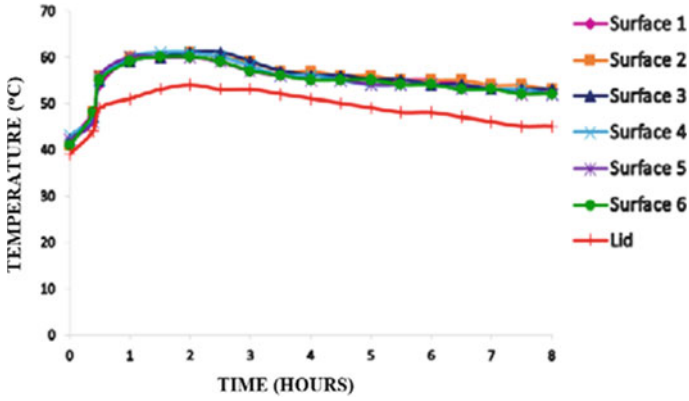


Fig. 8 Variation of surface temperatures of hexagonal TES unit with time

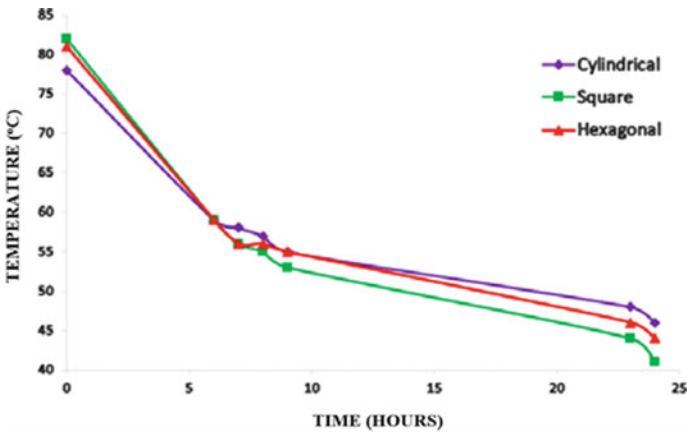


Fig. 9 Variation of water temperatures in different geometries of TES units with time

Outdoor Test: The outdoor test is conducted with the cylindrical-shaped TES unit charged with CBSC. The cooking pot having 1 kg of water is placed on the top of the absorber plate, and the whole assembly is open to direct sunlight. Figure 10 shows the variation of solar irradiance and temperatures of the absorber plate, cooking pot, water, and ambient air measured during the experiment conducted on 10 June 2021. The experiments began at 10 AM (IST) and took measurements at 15-min intervals. The ambient, water, TES surface, and absorber plate temperatures reached 32 °C, 86 °C, 91 °C, and 104 °C, respectively, at 1:15 PM, and the corresponding solar irradiance is observed to be 830 W/m². Later, the temperatures of the water, absorber plate, and cooking pot are decreasing. At 3 PM (IST), the cooking pot integrated TES unit is taken from the CBSC and placed in the thermal insulation box. Then, the water and TES container surface temperatures are, respectively, 62 and 65 °C.

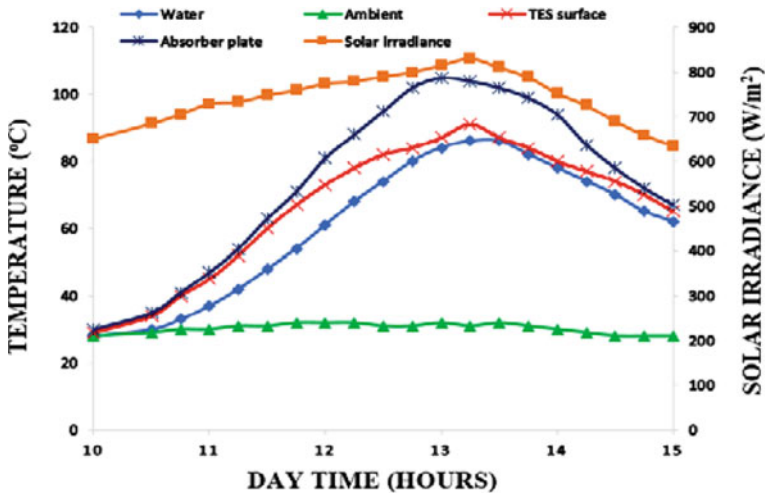


Fig. 10 Variation of water temperature and solar irradiance with time (10 June 2021)

Experimentation revealed that the cooking pot’s water keeps the temperature in the 55–60 °C range until 9 PM (IST).

4 Conclusions

Thermal energy storage (TES) units of various shapes (cylindrical, hexagonal, and square) incorporated with the cooking vessel used in solar cookers are designed, fabricated, and tested for the comparative performance study. In this work, we developed the TES unit to fill the heat storage material at the lateral and bottom sides and on the lid. Commercial-grade paraffin wax is used as the latent heat storage material. The results of the indoor test show that after 6 h, all geometries of TES units keep the water temperature at the same level as the melting point of paraffin wax (55–60 °C). However, cylindrical TES units perform best, followed by hexagonal, while square TES units perform least. The surface area-to-volume ratio is the lowest for cylindrical geometry and the highest for a square shape. The performance test on the cylindrical box solar cooker (CBSC) with the optimized cooking vessel incorporated with the TES unit is also conducted. The CBSC is used to charge the heat storage material during the daytime up to 3 PM (IST), and the TES unit discharges the thermal energy required for the night cooking. Research should focus on implementing solar cookers with efficient TES units by utilizing PCMs with high-energy density, high latent heat of fusion, and low-cost and low volume changes in future.

References

1. Anilkumar BC, Maniyeri R, Anish S (2020) Design, fabrication and performance assessment of a solar cooker with optimum composition of heat storage materials. *Environ Sci Pollut Res*. <https://doi.org/10.1007/s11356-020-11024-3>
2. Anilkumar, BC, Maniyeri R, Anish S (2021) Optimum selection of phase change material for solar box cooker integrated with thermal energy storage unit using multi-criteria decision-making. *J Energy Storage* 40(102807). <https://doi.org/10.1016/j.est.2021.102807>.
3. Anilkumar BC, Maniyeri R, Anish S (2021) Numerical investigation on the effect of various geometries in a solar box-type cooker: a comparative study, fluid mechanics and fluid power, LNME, Springer, https://doi.org/10.1007/978-981-16-0698-4_9
4. Aramesh M, Ghalebani M, Kasaeian A, Zamani H, Lorenzini G, Mahian O, Wongwises S (2019) A review of recent advances in solar cooking technology. *Renew Energy* 140:419–435
5. Arunachala UC, Kundapur A (2020) Cost-effective solar cookers: A global review. *Sol Energy* 207:903–916
6. Bhave AG, Kale CK (2020) Development of a thermal storage type solar cooker for high temperature cooking using solar salt. *Sol Energ Mater Sol Cells* 208:110394
7. Buddhi D, Sharma SD, Sharma A (2003) Thermal performance evaluation of a latent heat storage unit for late evening cooking in a solar cooker having three reflectors. *Energy Convers Manag* 44(6):809–817
8. Lecuona A, Nogueira J, Ventas R, Rodríguez-Hidalgo M, Legrand M (2013) Solar cooker of the portable parabolic type incorporating heat storage based on PCM. *Appl Energy* 111:1136–1146
9. Mawire A, Lentswe K, Owusu P, Shobo A, Darkwa J, Calautit J, Worall M (2020) Performance comparison of two solar cooking storage pots combined with wonderbag slow cookers for off-sunshine cooking. *Sol Energy* 208:1166–1180
10. Nahar NM (2003) Performance and testing of a hot box storage solar cooker. *Energy Convers Manag* 44:1323–1331
11. Nkhonjera L, Bello-Ochende T, John G, King'ondeu CK (2017) A review of thermal energy storage designs, heat storage materials and cooking performance of solar cookers with heat storage. *Renew Sustain Energy Rev* vol 75, pp 157–167
12. Omara AAM, Abuelnuor AAA, Mohammed HA, Habibi D, Younis O (2020) Improving solar cooker performance using phase change materials: a comprehensive review. *Sol Energy* 207:539–563
13. Ramadan MRI, Aboul-Enein S, El-Sebaai AA (1988) A model of an improved low cost indoor solar cooker in Tanta. *Sol Wind Technol* 5:387–393
14. Saxena A, Cuce E, Tiwari GN, Kumar A (2020) Design and thermal performance investigation of a box cooker with flexible solar collector tubes: An experimental research. *Energy*. <https://doi.org/10.1016/j.energy.2020.118144>
15. Saxena A, Karakilcik M (2017) Performance evaluation of a solar cooker with low cost heat storage material. *Int J Sustain Green Energy* 6(4):57–63
16. Sharma SD, Buddhi D, Sawhney RL, Sharma A (2000) Design, development and performance evaluation of a latent heat storage unit for evening cooking in a solar cooker. *Energy Convers Manag* 41(14):1497–1508
17. Thirugnanam C, Karthikeyan S, Kalaimurugan K (2020) Study of phase change materials and its application in solar cooker. *Mater Today: Proc* <https://doi.org/10.1016/j.matpr.2020.02.780>. [10.1016/S0196-8904\(99\)00193-4](https://doi.org/10.1016/S0196-8904(99)00193-4)
18. Vigneswaran VS, Kumaresan G, Sudhakar P, Santosh R (2017) Performance evaluation of solar box cooker assisted with latent heat energy storage system for cooking application. *IOP Conf Series: Earth Environ Sci* vol 67, 012017
19. Yuksel N, Arabacigil B, Avci A (2012) The thermal analysis of paraffin wax in a box-type solar cooker. *J Renew Sustain Energy* vol 4, 063126, pp. 1–9.

Automobile Air Conditioning Loads Modelling Using Heat Balance Method



Vanita Wagh and A. D. Parekh

Abstract Air conditioning is one of the key components used in the automobile for providing comfortable conditions. Before designing air conditioning (AC), one should know the heating/cooling load of the vehicle cabin. The heat balance method (HBM) is used for estimating heating/cooling load inside the vehicle cabin. For calculation purposes, a lump vehicle body is assumed. Toyota Fortuner vehicle in Surat region is undertaken for load calculation in the summer season. Solar radiation, metabolism of passengers, engine exhaust, and ventilation air are considered as a source of heat load. The total cooling load obtained in the vehicle cabin is around 4.1448 kW. The capacity of AC required is 7.415 kW to compensate for cooling load and the heat emitted by other components. The present study will be beneficial for an automotive designer to evaluate the capacity of automobile air conditioning systems correctly.

Keywords Automobile air conditioning system · Heating load · Cooling load · Heat balance method · Solar radiation

Abbreviations

Q_{Total}	Overall thermal load encountered by the cabin (W)
Q_{Met}	Metabolic load (W)
Q_{Dir}	Direct radiation load (W)
Q_{Dif}	Diffuse radiation load (W)
Q_{Ref}	Reflected radiation load (W)
Q_{Amb}	Ambient load (W)
Q_{Exh}	Exhaust load (W)

V. Wagh (✉)

Thermal System Design, S.V.N.I.T, Surat, Gujarat 395007, India

e-mail: vanitawagh13@gmail.com

A. D. Parekh

Department of Mechanical Engineering, S.V.N.I.T, Surat, Gujarat 395007, India

© The Author(s), under exclusive license to Springer Nature Singapore Pte Ltd. 2023

H. B. Mehta et al. (eds.), *Recent Advances in Thermal Sciences and Engineering*,

Lecture Notes in Mechanical Engineering, https://doi.org/10.1007/978-981-19-7214-0_3

Q_{Eng}	Engine load (W)
Q_{Ven}	Load generated due to ventilation (W)
Q_{AC}	Thermal load created by the AC cycle (W)
A_{Du}	DuBois body surface area (m^2)
L	Latitude angle ($^\circ$)
H	Hour angle ($^\circ$)
S	Surface area (m^2)
I_{Dir}	Intensity of direct radiation (W/m^2)
I_{Ref}	Intensity of reflected radiations (W/m^2)
I_{Dif}	Intensity of diffuse radiation (W/m^2)
C	Diffuse radiation factor
T_s	Average surface temperature ($^\circ C$)
T_i	Cabin temperature ($^\circ C$)
$h_{cabinair}$	Convective heat transfer coefficient of cabin (low-speed flow of air over a surface) ($W/m^2 K$)
h_{atmair}	Convective heat transfer of atmospheric air (free convection) ($W/m^2 K$)
T_o	Ambient temperature ($^\circ C$)
T_c	Comfort temperature ($^\circ C$)
S_{Exh}	Area of the bottom surface in contact with the exhaust pipe (m^2)
T_{Exh}	Exhaust gases temperature ($^\circ C$)
U	Overall heat transfer coefficient of the surface element in contact with the engine ($W/m^2 K$)
S_{Eng}	Surface area exposed to the engine temperature (m^2)
T_{Eng}	Engine temperature ($^\circ C$)
M_{ven}	Ventilation mass flow rate (kg/s)
e_o	Ambient enthalpy (kJ per kg of dry air)
e_i	Cabin enthalpy (kJ per kg of dry air)
T	Air temperature ($^\circ C$)
X	Humidity ratio (gram of water per gram of dry air)
P	Total air pressure (bar)
P_s	Water saturation pressure at temp T (bar)
t_c	Pull-down constant (s)
t_p	Pull-down time (s)
W	Weight of person (kg)
H	Height of person (cm)
k_{glass}	Thermal conductivity of glass ($W/m K$)
$k_{carbody}$	Thermal conductivity of car body ($W/m K$)
t_{glass}	Thickness of glass (mm)
$t_{carbody}$	Thickness of car body (mm)
M	Passenger metabolic heat production rate (W/m^2)
m_a	Mass flow of air (kg/s)
C_a	Specific heat of cabin air ($J/kg K$)
DTM	Diffuse thermal mass (J/K)

Greek Symbols

δ	Solar declination angle ($^{\circ}$)
β	Solar altitude angle ($^{\circ}$)
Φ	Solar azimuth angle ($^{\circ}$)
θ	Angle between the surface normal and the position of sun in the sky ($^{\circ}$)
τ	Surface element transmissivity
ρ_g	Ground reflectivity
Σ	Surface tilt angle measured from horizontal surface ($^{\circ}$)
ρ	Air density (kg/m^3)
ϕ	Relative humidity (%)

1 Introduction

The air conditioning system is an essential component that provides comfort conditions to passengers and is one of the major energy-consuming components. The USA alone consumes 7 billion gallons of fuel a year for air conditioning (AC) systems of light-duty vehicles [1].

Automobile makers are always in need of optimizing and improving the efficiency of AC systems without compromising on the performance so that the comfort temperature can be maintained.

Before designing any air conditioning system, one should know various types of heating/cooling load occurring inside the vehicle cabin, and these loads need to be computed. In the present paper, cooling load is calculated considering all the sources of heat gain for automobile vehicles. Location for input data is taken Surat, Gujarat. The date, time, and month are chosen for load calculations for 21 June afternoon.

2 Problem Description

AC loads are affected by surrounding parameters as well as the automobile components. Solar radiation and ambient temperature are the surroundings affecting parameters. However, the engine, ventilation, and insulation of the car also affect the cooling load.

3 Heat Load Calculation

Heat load calculation is done using HBM. For heat load calculation, Toyota Fortuner car cabin is considered. Total heat gain by cabin consists of nine different loads, which are described below. The total load can be positive or negative depending

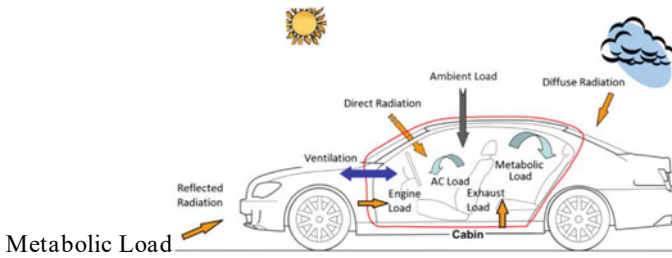


Fig. 1 Schematic representation of thermal load in vehicle cabin [2]

upon the requirement of comfort temperature condition inside with reference to outside condition. If the outside temperature is high, then the cabin heat load might be positive and vice versa.

Various loads which apply to the vehicle body are shown schematically in Fig. 1. Some of these loads are affected by body parts, whereas some are not affected irrespective of surface elements. All loads are calculated assuming quasi-steady-state conditions.

4 Metabolic Load

The human body performs metabolic activities. Because of these activities, constant heat and humidity are generated by perspiration. The amount of heat excreted by the human body is considered as heat gain by the cabin air and is called metabolic load [2].

Table 1 represents the weight and height of the passengers considered for metabolic load calculation (Table 2).

$$Q_{Met} = \sum_{Passengers} M \times A_{Du}$$

Table 1 Passenger data

S. No.	Passenger	Weight (kg)	Height (cm)
1	Driver	72	170
2	Male_1	66	165
3	Male_2	62	163
4	Female_1	64	168
5	Female_2	53	157
6	Child_1	36	140
7	Child_2	32	137

Table 2 Specifications for the driving condition [3]

Specification	Value
Date	June 21, 2020
Local time	13:00 to 16:00
Location	Surat, Gujarat
Ventilation flow	$0.01 \text{ m}^3 \text{ s}^{-1}$
Ground reflectivity	0.2
Ambient temperature	$34.4 \text{ }^\circ\text{C}$
Initial cabin temperature	$80 \text{ }^\circ\text{C}$
Ambient relative humidity	70 %
Cabin relative humidity	50 %
Comfort temperature	23°C
Pull-down time	600 s
Deep thermal mass	5600 JK^{-1}

$$A_{Du} = 0.202 W^{0.425} H^{0.725}$$

$$M_{\text{Driver}} = 37 \times 3.125 = 116.6425 \text{ W/m}^2$$

$$M_{\text{Others}} = 18 \times 3.125 = 56.745 \text{ W/m}^2$$

$$Q_1 = Q_{\text{Driver}} = 116.6425 \times 0.202 \times 72^{0.425} \times 1.7^{0.725}$$

$$Q_2 = 56.745 \times 0.202 \times 66^{0.425} \times 1.65^{0.725}$$

$$Q_3 = 56.745 \times 0.202 \times 62^{0.425} \times 1.63^{0.725}$$

$$Q_4 = 56.745 \times 0.202 \times 64^{0.425} \times 1.68^{0.725}$$

$$Q_5 = 56.745 \times 0.202 \times 53^{0.425} \times 1.57^{0.725}$$

$$Q_6 = 56.745 \times 0.202 \times 36^{0.425} \times 1.4^{0.725}$$

$$Q_7 = 56.745 \times 0.202 \times 32^{0.425} \times 1.37^{0.725}$$

$$Q_{\text{Met}} = Q_1 + Q_2 + Q_3 + Q_4 + Q_5 + Q_6 + Q_7$$

$$Q_{\text{Met}} = 718.91 \text{ W}$$

5 Radiation Load

$$Q_{\text{Dir}} = \sum_{\text{Surfaces}} S \times \tau \times I_{\text{Dir}} \times \cos\theta$$

Solar radiation generates a significant amount of heat. The heat gained because of solar radiation is called radiation load. According to ASHRAE [3], solar radiation heat load can be categorized into direct, diffuse, and reflected radiation loads.

$\delta = 23.45^\circ$ from ASHRAE Handbook < > for 21 June.

Location = Surat (21.17°N, 72.85°E)

$$L = 21.17^\circ$$

$$H = 15 \times (12 - \text{LST})^\circ$$

LST = Local Solar Time.

For 2 pm,

$$H = 15 \times (12 - 14)^\circ$$

$$H = -30^\circ$$

Afternoon, the hour angle is negative.

Solar Altitude Angle (β):

$$\sin(\beta) = \sin(\delta) \times \sin(L) + \cos(\delta) \times \cos(H) \times \cos(L)$$

$$\sin(\beta) = \sin(23.45) \times \sin(21.17) + [\cos(23.45) \times \cos(-30) \times \cos(21.17)]$$

$$\sin(\beta) = 0.8846$$

$$\beta = 62.2016^\circ$$

Solar Azimuth Angle (Φ):

$$\cos(\Phi) = \frac{\sin(\beta) \times \sin(L) - \sin(\delta)}{\cos(\beta) \times \cos(L)}$$

$$\cos(\Phi) = \frac{\sin(62.2) \times \sin(21.17) - \sin(23.45)}{\cos(62.2) \times \cos(21.17)}$$

$$\cos(\Phi) = -0.1804$$

$$\Phi = 100.3979^\circ$$

6 Direct Load

Solar radiation, which strikes directly the surface of the vehicle body, is considered as direct load.

$$Q_{Dir} = \sum_{Surface} S \times \tau \times I_{Dir} \times \cos(\theta)$$

$$I_{Dir} = \frac{A}{\exp\left[\frac{B}{\sin(\beta)}\right]}$$

A and B are constants tabulated in ASHRAE Handbook of Fundamentals [3] for different months (Fig. 2).

β is calculated based on position and time.

For 21 June,

$$A = 345 \text{ Btu/h.ft}^2,$$

$$B = 0.205$$

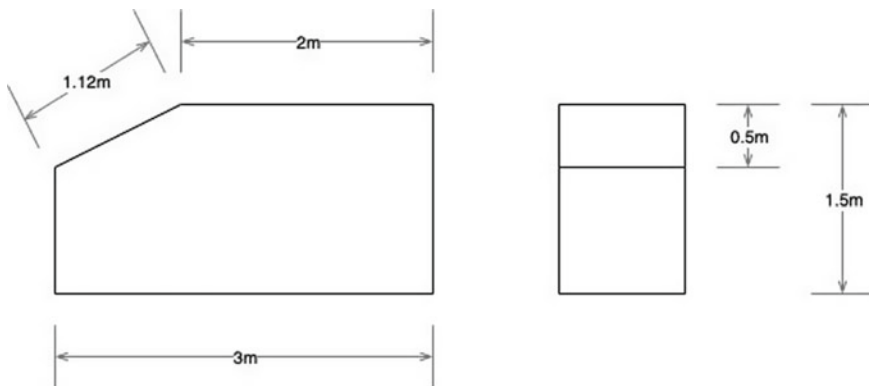


Fig. 2 Geometric diagram of cabin

Table 3 Properties of the vehicle cabin body

Property	Glass	Vehicle body
Conductivity (W/m K)	1.05	0.2
Density (kg/m ³)	2500	1500
Transmissivity	0.5	0
Absorptivity	0.3	0.4
Specific heat (J/kg K)	840	1000
Thickness (mm)	3	10

$$I_{Dir} = \frac{345 \times 3.1525}{\exp\left[\frac{0.205}{\sin(62.2)}\right]}$$

$$I_{Dir} = 862.6353 \text{ W/m}^2$$

$$\tau = 0.5[\text{From Table 3}]$$

$$S_{Dir} = S_1 + S_2$$

$$S_{Dir} = (1 \times 1.2) + (2 \times 1)$$

$$S_{Dir} = 3.2 \text{ m}^2$$

$$Q_{Dir} = \sum_{\text{Surface}} S \times \tau \times I_{Dir} \times \cos(\theta)$$

$$Q_{Dir} = 3.12 \times 0.5 \times 862.6353 \times \cos(27.7984)$$

$$Q_{Dir} = 1190.3904 \text{ W}$$

7 Diffuse Load

While significant solar radiation is due to direct strike, sometimes sunlight gets diffused by clouds, and the heat gained by this diffused sunlight is called diffused load.

The diffuse radiation heat gain is found by

$$Q_{\text{Dif}} = \sum_{\text{Surface}} S \times \tau \times I_{\text{Dif}}$$

$$I_{\text{Dif}} = C \times I_{\text{Dir}} \times \left[\frac{1 + \cos(\Sigma)}{2} \right]$$

$$C = 0.134$$

In most cases, the tilted surface faces due south.

The glass is tilted at an angle of latitude plus 10° with the horizontal and its pointing due south.

$$\Sigma = 21.17 + 10 = 31.7^\circ$$

$$I_{\text{Dif}} = C \times I_{\text{Dir}} \times \left[\frac{1 + \cos(\Sigma)}{2} \right]$$

$$I_{\text{Dif}} = 0.134 \times 862.6353 \times \left[\frac{1 + \cos(31.7)}{2} \right]$$

$$I_{\text{Dif}} = 107.2494 \text{ W/m}^2$$

$$Q_{\text{Dif}} = \sum_{\text{Surface}} S \times \tau \times I_{\text{Dif}}$$

$$Q_{\text{Dif}} = 3.12 \times 0.5 \times 107.2494$$

$$Q_{\text{Dif}} = 167.3090 \text{ W}$$

8 Reflected Radiation Load

Solar radiation reflected on surrounding surfaces like ground, wall, etc., is referred to as reflected radiation, and this radiation is also heat gain to the vehicle body.

Reflected radiation refers to the part of radiation heat gain that is reflected from the ground and strikes the body surfaces of the vehicle. The reflected radiation is calculated by

$$Q_{\text{Ref}} = \sum_{\text{Surface}} S \times \tau \times I_{\text{Ref}}$$

$$I_{\text{Ref}} = (I_{\text{Dir}} + I_{\text{Dif}}) \times \rho_g \times \left[\frac{1 - \cos(\Sigma)}{2} \right]$$

$\rho_g = 0.2$ (usually used for ground) [1]

$$I_{\text{Ref}} = (862.6353 + 107.2494) \times 0.2 \times \left[\frac{1 - \cos(31.17)}{2} \right]$$

$$I_{\text{Ref}} = 14.0017 \text{ W/m}^2$$

$$Q_{\text{Ref}} = \sum_{\text{Surface}} S \times \tau \times I_{\text{Ref}}$$

$$Q_{\text{Ref}} = 3.12 \times 0.5 \times 14.0017$$

$$Q_{\text{Ref}} = 21.8426 \text{ W}$$

9 Ambient Load

Heat load due to the difference between the temperature of cabin air and ambient is called ambient load. This load is mainly transferred through exterior convection, conducting through body panels, glasses, and interior convection.

$$Q_{\text{Amb}} = \sum_{\text{Surface}} S \times U \times (T_s - T_i)$$

$$S_{\text{Total}} = S_1 + S_2 + S_3 + S_4 + S_5 + S_6 + S_7$$

$$S_{\text{Total}} = (2 \times 1) + (1 \times 1.5) + (3 \times 1) + (1 \times 1) + (1.12 \times 1) \\ + [2 \times [(3 \times 1) + (2 \times 0.5) + (0.5 \times 0.5 \times 1)]]$$

$$S_{\text{Total}} = 17.12 \text{ m}^2$$

Overall heat transfer coefficient,

$$\frac{1}{U} = \frac{1}{h_i} + \frac{t}{k} + \frac{1}{h_o}$$

$$\frac{1}{U} = \frac{1}{h_{\text{cabinair}}} + \frac{t_{\text{glass}}}{k_{\text{glass}}} + \frac{t_{\text{carbody}}}{k_{\text{carbody}}} + \frac{1}{h_{\text{atmair}}}$$

Let,

$$h_{\text{cabin air}} = 10 \text{ W/m}^2\text{k}$$

$$h_{\text{atm air}} = 5 \text{ W/m}^2\text{k}$$

$$k_{\text{glass}} = 1.05 \text{ W/mk}$$

$$k_{\text{carbody}} = 0.2 \text{ W/mk}$$

$$t_{\text{glass}} = 3 \text{ mm}$$

$$t_{\text{carbody}} = 10 \text{ mm}$$

$$\frac{1}{U} = \frac{1}{10} + \frac{3 \times 10^{-3}}{1.05} + \frac{10 \times 10^{-3}}{0.2} + \frac{1}{5}$$

$$U = 2.834 \text{ W/m}^2\text{k}$$

Let,

$$T_c = 23^\circ\text{C}$$

$$T_o = 34.4^\circ\text{C}$$

$$T_i = 80^\circ\text{C}$$

$$T_s = \frac{T_i + T_c}{2} = \frac{80 + 23}{2}$$

Each surface element's heat gain or loss is the difference between the heat gained from the ambient by the surface and the heat released to the cabin by the surface. Thus, net absorbed heat is

$$Q_{\text{Amb}} = S \times U \times (T_o - T_s) - S \times U \times (T_s - T_i)$$

$$Q_{\text{Amb}} = S \times U \times (T_o - 2 \times T_s + T_i)$$

$$Q_{\text{Amb}} = 17.12 \times 2.834 \times \left(34.4 - 2 \times \left(\frac{23 + 80}{2} \right) + 80 \right)$$

$$Q_{\text{Amb}} = 553.1061 \text{ W}$$

10 Exhaust Load

The vehicle releases exhaust gas while operating. These exhaust gases can have temperatures as high as 1000 °C. At such a high temperature, exhaust gas transfers some of its heat to the cabin through the floor and amounts to the total heat load.

$$Q_{\text{Exh}} = S_{\text{Exh}} \times U \times (T_{\text{Exh}} - T_i)$$

$$T_{\text{Exh}} = 0.138 \times RPM - 17$$

For RPM = 3400, exhaust gases temperature will be

$$T_{\text{Exh}} = 0.138 \times 3400 - 17$$

$$T_{\text{Exh}} = 452.2 \text{ }^\circ\text{F}$$

$$T_{\text{Exh}} = 233.44 \text{ }^\circ\text{C}$$

$$T_{\text{Exh}} = 233.44 \text{ }^\circ\text{C}, T_i = 80 \text{ }^\circ\text{C}, U \simeq 0$$

$$Q_{\text{Exh}} \simeq 0W$$

11 Engine Load

Not only exhaust gas has a high temperature, but the engine of the conventional or hybrid vehicle also operates at high temperature, and the heat generated by the engine is considered as engine load. The equations described below are used for calculating the engine thermal load.

$$Q_{\text{Eng}} = S_{\text{Eng}} \times U \times (T_{\text{Eng}} - T_i)$$

$$T_{\text{Eng}} = -2 \times 10^{-6} \times RPM^2 + 0.0355 \times RPM + 77.5$$

From the Toyota Fortuner specifications,

RPM = 3400, displacement volume (V) = 2755 cm³, bore (D) = 95 mm = 9.5 cm,
n = 4

$$T_{\text{Eng}} = -2 \times 10^{-6} \times 3400^2 + 0.0355 \times 3400 + 77.5$$

$$T_{\text{Eng}} = 175.08^{\circ}\text{F}$$

$$T_{\text{Eng}} = 79.99^{\circ}\text{C} \cong 80^{\circ}\text{C}$$

$$\text{Volume} = n \times \frac{\pi}{4} \times D^2 \times L$$

$$2755 = 4 \times \frac{\pi}{4} \times 9.5^2 \times L$$

$$L = 75.08^{\circ}\text{F}$$

The area of the engine is

$$S_{\text{Eng}} = \pi \times R \times (R + L)$$

$$S_{\text{Eng}} = \pi \times 4.75 \times (4.75 + 9.7168)$$

$$S_{\text{Eng}} = 215.8818 \text{ cm}^2$$

$$S_{\text{Eng}} = 0.0216 \text{ m}^2$$

Overall heat transfer coefficient

$$\frac{1}{U} = \frac{1}{h_{\text{Engair}}} + \frac{t}{k} + \frac{1}{h_{\text{cabinair}}}$$

h_{air} for free convection of air

$$h_{\text{air}} = 5 \text{ W/m}^2\text{k}$$

$$k_{\text{dash}} = 0.035 \text{ W/mk (For lather insulation)}$$

$$t = 3 \text{ mm}$$

$$\frac{1}{U} = \frac{1}{5} + \frac{3 \times 10^{-3}}{0.035} + \frac{1}{5}$$

$$U = 2.0588 \text{ W/m}^2\text{k}$$

$$Q_{\text{Eng}} = S_{\text{Eng}} \times U \times (T_{\text{Eng}} - T_i)$$

$$Q_{\text{Eng}} = 0.0216 \times 2.0588 \times (80 - 80)$$

$$Q_{\text{Eng}} = 0W$$

12 Ventilation Load

Passenger's breathing causes CO₂ concentration to increase linearly over time, and this may cause suffocation to passenger. To avoid such a situation, flow of fresh air must be transferred to the cabin to maintain passenger's comfort. Research has shown that a minimum of 13% of fresh air is needed for the passenger to felt comfortable [4].

Air leakage happens in a different vehicle, and it is needed for passenger's comfort. This leakage can be considered a function of the pressure difference between the cabin and the surroundings and the vehicle's velocity and surrounding air. Air leakage for Toyota Fortuner car is around 0.02 m³/s at a pressure difference of 10 Pa [5].

Ambient pressure is slightly lower compared to car cabins because of air conditioning and ventilation. Hence, one should consider leakage airflow in the ventilation load. In steady-state operation, the built-up pressure is assumed to remain constant. Therefore, the incoming condition of airflow is considered the same as cabin air.

According to psychometric calculations, ventilation heat gain consists of both sensible and latent loads. The amount of thermal heat gain can be calculated from

$$Q_{\text{Ven}} = M_{\text{Ven}} \times (e_o - e_i)$$

Enthalpies are calculated from

$$e = 1006 \times T + (2.501 \times 10^6 + 1770 \times T) \times X$$

$$X = 0.62198 \times \frac{\phi \times P_S}{100 \times P - \phi \times P_S}$$

$$X \cong 0.622 \times \frac{\phi \times P_S}{100 \times P - \phi \times P_S}$$

Calculation of ambient enthalpy (e_o):

$\phi_{\text{Amb}} = 70\%$, $P = 1.013\text{bar}$, $P_S = 0.0545\text{bar}$ [at amb. temp. = 34.4 °C]

$$X_{\text{amb.temp.}} = 0.622 \times \frac{70 \times 0.0545}{100 \times 1.013 - 70 \times 0.0545}$$

$$X_{\text{amb. temp.}} = 0.02434 \text{ kg/kg of dryair}$$

$$e_o = e_{\text{amb}} = 1.006 \times T_{\text{amb}} + (2501 + 1.77 \times T_{\text{amb}}) \times X_{\text{amb. temp}}$$

$$e_o = e_{\text{amb}} = 1.006 \times 34.4 + (2501 + 1.77 \times 34.4) \times 0.02434$$

$$e_o = e_{\text{amb}} = 96.9628 \text{ kg/kg.}$$

Calculation of cabin enthalpy (e_i):

$$\phi_{\text{Cabin}} = 50\%, P = 1.013 \text{ bar}, P_s = 0.0281 \text{ bar [cabin temp.} = 23 \text{ }^\circ\text{C]}$$

$$X_{\text{cabin}} = 0.622 \times \frac{50 \times 0.0281}{100 \times 1.013 - 50 \times 0.0281}$$

$$X_{\text{cabin.}} = 0.00875 \text{ kg/kg of dryair}$$

$$e_i = e_{\text{amb}} = 1.006 \times T_{\text{cabin}} + (2501 + 1.77 \times T_{\text{cabin}}) \times X_{\text{cabin}}$$

$$e_i = e_{\text{amb}} = 1.006 \times 23 + (2501 + 1.77 \times 23) \times 0.00875$$

$$e_i = e_{\text{amb}} = 45.3779 \text{ kg/kg}$$

Let,

$$\text{ventilationflow} = 0.01 \text{ m}^3/\text{s} = Q,$$

$$\rho = \text{Airdensity} = 1.2 \text{ kg/m}^3$$

$$M_{\text{vent}} = Q \times \rho$$

$$M_{\text{vent}} = 0.01 \times 1.2$$

$$M_{\text{vent}} = 0.012 \text{ kg/s}$$

$$Q_{\text{vent}} = M_{\text{vent}} \times (e_o - e_i)$$

$$Q_{\text{vent}} = 0.012 \times (96.9628 - 45.3779)$$

$$Q_{\text{vent}} = 0.6190 \text{ kW}$$

$$Q_{\text{vent}} = 619.0 \text{ W}$$

The total load for Toyota Fortuner in Surat location is

$$Q_{\text{Vehicle}} = Q_{\text{Met}} + Q_{\text{Dir}} + Q_{\text{Dif}} + Q_{\text{Ref}} + Q_{\text{Amb}} + Q_{\text{Exh}} + Q_{\text{Eng}} + Q_{\text{Vent}}$$

$$Q_{\text{Vehicle}} = 718.91 + 1190.3904 + 167.3090 + 21.8426 \\ + 553.1061 + 0 + 0 + 619.0$$

$$Q_{\text{Vehicle}} = 3270.5581 \text{ W}$$

$$Q_{\text{Vehicle}} = 3.2705 \text{ kW}$$

13 AC Load

The responsibility of the air conditioning system is to compensate for other heat loads and provide comfort temperature to the passenger. In cold weather, AC provides

positive AC load (heating) and in cold weather, vice versa. While doing so, AC or heat pump cycle is providing thermal load.

$$Q_{AC} = -[Q_{Met} + Q_{Dir} + Q_{Dif} + Q_{Ref} + Q_{Amb} + Q_{Exh} + Q_{Eng} + Q_{Ven}]$$

$$-(m_a \times c_a + DTM) \times \frac{(T_i - T_{Comf})}{t_c}$$

$$t_c = \frac{t_p}{\ln[T_i - T_{Comf}]}$$

Let

$$t_p = 600 \text{ sec}$$

$$t_c = \frac{600}{\ln[80 - 23]}$$

$$t_c = 148.4027 \text{ s}$$

Let

$$m_a = 0.02 \text{ kg/s}$$

$$C_a = 721 \text{ J/kg k}$$

$$m_a = 0.02 \text{ kg/s}, C_a = 721 \text{ J/kg. k}$$

$$m_a = 0.02 \times 600 = 12 \text{ kg}$$

$$DTM = 5000 \text{ J/k}$$

$$Q_{AC} = -[718.9099 + 1190.3904 + 167.3090 + 21.8426$$

$$+ 553.1061 + 0 + 0 + 619.0]$$

$$- [(7.2 \times 721) + 5600] \times \frac{(80 - 23)}{148.4027}$$

$$Q_{AC} = -7415.3505 \text{ W}$$

$$Q_{Total} = Q_{Met} + Q_{Dir} + Q_{Dif} + Q_{Ref} + Q_{Amb} + Q_{Exh} + Q_{Eng} + Q_{Ven} + Q_{AC}$$

$$Q_{Total} = [718.9099 + 1190.3904 + 167.3090 + 21.8426 + 553.1061$$

$$+ 0 + 0 + 619.0 + (-7415.3505)]$$

$$Q_{\text{Total}} = -4144.7925 \text{ W}$$

$$Q_{\text{Total}} = -4.1448 \text{ kW}$$

14 Conclusions

Total cooling load obtained in the vehicle cabin is around—4.1448 kW. The capacity of AC required is —7.415 kW to compensate for cooling load and the heat emitted by other components.

Acknowledgements The authors would like to thank all the academicians/researchers whose work has been cited and used in this study. The authors also thank Sardar Vallabhbhai National Institute of Technology for all the support.

References

1. Johnson V (2002) Fuel used for vehicle air conditioning: a state-by-state thermal comfort-based approach. National Renewable Energy Laboratory
2. Fayazbakhsh MA, Bahrami M (2013) Comprehensive modeling of vehicle air conditioning loads using heat balance method. SAE International
3. Shank KW (1993) ASHRAE handbook of fundamental. American Society of Heating, Refrigerating, and Air Conditioning, Atlanta, GA
4. Arndt M, Sauer M (2004) Spectroscopic carbon dioxide sensor for automotive applications, sensors. Proceedings of IEEE, pp 252–255
5. Fletcher B, Saunders CJ (1994) Air change rates in stationary and moving motor vehicles. J Hazard Mater, pp 243–256
6. Vinofer BP, Rajakumar S (2016) Cooling load calculation and design of air conditioning system in automobile. Int J Res Soc Sci Human 6(1):94–103
7. Abdulsalam O, Santoso B, Aries D (2015) Cooling load calculation and thermal modelling for vehicle by MATLAB. Int J Innov Res Sci Eng Technol 4(5):3052–3060

Computational Modelling of Bioheat Transfer for Hyperthermia Using Finite Difference Method



Tarun Hegde and Ranjith Maniyeri

Abstract Bioheat transfer is a field which involves the study of thermal energy in living systems like tissues. Penne's bioheat transfer equation is a popular model used in this field. The objective of this study is to develop a computational model to understand the effect of different heating methods like magnetic hyperthermia and laser treatment for living tissues with an embedded tumour. This is done by solving Penne's bioheat transfer equation using finite difference method for a two-dimensional domain. Initially, Penne's model in its one-dimensional form is used to observe heat transfer in a living tissue. After validating the results, the model is extended to a two-dimensional domain with an embedded tumour. The properties of the healthy tissue and the tumour cells are considered to be different. Using different heating methods, the temperature of the tumour is raised to 40–43 °C to damage the tumour cells, and the time taken for necrosis is found. The results obtained will be useful for tumour detection and also its treatment.

Keywords Penne's bioheat transfer equation · Finite difference method · Magnetic hyperthermia · Laser · Tumour

Abbreviations

c_t	Specific heat of tissue $\text{J kg}^{-1}\text{K}^{-1}$
c_b	Specific heat of blood $\text{J kg}^{-1}\text{K}^{-1}$
T_a	Arterial temperature °C
T_c	Body core temperature °C
T_f	Surrounding air temperature °C

T. Hegde · R. Maniyeri (✉)
Biophysics Laboratory, Department of Mechanical Engineering, National Institute of Technology
Karnataka, Surathkal Mangalore, Karnataka 575025, India
e-mail: mrانji1@nitk.edu.in

T. Hegde
e-mail: tarun.181me280@nitk.edu.in

Q_m	Metabolic heat generation W m^{-3}
h_0	Heat convection coefficient $\text{W m}^{-2}\text{K}^{-1}$

Greek Symbols

ρ_t	Density of the tissue kg m^{-3}
ρ_b	Density of the blood kg m^{-3}
ω_b	Blood perfusion rate s^{-1}

1 Introduction

Computational fluid dynamics and heat transfer have a wide range of applications and can be used in improving our understanding of certain complex systems like living tissues. Cancer is one of the most widespread and fatal diseases across the world. Several methods of treatment for cancer have been developed over the years. Hyperthermia is a method where the temperature of the cancerous cells is raised above 43 °C. This can be done using laser treatment or magnetic hyperthermia. The main challenge in this is to ensure the surrounding healthy cells are not affected while heating the cancerous cells. Our aim is to observe the effect of magnetic hyperthermia and laser treatment along with convective heat transfer on a tissue with an embedded tumour.

A lot of researchers have been working on developing computational models to study detection and treatment of tumours. Pennes [9] came up with a bioheat transfer equation in 1948 by experimentally obtaining the temperature distribution in a human forearm. Deng and Liu [4] solved Penne's equation analytically using Green's function and applied the model with various boundary conditions and heating methods like point and spatial heating. Jiang et al. [6] have solved Penne's equation using finite difference method and observed the effects of thermo-physical properties and dimensions of the domain. Shen et al. [10] proposed another mathematical model in which the thermo-mechanical interactions were depicted at higher temperatures by treating the soft tissue as a thermo-poroelastic media. Ahmadikia et al. [1] used a thermal wave model which considers a relaxation time factor. An analytical solution was obtained from Laplace transformation method by Shih et al. [11]. Alternating direction implicit finite difference method was used to obtain temperature distributions in an irregular tissue by He et al. [5]. Akula and Maniyeri [2] have used Penne's thermal wave and dual phase lag models to simulate bioheat transfer and observe the time taken for tumour necrosis. Patil and Maniyeri [8] have used finite difference method to simulate bioheat transfer in a human breast cyst. Balusu et al. [3] have used finite element method to obtain the temperature distribution for a breast with a

cyst. By considering blood perfusion as a function of temperature, a more accurate temperature profile was obtained by Kengne et al. [7].

In this study, we simulate two different methods of heating, laser and magnetic hyperthermia, for hyperthermia and observe the time taken for necrosis. This is done by using finite difference method to discretize Penne's equation for a two-dimensional domain of the tissue with a tumour embedded in it. The properties of the healthy and cancerous cells are assumed to be different, and the numerical model is built by developing a code in C++ .

2 Mathematical Model

In order to validate the accuracy of the approach, a one-dimensional case is simulated initially. In a biological tissue, heat transfer occurs by conduction through the tissue and by convection due to the blood flowing through the arteries and veins within the tissues. This depends on various factors like blood perfusion rate and the heat generated internally due to metabolic activity of the cells. For our study, Penne's bioheat transfer equation (Pennes [9]) is used which assumes the blood and tissues to be at thermal equilibrium. Equation (1) shows Penne's model which is used.

$$\rho_t c_t \frac{\partial T}{\partial t} = \nabla(k \nabla T) + \rho_b c_b \omega_b (T_a - T) + Q_m + Q_r \quad (1)$$

Here ρ_t is tissue density (kg/m^3), c_t is specific heat of the tissue (J/kgK), T is temperature of the tissue, k is thermal conductivity (W/m^2) of the tissue, ρ_b is blood density (kg/m^3), c_b is specific heat of the blood (J/kgK), ω_b is blood perfusion rate (s^{-1}), T_a is the arterial temperature of blood, and Q_m is heat generated due to metabolism (W/m^3). To consider the effect of different heating methods during cancer treatment, an additional term Q_r is added to the right-hand side of Eq. (1).

Penne's equation is simulated with different boundary conditions and heating methods in a Cartesian coordinate system. The initial temperature distribution of the tissue is obtained by solving Eq. (1) for a steady-state condition, where $\frac{\partial T}{\partial t} = 0$ and $Q_r = 0$. Along with this, the following boundary conditions are used for a living tissue.

$$T = T_c, \text{ at } x = L \quad (2)$$

$$-k \frac{dT}{dx} = h_0 (T_f - T), \text{ at } x = 0 \quad (3)$$

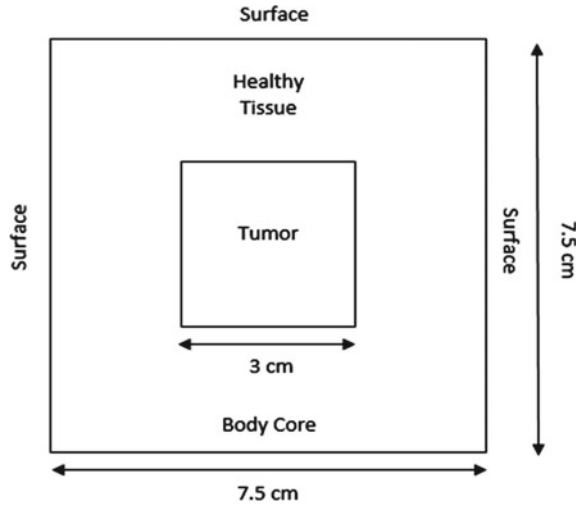
where T_c is the body core temperature which is assumed to be a constant at 37°C , h_0 is the apparent heat convection coefficient between the skin surface and the surrounding air which is taken as $10 \text{ W}/(\text{m}^2 \text{ } ^\circ\text{C})$, and T_f is the surrounding air temperature which

is 25 °C. For the one-dimensional case, $x = 0$ is considered to be the skin surface and $x = L$ is the body core.

3 Physical Problem Description

The numerical model is developed for a healthy tissue of size 7.5 cm X 7.5 cm. The size, position and number of tumours within the tissue can be changed according to our needs. Based on the position of the cells, the entire tissue can be divided into three regions. The first region consists of the cells located within the tumour. In this region, the heat generated due to metabolism is considered to be zero and where spatial or point heating is applied. Therefore, Q_m is zero and Q_r is added to the right side of Eq. (1). The second zone consists of cells which lie completely within the region of healthy tissues. Here, normal tissue properties are used, and Q_r is zero as the healthy cells might get damaged due to excess heating. Finally, the third region consists of cells located at the boundaries of the tumours. If the tumour lies in between two grid points, then the average properties of healthy tissue and tumour cells are taken. Figure 1 shows one of the cases simulated, where a 3 cm X 3 cm tumour is positioned in the middle of the square tissue. The bottom surface is considered as the body core at constant temperature, and the other three sides are exposed to an environment like air or a cooling medium.

Fig. 1 Physical model with a 3 cm X 3 cm tumour in the middle of the tissue



4 Methodology

For the one-dimensional case, Penne’s model is discretized using Crank–Nicolson scheme and solved using Thomas algorithm. To obtain the initial temperature distribution, the steady-state form of Eq. (1) is used along with Eqs. (2) and (3) as the boundary condition. For the unsteady simulation, the time step used is 1 s, the domain is divided into 101 nodes, and the total length of the domain is 3 cm.

The model was then extended to a two-dimensional domain which is shown in Fig. 1. The two-dimensional form of Penne’s equation is discretized using central difference scheme, and the unsteady term is discretized using Crank–Nicolson scheme. The bottom wall is considered to be the body core at constant temperature T_c which is around 37°C. The other three walls are considered to be exposed to the environment, and heat transfer takes place by conduction and convection to the environment. The boundary condition used for these walls is similar to the one used in Eq. (3). The discretized equations are solved using successive over relaxation method.

5 Results and Discussion

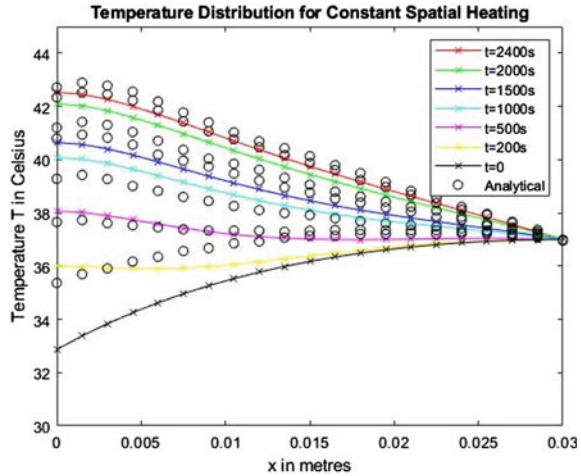
Validation: For validation, the analytical results from Deng and Liu [2002] were used. For our model, we have simulated two different cases. In one case, an adiabatic condition is assumed at the surface and a constant spatial heating source is used to heat the tissue. For the other case, sinusoidal spatial heating source for the tissue is used along with the adiabatic condition at the surface. The values for the various tissue properties used in our one-dimensional model are given in Table 1.

The heating source Q_r is calculated using Eq. (4) from Deng and Liu [4]. $P_0(t)$ is the time-dependent heating power on the skin surface, and η is the scattering coefficient.

Table 1 Tissue properties used in the 1D model

Property	Value for Tissue
ρ_t	1000 kg m ⁻³
ρ_b	1000 kg m ⁻³
c_t	4200 J kg ⁻¹ °C ⁻¹
c_b	4200 J kg ⁻¹ °C ⁻¹
T_a	37 °C
T_c	37 °C
k	0.5 W m ⁻¹ °C ⁻¹
ω_b	0.0005 s ⁻¹
Q_m	3380 Wm ⁻³

Fig. 2 Temperature distribution with adiabatic surface condition ($\eta = 200 \text{ m}^{-1}$, $P_0(t) = 250 \text{ Wm}^{-2}$)



$$Q_r(x, t) = \eta P_0(t) \exp(-\eta x) \quad (4)$$

For the constant spatial heating case, $P_0(t)$ is considered to be a constant, and for the sinusoidal spatial case, sinusoidal function is used to calculate $P_0(t)$.

Figure 2 shows the results obtained for constant spatial heating using finite difference method, and Fig. 3 shows the results for sinusoidal spatial heating. In both cases, the skin surface is assumed to have an adiabatic condition. The plots also show the analytical results from Deng and Liu [4] for the same conditions. The analytical solution was obtained from Green's function after ignoring the zero-order terms. This may be the reason for the slight difference between our numerical results and the analytical results of Deng and Liu [4]. However, there is satisfactory qualitative agreement between the results, and hence, we believe the model is valid and can be extended to a two-dimensional case.

Grid Independence Test: For selecting the appropriate grid size, various computational grids are considered and the time taken for necrosis of the tumour is observed. The physical domain is shown in Fig. 1. The time taken for necrosis is assumed to be the time taken to increase the temperature of the cancerous cells above 40°C . The computational time is also observed. For the heating term Q_r , magnetic hyperthermia using nanoparticles is used, and the power density is considered to be $1.5 \times 10^5 \text{ Wm}^{-3}$. This term is added to Penne's model only if the given cell lies within the tumour region. For healthy cells, Q_r is zero. The thermo-physical properties of the healthy tissue and tumour are different. The thermal conductivity k for healthy tissue is $0.42 \text{ W m}^{-1}\text{C}^{-1}$ and $0.56 \text{ W m}^{-1}\text{C}^{-1}$ for tumour. Blood perfusion rate ω_b for healthy tissue is 0.00018 s^{-1} and zero for tumour. Metabolic heat generation term Q_m is 450 W/m^3 for healthy tissue and zero for the tumour.

Table 2 shows the results of the grid independence test. From the table, we can see how by increasing the number of nodes, necrosis time changes. However, the

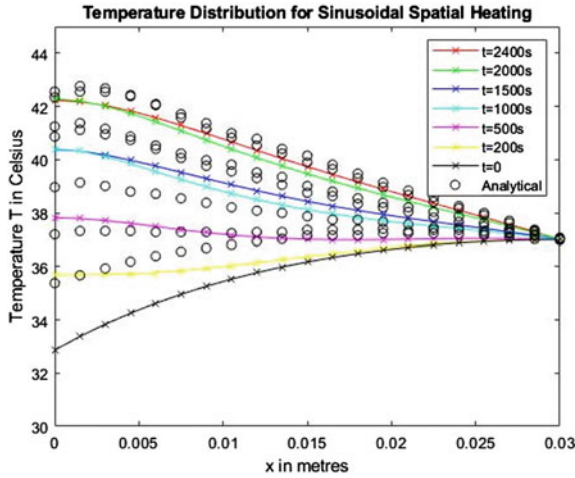


Fig. 3 Temperature distribution with adiabatic surface condition ($\eta = 200 \text{ m}^{-1}$, $P_0(t) = (250 + \cos(0.02t)) \text{ Wm}^{-2}$)

Table 2 Grid independence test results

Grid size	Necrosis time in seconds
71 × 71	884.56
81 × 81	900.53
91 × 91	913.15
101 × 101	923.38
111 × 111	931.82

computational time also increases. Since the values obtained from 101 × 101 grid and 111 × 111 grid are close, it is reasonable to select the 101 × 101 grid as our optimum domain as it takes lesser computational effort.

Tumour Detection: There are several methods to identify whether a given tissue is affected by cancer or not. Mammography is a medical imaging technique which uses a low dose of x-rays to visualize the interior of a breast. This procedure might be painful or cause some discomfort to the patients. Digital infrared thermal imaging (DITI) can be a suitable alternative. The developed numerical model can be used for this purpose by conducting a steady-state analysis and comparing the plots with thermal images captured for detecting tumours.

Figures 4 and 5 show the steady-state analysis for a healthy tissue and a tissue with a tumour embedded in it. In Fig. 5, the region within the black lines is the tumour region, and the dimensions are same as in Fig. 1. From these figures, we can see that the temperature within the tumour is slightly lower when compared to the case with no tumours. This is because we have considered the heat generated due to metabolism to be zero for cancerous cells.

Fig. 4 Temperature plot for steady-state analysis of a healthy tissue with no tumour

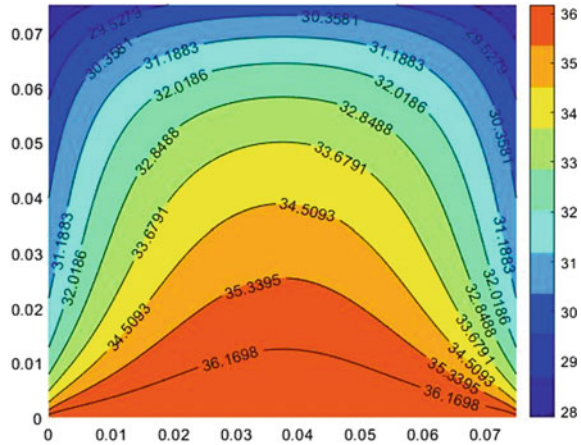


Fig. 5 Temperature plot for steady-state analysis of a tissue with an embedded tumour (3 × 3 cm)

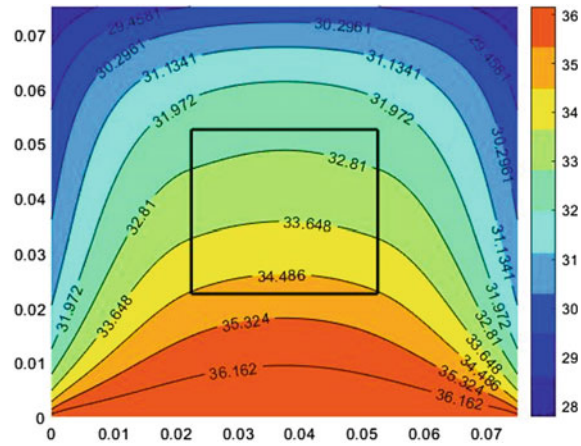
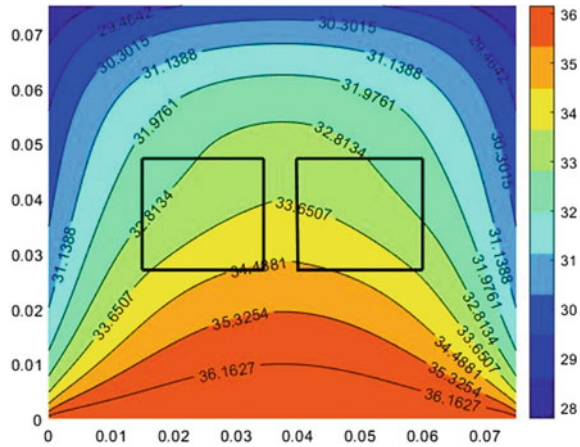


Figure 6 shows the effect of dual tumours on the temperature plot when a steady-state analysis is conducted for such a domain. Again we can see how the region with cancerous cells (located within the black boxes) has slightly lower temperature. Thus, as the size and number of tumours change, the temperature plots of the tissue are also affected.

Magnetic Hyperthermia: The cancerous cells can be damaged by raising its temperature to around 40–43 °C. There are several ways by which this can be done. Magnetic hyperthermia is a popular method to treat tumours. In this method, magnetic nanoparticles are inserted into the tumours, and their temperature is raised when an alternating magnetic field is applied. This causes the temperature of the surrounding tumour to also rise up. Care must be taken to ensure that the nanoparticles do not damage the

Fig. 6 Temperature plot for steady-state analysis of a tissue with dual tumours (2 X 2 cm each)



surrounding healthy tissue. Iron oxide, maghemite, is one of the most commonly used nanoparticles for magnetic hyperthermia.

Various parameters like mass of the nanoparticles used and strength of the magnetic field used affect the heating process. Since our aim is to visualize the effect of magnetic hyperthermia on tumours, the density of the absorbed power Q_r is used to simulate this process instead of quantifying mass and magnetic field strength. For our simulation, a power density range of 1.5×10^5 – 1.5×10^5 W/m³ is used as various researchers have used power density values around this range. Along with this, the time taken for necrosis is also observed. This is assumed as the time taken to increase the temperature of all the cells within the tumour region to a temperature above 40 °C. The domains used for this are similar to the ones shown in Figs. 5 and 6.

Figures 7, 8 and 9 show the temperature distribution obtained when simulating magnetic hyperthermia for a tissue with a single tumour embedded for various values of power density. From the figures, it can be seen that the temperature of the central region within the tumour also increases with increase in Q_r . Therefore, in order to reduce such high temperatures within the tissue, some form of cooling mechanism must be provided or the magnetic field must be temporarily switched off for some time. Figure 10 shows the effect of magnetic hyperthermia for a tissue with dual tumours. From these models, we can understand how the tissue can be affected during magnetic hyperthermia and allow us to select the appropriate power density value to avoid excessive damage.

Table 3 shows the necrosis time for the tumour for various values of power density Q_r . It can be observed that the time taken for necrosis reduces as Q_r increases. For Fig. 10, the necrosis time is 561.59 s.

Laser Treatment: Laser can be used to focus the energy on a specific area, and thus, it is used a lot in the medical field. It can be used in heating the tumour by focusing energy on the tumour region. By making use of endoscopy which is a lighted tube for looking at tissues inside the body, heat can be focused on the tumour region and

Fig. 7 Temperature distribution for a tissue with single tumour embedded and $Q_r = 1.5 \times 10^5 \text{W/m}^3$

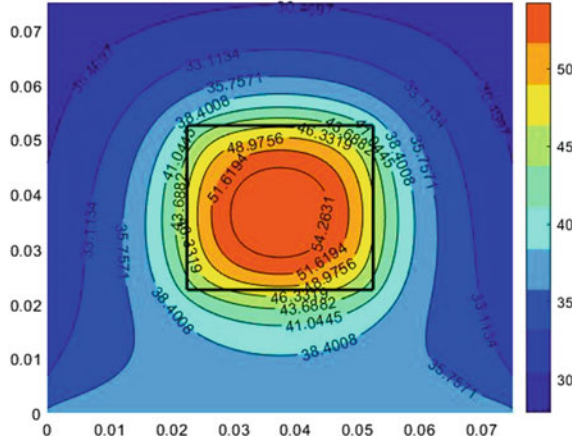


Fig. 8 Temperature distribution for a tissue with single tumour embedded and $Q_r = 2.0 \times 10^5 \text{W/m}^3$

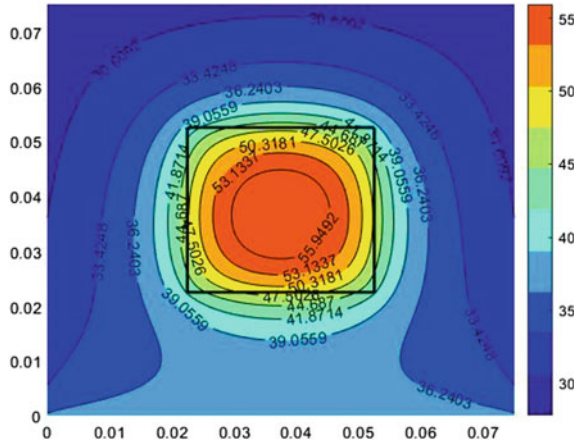


Fig. 9 Temperature distribution for a tissue with single tumour embedded and $Q_r = 2.5 \times 10^5 \text{W/m}^3$

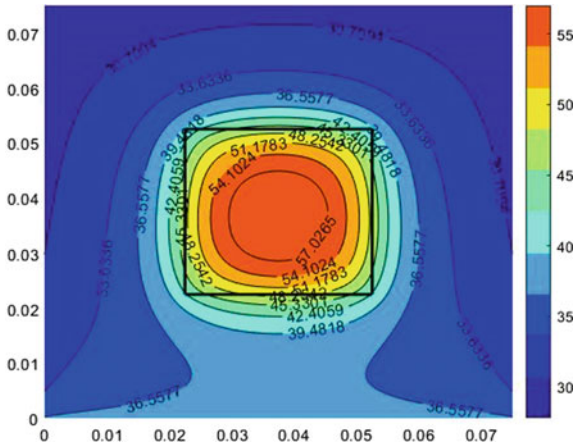


Fig. 10 Temperature distribution for a tissue with dual tumours embedded and $Q_r = 2.5 \times 10^5 \text{ W/m}^3$

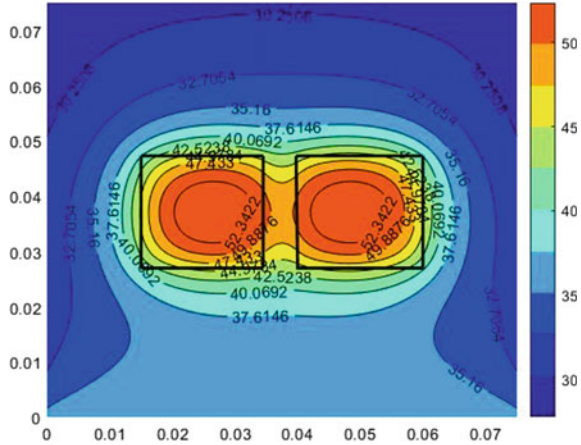


Table 3 Necrosis time for hyperthermia in single tumour tissues

Q_r (Wm^{-3})	Necrosis time in seconds
1.5×10^5	923.38
2.0×10^5	663.32
2.5×10^5	517.24

thus destroying them. For our study, Eq. (5) is used to calculate the heat provided to the tissues using laser.

$$Q_r(x, y, t) = \eta P_0 \exp(-\eta x) \tag{5}$$

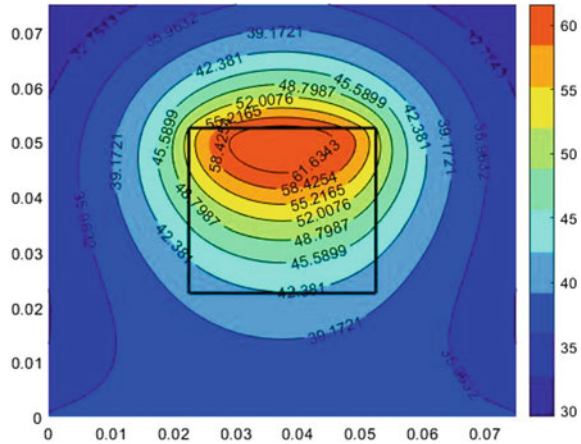
In Eq. (5), P_0 is the time-dependent heating power on the skin surface, η is the scattering coefficient, and x is the distance of the cell from the tumour surface. Therefore, the heat provided reduces exponentially along the length. Here, the laser is assumed to be focused on the top surface of the tumour.

Figure 11 shows the temperature distribution when laser treatment is applied to a tissue with a single tumour embedded in it. The necrosis time for this case was 3704.6 s. The plot also shows the effect of reduced strength of the heating source along the length of the tumour. Since the strength of the heating term reduces exponentially along the length, this method is most suitable when the tumour is located close to the surface.

6 Conclusions

In this work, a computational model is developed to solve Penne’s bioheat transfer equation for one- and two-dimensional cases using finite difference method. The one-dimensional results are validated with analytical results, and the given model

Fig. 11 Temperature distribution for a tissue with single tumour embedded and $P_0 = 2500\text{W/m}^2$



is extended to two-dimensional domain which had a tumour embedded in it. By conducting a steady-state analysis, tumours can be detected by using the model along with thermal images of the tissue. The developed numerical model is also used to simulate magnetic hyperthermia and laser treatment. The time taken for necrosis is also observed to decrease when the power density is increased in magnetic hyperthermia. Laser treatment was observed to be effective when the cancerous cells are located close to the outer surface. The given model can be used to understand the effect of magnetic hyperthermia and laser treatment on the tissue.

References

1. Ahmadikia H, Moradi A, Fazlali R, Parsa AB (2012) Analytical solution of non-Fourier and Fourier bio heat transfer analysis during laser irradiation of skin tissue. *J Mech Sci Technol* 26(6):1937–1947
2. Akula S, Maniyeri R (2020) Numerical simulation of bioheat transfer: a comparative study on hyperbolic and parabolic heat conduction. *J Braz Soc Mech Sci Eng* 42:1–13
3. Balusu K, Suganthi S, Ramakrishnan S (2014) Modelling bio-heat transfer in Breast Cysts using Finite Element analysis. In: 2014 international conference on informatics, electronics & vision (ICIEV), pp 1–4
4. Deng ZS, Liu J (2002) Analytical study on bioheat transfer problems with spatial or transient heating on skin surface or inside biological bodies. *J Biomech Eng* 124(6):638–649
5. He ZZ, Xue X, Liu J (2013) An effective finite difference method for simulation of bio heat transfer in irregular tissues. *J Heat Transf* 135(7):071003
6. Jiang SC, Ma N, Li HJ, Zhang XX (2002) Effects of thermal properties and geometrical dimensions on skin burn injuries. *Burns* 28(8):713–717
7. Kengne E, Mellal I, Hamouda M, Lakhssassi A (2014) A mathematical model to solve bio-heat transfer problems through a bio-heat transfer equation with quadratic temperature-dependent blood perfusion under a constant spatial heating on skin surface. *J Biomed Sci Eng* 7:721–730
8. Patil HM, Maniyeri R (2019) Finite difference method based analysis of bio-heat transfer in human breast cyst. *Thermal Sci Eng Prog* 10:42–47

9. Pennes HH (1948) Analysis of tissue and arterial blood temperatures in the resting human fore arm. *J Appl Physiol* 1(2):93–122
10. Shen W, Zhang J, Yang F (2005) Modeling and numerical simulation of bioheat transfer and biomechanics in soft tissue. *Math Comput Model* 41:1251–1265
11. Shih TC, Yuan P, Lin WL, Kou HS (2007) Analytical analysis of the Pennes bioheat transfer equation with sinusoidal heat flux condition on skin surface. *Med Eng Phys* 29(9):946–953

Application of Phase Change Material in Electronic Heat Dissipation: State-Of-The-Art



Kapil Kalra and Amit Arora

Abstract Increasing use of artificial intelligence is causing stronger and greater dependency on electronic devices, and efforts are ongoing to improve the hardware compactness. The power consumption of these devices is increasing continuously and so is the heat liberated by them. In order to avoid overheating of these devices and maintain them under controlled temperature limits, efficient and effective cooling techniques need to be explored. “Phase Change Materials” are a reliable solution, especially when the heat loads are intermittent. However, most of them have low thermal conductivities which need to be improved to pace the heat transfer process during its solidification and melting. Techniques like the incorporation of metallic foams and nanoparticles are very popular to improve the thermal conductivities of these materials. This article provides a review on use of phase change materials in integration with foams and nanoparticles in heat sinks. Last two decade’s published literature has been thoroughly studied, and all the major findings are discussed in an organized manner along with their pros and cons relevant to the subject matter.

Keywords Phase change material · Metallic foam · Nanoparticle

1 Introduction

In this modern era, the pace of development is greatly assisted by computing and electronic devices. These devices have now become the part and parcel of daily activities. With the increasing trends in technology, the performance and features of these devices are boosted along with a reduction in their sizes [1]. These advancements led to an increase in the input power and power density of these devices [2]. Due to this, the dissipated heat from these devices needs to be rejected out of the system at faster rates [3]. The performance of these devices greatly depends on the temperature at

K. Kalra (✉) · A. Arora

Department of Mechanical Engineering, Malaviya National Institute of Technology, Jaipur, India
e-mail: kapilkalra145@gmail.com

A. Arora

e-mail: amit.mech@mnit.ac.in

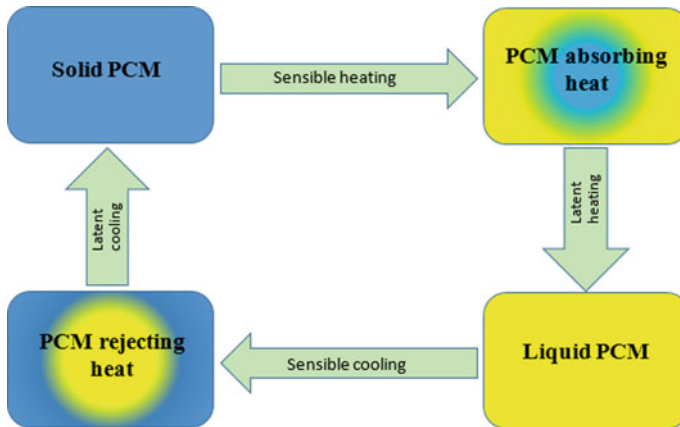


Fig. 1 Thermal charging and discharging of PCM

which they operate. According to the reports of the US Air Force survey, temperature-related failures account for more than 55% out of the total failures of these devices [4]. Thus, keeping the operating temperature within the controlled limits is getting difficult day by day.

Conventional cooling techniques, which are generally active cooling methods, employ fans or pumps to cool the circuits with forced convection mode of heat transfer [5]. However, this technique uses additional power, makes the system bulkier and more prone to mechanical vibrations [6]. Also, devices like laptops, mobiles, etc. have confined space where forced airflow is not much effective for cooling [7]. Passive cooling methods employing phase change materials (PCMs) are found to be of great potential in cooling for computers, smartphones, tablets and other electronic devices that operate intermittently [8]. At peak load condition, phase change materials absorb the heat by the virtue of their phase change process and release that absorbed heat at offload conditions [9] as shown in Fig. 1.

2 Operating Principle and Challenges

Amount of heat transfers in case of phase change process is far greater than the case of sensible heat transfer occurred in forced convection [9]. The operation of a heat sink can be divided into charging cycle and discharging cycle. In charging cycle, phase change material gains and stores the heat whereas in discharging cycle it expels the stored heat to the surrounding [10]. The temperature remains almost constant during heat absorption.

Due to their unique micro-encapsulation technology, phase change materials can be integrated invisibly with a wide range of devices. They are available in different temperature range for different kinds of applications [11]. The areas of application

of phase change materials cover solar energy utilization, building energy utilization [12], food refrigeration and transportation [13], space technology [14], lithium-ion battery cooling [15], military infrared camouflage [16], bio-pharmaceutical products [17].

An ideal phase change material should exhibit high thermal conductivity, chemical stability, high latent heat of fusion, low vapour pressure in the liquid phase, non-toxicity and compatibility with the construction materials. Paraffin waxes contain many of these properties out of several types of phase changing materials available [9], but incidentally, nearly, all of them have inherent low thermal conductivity. This slows down their cooling and heating processes during solidification and melting. Materials having high thermal conductivities, known as “Thermal Conductivity Enhancers” [18], are added to them to make them fit for cooling applications. The enhancement methods explored by researchers for the passive cooling of electronic devices till date can be classified into three categories. These categories are given below.

- (1) Foam matrix
- (2) Nanoparticles
- (3) Internal fins

Using internal fins with phase change material provides uniformity in the base temperature up to a certain level only. Foam matrix and nanoparticles form more uniform structures with phase change materials, and they make the overall heat sink lighter in weight and more compact as compared to that with internal fins. Accordingly, this article focuses on the use of nanoparticles and foam matrix with phase change materials and their performance with different parameters.

3 Heat Dissipation by PCM with Foam Matrix

Foams are porous matrix structures having interconnected paths for heat conduction [9] as shown in Fig. 2. They are light in weight, and they provide more uniformity in the heat distribution as compared to that of internal fins. Heat transfer due to conduction process dominates on natural convection heat transfer process due to flow resistance by use of foam in heat sink. Use of foams will be beneficial for heat sink applications if this increase in conduction rate is more than the decrease in natural convection rate. A heat sink having foam incorporated phase change material will have its performance affected by parameters like power level, foam size, and porosity, foam material, etc.

Power Level Power requirement of the electronic device is the amount of heat dissipated to a great extent. In an experimental study done by Rehman et al. [7], the heat loads were varied as 8 W, 16 W and 24 W by fixing the ambient conditions and volume fraction of the phase change material. They found that as power levels were increased the base temperature of the heat sink rises, and the uniformity in the

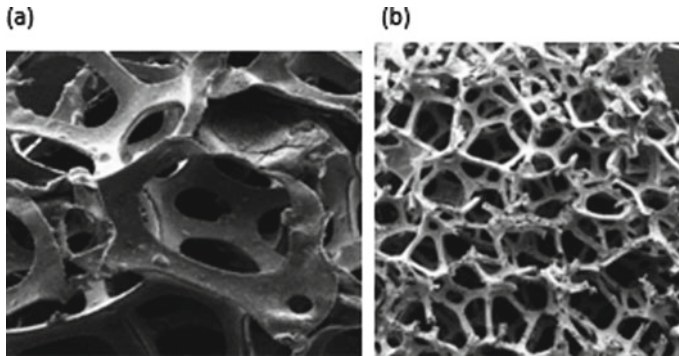


Fig. 2 Scanning electron microscope images of foams [7] **a** copper foam **b** nickel foam

temperature distribution increases. The use of phase change material was found to be the most effective at 24 W, and a reduction of 26% was obtained for copper foam with the 80% PCM volume fraction as compared with nickel foam heat sink without phase change material as shown in Fig. 3.

Orientation of the Sink As convection currents are involved in the melting process, the orientation of the sink came into the picture. In an experimental investigation, Baby and Balaji [19] took a heat sink with n-eicosane embedded in copper foam and studied the temperature variations for various orientations (0° , 25° , 45° , 60° , 75° , 90° , 110° , 130° , 150° , 180° and 210°) at 5 W. Among all the orientations, maximum time to reach a particular set point temperature was obtained for 0° which means this orientation has the maximum potential to keep the electronic device under safe limits. The orientation with 180° was found to have slightly poor performance due to the resistance offered gravity to convection currents. However, there was only

Fig. 3 Temperature versus time distribution for copper and nickel foam [7]

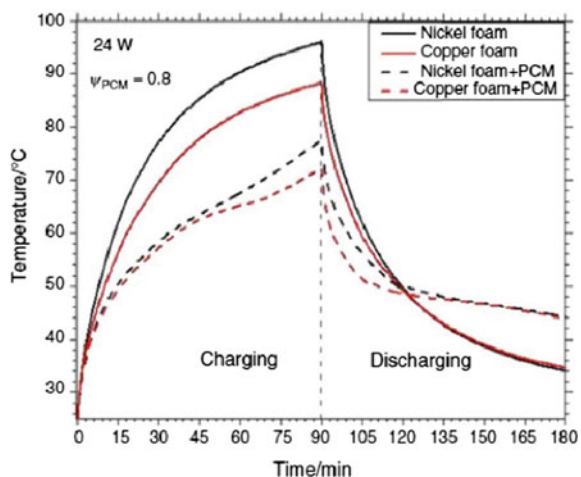
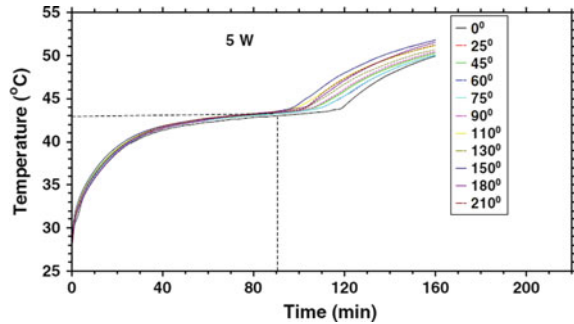


Fig. 4 Temperature versus time for different orientations [19]



a slight difference in the temperature distribution for all orientations as shown in Fig. 4 which lead the authors to conclude that the effect of orientation is not much significant in the heat sink having foam inserted phase change material.

Porosity and pore density Foam has voids present in it which can be measured in terms of porosity. More porosity means more voids that can be filled with air or any other material like phase change material. Foams with higher porosity make the heat sink lighter. Rehman and Ali [20] done an experimental study analysing the thermal performance of heat sink embedded in paraffin with two copper foam samples of different porosities and pore densities. Their results revealed that the copper foam with pore density of 15 PPI and 0.95 porosity showed more decrement in the base temperature as compared to another sample with pore density of 35 PPI and 0.97 porosity if phase change material has fixed volume fraction and power level. Tian and Zhao [21] varied the pore size and porosity of copper foam embedded in paraffin wax and found that the foam sample with 85% porosity has higher effective thermal conductivity than that of 95% porosity because of the more metallic structure present in it as shown in Fig. 5. Also, a smaller pore size (30 PPI) foam sample increases the area of contact between the paraffin wax and metallic structure, and hence, heat transfer rate increases.

In another experimental study, Qu et al. [22] varied the porosity and pore density independently, and Fig. 6 shows that the porosity influences the heat transfer rates more than pore density. Larger pore density means smaller pore size, and on fixing the pore density at 20 PPI, a smaller surface temperature was obtained for 0.90 porosity than that for 0.94 porosity, but the sample with 0.94 porosity took more time for melting.

4 Heat Dissipation by PCM with Nanoparticles

Addition of internal fins and metallic foams will improve thermal performance of phase change material, but it will increase weight of heat sink too. In order to make the heat sinks lighter, small quantity of nanoparticles are embedded in phase change

Fig. 5 Thermal conductivities for various pore sizes and porosities [21]

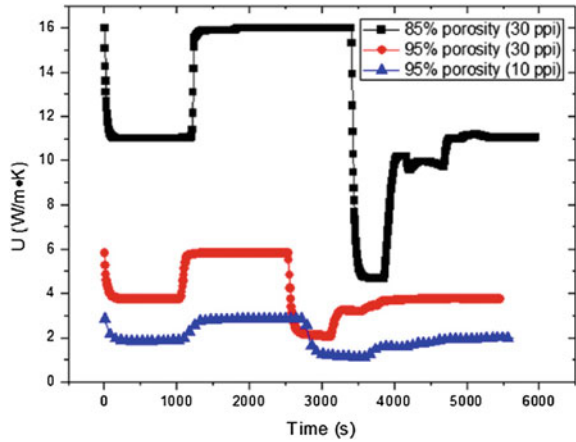
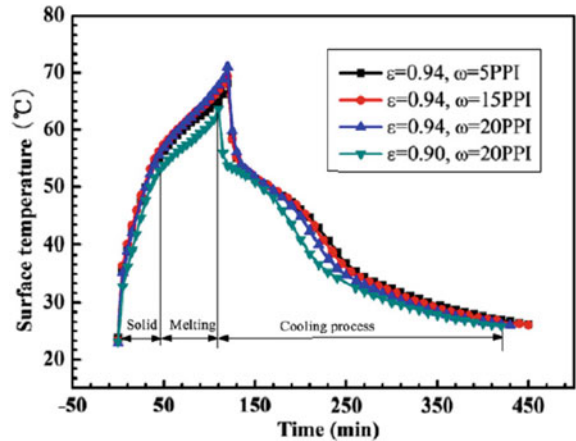


Fig. 6 Impact of pore density and porosity on surface temperature [22]



material. Nanoparticles have high thermal conductivity; thus, adding nanoparticles in the phase change material will improve its thermal conductivity, but it will increase its viscosity too. Increase in viscosity has negative effect as it dampers the velocity of natural convection currents and thus hinders the heat transfer rates. In order to use them for heat sink applications, the increase in thermal conductivity must be large enough to counter this negative effect too. This section deals with the effects of changing various parameters which are associated with the enhancement in thermal performance of phase change material with nanoparticles.

Power Level Time taken by phase change material depends strongly on the applied heat flux or power of the device. In a numerical study, Colla et al. [23] varied the power in step sizes of 10 W from 10 to 30 W for a phase change material-based heat sink enhanced with 0.5% and 1% alumina nanoparticles. Figures 7 and 8 revealed that the melting time for both RT 45 and RT 55 decreases and base temperature increases,

Fig. 7 Maximum junction temperature at different power levels [23]

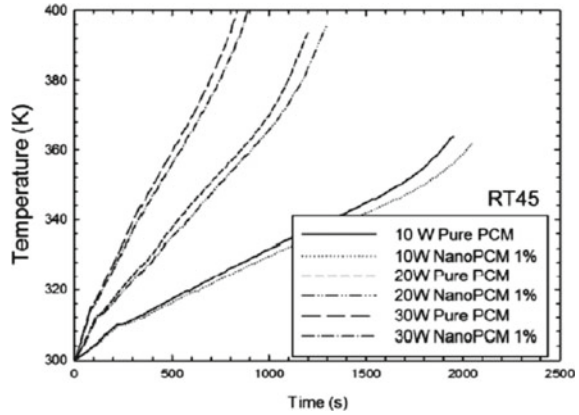
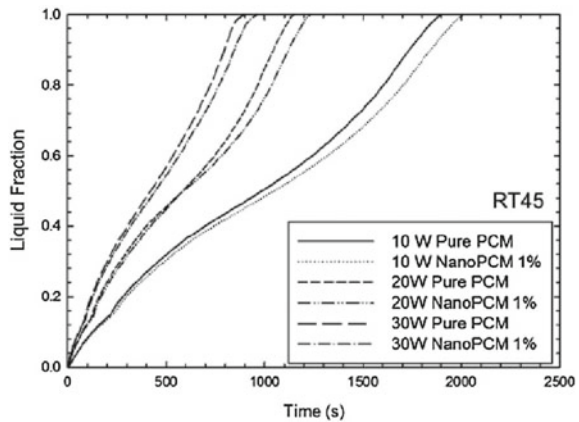


Fig. 8 Liquid fraction for different heat flow rates [23]



respectively, if the power level is increased from 10 to 30 W. Another experimental study conducted by Weinstein et al. [18] in which two power levels, namely 3 W and 7 W, were analysed for paraffin-based heat sink enhanced with nanofibres. They found that 3 W was not enough to completely melt the paraffin, but complete melting occurred for 7 W.

5 Weight Fraction

Various thermo-physical properties like thermal conductivity, dynamic viscosity, density, etc. of the nano-enhanced phase change material depend significantly on the weight fraction of the nanoparticles. In an experimental study, Weinstein et al. [24] took three graphite fibres, namely herringbone, ribbon, and platelet, and varied the weight fraction of nanofibers. The weight fraction of nanofibers that are taken into

Fig. 9 Thermal conductivity at different loading levels of Al_2O_3 in paraffin wax [25]

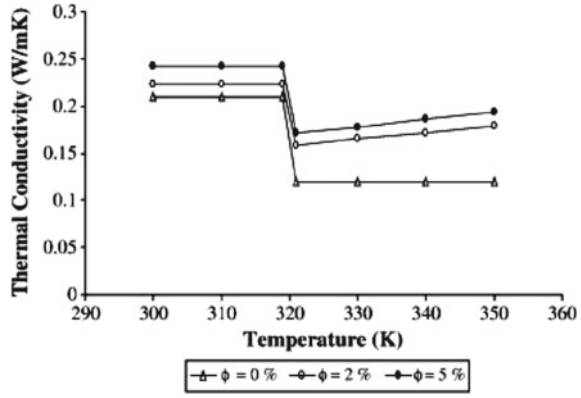
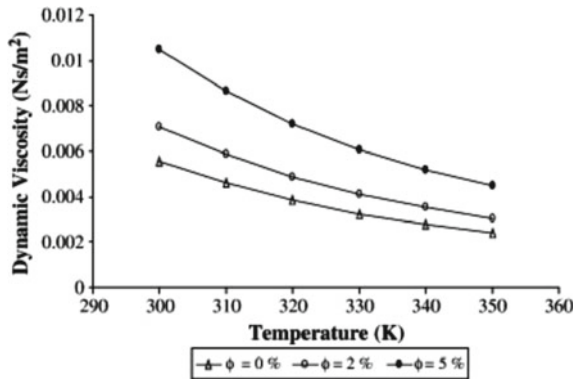


Fig. 10 Dynamic viscosity at different loading levels of Al_2O_3 in paraffin wax [25]



account were 0.25, 0.5, 1 and 5%. Their results revealed that adding nanoparticles in phase change material improves the thermal conductivity but up to a certain weight fraction only beyond which phase change material overheats as Rayleigh–Benard convection is suppressed.

In another numerical investigation, Arasu and Majumdar [25] studied the effect of varying volumetric concentrations of Al_2O_3 in paraffin wax. They found that both thermal conductivity and dynamic viscosity increase on increasing the concentration of the Al_2O_3 nanoparticles as illustrated in Figs. 9 and 10 (Table 1).

6 Conclusions

Low thermal conductivities of phase change materials delay the response of these materials to changing heat loads and lead to overheating in a confined area, particularly near the heat source. Among various techniques used for thermal conductivity enhancements, this article highlights the performance of foams embedded and

Table 1 Summary of some of the work performed by various authors

References	Nature of study	PCM	Foam/nanoparticles	Parameters
Marri and Balaji [26]	Experimental	n-eicosane	Open-cell aluminium foam	Porosity and PPI gradient
Zhao et al. [27]	Numerical	RT-82	Copper, aluminium, nickel and stainless steel foams	Pore size, interfacial gap thickness between the PCM and heated wall, pore height
Ferfera and Madani [28]	Experimental and numerical	Paraffin	Nickel and copper foams	Effective thermal conductivity, thermal diffusivity, and thermal effusivity
Li et al. [29]	Experimental and numerical	Paraffin	Open-cell copper foams	Porosity, pore density and internal temperature uniformity
Nie et al. [30]	Numerical 2D	RT-82	Copper foam	Geometrical modification
Zhou and Zhao [31]	Experimental	Paraffin wax RT 27 and calcium chloride hexahydrate	Copper foam and expanded graphite	Charging and discharging period, heat of fusion
Colla et al. [23]	Experimental and numerical	RT 45 and RT 55	Al ₂ O ₃	Power level, weight fraction and melting time
Weinstein et al. [24]	Experimental	Paraffin	Graphite fibres of different styles	Type of nanofiber, loading level and power level
Arasu and Majumdar [25]	Numerical	Paraffin	Al ₂ O ₃	Volumetric concentration of Al ₂ O ₃ and orientation of the heat sink and

nanoparticles embedded phase change material for heat sink applications based on various experimental, numerical and analytical studies. Following key conclusions are drawn from various published studies:

- Increasing power level harnesses the latent heat potential of phase change materials more, and hence, the effectiveness of using metallic foams increases.
- Orientation effects can be neglected for foam-enhanced phase change materials, but for nanoparticles-enhanced phase change materials, vertical orientation is preferred to take advantage of natural convection.

- Foam sample with higher pore density or smaller foam size has higher effective thermal conductivity and lower temperature difference because there is more contact area between phase change material and metal foam due to smaller size of foam.
- Addition of nanoparticles improves the thermal conductivity as well as other properties in which viscosity is important for heat convection. The magnitudes of viscosity and thermal conductivity decides whether conduction is dominant or convection.

References

1. Fok SC, Shen W, Tan FL (2010) Cooling of portable hand-held electronic devices using phase change materials in finned heat sinks. *Int J Therm Sci* 49(1):109–117
2. Li ZW, Lv LC, Li J (2016) Combination of heat storage and thermal spreading for high power portable electronics cooling. *Int J Heat Mass Transf* 1(98):550–557
3. Huang CH, Liu YC, Ay H (2015) The design of optimum perforation diameters for pin fin array for heat transfer enhancement. *Int J Heat Mass Transf* 1(84):752–765
4. Alawadhi EM, Amon CH (2000) Performance analysis of an enhanced PCM thermal control unit. In: *ITHERM 2000, the seventh intersociety conference on thermal and thermomechanical phenomena in electronic systems* (Cat. No. 00CH37069) 2000 May 23 (vol. 1, pp. 283–289). IEEE
5. Tomizawa Y, Sasaki K, Kuroda A, Takeda R, Kaito Y (2016) Experimental and numerical study on phase change material (PCM) for thermal management of mobile devices. *Appl Therm Eng* 5(98):320–329
6. Ge H, Liu J (2013) Keeping smartphones cool with gallium phase change material. *J Heat Transf* 135(5)
7. Ali HM (2019) Thermal performance analysis of metallic foam-based heat sinks embedded with RT-54HC paraffin: an experimental investigation for electronic cooling. *J Therm Anal Calorim* 6:1–2
8. Ashraf MJ, Ali HM, Usman H, Arshad A (2017) Experimental passive electronics cooling: parametric investigation of pin-fin geometries and efficient phase change materials. *Int J Heat Mass Transf* 1(115):251–263
9. Mancin S, Diani A, Doretto L, Hooman K, Rossetto L (2015) Experimental analysis of phase change phenomenon of paraffin waxes embedded in copper foams. *Int J Therm Sci* 1(90):79–89
10. Akula R, Gopinath A, Rangarajan S, Balaji C (2021) Experimental and numerical studies on heat transfer from a PCM based heat sink with baffles. *Int J Therm Sci* 159:106525
11. Bondareva NS, Sheremet MA (2018) Conjugate heat transfer in the PCM-based heat storage system with finned copper profile: application in electronics cooling. *Int J Heat Mass Transf* 1(124):1275–1284
12. Mahdaoui M, Hamdaoui S, Msaad AA, Kousksou T, El Rhafiki T, Jamil A, Ahachad M (2021) Building bricks with phase change material (PCM): thermal performances. *Constr Build Mater* 1(269):121315
13. Gin B, Farid MM (2010) The use of PCM panels to improve storage condition of frozen food. *J Food Eng* 100(2):372–376
14. Kansara K, Singh VK, Patel R, Bhavsar RR, Vora AP (2021) Numerical investigations of phase change material (PCM) based thermal control module (TCM) under the influence of low gravity environment. *Int J Heat Mass Transf* 1(167):120811
15. Huang R, Li Z, Hong W, Wu Q, Yu X. Experimental and numerical study of PCM thermophysical parameters on lithium-ion battery thermal management. *Energ Reports*

16. Xu R, Xia X, Wang W, Yu D (2020) Infrared camouflage fabric prepared by paraffin phase change microcapsule with good thermal insulating properties. *Colloids Surf A* 20(591):124519
17. Zhao J, Guo Y, Feng F, Tong Q, Qv W, Wang H (2011) Microstructure and thermal properties of a paraffin/expanded graphite phase-change composite for thermal storage. *Renew Energ* 36(5):1339–1342
18. Sahoo SK, Das MK, Rath P (2016) Application of TCE-PCM based heat sinks for cooling of electronic components: a review. *Renew Sustain Energ Rev* 1(59):550–582
19. Baby R, Balaji C (2013) Experimental investigations on thermal performance enhancement and effect of orientation on porous matrix filled PCM based heat sink. *Int Commun Heat Mass Transf* 1(46):27–30
20. Ali HM (2018) Experimental investigation on paraffin wax integrated with copper foam based heat sinks for electronic components thermal cooling. *Int Commun Heat Mass Transf* 1(98):155–162
21. Tian Y, Zhao CY (2011) A numerical investigation of heat transfer in phase change materials (PCMs) embedded in porous metals. *Energy* 36(9):5539–5546
22. Qu ZG, Li WQ, Wang JL, Tao WQ (2012) Passive thermal management using metal foam saturated with phase change material in a heat sink. *Int Commun Heat Mass Transfer* 39(10):1546–1549
23. Colla L, Ercole D, Fedele L, Mancin S, Manca O, Bobbo S (2017) Nano-phase change materials for electronics cooling applications. *J Heat Transf* 139(5)
24. Weinstein RD, Kopec TC, Fleischer AS, D'Addio E, Bessel CA (2008) The experimental exploration of embedding phase change materials with graphite nanofibers for the thermal management of electronics. *J Heat Transf* 130(4)
25. Arasu AV, Mujumdar AS (2012) Numerical study on melting of paraffin wax with Al₂O₃ in a square enclosure. *Int Commun Heat Mass Transfer* 39(1):8–16
26. Marri GK, Balaji C (2021) Experimental and numerical investigations on the effect of porosity and PPI gradients of metal foams on the thermal performance of a composite phase change material heat sink. *Int J Heat Mass Transf* 164:120454
27. Zhao C, Opolot M, Liu M, Bruno F, Mancin S, Flewell-Smith R, Hooman K (2021) Simulations of melting performance enhancement for a PCM embedded in metal periodic structures. *Int J Heat Mass Transf* 168:120853
28. Ferfera RS, Madani B (2020) Thermal characterization of a heat exchanger equipped with a combined material of phase change material and metallic foams. *Int J Heat Mass Transf* 1(148):119162
29. Li WQ, Qu ZG, He YL, Tao WQ (2012) Experimental and numerical studies on melting phase change heat transfer in open-cell metallic foams filled with paraffin. *Appl Therm Eng* 1(37):1–9
30. Nie C, Liu J, Deng S (2021) Effect of geometry modification on the thermal response of composite metal foam/phase change material for thermal energy storage. *Int J Heat Mass Transf* 165:120652
31. Zhou D, Zhao CY (2011) Experimental investigations on heat transfer in phase change materials (PCMs) embedded in porous materials. *Appl Therm Eng* 31(5):970–977

Experimental Study of Integrated Solar Dryer with and Without Reversed Absorber and Reflector



Vijay R. Khawale, Bhojraj N. Kale, and Sandeep Lutade

Abstract The aim of manuscript writing is to recommend a solar crop dryer with reversed absorber and reflector which collect the maximum possible solar emission. For experimentation, model was made adjustable such that it can satisfy the required conditions. The two types of solar dryer used are (1) Solar dryer without reversed absorber and reflector (2) Solar dryer with reversed absorber and reflector. The average collector efficiency (η_c), drying efficiency (η_d) and the picking efficiency (η_p) of multi-pass SCD with reversed absorber and reflector (SD6) values were 34%, 49% and 64%, respectively. Excel software was used to find the changes in moisture content with the time as well as constants by graphical method. These values show that SD6 is more capable than another solar dryer. The experimental data are more suitable for Pages' model than other models. Pages' model gives the best results with the maximum value of R^2 and the minimum value of MBE and RMSE. It has been found that SD6 is the most effective solar dryer and can be used to dry other agriculture food products also.

Keywords Flat plate collector · Solar crop dryer · Reversed absorber · Reflector · Red chilli

Nomenclature

DM	Drying model
DSD	Direct solar dryer
ISD	Indirect solar dryer
MC	Moisture content
SCD	Solar crop dryer

V. R. Khawale (✉)
Mechanical Department, YCCE, Nagpur, India
e-mail: vijay.khawale46@gmail.com

B. N. Kale · S. Lutade
Mechanical Department, DBACER, Nagpur, India

SD	Solar dryer
SD1	Single glazing solar dryer
SD2	Double glazing solar dryer
SD3	Multi-pass solar dryer
SD4	Single glazing SCD with reversed absorber and reflector
SD5	Double glazing SCD with reversed absorber and reflector
SD6	Multi-pass SCD with reversed absorber and reflector

1 Introduction

Drying is the process of removing moisture. Drying is a very important process to preserve an agricultural product for a long time because of which an agricultural product may be available in all the season. Open sun drying method is always used by a farmer to dry all agricultural products. Due to limitations such as no uniform drying of agricultural product and longer time required for drying and uncleanness during drying process, this method is not suitable for mass production. Conventional dryers can be used to dry an agricultural product. In conventional dryer, hygienic condition can be maintained, but it is costly due to the use of fuel as an energy source. Solar dryer is an emerging technique which has overcome these limitations. Solar dryer technology has various advantages like simple in design, low-cost energy source and maintain hygienic condition. The critical study of solar drying processes has great practical and economic importance. In designing the process, study of fundamentals and mechanisms, moisture level in the product and temperature required to dry the product are critical factors [1]. Many researchers have presented theoretical models of drying process in which heat and mass transfer are studied. Thin-layer models and simulations help for designing new dryer with improving its usefulness in existing applications [2]. In thin-layer model, the moisture in agriculture product can be measured at any time, and correlation can be developed with drying period. Most of the researchers have developed a specific type of solar dryer and conducted experimentation for specific type of agriculture product. Analysis has been done without putting any evidence that this dryer can be used for other agricultural product. Many researchers have proposed a different type of solar dryer which are classified into direct, indirect and hybrid solar dryer [3, 4]. SCD is an example of domestic and DSD where solar radiation direct falls on the food product [5]. In a direct solar dryer, the food product placed in the thin layer on perforated trays and opened to the direct solar emission. In ISD, the air gets heated initially in the collector, and then, it has passes through the product. Indirect solar dryer functions more effectively and can control the drying process. Shell dryer is an example of ISD present in the literature [6]. Indirect solar dryer with natural air circulation has been specially designed for particular type of agricultural product and may be used with additional source of energy to improve its performance. Singh et al. [7] have developed an efficient solar dryer specially to dry fruits, spices and vegetables and has a drying

capacity of about 1 kg per day. The solar dryer is featured by direct, indirect and hybrid with forced or natural circulation of air. For collecting maximum energy, the solar air collector is always inclined due south so that sun rays strike perpendicular throughout the day on collector. Manual tracking may be alternative, but it is not a practical. Solar air heater integrated with tracking system can be used to collect maximum heat energy, but it is very expensive. The solar air heater is designed to absorb the maximum solar radiation on a sunny day. Many researchers have proposed a new type solar dryer model, and the researcher has developed a specific type of solar dryer and conducted experimentation for specific type of agriculture product. Analysis has been done without putting any evident that this dryer can be used for other agriculture product. Many researchers have proposed a different type of solar dryer which are classified into direct, indirect and hybrid solar dryer [3, 4]. SCD is an example of domestic and DSD where solar radiation direct falls on the food product [5]. In a direct solar dryer, the food product placed in thin layer on perforated trays and opened to the direct solar emission. In ISD, the air gets heated initially in the collector, and then, it has passes through the product indirect solar dryer has functions more effectively and can be control over the drying process. Shell dryer is an example of ISD present in the literature [6]. Indirect solar dryer with natural air circulation has been specially designed for particular type of agriculture product and may be used with additional source of energy to improve the performance. Singh et al. [7] have been developed an efficient solar dryer specially used to dry fruits, spices and vegetables and drying capacity of about 1 kg per day. The solar dryer is featured by direct, indirect and hybrid with forced or natural circulation of air. For collecting maximum energy, the solar air collector always keeps inclined due south so that sunrays must strike perpendicular throughout the day on collector. Manual tracking may be alternative, but it is not a practical. Solar air heater integrated with tracking system can be used to collect maximum heat energy, but it is very expensive. The solar air heater is designed to absorb the maximum solar radiation in sunshine day. Using of single glazing, double glazing and multi-pass solar air collector can also improve the efficiency. Many researchers proposed new type solar dryer model and present a nature of drying behaviour of agricultural product [8–11]. Thin-layer drying model can be used easily as well as it gives accurate results. However, the rate of drying depends on the temperature of air and drying rate can be kept constant if temperature of air is maintained. The mathematical model [12] was used to examine the effect of various air passes within the SAC on the thermal efficiency and the temperature rise at different air mass flow rates. The result shows that the thermal efficiency of the SAC increases rapidly as the mass flow rate is increased. But, it is not possible to maintain the temperature constant throughout the day. Mwithiga and Kigo [13] have noted the effectiveness of tracking the sun on increasing the drying rate, but it is a costly affair. Fatouh et al. [14] observed the effect of drying air temperature and air velocity on the drying characteristics of the agricultural product. The drying rate can be achieved if considered parameters are within the limits. Singh et al. [15] noted that the leafy vegetables are dried in a short period than other vegetables. Abhay Bhanudas Lingayata, Chandramohana et al. [16] had designed a new indirect type of SD. From experimentation, it is interpreted that the drying rate is

dependent on air temperature and velocity. Vidhana et al. [17] had designed and constructed a mixed type of SCD and studied its performance by using a tomato. Nabnean et al. [18] had used a parabolic-shaped polycarbonate plate cover over a flat plate collector and noticed that the drying time is reduced significantly. Spall et al. [19] presented an innovative SD integrated with inclined reflective north wall (RNW). Result shows reduced drying time up to 20 and 15% under natural and forced convection modes, respectively. Hybrid indirect passive (HIP) solar dryer [20] suggested mass drying against a conventional active-mode solar photovoltaic and electric (SPE) dryer with an auxiliary thermal-backup and open sun drying (OSD). Mixed mode forced convection type (MFSCD) [21] takes less drying time, better dryer efficiency, improved quality of product than OSD, and payback period was found 0.65 Yrs. The [22] FPSAC examines for different air flow rates, found a strong positive effect of solar intensity on the temperature of absorber plate, glass cover and outlet air of collector. Solar cooker equipped with internal reflectors and a tracking-type bottom parabolic reflector (TBPR) [23] is able to attain the intermediate temperatures up to 140–150 °C. The spherical dimple plate solar air heater (SDPSAH), IIT (ISM) Dhanbad, India [24] shows the highest heat transfer rate, which is about 1.51 to 1.64 times higher than the corresponding FPSAH. Maiti et al. [25] developed a natural convection batch-type solar dryer fitted with North–South reflectors. At a high solar radiation, the collector efficiency had increased by 18.5%, and MC reduced from 83 to 12% (w.b) in 5 h. In multi-shelf side loading inclined solar cooker-cum-dryer (ISCCD) [26] integrated with single reflector north facing booster mirror (NFBM) shows significant improvement in performance of both cooking and drying operations particularly in winter months. Although this solar dryer had been developed for multi-purpose agricultural food drying, drying tests are still needed for specific agricultural products in order to study its performance and viability to use. In addition, solar drying can be considered as an advancement of natural sun drying, and it is an efficient technique of utilizing solar energy. Use of single glazing, double glazing and multi-pass solar air collector can also improve its efficiency. Glazing the dryer and solar air heater can be a practical solution.

The objective of this work is to recommend a SCD with reversed absorber and reflector to collect the maximum possible solar radiation. A novel SD has been projected by taking a reference of reported solar dryer in literature [27, 28] and introduces some new features which help to maximize the solar energy absorption. The principal modification was that, it includes indirect type of solar dryer using forced convection heat transfer with single pass, double pass and multi-pass arrangement. Firstly, it was very important to reduce the variation in air temperature throughout the day. Secondly, the drying period was long because drying started from 8 am to 5 pm for using the whole sunny day. The dryer was constructed, performed the experiment and compared with other solar dryers' performance. The drying characteristic was investigated by performing an experiment by using chilli.

2 Material and Methods

2.1 Experimental Apparatus

The size of solar air collector was $2 \times 1 \times 0.10$ m. Two black-painted absorber plates of aluminium were used. First, absorber plate was inclined at 30 degree to earth in south direction. Second absorber plate was horizontal and parallel with earth which was used as a bottom of collector and surrounded by a reflector. 4-mm-thin clear glass had been used as a glazing over top of solar collector. The solar collector integrated with a drying box of size $1 \times 1 \times 1$ m. All sides of box were insulated because of wood material. Two perforated trays of 5 kg capacity were used to store the chilli. Air fan was provided at the top side of dryer to control the air flow. This model was made adjustable such that it can work as a single pass, double pass and triple pass as well as with reflector and without reflector solar dryer. Reflector was of aluminium material. The solar heater is just south, tilted 30 degrees to the earth (Fig. 1).

2.2 Experimental Procedure

During the light hours, from 8 am to 6 pm, experimentation was carried out on designed solar dryer by using red chilli, and evaluation of the performance was noted. The two types of solar dryer were used, i.e. (1) Solar dryer without reversed absorber and reflector (2) Solar dryer with reversed absorber and reflector. 10 kg of red chilli was washed by potable water, and then, it was stored on a thin-layered perforated trays. Fan was started and set such that it maintains a 1 m/s velocity of air during drying process. Experimental readings were taken at an interval of 1 h and noted solar intensity, ambient air temperature, collector outlet air temperature, weight of chilli and air temperature at the dryer outlet. Measure the relative humidity of ambient air and dry air with a wet bulb hygrometer.

2.3 Performance Analysis

The performance of the solar dryer can be assessed from the thermal efficiency of collector or drying rate of the agricultural product [29].

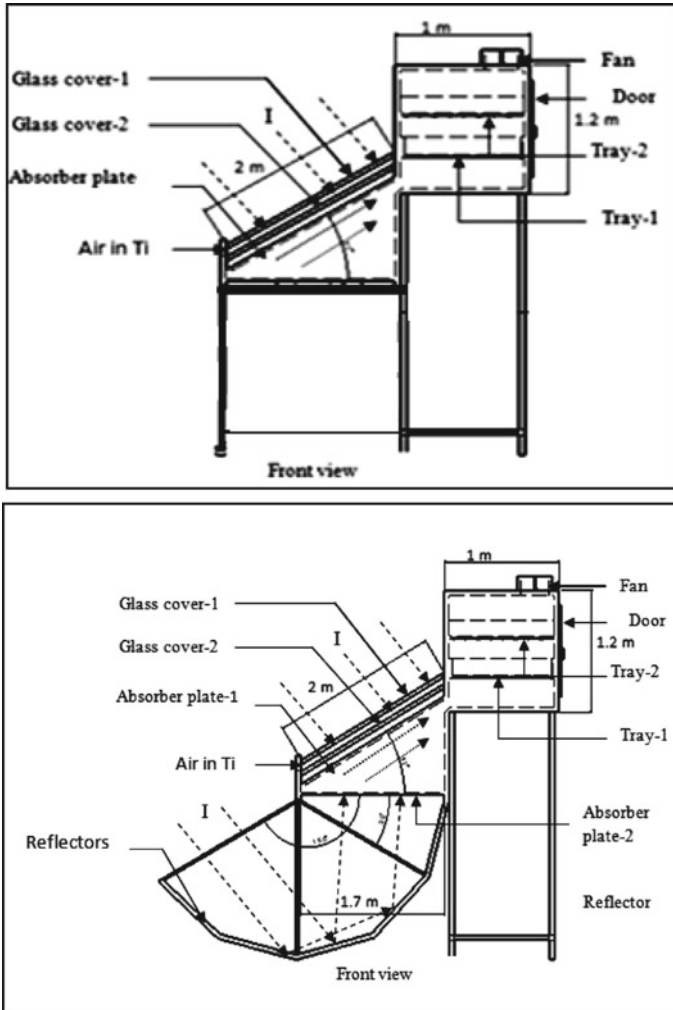


Fig. 1 a solar dryer without reversed absorber and reflector **b** solar dryer with reversed absorber and reflector

3 Drying Rate

Drying rate depends on various factors which have a very monotonous and time-consuming measuring and calculation. In thin-layered drying, Pathak et al. [30] noted that temperature of air, initial moisture percentage in product, velocity and relative humidity of air are various factors over which drying rate vary. For various products, drying rates have been successfully analysed by using Pages' equation [31]. The equation is as follows;

$$M_r = e^{-zt^n} \tag{1}$$

where

M_r —moisture ratio, t —drying time in hours, z and n are drying constants.

Moisture ratio given by equation:

Moisture Ratio

$$M_r = \frac{M_t - M_e}{M_o - M_e} = e^{-zt} \tag{2}$$

where

M_t —Instantaneous Moisture Content (% db),

M_e —Equilibrium Moisture Content (% db),

M_o —Initial Moisture Content (% db).

Following equation may be used to calculate moisture content on dry basis M_t (% db) [32]:

$$M_t = \frac{(W_t - W_d)}{W_d} \tag{3}$$

And the equation used to calculate moisture content on wet basis (% wb):

$$M_t = \frac{(W_t - W_d)}{W_t} \tag{4}$$

where

W_t —Weight of chilli at a time (t) (kg)

M_d —Mass of dry chilli (kg)

From exponential and Newtonian model [33], Page introduced an equation as

$$\text{Drying rate} \left(\frac{dm}{dt} \right) = -z(M_t - M_e) \tag{5}$$

z is drying rate constant, per hour.

By distinguishing, the drying model can be explained as follows

$$M_z = e^{-zt^n} \tag{6}$$

In deriving this equation, the resistance of water movement and gradient in the material is ignored. If the drying rate decreases at a constant temperature, pressure and humidity of the air, this equation is valid [34], which is characteristic of products with low moisture content (e.g. grains), negative sign of is important which shows the characteristics of drying process [35].

Moisture ratio

$$M_r = \frac{M_t - M_e}{M_o - M_e} = e^{-zt} \quad (7)$$

Collector efficiency

By using formula

$$\eta_c = \frac{\dot{m}a C_{pa} (T_o - T_i)}{[(I * A_{c1}) + (I_{eff} * A_{c2})]} \quad (8)$$

where

- $\dot{m}a$ —Mass of air flowing in collector and dryer per unit time
- C_{pa} —Specific heat of air at constant pressure
- T_o —Air temperature at collector exit
- T_i —Inlet temp. of air at collector entrance
- I —Solar emission on absorber plate I (Hourly)
- A_{c1} —Area of absorber plate-I
- I_{eff} —Actual solar emission on reversed absorber plate-II (Hourly)
- $(I_{eff} - \rho * I * A_R)$
- ρ —Reflectivity of reflector
- A_R —Area of reflector
- A_{c2} —Area of absorber plate-II

Dryer thermal efficiency

$$\eta_d = \frac{M_w H_{fg}}{\dot{m}a C_{pa} (T_d - T_i)} \quad (9)$$

where

- $\dot{m}a$ —Mass of air flowing per unit in the dryer
- C_{pa} —Specific heat of air at constant pressure
- T_d —Temperature of air in dryer
- T_i —Inlet air temperature at collector equal to ambient temp
- H_{fg} —Latent heat of water (evaporation)
- M_w —Mass of evaporated water.

Dryer pick-up efficiency

$$\eta_p = \frac{M_w}{\dot{m}a \Delta_t (W_{ce} - W_{ci})} \quad (10)$$

where

- M_w —Mass of evaporated water in time Δ_t
- $\dot{m}a$ —Air mass flow rate

W_{ce} —Humidity of air at dryer exit (Absolute)
 W_{pa} —Humidity of air at dryer inlet (Absolute)

4 Drying Model

Use the following model to find the best model described the characteristics of drying curves for drying of chilli in solar dryer [36–39].

Following equations were used to evaluate MBE and RMSE.

$$MBE = \frac{1}{N} \sum_{i=1}^N (M_{rpre, i} - M_{rexp, i})^2 \tag{11}$$

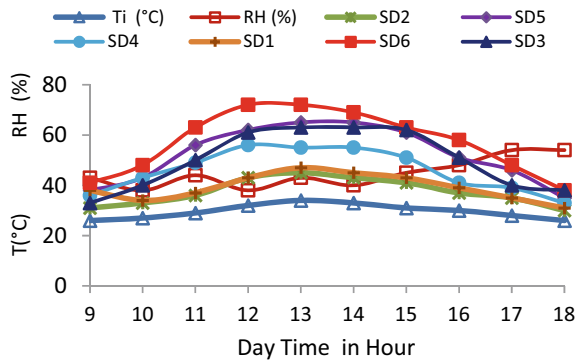
$$RMSE = \sqrt{\left[\frac{1}{N} \sum_{i=1}^N (M_{rpre, i} - M_{rexp, i})^2 \right]} \tag{12}$$

The best model is selected from the mean deviation error and the root mean square error of the determination coefficient R^2 . The higher R^2 value and the lower MBE and RMSE values are used to select the best model [40].

5 Results and Discussion

Six different types of solar dryers are used to dry the red chilli. The test was conducted on a sunny day. In a typical experimental run, the deviation in ambient temperature, relative humidity and air temperature at collector outlet of different types of solar dryer are shown in Fig. 2. Graphical presentation shows that the temperature of air rise in SD6 is more reducing the drying period of agricultural product.

Fig. 2 Deviation of relative humidity, ambient temperature and final temperature with day time (hr)



The average temperature of drying air was recorded about 57 and 50 °C for SD6 and SD5, respectively, at the inlet of the drier. During peak daylight hours, maximum temperature of drying air was recorded about 71 °C at the drier inlet. From the air temperature curves, it can be observed that the invented dryer may be used to dry a variety of farming product.

During the peak light hours, maximum intensity of solar energy was recorded about 905 W/m². The average dry and wet bulb temperature were recorded 32 °C and 25.8 °C correspondingly. The recorded relative humidity of air was about 32% at inlet and 70% at the exit of solar dryer chamber. Figures 3, 4 and 5 shows a variation in collector, drying and pick-up efficiency with a solar flux for all the dryers.

From Figs. 3, 4 and 5, it was observed that at an average value of $I_s = 675 \text{ w/m}^2$, $T_a = 34 \text{ }^\circ\text{C}$ and $m_a = 1.614 \text{ kg/min}$, collector efficiency (η_c) of SD6 & SD3 was 36% and 30%, respectively. It was noted that at an average value $I_s = 427 \text{ w/m}^2$, $T_a = 28 \text{ }^\circ\text{C}$ and $m_a = 1.614 \text{ kg/min}$, collector efficiency (η_c) values of SD5 & SD2 were 29.7% and 25%, respectively, and the collector efficiency values of SD1 and SD4 were 19% and 26%, respectively.

It was observed that dryer thermal efficiency (η_d) and pick-up efficiency (η_p) at an average value $I_s = 675 \text{ w/m}^2$, $T_a = 34 \text{ }^\circ\text{C}$ and $m_a = 1.614 \text{ kg/min}$, of SD6 and SD3,

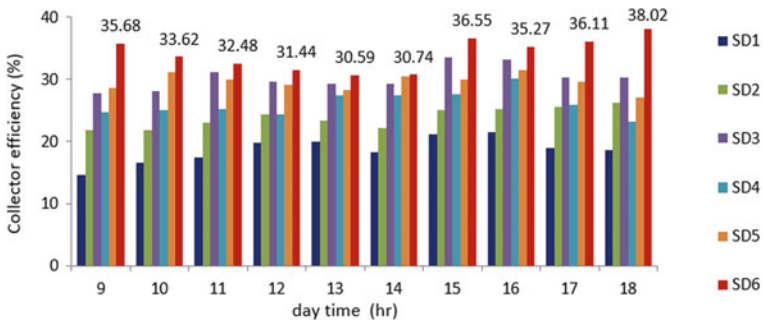


Fig. 3 Variation of collector efficiency with time (hr)

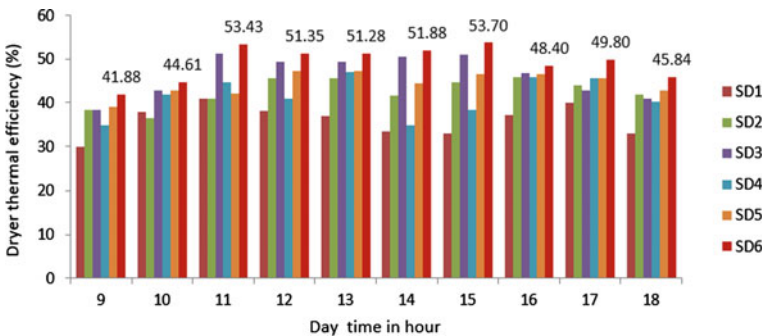


Fig. 4 Variation of drying thermal efficiency with time (hr)

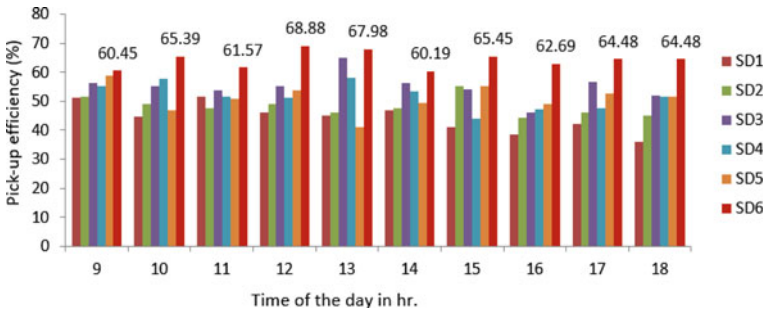


Fig. 5 Variation of pick-up thermal efficiency with time (hr)

were 49% and 46%; 64% and 55%, respectively. At an average value $I_s = 427\text{w/m}^2$, $T_a = 28^\circ\text{C}$ and $m_a = 1.614\text{ kg/min}$ the dryer thermal efficiency (η_d) and pick-up efficiency (η_p) of SD5 and SD2 were 45.5% and 38%; 54% and 50%, respectively. Dryer thermal efficiency (η_d) and pick-up efficiency (η_p) of SD4 and SD1 were 47.8% and 37.7%; 55% and 45%, respectively. From the above experiment, it was analysed that solar air heater with reversed absorber and reflector was more efficient than conventional SCD. This observation was validated with earlier studies that the heat gain by reversed absorber plate is noteworthy [41, 42].

The change of MC in red chilli with time for SD1, SD2, SD3, SD4, SD5 and SD6 is graphically represented in Fig. 6. The MC in fresh red chilli was nearly similar during all tests whereas the initial value was 4.1 kg/kg (db) and 3.9 kg/kg (db) for SD4 and SD1, respectively. From Fig. 7, it is manifested that drying rate more than SD1 in SD4. These results ensure that SD4 used forced convection and attained higher air temperature which increases moisture removal rate from red chilli. From Fig. 7, it is noted that, drying rate continuously goes on decreasing in all the cases, and drying period is less for SD4 as compare to SD1.

Figure 6 shows that in SD5, MC was for shorter period in the red chilli above the equilibrium MC than SD2. Figure 7 shows the contour of drying rate versus drying time. It was observed that the drying rate in SD5 is greater than SD2 due to higher

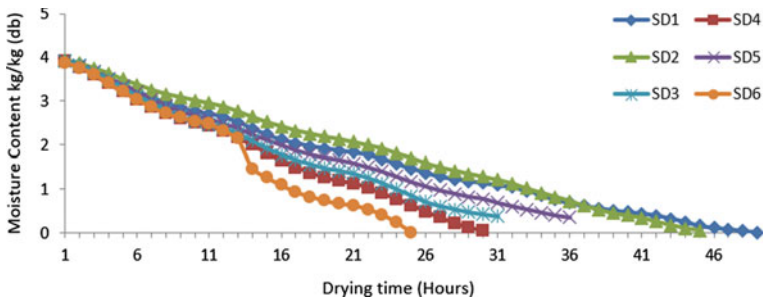


Fig. 6 Profile of the moisture content versus drying time

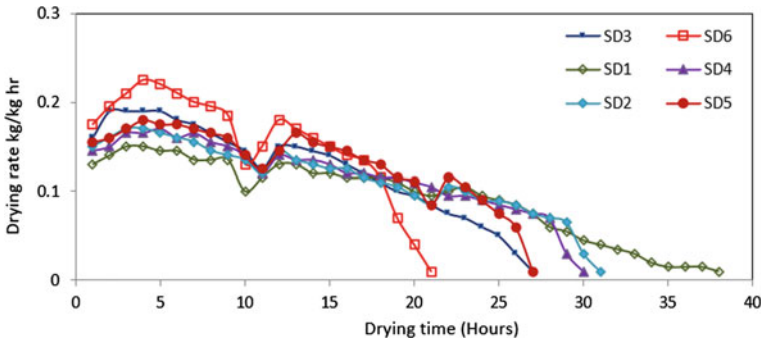


Fig. 7 Profile of drying rate versus drying time

drying air temperature and increases vapour pressure in the red chilli which reduces the effect of relative humidity during sunny day [43].

From Figs. 6 and 7, it is also observed that the MC in red chilli above the equilibrium MC in SD6 is reduced remarkably than SD1, SD2, SD3, SD4 and SD5. Drying rate is found to be higher in SD6 than in SD1, SD2, SD3, SD4 and SD5 because of high drying temperature and vapour pressure in the chilli which increased the rate of evaporation. Losses of heat to surrounding were reduced due to use of two glazing and air gain additional heat from reversed absorber [28].

Experimental data of drying chilli were used to describe the DM. Newton DM, Page DM and Henderson & Pabis DM was fitted with the experimental data of drying chilli. In the DM, the data of MC and drying time had been used. In all models, Excel software was used to find the changes in moisture content with the time as well as constants by graphical method. The best DM was decided from higher value of R² and lowest value of MBA and RMSE [44]. The best drying model was selected out of three drying models by drying red chilli, where constant mass flow rate was maintained. Table 1 shows the experimental constant values which fits in the DM. From Table 1, it has been noted that Pages’ DM is the most fitted DM to describe the drying curves of red chilli. The experimental data were fit to the Page’s DM than Newton’s and Henderson & Pabis DM. The Page’s DM gives best result with higher value of R² and lower values of MBE and RMSE (Table 2).

Table 1 Drying models

S. No	Model	Equation
1	NEWTON	$M_r = e^{-zt}$
2	PAGE	$M_r = e^{-zt^n}$
3	HENDERSON and PABIS	$M_r = a * e^{-zt^n}$

Table 2 Constants value fitting of DM

S. No	Solar dryer type	Thin-layer DM	Constant	DM constant	MBE	RMSE	R ²	
1	SD1	NEWTON	Z	0.060	0.00132	0.036	0.990	
			PAGE	Z	0.027	0.0020	0.014	0.998
				N	0.1212			
		HEDERSON and PABIS	A	0.8547	0.0173	0.132	0.990	
			Z	0.0610				
2	SD2	NEWTON	Z	0.080	0.00364	0.067	0.97	
			PAGE	Z	0.032	0.00044	0.021	0.994
				N	1.22			
		HEDERSON and PABIS	A	1.229	0.00364	0.060	0.97	
			Z	0.080				
3	SD3	NEWTON	Z	0.070	0.00194	0.044	0.99	
			PAGE	Z	0.0386	0.0001	0.009	0.99
				N	1.186			
		HEDERSON and PABIS	A	1.160	0.00108	0.033	0.994	
			Z	0.077				
4	SD4	NEWTON	Z	0.070	0.00382	0.062	0.974	
			PAGE	Z	0.029	0.00026	0.016	0.997
				N	1.252			
		HEDERSON and PABIS	A	1.492	0.00332	0.058	0.974	
			Z	0.075				
5	SD5	NEWTON	Z	0.08	0.00303	0.055	0.97	
			PAGE	Z	0.038	0.00114	0.0034	0.98
				N	1.161			
		HEDERSON and PABIS	A	1.230	0.00301	0.055	0.974	
			Z	0.080				
6	SD6	NEWTON	Z	0.1	0.0058	0.243	0.96	
			PAGE	Z	0.0398	0.004	0.021	0.995
				N	1.267			
		HEDERSON and PABIS	A	1.276	0.00379	0.062	0.969	
			Z	0.102				

6 Conclusion

After experimentation and comparison, it has been observed that the significant improvement found in solar dryer with reversed absorber and reflector was in thermal, drying and pick-up efficiency. Further, it has been pointed out that, at constant air

flow rate, the solar collector inlet and exit air temperature difference increases with the rise in solar irradiation.

The average collector efficiency (η_c) values are 26.11%, 29.56% and 34% for the SD4, SD5 and SD6, respectively. It displays that the collector efficiency (η_c) of SD6 is more than SD4 and SD5. The drying efficiency (η_d) values are 41%, 44% and 49%, and pick-up efficiency (η_p) value are 51%, 55% and 64% for the SD4, SD5 and SD6, respectively. These value shows that SD6 is more capable than SD4 and SD5.

Experimental data of drying chilli were used to describe the drying model. In all models, Excel software was used to find the changes in MC with the time as well as constants by graphical method. The best DM was decided from the highest value of R^2 and lowest value of MBA and RMSE. Table 1 shows the experimental constant values which is fitting in the DM. It has been noted that Pages' DM is the most fitted DM. The experimental data were appropriate for the Page's DM than Newton's and Henderson & Pabis DM. The Page's DM gives best result with the highest value of R^2 and lowest values of MBE and RMSE.

Finally, it has been found that SD6 is the most effective solar dryer than SD1, SD2, SD3, SD4 and SD5.

Solar dryer with reversed absorber and reflector is capable of reducing drying time as compared to the other solar dryer and OSD. In addition, the red chilli was completely protected from insects, dust and rain. This dryer can also be used to dry other agricultural food products and the products which are sensitive to the exposure of solar radiation.

In present study, it is difficult to cover the complete surface area of reflector by solar radiation during light hours. In future study, there is a need to develop a tracking system for a reflector to cover all the surface area of the reflector by solar radiation throughout the day.

References

1. McMinn WAM (2006) Thin-layer modelling of the convective, microwave, microwave convective and microwave- vacuum drying of lactose powder. *J Food Eng* 72:113–23
2. Kardum JP, Sander A, Skansi D (2001) Comparison of convective, vacuum and microwave drying of chlorpropamide. *Drying Technol* 19(1):167–83
3. Garg HP, Sharma S (1990) Mathematical modeling and experimental evaluation of a natural convection solar dryer. In: *Proceedings of 1st world renewable energy congress*, Reading, UK vol 2, p 904–8
4. Hallak H, Hilal J, Hilal F, Rahhal R (1996) The staircase solar dryer: design and characteristics. *Renew Energy* 7:177–83
5. Lawand TA (1996) A solar cabinet dryer. *Solar Energy* 10:158–64
6. Fournier M, Guinebault A (1995) The "shell" dryer-modeling and experimentation. *Renew Energy* 6:459–63
7. Singh PP, Singh S, Dhaliwal SS (2006) Multi-shelf domestic solar dryer. *Energy Convers Manage* 47:1799–815
8. Simal S, Femenia A, Garau MC, Rossello C (2005) Use of exponential, pages and diffusional models to simulate the drying kinetics of kiwi fruit. *J Food Eng* 66(3):323–8

9. Midilli A, Kucuk H (2003) Mathematical modeling of thin layer drying of pistachio by using solar energy. *Energy Convers Manage* 44(7): 1111–22
10. El-Beltagy A, Gamea GR (2007) Amer Essa AH Solar drying characteristics of strawberry. *J Food Eng* 78(2):456–64
11. Akpınar EK, Sarsilmaz C, Yildiz C (2004) Mathematical modeling of a thin layer drying of apricots in a solar energized rotary dryer. *Int J Energy Res* 28(8):739–52
12. Al Mahdi N, Al Baharna NS (1991) Thermal performance of an *n*-pass solar air heater. *Renew Energy* 1(3–4):527–532
13. Mwithiga G, Kigo SN.[2006], Performance of a solar dryer with limited sun tracking capability. *Journal of Food Engineering*.74:247–52.
14. Fatouh M, Metwally MN, Helali AB, Shedid MH (2006) Herbs drying using a heat pump dryer. *Energy Convers Manage* 47:2629–2643
15. Singh H, Singh AK, Chaurasia PBL, Singh A (2005) Solar energy utilization: a key to employment generation in the Indian Thar Desert. *Int J Sustain Energy* 24(3):129–42
16. Lingayata ABVP, Chandramohana VRK, Rajua VM (2020) A review on indirect type solar dryers for agricultural crops – Dryer setup, its performance, energy storage and important highlights. *Appl Energy* vol 258:114005
17. López-Vidaña Erick César César-Munguía Ana Liliab García-Valladares Octavio Pilatowsky Figueroa Isaac Brito Orosco Rogelio (2020) Thermal performance of a passive, mixed-type solar dryer for tomato slices (*Solanum lycopersicum*). *Renew Energy* 147:845–855
18. Nabnean S, Nimnuan P (2020) Experimental performance of direct forced convection household solar dryer for drying banana. *Case Stud Thermal Eng* 22:100787
19. Spall S, Sethi VP (2020) Design modeling and analysis of efficient multi-rack tray solar cabinet dryer coupled with north wall reflector. *Solar Energy* vol 211, pp 908–919
20. Ssemwanga M, Makule E, Kayondo SI et al (2020) Performance analysis of an improved solar dryer integrated with multiple metallic solar concentrators for drying fruits. *Solar Energy* vol 204, pp 419–428
21. Lakshmi DVN, Kumar PM, Layek A, Nayak PK (2019) Performance analyses of mixed mode forced convection solar dryer for drying of stevia leaves. *Solar Energy* vol 188, pp 507–518
22. Rani P, Tripathy PP (2020) Thermal characteristics of a flat plate solar collector: Influence of air mass flow rate and correlation analysis among process parameters. *Solar Energy* vol 211, pp 464–477
23. Tawfik MA, Sagade AA, Palma-Behnke R, El-Shal HM, Abd Allah WE (2021) Solar cooker with tracking-type bottom reflector: an experimental thermal performance evaluation of a new design. *Sol Energy* 220:295–315
24. Perwez A, Kumar R (2019) Thermal performance investigation of the flat and spherical dimple absorber plate solar air heaters. *Solar Energy* 193:309–323
25. Maiti S, Patel P, Vyas K, Eswaran K, Ghosh PK (2011) Performance evaluation of a small scale indirect solar dryer with static reflectors during non-summer months in the Saurashtra region of western India. *Solar Energy* 85(11):2686–2696
26. Singh M, Sethi VP (2018) On the design, modelling and analysis of multi-shelf inclined solar cooker-cum-dryer. *Solar Energy* vol 162 pp 620–636
27. Jain D, Jain RK (2004) Performance evaluation of an inclined multi-pass solar air heater with in-built thermal storage on deep-bed drying application. *J Food Eng* 65:497–509
28. Jain D (2007) Modeling the performance of the reversed absorber with packed bed thermal storage natural convection solar crop dryer. *J Food Eng* 78:637–647
29. Joshi CB, Gewali MB, Bhadari RC (2004) Performance of solar drying systems: a case study of Nepal. *J Inst Eng* 85:53–7
30. Pathak PK, Agrawal YC, Singh BPN (1991) Thin layer drying model for rapeseed. *Trans American Soc Agric Eng* 34(6):2505–8
31. Li YR, Morey V, Afinrud M (1987) Thin-layer drying rates of oilseed sunflower. *Trans American Soc Agric Eng* 30(4):1172–5
32. ASHRAE. *Fundamental handbook*; 2001 [Atlanta GA, USA]

33. Sun D, Woods JL (1994) Low-temperature moisture transfer characteristics of barley: thin-layer models and equilibrium isotherms. *J Agric Eng Res* 59:273–83
34. Nellist ME (1976) Exposed layer drying of ryegrass seeds. *J Agric Eng Res* 21:49–66
35. Fatouh M, Metwally MN, Helali AB, Shedid MH (2006) Herbs drying using a heat pump dryer. *Energy Convers Manage* 47:2629–43
36. Cakmak G, Yıldız C (2011) The drying kinetics of seeded grape in solar dryer with PCM-based solar integrated collector. *Food Bioproducts Process* 89:103–108
37. Midilli A, Kucuk H (2003) Mathematical modeling of thin layer drying of pistachio by using solar energy. *Energy Convers Manage* 44:1111–1122
38. Ong KS (1995) Thermal performance of solar air heaters: mathematical model and solution procedure. *Sol Energy* 55(2):93–109
39. I. Doymaz [2005], Sun drying of figs: an experimental study. *J Food Eng* 71(4):403–407
40. Günhan T, Demir V, Hancioglu E, Hepbasli A (2005) Mathematical modeling of drying of bay leaves. *Energy Convers Manage* 46(11–12):1667–1679
41. Goyal RK, Tiwari GN (1997) Parametric study of a reverse flat plate absorber cabinet dryer: a new concept. *Sol Energy* 60(1):41–48
42. Forsona FK, Nazhab MAA, Akuffoa FO, Rajakarunab H (2007) Design of mixed-mode natural convection solar crop dryers: application of principles and rules of thumb. *Renewable Energy* 32:2306–2319
43. Garg HP, Sharma VK, Mahajan RB, Bhargave AK (1985) Experimental study of an inexpensive solar collector cum storage system for agricultural uses. *Solar Energy* 35(4):321–31
44. Devahastin S, Pitaksuriyarat S (2006) Use of latent heat storage to conserve energy during drying and its effect on drying kinetics of a food product. *Appl Therm Engg* 26:1705–13

An Overview on Composites Used in Phase Change Materials for Battery Thermal Management System



Nishi Mehta, Shivam Prajapati, and Shulabh R. Yadav

Abstract Having a lightweight power source directly not solves all the problems. Due to the high discharge rate, these batteries (most commonly Li-ion) lead to excessive heating, and that might result in reduced efficiency, the life span of the battery or even result in an explosion. To prevent this overheating, BTMS is a necessary component that is mostly used in outdoor applications such as electric vehicles. Multiple attempts have been made over the years to enhance the performance of BTMS using external cooling media. Adding PCMs is one of the most explored methods. However, there does not exist such a review through which one can directly select a particular composite PCM as per the requirements. PCM usually has low thermal conductivity, low latent heat of fusion and leakage problems. To overcome these issues, different kinds of composites are added according to the prevailing operating conditions. In this review, an attempt has been made to organize most widely used advanced PCMs. After going through the various research articles of worldwide researchers, applications of PCMs and basic classification have been explained. Following that recent advancement in BTMS, PCM-based cooling, applications of PCM have been mentioned. In the end as a summary advantages of different composite PCMs based on their operating conditions have been discussed.

Keywords Battery thermal management system (BTMS) · Phase change material (PCM) · Thermal conductivity · Latent heat · Composites · Electric vehicles (EVs)

Author Contribution: Nishi Mehta, Shivam Prajapati, and Shulabh R. Yadav contributed equally to this work.

N. Mehta · S. R. Yadav
SVNIT, Surat, Gujarat, India

S. Prajapati (✉)
NIT, Agartala, Tripura, India
e-mail: prajapatishivam64@gmail.com

1 Introduction

These days everyone is talking about performance and environment-friendly compact and portable electronic energy sources. Lithium-ion batteries are very much suitable for such kind of applications [1]. These batteries have a very large number of charging-discharging cycles, so these are very economical. Li-ion batteries have a substantial energy density and have high decay. These high discharge rates are responsible for the high-temperature rise of these batteries. The Li-ion batteries are rated for their best performance between 20 and 60 °C [2]. If the temperature keeps increasing, it can result in thermal runaway, cause fire or explosion and increase the temperature more [3]. As it sounds, it is a very hazardous event. It can cause severe injuries or death of persons in close proximity to that. So, to prevent this high-risk and dangerous event, we need the battery thermal management system for such closely packed multiple small batteries. The lifespan of cells of these batteries can be increased by using the battery thermal management system (BTMS). By using the BTMS, the battery regulates the heat and maintains the temperature level under the safe zone [4]. Many attempts have been made to make BTMS better and better.

It is known that the basic methods of cooling are natural convection, forced convection and cooling through fins. Even in the battery thermal management system, people have tried and experimented with cooling through natural convection [5], effective cooling using fins as a heat transfer media. The PCMs' thermal conductivities can be enhanced by using the thermal fins in the setup. The experimental as well as the numerical investigation of about six different types of fin arrangements in BTMS was done by Shojaeefard et al. [6]. It was observed that the best cooling effect was provided by the BTMS having horizontal fins. Moreover, largest melt fraction of the PCM was also provided by this type of arrangement. Furthermore, an important observation was made regarding the manner of breaking of PCM. It was concluded that the fin arrangement as well as the fin orientation had a significant impact on it. Over time, as technology advanced, people introduced new materials having better thermophysical properties to use in these types of active and/or passive cooling systems of BTMS. Here, emphasis has been laid on application of such materials (i.e. Phase change materials).

An important method of thermal management of battery systems is the application of phase change materials in it. Primarily, the phase change materials are the high latent heat absorbing as well as releasing materials. They do this during the process of the phase change (as the name suggests) [7]. PCMs having thermophysical properties such as high thermal conductivity, high latent heat of fusion, high density and superheat transfer properties are preferred over other available PCMs as they enhance heat transfer effectively [8]. It is also used for the storage of thermal energy. Most commonly, these are used in automotive applications. As mentioned above, all of the electric vehicles (EVs) and hybrid electric vehicles (HEVs) have battery thermal management system, and with the help of PCM, the thermal management can be enhanced [9].

The PCMs can be classified as mentioned in Fig. 1 [10].

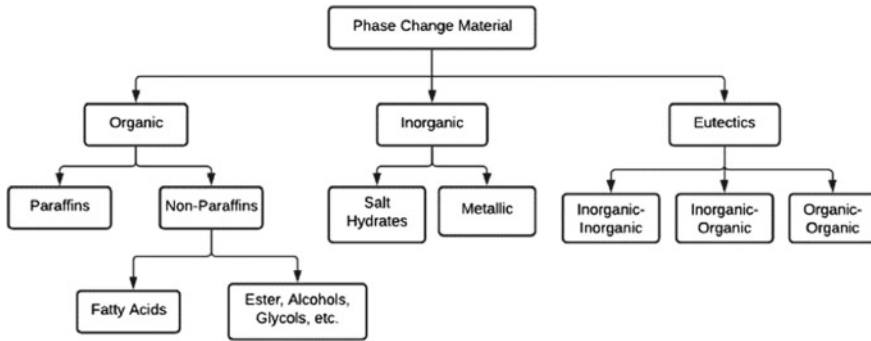


Fig. 1 Basic classification of PCMs [10]

2 Problem Description

Due to increase in demand for large energy consumptions, researchers are focussing more on development of phase change materials (PCMs). Due to excessive heating, the battery pack temperature increases highly which might even lead to explosion of the battery module. The main aim of this review paper is to explore the applications of PCMs in the thermal management of battery. It also contains the collections of different composites used to improve thermal conductivity of the PCM. Further, we have covered the influence of the characteristics of different PCMs on BTMS.

3 Recent Advancements in Battery Thermal Management System

The research in the field thermal management system of batteries has been done by many researchers since many years. This is because the battery packs have their safety issues due to excessive heating, especially those developed from the elevated temperature and the temperature having non-uniform distribution. It is observed that the maximum rise in temperature must not be greater than 65 °C [2] and also that the entire battery pack's maximum temperature difference should not be greater than 5 °C [11]. Therefore, some methods like air-based [12], liquid-based [13], and heat pipe-based cooling [18] are incorporated to minimize overheating in the battery. However, air-based cooling has not been very effective due to excessive heating of the batteries. Other possible method for thermal management is to control the dimensions of electrode and hence reduce the resistance which helps in the reduction of dissipated power and hence to prevent electrolyte explosion [15]. However, PCM-based cooling has been observed to have maximum efficiency in BTMS. Therefore, PCM-based cooling is described briefly.

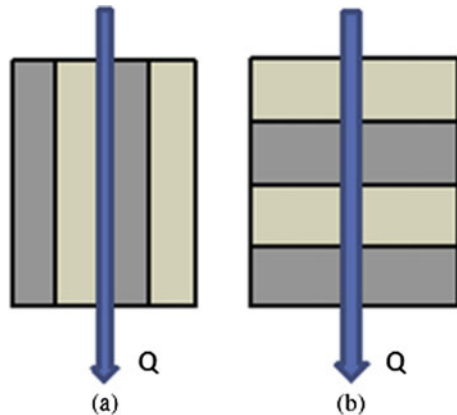
4 PCM-Based Cooling

It is known that during the process of phase transition, a high amount of storage as well as the liberation of latent heat is done by the PCMs. Owing to this reason, they have a wide application in the devices used for latent heat storage, popularly known as the latent heat storage units. The continuous increase in energy consumption in all the sectors is the reason for the rapid demand for PCM. Wu et al. experimented with a “thermal management system using copper mesh-enhanced composite phase change materials for the power battery pack.” An addition of the PCM plate which was enhanced with the mesh made up of mainly the copper metal, an increment in the performance of the uniformity of temperature and heat dissipation was observed. Greco et al. [16] presented a study on a 1D model for a cylindrical-shaped battery cell thermal investigation related to the combination of PCM and compressed expanded natural graphite. The bulk density of the graphite matrix is quite important parameter to determine the effectivity of the entire BTMS. Furthermore, the analysis of the electrochemistry and coupled thermal model were done for investigation of the passive cooling method of the PCM/compressed expanded natural graphite. This important analysis was done for cylindrical battery cell as well as the battery module [17]. The addition of composites with the PCM helps in limiting the rise in temperature in the lithium-ion batteries. Wang et al. [18] used paraffin/aluminium foam PCM for their experimental work. Two different models were presented to determine productive thermal conductivity of the PCM as shown in Fig. 2. A significant enhancement of the PCM’s thermal conductivity was done by adding the aluminium.

Figure 2a shows that the metal material and the filler are parallel to each other, and thermal conductivity in this case is maximum which can be proved from Eq. (1) shown.

$$\lambda_{\max} = (1 - \varepsilon)\lambda_{Al} + \varepsilon\lambda_{\text{PCM}} \tag{1}$$

Fig. 2 Effective thermal conductivity model **a** Parallel model and **b** Series model [18]



λ_{max} = Used composite material’s maximum equivalent coefficient ($\mathbf{W - m^{-1}K^{-1}}$)

λ_{Al} = Aluminium foam’s thermal conductivity

λ_{PCM} = PCM’s thermal conductivity ($\mathbf{W - m^{-1}K^{-1}}$)

ϵ = Porosity of aluminium foam.

5 Different BTMS with PCM Application

Rao et al. [13] increased an electric vehicle’s battery pack’s cycle life by designing a BTMS consisting of PCM coupled with a mini channel heat sink in a 3D battery model. Parameters like water mass flow rate, the temperature of change of PCM phase and PCM’s thermal conductivity were considered affecting parameters, and hence, they were numerically investigated. PCM’s thermal conductivity and temperature of phase change were known to have a significant impact on PCM’s liquid volume factor. As there was an increment in the heat sink’s channel number, a decrement was observed in the maximum temperature as well as maximum temperature difference of the battery module. See the Table 1 and Fig. 3.

The advantages of PCM coupled with mini channel heat sink over the only PCM in BTMS are as follows:

- Lower maximum temperature (320.6 K) than the temperature of only PCM BTMS (335.4 K).
- Comparatively higher effective thermal performance than the latter.

Chen et al. [19] analysed the design of BTMS having PCM and heat pipe (HP) (Fig. 4). The battery pack was entirely surrounded by PCM. The HP was divided into two types of sections, namely the evaporation and the condensation sections. The job of the evaporation section was to absorb the heat which was absorbed by the PCM, fitted in it, whereas the job of the condensation section was heat exchange with the flow of surrounding air. In this way, an overall system of an effective and speedy heat discharge was created in this design. The PCM used was a composite of extended graphite and paraffin. Its latent heat is 141.7 kJ/kg, and the range of change temperature of was between 315.15 K and 317.15 K. The value of surrounding temperature was 293.15 K. The convective heat transfer coefficient of the condensation section was considered as 50 W/m²K. HP had a starting temperature of 308.15 K. Different parameters of the surrounding environment and HP and PCM had an effect on the

Table 1 Optimum parameters for the maximum melted percentage of PCM (95.9%)

Temperature of phase change of PCM (K)	Thermal conductivity of PCM ($\mathbf{W - m^{-1}K^{-1}}$)	No. of channels in heat sink	Mass flow rate ($\frac{kg}{s}$)
308.15	0.6	8	$8 * 10^{-4}$

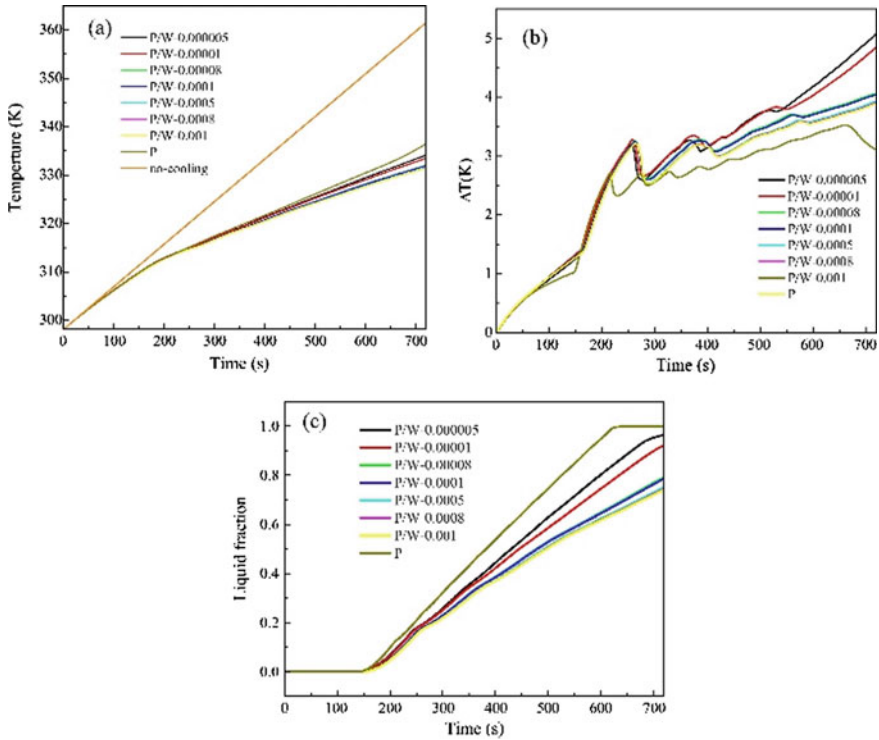


Fig. 3 **a** Maximum temperature, **b** temperature difference, **c** the liquid fraction of PCM versus time [13]

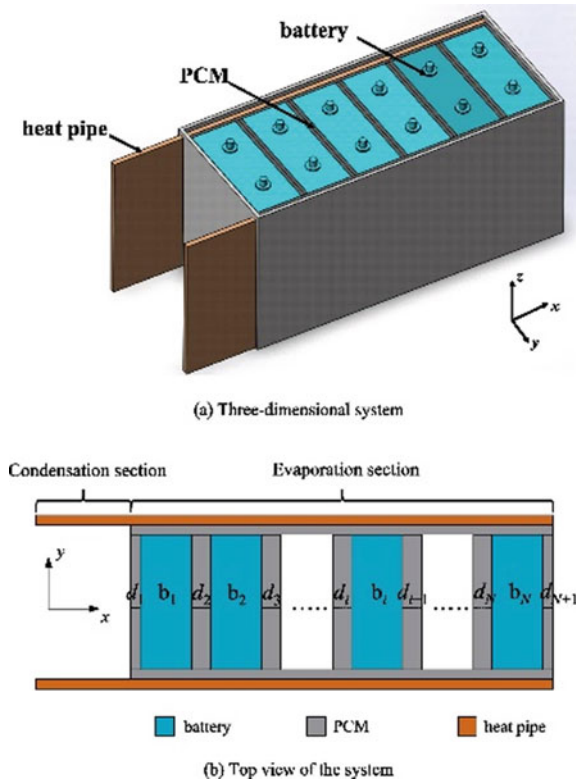
overall system, which was investigated using numerical methods. The temperature difference was reduced in the following ways:

- Enhancement in the coefficient of heat transfer of the surrounding environment.
- Increasing latent heat of PCM.
- Increasing thickness of PCM.
- Decreasing the ambient temperature.

Furthermore, increment in equivalent thermal conductivity of heat pipe at the initialization time and decrement in initialization temperature positively impacted the battery module’s heat dissipation. An increase in the battery pack’s temperature difference was observed when the PCM’s melting temperature was lowered than the heat pipe’s initialization temperature. PCM’s thickness distribution was optimized, which reduced the temperature difference by 30%, provided the initial thermal conductivity of the heat pipe was of small value as well as the ambient heat transfer coefficient was of moderate value.

Luo et al. [20] investigated a combination of electrically conductive PCM and expanded graphite (EG) phase change material for BTMS (Fig. 5). The primary

Fig. 4 Schematic of BTMS with heat pipe [19]



function of EG was to prevent liquid leakage of paraffin by providing a supporting matrix. Another important function which it served was the networking between electrical and thermal conduction. When EG had a weight percentage of 20%, the electrical resistance of paraffin was as low as 0.1–0.28 Ω -mm, and the paraffin’s thermal conductivity was increased up to 960%. This BTMS was analysed by numerical analysis. Also, a novel part of this system was the simultaneous heating and cooling procedure of the battery. Joule heating effect was employed for preheating of batteries, as well as the method of the storage of the thermal energy of the composite PCM was used to cool down the battery simultaneously. When the battery’s voltage was 3.4 V and consisted of the eight-cell module, the rate of heating of the composite PCM was 13.4 $^{\circ}\text{C}/\text{min}$. The maximum value of the difference of the temperature amongst the cells was found out to be of 3.3 $^{\circ}\text{C}$. Also, a good point observed was that a high-temperature reduction (34 $^{\circ}\text{C}$) was obtained even at a high discharge rate (3C). Because of this, a decrement in module’s temperature was obtained from 77 to 43 $^{\circ}\text{C}$. The overall range in which this composite PCM maintained the battery’s temperature between 20 and 55 $^{\circ}\text{C}$ during the entire discharging process. This temperature range was achieved for a seven-module battery pack even within the extremely varying battery temperature range of -40 to $+ 50$ $^{\circ}\text{C}$. The point is that the role of PCM

in this design was not only limited to cooling, but it also played the role of full-temperature thermal management because of the effect it had shown within the wide temperature range.

Yang et al. [21] explored the role of bionic liquid and neural networks along with PCM in BTMS. The BTMS was honeycomb-like. Furthermore, it comprised of a mini channel having bionic liquid flowing through it as well as the hexagonal cooling plate consisting of PCM. Also, the second-order circuital models and the CFD were used to computationally investigate the proposed BTMS's thermal performance. The value of applicable input parameters was discharge current of value of 32.2 A, inlet flow rate of 0.001 kg/s and 298.15 K as ambient temperature. The output value of the maximum temperature was 309.15 K that of temperature difference was of 3.8 K, as well as that of the pressure drop was obtained to be 11.95 Pa. The backpropagation neural network model had a significant role in this analysis. It was basically to estimate an appropriate flow rate through the inlet, considering the ambient temperature and the driving cycle condition. The BP neural network model gave the battery module's maximum stabilized temperature to be 312 K and difference of temperature to be 3.5 K. The main advantage of this BTMS was that it did not let temperature control fail, even when the PCM was melted completely.

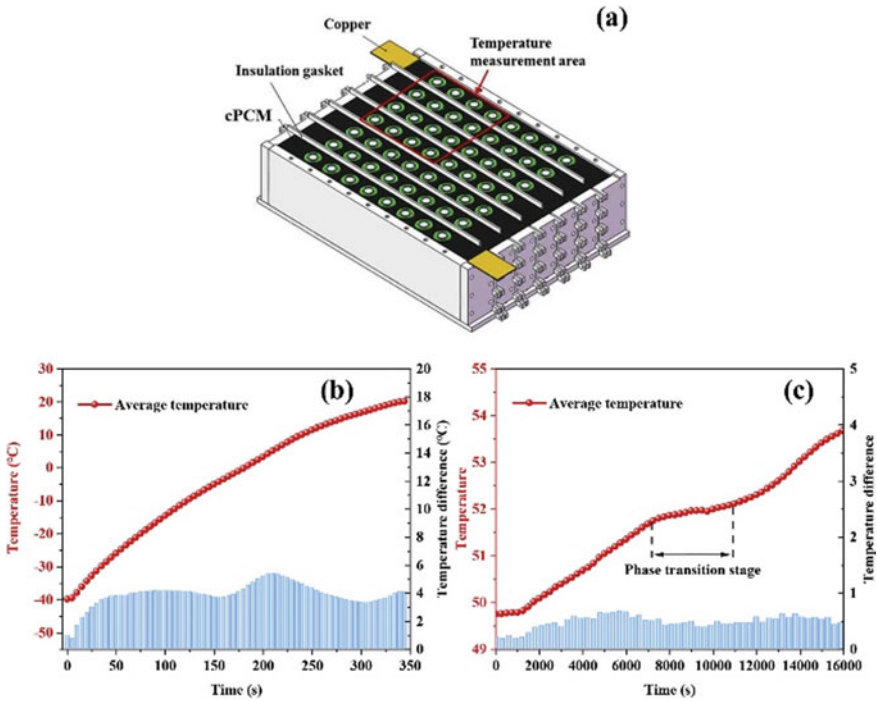


Fig. 5 Seven-module battery pack diagram with PCM/EG composite **a** temperature difference during heating, **b** cooling, **c** at 50 °C [20]

Wang et al. [22] designed a BTMS consisting of PCM combined with silicone. Paraffin was coated with silicone, and their thicknesses were optimized for improving the structural stability and thermal management performance. Ling et al. [23] used non-flammable inorganic PCM which had benefits of high thermal conductivity, small sub-cooling, high stability, and better cooling performance than some organic PCM. Nano-enhanced PCMs have also been used for BTMS [25]. It had the advantage of effective cooling, even at an elevated temperature of about 40 °C. Wang et al. [22] designed a passive cooling BTMS which investigating the impact of various important parameters of the PCM unit like thermal conductivity, viscosity, phase change latent heat, etc. on BTMS. The advantages of this BTMS were cost-effectiveness, good heat storage capacity, temperature equalization capability and mathematical function showing temperature retention).

6 Advantages of Different Composite PCMs

See Table 2.

7 Issues Faced by PCM in BTMS

The use of PCMs is an appealing technology storage of the thermal energy in the case of batteries which are widely used in the EVs. PCM is facing a lot of issues due to its relatively lesser thermal conductivity, leakage process and poor skeleton strength. Also, it is known that the widely used PCM in the BTMS is the paraffin (PA). However, one thing that adds to its drawback is its low thermal conductivity. One of the widely used methods to increase the thermal conductivity of the system is that of addition of metal foam or any other similar material [34], expanded graphite [35–38] and carbon fibre. The addition of composites might lead to both improvements of rising in temperature as well as some critical negative side effects like Wang et al.[28] found out that the addition of aluminium foam to the PCM can reduce the chances of natural convection occurring in the surrounding.

8 Conclusions

1. The parameters which controlled the difference in the temperature as well as the maximum value of the temperature in the battery module are mainly the PCM's thermal conductivity, the temperature at which it started to melt as well as its heat storage capacity, mainly that of the latent heat.

Table 2 Advantages of different composite PCMs

PCM/Composite	Pros of using this PCM	References
Copper Foam	<ul style="list-style-type: none"> • Enhancement of the paraffin’s thermal conductivity • Copper acts as a skeleton to the whole battery module 	[26, 27]
Paraffin	<ul style="list-style-type: none"> • Less expensive • High value of latent heat • Phase change temperature suitable to the given application 	[28, 29]
Paraffin/Aluminium Foam	<ul style="list-style-type: none"> • It has a cooling effect to limit the heating of the Li-ion battery 	[18]
Paraffin/Extended Graphite	<ul style="list-style-type: none"> • Improved structural strength and thermal conductivity 	[20]
Gypsum-based Composite	<ul style="list-style-type: none"> • Enhancement of the PCM’s thermal conductivity, even in the case of the dynamic simulations of the building structures comprising of the combination of the PCM and composite material 	[30]
Carbon Foam	<ul style="list-style-type: none"> • It gives porosity which ultimately improves thermal performance 	[31]
Paraffin + Silicone Composite	<ul style="list-style-type: none"> • It has reduction in battery module temperature at high discharge rate 	[22]
Graphene + Nanotubes	<ul style="list-style-type: none"> • It improves thermal conductivity of PCM • Restrains rise in temperature 	[32]
Phenolic Resin/PPE-PPO	<ul style="list-style-type: none"> • It provides high energy density and lower difference in temperature between the storage and release during the transition of the phase change 	[33]
Inorganic PCMs	<ul style="list-style-type: none"> • Better cooling performance than some organic PCMs • Small sub-cooling and high thermal stability 	[23]

2. Ambient conditions are the main key factor on which the performance of BTMS and battery module depends. The temperature of module will be dependent upon the decay rate and the ambient temperature. Higher ambient temperature would cause more temperature rise during operation. So, indoor applications would have less temperature difference, hence more stable operation and more effective thermal management.
3. Addition of composites to the PCM increases the PCM’s thermal conductivity; through this review paper, researchers would be able to select the most effective composite of PCM to be used on which research has been done till now and is most commonly used according to their purpose.
4. The uniformity of temperature distribution, maximum successful operating temperature, time taken to attain thermal stability are key factors to be considered while designing or selecting a BTMS for any specific application.

Keeping in mind the limitations of PCM, one should be very careful while selecting the proper composite. Some new composites such as nanomaterials, carbon nanotubes and bionic liquids can be explored in depth as these materials have more potential than normal organic, inorganic or eutectic PCMs. Further efforts can be performed to increase the battery module's operating temperature range and to reduce the time to achieve thermal stability and establish temperature uniformity by making some phenomenal changes in geometrical parameters.

References

1. Maleki H, Shamsuri AK (2003) Thermal analysis and modeling of a notebook computer battery. *J Power Sources* 115(1):131–136
2. Skerlos SJ, Winebrake JJ (2010) Targeting plug-in hybrid electric vehicle policies to increase social benefits. *Energy Policy* 38(2):705–708
3. Sun J, Li J, Zhou T, Yang K, Wei S, Tang N, Dang N, Li H, Qiu X, Chen L (2016) Toxicity, a serious concern of thermal runaway from commercial Li-ion battery. *Nano Energy* 27:313–319
4. Smith J, Singh R, Hinterberger M, Mochizuki M (2018) Battery thermal management system for electric vehicle using heat pipes. *Int J Therm Sci* 134:517–529
5. Akinlabi AH, Solyali D (2020) Configuration, design, and optimization of air-cooled battery thermal management system for electric vehicles: A review. *Renew Sustain Energy Rev* 125:109815
6. Shojaeefard MH, Molaeimanesh GR, Ranjbaran YS (2019) Improving the performance of a passive battery thermal management system based on PCM using lateral fins. *Heat Mass Transf* 55(6):1753–1767
7. Cabeza LF, Castell A, Barreneche CD, De Gracia A, Fernández AI (2011) Materials used as PCM in thermal energy storage in buildings: A review. *Renew Sustain Energy Rev* 15(3):1675–1695
8. Cascone Y, Perino M (2015) Estimation of the thermal properties of PCMs through inverse modelling. *Energy Procedia* 78:1714–1719
9. Jaguemont J, Omar N, Van den Bossche P, Mierlo J (2018) Phase-change materials (PCM) for automotive applications: A review. *Appl Therm Eng* 132:308–320
10. Rathod MK, Banerjee J (2013) Thermal stability of phase change materials used in latent heat energy storage systems: A review. *Renew Sustain Energy Rev* 18:246–258
11. Qu ZG, Li WQ, Tao WQ (2014) Numerical model of the passive thermal management system for high-power lithium ion battery by using porous metal foam saturated with phase change material. *Int J Hydrogen Energy* 39(8):3904–3913
12. Park H (2013) A design of air flow configuration for cooling lithium ion battery in hybrid electric vehicles. *J Power Sources* 239:30–36
13. Rao Z, Wang Q, Huang C (2016) Investigation of the thermal performance of phase change material/mini-channel coupled battery thermal management system. *Appl Energy* 164:659–669
14. Rao Z, Wang S, Wu M, Lin Z, Li F (2013) Experimental investigation on thermal management of electric vehicle battery with heat pipe. *Energy Convers Manage* 65:92–97
15. Verma A, Shashidhara S, Rakshit D (2019) A comparative study on battery thermal management using phase change material (PCM). *Thermal Sci Eng Prog* 11:74–83
16. Greco A, Jiang X, Cao D (2015) An investigation of lithium-ion battery thermal management using paraffin/porous-graphite-matrix composite. *J Power Sources* 278:50–68
17. Greco A, Jiang X (2016) A coupled thermal and electrochemical study of lithium-ion battery cooled by paraffin/porous-graphite-matrix composite. *J Power Sources* 315:127–139
18. Wang Z, Zhang Z, Jia L, Yang L (2015) Paraffin and paraffin/aluminum foam composite phase change material heat storage experimental study based on thermal management of Li-ion battery. *Appl Therm Eng* 78:428–436

19. Chen K, Hou J, Song M, Wang S, Wu W, Zhang Y (2021) Design of battery thermal management system based on phase change material and heat pipe. *Appl Therm Eng* 188:116665
20. Luo M, Song J, Ling Z, Zhang Z, Fang X (2021) Phase change material coat for battery thermal management with integrated rapid heating and cooling functions from -40°C to 50°C . *Materials Today Energy* 20:100652
21. Yang W, Zhou F, Liu Y, Xu S, Chen X (2021) Thermal performance of honeycomb-like battery thermal management system with bionic liquid mini-channel and phase change materials for cylindrical lithium-ion battery. *Appl Therm Eng* 188:116649
22. Wang J, Huang Q, Li X, Zhang G, Wang C (2021) Experimental and numerical simulation investigation on the battery thermal management performance using silicone coupled with phase change material. *J Energy Storage* 40:102810
23. Ling Z, Li S, Cai C, Lin S, Fang X, Zhang Z (2021) Battery thermal management based on multiscale encapsulated inorganic phase change material of high stability. *Appl Therm Eng* 193:117002
24. Wang Y, Wang Z, Min H, Li H, Li Q (2021) Performance investigation of a passive battery thermal management system applied with phase change material. *J Energy Storage* 35:102279
25. Jilte R, Afzal A, Panchal S (2021) A novel battery thermal management system using nano-enhanced phase change materials. *Energy* 219:119564
26. Zheng H, Wang C, Liu Q, Tian Z, Fan X (2018) Thermal performance of copper foam/paraffin composite phase change material. *Energy Convers Manage* 157:372–381
27. Wu W, Yang X, Zhang G, Ke X, Wang Z, Situ W, Li X, Zhang J (2016) An experimental study of thermal management system using copper mesh-enhanced composite phase change materials for power battery pack. *Energy* 113:909–916
28. Khateeb SA, Amiruddin S, Farid M, Selman JR, Al-Hallaj S (2005) Thermal management of Li-ion battery with phase change material for electric scooters: experimental validation. *J Power Sources* 142(1–2):345–353
29. Zhang X, Kong X, Li G, Li J (2014) Thermodynamic assessment of active cooling/heating methods for lithium-ion batteries of electric vehicles in extreme conditions. *Energy* 64:1092–1101
30. Toppi T, Mazzarella L (2013) Gypsum based composite materials with micro-encapsulated PCM: Experimental correlations for thermal properties estimation on the basis of the composition. *Energy Build* 57:227–236
31. Mesalhy O, Lafdi K, Elgafy A (2006) Carbon foam matrices saturated with PCM for thermal protection purposes. *Carbon* 44(10):2080–2088
32. Zou D, Ma X, Liu X, Zheng P, Hu Y (2018) Thermal performance enhancement of composite phase change materials (PCM) using graphene and carbon nanotubes as additives for the potential application in lithium-ion power battery. *Int J Heat Mass Transf* 120:33–34
33. Rodríguez F, Lopez BL (2016) Phenolic resin/PEO-PPO block copolymer composite materials as phase change materials (PCM) for latent heat thermal energy storage (LHTES). *J Energy Storage* 6:173–177
34. Samimi F, Babapoor A, Azizi M, Karimi G (2016) Thermal management analysis of a Li-ion battery cell using phase change material loaded with carbon fibers. *Energy* 96:355–371
35. Alrashdan A, Mayyas AT, Al-Hallaj S (2010) Thermo-mechanical behaviors of the expanded graphite-phase change material matrix used for thermal management of Li-ion battery packs. *J Mater Process Technol* 210(1):174–179
36. Wu W, Zhang G, Ke X, Yang X, Wang Z, Liu C (2015) Preparation and thermal conductivity enhancement of composite phase change materials for electronic thermal management. *Energy Convers Manage* 101:278–284
37. Ling Z, Chen J, Fang X, Zhang Z, Xu T, Gao X, Wang S (2014) Experimental and numerical investigation of the application of phase change materials in a simulative power batteries thermal management system. *Appl Energy* 121:104–113
38. Ling Z, Wang F, Fang X, Gao X, Zhang Z (2015) A hybrid thermal management system for lithium ion batteries combining phase change materials with forced-air cooling. *Appl Energy* 148:403–409

Effect of Semi-cylindrical Protrusions on Thermal Behaviour of SPHE



Darshilkumar N. Chhatrodiya, Kuldeep Parmar, Jay Chavda, Yash Kalola, and Vipul M. Patel

Abstract In the present work, a numerical investigation is carried out to study the heat transfer characteristic of a modified spiral plate heat exchanger (SPHE). First, SPHE with the plain surface is considered. The temperature data obtained for the plain SPHE from the present simulation is compared with the standard benchmark result. In order to improve heat transfer characteristics of SPHE, semi-cylindrical-shaped protrusions are provided at a regular interval on the surface of SPHE plates. Moreover, a parametric study is carried out to investigate the effect of size of protrusion ($r_i = 1.175$ to 3.175 mm) on temperature distribution and heat transfer rate. For the initial cases of $r_i (=1.175$ mm), the heat transfer rate decreases as compared to simple SPHE. With further increase in r_i , the heat transfer rate monotonically increases.

Keywords Spiral plate heat exchanger · Heat transfer enhancement · Semi-cylindrical protrusion · CFD

Nomenclature

$c_{p,h}$	Specific heat of hot fluid, J/kg K
$c_{p,c}$	Specific heat of cold fluid, J/kg K
G_k	Generation of turbulent kinetic energy, W/m ³
k	Thermal conductivity W/m-K
M_h	Mass flow rate of hot fluid, kg/s
M_c	Mass flow rate of cold fluid, kg/s
P	Pressure, Pa
Q	Heat transfer rate, W
r_i	Radius of protrusion, mm
T	Temperature, K

D. N. Chhatrodiya (✉) · K. Parmar · J. Chavda · Y. Kalola · V. M. Patel
Mechanical Engineering Department SVNIT, Surat, India
e-mail: ul7me108@med.svnit.ac.in

v	Velocity, m/s
V	Volume flow rate, m ³ /s

Greek Symbols

ε	Effectiveness
κ	Turbulent kinetic energy, J/kg
μ	Dynamic viscosity, Pa-s
μt	Turbulent viscosity, m ² /s
ρ	Density, kg/m ³
σ_k	Prandtl numbers for turbulent kinetic energy
σ_ε	Prandtl numbers for rate of dissipation
Φ	Volume concentration

Abbreviations

SPHE	Spiral plate heat exchanger
HTR	Heat transfer rate

1 Introduction

Heat exchangers are widely used for effective heat transfer between two or more fluids (liquid and/or gas). They can be seen in almost all industrial units such as chemical and hydrocarbon processing, oil refining, petrochemicals, edible oils, pulp, paper mills, and many more. Among commonly used heat exchangers, SPHE enjoys popularity because of its novel thermo-hydraulic performance. Rosenblad [1] proposed this revolutionary idea of SPHE. Then Beckmann and Loiacona [2] showed applications of SPHE. SPHEs have extraordinary thermal performance because of their geometry and counter-flow type arrangement. Geometry of SPHE contributes in decreasing the size of heat exchanger for same thermo-hydraulic performance; hence, SPHE is considered as a compact heat exchanger. SPHEs offer high resistance to fouling and are easy to clean as compared to Shell and tube heat exchangers. The spiral flow path constantly changes the flow direction and thus increases local turbulence that eliminates fluid stagnation zones. These factors increase heat transfer rate. The SPHEs are constructed by rolling a pair of plates in a special rolling machine with spacer studs, which are welded onto the plates, to obtain a pair of uniform spiral passages.

In early 1970, Minton [3] proposed a case study to identify SPHE design parameters. He used allowable pressure drop as a constraint to obtain the required design parameters such as spiral outer and inner diameter, plate width, and plate spacing. Moreover, he presented first-hand correlations of heat transfer coefficient and pressure drop based on plate curvature for laminar and turbulent flows. Further, in 1992, Martin [4] used the numerical method to study the heat transfer and pressure drop characteristics of SPHE and presented empirical relations. Detailed discussion on the geometry of SPHE was done by Dongwu [5]; he obtained formulas to calculate geometric parameters (i.e. number of turns, length of spirals) for spiral heat exchangers. Núñez et al. [6–8] used an alternate approach to obtain design parameters. They used pressure drop as design objective and obtained optimized geometric parameters and compared with the data reported by Minton [3]. Garcia and Moreles [9] proposed a numerical method to obtain thermal performance of SPHE in which outlet temperature, overall heat transfer coefficient, and performance parameters were obtained for given flow rate and temperature at the inlet. In a recent study, Sabouri et al. [10] proposed a modified algorithm based on pressured drop maximization. They tried to minimize dimensions of SPHE considering geometric restriction and cost minimization. Research conducted on SPHEs till now mainly focuses on designing SPHEs, performance evaluation, and optimizing design parameters of SPHEs. As per the authors' knowledge, no light has been put to enhance heat transfer in SPHE by passive heat transfer augmentation techniques. In the present work, protrusions on the surface of the spiral plate are provided to see their effect on overall heat transfer. The two-dimensional CAD model of both modified and simple SPHE is shown in Fig. 1a and b, respectively. The shape of protrusion is semi-cylindrical connecting end-to-end width of spiral plate at 10° intervals. In addition to the designing parameters considered by Núñez et al. [6], radius of protrusion (r_i) is also added as an additional parameter in the present work.

The focus of this work is to study the heat transfer rate of the modified SPHE. The surface protrusion size, i.e. radius of protrusion (r_i), is varied to see its effect on heat transfer rate and outlet temperature of both hot and cold fluid streams.

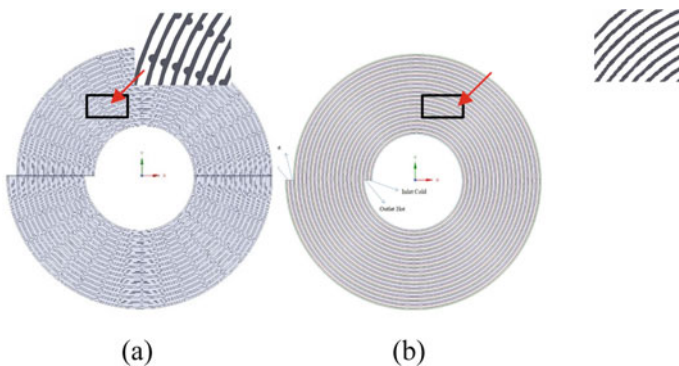


Fig. 1 Two-dimensional CAD model of **a** modified SPHE and **b** simple SPHE

The protrusion is intended to create disturbance in boundary layer growth, thereby increasing heat transfer rate. The main objective behind modification in the surface geometry of the SPHE is to enhance the heat transfer characteristics. A higher heat transfer rate is achieved by disturbing the development of the boundary layer and thereby increased mixing between fluid layers. The use of surface extensions, channel inserts, or geometrical modification of the flow duct is passive heat transfer augmentation techniques. These methods enhance the heat transfer coefficient of the equipment with a slight increase in pressure drop. Here modification in the fluid flow behaviour is achieved by the introduction of protrusions on the surface of the heat exchanging equipment. In this study, different radius of protrusions (r_i) ranging from 1.175 to 3.175 mm are considered. The hot and cold fluids are flowing at a mass flow rate of 0.7833 kg/s and 0.7444 kg/s, respectively. With equal mass flow rate, the effect of r_i on the temperature of the fluid streams and heat transfer rate are investigated.

2 Problem Description

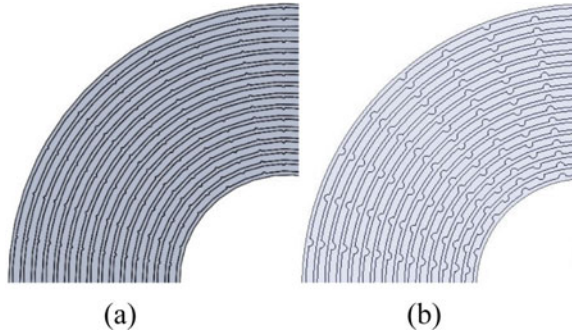
The computational domain in this work consists of two-dimensional spiral plates. The geometry of the considered problem is generated using solid works. The outer diameter, plate spacing, and core diameter are taken the same as reported by Núñez [7], and the values are given in Table 1.

The geometry of the protrusion is taken as hemispherical in 2D (semi-cylindrical in 3D), and it is provided at the opposite sides of the plates at 10° intervals. The radius of protrusions r_i is varied from 1.175 to 3.175 mm. Figure 2a shows modified SPHE with $r_i = 1.175$ mm and Fig. 2b shows the same with $r_i = 3.175$ mm.

Table 1 Operating conditions and design parameters

Conditions	Hot side	Cold side
Mass flow rate (kg/s)	0.7833	0.7444
Specific heat capacity (J/kg K)	2972.628	2763.288
Thermal conductivity of fluid (W/m K)	0.34789	0.32339
Inlet temperature ($^\circ\text{C}$)	200	60
Density (kg/m^3)	843	843
Viscosity (kg/m s)	0.00335	0.008
Plate material	SS312	
Thermal conductivity of plate (W/m-K)	17.3073	
Spiral outer diameter (m)	0.57	
Spiral inner diameter (m)	0.203	
Plate spacing (mm)	6.35	
Spiral plate width (m)	0.61	
Spiral plate thickness (mm)	3.175	

Fig. 2 Semi-cylindrical protrusion in SPHE **a** $r_i = 1.175$ mm and **b** $r_i = 3.175$ mm



3 Computational Model

Governing Equation: In order to investigate the performance of SPHE, the standard governing equations, such as mass, momentum, and energy equations, are solved using finite volume based commercial solver ANSYS-FLUENT 15.0. The thermal and physical properties of the fluid medium are taken as constant. The fluids are assumed to be Newtonian and incompressible in nature. The steady-state governing equations are expressed as.

Conservation of mass:

$$\nabla(\rho\mathbf{v}) = 0 \tag{1}$$

Conservation of momentum:

$$\nabla(\rho\mathbf{v}\mathbf{v}) = -\nabla P + \nabla(\mu\nabla \cdot \mathbf{v}) \tag{2}$$

Conservation of energy:

$$\nabla \cdot (\rho\mathbf{v}c_p T) = \nabla \cdot (k\nabla T) \tag{3}$$

In this simulation, realizable $K-\varepsilon$ turbulent model with enhanced wall treatment is employed. Two additional equations are also included, which are Prandtl number for turbulent kinetic energy (σ_k) and rate of dissipation (σ_ε) to incorporate eddy losses. These equations are as follows:

Turbulent kinetic energy:

$$\nabla \cdot (\rho V\kappa) = \nabla \cdot \{(\mu + \mu_t)/(\sigma_k \nabla x)\} + G_k - \rho\varepsilon \tag{4}$$

Rate of dissipation:

$$\nabla \cdot (\rho V \varepsilon) = \nabla \cdot \left\{ (\mu + (\mu_t / \sigma_\varepsilon)) \cdot \nabla_\varepsilon \right\} \cdot C_{1\varepsilon} \cdot (\varepsilon / K) \cdot G_k + C_{2\varepsilon} \rho (\varepsilon^2 / K) \quad (5)$$

G_k indicates generation of turbulent kinetic energy owing to the average velocity gradients, while σ_x and σ_ε denote effective Prandtl numbers for turbulent kinetic energy and rate of dissipation, respectively. Coefficients $C_{1\varepsilon}$ and $C_{2\varepsilon}$ are constants. μ_t represents eddy viscosity which is modelled by

$$\mu_t = (C_\mu \kappa^2) / \varepsilon \quad (6)$$

where C_μ is a constant equal to 0.09, other coefficients appearing in Eq. (4) and (5) are

$$C_{1\varepsilon} = 1.44, C_{2\varepsilon} = 1.92, \sigma_x = 1, \sigma_\varepsilon = 1.3$$

Computational Domain: The computational domain is discretized using structural grids. The spiral geometry is divided into quarter circles at each turn, and edge sizing is used for meshing protrusion and quarter circles. The mesh quality is checked using skewness. The average skewness is 0.1348 with a standard deviation of 0.11408 (Fig. 3).

Boundary Condition: Both hot and cold fluids enter in a counter-flow arrangement with uniform velocity and temperature profiles. At both, outlets relative zero pressure was applied. No-slip condition is maintained on the walls. The outermost and innermost plates are maintained in adiabatic condition. The values of various parameters taken during simulation are as follows: (Table 2).

At the inlets: Hot fluid: $T_{in} = 473.15 \text{ K min} = 0.7833 \text{ kg/s}$.

Cold fluid: $T_{in} = 333.15 \text{ K min} = 0.7444 \text{ kg/s}$.

At the outlets: $P_{gauge} = 0$.

At the walls: $\mathbf{v} = 0$.

Methodology: In order to simulate the problem numerically, ANSYS-FLUENT 15.0 is used. The coupling of velocity and pressure is handled using the SIMPLE

Fig. 3 Grid in spiral plate
radius $r_i = 3.175 \text{ mm}$

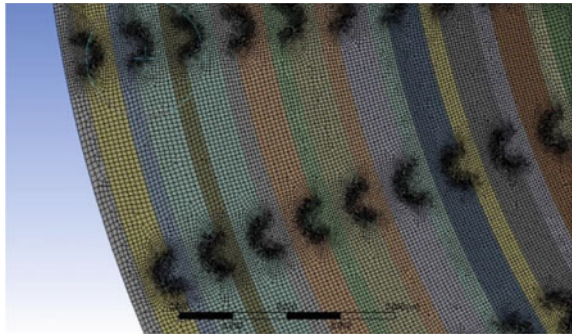


Table 2 Fluid and plate data

Properties	Hot stream	Cold stream	Plate (SS312)
Flow rate	0.7833 kg/s	0.7444 kg/s	–
Thermal conductivity	0.348 W/mK	0.322 W/mK	17.5 W/mK
Viscosity	3.35×10^{-3} kg/ms	8×10^{-3} kg/ms	–
Heat capacity	2973 J/kgK	2763 J/kgK	500 J/kgK
Density	843 kg/m ³	843 kg/m ³	7800 kg/m ³

algorithm, and the second-order upwind scheme is used for solving the governing equations. The convergence criteria for all variables were taken as 10^{-6} .

4 Results and Discussion

Grid Independency Test: To ensure that the numerical solutions are independent of the number of hexahedral cells, grid independency test was carried out for the protrusion of the size 1.175 mm. The outlet temperatures of both hot and cold fluids have been taken as parameters of interest. The obtained results are given in Table 3, and the corresponding variations are plotted in Fig. 4. It is observed that the outlet temperatures corresponding to element numbers 2248692 and 2,312,893 are almost identical. Hence, all simulations are performed at 2,248,692 number of elements.

Validation of numerical model: As per the authors' knowledge, the modified spiral heat exchanger is not investigated by the researchers. Hence, validation of the numerical model is performed by considering a simple spiral plate-based heat exchanger. The centre line temperature distribution for both cold and hot streams are compared with the work of Núñez et al. [7]. The corresponding values are summarized in Table 4.

From the centre line temperature comparison plot (see Figs. 5 and 6), it can be observed that the temperature distribution of the present results shows good agreement with the published work.

Table 3 Grid independency test

Sr. no	No of elements	Outlet temp (hot fluid) (K)	Outlet temp (cold fluid) (K)
1	1,296,205	400.85	415.001
2	1,866,873	400.48	415.420
3	2,146,071	401.84	413.849
4	2,248,692	403.09	412.469
5	2,312,893	403.09	412.472

Fig. 4 Grid independency test

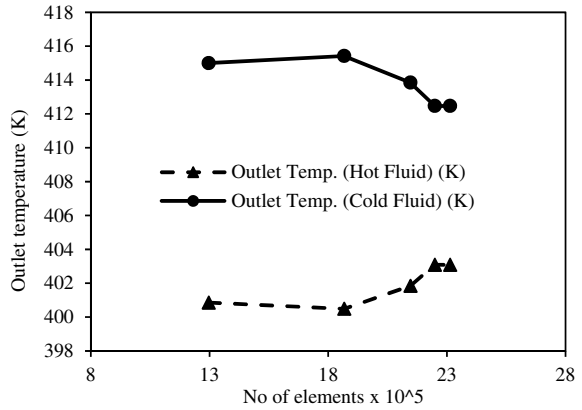
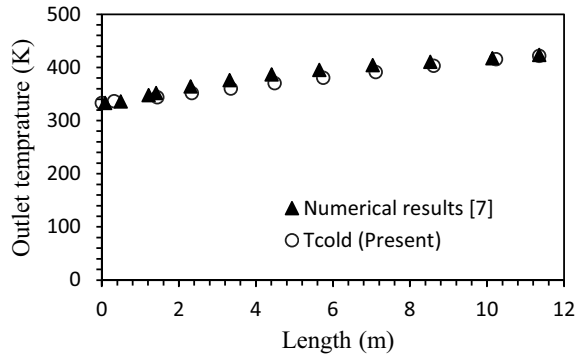


Table 4 Variation of temperature

Sr. no	Radius (mm)	Outlet temp (hot fluid) (K)	Outlet temp (cold fluid) (K)
1	0	394.57	422.12
2	1.175	403.09	412.47
3	1.650	397.48	418.82
4	2.175	391.65	425.43
5	2.650	387.97	429.60
6	3.175	380.34	438.23

Fig. 5 Comparison between numerical results for cold fluid stream



The present numerical model is further extended to see the effect of radius of protrusion on outlet temperature of both streams and overall heat transfer rate. The effect of r_i on outlet temperature is shown in Fig. 7.

It is expected that as heat transfer from hot stream to cold one takes place, the temperature of the cold stream increases and that of the hot stream decreases. The

Fig. 6 Comparison between numerical results for hot fluid stream

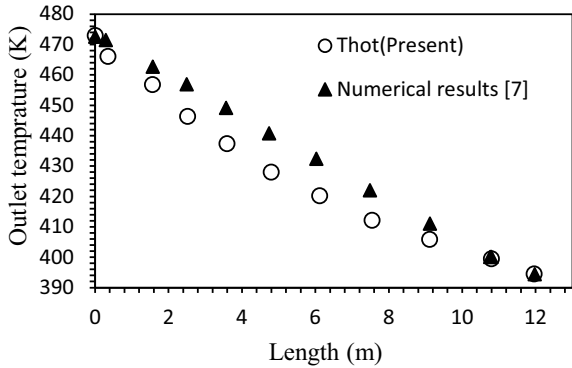
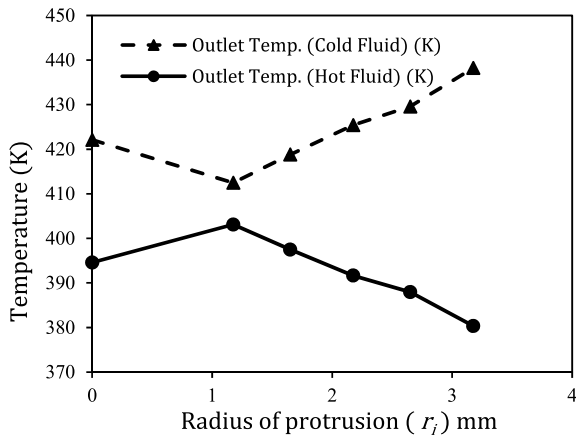


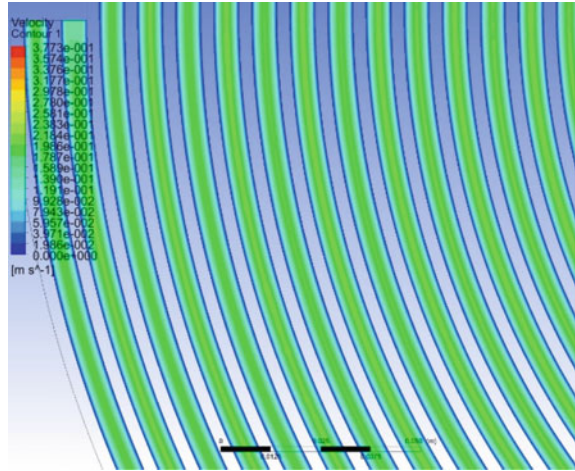
Fig. 7 Graph between outlet temperature and radius of protrusion



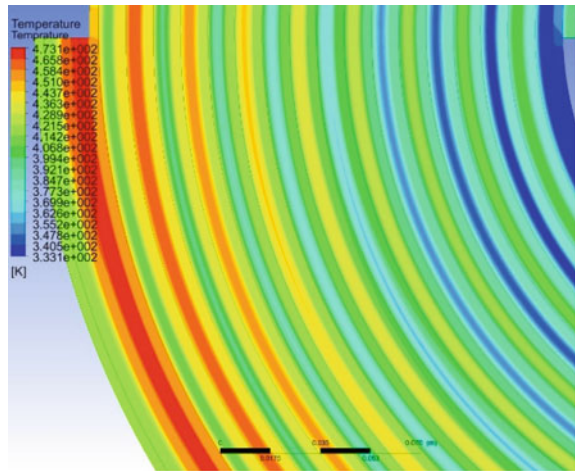
purpose of putting protrusion at regular intervals is to enhance the heat transfer. Hence, it is also expected that the outlet temperature of the hot stream should be lesser than the one obtained for plain SPHE. Likewise, the outlet temperature of the cold stream is expected to be higher than that of the plain SPHE. Surprisingly, for the initial radius of protrusion (i.e. $r_i = 1.175\text{mm}$), the outlet temperature of the hot stream is higher as compared to that of the plain SPHE case. Similar behaviour is observed for the cold stream, i.e. the outlet temperature of the cold stream for modified SPHE with $r_i = 1.175\text{mm}$ is lesser than that of the plain SPHE. In order to understand this contradiction, both velocity and temperature contours are compared for all the considered cases with and without protrusions. The velocity contour of plain SPHE, modified SPHE with $r_i = 1.175\text{mm}$ and $r_i = 3.175\text{mm}$ are shown in Figs. 8, 9, and 10, respectively.

The role of protrusion is to break the boundary layers and enhance the convective heat transfer by accelerating the flow. However, at $r_i = 1.175\text{mm}$, the acceleration of flow at the throat section (i.e. minimum cross-sectional area at the site of protrusion)

Fig. 8 a Velocity contour and **b** temperature contour for plain channel based SPHE protrusion radius $r_i = 1.175$ mm.



(a)

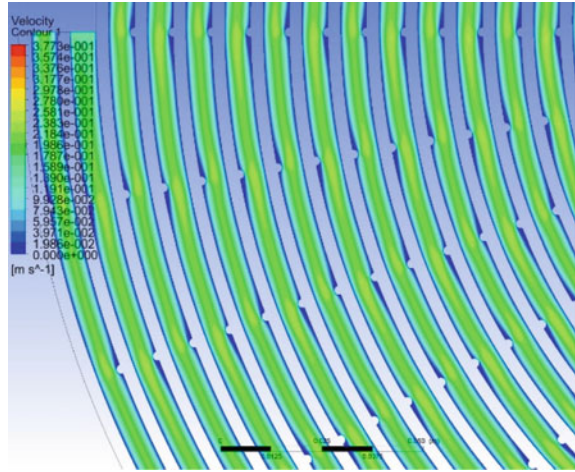


(b)

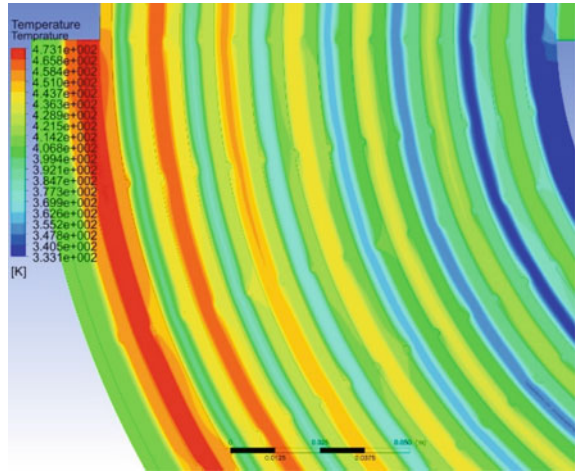
is not significant. Moreover, the thickening of the velocity boundary layer at the trailing side of the bump is also observed. The reduction in overall heat transfer at $r_i = 1.175$ mm can be attributed to the aforementioned observation.

With further increase in radius of protrusion, the contribution from convective heat transfer due to local acceleration of velocity increases. Hence, the resultant heat transfer rate shows favourable trend. The corresponding velocity contour is shown in Fig. 10.

Fig. 9 **a** Velocity contour and **b** temperature contour for modified SPHE with protrusion radius $r_i = 1.175$ mm.



(a)



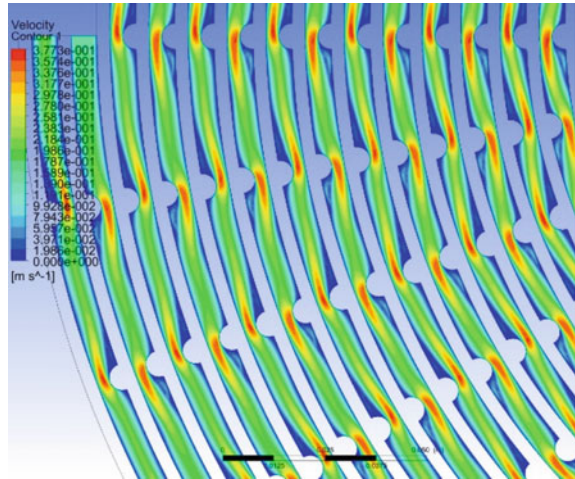
(b)

The heat transfer rate is calculated using Eq. (8). The calculated value of Q for all considered cases are given in Table 5 and plotted in Fig. 11.

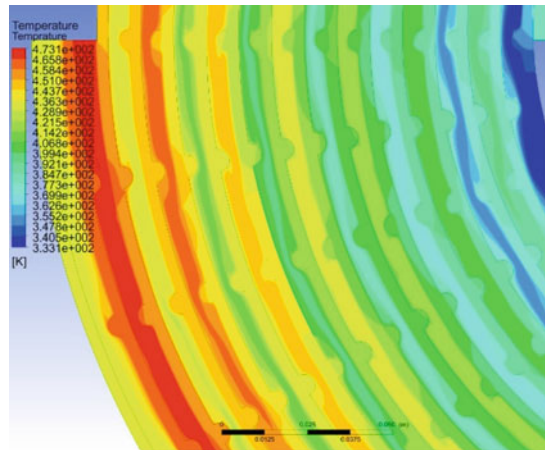
$$Q = M_h c_{p,h} (T_{h,o} - T_{h,i}) = M_c c_{p,c} (T_{c,o} - T_{c,i}) \tag{8}$$

The heat transfer rate decreases up to $r_i = 1.175$ mm and then increases monotonically up to $r_i = 3.175$ mm. The heat transfer rate for simple SPHE (i.e. $r_i = 0$ mm) is observed as 183.56 kW, whereas with protrusion of $r_i = 2.175$ mm, it increases

Fig. 10 **a** Velocity contour and **b** temperature contour for modified SPHE with protrusion radius $r_i = 3.175$ mm.



(a)

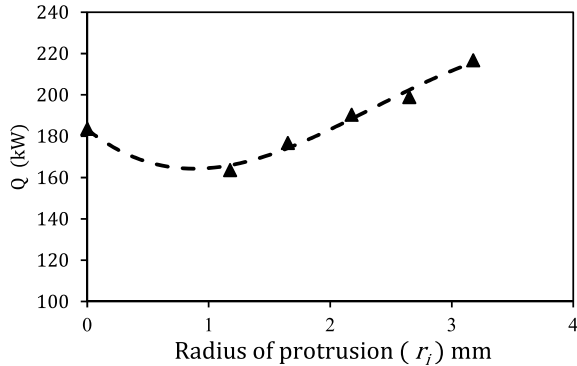


(b)

Table 5 Variation of heat transfer rate and radius of protrusion

r_i (mm)	0	1.65	1.175	2.175	2.65	3.175
Q (kW)	183.56	163.62	176.71	190.35	198.94	216.75

Fig. 11 Graph between heat transfer rate and radius of protrusion



to 190.35 kW. The reason for the initial decrement in Q and further enhancement in Q is already discussed.

5 Conclusion

In the present study, numerical investigation is carried out to study the effect of protrusion on heat transfer enhancement of SPHE. The important conclusion drawn from the study are as follows: at a lower radius of protrusion, particularly less than 2 mm, there is a decrease in the heat transfer. It is due to the thickening of the velocity boundary layer at the trailing edge of the protrusion. The corresponding decrease in velocity diminishes the convective heat transfer. With the increase in radius of protrusion, the flow accelerates and thus enhances the convective heat transfer. In future study, different shapes of protrusion like pin, triangular, and elliptic will be studied. The effect of changing configuration and number of protrusions on overall heat transfer coefficient and heat transfer rate will be studied to find the optimal design of the spiral heat exchanger.

References

1. Rosenblad CF (1935) Heat exchanger apparatus made of sheet metal. Patent No US2011201A
2. Hargis AM, Beckman AT, Loiacona JJ (1962) Application of spiral heat exchangers. Chem Eng Progr pp 62
3. Minton PE (1970) Designing spiral-plate heat exchangers. Chem Eng. Progr 11(1970):103–112
4. Martin H (1992) Heat exchangers. CRC Press—Taylor and Francis Group, Washington DC
5. Dongwu W (2003) Geometric calculations of the spiral heat exchanger. Chem Eng Technol Ind Chem-Plant Equip-Process Eng-Biotechnol
6. Picon Núñez M, Canizalez Davalos L, Morales Fuentes A (2006) Alternative design approach for spiral plate heat exchangers. Heat Transf Eng 27(6):12–21

7. Picon Núñez M, Canizalez Davalos L, Martinez Rodriguez G, Polley GT (2007) Shortcut design approach for spiral heat exchangers. *Food Bioprod Process* 85(4):322–327
8. Picon Núñez M, Canizalez Davalos L, Medina Flores JM (2009) Alternative sizing methodology for compact heat exchangers of the spiral type. *Heat Transf Eng* 30(9):744–750
9. Garcia MM, Moreles MA (2012) a numerical method for rating thermal performance in spiral heat exchangers. *Mod Appl Sci* 6:6
10. Shirazi AHS, Nasr MRJ, Ghodrat M (2020) Effects of temperature differences in optimization of spiral plate heat exchangers. *Process Integr Optim Sustain* 4(4):391–408
11. Mollicone JP, Battista F, Gaultieri P, Casciola CM (2017) Effect of geometry and reynolds number on the turbulent separated flow behind a bulge in a channel. *J Fluid Mech* 823(2017):100–133

Thermal Analysis for Solar Water Heater by Implementing Fins



Rushil Patel, Harshal Sonawane, Yogesh Mane, and Mandar Lele

Abstract Nowadays, there is huge energy demand, and this energy demand is fulfilled by fossil fuels, but these non-renewable resources will create crisis in future especially for developing countries. Hence, the implementation of renewable resources and increasing their dependency is a major concern. In this paper, simulation was done for one of the heat transfer augmentation techniques in the solar water heater that by implementing rectangular fins also without fins and different materials such as copper, stainless steel, and aluminium. The CAD model was created in Solid works, and thermal analysis was done in Autodesk Fusion 360. Finally, the result achieved was that the rectangular-based solar water fin tube had greater heat flow than the without fin solar water tube by 12 °C.

Keywords Renewable energy · Solar water heater · Flat plate collector · Fins · Heat transfer rate

1 Introduction

Renewable (flow/non-conventional) and non-renewable (finite/conventional) energy resources are the energy sources that human society utilizes on everyday schedule. The distinction between both energy sources is that renewable energy naturally replenishes themselves, whereas non-renewable energy cannot replenish themselves means they are restricted in supply and can't be utilized reasonably.

As human society is for the time being profoundly reliant upon non-renewable resources as its essential wellspring of energy, the major issue with non-renewable energy resources, aside from restricted supply is that consuming them discharges carbon dioxide into the air leading to a rise in global warming levels. So alternate energy sources, i.e. renewable energies such as sunlight, wind, hydro, tides, waves, and geothermal energy which are clean energy sources and are accessible in limitless supply, can be the significant supplier for power age, air warming and cooling, water

R. Patel (✉) · H. Sonawane · Y. Mane · M. Lele
Dr. Vishwanath Karad MIT WPU, Pune, India
e-mail: rushil2805@gmail.com

warming, cooling and transportation, and a lot more applications. Now as India is honoured with acceptable daylight and gets normal force of sun-based radiation of 200 MW/km^2 with a geological space of $3.287 \text{ million km}^2$ which adds up to 657.4 million MW , utilizing this free and environmentally clean energy not only resolves present-day but upcoming future challenges also. Thus, utilizing a solar water heater rather than an electric water heater for heating water is a far greater option in terms of any other non-renewable energy resources.

Solar water heater is a device which heats up the water by using sunlight; this energy is free and generates hot water for sanitary use throughout the year without emitting any carbon dioxide or other harmful gases. There are two kinds of solar water heater—(i) active system which is also known as forced circulation system which uses an electric pump, valves of controllers to circulate water through the tubes of collector and (ii) passive system which simply circulates water by means of natural convection between collector and reservoir/storage tank. The principle behind passive system working is that the water heats up in the tubes; its density decreases leading to the lighter weight of water and rises to the top of the collector and finally gets collected into reservoir/storage tank. Water that cools down in the reservoir/storage tank again goes back to the collector. For simulation, a passive system was used. Flat plate collector is the most common type of solar water collector used in domestic applications and some industrial applications. It is generally used for the temperature range of up to 100°C as it absorbs both direct and diffusive radiations. This flat plate collector consists of absorber tubes beneath which black coating is done to reduce convective losses and to this absorber tubes, fins were attached on the inner surface for simulation purpose.

2 Previous Work

Campo et al. [1] has shown that the fin efficiencies and tip temperatures of annular fins of uniform thickness by numerical analysis as it was extremely simple to apply multivariable regression analysis to the information as to produce minimal correlations equations for the forecasts of thermal amounts. This correlations equation can be utilized for the analysis for straight fins, where straightforward scientific articulations exist for assessment of two thermal amounts as far as single variable, dimensionless thermogeometric parameter [3].

Castell et al. [2] learned about what will be impact of using external vertical fins regarding phase change materials module with the end goal that improvement in the natural convection coefficient in water can be seen. Thus, by exploratory work for which two unique external vertical fins geometries were utilized, after-effect of increase of heat transfer area and heat transfer coefficient for natural convection was seen. By the utilization of fins, heat transfer coefficient up to 3 times bigger than the ones without fins and using greater fins permits achieving higher heat transfer coefficient esteem with a lower temperature difference in correlation with the more modest ones was seen and a significant term in a supply/stockpiling tank associated

with a solar system is that, time expected to heat the water to a valuable temperature and this time lessens by using external vertical fins in the phase change material module [6].

Ho et al. [3] led hypothetical test of double-pass sheet-and-tube solar water heaters with internal fins connected to it and outside recycle have been intended for broadening the heat transfer area and upgrading the convective heat transfer coefficient. With internal fins connected and recycle operation, the proficiency of collector can be improved by expanding the recycle ratio, number of fins appended, inlet water temperature, and mass flow rate diminishes with expanding number of pair of ducts. Albeit expanding recycle ratio, number of fins, inlet water temperature, and mass flow rate, it initiates higher dissipation at same time and the outcomes accomplished for modest quantity of hydraulic dissipated energy augmented were 24.3% [13].

Mokheimer [4] contemplated the performance of annular fins of different profiles exposed to locally factor heat transfer coefficient as performance of fins is communicated as far as fin efficiency and fin efficiency is an element of ambient temperature and fin geometry, creators likewise introduced fin efficiency bends for annular fins of rectangular, constant heat flow area, triangular, convex and concave parabolic of wide scope of radius ratios and dimensionless parameters [12].

Chabane et al. [5] experimentally investigated the thermal performance of a single pass solar air heater, and five fins were attached to it, and these all five fins were longitudinal fins which were fitted on the inferior side of the absorber plate with the end goal that increase in the rate of heat transfer can be seen and can easily deliver the flow of fluid in the channel. They also concentrated during the investigation about the impact of mass flow rate of air at outlet, temperature at outlet, heat transfer due to thickness of solar collector, and thermal efficiency. They played out the tests for two air mass flow rates, i.e. 0.012 and 0.016 kgs^{-1} and maximum efficiency values for 0.012 and 0.016 kgs^{-1} obtained with and without fins were 40.02%, 51.50% and 34.92%, 43.94%, respectively [10].

Murali et al. [6] reviewed how efficiency of energy storage and solar water collector of natural circulation solar water heating system can be improved by stratifying the water storage/recipient tank, and this stratification is accomplished by employing phase change material on the top of the storage tank and directed an examination whereby using circular fins around phase change material geometry of higher surface to volume ratio will work on the efficiency of solar water heating system for which heating and cooling tests have been performed with the assistance of home-grown solar water heater system of flat plate type collector and temperature distribution along the height of the storage tank, charging energy efficiency, and collector efficiency have been determined, and tests have been simulated in CFD fluent (version 6.3.26) software for validating the outcomes. The reproduction has been done by applying boundary conditions of the wall with convective heat flux and ambient temperature. The investigation showed that the arrangement among insightful and trial results has fundamentally improved, i.e. by using circular fins around phase change material geometry further developed the collector efficiency between 8.77% and 36.48% at 11:00 am and 3:30 pm, respectively [6].

Qiu et al. [7] considered heat transfer model of finned tube, and theoretical solution was gotten, and exactness of theoretical solution was approved utilizing mathematical simulation. They discovered outcome that by increasing the solar intensity on fin surface and decreasing height of the zone without solar radiation expands the heat transfer limit of finned tube. Additionally, by increasing the convective heat transfer coefficient of inner wall and inner diameter of copper tube can make fluid to absorb more heat acquiring from the fins presented to sunlight and by increasing the fins size over certain worth, the all-out heat transfer limit of finned tube stays unaltered with increasing height of the fins [9].

Singh et al. [8] looked into on solar energy collection and their application in their paper. A few of the most widely recognized types of the solar collector were introduced which incorporates flat plate collector, compound parabolic, evacuated tube, parabolic trough, Fresnel lens, and parabolic dish type collector. Likewise, applications of solar collector are water heating, space heating and cooling, refrigeration, industrial process heat, desalination, thermal power systems, solar furnaces, chemistry applications, and some more. It ought to be noticed that the applications of solar energy collectors are not restricted to the above regions as there are numerous different applications which are not depicted in their paper, either on the grounds that they are not completely evolved or are not developed at this point [8].

Balaji et al. [9] learned about the effect of fins with and without fins in solar flat plate water heater using data acquisition system. They showed how fins are frictionally drawn in with the inner side of the tube wall and is kept in axial flow direction of fluid flow path to such an extent that the outlet temperature of the fins absorber tube collector is 8 °C higher than plain tube collector. Additionally, it was tracked down that the rod extended surface gives higher outlet temperature when contrasted with the tube expanded surface, and there was low friction loss and pressure drop [10].

Jesurar et al. [10] investigated how micro-fin tube is a promising strategy for heat transfer expansion in heat transfer gadgets so led a trial where they zeroed in on outlet velocity, pressure drop, increasing rate of heat transfer by increasing area of the tube and principle obstacle of setting fins inside the water tube which makes water hindrance which was settled by putting require shape and size fins and further the outcomes showed that in morning because of low intensity, efficiency is extremely low however colossal ascent in the efficiency was found in afternoon. [6].

Cabeza et al. [11] summarized how phase change material modules with stratification can improve heat of hot water and for that experiment was performed under real operating conditions at the university of Lleida in Spain and a new phase change material, namely graphite compound with optimized thermal properties was used and final outcomes showed that 3 kg of phase change material compound is sufficient to remunerate a heat loss of 3 to 4 °C in 36 L of water which is likeness cooling down the genuine storage over a time of around 10 h [7].

Sheikh et al. [12] provided brief review about how the efficiency can be improved in pin fins by fluctuating boundaries like fin geometries, fin spacing, height, temperature distribution, and length to such an extent that increment in the warmth move can be accomplished. They have also reviewed how aluminium material for fins

is best suited than other fin materials and by increasing Reynold's number, rate of heat transfer for pin fins can be improved. Further, elliptical geometry can improve notable rate of heat transfer compared to other geometries like annular and eccentric fins [5].

Patil et al. [13] outlined how to manage the design thought of solar water heater with the end goal that boiling water for the home-grown and mechanical applications will be gotten. Also, appropriate selection of each component, desired capacity, location of installation, and correlations for design of collector parameters like cover materials, absorber plate materials, absorber and glazing, and coating assumes a significant part. Further, they have very much delineated the technique or steps for designing any ideal solar water warming framework in their paper [5].

Mohammed et al. [15] carried out analysis by creating a model and analysing it in Ansys CFD 14.0 in which solar flat plate collector is dissected for both with fins and without fins for development in heat transfer rate is broke down for both with fins and without fins for development in heat transfer rate. By analysing the results, they found that finned collector has more efficiency than no fin collector by 17.5% [5].

Ramasamy et al. [14] led an analysis to accomplish their motto which was to keep up with the velocity and temperature at the outlet of the sun powered water heater by choosing legitimate shape and measurements of fins. Likewise, keeping up with pressure drop, expanding heat move rate and expanding space of the cylinder were their other target. Thus, for accomplishing their motto they directed an examination in bright days and look at the thermal presentation of sunlight-based water heater with and without fins in their Tamil Nadu city and tabulated the readings of time, radiation, inlet temperature, outlet temperature, heat gain, heat available, with fins, without fins, and fin efficiency with time frame hour in a specific day a finally it was seen that temperature difference of 7 to 8 °C with fins and without fins was there [8].

Selvam et al. [16] explored how unique execution factors, for example, glassing, number of fins, number of passes, geometry of fins, site selection, etc., influence the heat transfer rate of the flat plate solar water heating system to acquire high temperature water for the home-grown and industrial applications. Also, in view of their writing overview they note if need to work on the thermal execution of the solar water heating system, fins gave internally to the absorber tubes is best fitted; modified fins give higher temperature compare to standard fins with proper pitch, multi-pass of water gives better outlet temperature and black painted clear toughened absorber glass of sandwich type gives better performance than higher thermal conductivity material like aluminium [7].

Bisen et al. [17] did CFD simulation in which three types of fins were taken for study, namely rectangular fin type, triangular fin type, and trapezoidal fin type with different type of perforation (without perforation, elliptical perforation, square perforation, and circular perforation), and they found out that triangular fin is most economical as its profile requires minimum material for construction, and overall cost is also less compared to rectangular and trapezoidal profile. Henceforth, triangular profile is more alluring in the light of the fact that for equivalent heat transfer it requires less volume contrast with different profiles. Temperature distribution for

every one of the three profiles of perforations diminishes along the length up to the tip of the fin, and minimum temperature was found at the tip of the triangular profile with circular perforation [7].

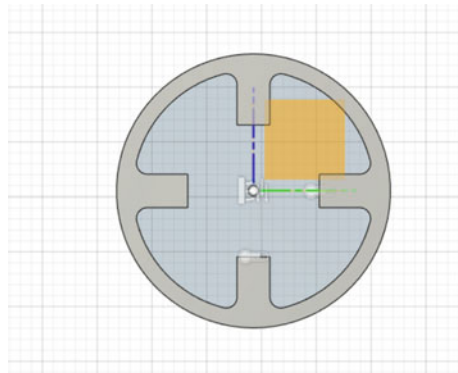
Badescu et al. [18] evaluated for enhance configuration just as functional boundaries in this paper for the instance of flat plate finned tube solar collectors. They thought about the two fins of uniform and variable thickness and the improvement cycle depended on the base expense per unit of helpful warmth transition model, and this warmth motion model was made relying upon a topographical area with a point-by-point meteorological information base accessible, and further the outcomes showed that the best monetary exhibition is acquired on account of balances with ideal variable thickness as the balances cross segment is near an isosceles triangle. The ideal distance between the tubes is expanded by expanding the channel liquid temperature, and it is bigger in the cold season contrasted with warm season [17].

3 Methodology

In this simulation, passive-type solar water heater with a flat plate collector was utilized. The heat transfer augmentation technique was applied to the absorber tubes of the collector. Fins were attached to the inner side of the tube of rectangular shape and different types of material, namely copper, aluminium, and stainless steel. The CAD model was generated in Solid works, and thermal analysis was carried out in Autodesk Fusion 360. The dimensions of the absorber tube were taken as outer diameter 25 mm and inner diameter 22 mm. The rectangular fin of length 5 mm and width 3 mm was attached by weld of 2 mm on inner surface of absorber tube as shown in Fig. 1.

The applied temperature for the absorber tube was 90 °C, and the temperature of the water was taken as 30 °C.

Fig. 1 Rectangular fin



4 Result and Discussion

Following is the result of the absorber tube without fins:

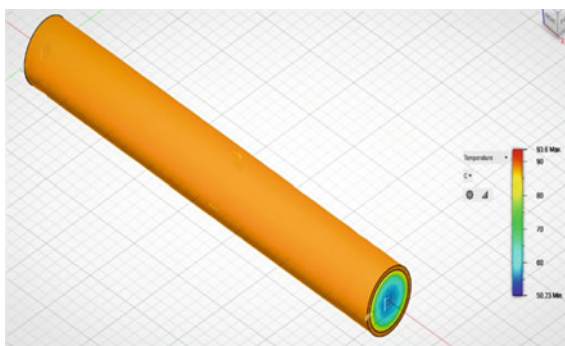
1. Copper and water

See Fig. 2.

2. Aluminium and water

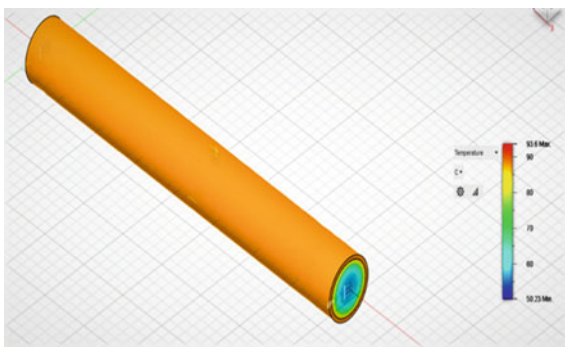
See Fig. 3.

Fig. 2 Copper tube without fins



Minimum	Maximum
50.24°C	93.6°C

Fig. 3 Aluminium tube without fins



Minimum	Maximum
50.23°C	93.6°C

3. Stainless steel and water

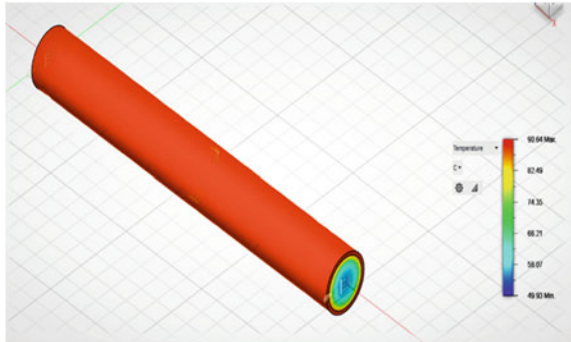
See Fig. 4.

Following is the result of the absorber tube rectangular fins:

1. Copper and water

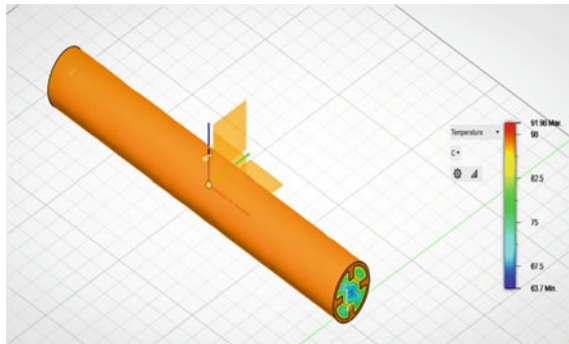
See Fig. 5.

Fig. 4 Stainless steel tube without fins



Minimum	Maximum
49.33°C	90.64°C

Fig. 5 Copper tube with rectangular fins



Minimum	Maximum
63.7°C	91.98°C

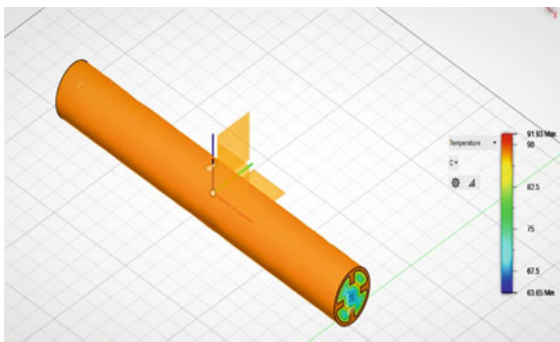
2. Aluminium and water

See Fig. 6.

3. Stainless steel and water

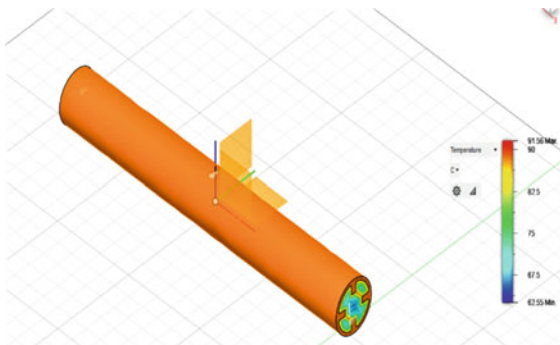
See Fig. 7.

Fig. 6 Aluminium tube with rectangular fins



Minimum	Maximum
63.65°C	91.93°C

Fig. 7 Stainless steel tube with rectangular fins



Minimum	Maximum
62.55°C	91.56°C

Combined result

Material	Without fin (°C)	Rectangular fin (°C)
Copper	50.24	63.70
Aluminium	51.23	63.65
Stainless steel	49.23	62.55

It was seen from above simulation that by using fins inside the absorber tubes proves to be more efficient in temperature distribution compared to absorber tubes without fins, whereas material of fins also plays major role in enhancement of temperature. It was found that copper fins were more effective in temperature distribution compared to aluminium and stainless steel, respectively. The temperature for copper absorber tubes without fins was found to be 50.24 °C and with fins was 63.70 °C. So, it was observed that there was rise in the temperature of water by 12 °C.

5 Conclusion

It can be concluded that by using copper rectangular fins, it is more beneficial in terms of temperature distribution, material cost, corrosion resistance, water hindrance, and other thermal parameters compared to aluminium rectangular fins and stainless steel rectangular fins. Hence, fin's shape and material play a critical part in working on the proficiency of the solar water heater. The temperature difference was recorded as 12 °C for copper absorber tubes without fins and with fins as stated above.

References

18. Badescu V (2006) Optimum fin geometry in flat plate solar collector systems. *Energy Convers Manage* 47(15):2397–2413
9. K. Balaji, S. Iniyar and A. Idrish Khan, 2015, Thermodynamic analysis of a solar flat plate water heater using extended surface absorber tube, *International solar energy society selection*.
11. L. F. Cabeza, M. Nogues, J. Roca, J. Illa, S. Hiebler and H. Mehling, 2003, Phase change material-module to improve hot water heat stores with stratification: first tests in a complete solar system, *International conference on thermal energy storage*, Vol. 1.
1. A. Campo and R. E. Stuffle, [1996], Symbolic mathematics for calculation of thermal efficiencies and tip temperatures in annular fins of uniform thickness, *International journal of heat mass transfer*, Vol. 40, No. 2, pp. 490–492.
2. Castell A, Sole C, Medrano M, Roca J, Garcia D, Cabeza LF (2006) Effect of using external vertical fins in phase change material modules for domestic hot water tanks. *Renewable energy and power quality journal* 1(4):118–123
5. Chabane F, Moumni N, Benramache S (2014) Experimental study of heat transfer and thermal performance with longitudinal fins of solar air heater. *J Adv Res* 5:183–192
3. Chii-Dong Ho and Tsung-Ching Chen (2007) Collector efficiency of double-pass sheet and tube solar water heaters with internal fins attached. *Tamkan journal of science and engineering* 10(4):323–334

4. Esmail and M. A. Mokheimer, (2002) Performance of annular fins with different profiles subject to variable heat transfer coefficient. *Int J Heat Mass Transf* 45(17):3631–3642
7. Guodong Qiu, Jian Sun, Lijun Nie, Yuanyang Ma, Weihua Cai and Chao Shene, 2020, Theoretical study on heat transfer characteristics of a finned tube used in the collector/evaporator under solar radiation, *Applied thermal engineering*, Vol. 165.
10. K. Jesurar, D. B. Sivakumar, B. Kumaragurubaran and T. Senthil Kumar, 2016, Heat enhancement in solar water heater, *International journal of engineering science and computing*, Vol. 6 (6).
6. Murali G, Mayilsamy K (2015) Effect of circular fins on latent heat storage to enhance solar water heater: an experimental study. *Appl Mech Mater* 787:13–17
13. P. P. Patil and Dr. D.S. Deshmukh, 2015, Design considerations for flat plate solar water heater system, *International journal of science, spirituality, business and technology*, Vol. 3 (2).
14. Sethuraman Ramasamy and Pakkirisamy Balashanmugam, 2015, Thermal performance analysis of the solar water heater with circular and rectangular absorber fins, *International journal of innovative science, engineering and technology*, Vol. 2 (1).
16. Selvam, Prathap and Dr. C. Sivarajan, 2019, A review of solar water heater performance factors, *International research journal of engineering and technology*, Vol. 6 (6).
15. Shakir MM, Dr. Sanke Narsimhulu, (2015) Solar flat plate collector heat transfer analysis in the raiser with helical fins. *International journal of engineering and science research* 5(5):352–356
12. Sheikh NN, Kumar B, Saini NK (2019) A Review Paper on Pin Fin Efficiency Enhancement. *Int J Appl Eng Res* 14(9):108–112
8. Singh I, Vardhan S, Singh S (2019) A review on solar energy collection for thermal applications. *International journal of advance and innovative research* 6(1):252–259
17. Virendra Bisen and N.K. Sagar, 2020, CFD analysis of heat transfer in annular fins of various profiles having different shapes of perforation, *International journal for research in applied science and engineering technology*, Vol. 8 (2).

Emission Analysis Through Numerical Simulation of Three-Way Catalytic Converter with Thermal Energy Storage



Sanket S. Keer, Gargee Pise, and M. R. Nandgaonkar

Abstract One of the methods implied by the automakers to meet regulations upon automotive emissions is application of catalytic converter. The major challenge associated with the catalytic converter is its inactivity in conversion of emission until it reaches the light-off temperature. This work is intended to employ a technique to minimize the time taken by catalytic converter to attain light-off temperature and reduce its inactive period. The effect of thermal heat storage system on the operation of catalytic converter is analyzed using ANSYS CHEMKIN Pro software. Accordingly, emission analysis using numerical simulation of catalytic converter with Phase Change Material (PCM) is done to calculate the improvement in the performance of catalytic converter. Phase Change Material ($Mg_{70}Zn_{24.9}Al_{5.1}$) with transition temperature of 613 K is formulated with catalytic converter, and simulation is done for three different loads (100%, 50%, and No load). During normal engine operation (charging period), PCM extracts some of the thermal energy from exhaust gas and stores in the form of sensible heat as well as latent heat. During engine off period, whatever heat is stored in PCM in the form of latent heat is transmitted back to substrate by undergoing partial or complete solidification to maintain substrate temperature in desired light-off temperature range for maximum conversion efficiency. The results from the simulation are substantiated experimentally. The results signify that application of PCM as a thermal energy storage leads to overall increment in the conversion efficiency during cold starting of the engine. This is evident from the continuous improvement of conversion of pollutants from exhaust gas in subsequent transient cycles.

Keywords Cold start emission · Catalytic converter · Light-off temperature · Conversion efficiency · Thermal energy storage · Phase change material · Numerical simulation · CHEMKIN

S. S. Keer (✉) · G. Pise · M. R. Nandgaonkar
College of Engineering, Pune, India
e-mail: keerss19.mech@coep.ac.in

Nomenclature

ΔH_m	Latent heat of fusion
Q_l	Heat loss to environment
R_{th}	Thermal resistance

1 Introduction

Automobiles constitute a larger part in atmospheric pollution. The exhaust flue gases from spark ignition engine contain oxides of nitrogen (NO_x), carbon monoxide (CO), and organic compounds that are unburnt hydrocarbons (HC). Though the CO and HC emissions are less in Compression-Ignition (diesel) engines, their main problem is the presence of particulate matter. Hike in environmental pollution is an important problem appearing and one of the reasons contributing to this is the internal combustion engines.

There are numbers of techniques available to reduce the pollution emitted from the vehicles like catalytic converter, improvement in combustion chamber, fuel additives, fuel pre-treatment, diesel particulate filter, use of alternate fuels, etc. Among all of them, use of catalytic converter based on noble group metal is very promising. Catalytic converters have proved to be one of the most effective method for minimizing toxic pollutants from internal combustion (IC) engines working under normal operating range. The fact that the conversion efficiency declines very swiftly for temperatures under light-off temperature and is very low during the starting and warming-up period is stated by Pardiwala [1]. The preferred method to elevate these activating temperatures is by means of engine-related measures like throttling of intake air, post-injection, and exhaust pipe fuel injection.

According to Sun [2], although the cold start segment corresponds to about 3% of total test time, it is responsible for more than 80% of total HC and CO emissions collected during the full cycle. Enhancement of conversion efficiency in cold starting conditions is required specifically in metro cities, where starting of vehicle in a day is more frequently. Among all techniques employed to reduce cold start period, some techniques like electrical or external combustion chamber heating of the catalyst and exhaust gas ignition systems are found to be successful. Although these techniques have enhancement in the performance, they require an external energy source making it less economical.

Enhancement in the performance of catalytic converter during cold start period has more scope for research. So, the present work is focused on the performance enhancement of catalytic converter of IC engine using thermal heat storage system at various operating conditions.

Table 1 PCM properties

	T(K)	Mg ₇₀ Zn _{24.9} Al _{5.1}	Zn _{85.8} Al _{8.2} Mg ₆
T _m (K)		613	617
ΔH _m (kJ/kg)		157	104
ρ(kg/m ³)	298	2820	6190
C _p (J/kg.K)	298	690	410
	573	830	530
k(W/m.K)	323	47	59
	573	59	55
	673	38	31

2 Problem Description

To reduce the warm up period of the catalytic converter, we can extract heat from the exhaust of an engine and employ it for heating. Filter regeneration with help of Phase Change Material (PCM) could be another option. PCM are the materials which are used to store the latent heat. The latent thermal energy storage system can be used to store the waste thermal energy, and same energy can be used to maintain the temperature of the catalytic converter during ‘engine off’ period. When next time we start the vehicle, the warm up period will get reduced or even completely eliminated. A PCM with transition (melting point) temperature slightly above the ‘light-off’ temperature of the catalytic converter can be used to maintain the temperature of catalytic converter.

The energy can be stored in the mode of heat using thermal energy storages. Several types of materials have been examined by the researchers for application as latent heat storage. Then again, the major shortcoming of such materials is their low thermal conductivity which is responsible for low heat transfer rates. Number of researches are embarked on in the last few years to solve this limitation.

As far as the thermal transport behavior of the thermal energy storage (TES) system is concerned, the application of metal/metal alloys as PCMs is a better alternative. Mg-Zn-Al eutectic alloys are found to be appropriate for this application based upon their physical properties. Risueño [3] studied the physical properties of two Mg-Zn-Al alloys, which are described in Table 1.

Table 1 represents the values of thermophysical properties of Mg₇₀Zn_{24.9}Al_{5.1} and Zn_{85.8}Al_{8.2}Mg₆ eutectic alloys. T_m denotes melting temperature.

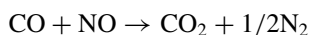
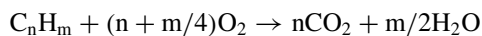
3 Numerical Simulation

Numerical simulation is proved to be a convenient and effective tool for the prediction of the performance of the catalytic converter. There are two approaches to carry out the numerical simulation of a catalytic converter. The first approach is to represent the

monolith as cluster of small individually reacting channels and then converge them as a thermal network model. The second approach is by approximating the monolith as a porous medium. According to Kumar [4], the latter is best suited for minimum time and space complexity. The effect of thermal heat storage system (PCM) on the performance of catalytic converter is studied using ANSYS CHEMKIN Pro software. All the prerequisites required for simulation of detailed chemical reactions have been obtained prior to this with the help of modeling and simulation performed in ANSYS Fluent. Accordingly, emission analysis using numerical simulation of catalytic converter with PCM is done to calculate the improvement in the performance of catalytic converter. The results from the simulation are validated with the experimental results performed. CHEMKIN Pro's ability of simulating precise, fast, and dynamic kinetic models yield it to be one of the most suitable kinetic simulation tools for estimating outputs in the product planning and design phase. Technologists can straightway explore the influence of design attributes on operation, emissions, and flame extinction using substantial, accurate fuel models to obtain the results which are essential for making key product development decisions. The software simulates realistic chemical reactors in practice so that we can assess exhaustive chemistry competently to simulate residue species formation and devastation.

Surface reaction mechanism Basically, a project in CHEMKIN requires two input files regarding mechanisms named as Gas-Phase Kinetics File and Surface Kinetics File. The conditions inside a substrate of catalytic converter like low pressure and temperature with short residence time of species allows us to neglect gas phase chemistry. Hence, the data regarding six elements: O, H, C, N, Rh, and Pt; nine species: O₂, C₃H₆, H₂, H₂O, CO₂, CO, NO, NO₂, and N₂ are included in Gas-Phase Kinetics input file. There are no reactions included in this file. For this application, surface chemistry occurring on the monolith substrate is more dominating than the gas phase chemistry.

The chemical reactions of the polluting contents in the exhaust gases into harmless components inside a monolithic three-way catalyst are represented generally as followed.



This kind of global chemistry is the basis upon which a literature by Chatterjee [5] is stated. The surface reaction mechanism stated in literature by Chatterjee [5] includes number of elementary reaction steps. Hence, the software helps us to employ a more detailed study to model the surface chemistry. The reactions considered for the simulation consists of 61 elementary reaction steps and 31 chemical species which includes dissociative oxygen adsorption, non-dissociative adsorption of C₃H₆, CO

and NO, the reaction of carbon dioxide (CO₂), water (H₂O), and nitrogen (N₂), and desorption of all species.

All the reactions stated by Chatterjee [5] and considered in simulation are represented in Table 2.

Simulation Set up For a substrate wrapped up in the PCM jacket, the rate of heat loss and surface temperature defers from the conventional catalytic converter. Hence, these two parameters will be the differentiating parameters used to simulate the catalytic converter with Phase Change Material. As a prerequisite of this simulation, the effect of PCM on the surface temperature of monolith substrate has already been studied in ANSYS Fluent and also validated with the experimental data. Hence, the obtained surface temperature profile of the catalytic converter is used for heat loss calculations from the reactor (Fig. 1).

The heat loss from a composite cylinder can be calculated using following equation by Incropera [6]:

$$Q_1 = \frac{T_{\text{substrate}} - T_{\text{ambient}}}{\text{Thermal Resistance}} \quad (1)$$

Here, the thermal resistance is offered by steel covers, PCM jacket, and insulation. The thermal resistance for cylindrical body is given by Incropera [6] as.

$$R_{\text{th}} = \frac{\ln\left(\frac{r_2}{r_1}\right)}{2\pi kl} \quad (2)$$

where r_1 and r_2 are the radii of inner and outer cylinders, k is the thermal conductivity of material, and l is the length of the cylinder.

Along with the heat loss, surface temperature is also an important parameter in the simulation. But the provision by the CHEMKIN Pro allows us to either enter a constant value of surface temperature or consider surface temperature equal to the gas temperature. Constant surface temperature cannot work for simulation as our surface temperature is going to vary with respect to time and also perform a vital role in simulation.

Hence, we are using surface temperature same as gas temperature. But, as this chemistry is dominated by surface reactions rather than gas phase chemistry, surface temperature profile is input instead of the gas temperature.

4 Results and Discussions

The simulation is performed to understand the effect of Mg₇₀Zn_{24.9}Al_{5.1} as a PCM on the performance of a three-way catalytic converter. Conversion efficiency is the performance parameter of a catalytic converter. Hence, all the results obtained are in terms of conversion efficiency of the residual gases, namely HC, CO, and NOx.

Table 2 Chemical reactions in catalytic converter (Chatterjee [5])

No	Reaction
(a)	C₃H₆ oxidation on Pt
A	Adsorption
1	$O_2 + Pt(s) + Pt(s) \rightarrow O(s) + O(s)$
2	$C_3H_6 + Pt(s) + Pt(s) \rightarrow C_3H_6(s)$
3	$C_3H_6 + O(s) + Pt(s) \rightarrow C_3H_5(s) + OH(s)$
4	$H_2 + Pt(s) + Pt(s) \rightarrow H(s) + H(s)$
5	$H_2O + Pt(s) \rightarrow H_2O(s)$
6	$CO_2 + Pt(s) \rightarrow CO_2(s)$
7	$CO + Pt(s) \rightarrow CO(s)$
B	Desorption
8	$O(s) + O(s) \rightarrow O_2 + Pt(s) + Pt(s)$
9	$C_3H_6(s) \rightarrow C_3H_6 + Pt(s) + Pt(s)$
10	$C_3H_5(s) + OH(s) \rightarrow C_3H_6 + O(s) + Pt(s)$
11	$H(s) + H(s) \rightarrow H_2 + Pt(s) + Pt(s)$
12	$H_2O(s) \rightarrow Pt(s) + H_2O$
13	$CO(s) \rightarrow CO + Pt(s)$
14	$CO_2(s) \rightarrow CO_2 + Pt(s)$
C	Surface reaction
C.1	C ₃ H ₅ (s) Oxidation [global reaction]
15	$C_3H_5(s) + 5O(s) \rightarrow 5OH(s) + 3C(s)$
C.2	C ₃ H ₆ (s) Consumption
16	$C_3H_6(s) \rightarrow H(s) + CC_2H_5(s)$
17	$CC_2H_5(s) + H(s) \rightarrow C_3H_6(s)$
18	$CC_2H_5(s) + Pt(s) \rightarrow C_2H_3(s) + CH_2(s)$
19	$C_2H_3(s) + CH_2(s) \rightarrow Pt(s) + CC_2H_5(s)$
20	$C_2H_3(s) + Pt(s) \rightarrow CH_3(s) + C(s)$
21	$CH_3(s) + C(s) \rightarrow C_2H_3(s) + Pt(s)$
C.3	CH _x Consumption
22	$CH_3(s) + Pt(s) \rightarrow CH_2(s) + H(s)$
23	$CH_2(s) + H(s) \rightarrow CH_3(s) + Pt(s)$
24	$CH_2(s) + Pt(s) \rightarrow CH(s) + H(s)$
25	$CH(s) + H(s) \rightarrow CH_2(s) + Pt(s)$
26	$CH(s) + Pt(s) \rightarrow C(s) + H(s)$
27	$C(s) + H(s) \rightarrow CH(s) + Pt(s)$
C.4	C ₂ H _x Oxidation
28	$C_2H_3(s) + O(s) \rightarrow Pt(s) + CH_3CO(s)$
29	$CH_3CO(s) + Pt(s) \rightarrow C_2H_3(s) + O(s)$

(continued)

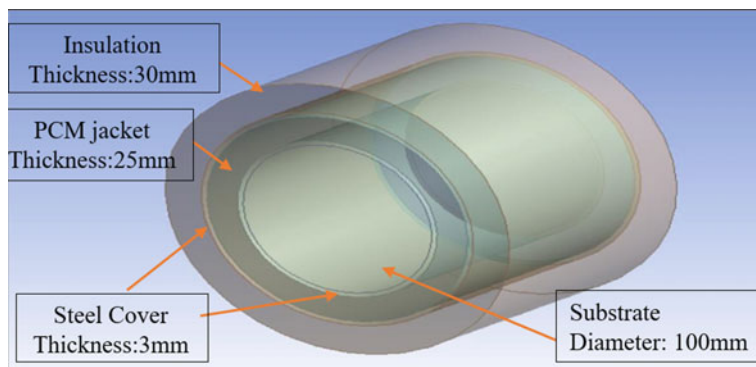
Table 2 (continued)

No	Reaction
30	$\text{CH}_3(\text{s}) + \text{CO}(\text{s}) \rightarrow \text{Pt}(\text{s}) + \text{CH}_3\text{CO}(\text{s})$
31	$\text{CH}_3\text{CO}(\text{s}) + \text{Pt}(\text{s}) \rightarrow \text{CH}_3(\text{s}) + \text{CO}(\text{s})$
C.5	CH_x Oxidation
32	$\text{CH}_3(\text{s}) + \text{O}(\text{s}) \rightarrow \text{CH}_2(\text{s}) + \text{OH}(\text{s})$
33	$\text{CH}_2(\text{s}) + \text{OH}(\text{s}) \rightarrow \text{CH}_3(\text{s}) + \text{O}(\text{s})$
34	$\text{CH}_2(\text{s}) + \text{O}(\text{s}) \rightarrow \text{CH}(\text{s}) + \text{OH}(\text{s})$
35	$\text{CH}(\text{s}) + \text{OH}(\text{s}) \rightarrow \text{CH}_2(\text{s}) + \text{O}(\text{s})$
36	$\text{CH}(\text{s}) + \text{O}(\text{s}) \rightarrow \text{C}(\text{s}) + \text{OH}(\text{s})$
37	$\text{C}(\text{s}) + \text{OH}(\text{s}) \rightarrow \text{CH}(\text{s}) + \text{O}(\text{s})$
C.6	H, OH, H ₂ O Surface Reactions
38	$\text{O}(\text{s}) + \text{H}(\text{s}) \rightarrow \text{OH}(\text{s}) + \text{Pt}(\text{s})$
39	$\text{OH}(\text{s}) + \text{Pt}(\text{s}) \rightarrow \text{O}(\text{s}) + \text{H}(\text{s})$
40	$\text{H}(\text{s}) + \text{OH}(\text{s}) \rightarrow \text{H}_2\text{O}(\text{s}) + \text{Pt}(\text{s})$
41	$\text{H}_2\text{O}(\text{s}) + \text{Pt}(\text{s}) \rightarrow \text{H}(\text{s}) + \text{OH}(\text{s})$
42	$\text{OH}(\text{s}) + \text{OH}(\text{s}) \rightarrow \text{H}_2\text{O}(\text{s}) + \text{O}(\text{s})$
43	$\text{H}_2\text{O}(\text{s}) + \text{O}(\text{s}) \rightarrow \text{OH}(\text{s}) + \text{OH}(\text{s})$
C.7	CO oxidation
44	$\text{CO}(\text{s}) + \text{O}(\text{s}) \rightarrow \text{CO}_2(\text{s}) + \text{Pt}(\text{s})$
45	$\text{CO}_2(\text{s}) + \text{Pt}(\text{s}) \rightarrow \text{CO}(\text{s}) + \text{O}(\text{s})$
46	$\text{C}(\text{s}) + \text{O}(\text{s}) \rightarrow \text{CO}(\text{s}) + \text{Pt}(\text{s})$
47	$\text{CO}(\text{s}) + \text{Pt}(\text{s}) \rightarrow \text{C}(\text{s}) + \text{O}(\text{s})$
(b)	NO reduction on Pt
A	Adsorption
48	$\text{NO} + \text{Pt}(\text{s}) \rightarrow \text{NO}(\text{s})$
B	Desorption
49	$\text{NO}(\text{s}) \rightarrow \text{NO} + \text{Pt}(\text{s})$
50	$\text{N}(\text{s}) + \text{N}(\text{s}) \rightarrow \text{N}_2 + \text{Pt}(\text{s}) + \text{Pt}(\text{s})$
C	NO surface reactions
51	$\text{NO}(\text{s}) + \text{Pt}(\text{s}) \rightarrow (\text{s}) + \text{O}(\text{s})$
52	$\text{N}(\text{s}) + \text{O}(\text{s}) \rightarrow \text{NO}(\text{s}) + \text{Pt}(\text{s})$
(c)	NO reduction and CO oxidation on Rh
A	Adsorption
53	$\text{O}_2 + \text{Rh}(\text{s}) + \text{Rh}(\text{s}) \rightarrow \text{O}(\text{Rh}) + \text{O}(\text{Rh})$
54	$\text{CO} + \text{Rh}(\text{s}) \rightarrow \text{CO}(\text{Rh})$
55	$\text{NO} + \text{Rh}(\text{s}) \rightarrow \text{NO}(\text{Rh})$
B	Desorption
56	$\text{O}(\text{Rh}) + \text{O}(\text{Rh}) \rightarrow \text{O}_2 + \text{Rh}(\text{s}) + \text{Rh}(\text{s})$

(continued)

Table 2 (continued)

No	Reaction
57	$\text{CO}(\text{Rh}) \rightarrow \text{CO} + \text{Rh}(\text{s})$
58	$\text{NO}(\text{Rh}) \rightarrow \text{NO} + \text{Rh}(\text{s})$
59	$\text{N}(\text{Rh}) + \text{N}(\text{Rh}) \rightarrow \text{N}_2 + \text{Rh}(\text{s}) + \text{Rh}(\text{s})$
C	NO/CO surface reactions
60	$\text{CO}(\text{Rh}) + \text{O}(\text{Rh}) \rightarrow \text{CO}_2 + \text{Rh}(\text{s}) + \text{Rh}(\text{s})$
61	$\text{NO}(\text{Rh}) + \text{Rh}(\text{s}) \rightarrow \text{N}(\text{Rh}) + \text{O}(\text{Rh})$

**Fig. 1** CAD representation of catalytic converter

The proportion of the constituents in the exhaust gas varies with the variation in load applied on the engine. Hence, the readings have been taken at different loads applied on the engine (100%, 50%, and No load). To understand the capacity of PCM to hold the heat and to transfer it back to the substrate, the experiment has been carried out in a specific pattern. The engine is allowed to run for 30 min with load applied. This is known as First Transient Cycle. It is followed by shutting off the engine for next 30 min and allowing PCM to transfer heat back to the substrate. Again, the engine is operated for another 30 min as Second Transient Cycle. For a second time, the engine is shut off for 30 min followed by Third Transient Cycle. As we are dealing with the improvement of conversion efficiency in starting period, we use initial few readings for comparison between with PCM and without PCM models. Comparison of conversion efficiency in Third Transient Cycle with First Transient Cycle will let us analyze the improvement in starting period emission control with the help of PCM employed. The effect of the PCM utilized is estimated by comparison between conversion efficiency with PCM and without PCM.

Figures 2 and 3 are the results of simulation for 100% load applied on the engine for First and Third Transient Cycle, respectively. On comparison of conversion efficiency between First and Third Transient Cycles for 100% load on engine, it is evident that the Conversion efficiency of HC is improved by 46.26%. Similarly, the Conversion efficiency of CO is improved by 6.37%. From the results of simulation, it can be

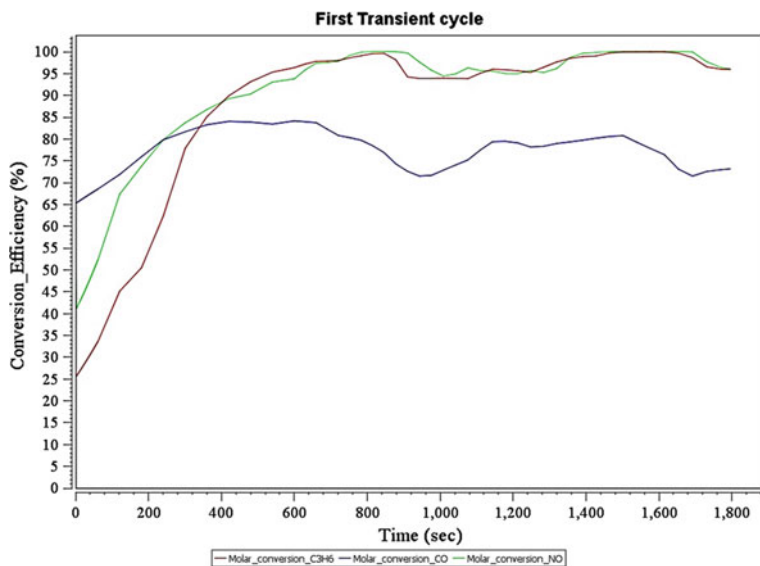


Fig. 2 First Transient Cycle for 100% load

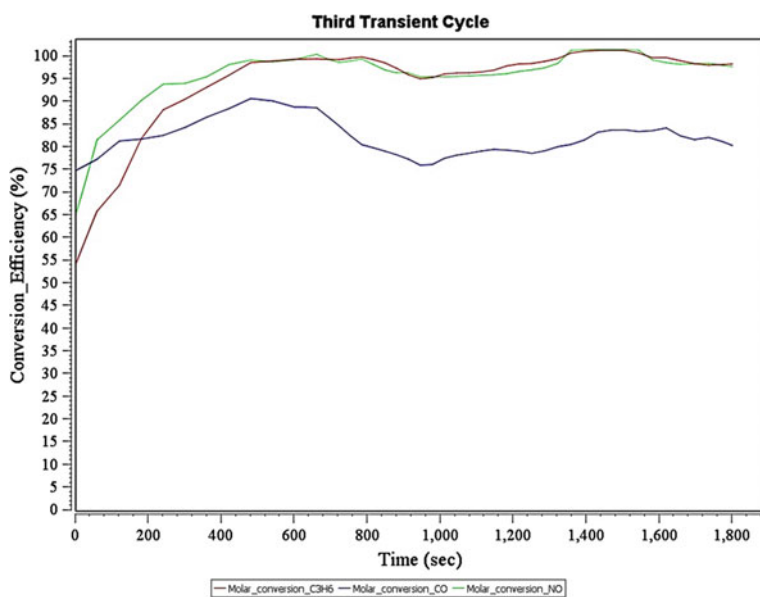


Fig. 3 Third Transient Cycle for 100% load

analyzed that the conversion efficiency of NOx has been improved by 23.61%. Similar improvement in Conversion efficiency for third transient cycles is observed for all other loads applied on the engine.

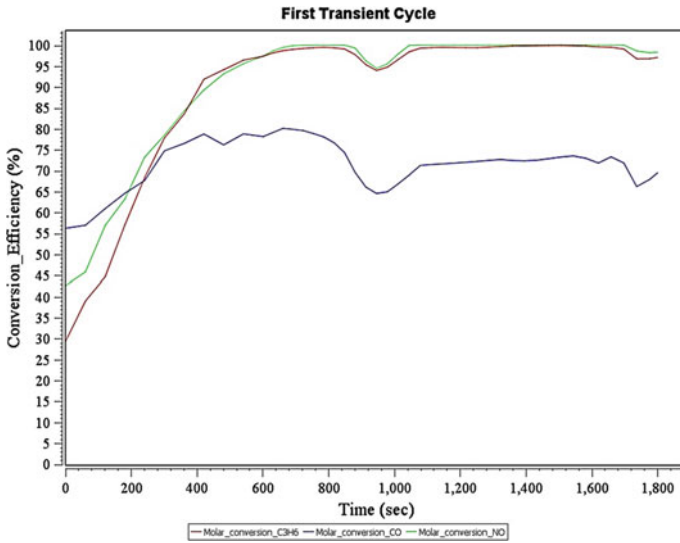


Fig. 4 First Transient Cycle for 50% load

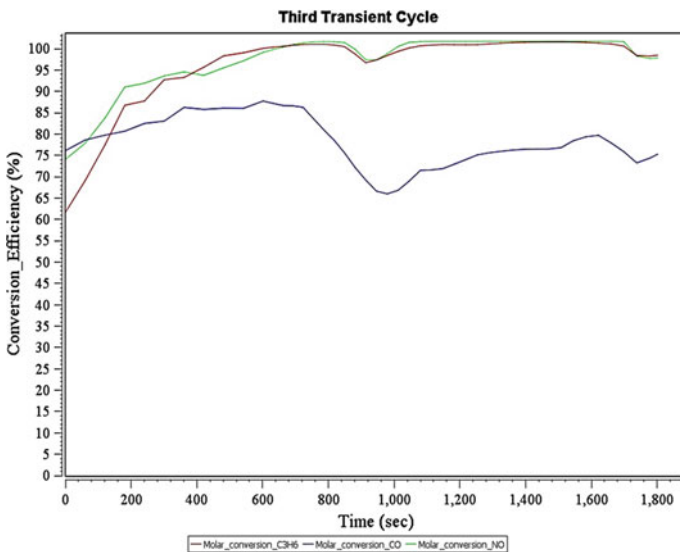


Fig. 5 Third Transient Cycle for 50% load

The comparison of conversion efficiency between First and Third Transient Cycles of 50% load (Figs. 4 and 5) yields that the Conversion efficiency of HC is improved by 41.92%. Here the conversion efficiency of CO is improved by 22.56%. It is evident that overall improvement of 35.87% is obtained in the conversion efficiency of NOx.

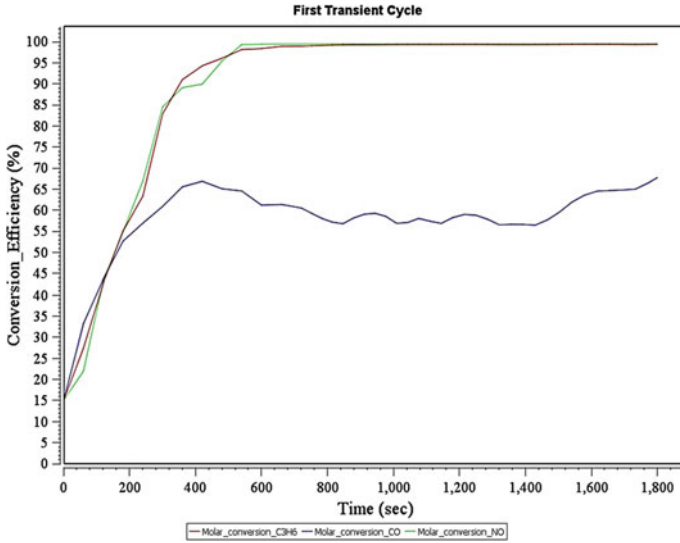


Fig. 6 First Transient Cycle for No load

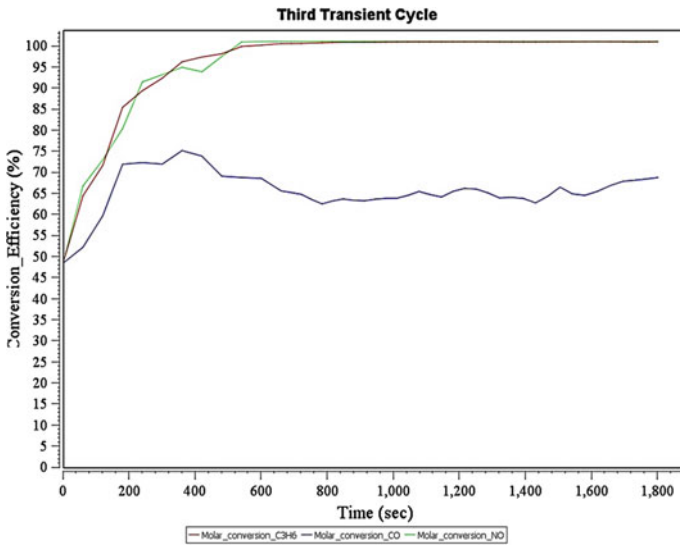


Fig. 7 Third Transient Cycle for No load

On comparison of conversion efficiency between First and Third Transient Cycles for No load on engine (Figs. 6 and 7), it is evident that the conversion efficiency of HC is improved by 45.38%. Similarly, the conversion efficiency of CO is improved by 26.70%. From the results of simulation, it can be analyzed that the conversion efficiency of NO_x has been improved by 53.10%.

The effect of Mg₇₀Zn_{24.9}Al_{5.1} as thermal energy storage is assessed by the percentage improvement in conversion efficiency of pollutants by catalytic converter with PCM. After studying the values of conversion efficiency during the starting period of transient cycles, it is evident that for all loads, the average improvement in the conversion of HC gas is 52.17%. The PCM jacket improves the conversion of CO gas by 18.01% and that of NO_x gas by 37.99% average for different loading conditions.

5 Conclusions

The results signify that application of PCM as a thermal energy storage leads to overall increment in the conversion efficiency during cold starting of the engine. This is evident from the continuous improvement of conversion of pollutants from exhaust gas in subsequent transient cycles.

Numerical simulation of catalytic converter with PCM simulates the chemical reactions occurring in the catalytic converter with the help of 61 reaction mechanisms. This simulation model is validated with the experimental work. The divergence attained between practical and simulated results for conversion of targeted pollutants, i.e., HC, CO, and NO_x is less than 5%.

The effect of catalytic converter with PCM is extensively the most for conversion of HC gas from the exhaust. There is also significant improvement in the conversion of NO_x gas during the cold starting period of engine. Considering the impact on conversion of CO gas, it is observed to be slightly lesser during heavy load condition but tend to improve at lower loads.

Acknowledgements The authors are thankful and extend their gratitude to College of Engineering, Pune, for providing useful softwares and laboratories for smooth completion of the work.

References

1. Pardiwala JM, Patel F, Patel S (2011) Review paper on catalytic converter for automotive exhaust emission international conference on current trends in technology. 'NUiCONE-2011' Nirma University, Ahmedabad
2. Sun J, Sivashankar N (1998) Issues in Cold start emission control for automotive IC engines. In: Proceedings of the American control conference, Philadelphia, Pennsylvania, pp 1372–1376
3. Risueño E, Faik A, Rodríguez-Aseguinolaza J, Blanco-Rodríguez P, Gil A, Tello M, D'Aguzzo B (2015) Mg-Zn-Al eutectic alloys as phase change material for latent heat thermal energy

- storage. In: International conference on concentrating solar power and chemical energy systems, SolarPACES 2014, pp 1006–1013
4. Kumar A, Mazumder S (2010) Toward simulation of full-scale monolithic catalytic converters with complex heterogeneous chemistry. *Comput Chem Eng*, pp 135–145
 5. Chatterjee D, Deutschmann O, Warnatz J (2001) Detailed surface reaction mechanism in a three-way catalyst. *Faraday Discuss*, 119:371–384
 6. Incropera P (2007) *Fundamentals of heat and mass transfer*. John Wiley & Sons, USA
 7. Bera P, Hegde MS (2010) Recent advances in auto exhaust catalysis. *J Indian Institute Sci*, pp 299–325
 8. Bokde KK, Waghmare AV (2013) Cold start performance enhancement of motorcycle catalytic convertor by latent heat storage system. *Int J Innov Res Sci Eng Technol* 2(2):372–377
 9. Braun J, Hauber T, Többen H, Windmann J, Zacke P (2002) Three-dimensional simulation of the transient behavior of a three-way catalytic converter SAE 2002 World Congress Detroit, Michigan
 10. Burch SD, Potter TF, Keyser MA, Brady MJ, Michaels KF (1995) Reducing cold-start emissions by catalytic converter thermal management. SAE International Congress and Exposition Detroit, Michigan
 11. Gao J, Tian G, Sornioti A, Karci AE, Palo RD (2018) Review of thermal management of catalytic converters to decrease engine emissions during cold start and warm up. *Appl Thermal Eng*
 12. Gumus M (2009) Reducing cold-start emission from internal combustion engines by means of thermal energy storage system. *Appl Thermal Eng* 29, pp 652–660
 13. Korin E, Reshef R, Tshernichovesky D, Sher E (1999) Reducing cold-start emission from internal combustion engines by means of a catalytic converter embedded in a phase-change material. In: *Proceedings of the institution of mechanical engineers vol 213, Part D*, pp 575–583
 14. Real M, Hedinger R, Pla B, Onder C (2019) Modelling three-way catalytic converter oriented to engine cold-start conditions. *Int J Engine Res*, pp 1–12
 15. Subramanian SP, Pandiyarajan V, Velraj R (2004) Experimental analysis of a PCM based I.C. engine exhaust waste heat recovery system. *Int Energ J* 5(2):81–92
 16. Sinha YK, Banjare YP (2015) Computational analysis of three-way monolithic catalytic converter using FVM tool ANSYS fluent. *Int J Eng Trends Technol (IJETT)* 26(3):174–181
 17. Venkatesh L, Logeshkumar R, Jayaprakash G, Dinesh N (2017) Control and reduction of emissions using catalytic converter. *Int Res J Eng Technol* 4(11):788–794

Optimization of 3D Plate Fin Heat Sinks Through Analytical Modelling



Niyaj Shikalgar, Pushkar Chitale, and S. N. Sapali

Abstract Heat sinks are the most integral part of electronic devices which help in the quick dissipation of heat and thus protect them from overheating. Due to continuous effort to increase the power density within minimum space, the design of highly efficient heat sinks has become mandatory for the proper functioning of devices. In this paper, a quick method to optimize the heat sinks with a fixed number of heat sources has been discussed. A new Analytical Model has been introduced that can perform temperature evaluations of electronic devices in a much shorter time and can be used as a replacement for CFD. The main goal of this paper is to present a Genetic Algorithm where the Analytical Model can be taken as an objective and can be checked for thousands of heat sink geometries for quick evaluation of highly efficient heat sink design. The resulting model applies to forced convection plate fin heat sinks with fully developed laminar airflow between channels.

Keywords Forced convection · Fully developed laminar flow · Genetic algorithm · Plate fin heat sinks

1 Introduction

Electronic components produce heat while working. This heat must be dissipated away continuously to keep their operating temperatures below the design limit and thereby increase their service life. Heat sinks cooled by natural or forced convection have served as a typical solution for the enhancement of the heat transfer from the electronic components. The extended surfaces of the heat sink generally provide a larger area for heat transfer and conduct heat.

Forced convection heat sinks are employed in most applications as they can remove large heat loads as compared to natural convection heat sinks. The performance of the heat sink is sensitive to its geometrical structure because overall heat transfer is constrained by the conduction resistance imposed by solid geometry

N. Shikalgar (✉) · P. Chitale · S. N. Sapali
Department of Mechanical Engineering, College of Engineering Pune, Pune, India
e-mail: nds.mech@coep.ac.in; niyaj.shikalgar@gmail.com

and convection resistance of the airflow in heat sink channels. Due to continuously increasing power densities, the optimal design of a heat sink by considering weight, space, and thermal constraints is a challenging task.

Typically, a heat sink has a base plate on which many eccentric components of different wattages and sizes are placed. Optimal design must minimize the component maximum temperature, heat sink weight, manufacturing, and operating costs. The main part of optimization is to find the correct temperature distribution by considering the heat spreading effect due to smaller-sized heat sources. The maximum temperature depends on the component locations, heat dissipation rates, heat sink dimensions, and flow conditions.

Computational Fluid Dynamics software is mostly preferred in industries to obtain the temperature field for single case calculation. However, CFD simulation of a single iteration takes a long time, and it depends on the skill and expertise of the user. To check hundreds of different geometries for optimization, CFD performs too slowly.

The main objective of this thesis is to model forced convection plate fin heat sinks analytically, which will perform quick temperature field evaluations accurately and can be capable of replacing the present CFD technique. This makes it possible to use the new model as a part of an effective multi-variable algorithm where it can be checked by varying different geometric parameters to get the optimum heat sink design. The important objectives of the paper are

- To develop an Analytical Model for quick prediction of electronic case temperatures for forced convection heat sinks.
- Test the model accuracy using CFD/experimental results
- Present the model used in the multi-variable algorithm for thermal performance or weight optimization.

1.1 Literature Review

There are different literature studies available for the modelling of heat sinks. However, many of those studies are based on very simple 1D mathematical modelling with many assumptions or are very complex (numerical analysis using CFD or FEM).

Optimal solutions for fins that take into consideration the effect of surface temperature distribution on heat transfer coefficient are presented by Kraus et al. [1]. Optimizing a single fin helps in understanding the effect of fin shape on the heat transfer efficiency of a single fin. However, fin array optimization is more complicated because flow between channels is also taken into consideration.

There are various studies presented by Bejan and Sciubba [2] for isothermal heat sink optimization based on forced convection. Optimal fin spacing has been obtained by various numerical and analytical approaches for various flow boundary conditions. The analytical formula was based on the intersection of asymptotes, which is a simple and effective way to obtain optimal fin spacing. Teeresta et al. [3] used the same method of the intersection of asymptotes to develop the composite solution for average Nusselt's number based on limiting cases of fully developed and

developing flow between isothermal parallel plates. Shah and London [4] developed a correlation for forced laminar and turbulent heat transfer coefficient as a function of the dimensionless parameter.

There are two- or three-dimensional models presented by Yovanovich et al. [5] coming from direct solving of heat transfer equation. They are more advantageous as they consider the realistic way of heat propagation. They take into consideration the real heat spreading effect in the baseplate due to smaller size heat sources. This spreading phenomenon is not properly explained in the 1D resistive model of Lee et al. [6].

There are different multi-objective optimization studies for isothermal arrays such as “minimum thermal resistance with fixed weight or pressure drop” and vice versa. Lindstedt and Karvinen [7] concluded that at least one design parameter from fin height, fin thickness, number of fins, and flow mean velocity must be fixed in the optimization to get meaningful geometry.

Lampio and Karvinen [8] developed a correlation for effective heat transfer coefficient of heat sink based on the energy balance of small control volume of flow region and carried out different multi-objective optimization on forced and natural convection heat sinks using Particle Swarm Algorithm.

The approach proposed in this work combines the fin or heat sink model with the base plate model to obtain an Analytical Model that will quickly predict the temperatures of components and can be taken to optimization routine to get the highly efficient heat sink design.

2 Methodology

Plate fin heat sinks are characterized by fins with the rectangular cross-sectional area having uniform spacing resulting in the formation of fin array. Above the fin array, there is a base plate of desired thickness over which different heat sources are mounted. Air is forced to flow through the channels with the help of a fan for cooling.

The heat sink model has been shown in Figs. 1 and 3. The important design parameters are fin height, number of fins, length of fins, the width of fin array, the thickness of fin, the space between the fins, and base plate thickness.

The development of the model starts by entering the input parameters which includes number, size, location, power wattage of each heat source, component package resistance details (thermal grease, ceramic pad, etc.), heat sink geometry (no of fins, geometry details), heat sink and fluid material, duct dimensions, the velocity of the fluid, and its properties at inlet temperature. Outputs are average component temperature; temperature contours on the base plate.

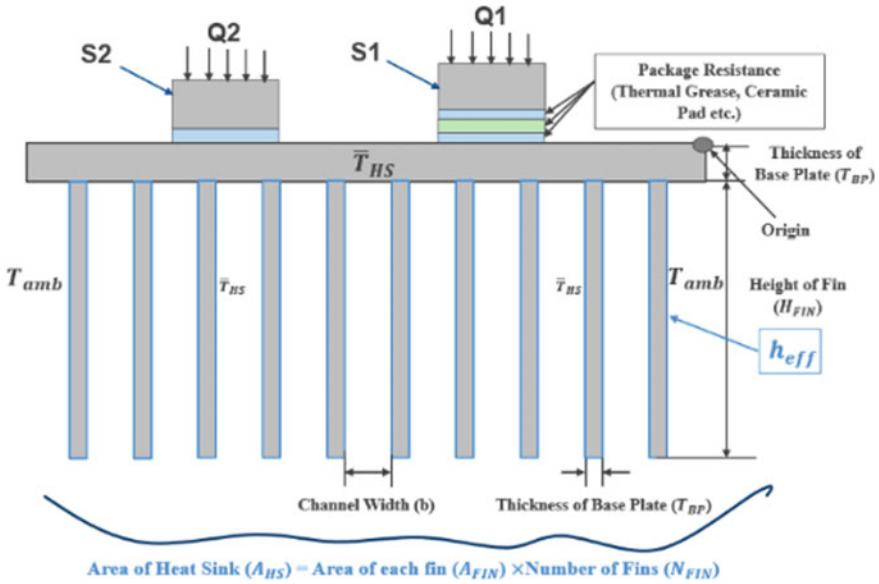


Fig. 1 Heat sink with electronic components

2.1 Determination of Equivalent Heat Transfer Coefficient

Equivalent heat transfer coefficient is the thermal parameter to be applied at the lower surface of the base plate which replaces the heat sink below and produces the same thermal effect as that of the heat sink under given conditions of fluid and ambient.

Airflow in the fin channels is in close resemblance with the flow between adjacent parallel plates. The mean Nusselt number (Nu) followed by average heat transfer coefficient (h) for forced laminar flow between adjacent parallel plates of length $L(m)$ is given by Shah and London [4].

$$Nu = 7.55 + \frac{0.024(L^*)^{-1.14}}{1 + 0.0358(L^*)^{-0.64}Pr^{-0.17}} \tag{1}$$

$$h = \frac{Nu \times d_h}{k_f} \tag{3}$$

where

- $L/(RePrd_h)$ Dimensionless length (L^*)
- $V_{ch}d_h/\nu$ Reynold's number (Re)
- $\mu C_p/k_f$ Prandtl's number (Pr)
- $4A_{cs}/P$ The hydraulic diameter of the channel (d_h)

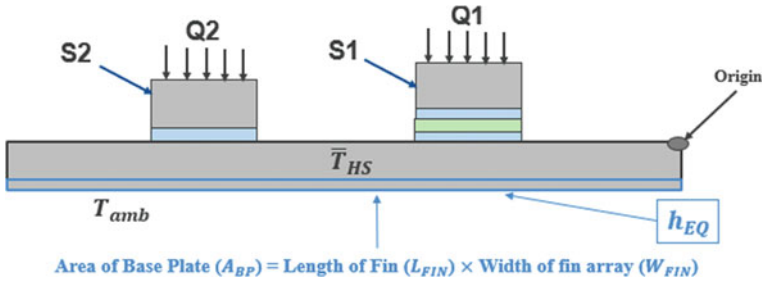


Fig. 2 Conversion of heat sink model into baseplate model

Lampio and Karvinen [8] developed an expression for effective heat transfer coefficient to be applied to heat sink based on mean Nusselt’s number as

$$h_{eff} = \frac{\rho V_{ch} b c_p}{2L_{FIN}} \left(1 - e^{-\frac{2hL}{\rho c_p V_{ch} b}} \right) \tag{3}$$

Equivalent heat transfer coefficient to be applied at the base plate surface can be obtained by energy balance (Figs. 1 and 2).

$$\begin{aligned} h_{eff} A_{HS} (\bar{T}_{HS} - T_{\infty}) &= h_{EQ} A_{BP} (\bar{T}_{HS} - T_{\infty}) \\ h_{EQ} &= h_{eff} A_{HS} / A_{BP} \end{aligned} \tag{4}$$

The equivalent heat transfer coefficient developed (h_{EQ}) is the characteristic of a heat sink that analyses its thermal behaviour. It is used as an input to the baseplate model.

2.2 Determination of Average Case Temperature of Electronic Components (Baseplate Model)

A general solution for thermal spreading resistance of eccentric heat sources on a rectangular base plate is developed by Yovanovich et al. [5]. It is valid for any number of heat sources, size, location, and power dissipation of heat sources. This analytical approach solves the 3D, steady-state Laplace equation using the method of separation of variables. The material is assumed to be isotropic and homogeneous.

$$\frac{\partial^2 T(x, y, z)}{\partial x^2} + \frac{\partial^2 T(x, y, z)}{\partial y^2} + \frac{\partial^2 T(x, y, z)}{\partial z^2} = 0 \tag{5}$$

The average temperature difference $\overline{\Delta T_{i,j}}$ between source j and ambient due to heat dissipation effect of source i is as follows:

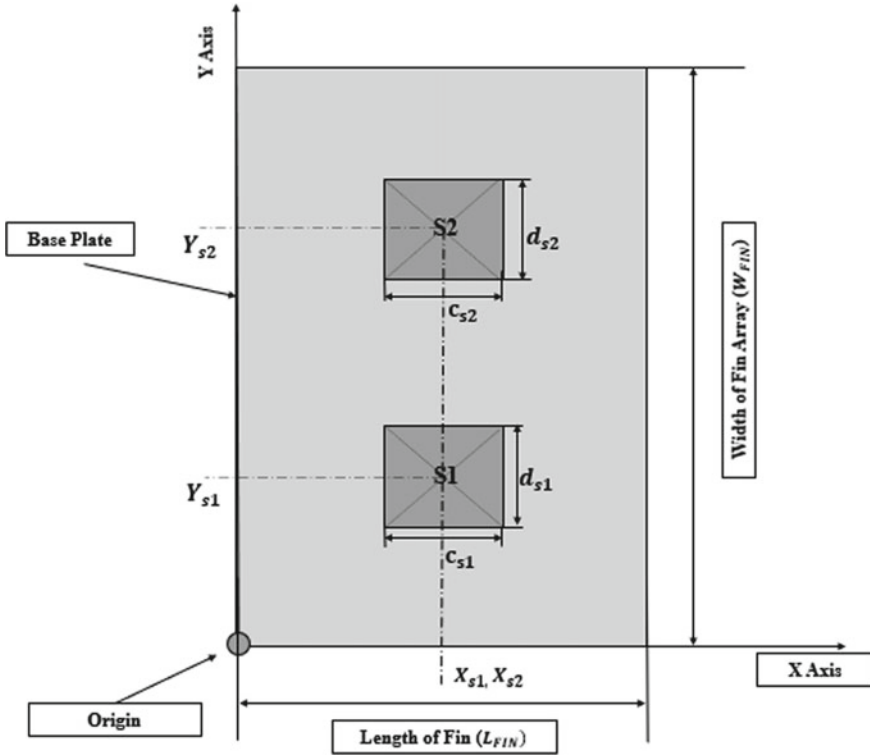


Fig. 3 Modelling of baseplate geometry and heat sources

$$\begin{aligned}
 \overline{\Delta T}_{i,j} = & A_0^i + 2 \sum_{m=1}^{\infty} A_m^i \frac{\cos(\lambda_m X_{s,j}) \sin\left(\frac{\lambda_m c_{sj}}{2}\right)}{\lambda_m c_{sj}} \\
 & + 2 \sum_{n=1}^{\infty} A_n^i \frac{\cos(\delta_n Y_{s,j}) \sin\left(\frac{\delta_n d_{sj}}{2}\right)}{\delta_n d_{sj}} \\
 & + 4 \sum_{m=1}^{\infty} \sum_{n=1}^{\infty} A_{mn}^i \frac{\cos(\delta_n Y_{s,j}) \sin\left(\frac{\delta_n d_{sj}}{2}\right) \cos(\lambda_m X_{cs,j}) \sin\left(\frac{\lambda_m c_{sj}}{2}\right)}{\lambda_m c_{sj} \delta_n d_{sj}} \quad (6)
 \end{aligned}$$

The average temperature difference $\bar{\theta}_j$ between the source j and the ambient due to cumulative effect of N number of sources is as follows:

$$\overline{\Delta T}_j = \bar{T}_j - T_{\text{amb}} = \sum_{i=1}^N \overline{\Delta T}_{i,j}$$

where

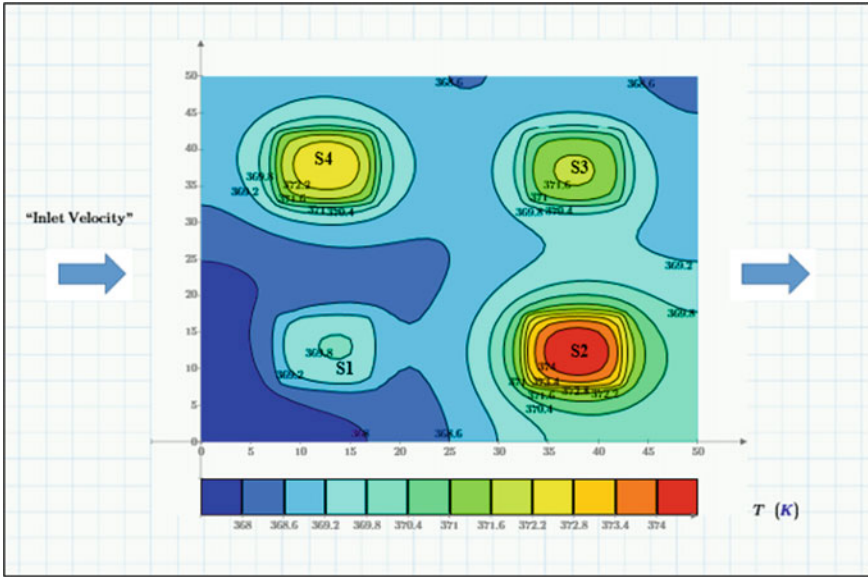


Fig. 4 Contour plots using MATHCAD

$$A_0^i = \frac{Q^i}{L_{FIN} W_{FIN}} \left(\frac{T_{BP}}{k_{BP}} + \frac{1}{h_{EQ}} \right)$$

A_m, A_n, A_{mn} are the Fourier coefficients, and $\lambda_m, \delta_n, \beta_{m,n}$ are the eigenvalues the details of which are shown in [4]. The case temperature of the component is given by

$$\bar{T}_{j_case} = \bar{T}_j + Q_j \times R_{package} \tag{8}$$

$R_{package}$ is the case to heat sink resistance due to thermal interface material layers like thermal grease, ceramic spacer, etc., which includes conductive and contact resistance between layers.

2.3 Comparison of Analytical Model with CFD

The analytical expressions (1–9) have been coded sequentially in PTC MATHCAD. A prototype of a heat sink has been modelled with four heat-dissipating sources. The geometry parameters, heat sink parameters, of the prototype which has been given as an input to the model are given in Tables 1 and 2. The package resistance is zero as heat sources are directly mounted on the baseplate. The heat sink has been tested in both CFD and MATHCAD models. Results for case temperature have been predicted

Table 1 Heat source parameters

Sources	Heat flux (Q) W/m ²	Location (X_s, Y_s) mm	Size (c_s, d_s) mm
S1	100,000	(12.5, 12.5)	(10, 10)
S2	250,000	(37.5, 12.5)	(10, 10)
S3	200,000	(12.5, 37.5)	(10, 10)
S4	150,000	(37.5, 37.5)	(10, 10)

Table 2 Heat sink parameters

Parameters	Symbol	
Inlet/Duct velocity	(U)	5 m/s
Ambient temperature	(T_{AMB})	25 °C
Number of sources	(N)	4
Number of fins	(N_{FIN})	15
Height of fins	(H_{FIN})	15 mm
Fin tip and base thickness	(t)	2 mm
Length of heat sink	(L_{FIN})	50 mm
Width of heat sink	(W_{FIN})	50 mm
Base plate thickness	(T_{BP})	10 mm
Heat sink material		Aluminium

in a very quick time (15 min for extracting inputs and 5–10 s for output) by the model. The model predicted temperatures are then compared with CFD temperatures, and results are expressed in terms of relative difference as given in Table 3.

The results showed that the Analytical Model results are within $\pm 1\%$ relative difference of what was predicted by CFD analysis of Test Prototype. The contour plots plotted through MATHCAD also show great similarity with CFD plots. After successful validation, the Analytical Model has been checked to various Industrial Test Cases to check for accuracy and sensitiveness. The results showed a maximum 3% relative difference for two heat sources (low heat flux), 2.3% for three heat sources

Table 3 Comparison between temperature prediction from CFD and analytical model

Sources	Case temperature (CFD model) (K)	Case temperature (analytical model) (K)	Relative percentage error
S1	370.55	369.434	-0.3
S2	376.97	373.574	-0.9
S3	374.43	371.89	-0.68
S4	373.09	371.119	-0.53
Equivalent heat transfer coefficient = 404 W/m ² K			
Weight of heat sink = 64 gm			

(moderate heat flux), 2% for four heat sources (high heat flux), and 1.2% relative difference for six heat sources (very high heat flux).

It can be concluded that the model error will go on decreasing as the number of heat sources, heat flux, and their area of contact with the base plate increases. This is because heat sources will occupy more surface of base plate thus helps in reducing the spreading resistance and thereby reduce the model near to the 1D model.

2.4 Evolutionary Computational Algorithm for Heat Sink Optimization

The Genetic Algorithm is an evolutionary algorithm and a heuristic search and optimization technique that mimics the process of natural evolution. It is mostly used to find the optimal or near-optimal solution for problems having a large number of variables and constraints. Heat sinks have several parameters bounded by upper and lower limits. The Analytical Model will be the objective function that must be optimized for maximum thermal performance or minimum weight satisfying all sets of constraints. The algorithm is applied over the prototype, and results are analysed. First, the optimization code is run for thermal performance optimization and then for weight optimization of the heat sink.

• **Problem Formulation**

Find	$x = (L_{FIN}, W_{FIN}, H_{FIN}, T_{FIN}, N_{FIN}, T_{BP})$
To minimize	$f(x) = T_{avg}(x)$ or $m(x)$
Subject to	<ul style="list-style-type: none"> • $F = \{x \in R^6 lb \leq x \leq ub; g_i(x) \leq 0, i = 1 - 6\}$ • $lb = \min(L_{FIN}, W_{FIN}, H_{FIN}, T_{FIN}, N_{FIN}, T_{BP})^T$ • $ub = \max(L_{FIN}, W_{FIN}, H_{FIN}, T_{FIN}, N_{FIN}, T_{BP})^T$
Constraints	<ul style="list-style-type: none"> • $g_1 = L_{FIN} W_{FIN} T_{BP} \rho_{FIN} + N_{FIN} L_{FIN} H_{FIN} T_{FIN} \rho_{FIN} - m_{min} \leq 0$ • $g_2 = -(L_{FIN} W_{FIN} T_{BP} \rho_{FIN} + N_{FIN} L_{FIN} H_{FIN} T_{FIN} \rho_{FIN} - m_{max}) \leq 0$ • $g_3 = T_{BP} + H_{FIN} - H_{FIN-MAX} \leq 0$ • $g_4 = b_{min} - \frac{W_{FIN} - N_{FIN} \times T_{BP}}{N_{FIN} - 1}$ • $g_5 = (T_1, T_2, \dots, T_N) \leq T_{allowable}$

From the heat sink formulation, the parameters of the prototype have been varied between lower and upper limits. The lower limits are generally fixed by strength constraints and the upper limit by weight, space, cost, and design constraints. According to [9] and [10], at most three parameters of the heat sink, we can vary by keeping all parameters constant to get the optimal solution. For more than three

Table 4 Variation of geometry parameters

Parameters	N_{FIN}	H_{FIN} (mm)	T_{FIN} (mm)	T_{BP} (mm)
Lower bound	5	5	1	10
Upper bound	20	25	2	10

Table 5 Optimized parameters for maximum thermal performance

Parameters	Reference model	Optimized model	Relative percentage difference (%)
Heat transfer coefficient	404 W/m ² K	804 W/m ² K	+100
Number of fins	15	19	+26.67
Height of fins	15 mm	25 mm	+66.67
Thickness of fins	2 mm	1 mm	-50
Channel velocity	3.752 m/s	4.327 m/s	+15.33
Channel width	1.429 mm	1.713 mm	+19.87
Weight of heat sink	64 gm	64 gm	0

Table 6 Optimized temperature of sources

Sources	Reference temperatures (K)	Optimized temperatures (K)	Relative percentage difference (%)
S1	369.434	334.384	-9.487
S2	373.574	338.469	-9.397
S3	371.89	336.822	-9.43
S4	371.119	336.031	-9.45

variable parameters, the algorithm will give multiple optimal solutions which result in different outputs after every run. In this case, parameters such as the number of fins, the height of fins, and thickness of fin have been varied for constant base plate thickness, and optimization of the prototype is carried out for both performance and weight. The variation of parameters selected has been given in Table 4.

Optimization takes 1–2 h depending upon the number of parameters and complexity of geometry. The result for thermal performance optimization by keeping weight constant has been given in Table 5, and weight optimization for constant thermal performance has been given in Table 7.

3 Results

Genetic Algorithm has been tested for optimization with the probability of crossover (P_c) as 0.8, probability of mutation (P_m) as 0.2, and distribution index for both

Table 7 Optimized parameters for minimum weight

Sources	Reference model (K)	Optimized model (K)	Relative percentage difference (%)
Weight of heat sink	64 gm	30 gm	-53.13
Number of fins	15	18	+20
Height of fins	15 mm	12.4 mm	-17.33
Thickness of fins	2 mm	1 mm	-50
Channel velocity	3.752 m/s	3.793 m/s	+1.09
Channel width	1.43 mm	1.878 mm	+31.33
Equivalent heat transfer coefficient	404 W/m ² K	404 W/m ² K	0

crossover (etac) and mutation (etam) as 3. After successful optimization, the results showed that for the same weight of heat sink, thermal performance of heat sink has been increased by 100%, and temperatures of components have been decreased by an average of 9%. On the other hand, for the same thermal performance, the weight of the heat sink has been reduced by 53%.

4 Conclusions

Analytical Model developed for the plate fin heat sinks has accurately predicted the Electronic Sources Temperatures. Due to its fast prediction, users can perform multiple modifications in the design and can perform optimization of heat sink making it a suitable option as a replacement for CFD technique. Genetic Algorithm has been successfully applied to quickly predict the heat sink parameters that will enhance the thermal performance and reduce the weight by satisfying all the constraints.

References

1. Kraus AD, Aziz A, Welty J (2001) *Extended surface heat transfer*. Wiley, New York
2. Bejan A, Sciubba E (1992) The optimal spacing of parallel plates cooled by forced convection. *Int J Heat Mass Transf* 35(12):3259-3264
3. Teertstra P, Yovanovich MM, Teerstra P, Culham JR, Lemczyk T (1999) Analytical forced convection modeling of plate-fin heat sink. In: 15th IEEE semi-therm symposium
4. Shah RK, London AL (1978) *Laminar flow forced convection in ducts*. Academic Press, New York
5. Yovanovich MM, Muzychka YS, Culham JR (2003) Thermal spreading resistance of eccentric heat sources on rectangular flux channels. *J Electron Packag* 125(2):178-185

6. Lee S, Song S, Au V, Moran KP (1995) Constriction/spreading resistance model for electronics packaging. In: Proceedings of the 4th ASME/JSME thermal engineering joint conference, Hawaii, vol 4, pp 199–206
7. Lindstedt M, Karvinen R (2012) Optimization of isothermal plate-fin arrays with laminar forced convection. *J Enhanced Heat Transf* 19(6):535–547
8. Lampio K, Karvinen R (2013) Multi-objective optimization of electronics heat sink geometries. In: Proceedings of IWHT, Oct 18–21
9. Shikalgar ND, Sapali SN (2019) Energy and exergy analysis of a domestic refrigerator: approaching a sustainable refrigerator. *J Thermal Eng* 5(5):469–481. <https://doi.org/10.18186/thermal.624159>
10. Shikalgar ND, Sapali SN (2018) Numerical and thermal analysis of condensers applied to domestic refrigerator. *Int Rev Mech Eng* 11(7):481–485. <https://doi.org/10.15866/ireme.v11i7.12849>
11. Castelan A, Cougo B, Brandelero J, Flumian D, Meynard T (2015) Optimization of forced-air cooling system for accurate design of power converters. In: IEEE 24th international symposium on industrial electronics (ISIE), pp 367–372

Comparative Energy Analysis of R1234yf and R134a Refrigerants



Vanita Wagh and A. D. Parekh

Abstract Under the Kyoto protocol, all automobile air conditioning systems should use low global warming potential (GWP) refrigerant. Kyoto committee has defined low refrigerants which have GWP less than 150. Currently, popular R134a refrigerant has a GWP of 1430, which is very high. Newly researched R1234yf refrigerant has a GWP of 4. The present paper compares the energy analysis of the R1234yf refrigerant system with the R134a refrigerant system. For developing a computation energy analysis model, engineering equation solver (EES) software has been used. Refrigeration effect, compressor work, coefficient of performance (COP) and 2nd law of efficiency are compared based on evaporator temperature, condenser temperature, degree of superheating, degree of subcooling and isentropic efficiency. This study proposes that R1234yf refrigerant will be a suitable replacement for R134a refrigerant.

Keywords Automobile refrigerant · Energy analysis · Refrigeration effect · Compressor work · Coefficient of performance · 2nd law efficiency

Nomenclature

COP_{act}	Actual coefficient of performance
COP_{rev}	Reversible coefficient of performance
h_1	Specific enthalpy at evaporator outlet (kJ/kg)
h_{1a}	Specific enthalpy at superheater outlet (kJ/kg)
h_2	Specific enthalpy at compressor outlet (kJ/kg)
h_{2a}	Specific enthalpy at isentropic compressor outlet (kJ/kg)
h_{2b}	Specific enthalpy at condenser inlet (kJ/kg)

V. Wagh (✉)

Thermal System Design, S.V.N.I.T, Surat, Gujarat 395007, India

e-mail: vanitawagh13@gmail.com

A. D. Parekh

Department of Mechanical Engineering, S.V.N.I.T, Surat, Gujarat 395007, India

h_3	Specific enthalpy at condenser outlet (kJ/kg)
h_{3a}	Specific enthalpy at sub-cooler outlet (kJ/kg)
h_4	Specific enthalpy at evaporator inlet (kJ/kg)
\dot{m}_r	Mass flow rate of refrigerant (kg/s)
Q_{Evap}	Heat absorbing rate in evaporator (kJ/kg)
Q_{Cond}	Heat rejection rate in condenser (kJ/kg)
RE	Refrigeration effect (kJ/kg)
T_{Evap}	Evaporator temperature ($^{\circ}\text{K}$)
T_{Cond}	Condenser temperature ($^{\circ}\text{K}$)
T_{Sup}	Degree of superheating ($^{\circ}\text{K}$)
T_{Sub}	Degree of subcooling ($^{\circ}\text{K}$)
W_{Comp}	Work required to compressor (kJ/kg)

Greek Symbols

η_c	Isentropic efficiency of compressor
$\eta_{\text{2nd law}}$	Second law efficiency

1 Introduction

A refrigerant is a crucial part of the air conditioning system for absorbing/removing heat and cooling the surrounding. Usually, air conditioning unit contains R134a refrigerant. R134a refrigerant has a global warming potential (GWP) score of 1430. The GWP score of 1430 indicates that 1 kg of heat trapped by R134a is equivalent to 1430 kg of heat trapped by CO_2 over a specific time period [1].

Allowing refrigerants to have such harmful potential causes depletion of the ozone layer in the stratosphere. Hence, controlling the greenhouse gas emission from vehicles is crucial to conserve the earth for future generations.

Therefore, international organizations made a law Kyoto protocol. Under the Kyoto protocol, all these refrigerants should have a GWP score below 150. To concur with this problem, Honeywell and DuPont chemical companies developed R1234yf refrigerant. R1234yf refrigerant has 4 GWP, which is 325 times smaller than R134a and 38 times smaller than the maximum allowed GWP score.

This paper focuses on studying R1234yf as a refrigerant in automobile air conditioning systems and energy analysis of R1234yf systems concerning R134a systems.

Table 1 Operating conditions for energy modelling [2]

Specification	Value
\dot{m}_r (kg/s)	1 (Constant)
T_e (°C)	-40 °C to 20 °C
T_c (°C)	35 °C to 55 °C
T_{Sub} (K)	5(K)
T_{Super} (K)	5(K)
η_c	0.85

2 Problem Description

Refrigerant is a critical part of the automobile air conditioning system. Under the Kyoto protocol, automobile manufacturers need to integrate refrigerants having a GWP value of less than 150. Before designing an AC system for replacement refrigerant, one should confirm if the refrigerant is performing better or similar to the refrigerant used in the existing AC system. This paper aims to find whether the R1234yf system can energy-wise perform comparatively similarly or better to the R134a system.

2.1 Method

For comparative analysis of energy for the R1234yf system and R134a system, we have modelled the system in EES software. We have simulated the refrigeration cycle as the data mentioned in Table 1. From simulated data, compared refrigeration effect, compressor work, COP and 2nd law of efficiency by varying evaporator temperature, condenser temperature, degree of superheating, degree of subcooling and isentropic efficiency. Details for the refrigeration cycle and equations are mentioned below.

2.2 Refrigeration Cycle

Refrigerant enters into the compressor at low-pressure and low-temperature vapour. In the compressor, the pressure and temperature of the refrigerant are increased. It is released as superheated gas. This hot pressurized gas then enters into the condenser, where the heat from the refrigerant gets released to the surroundings as it cools and condensed completely. This cooled high-pressure liquid refrigerant then passes through the expansion valve, which abruptly reduces the pressure, causing the temperature to drop rapidly. Next, it enters into the evaporator as a combination of gas and liquid at low temperature where it accepts heat from the surrounding, thus

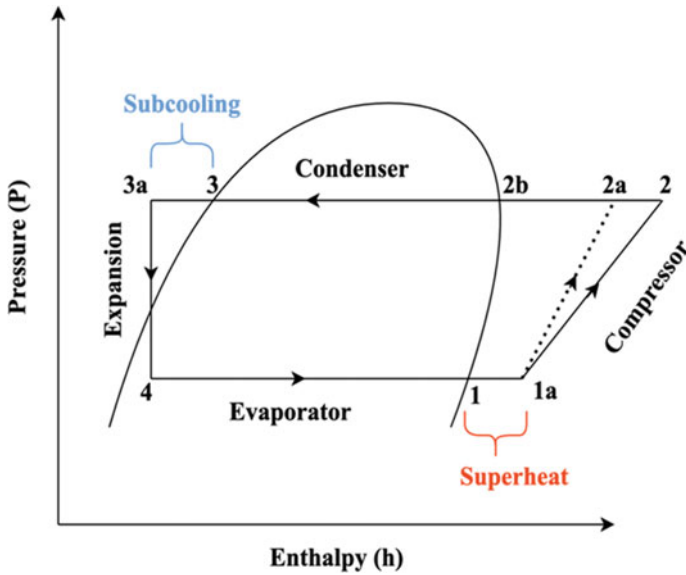


Fig. 1 p-h diagram of VCR cycle with superheating and subcooling

getting converted into vapour completely. After the evaporator, the refrigerant enters into the compressor, and so, the cycle will continue (Fig. 1).

Evaporator

$$Q_{\text{Evap}} = \dot{m}_r \times (h_{\text{Evap,out}} - h_{\text{Evap,in}})$$

$$Q_{\text{Evap}} = \dot{m}_r \times (h_1 - h_4)$$

$$RE = Q_{\text{Evap}}$$

Compressor

$$W_{\text{Comp}} = \dot{m}_r \times (h_{\text{Comp,out}} - h_{\text{Comp,in}})$$

Considering superheating from point 1 to point 1a. So, the compression starts at point 1a.

$$W_{\text{Comp}} = \dot{m}_r \times (h_{\text{Comp,out}} - h_{\text{Comp,in}})$$

$$W_{\text{Comp}} = \dot{m}_r \times (h_{2a} - h_{1a})$$

For the isentropic efficiency of the compressor,

$$\eta_c = \frac{T_{2a} - T_{1a}}{T_2 - T_{1a}}$$

$$W_{\text{Comp}} = \dot{m}_r \times (h_2 - h_{1a})$$

Condenser

$$Q_{\text{Cond}} = \dot{m}_r \times (h_{\text{Cond,in}} - h_{\text{Cond,out}})$$

$$Q_{\text{Cond}} = \dot{m}_r \times (h_{2b} - h_3)$$

For subcooling in the condenser,

$$Q_{\text{Cond}} = \dot{m}_r \times (h_{2b} - h_{3a})$$

Expansion Valve

$$h_{\text{Exp,in}} = h_{\text{Exp,out}}$$

$$h_3 = h_4$$

For subcooling, $h_3 = h_4$

Actual coefficient of performance

$$\text{COP}_{\text{act}} = \frac{\text{Desired Effect}}{\text{Power Input}}$$

$$\text{COP}_{\text{act}} = \frac{\text{RE}}{W_{\text{Comp}}}$$

Reversible or Carnot coefficient of performance

$$\text{COP}_{\text{rev}} = \frac{T_{\text{Evap}}}{T_{\text{Cond}} - T_{\text{Evap}}}$$

Second law efficiency

$$\eta_{\text{2nd law}} = \frac{\text{COP}_{\text{act}}}{\text{COP}_{\text{rev}}}$$

Note—all equations are taken from [1, 3–5].

3 Results and Discussion

3.1 Effect of Evaporator Temperature

For Figs. 2, 3, 4 and 5, as evaporator temperature is increased, the effect on both the refrigerant is as following.

- Refrigeration effect increases

Fig. 2 Refrigeration effect versus evaporator temperature for R1234yf and R134a

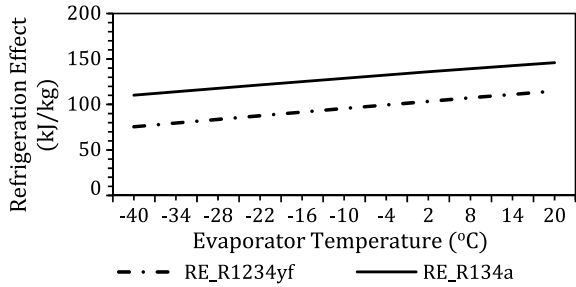


Fig. 3 Compressor work versus evaporator temperature for R1234yf and R134a

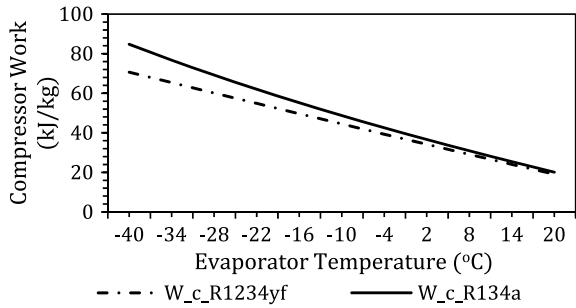


Fig. 4 Actual COP versus evaporator temperature for R1234yf and R134a

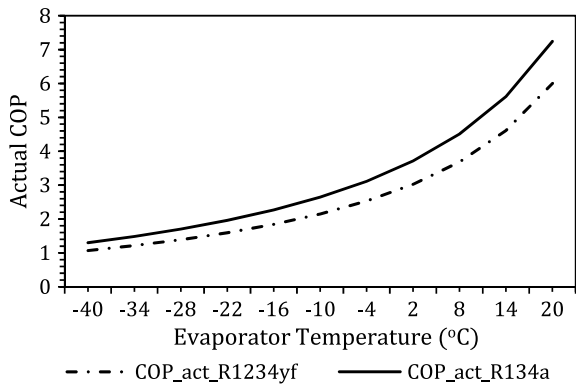
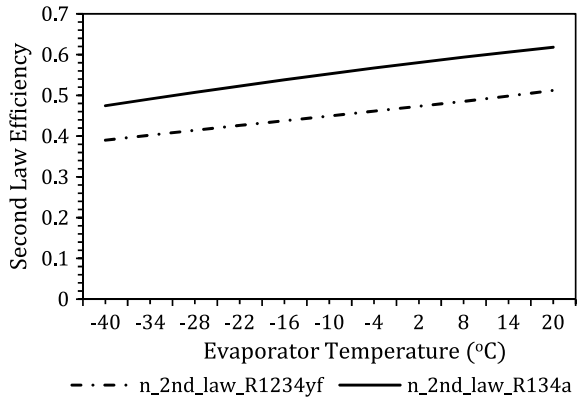


Fig. 5 Second law efficiency versus evaporator temperature for R1234yf and R134a



- Compressor work decreases
- COP increases exponentially
- 2nd law of efficiency increases.

Compressor work for R134a is significantly more extensive than R1234yf for -40 °C. But, as evaporator temperature increases, compressor work for both of the refrigerants converges. COP is nearly the same for the R1234yf system and R134a system, but as evaporator temperature increases, both systems start to diverge while growing exponentially. R1234yf systems are underperforming R134a systems for the 2nd law of efficiency and COP by a significant value. For compressor work, R1234yf is performing better compared to R134a systems.

3.2 Effect of Condenser Temperature

For Figs. 6, 7, 8 and 9, as condenser temperature is increased, the effect on both the refrigerant is as following.

Fig. 6 Refrigeration effect versus condenser temperature for R1234yf and R134a

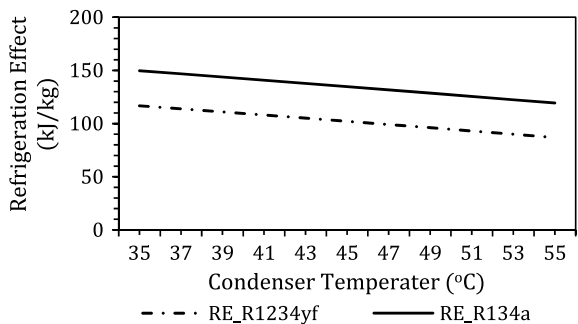


Fig. 7 Compressor work versus condenser temperature for R1234yf and R134a

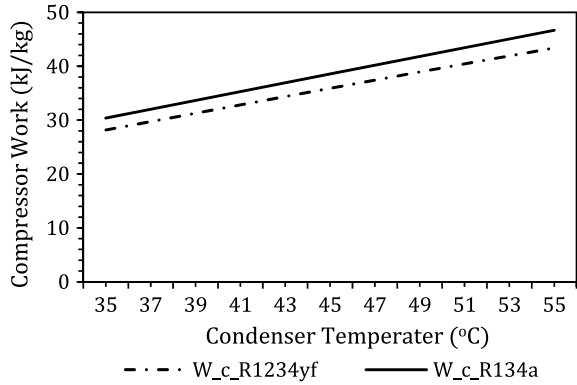


Fig. 8 Actual COP versus condenser temperature for R1234yf and R134a

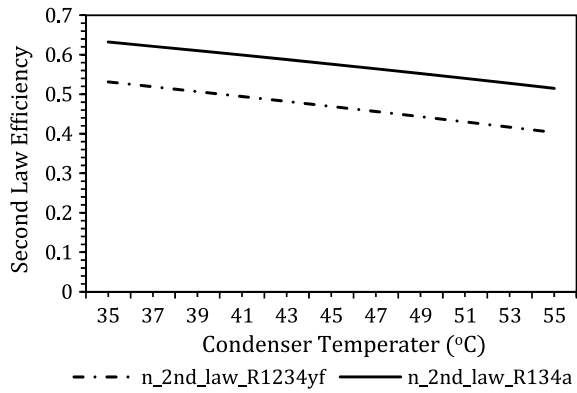
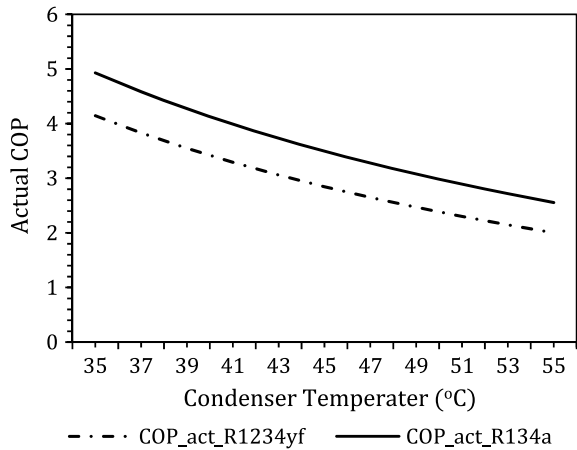


Fig. 9 Second law efficiency versus condenser temperature for R1234yf and R134a



- Refrigeration effect decreases
- Compressor work increases
- COP decreases
- 2nd law of efficiency decreases slowly.

R1234yf systems are underperforming R134a systems for refrigeration effect, COP and 2nd law of efficiency by a significant value. For compressor work, R1234yf is performing better compared to R134a systems.

3.3 Effect of Suction Vapour Superheat

For Figs. 10, 11, 12 and 13, as the degree of superheating is increased, the effect on both the refrigerant is as following.

Fig. 10 Refrigeration effect versus degree of superheating for R1234yf and R134a

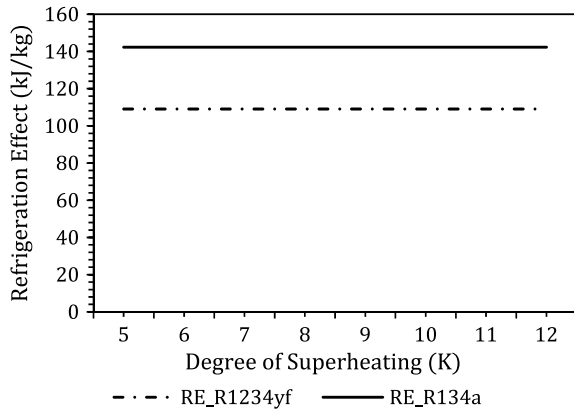


Fig. 11 Compressor work versus degree of superheating for R1234yf and R134a

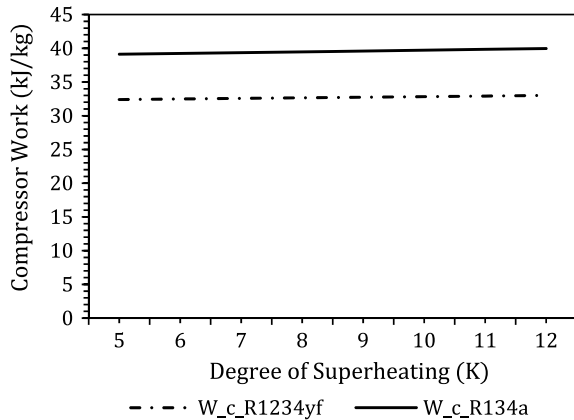


Fig. 12 Actual COP versus degree of superheating for R1234yf and R134a

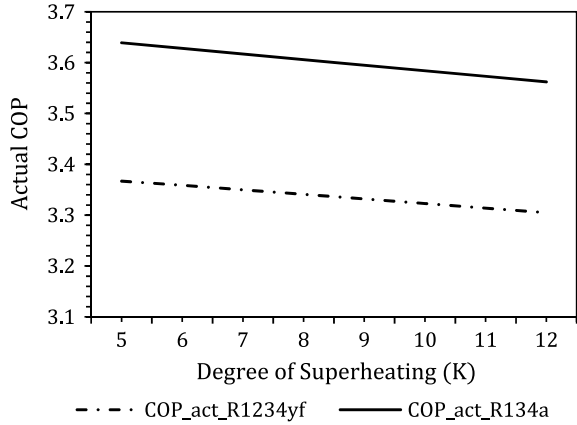
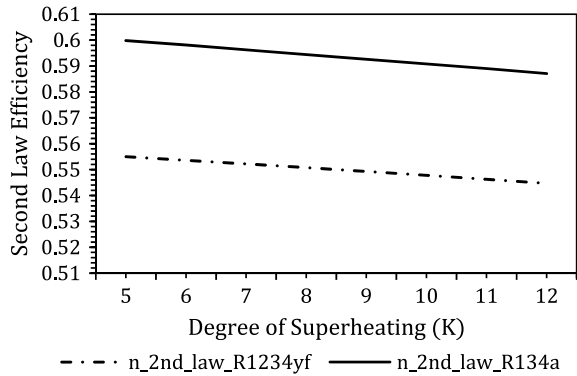


Fig. 13 Second law efficiency versus degree of superheating for R1234yf and R134a



- The refrigeration effect remains constant
- Compressor work increases
- COP decreases very slowly
- 2nd law of efficiency decreases very slowly.

R1234yf systems are underperforming R134a systems for refrigeration effect, COP and 2nd law of efficiency by a significant value. For compressor work, R1234yf is performing better compared to R134a systems.

3.4 Effect of Liquid Subcooling

For Figs. 14, 15, 16 and 17, as the degree of subcooling is increased, the impact on both the refrigerant is as following.

- Refrigeration effect increases

Fig. 14 Refrigeration effect versus degree of subcooling for R1234yf and R134a

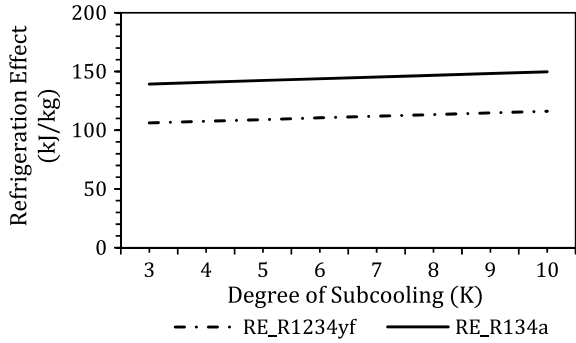


Fig. 15 Compressor work versus degree of Subcooling for R1234yf and R134a

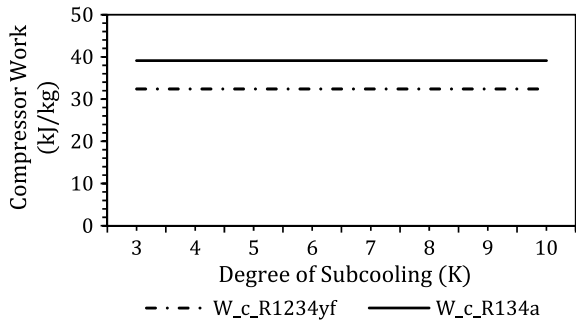
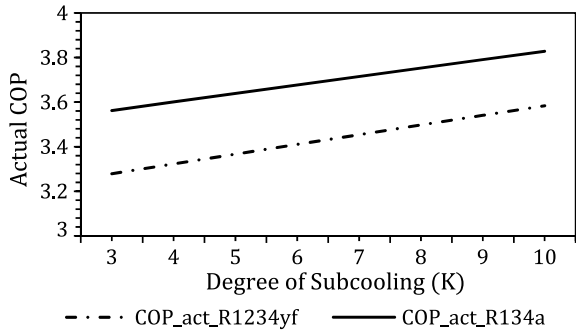


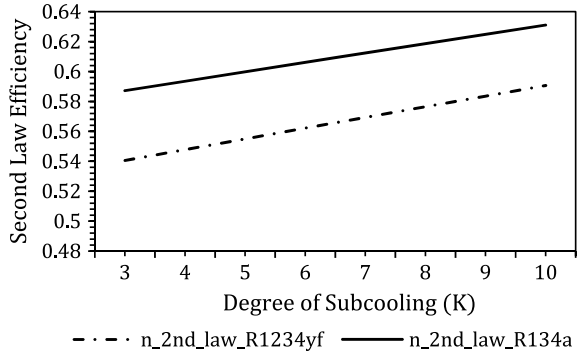
Fig. 16 Actual COP versus degree of subcooling for R1234yf and R134a



- Compressor work remains the same
- COP increases
- 2nd law of efficiency increases.

R1234yf systems are underperforming R134a systems for refrigeration effect, COP and 2nd law of efficiency by a significant value. For compressor work, R1234yf is performing better compared to R134a systems.

Fig. 17 Second law efficiency versus degree of subcooling for R1234yf and R134a



3.5 Effect of Isentropic Efficiency

For Figs. 18, 19, 20 and 21, as isentropic efficiency is increased, the impact on both the refrigerant is as following.

Fig. 18 Refrigeration effect versus isentropic efficiency of compressor for R1234yf and R134a

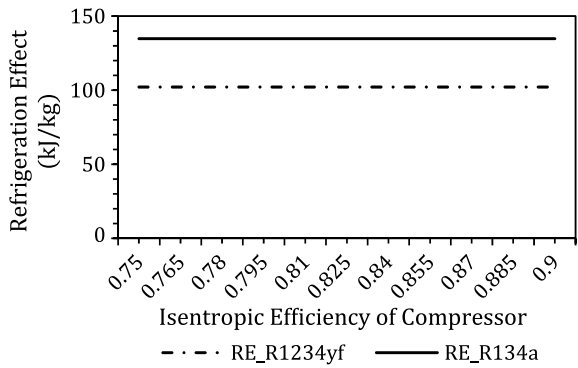


Fig. 19 Compressor work versus isentropic efficiency of compressor for R1234yf and R134a

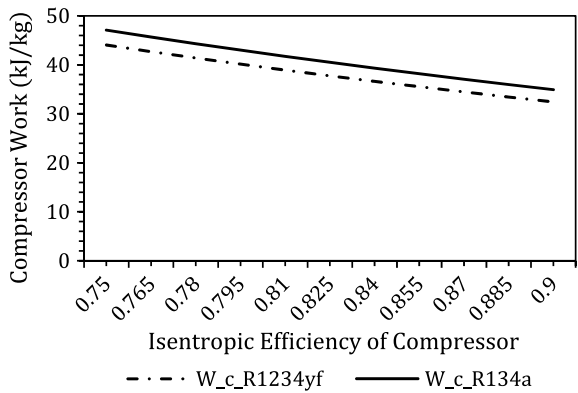


Fig. 20 Actual COP versus isentropic efficiency of compressor for R1234yf and R134a

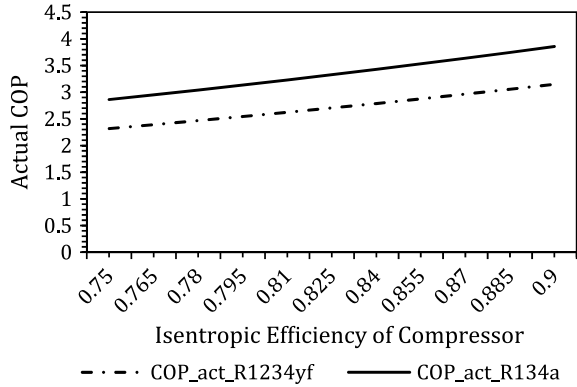
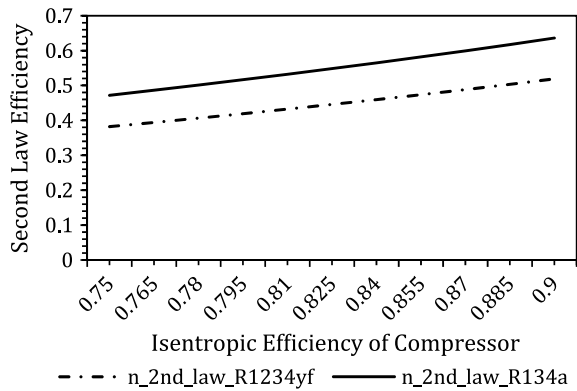


Fig. 21 Second law efficiency versus isentropic efficiency of compressor for R1234yf and R134a



- The refrigeration effect remains constant
- Compressor work decreases
- COP increases
- 2nd law of efficiency increases.

R1234yf systems are underperforming R134a systems for refrigeration effect, COP and 2nd law of efficiency. For compressor work, R1234yf is performing as better as R134a systems.

4 Conclusions

R1234yf refrigerant systems are slightly underperforming compared to R134a refrigerant systems for refrigeration effect, COP and 2nd law of efficiency. R1234yf is performing better only in the case of compressor work. Refrigeration effect, compressor work, COP and 2nd law of efficiency show different behaviour for

evaporator temperature, condenser temperature, degree of superheating, degree of subcooling and isentropic efficiency. It can be concluded that R1234yf systems can be made as performant as the R134a system by making minor modifications.

Acknowledgements The authors would like to thank all the academicians/researchers whose work has been cited and used in this study. The authors also thank Sardar Vallabhbhai National Institute of Technology for all the support.

References

1. Cho H, Park C (2016) Experimental investigation of performance and exergy analysis of automotive air conditioning systems using refrigerant R1234yf at various compressor speeds. *Appl Therm Eng* 101:30–37
2. Saini VS, Kumar B (2015) Exergy analysis of vapour compression refrigeration cycle based automotive air conditioner using eco friendly refrigerants. *Int J Tech Res (IJTR)* 4(2):99106
3. Belman-Flores JM, Rangel-Hernandez VH, Uson S, Rubio-Maya C (2017) Energy and exergy analysis of R1234yf as drop-in replacement for R134a in a domestic refrigeration system. *Energy* 132:116–125
4. Cho H, Lee H, Park C (2013) Performance characteristics of an automobile air conditioning system with internal heat exchanger using refrigerant R1234yf. *Appl Therm Eng* 61(2):563–569
5. Vaghela JK (2016) Comparative evaluation of an automobile air—conditioning system using R134a and its alternative refrigerants. *Energy Procedia* 109:153–160

Recent Trends in Artificial Intelligence-Inspired Electronic Thermal management—A Review



Aviral Chharia, Nishi Mehta, Shivam Gupta, and Shivam Prajapati

Abstract The rise of computation-based methods in thermal management has gained immense attention in recent years due to its ability to solve complex ‘physics’ problems, which are otherwise difficult to be approached using conventional techniques. Thermal Management is required in Electronic systems to keep them from overheating and burning, enhancing their efficiency and lifespan. For a long time, numerical techniques have been employed to aid in the thermal management of electronics. However, they come with some limitations. To increase the effectiveness of traditional numerical approaches and address their drawbacks, researchers have looked at using Artificial Intelligence (AI) at various stages of the thermal management process. The present study discusses in detail, the current uses of computation-based methods, especially deep learning in the domain of electronic thermal management.

Keywords Electronic thermal management · Artificial Intelligence · Machine learning · Deep learning · Reinforcement learning

1 Introduction

Thermal management is the technique of controlling temperatures for enhancing system performance. One of the recent works in thermal management was by Zhao

A. Chharia (✉)

Department of Mechanical Engineering, Thapar Institute of Engineering and Technology, Patiala, Punjab, India

e-mail: achharia_be18@thapar.edu

N. Mehta

Department of Mechanical Engineering, Sardar Vallabhbhai National Institute of Technology, Surat, Gujarat, India

S. Gupta

Department of Mechanical Engineering, Indian Institute of Technology (ISM), Dhanbad, India

S. Prajapati

Department of Mechanical Engineering, National Institute of Technology, Agartala, India

© The Author(s), under exclusive license to Springer Nature Singapore Pte Ltd. 2023

H. B. Mehta et al. (eds.), *Recent Advances in Thermal Sciences and Engineering*,

Lecture Notes in Mechanical Engineering, https://doi.org/10.1007/978-981-19-7214-0_13

et al. [1]. They developed a heat pump system combined with an innovative vehicle thermal management system (VTMS) to compensate for performance loss caused due to the electric heater in the cabin of fuel cell vehicles. Moore et al. [2] investigated the capability of various materials and cubic crystals for the thermal management of electronic devices. Ghosh et al. [3] carried out experiments to determine the thermal conductivity of graphene and concluded it to be helpful as a material for thermal management in various nanoelectronic circuits. Another work by Pesaran et al. [4] carried out comparative studies on various types of cooling for thermal management of electric and hybrid electric vehicles. Beircuk et al. [5] combined single-wall nano-tubes with industrial epoxy to enhance the thermo-mechanical properties of the epoxy. They found the entire material to be quite valuable for thermal management. Zweben et al. [6] explored various composite materials with higher conductivities than aluminum alloys and examined their properties and applications in different areas of thermal management. Kercher et al. [7] experimented with microjet technology for cooling electronics and found it more effective than the unforced cooling technology. They compared it with standard cooling-fan technology. Mudawar et al. [8] explored various advanced cooling methods like jet impingement cooling, detachable heat sinks, etc. Gallego et al. [9] developed and experimented on carbon foam for thermal management and found it more effective than conventional heat sinks.

Kandasamy et al. [10] experimentally investigated the effectiveness of an innovative phase change material (PCM) package for electronics thermal management. Further, the work numerically confirmed PCMs to be suitable for application in transient electronic cooling. Mallik et al. [11] worked on finding materials that were more thermally conductive than aluminum, mainly for automotive electronic cooling. Xin et al. [12] fabricated large-area freestanding graphene papers with extremely high thermal conductivity ($1238.3\text{--}1434 \text{ Wm}^{-1} \text{ K}^{-1}$) with electrospray deposition combined with a continuous roll process.

Artificial intelligence (AI) has gotten much attention in recent years because of its vast possibilities. Using AI-based optimization, prediction, etc., researchers have proposed various novel methods that have surpassed conventional techniques in both accuracy, robustness, and time taken to be implemented. However, the present literature lacks an in-depth study of the various AI-based techniques that have been used in thermal management. In this work, we aim to provide an in-depth review of recent developments in AI-inspired thermal management techniques, mainly focusing on its applications in single-core and multicore processors, high accuracy determination of thermo-physical properties impacting thermal management, predicting the thermal conductivity of composites, system performance prediction accuracy, connection establishing, decision-making for the best configuration/method and parameter optimization among others. The study also provides an in-depth look at the most current advancements in AI approaches used in the thermal management literature.

2 Recent Advances in Artificial Intelligence in Thermal Management Literature

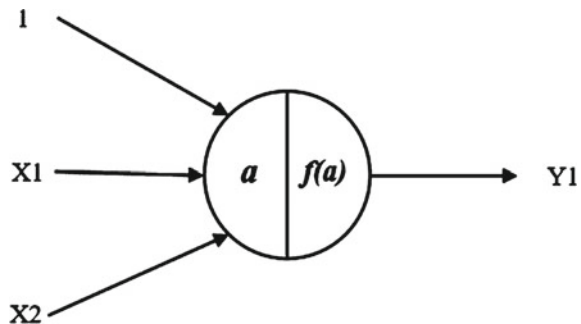
Machine learning (ML) is one of the most rapidly evolving technical disciplines today [13], and it has been used in various domains, including thermal management. Mitchell [14] defined ML as the study of a new class of algorithms that automatically improve their performance over a task ‘ T ’ as measured by the performance metrics ‘ P ’, through experience ‘ E ’. The last decade has witnessed a rapid rise in AI algorithms mainly due to the increased computational power of processors (Fig. 1).

Artificial Neural Networks Artificial neural networks (ANNs) are computing systems that are inspired by the biological neural networks that make up brains. During training neural networks, the main objective is to find a suitable ‘loss’ function and minimize it through computational techniques. One of the widely used optimization techniques includes stochastic gradient descent (SGD). SGD entails displaying the input vector for several examples, computing the outputs and errors, calculating the average gradient for those samples, and changing weights as required [15]. The method is repeated for a large number of tiny sets of samples from the training set until the loss function’s average no longer decreases. Stacking up multiple neural networks forms a deep learning (DL) model. The most commonly used loss functions include binary cross-entropy loss, mean square error, etc.

Solving PDEs with Physics-Informed Neural Networks Recently introduced, physics-informed neural networks [16] are particularly trained to solve supervised learning problems. These form a new class of data-efficient universal function approximators that encode physical laws of nature, naturally as initial input. Presently, these are employed for obtaining data-driven solutions and data-driven discovery of partial differential equations (PDEs) (Fig. 2).

Convolutional Neural Networks CNNs take high-dimensional data in the form of matrices, for example, a colored image made of three 2D arrays having pixel intensities in the RGB color channel [17]. The architecture of a CNN consists of multiple layers, which includes—convolutional layers and pooling layers. A convolutional layer’s units are arranged in feature maps, with each unit linked to local regions in the preceding layer’s feature maps. The outcome of this locally weighted sum is then

Fig. 1 Architecture of the simplest possible neuron



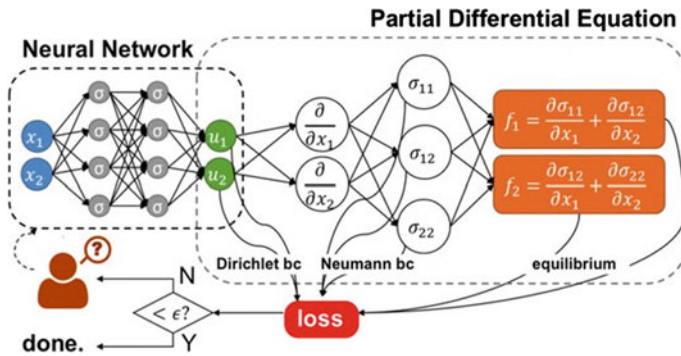


Fig. 2 Physics-informed neural network [16]

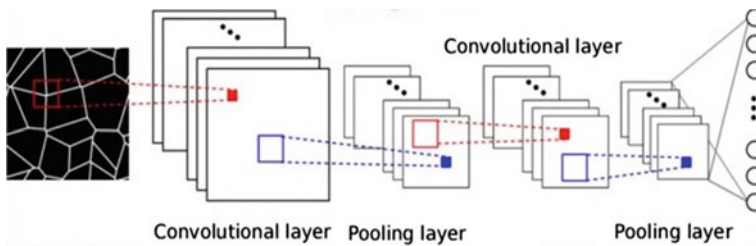


Fig. 3 CNN with convolutional and pooling layers

processed through a nonlinearity (mostly ReLU). The 3D equivalent of CNNs is 3D CNNs which is used when the data comprises 3D matrices. In thermal management, most authors have used CNN-based transfer learning [18] on pre-trained datasets like ImageNet [19] (Fig. 3).

Other Deep Learning Architectures and Domains Other DL architectures [20] widely used in thermal management include long short-term memory (LSTM) networks, recurrent neural networks (RNNs), reinforcement learning, etc. Table 1 presents an in-depth analysis of various recent works in thermal management involving ML and DL techniques.

3 Thermal Management Assisted by ML, Deep Learning and Other AI Domains

This section discusses in detail the role of artificial intelligence techniques in thermal management.

ML-Based Thermal Design Parameters Optimization in MPSoCs The enhanced performance of high-efficiency video coding (HEVC) increases the

Table 1 In-depth collection of the various recent works in thermal management involving ML and DL techniques

References	Major advances in thermal management	Applications/role of AI
[21]	Determined the thermal properties of composite PCMs like paraffin and copper foam used for thermal management of a Li-ion battery pack	Combined CNN with FEM. Using thermal properties, an image dataset was created and used for training the CNN. The study concluded that the combination of CNN with FEM was more accurate in determining the effectiveness of the BTMS compared to FEM alone
[22]	Improving the transient thermal performance of thermal energy storage units using ML	Used nearest neural search and ANNs to determine PCM melt fraction more accurately compared to conventional approaches
[23]	DL was used to predict the composite's thermal conductivity from a section picture	CNNs are used to extract geometric features of the components, which helps in establishing structure–property linkages
[23]	Predicting thermal conductivity of composites	Used various CNN architectures to establish structure and property linkage to determine composite's thermal conductivity
[24]	Thermal management of multi-processor systems-on-chips (MPSoCs)	Developed the approach for selecting best encoder configuration and core frequency using AI for temperature maintenance of MPSoCs
[25]	Efficiently managing energy utilized by data centers through reinforcement learning	A DPM technique based on reinforcement learning
[26]	Dynamic thermal management (DTM) of multimedia application using reinforcement learning	Aimed to maximize the average long-term application by trial-and-error interaction with a dynamic environment and is developed by π learning policy mapping between states and actions. It is used to control the optimum temperature of any multimedia application using ML
[27]	Energy minimization on multicore chips using supervised learning	A probability-based learner is built using supervised learning to estimate the processor's performance state for every incoming task, thus using the former knowledge to minimize energy requirement

(continued)

Table 1 (continued)

References	Major advances in thermal management	Applications/role of AI
Liu et al. [41]	Enhanced Q-learning algorithms-based novel power management techniques	Model-free online algorithms are presented for dynamic power management with performance constraints. Using ML algorithms, it can adapt itself to the changing performance constraint during runtime
[28]	Proposes an adaptive learning tree and idle period clustering-based new DPM scheme	Uses an algorithm based on adaptive learning tree to predict the future idle periods with high accuracy by applying binary and multi-varied sequences

complexity of computational methods. This increases the temperature of multi-processor systems-on-chip (MPSoCs) due to increased power consumption. Iranfar et al. [24] proposed an approach for thermal and power management using AI. It learned the best encoder configuration and core frequency for every individually running video stream running in the MPSoC. The parameters used for determining them were obtained from frame compression, performance, temperature, and the total power. This approach was further experimented by implementing it on an enterprise multicore server and compared with conventional methods. The approach was advantageous as these parameters were improved compared to the conventional techniques, as shown in Table 2. Furthermore, this improvement was achieved with no compromise on power or decrement of compression.

Improving Transient Performance in Thermal Energy Storage Units using Nearest Neighbor Search and ANNs [22] improved the transient performance of thermal energy storage units using PCM for latent heat storage by thermal management by applying ML. In a phenomenon known as subcooling, the solidification of PCM is initialized by significantly reducing the temperature below the melting point of the PCM. The cold finger technique is used for initiating the solidification of PCM. In this technique, a little unmelted part is kept in the PCM for initializing the nucleation and solidification of the remaining PCM. The intended melt fraction of PCM in this technique can be predicted accurately by using the ML technique. This is different from conventional methods, where accuracy is increased at the cost of storage capacity. Conventional techniques consisting of physics-based prediction methods had some limitations, including-

- (a) High uncertainties in measurement.

Table 2 Percentage increase in various parameters by employing ML methods over conventional approaches

Parameter	Increase over conventional methods
Video quality	17% increase
Video performance	11% increase
Avg. temperature	12% decrease

- (b) Limited accuracy in real-time predictions.
- (c) Limited operating conditions where it can be applied.

To overcome these limitations, the nearest neighbor search and ANNs were combined, and the melt fraction of PCM was determined with significantly high accuracy. Therefore, this technique can be considered beneficial during the ending of the process (the stage in which PCM has a higher melt fraction). However, it cannot be considered beneficial for the stage having a lower melt fraction of PCM, based on its accuracy compared to physics-based solvers.

3D CNNs for Thermal Management in Composites Through Structure–Property Linkage Thermal conductivity is an essential parameter in thermal management by composites. Solving PDEs and effective medium theory is the conventional methods to determine effective thermal conductivity. The linkage of structure and property could be established through various ML methods. CNNs perform generative as well as descriptive tasks. It uses machine vision having image/video recognition, recommender systems, and natural language processing in order to do so. The thermal conductivity of composites using various CNNs was predicted by [23]. 3D CNNs can more accurately establish the linkage of structure and property. The prediction accuracy of ML methods depends on microstructure-representing features. The 2D cross-sectional images and 2D CNNs can very well predict the effective thermal conductivity of 3D composites. Also, they are easier to obtain than 3D microstructure images. 2D CNNs can predict both isotropic particle-filled and anisotropic stochastic complex composites by taking 2D images in a proper direction with respect to fillers. Cross-sectional images along the direction of heat flow were found to be beneficial compared to those perpendicular to the direction of heat flow.

Integrating CNNs with FEA for Thermal Management in CPCMs [21] determined the thermal properties of composite PCMs like paraffin and copper foam used for thermal management of a Li-ion battery pack by combining CNN with the finite element method (FEM). First, the FEM was used for modeling the microstructure of CPCMs. Then, thermal properties were used to create an image dataset, which was further used for training and testing the performance of CNN. Image classification was done using a popular network architecture. This procedure predicted the thermal characteristics of the CPCMs. They were used in Newman's battery model to simulate the Li-ion battery's cell's heat generation and electrochemical response. Paraffin had the leading role in thermal management, in which the copper foam acted as a thermal conductivity enhancer. The thermal management effectiveness of the battery pack was determined by the multiscale model developed by FEM. Here also, the thermal characteristics which were determined by the combination of CNN and FEM were used. Finally, it was concluded that the combination of CNN with FEM was more accurate for determining the battery thermal management system's effectiveness compared to only FEM.

Reinforcement Learning for Thermal Management in HPC Systems With the increase of power demands for high-performance computing (HPC) systems, this is high time that researchers should focus more on the thermal management of such systems as the CPU. They are designed for very low maximum power rating

having minimum performance [29] for specific high graphic applications keeping in mind the dynamic management of the control unit. Specific ML techniques can be implemented to control the thermal management of multimedia applications' computational intensity. Dynamic thermal management (DTM) has also been used in balancing the temperature of different computer systems like servers [30], embedded systems [31], and general-purpose computers [32]. Work done by [26] presented a study on DTM using reinforcement learning. It works on changing temperature and switching patterns workload by looking at the control unit's temperature sensor and event counters. This learning [33] consists of

- (a) An agent, with a finite action, set \mathbf{A} .
- (b) Environment space is represented by \mathbf{S} .
- (c) A policy of π representing the behavior of the learning agent at any specified time. It can also be defined as the mapping from the set of environment states to the set of actions, i.e., $\pi: \mathbf{S} \rightarrow \mathbf{A}$.

They used dynamic voltage and frequency scaling (DVFS) for controlling the operating temperature. ML finds the easiest thermal management method, which ultimately helps decrease the high-temperature hotspot, unlike standard DTM methods.

Bayesian Learning, Reinforcement Learning, and Regression Analysis for Dynamic Voltage and Frequency Prediction Modern multicore processors suffer higher power densities due to the high integration density and various obstructions of voltage scaling. Sometimes, these issues might lead to high-temperature spots, which will decrease the overall efficiency and may cause inconsistent aging, increase the chances of chip failures, degrade reliability, and ultimately reduce the system's performance [34]. Thus, effective thermal management practices are becoming more relevant than ever. However, the main goal remains to prevent chips from possible overheating while not sustaining unbearable cooling costs, thus guaranteeing to continue technology scaling trends feasible [35]. Moreover, minimizing overall energy consumption or energy management while not suppressing the battery lifetime and performance of the system is another significant problem. Overall system performance maximization is typically the most chased optimization goal. However, thermal constraints are the major limiting factors for maximizing performance, especially in modern chips with very high power densities due to the dark silicon problem [36].

Q-Learning for Lagrangian Multiplier Adaption for Minimizing Power in Single-Core Systems [28] propose a DPM technique for a random number of sleep states that shutdown the idle components based on adaptive learning trees and idle period clustering. The proposed methodology correlates with advanced branch prediction schemes to lessen the penalty of mispredicted branches. Also, based on the transition time between sleep states and the expected duration of the next idle period, authors derive a function that selects the optimal sleep state in which to set the core to reduce the energy consumption. Tan et al. [37] propose a DPM technique to minimize average power consumption for an arbitrary number of sleep states under a given performance constraint. The methodology enhances the traditional Q-learning

algorithm that proposes a linear adaption of Lagrangian multiplier to minimize the power consumption while delivering the exact needed performance. Thus, the authors present an iterative algorithm that adjusts the Lagrangian multiplier to the optimal value.

Supervised Learning-Based Power Management Model For Energy Minimization in Multicore Systems The work in [27] portrays a supervised learning-based power management model for energy minimization on a multicore chip with per-core DVFS. A probability-based learner is used as the power manager to predict the processor's performance state for every incoming task by examining some commonly available input features and then uses this predicted state to suggest the optimal power management action from a pre-computed policy table. The chief objective of the power manager is to derive a DVFS policy for picking the frequency/voltage levels of the cores that reduces the overall energy consumption based on the load conditions and workload characteristics.

Reinforcement Learning-based Dynamic Power Management The work in [25] proposes a reinforcement learning-based DPM structure for data centers that try to reduce the overall energy utilization of a server pool while sustaining a reasonable average job response time. In [38], authors developed an ML-based thermal management model that employs a heuristic to bound the learning space by assigning a particular set of available actions to all existing states. The purpose of this work is to accelerate the performance while minimizing the thermal stresses under thermal and power constraints by transferring tasks between cores and by selecting the frequency/voltage levels of every core.

4 Discussion and Conclusions

AI has been immensely used in electronic thermal management. This work provides an in-depth review of recent developments in AI-inspired thermal management. The present study mainly focuses on the following aspects of electronic thermal management. The study concludes that,

- (1) Various ML algorithms (like reinforcement learning) could be used in high graph applications for DTM.
- (2) AI techniques can be used for thermal management without compromising the quality of output. Hence, they are more effective compared to conventional methods.
- (3) Next, we have portrayed an overview of various research developments that aim to use ML and DL techniques to efficiently manage the power and thermal supply of single-core and multicore processors.

The major advantage of using ML is its ability to adapt instantaneously to varying system conditions and workloads, learning from past events to improve themselves. AI-based approaches have been shown to improve management decisions. By going through the current review, one can look into the recent developments in thermal

management techniques and make them more accurate, efficient, and time-saving by developing and deploying appropriate AI models.

References

1. Zhao Z, Wang T, Zhang B, Wang Y, Bao C, Ji Z (2021) Analysis of an integrated thermal management system with a heat-pump in a fuel cell vehicle. *AIP Adv* 11(6):065307
2. Moore AL, Shi L (2014) Emerging challenges and materials for thermal management of electronics. *Mater Today* 17(4):163–174
3. Ghosh DS, Calizo I, Teweldebrhan D, Pokatilov EP, Nika DL, Balandin AA, Bao W, Miao F, Lau CN (2008) Extremely high thermal conductivity of graphene: prospects for thermal management applications in nanoelectronic circuits. *Appl Phys Lett* 92(15):151911
4. Pesaran AA (2001) Battery thermal management in EV and HEVs: issues and solutions. *Battery Man* 43(5):34–49
5. Biercuk MJ, Llaguno MC, Radosavljevic M, Hyun JK, Johnson AT, Fischer JE (2002) Carbon nanotube composites for thermal management. *Appl Phys Lett* 80(15):2767–2769
6. Zweben C (1998) Advances in composite materials for thermal management in electronic packaging. *Jom* 50(6):47–51
7. Kercher DS, Lee JB, Brand O, Allen MG, Glezer A (2003) Microjet cooling devices for thermal management of electronics. *IEEE Trans Compon Packag Technol* 26(2):359–366
8. Mudawar I (2001) Assessment of high-heat-flux thermal management schemes. *IEEE Trans Compon Packag Technol* 24(2):122–141
9. Gallego NC, Klett JW (2003) Carbon foams for thermal management. *Carbon* 41(7):1461–1466
10. Kandasamy R, Wang XQ, Mujumdar AS (2007) Application of phase change materials in thermal management of electronics. *Appl Therm Eng* 27(17–18):2822–2832
11. Mallik S, Ekere N, Best C, Bhatti R (2011) Investigation of thermal management materials for automotive electronic control units. *Appl Therm Eng* 31(2–3):355–362
12. Xin G, Sun H, Hu T, Fard HR, Sun X, Koratkar N, Borca-Tasciuc T, Lian J (2014) Large-area freestanding graphene paper for superior thermal management. *Adv Mater* 26(26):4521–4526
13. Jordan MI, Mitchell TM (2015) Machine learning: trends, perspectives, and prospects. *Science* 349(6245):255–260
14. Mitchell TM (1997) *Machine learning*. McGraw-Hill Inc., New York
15. LeCun Y, Bengio Y, Hinton G (2015) Deep learning. *Nature* 521(7553):436–444
16. Raissi M, Perdikaris P, Karniadakis GE (2019) Physics-informed neural networks: A deep learning framework for solving forward and inverse problems involving nonlinear partial differential equations. *J Comput Phys* 378:686–707
17. Chharia A, Upadhyay R (2020) Deep recurrent architecture based scene description generator for visually impaired. In 2020 12th international congress on ultra modern telecommunications and control systems and workshops (ICUMT). IEEE, pp 136–141. <https://doi.org/10.1109/ICUMT51630.2020.9222441>
18. Krizhevsky A, Sutskever I, Hinton GE (2017) ImageNet classification with deep convolutional neural networks. *Commun ACM* 60(6):84–90
19. Deng J et al (2009) ImageNet: a large-scale hierarchical image database. In 2009 IEEE conference on computer vision and pattern recognition, IEEE, pp 248–255
20. Goodfellow I, Bengio Y, Courville A (2016) *Deep learning*. MIT Press, Cambridge, Massachusetts. Available at: <http://www.deeplearningbook.org>
21. Kolodziejczyk F, Mortazavi B, Rabczuk T, Zhuang X (2021) ‘Machine learning assisted multi-scale modeling of composite phase change materials for Li-ion batteries’ thermal management. *Int J Heat Mass Transf* 172:121199

22. Shettigar N, Banerjee D, Truong M, Thyagarajan A, Bamido A, Meza A, Kumar N, (2020) Application of machine learning for enhancing the transient performance of thermal energy storage platforms for supplemental or primary thermal management. In Heat transfer summer conference, vol 83709. American Society of Mechanical Engineers, pp V001T02A014
23. Rong Q, Wei H, Huang X, Bao H (2019) Predicting the effective thermal conductivity of composites from cross sections images using deep learning methods. *Compos Sci Technol* 184:107861
24. Iranfar A, Zapater M, Atienza D (2017) Work-in-progress: a machine learning-based approach for power and thermal management of next-generation video coding on mpsoCs. In: 2017 International conference on hardware/software codesign and system synthesis (CODES+ISSS). IEEE, pp 1–2
25. Lin X, Wang Y, Pedram M (2016) A reinforcement learning-based power management framework for green computing data centers. In: 2016 IEEE international conference on cloud engineering (IC2E). IEEE, pp 135–138
26. Yang et al (2011) Dynamic thermal management for multimedia applications using machine learning. In: 2011 48th ACM/EDAC/IEEE design automation conference (DAC). IEEE, pp 95–100
27. Jung H, Pedram M (2010) Supervised learning based power management for multicore processors. *IEEE Trans Comput Aided Des Integr Circuits Syst* 29(9):1395–1408
28. Chung EY, Benini L, De Micheli G (1999) Dynamic power management using adaptive learning tree. In: 1999 IEEE/ACM international conference on computer-aided design. Digest of Technical Papers (Cat. No.99CH37051). IEEE, pp 274–279
29. Brooks et al (2001) Dynamic thermal management for high-performance microprocessors. In Proceedings HPCA seventh international symposium on high-performance computer architecture, pp 171–182
30. Pakbazni et al (2010) Temperature-aware dynamic resource provisioning in a power-optimized datacenter. In: 2010 Design, automation and test in Europe conference and exhibition. IEEE, pp 124–129
31. Zhang et al (2010) Thermal aware task sequencing on embedded processors. In: Design automation conference. IEEE, pp 585–590
32. Cochra et al (2010) Consistent runtime thermal prediction and control through workload phase detection. In: Design automation conference. IEEE, pp 62–67
33. Sutton et al (1998) Reinforcement MIT Press
34. P.D. SM et al (2017) ‘a scalable network-on-chip microprocessor with 2.5D integrated memory and accelerator. *IEEE Trans Cir Syst I Regular Papers* 64(6):1432–1443
35. Pagani S et al (2020) Machine learning for power, energy, and thermal management on multicore processors: a survey. *IEEE Trans Comput Aided Des Integr Circuits Syst* 39(1):101–116
36. Esmaeilzadeh H et al (2011) Dark silicon and the end of multicore scaling. *ACM SIGARCH Comp Archit News* 39(3):365–376
37. Tan Y, Liu W, Qiu Q (2009) ‘Adaptive power management using reinforcement learning’. In: Proceedings of the 2009 international conference on computer-aided design—ICCAD ’09. ACM Press, New York, p 461
38. Iranfar A, et al (2015) A heuristic machine learning-based algorithm for power and thermal management of heterogeneous MPSoCs. In: 2015 IEEE/ACM international symposium on low power electronics and design (ISLPED). IEEE, pp 291–296. <https://doi.org/10.1109/ISLPED.2015.7273529>
39. Srinivasan et al (2003) Predictive dynamic thermal management for multimedia applications. In: Proceedings of the 17th annual international conference on supercomputing, pp 109–120
40. Rong et al (2019) Predicting the effective thermal conductivity of composites from cross sections images using deep learning methods. *Compos Sci Technol* 184:107861
41. Liu W, Tan Y, Qiu Q (2010) Enhanced Q-learning algorithm for dynamic power management with performance constraint. In: 2010 Design, automation & test in europe conference & exhibition, pp 602–605. IEEE. <https://doi.org/10.1109/DATE.2010.5457135>

Investigation on Heat Transfer Performance of Nanofluids



Shankar Durgam and Ganesh Kadam

Abstract Nanofluid is prepared by dissolving nanoparticles less than 100 nm in a base fluid. Various studies have shown that nanofluid provides a higher heat transfer rate compared to its base for similar flow conditions. It promises better heat transfer properties and can be used as an alternative to traditional heat transfer fluids. Different numerical models like single-phase, Eulerian and mixture model investigated to understand heat transfer performance. Thermal properties used in this study are calculated using a machine learning model. Numerical result characterizing heat transfer rate and heat transfer performance factor is presented. Result shows that Eulerian model for single-phase flow and k - ω Baseline Turbulence Model (BSL) for two-phase flows predict result more accurately. Use of nanofluid instead of base fluid laminar flow did not result in a significant increment of heat transfer rate but in the case of turbulent flow it increases significantly along with thermal performance factor.

Keywords Nanofluids · Machine learning models · Two-phase models · Single-phase model · Thermal performance factor

Nomenclature

T	Temperature of nanofluid ($^{\circ}\text{C}$)
ρ	Density of nanoparticle (kg/m^3)
k	Thermal conductivity ($\text{W}/(\text{m K})$)
\vec{g}	Gravitational acceleration (m/s^2)
C_p	Specific heat capacity ($\text{J}/(\text{kg K})$)
\vec{F}	External body force (N)
P	Pressure (N/m^2)
S	Source terms

S. Durgam (✉) · G. Kadam
Department of Mechanical Engineering, College of Engineering Pune, Pune 411005, India
e-mail: sodiitm@gmail.com

H	Sensible enthalpy (J)
m	Mass flow rate (kg/s)
\bar{v}	Time average velocity (m/s)

1 Introduction

Different experimental and numerical studies are done to study conduction of nanofluids as heat transfer fluid. Choi and Eastman [1] studied it for copper nanophase materials-based nanofluid. In this experimental study authors concluded use of nanofluid to reduce pumping power to achieve same heat transfer rate. It found that to increase heat transfer rate by factor two conventional methods need to increase pumping power by factor 10 but with use of nanofluid same result can be achieved without increasing pumping power. Leong et al. [2] studied ethylene glycol-copper oxide (EG-CuO) nanofluid in cooling system of automotive and increased heat transfer coefficient which is compared with it and achieved through a base fluid. Result indicated 3.8% improvement in a heat transfer rate for 2% volume concentration. Bozorgan et al. [3] studied use of copper oxide-water (CuO-H₂O) in radiator of diesel engine using numerical analysis. The result found an increase in the heat transfer rate by 10% for 2% nanoparticles volume fraction. Gulhane et al. [4] studied experimentally aluminum oxide-water (Al₂O₃-H₂O) nanofluid at a low volume fraction in the car radiator. The result of this experimental investigation has shown that heat transfer rate increases with increment in nanoparticle concentration. Ali et al. [5] studied zinc oxide (ZnO) nanoparticles-based nanofluid for the different volumetric concentrations for the turbulent flow with Reynolds number varying from 17,500 to 27,600. The result showed increase in heat transfer coefficient for all concentrations of the nanoparticles. The highest increment found was 46% compared to the base fluid with a 2% volume fraction of nanoparticles. Elbadawy et al. [6] studied flow of Al₂O₃-water and CuO-water in a radiator numerically to study its performance. The result shown that with use of nanofluid instead of base fluid, volume of the radiator is reduced significantly along with the rise in pumping power. In radiator it depends on volume concentration of nanoparticles and Reynolds number. The optimum concentration of nanoparticle found to be 4.5% for both nanofluids.

However few researchers found fall in heat transfer rate instead of rise with use of nanofluid as a heat transfer fluid. Rashmi et al. [7] investigated heat transfer in natural convection with Al₂O₃-water nanofluids. The author found a fall in heat transfer rate as nanoparticle volume fraction increases, and this decrease is attributed to effect of dynamic viscosity. All this controversy reported in the case of nanofluid use in natural convection but to the best of our awareness no such case is found in case of mixed and forced convective heat transfer. In this study properties used were calculated using different analytical models. Focus of this study is about forced convection for laminar and turbulent flow through pipe using thermal properties calculated by machine learning model.

2 Modeling Methodology

The researchers presented two principal methodologies to study the nanofluids using numerical methods. In single-phase model, it is considered that base fluid and nanoparticles are flows with same velocity and thermal equilibrium. In the multiphase method, it is not necessary.

Continuity equation

$$\frac{\partial \rho}{\partial t} + \Delta \cdot (\rho \vec{v}) = 0$$

Momentum equation

$$\frac{\partial}{\partial t} \rho \vec{v} + \Delta \cdot (\rho \vec{v} \vec{v}) = -\Delta p + \rho \vec{g} + \vec{F}$$

Energy equation

$$\frac{\partial}{\partial t} (\rho H) + \Delta \cdot (\vec{v} \rho H) = \Delta \cdot (k \Delta T) + S$$

In multiphase model it is assumed that base fluid and nanoparticles have strong coupling and both of them flow in the same velocity. In the governing equation interaction between them is taken into account. Two main models are used in laminar fluid flow; they are Eulerian model and mixture model. Eulerian model allows to model multiphase, interacting phase separately, and in its momentum, continuity equations are solved separately for each phase. In multiphase mixture model it assumed strong coupling between nanoparticles and base fluid and both have same local velocity for short spatial length. Interaction between phases is taken into consideration while solving governing equations.

The turbulent model takes into account the number of parameters. Different turbulent models can be used depending on accuracy, computational time and cost. Mustafa et al. [8] did numerical simulation on two-phase flows of Al_2O_3 -based nanofluid to study its convective heat transfer performance. The result shows that ω -based models predict heat transfer performance better than ε -based model. In this study turbulent flow of nanofluid for this heat transfer performance is investigated using Std. k - ω and BSL k - ω model. Standard k - ω (Std. k - ω) model is elicited from Wilcox et al. [9] model. BSL k - ω model is elicited from Menter [10] model. In BSL k - ω model Std. k - ω model and k -epsilon model are added together by multiplying a blending function. In this study artificial neural network machine learning model is used to calculate viscosity and thermal conductivity of the nanofluid and mixture model is used to predict density and heat capacity.

3 Results and Discussion

Grid sensitivity is carried using a single-phase model for both turbulent flow and laminar flow models to find the appropriate size of the mesh. This test is carried out by varying number of the elements against the evaluated heat transfer rate for similar flow and geometry conditions. Figure 1 is the result of the grid-independent test carried out for the laminar flow model. For the laminar model a 2D channel with $7 * 1000$ mm with flow of water with Reynolds number 400 is subjected to heat flux of $10,500 \text{ W/m}^2$. Figure 1 displays the changes of the heat transfer rate with a number of elements. It is observed that the grids with a number of elements 62,899 give acceptable results as differences detected are quite less and can be ignored. Similarly, for the turbulent model a 2D channel with $7.5 * 1500$ mm with flow of water with Reynolds number 6000 is exposed to a constant heat flux of $10,500 \text{ W/m}^2$. Figure 2 shows a variation of the heat transfer coefficient with number of elements. It is found that the grids with number of elements 88,800 give the most reasonable results.

Validation of numerical findings is done against existing experimental results for laminar and turbulent flows. Besides that, accuracy of two-phase, single-phase Eulerian and two-phase mixture model for laminar flow is investigated. Figure 3 represents a comparison of heat transfer coefficient by numerical method against experimental result by Almohammadi et al. [11]. In this investigation $\text{Al}_2\text{O}_3\text{-H}_2\text{O}$ nanofluid with average nanoparticle size 15 nm and volume fraction 1% is used. Properties used to calculate parameters like velocity are calculated using machine learning model which is discussed in the previous section. The result shows that among all numerical model two-phase Eulerian model predicts heat transfer more accurately while two-phase mixture model overpredicts and single-phase underpredicts it. RMSE values of all three numerical models are compared. Result shows that

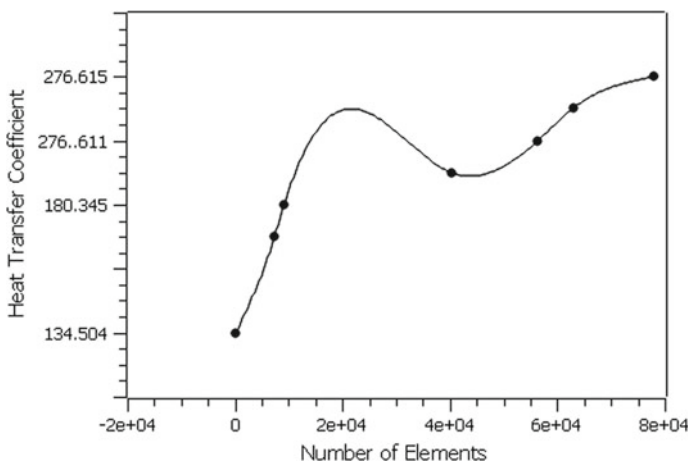


Fig. 1 Grid-independent test based for laminar flow

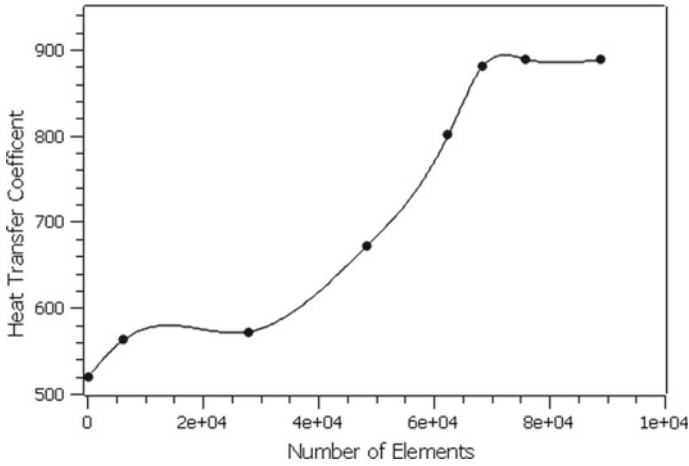


Fig. 2 Grid-independent test based for turbulent flow

a value of RMSE is lowest for the Eulerian model (76.92) compared to single-phase (191.56) and mixture model (152.36); hence Eulerian model is selected for further investigation of nanofluid flow in the laminar zone.

Mustafa et al. [8] in his investigation shown that ω -based model is more accurate than ε -based model. In this study numerical investigation is carried out using Eulerian Std. $k-\omega$ model and BSL $k-\omega$ model, and its result is related with experimental study of Heyhat et al. [12]. In this study Al_2O_3 nanoparticles with size 45 nm and volume concentration 1% and 2% are used. Nanofluid with varying Reynolds number

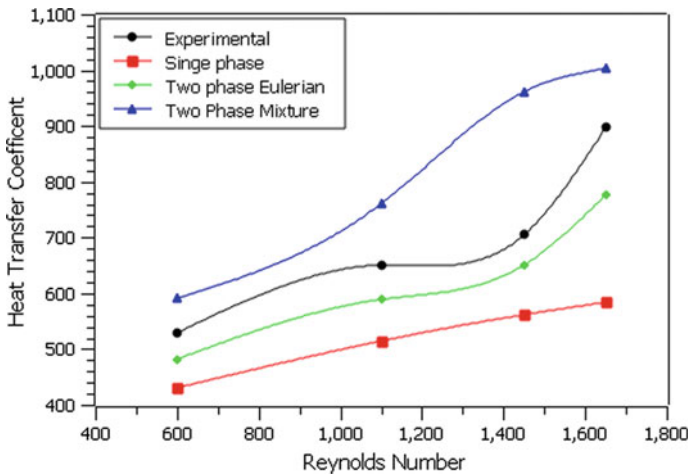


Fig. 3 Comparison of experimental value of heat transfer coefficient predicted by various numerical models of $Al_2O_3-H_2O$ nanofluid at laminar flow

from 4000 to 12,000 flows through 2D channel of size 7.5 * 1500 mm subjected to constant temperature wall at 373 K. The result of numerical models is compared to the experimental result to find out an accurate model to predict heat transfer coefficient. Figure 4 is a comparison of numerical model prediction and experimental result for 1% nanoparticle volume fraction, and Fig. 5 is a comparison for 2% volume concentration. Properties used to calculate parameters like velocity are calculated using a machine learning model which is discussed in the previous section. Comparison of RMSE values for the Std. $k-\omega$ model and BSL $k-\omega$ model is done, and the value of RMSE of Std. $k-\omega$ and BSL $k-\omega$ models is 553.79 and 276.35 for 1% concentration and 273.91 and 159.62 for 2% volume concentration, respectively. From the result it can conclude that numerical models overpredict heat transfer coefficient for 1% volume concentration of nanoparticles compared to the 2% volume concentration; furthermore BSL $k-\omega$ model predicts it more accurately than the standard (Std.) $k-\omega$ model; hence BSL $k-\omega$ model is selected for further investigation of nanofluid flow in the turbulent zone.

In this section numerical investigation is carried out using the BSL $k-\omega$ model. In it a two-dimensional horizontal pipe of length 1500 mm and diameter 7.5 mm is considered for the study. Heat transfer performance is investigated for Al_2O_3 and CuO -type nanofluid. For this study a pipe inlet with uniform velocity as well as uniform temperature (298 K) is stated. Properties used to calculate parameters like velocity are calculated using the machine learning model which is discussed in the previous section. For both types of nanofluids 50 nm-sized nanoparticle is selected, and a no-slip boundary condition is introduced on pipe wall with a constant temperature.

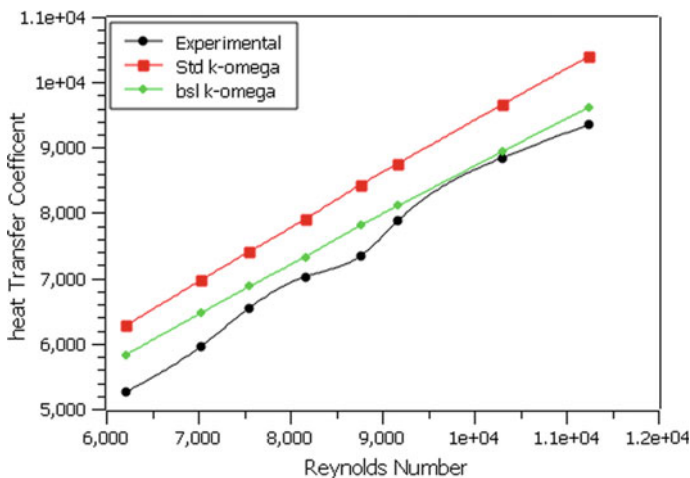


Fig. 4 Comparison of experimental value of heat transfer coefficient predicted by various numerical models of $\text{Al}_2\text{O}_3\text{-H}_2\text{O}$ nanofluid at 1% volume fraction of nanoparticles

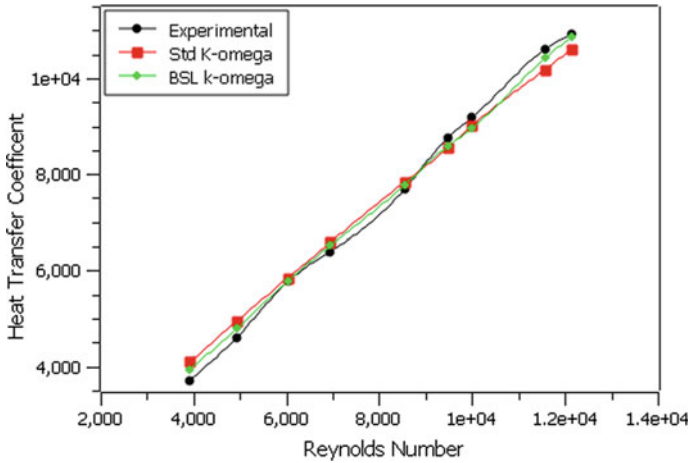


Fig. 5 Comparison of experimental value of heat transfer coefficient predicted by various numerical models of $\text{Al}_2\text{O}_3\text{-H}_2\text{O}$ nanofluid at 2% volume fraction of nanoparticles

The ratio of heat transfer rate is presented and discussed in this section to understand heat transfer behavior. Figures 6 and 7 show a change in heat transfer rate ratio of $\text{Al}_2\text{O}_3\text{-H}_2\text{O}$, CuO-EG nanofluid with varying Reynolds number and concentration of nanoparticles. The heat transfer coefficient ratio aggrandizes with an increment in volume fraction for both nanofluids but this rise is significant compared to the rise in laminar flow for same nanofluid and volume concentration. It interesting to see that this ratio is higher at low Reynolds number and starts decreasing slightly with an increase in Reynolds number in a turbulent region. It further demonstrates that this ratio is constant in case of CuO-EG nanofluid for all value of Reynolds number. Like laminar flow ratio increases with increase in volume fraction but this rise is more in case of turbulent flow which makes nanofluid ideal candidate for application in turbulent flow region. The highest rise in heat transfer rate ratio is for 2.5% nanoparticle volume fraction, and its values are 1.66 and 1.72 for $\text{Al}_2\text{O}_3\text{-water}$ and CuO-EG nanofluid, respectively.

From above investigation, it can be concluded that with rise in nanoparticles volume fraction heat transfer coefficient rises significantly for both nanofluids in the turbulent region. Figures 8 and 9 show change in thermal performance factor of $\text{Al}_2\text{O}_3\text{-water}$ and CuO-EG nanofluid for different volume fractions and Reynolds numbers. Its values rise with an increase in volume fraction of nanoparticles but its rise is more significant in case of CuO-EG nanofluid compared with $\text{Al}_2\text{O}_3\text{-water}$ nanofluid. It indicates that the rise in heat transfer rate is feasible when volume fraction and Reynolds number are considered with penalty rise in friction coefficient with rise in pumping power.

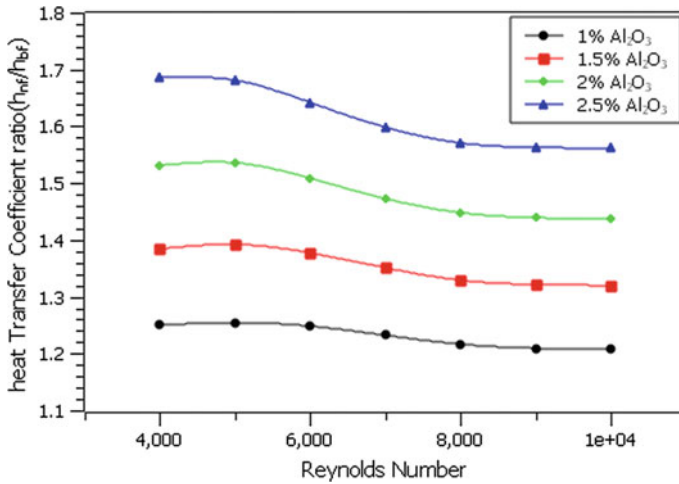


Fig. 6 Effect of nanoparticle volume fraction on the heat transfer coefficient ratio of Al₂O₃-water nanofluid at the Reynolds number

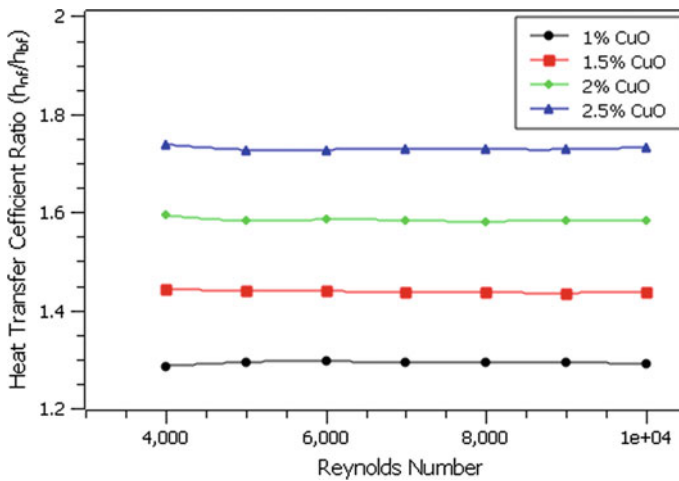


Fig. 7 Effect of nanoparticle volume fraction on the heat transfer coefficient ratio of CuO-EG nanofluid at the Reynolds number

4 Conclusion

Numerical study of forced convection flow has been done under turbulent flow and laminar flow regimes. An investigation is carried out to study heat transfer performance of nanofluid. Properties used to calculate parameters like velocity are calculated using a machine learning model. In this investigation heat transfer coefficient

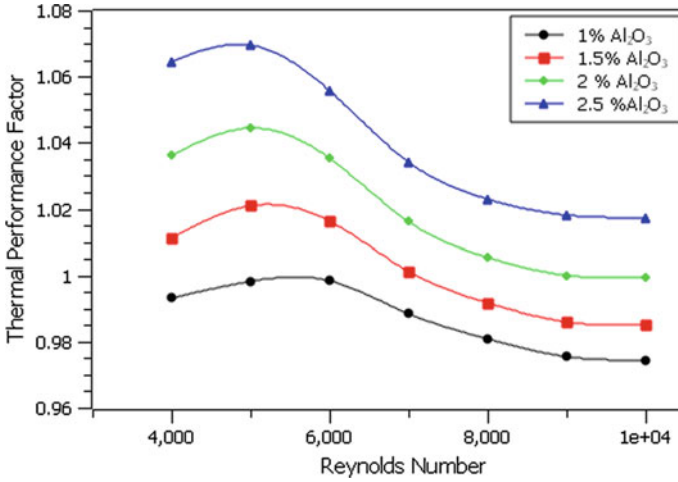


Fig. 8 Effect of nanoparticle volume fraction on the thermal performance factor of Al₂O₃-water nanofluid at the Reynolds number

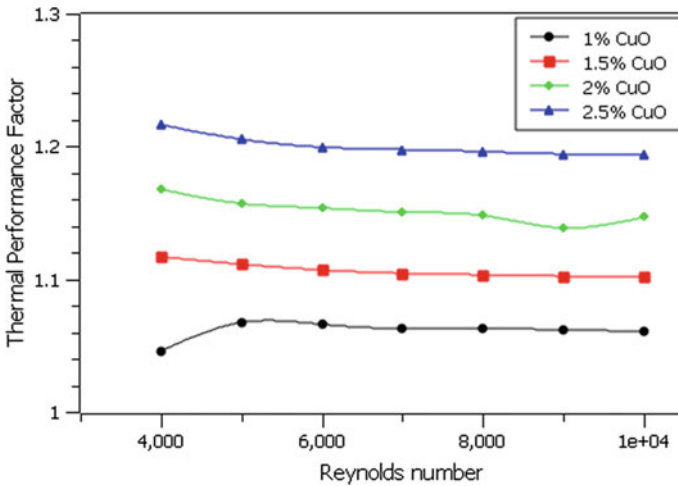


Fig. 9 Effect of nanoparticle volume fraction on the thermal performance factor of CuO-EG nanofluid at the Reynolds number

ratio is found higher than unity for both laminar and turbulent flows but in case of laminar flow, it starts decreasing with an rise in Reynolds number and reaches to almost unity for high Reynolds number in a laminar zone. In contrast to that in turbulent flow it remains constant or in some cases decreases slightly in the same nanofluids. In the case of thermal performance factor, it remains lower than unity

for laminar flow conditions. In turbulent flow it remains higher than unity and it improves with an increase in nanoparticles concentration.

References

1. Choi SUS, Eastman JA (1995) Enhancing thermal conductivity of fluids with nanoparticles. In: ASME international mechanical engineering congress, Nov 12–17,1995, San Francisco, CA
2. Leong KY, Saidur R (2010) Thermal Eng. 30, performance investigation of an automotive car radiator operated with nanofluid-based coolants (nanofluid as a coolant in a radiator). Appl Therm Eng 30:2685–2692
3. Bozorgan N, Krishnakumar K, Bozorgan N (2012) Numerical study on application of CuO-water nanofluid in automotive diesel engine radiator. Mod Mech Eng 2:130–136
4. Gulhane A, Chincholkar SP (2017) Experimental investigation of convective heat transfer coefficient of Al₂O₃/water nanofluid at lower concentrations in a car radiator. Heat Transfer—Asian Res 1–11
5. Ali HM, Ali H, Liaquat H, Maqsood HTB, Nadir MA (2020) Energy 84, experimental investigation of convective heat transfer augmentation for car radiator using ZnO-water nanofluids. J Therm Sci 29(4):1010–1024
6. Elbadawy I, Elsebay M, Shedid M, Fatouh M (2018) Reliability of nanofluid concentration on the heat transfer augmentation in engine radiator. Int J Autom Tech 19:233–243
7. Rashmi W, Ismail AF, Khalid M, Faridah Y (2011) CFD studies on natural convection heat transfer of Al₂O₃-water nanofluids. Heat Mass Transf 47:1301–1310
8. Mustafa Kemal Isman (2020) Numerical studies on convective heat transfer of Al₂O₃ nanofluid in circular pipe. Heat Mass Transf 56:1421–1428
9. Wilcox DC (1998) Turbulence modeling for CFD. DCW Industries Inc., La Canada, California, p 1998
10. Menter FR, Two-equation Eddy-viscosity turbulence models for engineering applications. AIAA J 32(8):1598–160
11. Almohammadi H, Vatan SN, Esmaeilzadeh E, Motezaker A, Nokhosteen A (2012) Experimental investigation of convective heat transfer and pressure drop of Al₂O₃-water nanofluid in laminar flow regime inside a I circular tube. World Acad Sci Eng Technol Int J Mech Mechatron Eng 6(8)
12. Heyhat MM, Kowsary F, Rashidi AM, Alem Varzane Esfehiani S, Amrollahi A (2012) Experimental investigation of turbulent flow and convective heat transfer characteristics of alumina water nanofluids in fully developed flow regime. Int Commun Heat Mass Transfer 39:1272–1278

A Comprehensive Review on Nano-additives for the Enrichment of Diesel and Biodiesel Blends for Engine Applications



**Gandhi Pullagura, Srinivas Vadapalli, V. V. S. Prasad,
Venkateswarlu Velisala, Kodanda Rama Rao Chebattina,
and Abdul Razack Mohammad**

Abstract Ever-increasing energy needs combined with the exhaustion of fossil fuels and rapid fuel consumption rates, together with the release of harmful emissions, prompted extensive investigations on alternative fuels. Better fuel combustion and reduction in ecologically harmful emissions are the main concern for modern alternative fuel research. The exploitation of alternative fuels, biodiesels, is a promising option to meet the current energy requirements in an eco-friendly manner. This sustainable approach seizes the attention of many researchers throughout the world since biodiesel has promising characters like biodegradability, oxygenated, less combustible, non-hazardous, sulfur-free, and renewable nature. However, the direct usage of biodiesel directly in engines has its own set of drawbacks that can be controlled by using additives. In this respect, fuel additives become indispensable for improving biodiesel fuel properties and reducing engine emissions. Therefore, the present review aimed to summarize the significant published work on engine performance and emission features of biodiesel fuels from non-edible sources and their blends with nanoparticles. This review will be helpful to the researchers to know the up-to-date knowledge of biodiesel fueled compression ignition engines.

Keywords Alternative fuels · Biodiesel · Nano-additives · CI engine · Performance · Emissions

Nomenclature

ASTM American Society for Testing and Materials

G. Pullagura (✉) · S. Vadapalli · K. R. R. Chebattina · A. R. Mohammad
GITAM Deemed to be University, Visakhapatnam, India
e-mail: gpullagu@gitam.edu

V. V. S. Prasad
Andhra University, Visakhapatnam, India

V. Velisala
Damacharla Anjaneyulu Government Polytechnic, Ongole, Andhra Pradesh, India

© The Author(s), under exclusive license to Springer Nature Singapore Pte Ltd. 2023
H. B. Mehta et al. (eds.), *Recent Advances in Thermal Sciences and Engineering*,
Lecture Notes in Mechanical Engineering, https://doi.org/10.1007/978-981-19-7214-0_16

AC	Air-cooled
ANP	Aluminum nanoparticle
AgO	Silver oxide
Al ₂ O ₃	Aluminum oxide
BTE	Brake thermal efficiency
BSFC	Brake specific fuel consumption
BD	Biodiesel
B5A90	B5 + 90 ppm Al ₂ O ₃
B5A60	B5 + 60 ppm Al ₂ O ₃
B10A90	B10 + 90 ppm Al ₂ O ₃
CeO ₂	Cerium oxide
CO	Carbon monoxide
CO ₂	Carbon dioxide
CO ₃ O ₄	Cobalt oxide
CuO	Copper oxide
CNT	Carbon nanotube
CuO	Copper oxide
COME	Corn oil methyl ester
CVOME	Corn vegetable oil methyl ester
CR	Compression ratio
DI	Direct injection
Fe ₃ O ₄	Iron oxide
GO	Graphene oxide
HC	Hydrocarbon
IL	Inline
IP	Injection pressure
IT	Injection timing
INPs	Iron nanoparticles
JBD	Jatropha biodiesel
JB20D	Jojoba biodiesel 20% + 80% diesel
LGO	Lemongrass oil
Mg-AI	Magnalium
MME	Mahua methyl ester
MWCNTs	Multiwall carbon nanotubes
MgO	Magnesium oxide
Mg/lit	Milligram per liter
NBD	Neem biodiesel
NOx	Oxide of nitrogen
PB30INP50	Palm biodiesel 30 + 50 ppm INP
PB30INP75	Palm biodiesel 30 + 70 ppm INP
PSBD	Palm stearin biodiesel
ppm	Parts per million
SiO ₂	Silicon dioxide
TiO ₂	Titanium oxide
Wc	Water-cooled

WCO	Waste cooking oil
ZnO	Zinc oxide
ZrO ₂	Zirconium oxide

1 Introduction

Exhaustion of fossil fuels and the rise in the requirements of petroleum-based energy resources now has become a significant apprehension for researchers. Diesel engines are indispensable for developing countries due to their advantages like higher mileage capacity, reliability & durability compared to other fossil fuels [1]. Consequently, petroleum-based fuels have become vital in industrial, agricultural, and transportation segments despite their limited availability. Furthermore, the intense exploitation of petroleum products gives rise to the release of detrimental toxins into the environment [2]. The quality and the proportion of derivatives emitted by these petroleum products fall short of strict emission standards. Contaminants, such as NO_x, CO_x, VOCs, soot, particulate matter, and formaldehyde discharged due to diesel fuel combustion, play an influential role in the existence and persistence of severe health hazards and ecological deprivation [3, 4]. Furthermore, exhaust emissions also discharge smog and increase greenhouse gas release, eventually contributing to global warming. Environmental concerns and excessive burning of diesel fuel necessitate the use of alternative fuels.

1.1 Biodiesel as an Alternative Fuel

In cognizance of increased energy needs and environmental concerns, the exploitation of fossil fuels has forced many researchers to investigate the scenarios of the utilization of alternative energy resources to substitute petroleum-based fuels and their products [5, 6]. Biodiesel has emerged as the most promising substitute for diesel [7]. It is an unconventional fuel that can be prepared directly from edible and non-edible oils derived from plants, waste cooking oils, and animal fats like tallow and lard [8]. It has become an excellent substitute for diesel engines due to its biodegradability, non-explosive nature, less combustible, oxygenated, non-hazardous, and eco-friendly [9]. Additionally, soot emission [10, 11] was found to be decreased significantly, owing to the absence of sulfur and aromatics [12] and the existence of fuel-bound oxygen [13]. Nevertheless, the exploitation of biodiesel has increased the market price of both edible oils and biodiesel, leading to food scarcity concerns. Consequently, to surmount food necessities globally, sources of biomass should be inedible [14]. Plants are the chief producers of most non-edible oils that do not need plenty of water and can be grown in infertile lands using wastewater [14]. Besides, non-edible oils are highly resistant to pests and related diseases. Biodiesel

is prepared from a variety of readily available non-edible feedstocks, namely oil palm, Jatropha, Karanja, Grapeseed, Madhuca, Ricinus, Cottonseed, Tobacco seed, Rubber seed, Lemongrass, Rice bran, Azadirakta, etc. Recent studies have reported microalgae as yet another promising feedstock for the production of biodiesel [15–17]. However, biodiesel usage in CI engines has few restrictions, for example, a small decline in the economy of the fuel on an energy basis (up to 10%), slightly elevated density, low volatility, high iodine number [18], and a rapid burn rate owing to the availability of fuel-bound oxygen [19]. Moreover, reduced fuel atomization, lesser cloud and pour points, fusing of the piston ring, increased NO_x emission and cold ignition problems, poor spray characteristics, and lesser heat content [8, 20]. These shortcomings can be overpowered by implementing a few moderately novel methods, for instance, usage of fuel additives and hybrid fuel, which gives rise to the improvement of engine performance and reduced exhaust emissions [21].

1.2 Significance of Additives

Additives majorly constitute various chemical compounds added to improve the fuel properties by blending them with petroleum-based or other fuel substitutes. The main uses of fuel additives are the formation of deposits and rust, oxidation stability while stocking up fuel for longer periods of time, cold flow characteristics, and contagion [22, 23]. Different types of additives are used in fuel modification based on the problems associated with that test fuel. For example, metal or metal oxide-based additives, oxygen-containing additives, nanoparticle-based additives, antioxidant-based additives, polymeric additives, the broad classification of additives based on their properties are tabulated in Table 1. The exploitation of oxygenated/alcohol-based additives as blending agents significantly reduces the emission of particulate matter and modifies the physio-chemical characteristics of particles; therefore, their toxicological nature [24]. Alcohols like methanol, ethanol, butanol, Isopropyl, n-pentanol, dimethyl ether, diethyl ether, 2, 5-dimethylfuran, dimethyl carbonate, diethyl adipate, triacetin, diethylene glycol, etc. are widely used in fuel modification. Low viscosity and density of alcohol mixed fuel may enhance fuel atomization and fuel–air mixing, therefore reducing the emission parameters [25].

Specific metals and their oxides were applied to the fuels in micro or nano-sized ranges by ppm or fractions by weight. Metals such as Fe, Al, Mg, Mn, Ag, Au, Cu, boron (B), graphene, Si. [2], and metal oxides such as Al_2O_3 , Co_3O_4 , CeO_2 , TiO_2 , ZnO, CuO, Fe_3O_4 . [2, 9] are used as fuel enhancement additives. Metal alloys such as Mg–Al and CNT are also used as metal-based additives that bring changes in fuels physio-chemical properties and improve their overall performance [2]. Various chemical and metal-based nanoparticles have been used to ensure the complete combustion of biodiesels, enhances the characteristics of diesel fuels [26]. These additives will help biodiesel to improve performance, combustion, and emission parameters in diesel engines in terms of environmental regulations. The choice of additives will depend on the problems encountered with that biodiesel fuel, such as the viscosity

Table 1 Types of fuel additives are based on their applications and examples

S. No.	Type of fuel additives	Examples	Applications
1	Metal/metal oxide-based additives	Alumina, magnesium, copper, cerium, titanium oxide, zinc oxide, iron oxide, ferro-fluids, etc.	Function as a catalyst for the combustion improvement Enhances the performance Decreases emissions
2	Antioxidant additives	Phenylene diamine, Alkylated phenol antioxidants	Enhances stability of biodiesel Decrease the cylinder temperature during combustion A decrease in NOx emission
3	Oxygenated/higher alcohols-based additives	Alcohols (methanol ethanol, butanol, Isopropyl, n-pentanol, etc.), dimethyl ether, diethyl ether, 2,5-dimethylfuran, dimethyl carbonate, diethyl adipate, triacetin, diethylene glycol	Enhances the combustion progression Improves the performance factors like octane rating Reduces emission of particulate matter
4	Lubricant additives	Sulfurized lard oils, Chlorinated paraffin, Phosphate esters, calcium sulfonates, vegetable oils	Enhances the tribological properties Benefits of both environmental and consumer lubricant additives, for example, fuel economy and exhaust emissions Furthermore, the health and safety aspects of additive production are considered
5	Cetane number improver additives	Ethyl hexyl nitrate, alkyl nitrate, peroxide compounds, methyl oleate, di-methyl propane (DMP) or neopentane, di-tertiary-butyl peroxide (DTBP) 2-ethylhexyl nitrate (EHN)	Lowers the Ignition delay Improves cetane index
6	Ignition boost additives	Chlorinated paraffin, sulfurized lard oils, Phosphate esters, calcium sulfonates	Reduction in ignition lag Decrease the noise Reduction of harmful emissions

(continued)

index, density, toxicity, self-ignition point, cetane number, additive solubility, flash point, and cost-effective probabilities of fuel amalgamations. Several research studies have established that the inclusion of metal-based additives in the form of nanoparticles to biodiesel acts as catalysts in improving engine combustion, performance and providing excellent fuel properties [27–30].

Table 1 (continued)

S. No.	Type of fuel additives	Examples	Applications
7	Polymer additives	Polyethylene, Polypropylene, Polystyrene, Polyvinylchloride, Polyethylene terephthalate, Polycarbonate (bisphenol A), unsaturated polyester, Acrylonitrile butadiene styrene, household PSW mixture	Reduces emissions Improves performance

The addition of nano-additives contributes to considerable changes in the chemical properties of biodiesel and increases the oxidation properties [31, 32]. Biodiesel nano-additive blends have several advantages corresponding to engine efficacy and emissions [33]. The catalytic nature of nanoparticles gives superior combustion [34], a short ignition period [35], excellent efficiency [36], and low NOx emissions [9]. They also help to improve thermophysical properties, including a high surface area to volume ratio and thermal conductivity. Furthermore, nano-additives enhance the flashpoint, kinematic viscosity, and calorific values of the diesel, biodiesel, and blends, as shown by Hosseini et al. [37] and Gumus et al. [38]. In a few research studies, the use of metal-based nanoparticles was reported to decrease the ignition delay and to facilitate trouble-free engine performance of biodiesel and diesel fuel [33, 38, 39]. Simple steps involved in the formulation of nano-fuel blend using biodiesel (MME) and graphene nanoparticles (GNPs), characterization of performance, and emission parameters are depicted in Fig. 1.

Nanoparticles as additives in diesel and biodiesels were manifested as most efficient in terms of improvement in engine parameters [35, 40, 41]. More recent nanotechnology developments enable particle sizes <100 nm without much complexity for engine fuels to facilitate all the benefits, as mentioned earlier. The blending of nano-additives-diesel/biodiesels was accomplished using ultrasonication, where sound waves of high frequency were used. Surfactants or dispersants are commonly used to make solutions more stable to prevent the agglomeration of nano-additives in the modified fuels [42, 43]. SEM and TEM are the most valuable aids to examine the nanoparticle size, shape, and distribution [44]. SEM images of few nanoparticles were shown in Fig. 2. Nanoparticles (CNTs, TiO₂, SiO₂, GNP, ZrO₂, and Al₂O₃) were dispersed into the biodiesel blend separately. The clustering of nanoparticles to form a micro-emulsion was observed along with sedimentation. The nano-additives-fuel blends should be utilized soon after the formulation to circumvent nanoparticle deposition or sedimentation [39, 42].

The fuel blends were tested for stability and phase partition. Small-sized nanoparticles improve fuel stability, avoid clogging as well as troubles of fuel atomization in fuel injectors. Saravankumar et al. [45] observed SiO₂ nanoparticles under SEM at 20,000X magnification, which revealed the spherical shape of SiO₂ having a smooth

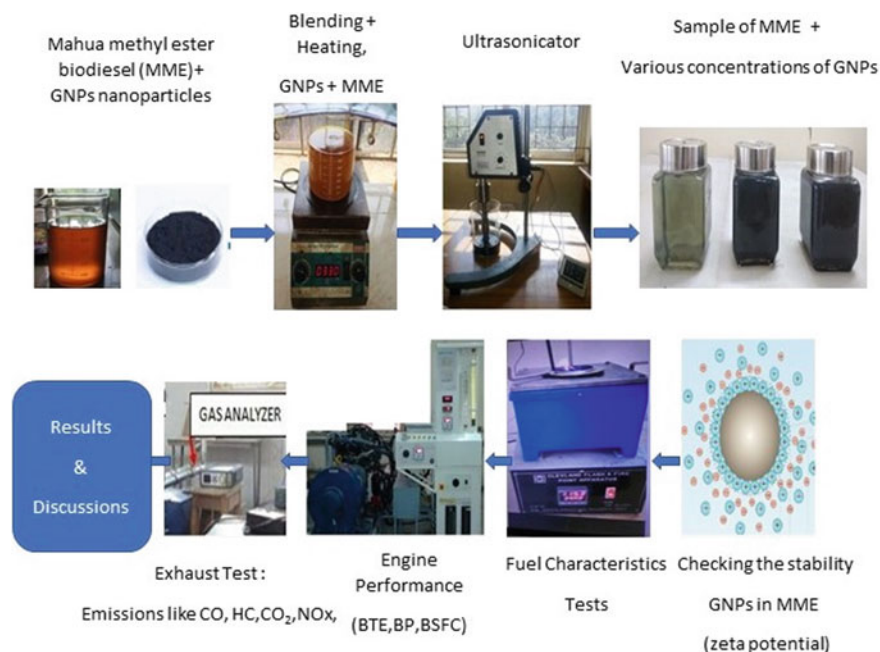


Fig. 1 Schematic diagram showing steps involved in nanoparticle-diesel-biodiesel emulsion fuel

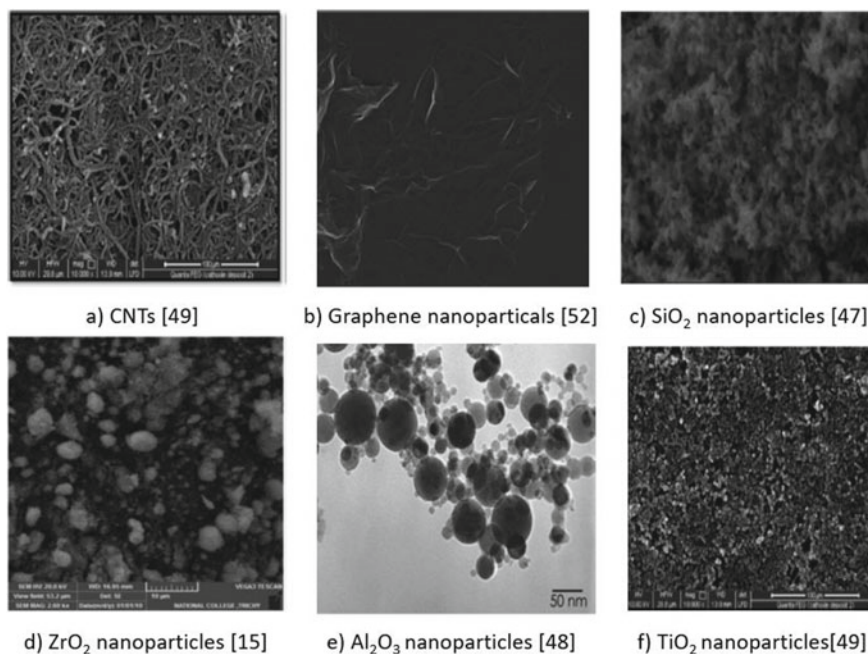


Fig. 2 Nanofluid blends SEM Images (adapted from [15, 46, 47, 49, 52] with permission)

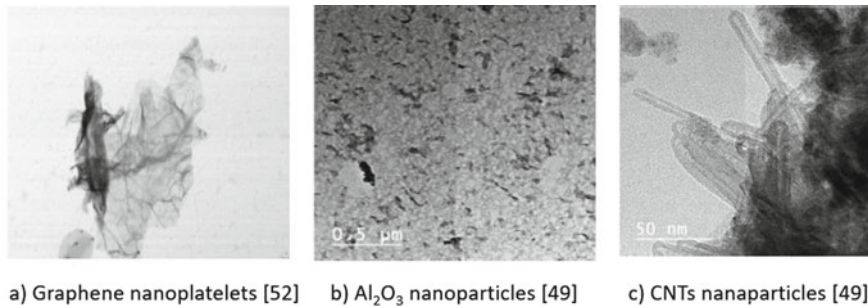


Fig. 3 TEM Images of nanoparticles (adapted from [50] and [47] with permission)

surface with an average particle size of 35 nm. Hence it was concluded that nanoparticles having a smaller diameter than that of the fuel injector nozzle avoid any overt obstacles in fuel flow in the nozzle. Likewise, ZrO₂ nanoparticles observed under 50,000X magnification showed a size variation between 38.13 and 43.54 nm [15]. SEM analysis of Al₂O₃ nanoparticles revealed the size variation of 32–48 nm [46]. The above experimental results demonstrate the positive effects of metal-based nano-additives on the CI engine. Similarly, the distribution of nano-additives in biodiesel blends improves the stability as depicted in TEM images [47] (Fig. 3).

In this review, the focus is laid to comprehend the expertise and information related to fuel modification by introducing nano-additives for metal and metal oxide to boost efficiency and minimize diesel engine emissions. The authors have attempted a thorough analysis in listing out different biodiesels from non-edible sources, biodiesel with nano-metal-based additives, and their effect on engine performance and emission characteristics at different operating conditions. This paper also reports the results of several studies conducted by various researchers on the impact of nano-fuel additives on fuel properties that would assist students, research scholars, and engineers.

1.3 Effect of nano-additives on fuel properties

Several researchers investigated the effects of nano-additives on fuel properties like calorific value, viscosity, cetane number, and flash point, etc. Nano-additive biodiesel blends were found to exert some positive effects on fuel properties [48]. The physical and chemical properties of diesel–biodiesel with nano-metal additive blends reported in recent studies are summarized in Table 2. The addition of Al₂O₃ and CuO to neat diesel slightly increased the flashpoint and cetane index at the dosage level of 50 ppm, whereas there is no considerable change in the kinematic viscosity [38].

Table 2 Physio-chemical properties of diesel–biodiesel and nano-additive blended fuel

S. No.	Fuel	Composition of additives	Kinematic viscosity (@ 40 °C cst)	Flash point (°C)	Calorific value (MJ/kg)	Cetane number	References
1	DIESEL	–	3.6	60	–	53.8	[30]
2	DIESEL + CuO	50 ppm	3.5	66	–	54.5	
3	DIESEL + Al ₂ O ₃	50 ppm	3.5	68	–	54.4	
4	DIESEL	–	2.9	76	44.12	50	[49]
5	LGO + CeO ₂	30 ppm	4.99	67	36.2	48.8	
6	JB20	–	3.33	–	41.142	51.6	[50]
7	JB20 + GNPs	25 ppm	4.05	–	41.160	52.3	
8	JB20 + GNPs	50 ppm	4.18	–	41.190	53.5	
9	JB20 + GNPs	75 ppm	4.21	–	41.210	55.2	
10	JB20 + GNPs	100 ppm	4.22	–	41.230	57.4	
11	DIESEL	–	2.55	49	45.2	51	
12	MME20	–	3.29	65	42.4	57	
13	MME50	–	4.55	89	41.4	54	
14	MME 20 + T	50 ppm	3.21	67	42.6	57	
15	MME 50 + T	50 ppm	4.56	94	41.6	54	
16	MME 20 + ZnO	100 ppm	3.92	65	42.6	57	
17	MME 50 + ZnO	100 ppm	4.87	98	41.6	54	
18	JAT B20	–	4.106	85.2	41.579	47.78	[47]
19	PUN B20	–	5.062	102.4	42.374	48.63	
18	JAT B20 + Al ₂ O ₃	100 ppm	4.234	90.1	44.998	46.6	
19	PUN B20 + Al ₂ O ₃	100 ppm	4.756	103.2	44.124	48	
20	PSBD	–	4.28	140	37.510	–	[38]

2 Effects of Nano-additives on Engine Performance

This segment describes the outcomes of several investigations on various metal-based nano-additives used in CI engines and their impact on performance characteristics, namely brake specific fuel consumption (BSFC) and brake thermal efficiency (BTE). Results of a difference of dosage levels of nano-additives on engine performance at peak load and their comparisons are furnished in Table 3. Most researchers proved that BTE was enhanced, and BSFC was decreased with an increase in the dosage rate of nano-additives.

2.1 Brake Specific Fuel Consumption (BSFC)

BSFC determines the expenditure of fuel provided to the engine for increasing brake power. In a study executed by Annamalai et al. [49], CeO₂ nanoparticles of 30 ppm, when added to Lemongrass Oil (LGO) emulsion fuel, significantly lowered BSFC in a single-cylinder diesel engine. This is attributed to the quick rate of evaporation of LGO nano-emulsion due to the accumulation of CeO₂ nanoparticles resulting in reduced energy consumption. BSFC of LGO nano-emulsion was reported to be 12.99 MJ/kW-h. Gumus et al. [38] used CuO, and Al₂O₃ nanoparticles at a dosage of 50 ppm led to a decrease in BSFC up to 0.5% and 1.2% at normal engine speed, respectively. This is due to the additional oxygen supply and constructive impacts of nano-additives on biodiesel physical properties, which increased the combustion efficiency. In another report by EL-Seesy et al. [53], BSFC was found to decrease considerably with the addition of 40 mg/l of MWCNTs in Jojoba methyl ester blended up to 16%. MWCNTs hasten the complete combustion resulting in elevated cylinder gas pressure. This is due to the high surface-to-volume ratio of MWCNTs, which improved the heat transmission among the particles and fuel droplets, consequently promoting the fuel droplet atomization and combustion process.

2.2 Brake Thermal Efficiency (BTE)

Several research studies reported that nano-additives have positive effects on brake thermal efficiency. Annamalai et al. [49] experimentally investigated the dosing of CeO₂ nanoparticles at 30 ppm concentration and found that the BTE of LGO nano-emulsion was increased by 17.02% because of micro explosion and secondary atomization of fuel, which resulted in faster evaporation of fuel [56]. Likewise, a maximum BTE of 31.62% was obtained with CeO₂ nanoparticles blended with Canola biodiesel. CeO₂ nanoparticles in the fuel facilitate complete combustion and act as oxygen barriers, liberating and accumulating oxygen based on the partial pressure of oxygen [57]. In another study, BTE was improved with the addition of

Table 3 Engine performance and emissions characteristics of nanoparticles doped fuels under different engine operating conditions

Engine specification	Base fuel	Operating condition	Nano-additive	Composition	Performance results	Emission results	References
1-cylinder, 4-stroke, DI diesel engine, Kirloskar Av1	Mahua biodiesel blend	Constant speed of 1500 rpm, CR-17.5:1, IT-23° (b TDC)	Aluminum oxide (ANPs)	50 ppm 100 ppm	Increased BTE Decreased BSFC	Lower CO, UHC, and higher NOx	[46]
1-cylinder, 4-stroke DI- WC engine	Oenothera lamarekiana biodiesel	Compression ratio 17.5 (variable)	Graphene oxide	50 ppm	Increased BTE	Reduction in NOx, UHC, and CO	[48]
1-cylinder, 4-stroke diesel engine, Kirloskar	Lemongrass Oil (LGO) emulsion fuel	1500 rpm and different load CR-17.5:1, IT-23° (b TDC), IP 200 bar	CeO ₂	30 ppm	Increased BTE AND slightly decreased BSFC	Reduction in CO, HC, and NOx	[49]
1-cylinder, 4-stroke, WC-diesel engine	Palm biodiesel	Constant speed of 1500 rpm, CR-17.5:1, IT-23° (b TDC)	Iron nanoparticles (INP)	50 ppm 75 ppm	Increased BTE Decreased BSFC	Lower CO and NOx	[32]
4-stroke, DI, air-cooled DIESEL engine	Waste cooking oil	CR-17.5:1, injection timing 60° (b TDC)	Alumina nanoparticles	30 ppm 60 ppm 90 ppm	Increased BTE Decreased BSFC	Reduction in CO and UHC	[38]
1-cylinders, diesel engine model/HATZ- 1B30-2	Jojoba methyl ester	Constant speed of 2500 rpm with different engine loads, CR-21.5:1	MWCNTs	20 mg/l	Increased BTE Decreased BSFC	Reduction in NOx, UHC, and CO	[53]

(continued)

Table 3 (continued)

Engine specification	Base fuel	Operating condition	Nano-additive	Composition	Performance results	Emission results	References
Kirloskar, air-cooled, diesel engine	Mahua biodiesel	Constant speed of 1500 rpm, CR-18.5:1, IT 23° (b TDC)	TiO ₂	100 ppm 200 ppm	- -	Lower CO, HC, and NOx	[33]
1-cylinder, direct injection diesel engine	Pongamia methyl ester (PMEB25)	Constant speed of 1500 rpm, CR-16.5:1	Al ₂ O ₃	50 ppm 100 ppm	Increased BTE, reduced BSFC	Reduction in CO, HC, Smoke, and increased NOx emission	[54]
1-cylinder, diesel engine,	Microalgae biofuel	Constant speed of 1500 rpm, CR-16.5:1, IT-23° (b TDC), IP-210 bar	(ZrO ₂)	50 ppm 100 ppm	- -	Lower CO, UHC, and smoke emissions	[15]
1-cylinder, 4-stroke, diesel engine, Kirloskar	Jatropha methyl esters Pongamia methyl esters	Constant speed 1500 rpm and different load	Al ₂ O ₃ ,	100 ppm	Increased BTE and decreased BSFC	- Max reduction of CO, HC, NOx emission	[52]
Kirloskar TV1 diesel engine	Waste cooking oil	Constant speed of 1500 rpm, CR-17.50	(MgO)	20, 30, 40 and 50 ppm	Increased BTE	Lower CO, UHC, and smoke. Higher NOx	[55]
1-cylinder, 4-stroke DI diesel engine,	Mahua methyl ester biodiesel	Constant speed of 1500 rpm, different load, IT-23° (b TDC), IP 210 bar	(ZnO)	50 ppm 100 ppm	Increased BTE, SFC is similar to diesel Increased BTE	Lower NOx, CO, and HC -	[51]

MWCNTs in Jojoba methyl ester blended up to 15% comparing to JB20D blended fuel [53]. The experimental investigation conducted with INP and Palm biodiesel blend has shown enhanced BTE up to 3%. Interestingly, increased concentrations of INP in biodiesel blends have increased the fuel blends viscosity, which results in lower combustion due to poor atomization. Conversely, INP also enhances combustion and offers added surface energy for improved atomization [32]. PB30INP50 fuel blend demonstrated elevated BTE than the PB30INP75 sample at high load settings, which is correlated to the oxygen content of biodiesel samples [58].

3 Effects of Nano-additives on Engine Emission Characteristics

The major concern for researchers from diesel engines is emission characteristics of fuel used since it has to meet the existing environmental standards. In general, HC, CO, CO₂, NO_x, and smoke are emitted by diesel engines. This part of the paper explicitly reviewed the up-to-date research reports on the role of nano-additives in checking diesel engine emissions. Summary of emission parameters by previous researchers and their comparative study were shown in Table 3.

3.1 Effect on Hydrocarbon (HC) Emission

Hydrocarbons are released during the partial combustion of fuels. Many researchers demonstrated lower HC emissions when metal-based nano-additives were used in biodiesel blends. Annamalai et al. [49] achieved a 16.03% reduction in HC emission using CeO₂ nanoparticles with LGO nanoemulsion since CeO₂ acts as an oxygen buffer and facilitates complete combustion of carbon particles present in the engine combustion chamber, resulting in lower HC emissions. Similarly, Gumus et al. [38] reported lower HC emissions up to 13% and 8% using Al₂O₃ and CuO nanoparticles, respectively. In another study by Anbarasu et al. [57], HC emissions were significantly lowered up to 50–60% when CeO₂ was dosed with COME. Likewise, MME blended with TiO₂ at 200 ppm concentration showed a 3.8% reduction in HC emissions as TiO₂ nanoparticle function as an oxidation catalyst reducing the activation temperature of carbon particle combustion and improve HC oxidation [33]. Moreover, Al₂O₃ nanoparticles also contribute to lower HC emissions up to 20.56% when mixed with WCO biodiesel [9].

3.2 *Effect on Carbon Monoxide (CO) Emission*

CO is one of the derivatives of incomplete combustion of hydrocarbons. Elevated concentrations of CO can result in adverse environmental effects as well as various physiological, pathological changes and, ultimately, death. For this reason, the reduction of CO emission becomes an essential characteristic of any fuel to be used. Several researchers investigated the use of various metal nano-additives to lower the CO emissions and established that these nanoparticles have adequate surface contact area to raise the chemical reactivity successively reduce the ignition delay. In addition, they enhance the extent of fuel–air mixing ensuring complete combustion. A decrease in viscosity of fuel improves fuel atomization and significantly contributes to lowering CO emissions [52, 59]. CO emissions were reduced up to 15.69% at full load conditions when CeO₂ nanoparticles were mixed with LGO biodiesel [49]. Gumus et al. [38] compared the impact of Al₂O₃ and CuO nano-additives in neat diesel to obtain lower CO emissions up to 11% and 5%, respectively. Similarly, TiO₂ nanoparticles at 200 ppm when blended with MME showed a 9.3% reduction in CO emissions at peak brake power [33]. Palm biodiesel dosed with INP at 30 ppm recorded a 56% reduction in CO emissions [32].

3.3 *Effect on Carbon Dioxide (CO₂) Emission*

During the complete combustion of fuel in the engine, CO₂ emissions were released. However, an increase in CO₂ emissions impinges much on ecological balance. In general, it was observed that during the combustion process, most of the CO would be converted into CO₂ in the presence of nano-additives since they provide extra oxygen to improve combustion. Consequently, more CO₂ emissions will be released. In line with this, Pongamia biodiesel without nano-additives showed lower emissions than with the addition of Al₂O₃ nanoparticles [52]. Similarly, increased CO₂ emissions were observed with *Oenothera Lamarckiana* biodiesel and GO nanoparticle blends, which is in accordance with several previous studies reporting a rise in CO₂ emissions with a decrease in CO emissions [48].

3.4 *NO_x Emission*

During the combustion process, the diesel engine releases NO_x, which fundamentally comprises nitric oxide (NO) and nitrogen dioxide (NO₂). NO_x contributes to a broad range of environmental effects, including the formation of acid rains and severe health hazards [60]. Therefore, to increase the quality of diesel fuel, various metal and metal oxide additives were doped with diesel for attaining complete combustion of fuel and decreasing the number of exhaust gases [61]. NO_x emission was reduced

by 24.8% with the accumulation of CeO₂ nanoparticles since it acts as a reducing agent. Besides, the thermal stability of CeO₂ ensured stable soot formation resulting in decreased NO_x [49]. Likewise, diesel fuel with Al₂O₃ and CuO additives showed lower NO_x emissions decreased by 6% and 2%, respectively [38]. Another study by Anbarasu et al. [57] reported the lower NO_x emission for CeO₂ nanoparticle blended fuel up to 11.7% at maximum load since the burnt hydrogen resulted in a complete combustion process. A significant reduction in NO_x emissions up to 6.6% was obtained with MME, and TiO₂ nanoparticle blends as the nano-additives ensure superior thermal conductivity and assist lesser ignition delay [33].

3.5 *Effect on Smoke Emission*

Smoke is primarily generated in the fuel-rich zone, where it is produced up to a large extent at peak load conditions. The catalytic nature of nano-additives and their higher surface-volume ratio provides better combustion and, ultimately, minimal smoke formation. Smoke opacity indicates the soot concentration in exhaust emissions, wherein it depends on oxidation and soot formation. The smoke opacity also determines the extent of pollution in the atmospheric air. An increase in the concentration of nanoparticles decreases the smoke opacity owing to the superior catalytic nature of the additive present in the fuel blend [53]. LGO and CeO₂ nanoparticle blends showed reduced smoke opacity emission up to 6.4% due to complete combustion, a rapid rate of evaporation, and enhanced ignition characteristics facilitated by CeO₂ [49]. Similarly, lower smoke emissions were obtained when canola biodiesel and CeO₂ fuel blends were used [57].

4 **Concluding Remarks and Future Prospects**

The present review gives a comprehensive description of the role of nano-additives, specifically metal-based nanoparticles, with an emphasis on pointers such as improving thermophysical properties of the fuel, stability as well as enhancing the performance and emissions characteristics. However, the selection of nano-additives based on the fuel properties to be improved will be helpful in accomplishing promising results. Subsequent conclusions can be drawn from the analysis of the above kinds of literature.

- It can be concluded that even though there is a slight increment in flash point, viscosity, and density of fuel, nanoparticle biodiesel blends advanced the calorific value and cetane number.
- Apparently, the rate of fuel combustion has improved with the addition of nano-additives owing to enhancement in catalytic activity, heat transfer, air–fuel mixing rate, as evidenced in previous studies.

- It is also observed that a decrease in BSFC was associated with an increase in nanoparticle dosage as the calorific value is increased, resulting in incomplete combustion of fuel. Conversely, higher BTE was achieved by high dosage rates of nano-additives.
- Most of the reports showed a decrease in NO_x owing to more cetane number and a drop in HC due to a greater evaporation rate and catalytic oxidation.
- As reported in various studies, the presence of nano-additives increases the CO₂ emission since they provide extra oxygen to improve combustion.
- Many researchers reported that the catalytic nature of nano-additives and their higher surface-volume ratio provides better combustion and, ultimately, minimal smoke formation. An increase in the concentration of nanoparticles decreases the smoke opacity owing to the superior catalytic nature of the additive present in the fuel blend.
- It was reported that the increase and decrease in CO emissions were due to better ignition characteristics with nano-additives. CO emission increases with an increase in the dosage of nano-additives.

However, future research investigations should be carried out to address the following concerns related to the practical applications of biodiesel/diesel additives:

- Metallic and metal oxide-based additives should be further investigated to comprehend their exact action mechanisms and their biosafety issues to address environmental concerns.
- Further, experimental studies are warranted to understand the nature and quantity of nanoparticles to be used with various biodiesel blends. Besides, the stability characteristics of nano-additive and biodiesel blends under different working conditions must be addressed precisely.
- In addition, extensive research should be performed to trap unburned nanoparticles from diesel engine exhaust in order to protect the environment.
- Durability tests may be indispensable for the exploitation of nano-additives in diesel engines for consideration in future research investigations.

Acknowledgements The authors wish to convey their heartfelt thanks to the Department of Mechanical Engineering, GITAM Deemed to be University, Visakhapatnam Campus, for their support in carrying out the research work.

References

1. Casanave D, Duplan JL, Freund E (2007) Diesel fuels from biomass. *Pure Appl Chem* 79(11):2071–2081
2. Shaafi T, Sairam K, Gopinath A, Kumaresan G, Velraj R (2015) Effect of dispersion of various nanoadditives on the performance and emission characteristics of a CI engine fuelled with diesel, biodiesel and blends—a review. *Renew Sustain Energy Rev* 49:563–573

3. McCarthy P, Rasul MG, Moazzem S (2011) Analysis and comparison of performance and emissions of an internal combustion engine fuelled with petroleum diesel and different biodiesels. *Fuel* 90(6):2147–2157
4. Shrivastava N, Khan ZM (2018) Application of soft computing in the field of internal combustion engines: a review. *Arch Comput Meth Eng* 25(3):707–726
5. Ahmad AL, Yasin NM, Derek CJC, Lim JK (2011) Microalgae as a sustainable energy source for biodiesel production: a review. *Renew Sustain Energy Rev* 15(1):584–593
6. Pullagura G, BabjiAlapati M, Prakash R (2012) Effect of hydrogen enrichment on the combustion characteristics of a biofuel diesel engine. *IOSR J Eng* 2(1):001–006
7. Chen KS, Lin YC, Hsieh LT, Lin LF, Wu CC (2010) Saving energy and reducing pollution by use of emulsified palm-biodiesel blends with bio-solution additive. *Energy* 35(5):2043–2048
8. Palash SM, Kalam MA, Masjuki HH, Masum BM, Fattah IR, Mofijur M (2013) Impacts of biodiesel combustion on NOx emissions and their reduction approaches. *Renew Sustain Energy Rev* 23:473–490
9. Hosseini SH, Taghizadeh-Alisaraei A, Ghobadian B, Abbaszadeh-Mayvan A (2017) Effect of added alumina as nano-catalyst to diesel-biodiesel blends on performance and emission characteristics of CI engine. *Energy* 124:543–552
10. Ogunkoya D, Roberts WL, Fang T, Thapaliya N (2015) Investigation of the effects of renewable diesel fuels on engine performance, combustion, and emissions. *Fuel* 140:541–554
11. Suh HK, Lee CS (2016) A review on atomization and exhaust emissions of a biodiesel-fueled compression ignition engine. *Renew Sustain Energy Rev* 58:1601–1620
12. Atabani AE, Badruddin IA, Badarudin A, Khayoon MS, Triwahyono S (2014) Recent scenario and technologies to utilize non-edible oils for biodiesel production. *Renew Sustain Energy Rev* 37:840–851
13. Boehman A, Alam M, Song J, Acharya R, Szybist J, Zello V, Miller K (2003) Fuel formulation effects on diesel fuel injection, combustion, emissions and emission control (No. CONF-200308–104). The Energy Institute The Pennsylvania State University; ConocoPhillips (US)
14. Atabani AE, da Silva César A (2014) *Calophyllum inophyllum* L.-A prospective non-edible biodiesel feedstock. Study of biodiesel production, properties, fatty acid composition, blending and engine performance. *Renew Sustain Energy Rev* 37:644–655
15. Venkatraman V, Sugumar S, Sekar S, Viswanathan S (2019) Environmental effect of CI engine using microalgae biofuel with nano-additives. *Energy Sour Part A Recov Utiliz Environ Eff* 41(1):2429–2438
16. Prabhu A, Venkata Ramanan M, Jayaprabakar J (2020) Effect of compression ratio on the performance of CI engine fuelled with freshwater algae biodiesel. *Int J Ambient Energy* 41(1):80–83
17. Nautiyal P, Subramanian KA, Dastidar MG, Kumar A (2020) Experimental assessment of performance, combustion and emissions of a compression ignition engine fuelled with *Spirulina platensis* biodiesel. *Energy* 193:116861
18. Canakci M (2009) NOx emissions of biodiesel as an alternative diesel fuel. *Int J Veh Des* 50(1–4):213–228
19. Xue J, Grift TE, Hansen AC (2011) Effect of biodiesel on engine performances and emissions. *Renew Sustain Energy Rev* 15(2):1098–1116
20. Mofijur M, Atabani AE, Masjuki HA, Kalam MA, Masum BM (2013) A study on the effects of promising edible and non-edible biodiesel feedstocks on engine performance and emissions production: a comparative evaluation. *Renew Sustain Energy Rev* 23:391–404
21. Kadarohman A, Hernani, Khoerunisa F, Astuti RM (2010) A potential study on clove oil, eugenol and eugenyl acetate as diesel fuel bio-additives and their performance on one cylinder engine. *Transport* 25(1):66–22. Shah PR, Ganesh A (2016) A comparative study on influence of fuel additives with edible and non-edible vegetable oil based on fuel characterization and engine characteristics of diesel engine. *Appl Therm Eng* 102:800–812
22. Hosseinzadeh-Bandbafha H, Tabatabaei M, Aghbashlo M, Khanali M, Demirbas A (2018) A comprehensive review on the environmental impacts of diesel/biodiesel additives. *Energy Convers Manage* 174:579–614

23. Surawski NC, Miljevic B, Ayoko GA, Elbagir S, Stevanovic S, Fairfull-Smith KE, Bottle SE, Ristovski ZD (2011) Physicochemical characterization of particulate emissions from a compression ignition engine: the influence of biodiesel feedstock. *Environ Sci Technol* 45(24):10337–10343
24. Rakopoulos DC, Rakopoulos CD, Kyritsis DC (2016) Butanol or DEE blends with either straight vegetable oil or biodiesel excluding fossil fuel: comparative effects on diesel engine combustion attributes, cyclic variability and regulated emissions trade-off. *Energy* 115:314–325
25. Wu Z, Li X, Liu W, Zhong Y, Gan Q, Li X, Wang H (2017) Materials chemistry of iron phosphosulfide nanoparticles: synthesis, solid state chemistry, surface structure, and electrocatalysis for the hydrogen evolution reaction. *ACS Catal* 7(6):4026–4032
26. Kumar S, Dinesha P, Bran I (2017) Influence of nanoparticles on the performance and emission characteristics of a biodiesel fuelled engine: an experimental analysis. *Energy* 140:98–105
27. Praveen A, Rao GLN, Balakrishna B (2018) Performance and emission characteristics of a diesel engine using *Calophyllum inophyllum* biodiesel blends with TiO₂ nanoadditives and EGR. *Egypt J Pet* 27(4):731–738
28. Debbarma S, Misra RD (2017) Effects of iron nanoparticles blended biodiesel on the performance and emission characteristics of a diesel engine. *J Energy Resour Technol* 139(4)
29. Pandian AK, Ramakrishnan RBB, Devarajan Y (2017) Emission analysis on the effect of nanoparticles on neat biodiesel in unmodified diesel engine. *Environ Sci Pollut Res* 24(29):23273–23278
30. Shaafi T, Velraj RJRE (2015) Influence of alumina nanoparticles, ethanol and isopropanol blend as additive with diesel–soybean biodiesel blend fuel: combustion, engine performance and emissions. *Renew Energy* 80:655–663
31. Shukla AK, Iravani S (2017) Metallic nanoparticles: green synthesis and spectroscopic characterization. *Environ Chem Lett* 15(2):223–231
32. Devarajan Y, Munuswamy DB, Mahalingam A (2018) Influence of nano-additive on performance and emission characteristics of a diesel engine running on neat neem oil biodiesel. *Environ Sci Pollut Res* 25(26):26167–26172
33. Alagu K, Nagappan B, Jayaraman J, Dhas AAG (2018) Impact of antioxidant additives on the performance and emission characteristics of CI engine fuelled with B20 blend of rice bran biodiesel. *Environ Sci Pollut Res* 25(18):17634–17644
34. Anbarasu M, Anandan M, Chinnasamy E, Gopinath V, Balamurugan K (2015) Synthesis and characterization of polyethylene glycol (PEG) coated Fe₃O₄ nanoparticles by chemical co-precipitation method for biomedical applications. *Spectrochim Acta Part A Mol Biomol Spectrosc* 135:536–539
35. Venu H, Madhavan V (2016) Effect of Al₂O₃ nanoparticles in biodiesel-diesel-ethanol blends at various injection strategies: performance, combustion and emission characteristics. *Fuel* 186:176–189
36. Devarajan Y, Munuswamy DB, Mahalingam A (2019) Investigation on behavior of diesel engine performance, emission, and combustion characteristics using nano-additive in neat biodiesel. *Heat Mass Transf* 55(6):1641–1650
37. Gumus S, Ozcan H, Ozbey M, Topaloglu B (2016) Aluminum oxide and copper oxide nanodiesel fuel properties and usage in a compression ignition engine. *Fuel* 163:80–87
38. Saxena V, Kumar N, Saxena VK (2017) A comprehensive review on combustion and stability aspects of metal nanoparticles and its additive effect on diesel and biodiesel fuelled CI engine. *Renew Sustain Energy Rev* 70:563–588
39. Devarajan Y, Nagappan B, Subbiah G (2019) A comprehensive study on emission and performance characteristics of a diesel engine fueled with nanoparticle-blended biodiesel. *Environ Sci Pollut Res* 26(11):10662–10672
40. Kumar S, Dinesha P, Bran I (2019) Experimental investigation of the effects of nanoparticles as an additive in diesel and biodiesel fuelled engines: a review. *Biofuels* 10(5):615–622
41. Fuskele V, Sarviya RM (2017) Recent developments in nanoparticles synthesis, preparation and stability of nanofluids. *Mater Today Proc* 4(2):4049–4060

42. Paramashivaiah BM, Rajashekhar CR (2016) Studies on effect of various surfactants on stable dispersion of graphene nano particles in simarouba biodiesel. In: IOP conference series: materials science and engineering, vol 149, no 1. IOP Publishing, pp 012083
43. Cao A, Xu C, Liang J, Wu D, Wei B (2001) X-ray diffraction characterization on the alignment degree of carbon nanotubes. *Chem Phys Lett* 344(1–2):13–17
44. Saravankumar PT, Suresh V, Vijayan V, Godwin Antony A (2019) Ecological effect of corn oil biofuel with SiO₂ nano-additives. *Energy Sour Part A Recov Utiliz Environ Eff* 41(23):2845–2852
45. Aalam CS, Saravanan CG (2017) Effects of nano metal oxide blended Mahua biodiesel on CRDI diesel engine. *Ain Shams Eng J* 8(4):689–696
46. Gad MS, Jayaraj S (2020) A comparative study on the effect of nano-additives on the performance and emissions of a diesel engine run on Jatropha biodiesel. *Fuel* 267:117168
47. Hoseini SS, Najafi G, Ghobadian B, Ebadi MT, Mamat R, Yusaf T (2020) Performance and emission characteristics of a CI engine using graphene oxide (GO) nano-particles additives in biodiesel-diesel blends. *Renew Energy* 145:458–465
48. Annamalai M, Dhinesh B, Nanthagopal K, SivaramaKrishnan P, Lalvani JIJ, Parthasarathy M, Annamalai K (2016) An assessment on performance, combustion and emission behavior of a diesel engine powered by ceria nanoparticle blended emulsified biofuel. *Energy Convers Manage* 123:372–380
49. El-Seesy AI, Hassan H, Ookawara S (2018) Effects of graphene nanoplatelet addition to jatropha Biodiesel-Diesel mixture on the performance and emission characteristics of a diesel engine. *Energy* 147:1129–1152
50. Seela CR, Ravi Sankar B (2020) Investigations on CI engine with nano-sized zinc oxide added Mahua Methyl Ester blends. *Int J Ambient Energy* 41(2):146–151
51. Prabhu A, Reddy BK, Nagappan M, Bharath N (2020) Effect of Al₂O₃ nano-additives on the performance and emission characteristics of jatropha and pongamia methyl esters in compression ignition engine. *Int J Ambient Energy* 41(5):528–532
52. El-Seesy AI, Abdel-Rahman AK, Bady M, Ookawara S (2017) Performance, combustion, and emission characteristics of a diesel engine fueled by biodiesel-diesel mixtures with multi-walled carbon nanotubes additives. *Energy Convers Manage* 135:373–393
53. Sivakumar M, Sundaram NS, Thasthagir MHS (2018) Effect of aluminium oxide nanoparticles blended pongamia methyl ester on performance, combustion and emission characteristics of diesel engine. *Renew Energy* 116:518–526
54. Ranjan A, Dawn SS, Jayaprabakar J, Nirmala N, Saikiran K, Sriram SS (2018) Experimental investigation on effect of MgO nanoparticles on cold flow properties, performance, emission and combustion characteristics of waste cooking oil biodiesel. *Fuel* 220:780–791
55. Kumar SM, Kerihuel A, Bellettre J, Tazerout M (2005) Effect of water and methanol fractions on the performance of a CI engine using animal fat emulsions as fuel. *Proc Inst Mech Eng Part A J Power Energy* 219(7):583–592
56. Anbarasu A, Karthikeyan A (2016) Performance and emission characteristics of a diesel engine using cerium oxide nanoparticle blended biodiesel emulsion fuel. *J Energy Eng* 142(1):04015009
57. Jena J, Misra RD (2014) Effect of fuel oxygen on the energetic and exergetic efficiency of a compression ignition engine fuelled separately with palm and karanja biodiesels. *Energy* 68:411–419
58. Soudagar MEM, Nik-Ghazali NN, Kalam MA, Badruddin IA, Banapurmath N, Khan TY, Bashir MN, Akram N, Farade R, Afzal A (2019) The effects of graphene oxide nanoparticle additive stably dispersed in dairy scum oil biodiesel-diesel fuel blend on CI engine: performance, emission and combustion characteristics. *Fuel* 257:116015
59. Mauzerall DL, Sultan B, Kim N, Bradford DF (2005) NO_x emissions from large point sources: variability in ozone production, resulting health damages and economic costs. *Atmos Environ* 39(16):2851–2866

60. Raju VD, Kishore PS, Nanthagopal K, Ashok B (2018) An experimental study on the effect of nanoparticles with novel tamarind seed methyl ester for diesel engine applications. *Energy Convers Manage* 164:655–666
61. Lenin MA, Swaminathan MR, Kumaresan G (2013) Performance and emission characteristics of a DI diesel engine with a nanofuel additive. *Fuel* 109:362–365

Convective-Radiative Heat Transfer in a Rotating Cubic Cavity with a Local Heat Source



S. A. Mikhailenko and M. A. Sheremet

Abstract Convective heat and mass transfer under influence of thermal radiation in a rotating cubic cavity with heat source has been investigated numerically. Vertical left and right walls are cooled, while other walls of the cavity are thermally insulated. The cavity has heat source on the bottom wall and it rotates at a constant angular velocity in counterclockwise direction relative to the z -axis. Mathematical model has been formulated using the dimensionless non-primitive parameters and worked out by the finite difference method on a uniform grid. The results have been presented for a wide range of surface emissivity, Rayleigh and Taylor numbers.

Keywords Numerical simulation · Natural convection · Surface radiation · Rotating cavity

Nomenclature

c	Heat capacity ($\text{J kg}^{-1} \text{K}^{-1}$)
F_{k-i}	View factor between k -th portion and i -th portion of the chamber
g	Gravity acceleration (M s^{-2})
H	Size of the chamber (M)
J_k	Radiosity for the k -th portion (W m^{-2})
N_{rad}	Radiation parameter

Greek Symbol

θ Dimensionless temperature

S. A. Mikhailenko (✉) · M. A. Sheremet
Laboratory on Convective Heat and Mass Transfer, Tomsk State University, 634050 Tomsk, Russia
e-mail: stepanmihaylenko@gmail.com

1 Introduction

Convective heat transfer analysis is important in a wide variety of engineering applications. It is equally important to take into account the heat exchange by radiation. Heat transfer can be enhanced with the right choice of materials and their reflective properties. An interesting area of research is heat transfer under rotational conditions. Rotating systems are often encountered when solving many technical problems, for example, designing rotary heat exchangers [1] or designing cooling systems for electronic equipment [2, 3].

Thus, mixed convection in a partially heated ventilated cavity has been investigated by Doghmi et al. [4]. A heat source simulating an integrated electronic device is located on the left wall of the cavity. The opposite wall is cooled and has a ventilation opening. It has been established that conduction is the main mechanism of energy transfer at low Reynolds numbers. The best thermal performance is observed when the size of the heater is reduced. Three-dimensional natural convection in a cubic cavity has been examined by Wang et al. [5]. The investigation has been performed for high Rayleigh numbers. It has been found that the Nusselt number on the hot wall sharply decreases near the adiabatic walls, which means that the intensity of convection in the center of the cavity is stronger than in the region near the adiabatic walls. But the influence of adiabatic walls on the total heat transfer decreases with increasing Ra. Ouakarrouch et al. [6] have studied the heat transfer by conduction, convection and radiation through alveolar building walls. The authors argue that heat transfer through alveolar structures increases significantly when radiative heat transfer is taken into account.

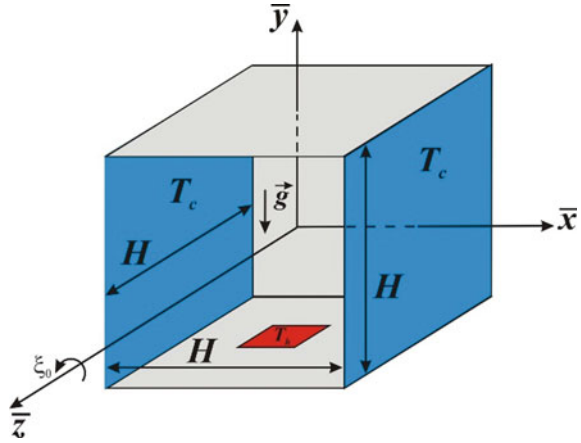
In this paper, we consider convective-radiative heat transfer in a cubic rotating cavity with an energy source.

2 Problem Description

Figure 1 shows the solution area for the problem under consideration. There is a cubic cavity of size H , the left wall and the right one are cooled, and all other walls are thermally insulated. The cavity has square heater size of h in the center of the bottom wall. The cavity rotates with a constant angular velocity ξ_0 around an axis passing through the center of the solution region parallel to the z -axis. The inner surfaces of the walls are gray emitters and reflectors of thermal radiation energy. The cavity is filled with a fluid that satisfies the Boussinesq approximation. A liquid with $Pr = 0.7$ is Newtonian and incompressible, and all physical parameters are independent of temperature. The liquid filling the cavity is transparent to radiation. The flow is laminar.

The system of equations describing the fluid motion and heat transfer is written using the dimensionless variables “vector potential functions and vorticity vector” as follows:

Fig. 1 Considered sketch, coordinates and thermal conditions



$$\nabla^2 \psi_x = -\omega_x, \nabla^2 \psi_y = -\omega_y, \nabla^2 \psi_z = -\omega_z \tag{1}$$

$$\frac{\partial \theta}{\partial \tau} + u \frac{\partial \theta}{\partial x} + v \frac{\partial \theta}{\partial y} + w \frac{\partial \theta}{\partial z} = \frac{1}{\text{Pr} \cdot \sqrt{\text{Ta}}} \left(\frac{\partial^2 \theta}{\partial x^2} + \frac{\partial^2 \theta}{\partial y^2} + \frac{\partial^2 \theta}{\partial z^2} \right) \tag{2}$$

$$\begin{aligned} & \frac{\partial \omega_x}{\partial \tau} + u \frac{\partial \omega_x}{\partial x} + v \frac{\partial \omega_x}{\partial y} + w \frac{\partial \omega_x}{\partial z} - \omega_x \frac{\partial u}{\partial x} - \omega_y \frac{\partial u}{\partial y} - \omega_z \frac{\partial u}{\partial z} \\ &= \frac{1}{\sqrt{\text{Ta}}} \left(\frac{\partial^2 \omega_x}{\partial x^2} + \frac{\partial^2 \omega_x}{\partial y^2} + \frac{\partial^2 \omega_x}{\partial z^2} \right) - \frac{\text{Ra}}{\text{Pr} \cdot \text{Ta}} \frac{\partial \theta}{\partial z} \cos(\tau) \\ &+ \frac{\text{Ra}_\xi}{\text{Pr} \cdot \text{Ta}} y \frac{\partial \theta}{\partial z} + 2 \frac{\partial u}{\partial z} \end{aligned} \tag{3}$$

$$\begin{aligned} & \frac{\partial \omega_y}{\partial \tau} + u \frac{\partial \omega_y}{\partial x} + v \frac{\partial \omega_y}{\partial y} + w \frac{\partial \omega_y}{\partial z} - \omega_x \frac{\partial v}{\partial x} - \omega_y \frac{\partial v}{\partial y} - \omega_z \frac{\partial v}{\partial z} \\ &= \frac{1}{\sqrt{\text{Ta}}} \left(\frac{\partial^2 \omega_y}{\partial x^2} + \frac{\partial^2 \omega_y}{\partial y^2} + \frac{\partial^2 \omega_y}{\partial z^2} \right) + \frac{\text{Ra}}{\text{Pr} \cdot \text{Ta}} \frac{\partial \theta}{\partial z} \sin(\tau) \\ &- \frac{\text{Ra}_\xi}{\text{Pr} \cdot \text{Ta}} x \frac{\partial \theta}{\partial z} + 2 \frac{\partial v}{\partial z} \end{aligned} \tag{4}$$

$$\begin{aligned} & \frac{\partial \omega_z}{\partial \tau} + u \frac{\partial \omega_z}{\partial x} + v \frac{\partial \omega_z}{\partial y} + w \frac{\partial \omega_z}{\partial z} - \omega_x \frac{\partial w}{\partial x} - \omega_y \frac{\partial w}{\partial y} - \omega_z \frac{\partial w}{\partial z} \\ &= \frac{1}{\sqrt{\text{Ta}}} \left(\frac{\partial^2 \omega_z}{\partial x^2} + \frac{\partial^2 \omega_z}{\partial y^2} + \frac{\partial^2 \omega_z}{\partial z^2} \right) + \frac{\text{Ra}}{\text{Pr} \cdot \text{Ta}} \left\{ \frac{\partial \theta}{\partial x} \cos(\tau) \right. \\ &\left. - \frac{\partial \theta}{\partial y} \sin(\tau) \right\} - \frac{\text{Ra}_\xi}{\text{Pr} \cdot \text{Ta}} \left\{ y \frac{\partial \theta}{\partial x} - x \frac{\partial \theta}{\partial y} \right\} + 2 \frac{\partial w}{\partial z} \end{aligned} \tag{5}$$

Here Ra is the Rayleigh number; Pr is the Prandtl number; Ta is the Taylor number; ψ_x, ψ_y, ψ_z are dimensionless vector potential functions; $\omega_x, \omega_y, \omega_z$ are the dimensionless vorticity components; x, y, z are the dimensionless coordinates; u, v, w are the dimensionless velocity components; τ is the dimensionless time.

Research is carried out under the following initial and boundary conditions:

$$\tau = 0 :$$

$$\psi_x = \psi_y = \psi_z = \omega_x = \omega_y = \omega_z = \theta = 0$$

$$\text{for } -0.5 \leq x \leq 0.5, -0.5 \leq y \leq 0.5 \text{ and } -0.5 \leq z \leq 0.5;$$

$$\tau > 0 :$$

$$\psi_x = \frac{\partial \psi_y}{\partial y} = \psi_z = 0, \vec{\omega} = -\nabla^2 \vec{\psi}, \theta = 1$$

for heater surface;

$$\frac{\partial \psi_x}{\partial x} = \psi_y = \psi_z = 0, \vec{\omega} = -\nabla^2 \vec{\psi}, \theta = 0$$

$$\text{for } x = -0.5 \text{ and } x = 0.5, -0.5 \leq y \leq 0.5 \text{ and } -0.5 \leq z \leq 0.5;$$

$$\psi_x = \frac{\partial \psi_y}{\partial y} = \psi_z = 0, \vec{\omega} = -\nabla^2 \vec{\psi}, \frac{\partial \theta}{\partial y} = N_{\text{rad}} Q_{\text{rad}}$$

$$\text{for } y = -0.5 \text{ and } y = 0.5, -0.5 \leq x \leq 0.5 \text{ and } -0.5 \leq z \leq 0.5;$$

$$\psi_x = \psi_y = \frac{\partial \psi_z}{\partial z} = 0, \vec{\omega} = -\nabla^2 \vec{\psi}, \frac{\partial \theta}{\partial z} = N_{\text{rad}} Q_{\text{rad}}$$

$$\text{for } z = -0.5 \text{ and } z = 0.5, -0.5 \leq y \leq 0.5 \text{ and } -0.5 \leq z \leq 0.5;$$

where N_{rad} is the radiative number, Q_{rad} is the dimensionless radiative heat flux.

The net-radiative technique is used to analyze radiative heat transfer between surfaces. The dimensionless density of the radiation flux Q_{rad} supplied to the k -th surface is determined using the effective radiation flux density R_k for the k -th surface:

$$Q_{\text{rad},k} = R_k - \sum_{i=1}^N F_{k-i} R_i \quad (6)$$

$$R_k = (1 - \varepsilon_k) \sum_{i=1}^N F_{k-i} R_i + \varepsilon_k (1 - \zeta)^4 \left(\Theta_k + 0.5 \frac{1 + \zeta}{1 - \zeta} \right)^4 \quad (7)$$

Here F_{k-i} is the form factor, ε_k is the surface emissivity, θ_k is the temperature of the k -th surface.

The intensity of heat transfer is determined using the average convective and radiative Nusselt numbers on the heater surface:

$$\overline{Nu}_{con} = \frac{1}{0.04} \int_{-0.1}^{0.1} \int_{-0.1}^{0.1} \left. \frac{\partial \theta}{\partial y} \right|_{y=-0.5} dx dz,$$

$$\overline{Nu}_{rad} = \frac{N_{rad}}{0.04} \int_{-0.1}^{0.1} \int_{-0.1}^{0.1} Q_{rad}|_{y=-0.5} dx dz$$

The system of the control equations for mass, momentum and energy in the rotating cubic cavity with heat source has been worked out using the finite difference method with the uniform grid. The Poisson equations for the vector potential functions (1) have been approximated using the central differences. The resulting system of linear algebraic equations has been solved by the successive over-relaxation method. The equations for the vorticity components (2)–(4) and temperature (5) have been solved on the basis of the locally one-dimensional Samarskii scheme. Diffusion terms have been approximated by central differences, convective ones using the monotonic scheme of A. A. Samarskii. The resulting systems of equations have been solved by the Thomas algorithm.

The developed computational model and numerical technique have been verified using the problem of convective heat transfer in a rotating cavity [7]. Table 1 shows a comparison of the average convective Nusselt number on the heated wall for different values of the grid parameters. The obtained data are well comparable with the data obtained by other authors [7].

Results have been obtained for a wide range of defining characteristics including Prandtl number ($Pr = 0.7$), Rayleigh number ($Ra = 10^3-10^6$), Taylor number ($Ta = 10^3-10^6$), and surfaces emissivity ($\epsilon = 0.0-0.9$). The results have been obtained after numerous revolutions of the cavity to establish periodic changes in heat and mass transfer parameters. The average convective Nusselt number, average radiative Nusselt number and average total Nusselt number have been used to describe the effects of Ra , Ta and ϵ .

Thus Fig. 2 demonstrates the effect of the Rayleigh number on the average convective, radiative and total Nusselt numbers during two revolutions of the cavity. Rise of the Rayleigh number illustrates an increase in the average convective Nusselt number with an increment of amplitude, while variation of the average radiative Nusselt number is not so essential.

Table 1 Average Nusselt number values with different times

τ	Results 120^3	Results 60^3	Data [7] 40^3	Data [7] 30^3
0.05	4.62237	4.74687	4.727	4.773
0.10	4.04754	4.13487	4.152	4.182
0.15	3.88969	3.97597	3.987	4.020
0.20	3.84627	3.93464	3.939	3.971
S.S	3.8325	3.92142	3.926	3.956

Fig. 2 Time-profiles of average convective Nusselt number, average radiation Nusselt and total Nusselt number during two revolutions for $Ta = 10^4$ and $\varepsilon = 0.9$

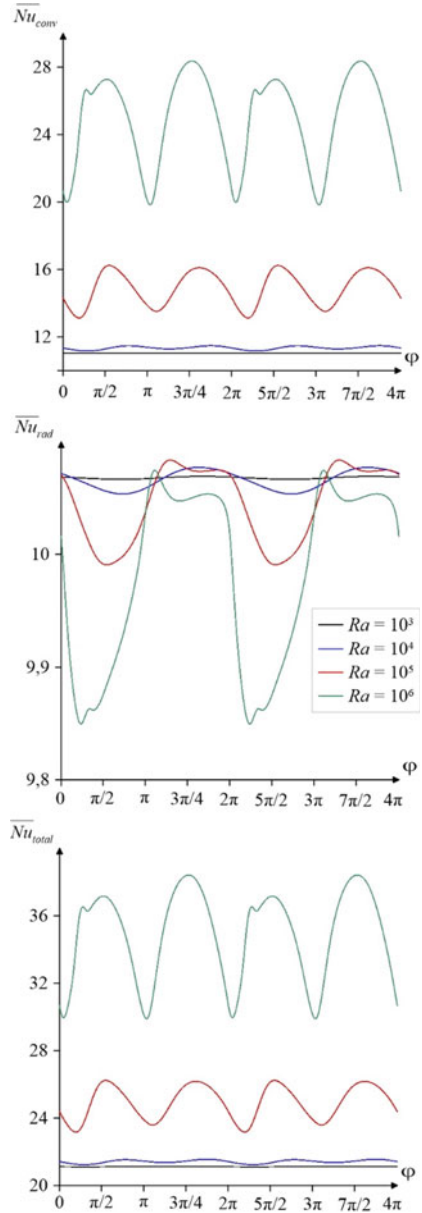
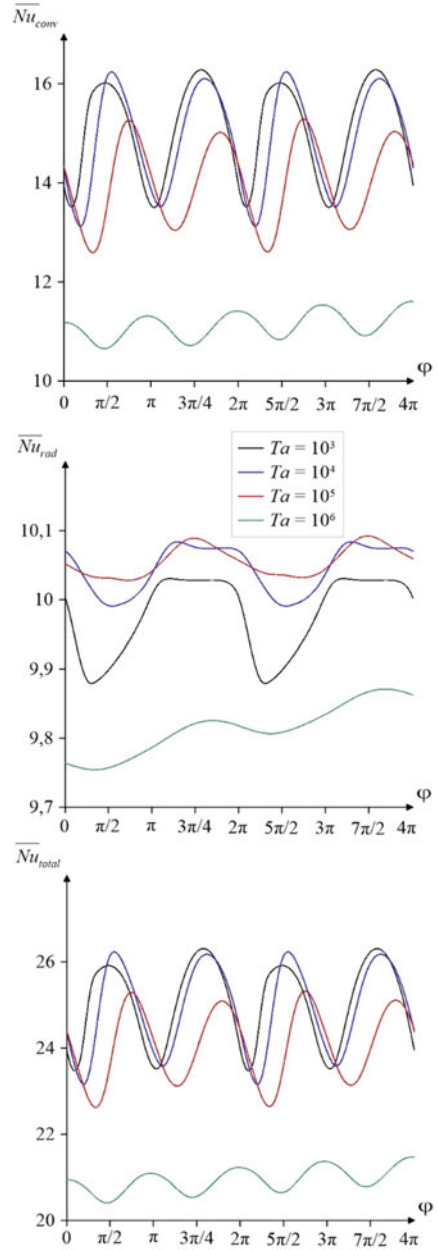


Figure 3 shows profiles of the average Nusselt numbers with the Taylor number for $Ra = 10^5$ and $\varepsilon = 0.9$. It should be noted a raise of the Taylor characterizes an attenuation of the convective heat transfer and as a result the average convective Nusselt number decreases with Ta . At the same time, the behavior of the average radiative Nusselt number is similar to an influence of Ra .

Fig. 3 Time-profiles of average convective Nusselt number, average radiation Nusselt and total Nusselt number during two revolutions for $Ra = 10^5$ and $\varepsilon = 0.9$



3 Conclusions

Convective-radiative heat transfer in a rotating cubic cavity with a local heat source has been studied numerically. Mathematical model has been formulated using non-primitive variables “vector potential functions—vorticity vector” and solved using the finite difference procedure on the uniform grid. Results have been obtained for a wide range of governing parameters. The influence of the Rayleigh number, the Taylor number and surface emissivity has been described. It has been found that a raise of the Rayleigh number characterizes the heat transfer enhancement, while a growth of the Taylor number reduces the energy transport intensity.

Acknowledgements The reported study was funded by RFBR, project number 20-31-90081.

References

1. Huang S-C, Wang C-C, Liu Y-H (2017) Heat transfer measurement in a rotating cooling channel with staggered and inline pin-fin arrays using liquid crystal and stroboscopy. *Int J Heat Mass Transf* 115:364–376
2. Jin LF, Tou KW, Tso CP (2005) Experimental and numerical studies on a rotating cavity with discrete heat sources with conjugate effects. *Experim Heat Transfer* 18:259–277
3. Tso CP, Jin LF, Tou KW (2007) Numerical segregation of the effects of body forces in a rotating, differentially heated enclosure. *Num Heat Transfer A* 51:85–107
4. Doghmi H, Abourida B, Belarche L, Sannad M, Ouzaouit M (2018) Three-dimensional mixed convection heat transfer in a partially heated ventilated cavity. *Therm Sci* 193–193. <https://doi.org/10.2298/TSCI180410193D>
5. Wang P, Zhang Y, Guo Z (2017) Numerical study of three-dimensional natural convection in a cubical cavity at high Rayleigh numbers. *Int J Heat Mass Transf* 113:217–228
6. Ouakarrouch M, Azhary KE, Laaroussi N, Garoum M, Feiz A (2019) Three-dimensional numerical simulation of conduction, natural convection, and radiation through alveolar building walls. *Case Stud Constr Mater* 11:e00249
7. Lee TL, Lin TF (1996) Transient three-dimensional convection of air in a differentially heated rotating cubic cavity. *Int J Heat Mass Transf* 39(6):1243–1255

Performance Analysis of IC Engine Using Parabolic Fin



Ruchika Dnyaneshwar Lande, Onkar Pravinrao Ajegaonkar,
Swapnil Suresh Nikam, Yogesh Mane, and Mandar M. Lele

Abstract Fins are set on the surface of the cylinder to improve the quantity of heat exchange by convection. Addition of fins can increase the heat transfer from the surface by several folds. IC engine is used to generate the mechanical power from chemical energy contain in a fuel which released to combustion of fuel inside the engine. If excessive heat is not removed, engine components may fail due to excessive temperature. Only approximately 30% of energy released is converted into useful work, the remaining 70% must be removed from the engine to prevent engine parts from melting. To determine the heat transfer rate associated with the fin, we must first obtain the temperature distribution along the fin. The variety of fins are available to enhance heat transfer rate including parabolic concave/convex, triangular, rectangular, trapezoidal, circular and so on. But some of the profiles are difficult to manufacture. In this paper, performance of convex parabolic fin was investigated by Ansys software. In the analysis part total five cases of parabolic fin were considered by varying fin base width, tip width, pitch length, number of fins and fin diameter. Temperature variation of all five cases described in this paper were analyzed by using Ansys software.

Keywords Internal combustion engine · Ansys (steady state thermal) · Parabolic fin

1 Introduction

A growing number of engineering disciplines are concerned with energy transitions requiring the rapid movement of heat. They produce an expanding demand for high performance heat transfer components with progressively smaller weights, volumes, costs, or accommodating shapes. Finned surface is commonly used in practice to enhance the heat transfer and they often increase the rate of heat transfer from a

R. D. Lande · O. P. Ajegaonkar (✉) · S. S. Nikam · Y. Mane · M. M. Lele
School of Mechanical Engineering, Dr. Vishwanath Karad MIT World Peace University, Pune,
India
e-mail: onkarajegaonkar1998@gmail.com

surface several fold. Fins are seen every day in a daily life like Automobile, Electronics atoms (which need heat rejection, heat sink, etc.). The importance of heat transfer is because the heat generation due to combustion in internal combustion engine. Commonly, these devices need some additional cooling in order to avoid the excessive temperature inside it.

Energy produced in IC engine is due to fuel inside the combustion chamber. When fuel burns heat generates and out of it. Only approximately, out of total 30% of energy converted into useful work and remaining 70% is exhausted to atmosphere through fins by mode of convection. Amount of heat transfer through extended surface by conduction and distribution of temperature in fin is depending upon both properties of fin material and engine outside the fluid. Magnitude of enhancement of heat transfer is proportional to fin thickness and its thermal conductivity. The thermodynamic properties of material along with its shape (Geometry) also have significant impact on heat convection process. To enhance the efficiency we need to keep in mind these points and focus on that heat transfer plays a major role in design and development of engine.

One key requirement in performance enhancement of engine is the cooling system which keeps all the part at the low temperature and prevent it from melting. The fins around the cylinder head of reciprocating engine improves the normal cooling action, as it increases the area of the cylinder and thus provide greater heat transfer. In this paper for the performance analysis of IC engine the study of parabolic fins was done. For this analysis different cases are considered by varying Base width, Tip width and pitch of parabolic fin.

2 Literature Review

Kumar et al. [1]: A Review Paper on Improving the Efficiency of IC Engine Fins by Varying its Material and Shape. In this paper the heat transfer rate of cooling fins by changing the fin geometry is done. So there is a big demand on a cooling system. The main purpose that the engines fails is the overheating. So for that purpose the cooling plays a crucial role. And it is necessary to keep all the parts kept at the low temperature. The conductive heat transfer is directly proportional to the temperature difference between the materials. So if engine metal is 260 °C and the air is at 30 °C then there is a 230 °C temperature difference for the cooling. The calculation & Analysis was done on this work to get a better understanding on cooling fins performance when it's geometry was changed. Here the thickness and the shape along with material plays a crucial role in the heat transfer of the fins. After the calculations and the analysis made, Elliptical shaped fins gives the better result than the triangular and the rectangular shape fins. And it also concluded that the thickness of the fins plays an important role in the increase in heat transfer. But we have to understand that while reducing the thickness we have to consider the strength of the fins that can withstand the working temperatures.

Alam and Tiwari [2] Increase the Efficiency of Internal Combustion Engine Fin by Replacing the Conventional Fin with Parabolic Fin. In this research researcher changes the pitch length from 11 mm, 13 mm and 15 mm, respectively. When base width increases efficiency increases of the fin. At last the fin having 5 mm base width and 15 mm pitch length has maximum efficiency in all cases.

Sorathiya et al. [3]: have researched in their “Review Paper on Effect of Cylinder Block Fin Geometry on Heat Transfer Rate of Air-Cooled 4S SI Engine” that there are several geometries of fins are available in the two wheeler engine cylinder. These geometries vary from company to company. They have did the comparative study of few models of engine & ultimately concluded that if the configuration of fin cross section, geometry is changed from conventional one, the contact time of air and fin can be increased, thus the heat carrying capacity can also be improved.

Rao and Vardhan [4]: Thermal analysis of engine cylinder fins by varying its geometry and material. In this research thermal analysis is done with the help of ANSYS. Shape and geometry of fin are most important parameters for fins which are considered in the research. Shape—Rectangular and Circular. Thickness—3 mm and 2.5 mm. Circular fin increases the heat transfer rate. The weight of fin body reduces due to circular shape. Efficiency and effectiveness is also increases in case of circular type fin.

Agarwal etc. [5] simulated the heat transfer in motor cycle engine fan using CFD analysis. It is observed that ambient temperature reduces to the very low value; it results in over cooling and poor efficiency of the engine. They have concluded that over cooling also affects the engine efficiency.

Magarajan et al. [6] have studied heat release of engine cylinder cooling fins with six numbers of fins having pitch of 10 and 20 mm, and are calculated numerically using commercially available CFD tool Ansys Fluent. The engine was at 150 C and the heat release from the cylinder was analyzed at a wind velocity of 0 km/h. Their CFD results were mostly same as that of the experimental results. So, they concluded that it is possible to modify the fin geometry and predict those results, changes like tapered fins, providing slits and holes in fins geometry can be made and the optimization of fins can be done.

Sateesh Modeling and Simulation of Fins for 150cc Engine [7]: In this research the thickness of the model is change from 3 to 2. 8 mm. Fins material is AL204, CI and AL6061. On the basis of thermal conductivities and densities the original material is changed for this model. For the thermal analysis 3 metals are selected—Cast iron, aluminum Alloy 204 and aluminum alloy 6061. For better efficient fin aluminum alloy 6061 is suitable because of curved slope and thickness 2.5 mm.

3 Computational Analysis

3D Geometry was created in Ansys (steady state thermal) to carry out simulations, after getting the data from the simulation the aim was to find out the efficiency of various conditions.

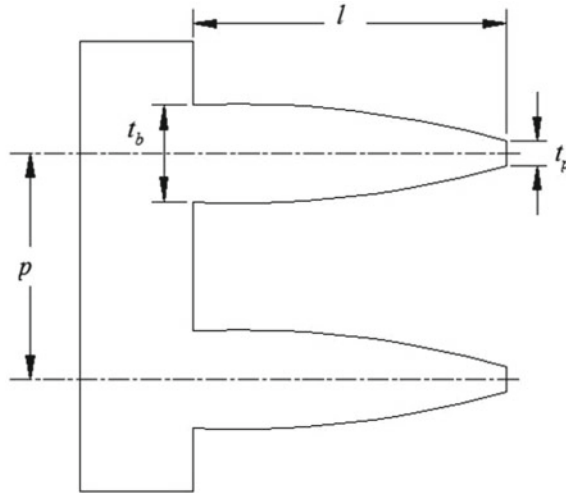


Fig. 1 Description of parabolic fin

3D Modeling and Simulations—Geometry of 3D axis—symmetric parabolic fin was created as shown in Fig. 1.

Where

- l Length of fin
- t thickness of fin
- p pitch of fin
- T temperature
- A area of fin
- w width of fin
- h convection heat transfer coefficient
- η efficiency of fin
- ϵ effectiveness of fin.

(a) Material Specification

Sr. No.	Specification	Value
1	Conductivity	167 W/m ² k
2	Density	2700 kg/m ²
3	Specific heat	896 J/kg K
4	Young modulus	68.9 Gpa
5	Poisson's ratio	0.33

(b) Fin Dimensions

After selecting material for fin, the dimensions were selected. Figure 2 shows the parabolic fin with detailed dimensions.

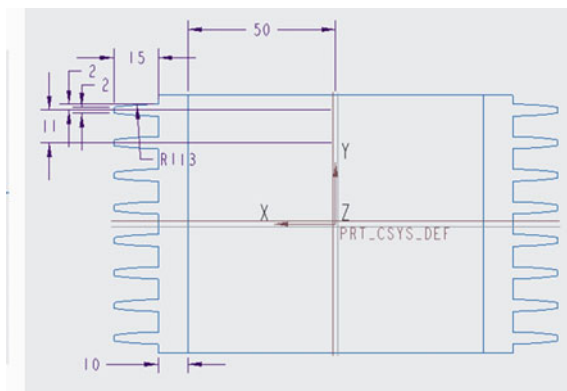


Fig. 2 Detailed dimensions of parabolic fin

where

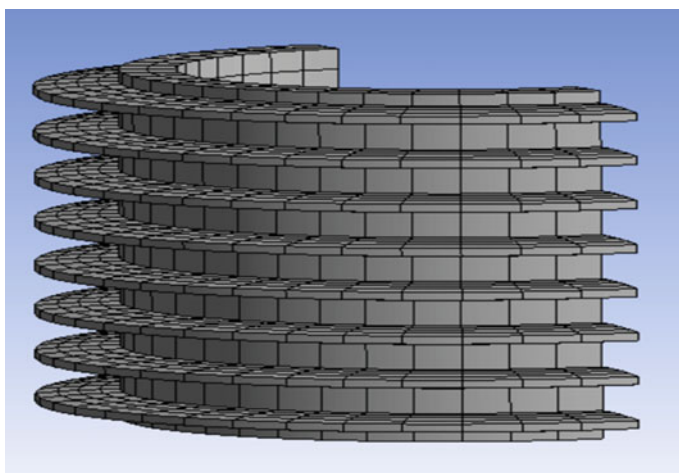
l 60 mm

t_p 2 mm

P 11 mm

t_b 4 mm

(c) Meshing



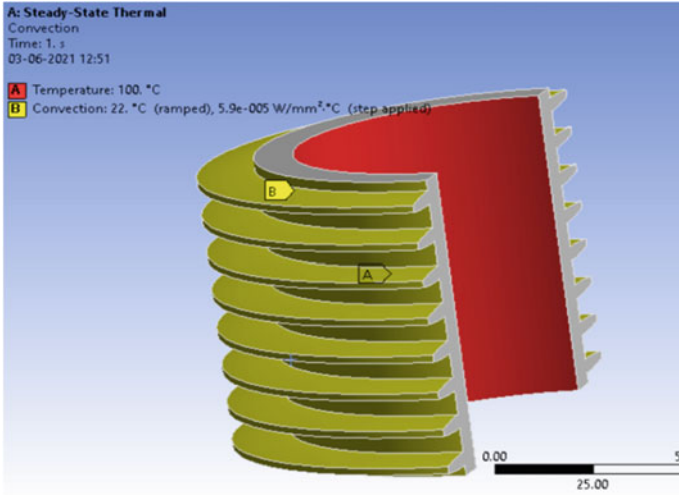
(d) Loading Conditions

Inner Temp: 100 °C.

Convection coefficient: $5.9e-6 \text{ W/mm}^2$.

Total Number of Nodes = 9519.

Total Number of Elements = 1452.



(e) Various Cases

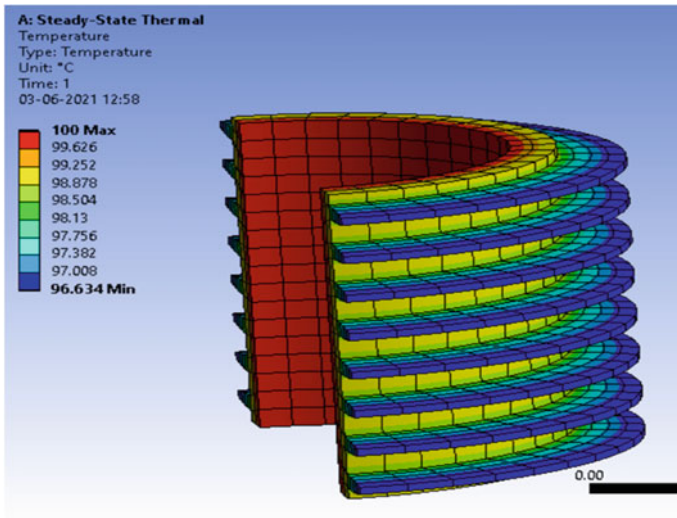
See Table 1.

Table 1 Varies cases considered for parabolic fin

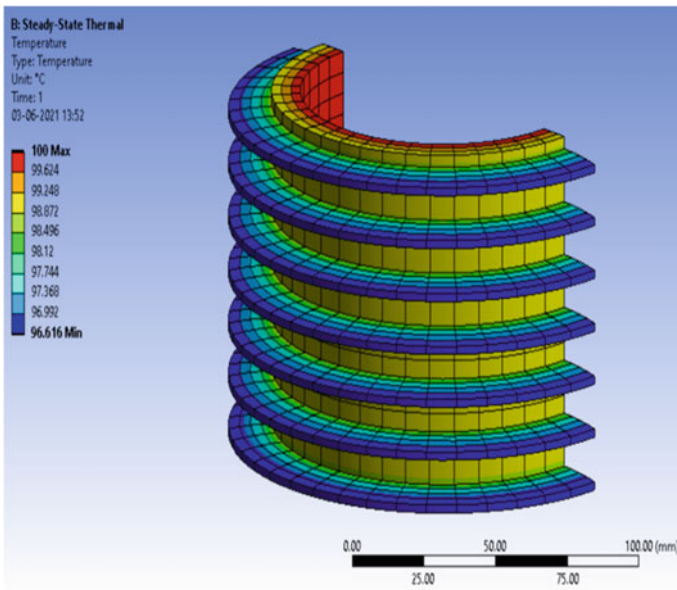
Case	Base width (mm)	Tip width (mm)	Pitch length (mm)	No. of fins	Fin dia. (mm)
1	4	2	11	7	113
2	4	2	13	8	113
3	5	1	11	7	113
4	5	1	13	8	113
5	4	2	11	7	50

Analysis

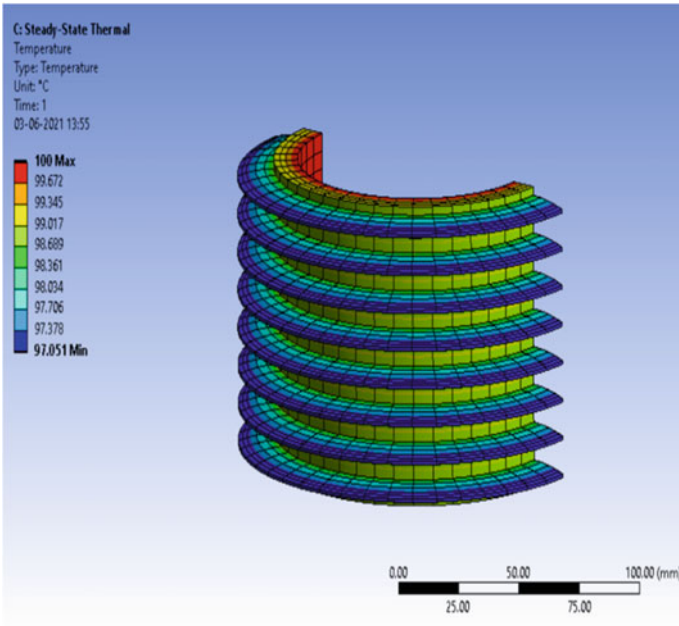
Analysis of case 1



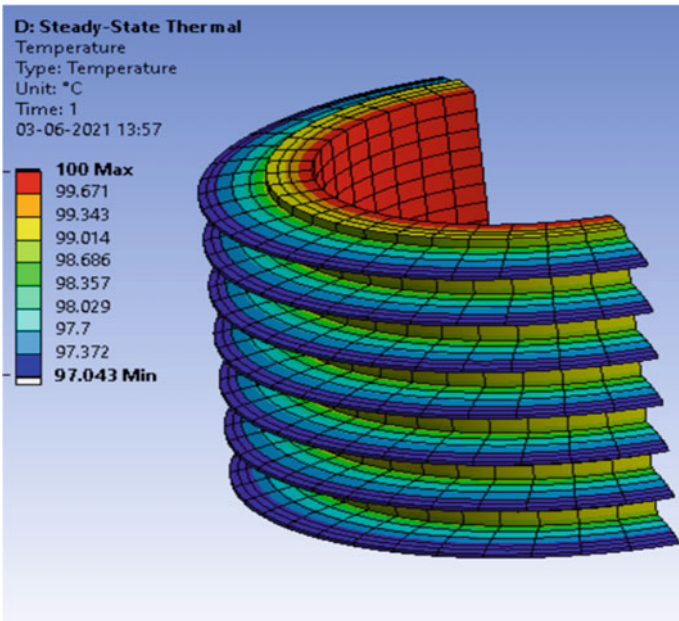
Analysis of case 2



Analysis of case 3



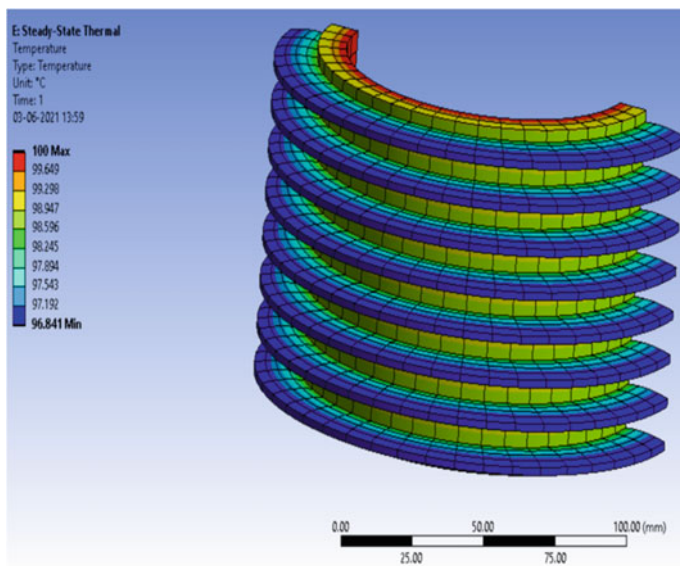
Analysis of case 4



Analysis of case 5

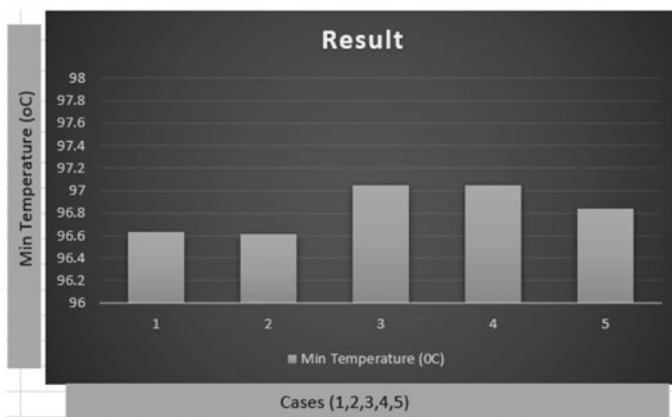
Table 2 Result table

Case	Minimum temperature (°C)
1	96.634
2	96.616
3	97.051
4	97.043
5	96.841



Result Table

See Table 2.



4 Discussion

From Tables 1 and 2,

(1) In the first two cases (case 1 and case 2):

With number of fins 7 and 8 for case 1 and case 2, Pitch length of fin was considered as 11 and 13 mm, respectively, by keeping fin base width and tip width constant. For the case 1 the minimum temperature variation obtained was greater than case 2 which is 96.634 °C.

(2) In the second two cases (case 1 and case 3):

Fin base width and tip width was considered as 4–2 mm and 5–1 mm, respectively, by keeping pitch length and number of fins constant. For the case 3 the minimum temperature variation obtained was greater than case 1 which is 97.051 °C.

(3) In the third two cases (case 3 and case 4):

With number of fins 7 and 8 for case 3 and case 4, Pitch length of fin was considered as 11 and 13 mm, respectively, by keeping fin base width and tip width constant. For the case 3 the minimum temperature variation obtained was greater than case 4 which is 97.051 °C.

5 Conclusion

From the above discussion it can be conclude that, the performance of fin with 5 mm base width, 1 mm tip width, 11 mm pitch length along with 7 number of fins, i.e., third case is better as compared to other four cases.

Thus, the performance of convex parabolic fin by considering third case gives the better heat transfer.

References

1. Kumar V, Jain SK et al (2016) A review paper on improving the efficiency of IC engine fins by varying its material and shape. *Int J Rec Develop Eng Technol* 5(6). www.ijrdet.com. ISSN 2347-6435 [Online]
2. Alam S, Tiwari G (2015) Increase the efficiency of internal combustion engine fin by replacing the conventional fin with parabolic fin. *Int J Analyt Experim Fin Elem Anal (IAEFEA)* 2(2):80–84. e-ISSN: 2394-5141, ISSN: 2394-5133
3. Sorathiya AS, Parmar AKN, Rathod PP, Review paper on effect of cylinder block fin geometry on heat transfer rate of air-cooled 4S SI engine
4. Rao NPR, Vardhan TV (2013) Thermal analysis of engine cylinder fins by varying its geometry and material. *Int J Eng Res Technol (IJERT)* 2(8)

5. Agarwal P et al (2011) Simulated the heat transfer in motor cycle engine fan using CFD analysis: heat transfer simulation by CFD from fins of an air cooled motorcycle engine under varying climatic conditions. In: Proceedings of the world congress on engineering 2011, vol 3, WCE 2011, Jul 6–8. ISBN: 978-988-19251-5-2, 2011, London, UK
6. Thiagarajan C, Prabhakar M et al (2020) Heat transfer analysis and optimization of engine cylinder liner using different materials. In: Proceedings, department of mechanical engineering, Aarupadai Veedu institute of technology, Vinayaka mission research foundation, Deemed to be university, Tamil Nadu, India Materials Today. <https://doi.org/10.1016/j.matpr.2020.06.173>
7. Chaitanya PS, Rani BS et al (2014) Thermal analysis of engine cylinder fin by varying its geometry and material. IOSR J Mech Civ Eng (IOSR-JMCE) 11(6):37–44. e-ISSN: 2278-1684, ISSN: 2320-334X, Ver. I (Nov–Dec 2014). www.iosrjournals.org

Numerical Study on Operating Temperature of PV and PV-PCM Systems



Deepak Kumar Sharma, Manish K. Rathod, and Purnanand V. Bhale

Abstract Photovoltaic (PV) is the best-known method for generating electricity from solar and this module has an efficiency in the range of 6–18%. Further, the electricity generating efficiency of solar cells decreases with the rise in operating temperature. Because of that it is required to maintain a low temperature of PV module using different cooling techniques. The main objective is to study the application of phase change material (PCM) as heat sink on the thermal performance of PV panel operating under actual weather conditions. Initially, a one-dimensional, transient mathematical model is developed to determine temperature variation of conventional PV panel under actual environmental conditions. It is found that the maximum solar cell temperature difference achieved between conventional PV and PV-PCM system at around 10 h which is 24.87 °C approximately 35.08% lower temperature.

Keywords Photovoltaic · Phase change material · PV/T system · Solar cell temperature

Nomenclature

A	Area of PV module (m^2)
C_p	Specific heat ($\text{J/kg}\cdot\text{K}$)
f_l	Liquid fraction
h	Convective heat transfer coefficient ($\text{W/m}^2\cdot\text{K}$)

D. K. Sharma (✉) · M. K. Rathod · P. V. Bhale
Mechanical Engineering Department, Sardar Vallabhbhai National Institute of Technology,
Surat 395007, India
e-mail: ds19me005@med.svnit.ac.in

M. K. Rathod
e-mail: mkr@med.svnit.ac.in

P. V. Bhale
e-mail: pvbhale@med.svnit.ac.in

I_t	Solar radiation (W/m^2)
k	Thermal conductivity of PCM ($\text{W}/\text{m}\text{-K}$)
LH	Latent heat of PCM (kJ/kg)
t	Thickness of PCM (cm)
T	Temperature ($^{\circ}\text{C}$)
T_m	Melting point of PCM ($^{\circ}\text{C}$)
U	Overall heat transfer coefficient ($\text{W}/\text{m}^2\text{-K}$)

Greek Symbols

η	Efficiency
β	Packing factor
σ	Stefan-Boltzmann constant ($\text{W}/\text{m}^2\text{-K}^4$)
α	Absorptivity
μ	Viscosity ($\text{kg}/\text{m}\text{-s}$)
ρ	Density of PCM (kg/m^3)
τ	Transmissivity
ε	Emissivity

1 Introduction

Nowadays, crude oil, followed by coal and natural gas is the world's biggest share of energy demand. In the previous two centuries, usage of fossil fuels has risen fast resulting leads to reserve depletion and high energy requirement. An energy crisis is a major disruption of the supply of energy to the economy, owing to causes such as over-consumption, overpopulation, ageing and energy waste. Performance of PV mainly depends on the types of PV module. The electrical performance is mainly affected by the types of PV used. A standard PV module depending on the kind of solar cell, 6–20% of incoming solar energy is converted into electricity but it is depending on location and climate condition. Remaining amount of solar radiation increasing solar cell temperature [1].

Reference [2] performed experimental study on mono-Si PV to observe the effect of temperature on performance factors under fixed light intensity. They conclude that as temperature increases open circuit voltage, maximum power output, efficiency and fill factor decrease but slight increment in short circuit current it due to because of rise in charge carrier generation. Reference [3] performed numerical investigation on PV with MATLAB to evaluate the effect of temperature on efficiency. They observed – 0.5%/degree Celsius temperature coefficient. Reference [4] studied the a-Si, mono-c and multi-c modules have examined temperature dependency coefficients utilizing 3

stand-alone photovoltaic systems in Malaysia and conclude that the temperature coefficient for a-Si, mono-Si and multi-Si was found to be $-0.1036 \text{ W/}^\circ\text{C}$, $-0.2525 \text{ W/}^\circ\text{C}$ and $-0.1742 \text{ W/}^\circ\text{C}$, respectively.

Reference [5] performed numerical study with steady state condition to analyse the effect on performance of single pass and double pass air in PV/T collector. They observed a double pass system has been shown to offer greater performance than one pass panel. Reference [6] noted that air-based PV/T can reach 8.4% electrical efficiency and 42% thermal efficiency. Due to the weak thermal characteristics of air, the electrical efficiency increase in air-based PV/T is small. Better liquid thermal characteristics make it more efficient for cooling PV panels compared with air.

Reference [7] reported an overall efficiency of 58% for a water-based PV/T system based on a numerical model. However, the water-based system also confronts certain disadvantages as heat recovery efficiency decreases over time as the water temperature increases. Reference [8] investigated experimental and numerical study to increase in efficiency of the system by providing active water cooling system. They concluded that approximate 20% in solar cell temperature and 9% improvement in efficiency of the system. However, the major disadvantage of air and water-based PV/T system is that it fails to provide the domestic hot water requirement specially on cloudy days. This inspired the creation of refrigerant-based PV/T collectors.

Reference [9] performed experimental study at China with rotary variable speed compressor using (R410a) refrigerant with electronic expansion valve. They concluded that obtained COP 4.7 and 15.4% electrical efficiency. Reference [10] performed experimental study on refrigerant-based PV/T they conclude that 15.2% improvement in electrical efficiency and achieved 2.96 COP of the system. It confronts numerous problems, such as coolant leakage, uneven cooling distribution in evaporator tubes and evaporator tube length.

A phase change material (PCM) is a substance that releases/absorbs good amount of energy to offer good heat/cooling throughout the phase transition, i.e. from solid to liquid or liquid to solid by absorbing or realizing large amount heat in from of latent heat. The energy received or released during fusion is known as the latent fusion this process occurred at almost constant temperature [11].

It is concluded from the literature survey that the PCM-based PV/T is a recently developing technology and investigation into this subject showed that the technology may greatly increase the solar utilization over the air, water and refrigerant-based system and therefore it has the potential to interchange the conventional system in the near future.

2 Thermal Modelling

In this study 1-D transient, mathematical model is developed to study PV system using MATLAB under the actual environmental conditions. Numerical model is developed to evaluate the variation of solar cell temperature for two cases, i.e. (i) Conventional PV panel (ii) PV with PCM.

2.1 Temperature Variation of Conventional PV Panel Under Actual Environmental Conditions

In order to write the energy balance equations of PV module following assumptions are made.

- Transient variation in temperature of PV is considered to be per minute from sun rise to sun set.
- As the thickness of the solar panel is small compared to the area of the panel, the heat transfer from the lateral surfaces is neglected.
- The temperatures are represented at the geometric centres of every component.
- Thermo-physical properties are assumed constant with respect to the operating temperature.
- Ambient air velocity is taken constant value, i.e. ($V_{air} = 1$ m/s)

To study the temperature variation of glass, solar cell and tedlar following equations are used. Finite Volume Method approach is used and with the help of the discretization technique, a MATLAB code is developed (Fig. 1).

The governing equations for energy balance across the PV panel are given below [12].

Glass

$$\begin{aligned}
 M_p C_{pg} \frac{dT_g}{dt} = & I_t \alpha_g A_m - h_{ga}^c (T_g - T_a) \\
 & - \sigma A_m \epsilon_g (T_g^4 - T_{sky}^4) + \sigma A_m \epsilon_{cg} (T_c^4 - T_g^4) \\
 & + h_{cg} A_m (T_c - T_g)
 \end{aligned}
 \tag{1}$$

where the heat transfer coefficient, temperature of sky and effective emissivity of glass-cell system can be calculated from following relations

$$h_{ga}^c = 2.8 + 3V_{air} \tag{1a}$$

$$T_{sky} = T_a - 6 \tag{1b}$$

$$\frac{1}{\epsilon_{cg}} = \frac{1}{\epsilon_c} + \frac{1}{\epsilon_g} - 1 \tag{1c}$$

Solar cell

Fig. 1 Conventional PV module



$$\begin{aligned}
 M_c C_{pc} \frac{dT_c}{dt} = & I_t \alpha_c \tau_g (1 - \eta_c) - h_{cg}^c A_m (T_c - T_g) \\
 & - \sigma A_m \varepsilon_{cg} (T_c^4 - T_g^4) - \sigma A_m \varepsilon_{cg} (T_c^4 - T_g^4) \\
 & - h_{cted}^c A_m (T_c - T_{ted})
 \end{aligned} \quad (2)$$

$$h_{cted}^c = \frac{1}{\frac{t_c}{2k_c} + \frac{t_{ted}}{2k_t}} \quad (2a)$$

Tedlar

$$M_t C_{pt} \frac{dT_t}{dt} = h_{cted}^c A_m (T_c - T_t) - U_{t-a} A_m (T_t - T_a) \quad (3)$$

$$U_{t-a} = \frac{1}{\frac{t_{ted}}{2k_t} + \frac{1}{h_{ta}}} \quad (3a)$$

$$h_{ta} = 2.8 + 3V_{air} \quad (3b)$$

2.2 Temperature Variation of PV-PCM System Under Actual Environmental Conditions

To evaluate the temperature of PV-PCM system, the conduction model is used for PCM. Enthalpy technique is used for numerical modelling of PCM. In order to write the energy balance equations of PV-PCM system following assumptions are made for melting and solidification process of PCM.

- PCM is homogeneous in nature.
- Thermo-physical properties of the PCM are constant with temperature.
- The flow of the liquid PCM is considered to be laminar and incompressible Newtonian fluid flow (Fig. 2).

The governing equations for glass and solar cell are same as Eqs. (1–2).

Tedlar

Fig. 2 PV panel with PCM

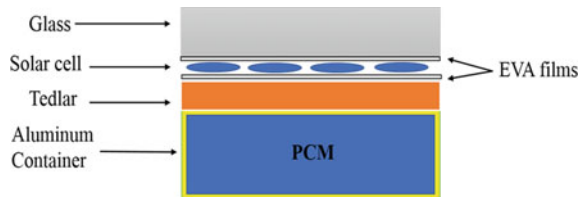


Fig. 3 PCM layers encapsulated aluminium base



$$M_{ted}C_{p\text{ted}} \frac{dT_{ted}}{dt} = h_{cted}^c A_m (T_c - T_{ted}) - h_{t-a} A_m (T_{ted} - T_a) \tag{4}$$

$$h_{t-a} = \frac{1}{\frac{t_{ted}}{2k_t} + \frac{2}{2k_{al}}} \tag{4a}$$

Top layer of aluminium

$$M_{Al}C_{pAl} \frac{dT_{Al}}{dt} = h_{cted}^c A_m (T_c - T_{ted}) - h_{Al-pcm} A_m (T_{Al} - T_{pcm}(1)) \tag{5}$$

$$h_{Al-pcm}^c = \frac{1}{\frac{t_{Al}}{2k_{Al}} + \frac{\Delta y_{pcm}}{2k_{al}}} \tag{5a}$$

For the PCM layers, the following equations are used to find temperature variations of different components of PV-PCM system as shown in the Fig. 3.

PCM layers

PCM is divided in N number of layers.

$$i = 1; \quad h(1, j) = h(1, j - 1) + \frac{dt}{\rho_{pcm}} \left(h_{Al-pcm}^c \frac{T_{(Al-1, j-1)} - T_{(1, j-1)}}{\Delta y} - k_{pcm} \frac{T_{(1, j-1)} - T_{(1, j-1)}}{\Delta y^2} \right) \tag{6}$$

$$2 < i < N - 1; \quad h_{(i, j)} = h_{(i, j-1)} + \frac{dt \cdot k_{pcm}}{\rho_{pcm}} \left(\frac{T_{(i+1, j-1)} + T_{(i-1, j-1)} - T_{i, j-1}}{\Delta y^2} \right) \tag{7}$$

$$i = N; \quad h(N, j) = h(N, j - 1) + \frac{dt}{\rho_{pcm}} \left(k_{pcm} \frac{T_{(N-1, j-1)} - T_{(N, j-1)}}{\Delta y^2} - h_{al-pcm}^c \frac{T_{(N, j-1)} - T_{(al2, j-1)}}{\Delta y} \right) \tag{8}$$

After evaluating the enthalpy for each layer of PCM, enthalpy is converted in to the temperature by following equations

$$T = \begin{cases} h/C_p & h < C_p T_m \\ T_m & C_p T_m < h < C_p T_m + LH \\ (h - LH)/C_p & h > C_p T_m + LH \end{cases} \tag{9}$$

$$f_l = \begin{cases} 0 & h < C_p T_m \\ (h - C_p T_m)/LH & C_p T_m < h < C_p T_m + LH \\ 1 & h > C_p T_m + LH \end{cases} \quad (10)$$

Bottom layer of aluminium

$$M_{Al} C_{pAl} \frac{dT_{Al}}{dt} = U_{Al-air}^c A_m (T_{Al} - T_{air}) \quad (11)$$

$$U_{Al-air}^c = \frac{1}{\frac{t_{Al}}{2k_{Al}} + \frac{1}{h_{Al-air}^c}} \quad (11a)$$

$$h_{Al-air} = 2.8 + 3V_{air} \quad (11b)$$

The dimensions and properties of the materials are listed in Tables 1 and 2.

Table 1 Properties of PV module

Parameters	Values
Area of PV module	1.01*0.665 m ²
Packing factor	0.9
Thickness of glass	0.0032 m
Thickness of solar cell	0.0005 m
Thickness of tedlar	0.0005 m
Emissivity of glass	0.95
Absorptivity of glass	0.05
Specific heat of glass	500 J/kg-K
Density of glass	3000 kg/m ³
Thermal conductivity of glass	1.8 W/m-K
Transmissivity of glass	0.95
Emissivity of solar cell	0.85
Absorptivity of solar cell	0.92
Specific heat of solar cell	710 J/kg-K
Density of solar cell	2285 kg/m ³
Thermal conductivity of solar cell	148 W/m-K
Emissivity of tedlar	0.35
Specific heat of tedlar	560 W/m-K
Efficiency of solar PV module	15%

Table 2 Properties of PCM (RT25) and aluminium [13]

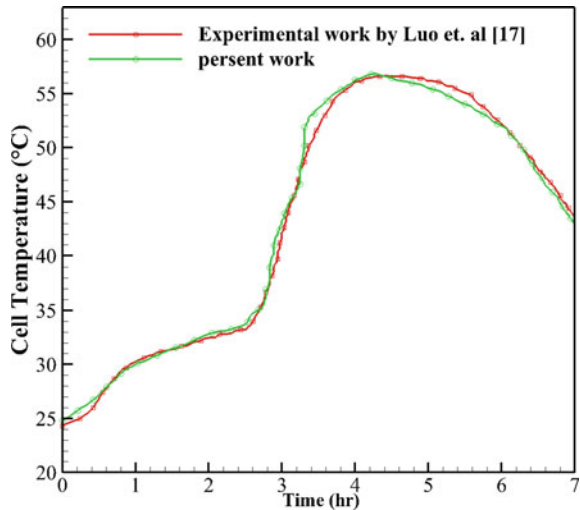
Parameters	Values
Density of PCM	785 kg/m ³
Specific heat of PCM	2000 J/kg-K
Latent heat of PCM	165 kJ/kg
Thermal conductivity of PCM	0.20 W/m-K
Melting temperature of PCM	299.75 K
Density of Aluminium	2700 kg/m ³
Specific heat of Aluminium	910 J/kg-K
Thermal conductivity of Aluminium	237 W/m-K

3 Validation of Numerical Model

The published experimental and numerical work of [14] is used to validate the developed numerical model. The same geometry with equal dimensions and the same material are used in the developed MATLAB code to predict temperature values. These studies were performed for 7 h.

Comparison of solar cell temperature of conventional PV with PCM panel between experimental result and simulated result is shown in Fig. 4. The analysis reveals that the results of the simulation are well consistent with the test result. The maximum relative error is 6.31% obtained at 3.3 h. Therefore, this model can be regarded as adequate and precise enough to simulate the temperature of the PV panel attached with PCM.

Fig. 4 Comparison of PV-PCM system temperature between present study and previous literature



4 Results and Discussion

To evaluate temperature variation of glass, solar cell and tedlar under the actual environmental conditions of Surat city (21.1702°N, 72.8311°E), solar radiation and ambient temperature are taken for a typical sunny day (31st March 2021). These data are taken for 12 h duration, i.e. from 6.00 AM to 6.00 PM. The radiation intensity varies from 13 W/m² to 1003.67 W/m² and the maximum radiation is achieved at 368 min means at 12.08 PM, the similarly ambient temperature varies from 25.91 °C to 39.64 °C and maximum temperature is achieved at 431 min means 1.11 PM. The ambient parameters (Solar irradiation, ambient temperature) are obtained from the weather station (Make: Davis-B) which is installed at the ‘Renewable energy laboratory’ at SVNIT, Surat. The variation of radiation and ambient temperature are shown in Figs. 5 and 6, respectively.

The weather station records radiation and temperature value in every minute of time interval. It is recorded total radiation values incident on horizontal surface. So with the help of standard relations, the available radiation is find out on tilted surfaces, i.e. at latitude of Surat city.

The studies were performed on PV module without PCM. Figure 7 shows that the temperatures of PV module increases as the solar radiation increases, reaches a maximum value at some instant, and then starts decreasing. it is observed that in PV panel maximum temperature 82.7 °C achieved by solar cell at 12.15 h. And lowest peak temperature 77.6 °C achieved by glass at 12.15 h in 12 h time duration. The difference between peak temperatures are 5.1 °C, i.e. approximately 6.58%.

This numerical investigation is also performed on PV module with PCM. From Fig. 8, it is observed that in PV panel maximum temperature 76.2 °C achieved by solar cell at 13.18 h. And lowest peak temperature 75.1 °C achieved by glass at

Fig. 5 Actual radiation variation with time

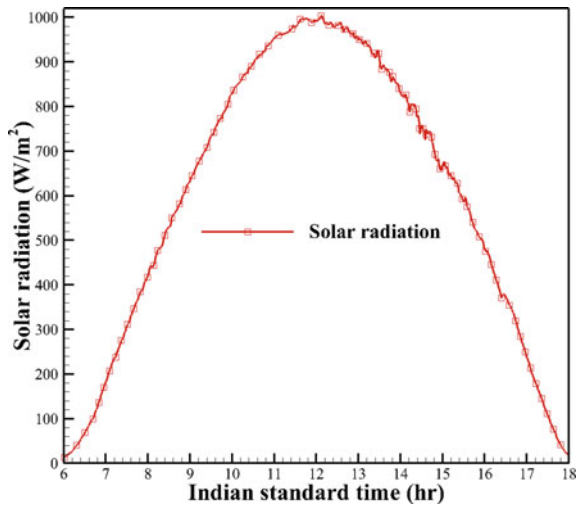


Fig. 6 Actual ambient temperature variation with time

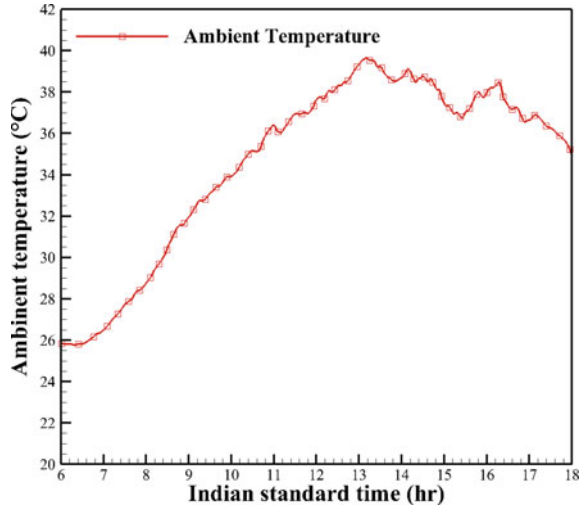
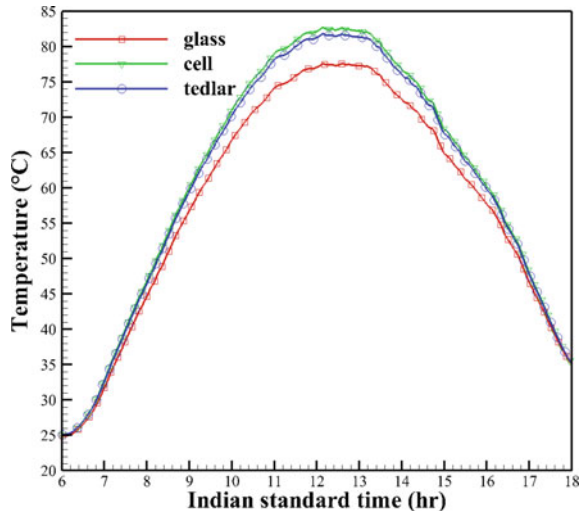


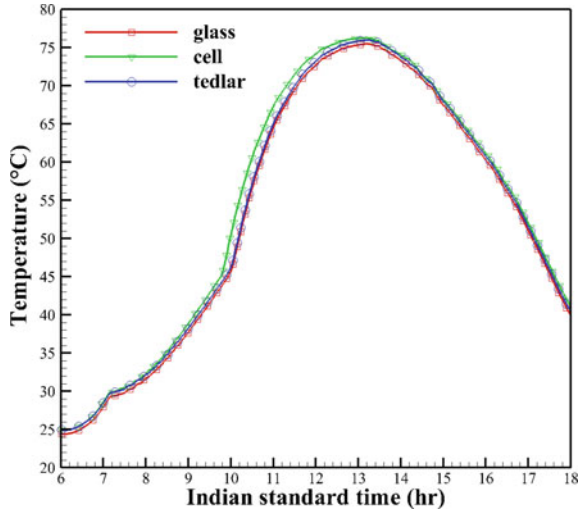
Fig. 7 Temperature variation of PV panel with time



13.18 h in 12 h time duration. The difference between peak temperatures are 1.1 °C, i.e. approximately 1.46%.

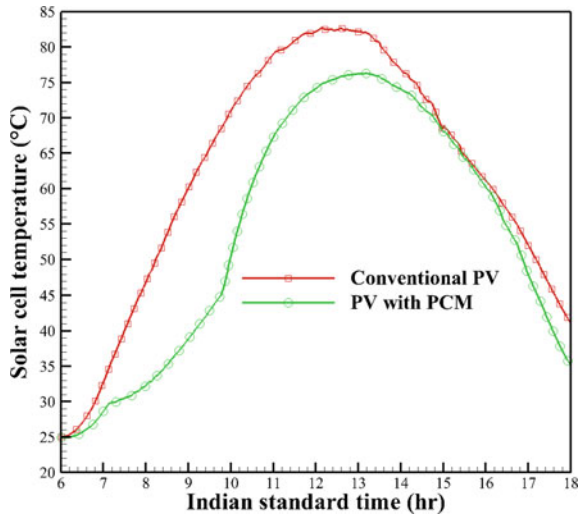
The difference between peak temperatures of both the cases is approximately 6.5 °C which is approximately 8.5%. This is because the excess solar energy that is not converted into electrical energy is stored by PCM in the form of latent heat, which takes place at nearly constant melting temperature. In the other case of the conventional PV module, all the excess energy is stored in the form of sensible heat that gives a significant rise in solar cell temperature. It is also observed from Fig. 9 that peak of solar cell temperature shift in rightward direction. The maximum

Fig. 8 Temperature variation of PV-PCM system with time



solar cell temperature difference achieved between PV without PCM and PV with PCM system at 9.98 h which is 24.87 °C approximately 35.08% lower temperature achieved.

Fig. 9 Comparison of solar cell temperatures with time



5 Conclusions

A numerical study is carried out to evaluate the thermal performance of PV panel cooled by PCM and these results are compared with the performance of conventional PV panel module. The study is carried out for climate conditions of Surat city and the following are the conclusions of the present work.

- The utilization of PCM for cooling PV panel can reduce solar cell temperature significantly.
- The maximum solar cell temperature difference achieved between conventional PV and PV-PCM system at 239 min, i.e. at 9.59 AM which is 24.87 °C approximately 35.08% lower temperature.
- The difference between peak temperatures of solar cell in both case is approximately 6.5 °C which is approximately 8.5%.

References

1. Dubey S, Sarvaiya JN, Seshadri B (2013) Temperature dependent photovoltaic (PV) efficiency and its effect on PV production in the world—a review. *Energy Procedia* 33:311–321
2. Chander S, Purohit A, Sharma A, Nehra SP, Dhaka MS (2015) Impact of temperature on performance of series and parallel connected mono-crystalline silicon solar cells. *Energy Rep* 1:175–180
3. Alkuhayli A, Telba A (2021) Effect of high temperature on the efficiency of grid-connected PV system proceedings of the world congress on engineering. London, UK
4. Shaari S, Sopian K, Amin N, Kassim MZ (2009) The temperature dependence coefficients of amorphous silicon and crystalline photovoltaic modules using Malaysian field test investigation. *Am J Appl Sci* 6(4):586
5. Sopian K, Yigit KS, Liu HT, Kakac S, Veziroglu TN (1996) Performance analysis of photovoltaic thermal air heaters. *Energy Convers Manage* 37(11):1657–1670
6. Solanki SC, Dubey S, Tiwari A (2009) Indoor simulation and testing of photovoltaic thermal (PV/T) air collectors. *Appl Energy* 86:2421–2428
7. Tiwari A, Sodha MS (2006) Performance evaluation of solar PV/T system: an experimental validation. *Sol Energy* 80:751–759
8. Bahaidarah H, Subhan A, Gandhidasan P, Rehman S (2013) Performance evaluation of a PV (photovoltaic) module by back surface water cooling for hot climatic conditions. *Energy* 59:445–453
9. Zhou J, Zhao X, Ma X, Qiu Z, Ji J, Du Z, Yu M (2016) Experimental investigation of a solar driven direct-expansion heat pump system employing the novel PV/micro-channels-evaporator modules. *Appl Energy* 178:484–495
10. Vaishak S, Bhale PV (2021) Performance analysis of a heat pump-based photovoltaic/thermal (PV/T) system. *Clean Technol Environ Policy* 23(4):1121–1133
11. Ma T, Yang H, Zhang Y, Lu L, Wang X (2015) Using phase change materials in photovoltaic systems for thermal regulation and electrical efficiency improvement: a review and outlook. *Renew Sustain Energy Rev* 43:1273–1284
12. Tiwari GN, Tiwari A (2016) *Handbook of solar energy: theory, analysis and applications*. Springer
13. Khanna S, Reddy KS, Mallick TK (2018) Optimization of finned solar photovoltaic phase change material (finned pv pcm) system. *Int J Therm Sci* 130:313–322

14. Luo Z, Huang Z, Xie N, Gao X, Fang Y (2017) Numerical and experimental study on temperature control of solar panels with form-stable paraffin/expanded graphite composite PCM. *Energy Convers Manage* 149:416–423

Aluminum Oxide as Potential Additives to N-Butanol-Diesel Blends on Emission and Performance Characteristics of the Diesel Engine



Gandhi Pullagura, Srinivas Vadapalli, V. V. S. Prasad, Suryanarayana Varma Datla, Arhun Jaya Sai Makkena, Ashok Srinivas Reddy Chilla, Venkateswarlu Velisala, and Kodanda Rama Rao Chebattina

Abstract In the current investigation, nanoparticles for engine applications were analyzed in the CI engine to enhance performance and reduce emissions. Aluminum oxide nanoparticles (ANPs) are used as an additive in 20% n-butanol in diesel (But20) blend. Al_2O_3 nanoparticles were added to the n-butanol-diesel blend in different proportions (50, 75, and 100 ppm). Cetyl trimethyl ammonium bromide (CTAB) as a stability enhancer for stable dispersion of nanoparticles. The But20 + Al_2O_3 fuel blends were evaluated for their thermophysical characteristics like flash point, viscosity, density, and performance evaluation at various engine loads. The nano fuel blends showed excellent stability and homogeneity in the diesel engine. FESEM images of nanoparticles reveal the spherical morphology of nanoparticles, and FT-IR results show the chemical stability of nanoparticles. Besides, these nano additives help to reduce air pollution because of the more oxygen content of butanol. Similarly, brake-specific fuel consumption decreased by 20.23%, whereas BTE improved by 7.31% compared to B20 without additives. In addition, nano fuel with But20 + 75 ppm ANPs significantly reduced the CO, UHC, and NO_x emissions by 22.04%, 21.07%, and 14.47%, respectively. In summary, ANPs, n-butanol diesel fuel additives have shown the better alternative to regular diesel to boost the overall engine efficiency and emission properties.

Keywords n-Butanol-diesel blend · Al_2O_3 nanoparticles · Diesel engine performance · Emissions

G. Pullagura (✉) · S. Vadapalli · S. V. Datla · A. J. S. Makkena · A. S. R. Chilla · K. R. R. Chebattina
GITAM Deemed to be University, Visakhapatnam, India
e-mail: gpullagu@gitam.edu

V. V. S. Prasad
Andhra University, Visakhapatnam, India

V. Velisala
Damacharla Anjaneyulu Government Polytechnic, Ongole, Andhra Pradesh, India

Nomenclature

ANPs	Aluminum oxide nanoparticles
BSFC	Brake specific fuel consumption, kg/kWh
BTE	Brake thermal efficiency, %
IMEP	Indicated mean effective pressure.
CO	Carbon monoxide, %
CTAB	Cetyl trimethyl ammonium bromide
	But20 20% n-butanol + 80% diesel fuel
	But20 + 50ppm ANPs
	But20 + 75ppm ANPs
	But20 + 100ppm ANP
FESEM	Field emission scanning electron microscope
FT-IR	Fourier transform infrared spectroscopic.
NOx	Nitrogen oxides
rpm	Revolution per minute
UHC	Unburnt hydrocarbon, ppm

1 Introduction

Conservation of energy resources and ecological balance regulating the engine emissions require cleaner ignition and complete combustion [1–4]. Over the last few decades, energy needs have increased tremendously [5]. Even though conventional fuels (gasoline and diesel) are used widely, they increase the exhaust emissions that limited their use. Therefore, many researchers [5–8] focused on sustainable alternative fuels to overcome this issue. On the other hand, petroleum-based energies are vital for transport, industrial growth, and agriculture [9, 10]; however, overexploitation leads to the depletion of fossil fuels. As per the survey conducted by the International Energy Agency, worldwide energy usage by the year 2025 will grow about 42% [11]. Overexploitation of fossil fuels releases toxic exhaust emissions, which result in global warming, adverse changes to the environment, and diminishing oil reserves [12]. Excessive diesel fuel use in large quantities of transportation increases the emission, thus accelerating global warming, adverse changes to the environment, and diminishing oil reserves. Recent studies [13, 14] emphasized that diesel particulate and diesel catalyst filters effectively regulate gas emissions, respectively. Finally, the most recommended alternative to enrich diesel fuel includes the use of oxygenated fuels [15, 16] and incorporation of nanoparticles [17, 18], minimizing pollutant emissions and increasing the combustion properties. Recently, researchers [19] showed that nano additives to fuel mixture facilitates reduced fuel consumption, exhaust emissions, and overall costs.

In view of this, the application of nano additives in diesel and biodiesel has a significant impact on nanotechnological derivatives as they reduce pollutant emission and improve engine performance [20, 21]. Nanoparticles were established as the most promising additives compared to other additives. Furthermore, the addition of nano additives facilitated improved heating value and cetane number and a significant increase in the properties of the fuel [22, 23]. In addition, they also help in increasing the rate of droplet evaporation, energy storage on surfaces, increased surface area, reduced ignition delay, and improved catalytic activity [19]. Nanoparticles can be proved as promising alternatives to accomplish the current objective as they can facilitate homogenous mixing of additives in the fuel. The greatest critical problem with petrochemicals is the dispersion of hazardous pollutants, for example, CO, CO₂, NO_x, and CH [23–29]. Several studies emphasized the use of modified fuels with the addition of organic and metal oxides (CuO, ZnO, MnO, GO, and SnO) to protect the environment from harmful emissions [30]. Gumus et al. [31] studied the impact of adding CuO and Al₂O₃ to traditional diesel fuel on emission parameters of diesel engines. The observations show that carbon monoxide (CO), hydrocarbon (HC), and NO_x decreased by 11.01%, 13.1%, and 6.2%, respectively. Similarly, adding 0.1 percentage by volume of Al₂O₃ nano additives increases combustion of gasoline spray characteristics, and CO emission decreased by 7% [32].

Moreover, nanoparticles help in achieving high surface area, combustion, and prevent CO formation. Additionally, a mixture of biodiesel blend and Al₂O₃ nano additives showed very fewer exhaust emissions and excellent engine performance. Experimental findings reveal that CO, HC, NO_x, and smoke concentrations were decreased by 70%, 60%, 80%, and 35%, respectively [33].

The present research investigation aims to evaluate the effect of nano additives of Al₂O₃ nanoparticles at different proportions (50, 75, and 100 ppm) and alcohol n-butanol-diesel simultaneously on fuel combustion. Further, examination of emissions and performance of a diesel engine was tested at different loads. Eventually, better engine performance and less harmful emissions were achieved using a combination of nano additive and an oxygenate additive simultaneously, which is proved as the novel approach with significant advantages.

2 Preparation of a Fuel Blend Using Nanoparticles and Equipment

Nanoparticles of Al₂O₃ (purity, 99.5%, and size, 30 nm) purchased from Platonic Nanotech Private Limited-Kachwa Chowk, Dist: Godda, Jharkhand, n-butanol purchased from Sigma Aldrich, and all the chemicals and surfactants are AR grade were used in the present investigation (Tables 1 and 2). The specifications of Al₂O₃ provided by the supplier and n-butanol [27] are given in Tables Numbers. 1 and 2. The fuel blends are prepared with a four-carbon alcohol n-butanol (C₄H₉OH), respectively. Al₂O₃ and n-butanol blends were sonicated along with surfactants using an

ultra-probe sonicator available at GITAM. The sonication is done at time intervals of 10 min for ten cycles. The blend prepared was tested for its stability for one month and observed no deposition or formation of accumulates in the fuel blend. The blend was mixed well before testing to avoid the deposition of nanoparticles in the solution or tubes. The nanofluids were prepared in three concentrations of Al_2O_3 : 50 ppm, 75 ppm, and 100 ppm. The obtained nanofluid samples appear to be milky white for all three cases, including But20 + 50 ppm, But20 + 75 ppm, and But20 + 100 ppm. The properties of diesel, But20 without, and with Al_2O_3 nanoparticles as shown in Tables 3 and 4.

Technical details of the test engine were shown in Table no. 4. Complete diagrammatic illustration of the trial setup as depicted in Fig. 1. The experiments were performed at room temperature. The CI engine's indicated mean effective pressures (IMEPs) were measured at 1500 rpm for different load conditions of 0.5 to 4.5 bar. The injection pressure of the fuel was kept constant at 200 bar for all test fuels. The experiments were carried out using diesel as reference fuel and n-butanol-diesel blend (But20), But20 + 50 ppm ANPs, But20 + 75 ppm ANPs, and But20 + 100 ppm ANPs. The engine emissions and performance measurements were recorded from

Table 1 Specifications of the Al_2O_3 nanoparticles

Manufacturer	Platonic Nanotech Private Limited-Kachwa Chowk, Dist.: Godda, Jharkhand
Chemical name	Alumina (Al_2O_3)
Appearance	White power
Purity	>99%
Specific surface area (SSA)	30 m^2/g
The average diameter of particle size	25 nm
Bulk density (%)	0.43
Sulfation assay ($\leq\%$)	0.42
Loss on drying ($\leq\%$)	0.92
Mg \leq ppm	$\leq 0.003\%$
Fe \leq ppm	≤ 0.007
Si \leq ppm	≤ 0.006

Table 2 n-butanol specification [27]

Specifications	Values
Melting point	$-89.6\text{ }^\circ\text{C}$, ($-129.5\text{ }^\circ\text{F}$, 183.4 K)
Boiling point	$117.6\text{ }^\circ\text{C}$, ($243.8\text{ }^\circ\text{F}$, 390.6 K)
Viscosity	2.96 cSt ($25\text{ }^\circ\text{C}$)
Solubility in water	73 g/L ($20\text{ }^\circ\text{C}$)
Molar mass	74.132 g mol^{-1}
Density	0.81 g/cm^3

Table 3 Properties of diesel, But20 without and with ANPs samples

Properties	Diesel	But20	But20 + 50 ppm	But20 + 100 ppm	But20 + 75 ppm
Density kg/m ³ at 15 °C	842.5	858.4	870.6	886.9	878.2
Calorific value kJ/kg	44,400	43,758	45,860	47,960	46,090
Kinematic viscosity cSt at 40 °C	2.77	3.224	3.125	2.845	3.054
Cetane number	51.01	52.5	54.2	58.26	55.46
Flash point °C	55	81	82	86	83
Pour point °C	-3	4.57	4.72	4.62	4.53
Copper strip corrosion	1	1	-	-	-

Table 4 Test engine technical specifications are listed below [34]

Parameters	Values
Make	Kirloskar
Type/number of cylinders	Single-cylinder/four-stroke
Various loads at a constant speed	1500 rpm
Variable compression ratio	16 to 18
Rated power	5.2 kW @ 1500 rpm
Injection point variation	23°BTDC
Cylinder diameter	87.5 mm
Stroke length	110 mm
Orifice diameter	20 mm
Connecting rod length	234 mm
Dynamometer arm length	185 mm
Loading	Eddy current dynamometer
Lubricating system	Forced feed system
Type of cooling	Water-cooled direct injection

the engine at a steady-state condition. To avoid thermal breakdown and certify that the fuel set up of the engine was clean of any previous fuel residues, the engine was operated with diesel in no-load at a constant speed of 1000 rpm before each subsequent test. Experiments were conducted in duplicates for every fuel test to prevent errors during testing and get further accurate results. Before the tests, all sensors and instruments were calibrated. The highest uncertainty in brake thermal efficiency, SFC, HC, CO, and NO_x emissions were $\pm 1.6\%$, 1.2% , $\pm 0.02\%$ Vol., ± 1 ppm, and ± 1 ppm, respectively. Brake power, exhaust gas temperature, and engine speed,

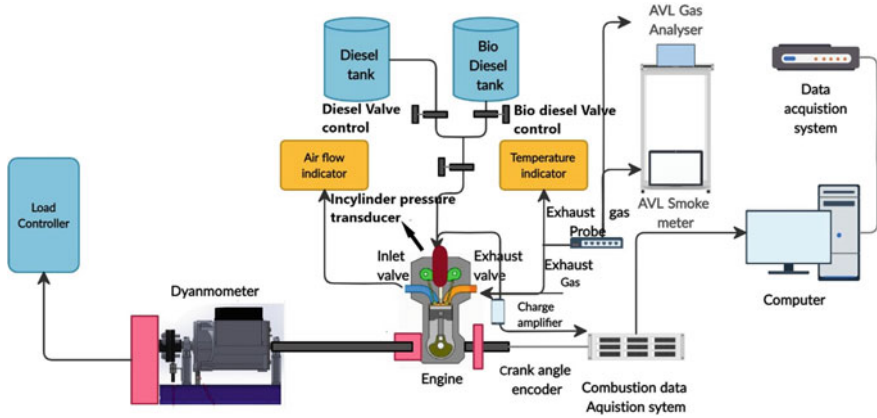


Fig. 1 Experimental setup is depicted in this diagram

overall ambiguities in readings were noted to be 0.6%, 0.2%, and 0.15% (± 2 rpm), respectively. The overall cumulative error uncertainty percentage is 2.52%.

Where

- $THER_u$ Brake thermal efficiency uncertainty.
- SFC_u Specific fuel consumption uncertainty.
- EGT_u Exhaust gas temperature uncertainty.
- BP_u Brake power uncertainty.
- UHC_u UHC emission uncertainty.
- CO_u CO emission uncertainty.
- NOx_u NOx emission uncertainty.
- N_u Engine speed uncertainty.

Total percentage uncertainty of this experiment

$$\begin{aligned}
 &= \sqrt{(THER_u)^2 + (SFC_u)^2 + (UHC_u)^2 + (CO_u)^2 + (NOx_u)^2 + (EGT_u)^2 + (BP_u)^2 + (textNu)^2} \\
 &= \sqrt{(1.6)^2 + (1.2)^2 + (1)^2 + (0.02)^2 + (1)^2 + (0.2)^2 + (0.6)^2 + (0.15)^2} \\
 &= \pm 2.52
 \end{aligned}$$

3 Result and Discussions

3.1 Characterization of Al_2O_3 Nanostructures

The surface morphology and the average particle size of Al_2O_3 nanoparticles were analyzed on a field emission scanning electron microscope (FESEM) on model:

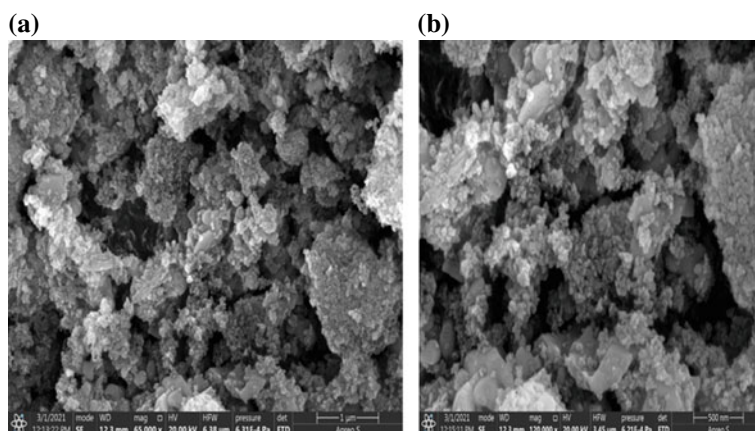


Fig. 2 **a** FESEM at 1 μm at 65,000X magnification level. **b** FESEM at 500 nm at 120,000X magnification level

Apereo LoVac, Central Analytical Laboratory, available BITs Pilani Hyderabad Campus. Figures 2a and b represents the FESEM image of Al_2O_3 nanoparticles. FESEM images were captured at 65,000X and 120,000X magnification. The image reveals that Al_2O_3 nanoparticles were round and smooth-surfaced with an average particle size of 30 nm, considering the nanoparticle's size smaller than the nozzle diameter of the fuel injector without obstructing the fuel flow in the nozzle.

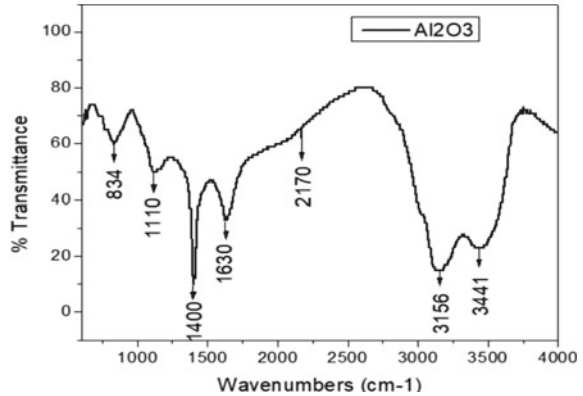
Fourier transform infrared spectroscopy (FT-IR) is utilized to analyze the chemical properties in a qualitative manner. The Al_2O_3 nanoparticles were studied using FT-IR (Bruker-Spectrum Model Vertex 70) in the wavelength of $400\text{--}4000\text{ cm}^{-1}$ to decipher functional groups and the peaks related to various vibrations, as depicted in Fig. 3. The figure shows that peaks observed at $3600\text{--}2500\text{ cm}^{-1}$ correspond to $\gamma\text{-Al}_2\text{O}_3$ containing different -OH groups on the exterior. The peaks recorded below 1110 cm^{-1} were related to Al-O vibrations. A sharp band at 1630 cm^{-1} signifies the scissoring vibrations of two O-H bonds in physically adsorbed water molecules or is also attributed to the minute quantity of adsorbed contaminants like CO_2 or carbonates [35]. The FT-IR analysis is comparable to that described for $\gamma\text{-Al}_2\text{O}_3$ nano additives by Ledwa et al. [36].

4 Engine Performance

4.1 Brake Specific Fuel Consumption

Figure 4 demonstrates the brake-specific fuel consumption versus IMEP for the tested fuels. The BSFC can be used to indicate how effective the fuel supplied for power generation is used by the engine. The key explanation for the BSFC increase may be

Fig. 3 Fourier transform infrared spectroscopy



the compared to diesel, B20 has a lower calorific value (Table 3); previous studies have recorded this pattern of B20 [37, 38]. The addition of nanoparticles as a fuel catalyst enhances the combustion process, reducing specific fuel consumption in But20 blends at all load conditions. A comparison of the ANP additions revealed that But20 + 75 ppm significantly reduced the BSFC by 30.23%, while But20 + 100 ppm and But20 + 50 ppm significantly reduced the BSFC by 26.47% and 17.64%, respectively, compared to But20. Improved BSFCs have been observed for blended Al₂O₃ nanoparticles due to improved atomization and excellent combustion characteristics [33]. More oxygen and the beneficial impacts of nano additives on the physical characteristics of diesel fuel contribute to an improvement in the efficiency of combustion, which decreases BSFC. The results appeared significant with reductions in the BSFC by adding 50, 75, and 100 ppm of ANPs to But20 of 6.66%, 20.33%, and 16.67%, respectively, compared with standard diesel for various engine loads (Fig. 4). At full load condition, But20 + 75 ppm ANPs are identified to have a reported minimum value. Previous studies revealed that when TiO₂ nano additives were applied to a fuel blend compared to diesel fuel, the BSFC decreased by 13.22 and 21.28% [39, 40].

4.2 Brake Thermal Efficiency

The effect of adding ANPs to the But20 on the BTE in various engine loads is shown in Fig. 5. When comparing B20 combustion to diesel fuel combustion, the BTE increased by 1.96% because the oxygenated fuel molecule structure has a greater oxygen concentration formed from fuel [41]. The results indicated that the increases in BTE were 5.14, 7.31, and 6.06% from the combustion of But20 + 50 ppm ANPs, But20 + 75 ppm ANPs, and But20 + 100 ppm ANPs, respectively, in comparison with But20 combustion without additives (Fig. 5). The presence of nano Al₂O₃ particles increases the combustion phenomena. Thus, it increases the heat release

Fig. 4 Brake specific fuel consumption variation with engine load

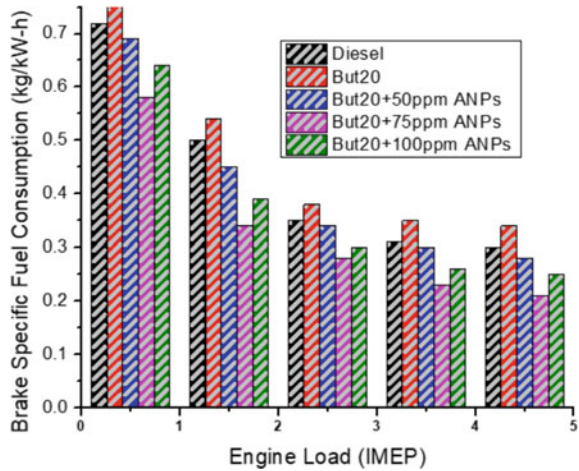
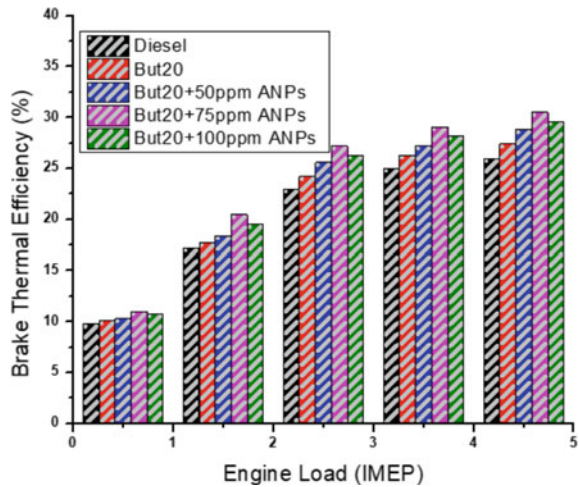


Fig. 5 Brake thermal efficiency variation with engine load



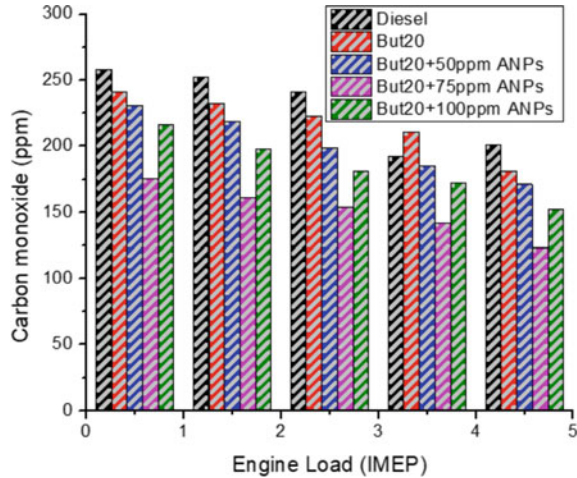
rate, better atomization, increased evaporation rate, and better air–fuel mixing [31, 32], which mainly contributes to the major improvement in BTE.

5 Influence of Nano Additives on Emission Characteristics

5.1 Carbene Monoxide (CO)

Figure 6. reveals the impact of CO emissions caused by various ANPs to But20 concentrations for various engine loads. It is observed that with an increase in engine

Fig. 6 Carbon monoxide emissions variation with engine load

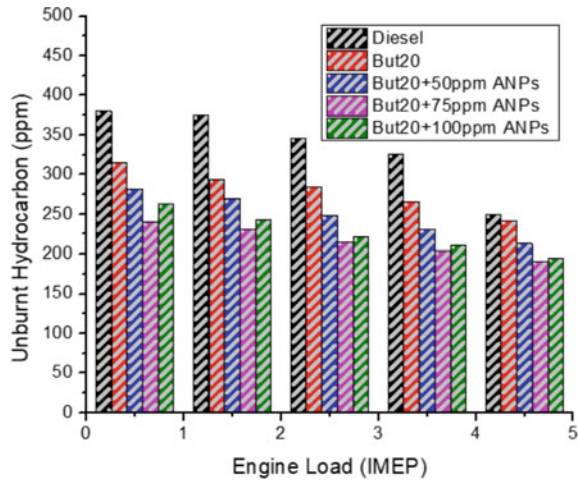


load, CO formation decreases. In the literature [42], the smaller quantity of CO emissions generated by But20 combustion than standard diesel combustion has already been stated. When ANPs were applied to the But20 in different engine loads, it resulted in a small reduction in CO emissions compared to the But20 without additives. The CO emissions decreased by 5.52, 22.04, and 16.02% for But20 + 50 ppm ANPs, But20 + 75 ppm ANPs, and But20 + 100 ppm ANPs, respectively, compared to But20 without additives. A study of the nanoparticle concentration revealed a large decrease in CO emissions when 75 ppm of ANPs is applied to the But20 compared to the other ANPs concentrations (Fig. 6).

5.2 Unburnt Hydrocarbon (UHC)

UHC concentration was reduced as nano additives were applied to But20 at various engine loads (Fig. 7). At lower engine loads, the concentration of UHC was elevated, and as engine load increased, the concentration of HC decreased. A decrease in HC emissions leads to an increase in combustion temperature in the combustion chamber [42]. When Al_2O_3 nano additives of 50, 75, and 100 ppm were added to But20, the concentration of UHC was reduced by 14.8%, 23.6%, and 22%, respectively, compared to standard diesel (Fig. 7). The catalytic nature of ANPs facilitated the oxidation of HCs in the But20. As 50, 75, and 100 ppm of ANPs were added to But20, HC emissions were reduced by 11.98%, 21.07%, and 19.42%, respectively, compared to B20 without additives. The nanoparticles' broad surface area and oxygen content may have aided the combustion procedure and extended the period required for the oxidation of HC [43]. Because of their high thermal conductivity, nanoparticles in fuel blends boost combustion parameters, resulting in total combustion and improved air–fuel blends, lowering HC emissions [44].

Fig. 7 Hydrocarbon emissions variation with engine load



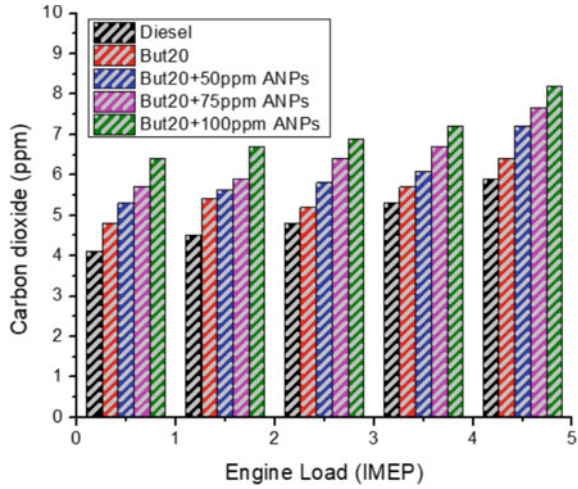
5.3 Carbone Dioxide (CO_2)

The concentration of CO_2 emissions for various concentrations of ANPs applied to But20 under different engine loads are shown in Fig. 8. In comparing combustions of But20 and But20 + ANPs to diesel fuel, the average increase in CO_2 emissions was 8.63% and 25.01%, respectively. Another comparative study of But20 without ANPs additives with But20 and But20 + ANPs revealed a 16.12% rise in CO_2 emissions. The nanoparticle additives might be the primary cause for the improved combustion process. The addition of nanoparticles to But20 resulted in higher CO_2 concentrations, which improved the combustion process. Furthermore, compared to B20 and diesel, the addition of nanoparticles resulted in lesser CO emission (Fig. 6) throughout the combustion procedure, which may result in elevated CO_2 emissions (Fig. 8) [45].

5.4 Oxides of Nitrogen (NO_x)

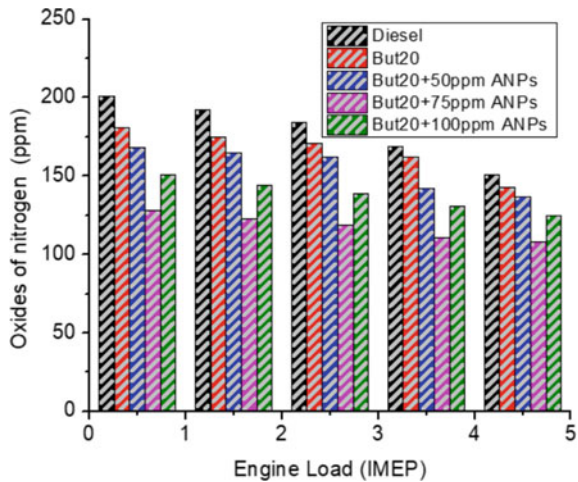
Figure 9 shows NO_x emissions in the exhaust gas under different engine loads for diesel, But20, and But20 + ANPs. A substantial reduction in NO_x emissions was observed when ANPs were supplemented to But20 for various engine loads. To ensure that HC compounds undergo the least amount of thermal breakdown, the catalytic behavior of ANPs improved the combustion procedure. The supplementation of ANPs to the diesel—n-butanol blend improved the fuel blend thermal conductivity, reducing the ignition delay time and improving its consumption. This kind of progress improves the overall performance of CI engines [43]. The addition

Fig. 8 Variation carbone dioxide with engine load



of nanoparticles reduces the potential for thermal NO_x formation in the combustion process by lowering active radicals. Venu and Madhavan [46] found a similar pattern in their experimental research. Furthermore, Attia et al. [33] found that adding nanoparticles to biodiesel blends reduces NO_x emissions. Figure 9 shows, as compared to diesel fuel, NO_x emissions for But20 + 50 ppm ANPs, But20 + 75 ppm ANPs, and But20 + 100 ppm ANPs decreased by 4.19%, 14.47% and 12.58%, respectively. Furthermore, compared to the other concentrations, adding 75 ppm ANPs to But20 had the strongest effect on NO_x reduction.

Fig. 9 Oxides of nitrogen emissions variation with engine load



6 Conclusions

The present study deals with the exploitation of Al_2O_3 by using n-butanol-diesel (But20) and diesel blends. Primarily, the diesel engine was run with pure diesel 100% and B20 followed by nano fuel blends But20 + ANP50ppm, But20 + 75 ppm, and But20 + ANP100 ppm. The effects of adding three concentrations of ANPs (50, 75, 100 ppm) to But20 on emissions characteristics and engine performance at various engine loads were studied experimentally. The key findings can be revealed as follows, according to the results of this study:

- The slightest drop in BSFC was accomplished for But20 + 75 ppm ANPs when compared to other concentrations. Furthermore, for different engine loads, But20 + 75 ppm ANPs resulted in the highest increase in BTE of 7.31%, compared to But20 without nano additives. The addition of 75 ppm ANPs to the But20 has a constructive influence on engine performance.
- The highest reduction in CO was 22.04%, and UHC emissions were 21.07% for But20 + 75 ppm ANPs.
- The smallest amount of NO_x emission was 14.47% when 75 ppm ANPs were added to the But20.
- To achieve the greatest improvement in engine emissions and performance, the proposed quantity of Al_2O_3 nanoparticles is 75 ppm. Therefore, it was finally concluded that nano additive But20 blends decreases the emission parameters and delivers better performance to the diesel engine.

Acknowledgements The authors wish to convey their heartfelt thanks to the Department of Mechanical Engineering, GITAM Deemed to be University, Visakhapatnam Campus, for their encouragement in carrying out the research work.

References

1. Deng B, Li Q, Chen Y, Li M, Liu A, Ran J, Xu Y, Liu X, Fu J, Feng R (2019) The effect of air/fuel ratio on the CO and NO_x emissions for a twin-spark motorcycle gasoline engine under wide range of operating conditions. *Energy* 169:1202–1213
2. Yüksel F, Yüksel B (2004) The use of ethanol-gasoline blend as a fuel in an SI engine. *Renew Energy* 29(7):1181–1191
3. Elfasakhany A (2018) Exhaust emissions and performance of ternary iso-butanol–bio-methanol–gasoline and n-butanol–bio-ethanol–gasoline fuel blends in spark-ignition engines: assessment and comparison. *Energy* 158:830–844
4. Tornatore C, Marchitto L, Valentino G, Corcione FE, Merola SS (2012) Optical diagnostics of the combustion process in a PFI SI boosted engine fueled with butanol–gasoline blend. *Energy* 45(1):277–287
5. Samuel OD, Okwu MO, Amosun ST, Verma TN, Afolalu SA (2019) Production of fatty acid ethyl esters from rubber seed oil in hydrodynamic cavitation reactor: study of reaction parameters and some fuel properties. *Ind Crops Prod* 141:111658

6. Pullagura G, Kumar KR, Verma PC, Jaiswal A, Prakash R, Murugan S (2012) Experimental investigation of hydrogen enrichment on performance and emission behavior of CI engine. *Int J Engi Sci Technol* 4(3):1223–1232
7. Shrivastava P, Verma TN, Samuel OD, Pugazhendhi A (2020) An experimental investigation on engine characteristics, cost and energy analysis of CI engine fuelled with Roselle, Karanja biodiesel and its blends. *Fuel* 275:117891
8. Samuel OD, Okwu MO (2019) Comparison of response surface methodology (RSM) and artificial neural network (ANN) in modeling of waste coconut oil ethyl esters production. *Energy Sour Part A Recov Util Environ Effects* 41(9):1049–1061
9. Demirbaş A (2002) Biodiesel from vegetable oils via transesterification in supercritical methanol. *Energy Convers Manage* 43(17):2349–2356
10. Pullagura G, BabjiAlapati M, Prakash R (2012) Effect of hydrogen enrichment on the combustion characteristics of a biofuel diesel engine. *IOSR J Eng* 2(1):001–006
11. Abbaszaadeh A, Ghobadian B, Omidkhal MR, Najafi G (2012) Current biodiesel production technologies: a comparative review. *Energy Conv Manage* 63:138–148
12. Chaichan MT (2018) Combustion and emission characteristics of E85 and diesel blend in conventional diesel engine operating in PPCI mode. *Therm Sci Eng Progr* 7:45–53
13. Fayad MA, Fernandez-Rodriguez D, Herreros JM, Lapuerta M, Tsolakis A (2018) Interactions between after-treatment systems architecture and combustion of oxygenated fuels for improved low-temperature catalysts activity. *Fuel* 229:189–197
14. Rodríguez-Fernández J, Lapuerta M, Sánchez-Valdepeñas J (2017) Regeneration of diesel particulate filters: effect of renewable fuels. *Renew Energy* 104:30–39
15. Zhang ZH, Balasubramanian R (2015) Effects of oxygenated fuel blends on carbonaceous particulate composition and particle size distributions from a stationary diesel engine. *Fuel* 141:1–8
16. Wei L, Cheung CS, Ning Z (2018) Effects of biodiesel-ethanol and biodiesel-butanol blends on the combustion, performance and emissions of a diesel engine. *Energy* 155:957–970
17. Devarajan Y, Nagappan B, Subbiah G (2019) A comprehensive study on emission and performance characteristics of a diesel engine fueled with nanoparticle-blended biodiesel. *Environ Sci Pollut Res* 26(11):10662–10672
18. Al-Shara NK, Sher F, Iqbal SZ, Sajid Z, Chen GZ (2020) Electrochemical study of different membrane materials for the fabrication of stable, reproducible and reusable reference electrodes. *J Energy Chem* 49:33–41
19. Saraee HS, Taghavifar H, Jafarmadar S (2017) Experimental and numerical consideration of the effect of CeO₂ nanoparticles on diesel engine performance and exhaust emission with the aid of artificial neural network. *Appl Therm Eng* 113:663–672
20. Rai PK, Kumar V, Lee S, Raza N, Kim KH, Ok YS, Tsang DC (2018) Nanoparticle-plant interaction: implications in energy, environment, and agriculture. *Environ Int* 119:1–19
21. Venkatesan H, Sivamani S, Sampath S, Gopi V, Kumar D (2017) A comprehensive review on the effect of nano metallic additives on fuel properties, engine performance and emission characteristics. *Int J Renew Energy Res (IJRER)* 7(2):825–843
22. Hashemzahi M, Pirouzfzar V, Nayebzadeh H, Alihosseini A (2020) Application of response surface methodology to optimize high active Cu-Zn-Al mixed metal oxide fabricated via microwave-assisted solution combustion method. *Adv Powder Technol* 31(4):1470–1479
23. Zamankhan F, Pirouzfzar V, Ommi F, Valihesari M (2018) Investigating the effect of MgO and CeO₂ metal nanoparticle on the gasoline fuel properties: empirical modeling and process optimization by surface methodology. *Environ Sci Pollut Res* 25(23):22889–22902
24. Heydari S, Pirouzfzar V (2016) The influence of synthesis parameters on the gas selectivity and permeability of carbon membranes: empirical modeling and process optimization using surface methodology. *RSC Adv* 6(17):14149–14163
25. Yang WM, An H, Chou SK, Chua KJ, Mohan B, Sivasankaralingam V, Raman V, Maghbouli A, Li J (2013) Impact of emulsion fuel with nano-organic additives on the performance of diesel engine. *Appl Energy* 112:1206–1212

26. Ciambelli P, Sannino D, Sarno M (2005) Carbon nanotubes, building blocks of nanotechnology. *Chim Oggi* 23(2):22–26
27. Jin C, Yao M, Liu H, Chia-fon FL, Ji J (2011) Progress in the production and application of n-butanol as a biofuel. *Renew Sustain Energy Rev* 15(8):4080–4106
28. Hansen AC, Zhang Q, Lyne PW (2005) Ethanol–diesel fuel blends—a review. *Biores Technol* 96(3):277–285
29. Pirouzfard V, Omidkhan MR (2016) Mathematical modeling and optimization of gas transport through carbon molecular sieve membrane and determining the model parameters using genetic algorithm. *Iran Polym J* 25(3):203–212
30. Sehar S, Sher F, Zhang S, Khalid U, Sulejmanović J, Lima EC (2020) Thermodynamic and kinetic study of synthesized graphene oxide-CuO nanocomposites: a way forward to fuel additive and photocatalytic potentials. *J Mol Liq* 313:113494
31. Gumus S, Ozcan H, Ozbey M, Topaloglu B (2016) Aluminum oxide and copper oxide nano diesel fuel properties and usage in a compression ignition engine. *Fuel* 163:80–87
32. El-Seesy AI, Attia AM, El-Batsh HM (2018) The effect of aluminum oxide nanoparticles addition with Jojoba methyl ester-diesel fuel blend on a diesel engine performance, combustion and emission characteristics. *Fuel* 224:147–166
33. Attia AM, El-Seesy AI, El-Batsh HM, Shehata MS (2014) Effects of alumina nanoparticles additives into jojoba methyl ester-diesel mixture on diesel engine performance. *ASME Int Mech Eng Congr Expo*
34. Sandhi RS, Chebattina KRR, Sambana NR, Vadapalli S, Pullagura G, Pathem UC (2021) Evaluation of TiO₂ nanoparticles as an additive in diesel-n-Butanol-bombax ceiba biodiesel blends for enhance performance and emissions control of a CI engine. *Journal* 39(6):1930–1936. <http://iicta.org/journals/ijht>
35. Wang S, Li X, Wang S, Li Y, Zhai Y (2008) Synthesis of γ -alumina via precipitation in ethanol. *Mater Lett* 62(20):3552–3554
36. Ledwa KA, Kępiński L (2017) Dispersion of ceria nanoparticles on γ -alumina surface-functionalized using long-chain carboxylic acids. *Appl Surf Sci* 400:212–219
37. Lapuerta M, Armas O, Rodriguez-Fernandez J (2008) Effect of biodiesel fuels on diesel engine emissions. *Prog Energy Combust Sci* 34(2):198–223
38. Hajbabaie M, Johnson KC, Okamoto R, Durbin TD (2013) Evaluation of the impacts of biofuels on emissions for a California certified diesel fuel from heavy-duty engines. *SAE Int J Fuels Lubr* 6(2):393–406
39. Fangsuwannarak K, Triratanasirichai K (2013) Effect of metalloid compound and bio solution additives on biodiesel engine performance and exhaust emissions. *Am J Appl Sci* 10(10):1201
40. D’Silva R, Binu KG, Bhat T (2015) Performance and emission characteristics of a CI engine fuelled with diesel and TiO₂ nanoparticles as fuel additive. *Mater Today Proc* 2(4–5):3728–3735
41. Fayad MA (2020) Investigating the influence of oxygenated fuel on particulate size distribution and NOx control in a common-rail diesel engine at rated EGR levels. *Therm Sci Eng Progr* 100621
42. Dhahad HA, Chaichan MT, Megaritis T (2019) Performance, regulated and unregulated exhaust emission of a stationary compression ignition engine fueled by water-ULSD emulsion. *Energy* 181:1036–1050
43. Wu Q, Xie X, Wang Y, Roskilly T (2018) Effect of carbon coated aluminum nanoparticles as additive to biodiesel-diesel blends on performance and emission characteristics of diesel engine. *Appl Energy* 221:597–604
44. Dhahad HA, Chaichan MT (2020) The impact of adding nano-Al₂O₃ and nano-ZnO to Iraqi diesel fuel in terms of compression ignition engines’ performance and emitted pollutants. *Therm Sci Eng Progr* 18:100535
45. Hassan MHA, Sher F, Zarren G, Suleiman N, Tahir AA, Snape CE (2020) Kinetic and thermodynamic evaluation of effective combined promoters for CO₂ hydrate formation. *J Nat Gas Sci Eng* 78:103313
46. Venu H, Madhavan V (2016) Effect of Al₂O₃ nanoparticles in biodiesel-diesel-ethanol blends at various injection strategies: performance, combustion and emission characteristics. *Fuel* 186:176–189

47. Fayyazbakhsh A, Pirouzfard V (2017) Comprehensive overview on diesel additives to reduce emissions, enhance fuel properties and improve engine performance. *Renew Sustain Energy Rev* 74:891–901
48. Fayyazbakhsh A, Pirouzfard V (2016) Investigating the influence of additives-fuel on diesel engine performance and emissions: analytical modeling and experimental validation. *Fuel* 171:167–177
49. Khorramshokouh S, Pirouzfard V, Kazerouni Y, Fayyazbakhsh A, Abedini R (2016) Improving the properties and engine performance of diesel–methanol–nanoparticle blend fuels via optimization of the emissions and engine performance. *Energy Fuels* 30(10):8200–8208
50. Hashemzahi M, Pirouzfard V, Nayebzadeh H, Alihosseini A (2020) Effect of synthesizing conditions on the activity of zinc-copper aluminate nanocatalyst prepared by microwave combustion method used in the esterification reaction. *Fuel* 263:116422
51. Raman LA, Deepanraj B, Rajakumar S, Sivasubramanian V (2019) Experimental investigation on performance, combustion and emission analysis of a direct injection diesel engine fuelled with rapeseed oil biodiesel. *Fuel* 246:69–74

Analytical Study of Thermal Stresses Generated in a Carbon Fiber-Reinforced Wheel Hub



Prasanna Kadambi, Bikash Prasad, Pranay Luniya, Parth Kulkarni, Sandip T. Chavan, and Yogesh G. Mane

Abstract The automobile sector has shown a year-on-year growth in terms of vehicles being disposed and revenue being generated. This drives the motive to conduct intensive research in this area to in order to suffice to change in dynamic needs of industries. Material selection and usage in development of automotive parts can be considered as a significant field of opportunity in terms of introducing heterogeneous combinations to achieve enhanced performance in vehicles. Among this, composites have tend to attract a lot of attention, in terms of manufacturing feasibility and the freedom of developing desired mixture of properties. Moreover with the advancements in additive manufacturing and hybrid manufacturing techniques, composites can be processed with more ease to form finished products with upgraded characteristics. Most of the literature in this area has focused on identifying the mechanical superiority of composites over metals (aluminum, steel). However, a comparatively less amount of work has been done on investigating the thermal behavior of composites. Thus, this paper intends to evaluate the thermal performance of a wheel hub developed using fiber-reinforced composite, during braking conditions in an ATV.

Keywords All-terrain vehicle · Composite · Thermal stresses · Wheel hub

Nomenclature

M	Gross weight of the vehicle
T	Time required for braking
U	Overall heat transfer coefficient
Y	Young's modulus
V	Velocity of the vehicle
W_d	Weight distribution of vehicle (front: Rear)

P. Kadambi · B. Prasad · P. Luniya (✉) · P. Kulkarni · S. T. Chavan · Y. G. Mane
School of Mechanical Engineering, MITWPU, Pune 411038, India
e-mail: pranayluniya16@gmail.com

Greek Symbols

α	Coefficient of linear expansion
σ_t, σ_c	Tensile strength, compressive strength
μ	Coefficient of friction

1 Introduction

Wheel assemblies used in automobiles consist of hub, knuckle, bearings, wheel hub and wheel usually integrated as unibody or part components.

A wheel hub is the mounting part for the wheel of a vehicle, housing the wheel bearings as well as supports the lugs. Knuckle and the hub assembly are used to provide support to the vertical load acting on the vehicle. The materials used for these components are mainly cast iron, mild steel, aluminum alloys, ductile iron and steel. However, with the growing demand of innovation in automotive technologies, reinforced composite structures need to be used to establish the feasibility of utilizing un-conventional materials by harnessing tools such as computer-aided design and engineering analysis [1]. In this study, we have considered carbon fiber (CF) and nylon-based continuous filament/fibers to additively manufacture a rear wheel hub of an all-terrain vehicle (ATV) and test it for performance characteristics. This continuous filament of carbon fiber is filled with nylon 6–6/nylon-12, which makes it 2.5 times stronger and stiffer than usual metallic materials like steel and aluminum [2, 3].

Since the wheel hub is subjected to both mechanical and thermal loads during braking, it is necessary to evaluate the thermal stresses, in order to understand its behavior to such hybrid loading conditions. Moreover, a comparative study has been established between metallic materials (Al-6061, E24 steel) and composites to illustrate the advantages of further research in this area.

2 Material Characteristics

Material selection for wheel hub is selected on the basis of properties such as tensile and compressive strength, resistance to axial, longitudinal and lateral loads due to the road surface (impact and gradual), fatigue behavior, machinability and ease of manufacturing. Based on this, commercially available materials for wheel hubs used for manufacturing are cast iron [4], wrought iron and mild steel [5]. However, in order to meet the objective of this research, CF+nylon-based fibers were the ideal choice to reduce weight, cost and their ability to modify and improve their properties

Table 1 Properties of CF+nylon continuous fibers [9]

Property	ρ (g/cm ³)	σ_t (MPa)	σ_c (MPa)	Y (GPa)	k (W/mK)	U (W/m ² K)	α (μ m/m ^o C)
Value	1.4	790	650	60	10.45	10	25

by additive manufacturing, allows the component to give the enhanced results [6–8]. Table 1 illustrates the material properties of CF+nylon-based continuous fibers utilized in additive manufacturing of a wheel hub.

3 Analytical Study

As mentioned above, this study analyzes the thermal characteristics and heat transfer through a CF+nylon-based wheel hub, during braking conditions in an ATV. During braking, heat is generated due to change in kinetic energy of the vehicle, which is converted to heat energy due to friction between the brake pad and brake rotor surface. Since the brake rotor is in contact with the rear part of the wheel hub, via bolted connections, some of the heat is transferred to the wheel hub via heat transfer methods such as conduction and convection [10].

This study aims to determine the thermal stresses induced in the rear section of wheel hub, due to the temperature variations, which can be a possible cause of failure of the component. The study involves some set of input variables (vehicle parameters, braking system properties), which were taken from the university’s BAJA vehicle (Tables 2 and 3).

Table 2 Vehicle characteristics and braking system properties

Parameter	Value
Vehicle characteristics	
M (kg)	200
V (km/hr)	60
W _d	4:6
Braking system properties	
T (in sec)	2.5
Deceleration rate (in g’s)	0.8
Brake rotor size (outer dia, inner dia) (in mm)	(140, 46)
μ	0.35
Brake rotor material	AL 7075-T6

Table 3 Brake rotor material characteristics

Property	ρ (g/cm ³)	σ_t (MPa)	Y (GPa)	k (W/mK)	U (W/m ² K)	α (μ m/m ^o C)
Value	3	560	70	130	25	23

In order to determine the maximum temperature which reaches on the surface of the wheel hub attached to the brake rotor due to the above mentioned braking parameters, can be given by a steady state-thermal analysis done on the brake rotor. As temperature reached after braking is low, therefore thermal properties varying over period of time can be neglected. Thermal analysis is also used to study temperature distribution during braking. This temperature distribution will yield the maximum temperature that reaches near the surface of the wheel hub and will help in determining the thermal stresses induced in the wheel hub.

For rear brake rotor,

Change in kinetic energy (KE)

$$\begin{aligned} \text{KE} &= \frac{1}{2} \times (MV^2) = \frac{1}{2} \times (200 \times (16.66)^2) \\ \text{KE} &= 27755.56 \text{ J} \end{aligned}$$

From the above mentioned weight distribution parameter

$$\begin{aligned} \text{Heat generated} &= 27755.56 \times 0.6 \times 0.5 \\ &= 8326.668 \text{ J} \end{aligned}$$

Area of rubbing surface

$$\text{Area} = \pi/4 \times (0.14^2 - 0.09^2) \times 2 = 0.07225 \text{ m}^2$$

Heat flux through the brake rotor

$$\begin{aligned} \text{Heat flux} &= \text{Heat generated/area of rubbing surface} \\ &\quad \times \text{braking time} \\ \text{Heat flux} &= 8326.668/0.07225 \times 2.5 \\ \text{Heat flux} &= 0.1904 \text{ W/mm}^2 \end{aligned}$$

Now in order to determine temperature distribution, analysis was carried out on ANSYS steady state thermal module (Figs. 1, 2, 3, 4 and 5).

As evident from the temperature profile, the temperature near the surface of the wheel hub is around ~40 °C. Hence, the thermal stresses can be calculated by

$$\text{Thermal stress} = FA = Y \times (L - L_o)/L_o$$

where

$$\text{Deflection} = (L - L_o)$$

$$L - L_o = \alpha \times (\Delta T),$$

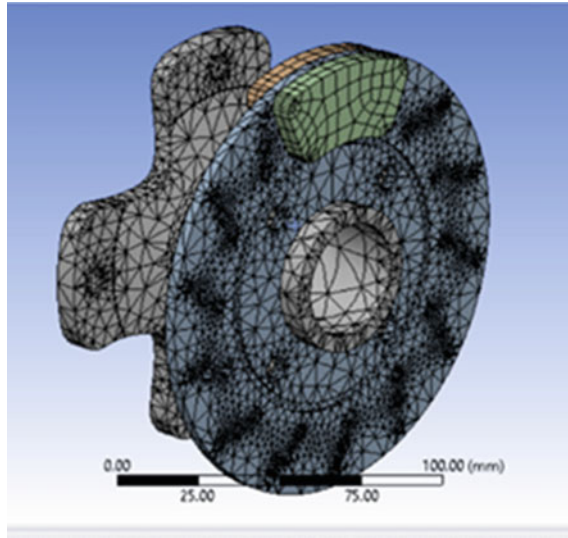


Fig. 1 Meshed view of components involved

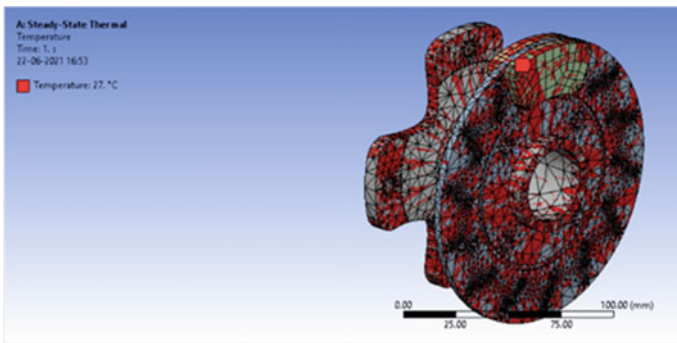


Fig. 2 Initial temperature set at 27 °C

where $\Delta T = T_{\max} - T_o$

$$T_{\max} = 40 \text{ }^\circ\text{C}, T_o = 27 \text{ }^\circ\text{C}, L_o = 0.006 \text{ m}$$

Hence, $\Delta T = 13 \text{ }^\circ\text{C}$.

This gives deflection as

$$\text{Deflection} = 25 \times (13) = 325 \times 10^{-6} \text{ m}$$

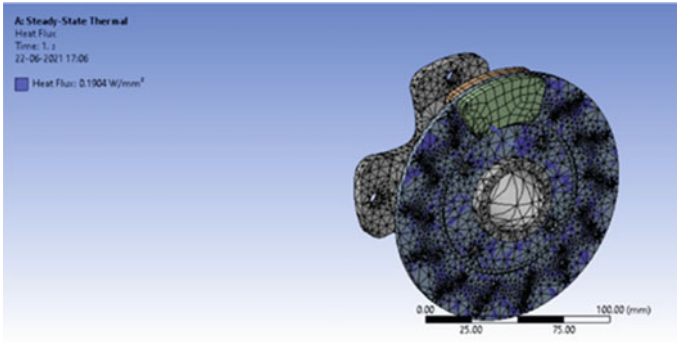


Fig. 3 Heat flux through the brake rotor surface

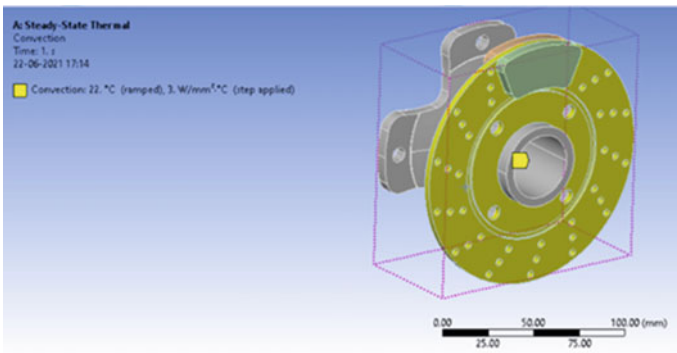


Fig. 4 Convection at the surface of brake rotor

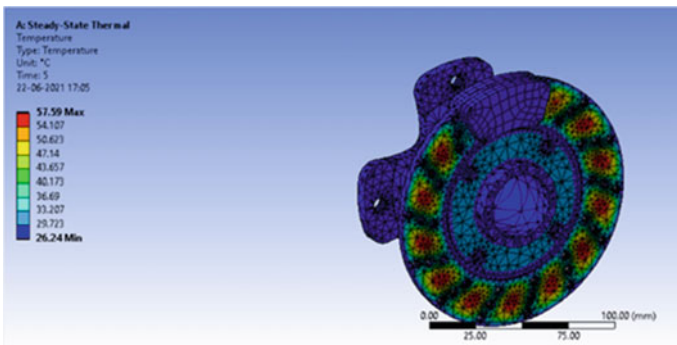


Fig. 5 Temperature distribution at the surface

Table 4 Properties of EN24 steel and AL-6061-T6

Parameter	EN24 steel	AL-6061-T6
Young's modulus (GPa)	190	68
Thermal conductivity (W/mK)	51.9	202
Coefficient of thermal expansion ($\mu\text{m/m } ^\circ\text{C}$)	13	23
Overall heat transfer coefficient ($\text{W/m}^2 \text{ K}$)	7.9	25

$$\text{Thermal stresses} = 60 \times 0.000325/0.006$$

$$\text{Thermal stresses} = 3.25 \text{ N/m}^2$$

4 Comparative Study

From the above analytical study, we were able to obtain thermal stresses induced in the wheel hub made of CF+nylon. In order to draw a significant inference from the study, a comparative analysis was done with stock materials used for wheel hubs commercially, to understand the difference of performance characteristics.

For this purpose, EN24 and AL-6061-T6 was used, whose properties have been enlisted below in Table 4.

Following the same procedure as in Sect. 3, the thermal stresses obtained for the stock materials were as follows

$$\text{Thermal stress(EN24 Steel)} = 5.35 \text{ N/m}^2$$

$$\text{Thermal stress(AL - 6061 - T6)} = 4.38 \text{ N/m}^2$$

5 Conclusion

After evaluating thermal stress-based results induced in the wheel hub during braking conditions, it can be concluded that wheel hubs made out of CF+Nylon can be a suitable material to avoid failure due to heat transferred from brake rotor to the hub. Moreover, with the rapid improvisation in manufacturing techniques, the ability to fabricate parts out of composite materials becomes more feasible. Even though, the difference between the magnitude of thermal stresses for CF+nylon and stock materials (steel and aluminum) is quite less for an ATV-based application, yet the study produces significant results and the potential to display better thermal performance in vehicles in which brake rotors temperatures can reach as high as $300 \text{ } ^\circ\text{C}$.

References

1. Poojari M, Kamarthi A, Shetty KK, Sanil AP, Palan KV (2019) Design and analysis of the wheel hub for an all-terrain vehicle with the plastic polymer: nylon-6,6. *J Mech Eng Res Dev* 42(5):119–123. <https://doi.org/10.26480/jmerd.05.2019.119.123>
2. Verma H, Kumar S, Singh R, Kumar R (2020) Design and development of the front wheel hub for all-terrain vehicle (ATV) 17(1):49–62
3. van de Werken N, Tekinalp H, Khanbolouki P, Ozcan S, Williams A, Tehrani M (2020) Additively manufactured carbon fiber-reinforced composites: state of the art and perspective. *Addit Manufact* 31. <https://doi.org/10.1016/j.addma.2019.100962>
4. Xiao B, Fan ZT, Jiang WM, Liu XW, Long W, Hu Q (2014) Microstructure and mechanical properties of ductile cast iron in lost foam casting with vibration. *J Iron Steel Res Int* 21(11):1049–1054. [https://doi.org/10.1016/S1006-706X\(14\)60182-5](https://doi.org/10.1016/S1006-706X(14)60182-5)
5. ‘Design and analysis of ATV rear wheel hub having light weight and high torque carrying capability 3(7):145–147 (2018)
6. Ibrahim Y, Elkholy A, Schofield JS, Melenka GW, Kempers R (2020) Effective thermal conductivity of 3D-printed continuous fiber polymer composites. *Adv Manuf: Polym Compos Sci* 6(1):17–28. <https://doi.org/10.1080/20550340.2019.1710023>. Taylor and Francis
7. Mohammadizadeh M, Fidan I (2019) Thermal analysis of 3d printed continuous fiber reinforced thermoplastic polymers for automotive applications. *Solid freeform fabrication 2019: proceedings of the 30th annual international solid freeform fabrication symposium—an additive manufacturing conference, SFF 2019*, pp 899–906
8. Sanei SHR, Popescu D (2020) 3d-printed carbon fiber reinforced polymer composites: a systematic review. *J Compos Sci* 4(3). <https://doi.org/10.3390/jcs4030098>
9. Calignano F, Lorusso M, Roppolo I, Minetola P (2020) Investigation of the mechanical properties of a carbon fibre-reinforced nylon filament for 3d printing. *Machines* 8(3):1–13. <https://doi.org/10.3390/machines8030052>
10. Talati F, Jalalifar S (2009) Analysis of heat conduction in a disk brake system. *Heat Mass Transfer/Waerme-und Stoffuebertragung* 45(8):1047–1059. <https://doi.org/10.1007/s00231-009-0476-y>

Estimation of Emissivity of the Surface Using Jaya Algorithm



Sanil Shah and Ajit Kumar Parwani

Abstract In this work, a one-dimension heat conduction problem has been considered with one of the boundary surfaces has been subjected to high temperature, while the other boundary surface is radiating in a vacuum whose emissivity is unknown. The unknown total hemispherical emissivity is estimated from the simulated temperature distribution of one-dimension opaque material by using the Jaya algorithm. Jaya algorithm is a stochastic algorithm that requires few parameters for its search operation and has been effective in solving inverse problems. The algorithm has been tested with different numbers and positions of sensors. The results indicate that the Jaya algorithm is an accurate and stable algorithm for the estimation of emissivity of opaque surfaces.

Keywords Emissivity · Inverse heat transfer · Jaya algorithm

Nomenclature

k	Thermal conductivity (W/mK)
L	Rod length (m)
M	Number of sensors
M_e	Radiant emittance (W/m ²)
n	Number of runs
P	Number of population
T	Temperature (K)
SD	Standard deviation

S. Shah · A. K. Parwani (✉)

Department of Mechanical and Aerospace Engineering, Institute of Infrastructure, Technology, Research and Management Ahmedabad, Ahmedabad, India

e-mail: ajitkumar.parwani@iitram.ac.in

Greek Symbols

ε	Hemispherical emissivity
σ	Stephen-Boltzmann constant ($\text{W/m}^2\text{K}^4$)

1 Introduction

In most high-temperature heat transfer processes, radiative heat transfer is the critical mode of heat transfer. Many industrial applications like boilers, furnaces, gas turbines, etc., due to their high-temperature applications are analysed by considering radiative heat transfer. Radiation is the surface phenomenon [1] and for designing any heat transfer equipment, proper knowledge of its radiative properties is essential. For heat transfer surfaces, hemispherical emissivity or emissivity (ε) is a critical property. It is defined as the ratio of radiation emission of that surface (M_e) to the radiation emission of the black body (M_{eb}) at the same temperature given by the following equation:

$$\varepsilon = \frac{M_e}{M_{eb}} \quad (1)$$

Estimation of emissivity is important for space applications, remote sensing satellites, solar applications, and other industrial applications [2]. Various methods are available for emissivity measurement [3] but all are based on the laboratory conditions. The main challenge in measuring emissivity is in situ measurement. For example, remote sensing satellites require the value of earth's surface emissivity, clouds' emissivity, and other objects' emissivity while travelling through the space to calculate other associated parameters for weather forecasting. It is next to impossible to measure emissivity directly, and hence, inverse methods are used for estimating for the same. Inverse heat transfer techniques (IHTT) are most widely used for estimating boundary heat flux, thermophysical properties, and radiative properties [4]. Firstly, the direct or forward heat transfer problem is solved with the known value of the quantity. IHTT uses the least square-based objective function consisting of the difference between measured temperatures and estimated temperatures by the inverse algorithm. All inverse algorithms are optimization-based algorithms. There are two main categories of inverse algorithms: stochastic and deterministic. Deterministic algorithms are gradient-based, while the stochastic method is search-based algorithms. Many researchers used deterministic, stochastic, and combination of both (called hybrid) for solving several inverse problems [5–7].

The current work focuses on estimating the emissivity of a grey surface for a one-dimensional heat conduction problem by using the newly developed Jaya algorithm. Jaya is a population-based algorithm or stochastic method developed by Rao

[8]. It has a simple structure and is used for solving several optimization problems [9, 10]. This algorithm is successfully implemented for estimating the thermal contact conductance between two bars as well as between two periodically contacting surfaces [11]. Also, it can be used as an enhancement algorithm for the deterministic algorithm like the traditional conjugate gradient method [12]. In the current work, the steady-state one-dimensional heat conduction-radiation problem is considered. The left boundary has a high temperature, while the right boundary is emitting radiation in a vacuum. The emissivity of the right boundary is estimated by the Jaya algorithm. The effect of the number of sensors and the effect of population size have been considered in the current analysis.

2 Problem Description

Figure 1 shows a one-dimensional rod having a length $L = 100$ mm. The rod is insulated from top and bottom, and heat can only be transferred in one direction. The left boundary has a high temperature while the right boundary is emitting heat by radiation in the vacuum.

The governing steady-state one-dimensional heat transfer equation is given by

$$\frac{\partial^2 T}{\partial x^2} = 0 \tag{2}$$

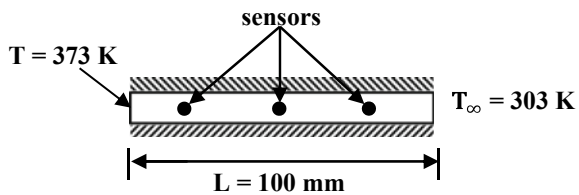
Subjected to following boundary conditions

$$T = 373 \text{ K at } x = 0 \tag{2a}$$

$$-k \frac{\partial T}{\partial x} = \sigma \varepsilon (T^4 - T_\infty^4) \text{ at } x = L \tag{2b}$$

where k and σ are the material thermal conductivity and the Stephen-Boltzmann constant, respectively, the values of which are taken as 385 W/mK and 5.67×10^{-8} W/m²K⁴, respectively. The value of vacuum temperature T_∞ is considered as 303 K. The sensors are shown in Fig. 1 used for measuring the temperatures at a

Fig. 1 Computational domain



particular location. Those measured temperature values are used in the Jaya algorithm for the estimation of emissivity.

Jaya algorithm The Jaya algorithm minimizes the least square-based objective function given by

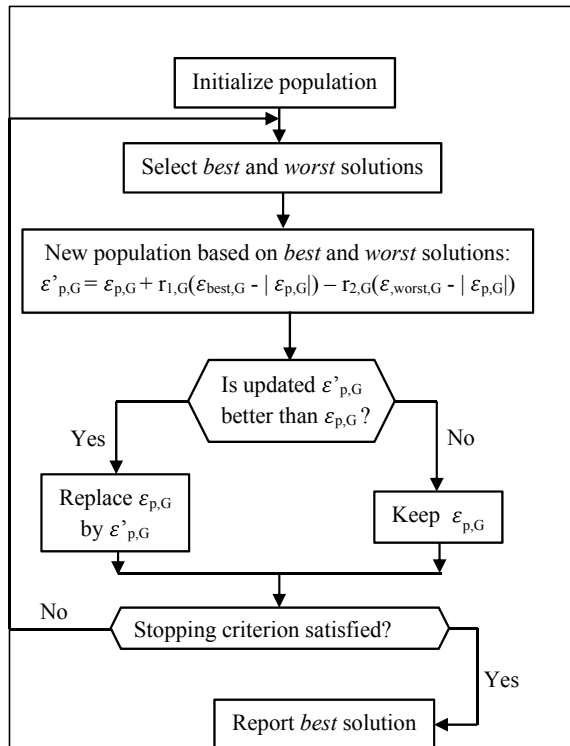
$$J(\varepsilon) = \sum_{m=1}^{m=M} (T_a(m) - T_e(m))^2 \tag{3}$$

where M is the number of sensors, T_a is measured temperature, and T_e is estimated temperature. To minimize the objective function $J(\varepsilon)$, Jaya uses the following computational algorithm as shown in Fig. 2.

Assuming at a particular generation (G), there is P number of populations ($p = 1, 2, \dots, P$). Let the *best* candidate gives the best value of the objective function, and the *worst* candidate gives the worst value of the same. If $\varepsilon_{p,G}$ is the value of p th candidate during G th generation, then this value is modified according to the following equation:

$$\varepsilon'_{p,G} = \varepsilon_{p,G} + r_{1,G}(\varepsilon_{best,G} - |\varepsilon_{p,G}|) - r_{2,G}(\varepsilon_{worst,G} - |\varepsilon_{p,G}|) \tag{4}$$

Fig. 2 Jaya algorithm



where $\varepsilon'_{p,G}$ is updated value of variable $\varepsilon_{p,G}$, $\varepsilon_{best,G}$, and $\varepsilon_{worst,G}$ are *best* and *worst* solutions at given population. Here, $r_{1,G}$ and $r_{2,G}$ are random numbers during G th generation and their range is $[0, 1]$. The algorithm terminates once the value of an objective function reaches beyond the particular value. This is called termination criterion which is given by

$$J(\varepsilon) < \Delta \tag{5}$$

where Δ is a small value. For the current analysis, it is taken as 10^{-8} .

3 Results and Discussion

Figure 3 shows the effect of population on the performance of the Jaya algorithm. Total five ($M = 5$) sensors are used where the distance between each sensor is 20 mm. The accuracy of the algorithm is measured from statistical analysis where first the algorithm is tested for 20 runs (n), and then, the standard deviation of that data is determined from the following equation:

$$SD = \sqrt{\frac{\sum(\varepsilon_m - \varepsilon_{est})^2}{n}} \tag{6}$$

where ε_m is the mean emissivity which is actual emissivity for this case and ε_{est} is the estimated emissivity at a given run and n is the total number of runs. From Fig. 3, it is clear that the Jaya algorithm accuracy increases with the population. The algorithm has maximum SD for $P = 20$ ($SD = 0.02927$) and minimum for $P = 80$ ($SD = 0.00665$).

The number of sensors (M) also has an influence on the accuracy of the algorithm. Figure 4 shows the performance of the Jaya algorithm at the different number of sensors with $P = 80$. Two, three, and five sensors are used. Two sensors ($M = 2$) are located at 30 mm and 70 mm from the left boundary, while the other three (M

Fig. 3 Performance of Jaya algorithm at different populations (P)

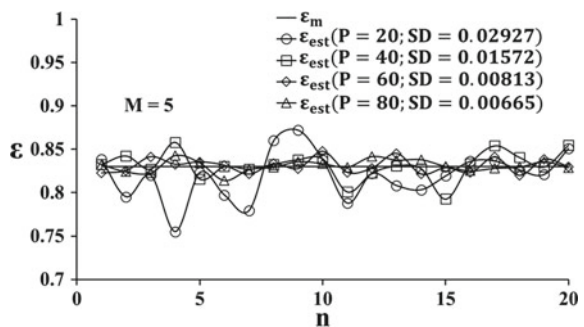
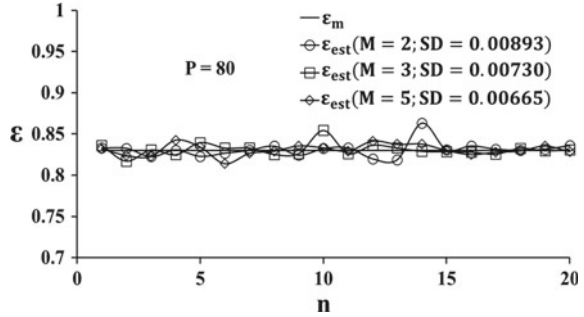


Fig. 4 Performance of the Jaya algorithm with different number of sensors (M)



= 3) sensors are located at 30 mm, 60 mm, and 90 mm from the left boundary. From Fig. 4, the performance of the algorithm increases with the number of sensors. The maximum accuracy found with $M = 5$ ($SD = 0.00665$), and minimum accuracy found with $M = 2$ ($SD = 0.00730$).

4 Conclusions

Hemispherical emissivity (ϵ) of grey surface for transient one-dimensional heat conduction problem has been estimated by newly developed stochastic Jaya algorithm. The performance of the Jaya algorithm has been verified by statistical analysis where the standard deviation (SD) of estimated emissivity is derived from the particular number of algorithm runs. The effect of number of population (P) and the number of sensors (M) on the performance of the Jaya algorithm is checked. The performance of the Jaya algorithm increases with population. Also, the algorithm’s accuracy increases with the number of sensors.

Acknowledgements This work is supported by the grant of SERB division, Department of Science and Technology, Government of India, and the authors greatly appreciate the financial contribution towards this research.

References

1. Incropera FP, Dewitt DP, Bergman TL, Lavine AS (2007) Fundamentals of heat and mass transfer. Wiley
2. Balaji C (2014) Essentials of radiation heat transfer. Wiley
3. Zhu C, Hobbs MJ, Willmott JR (2020) An accurate instrument for emissivity measurements by direct and indirect methods. Meas Sci Technol 31(044007)
4. Ozisik MN, Orlande HRB (2000) Inverse heat transfer: fundamentals and applications. Taylor and Francis, New York
5. Huang CH, Ozisik MN (1992) Inverse problem of determining unknown wall heat flux in laminar flow through parallel plate duct, Numer. Heat Transfer A 21:55–70

6. Parwani AK, Talukdar P, Subbarao PMV (2013) Simultaneous estimation of strength and position of heat source in participating medium using DE algorithm. *J Quant Spectrosc Radiat Transf* 127:130–139
7. Parwani AK, Talukdar P, Subbarao PMV (2013) Performance evolution of hybrid differential evolution approach for estimation of the strength of heat source in a radiatively participating medium. *Int J Heat Mass Transfer* 56:552–560
8. Rao RV (2016) Jaya: a simple and new optimization algorithm for solving constrained and unconstrained optimization problems. *Int J Ind Eng Computations* 7:19–34
9. Rao RV, Rai DP, Ramkumar J, Balic J (2016) A new multi objective Jaya algorithm for optimization of modern machining processes. *Adv Prod Eng Manag* 11:271–286
10. Rao RV, Saroj A (2017) Constrained economic optimization of shell-and-tube heat exchangers using elitist-Jaya algorithm. *Energy* 128:785–800
11. Parikh M, Shah S, Vaghela H, Parwani AK (2021) A comprehensive experimental and numerical estimation of thermal contact conductance. *Int J Therm Sci* 172(107285)
12. Shah S, Parwani AK (2020) Estimation of time-varying heat flux for one-dimensional heat conduction problem by hybrid inverse method. In: Parwani A, Ramkumar P (eds) *Recent advances in mechanical infrastructure*

Development of an Empirical Model for the Prediction of Thermoelectric Behavior of Lithium Iron Phosphate Pouch Cell Under Different Discharge Rates



Indraneel Naik, Pravin Nemade, and Milankumar Nandgaonkar

Abstract Broader adoption of electric vehicles is still facing barriers. When subjected to larger electric current, batteries cause high internal heat generation and thus are subjected to high temperature, impacting their performance, life and safety. Thermal management systems are in place to control the battery temperature in such scenarios. They should be optimized for the current demand; since they exert an additional burden on the overall system. This paper experimentally investigates the effect of varying electric current on the battery's thermal and electrical performance. Doubling the discharge rate is found to more than double the temperature rise and quadruple the temperature rise rate. The transient voltage profile drops, and hence energy delivered decreases by 3%. This paper proposes an empirical model for gaging the battery's thermal and electrical performance sensitivity toward varying discharge rates and optimizing the thermal management system accordingly. The inputs for the model are derived from the galvanostatic discharge test, and the model validation is carried out from a constant-current discharge test. The establishment of the model provides a promising way of optimizing battery thermal management systems considering their impact on the overall powertrain's performance, life, safety and cost.

Keywords Lithium-ion battery · Empirical model · Thermoelectric performance · Electric vehicles · Thermal management system

Nomenclature

BMS	Battery management system
CC	Constant current
DoD	Depth of discharge
EV	Electric vehicle
HEV	Hybrid electric vehicles

I. Naik (✉) · P. Nemade · M. Nandgaonkar
College of Engineering Pune, Pune, India
e-mail: indraneelnaik26@gmail.com

LFP	Lithium iron phosphate
OCV	Open-circuit voltage
PHEVs	Plug-in hybrid electric vehicles
SEI	Solid electrolyte interface

Symbols

A	Surface area m^2
C	Specific heat capacity $[J/kg.K]$
DoD	Depth of discharge –
h	Convective coefficient W/m^2K
I	Discharge current A
m	Mass of the cell kg
η	Overpotential mV
Q_T	Total theoretical cell capacity Ah
q_{gen}	Heat generated per second W
q_{sink}	Heat removed per second W
T	Temperature K
T_{ref}	Reference temperature, 298 K
U	Open-circuit voltage $[kg \cdot m^2 \cdot s^{-3} \cdot A^{-1}]$
Y	Conductance $[kg^{-1} \cdot m^{-2} \cdot s^3 \cdot A^2]$

1 Introduction

EVs are taking over the automotive market. The rate of increase in the total number of on-road EVs over the last couple of years is appreciable (*Global EV Outlook-2019, Scaling up the transition to electric mobility, IEA Technology report—May 2019*, 2019). The rising popularity of the EVs is not just because of their “zero tailpipe emissions” tag. Due to the low cost/ km of EVs, rising prices and scarcity of conventional fuels, government policies, lesser noise and vibration leading to lower discomfort, the pure EVs, HEVs, PHEVs will be some of the most sustainable options in the mobility sector [1]. The recent technology advancements combine IoT with existing EV architecture that has revolutionized the mobility concept all over the globe. The full-fledged implementation of EVs is still facing resistance, the root cause of which can be traced down to the temperature sensitivity of the battery affecting its performance, life and safety. These, in turn, affect the total cost of ownership of an EV, including the cost of purchase, operation and maintenance that raises a question on the viability of EVs as a pocket-friendly option. This paper takes an overview of the factors that affect the performance of the battery, which amounts to the majority of the cost of an EV and proposes guidelines to model the

battery to optimize the performance of a battery thermal management system that essentially improves the performance, life and safety of the battery.

The implementation of EVs is yet to occur since some roadblocks need to be addressed, such as battery replacement cost, charging infrastructure, power deliverable and single charge range [2]. In developing nations like India, which need to cater to the mobility requirements of millions of people, also meeting the “Go-Green” goals, the cost of EV is of primary concern. Though EV’s running cost/km is far less than conventional alternatives, the battery replacement cost eliminates all the advantages gained [3]. Improvement in battery performance and life can be brought about by maintaining the battery temperature within a band of 25–40 °C. Researchers worldwide are striving to devise innovative and cost-effective methods of battery thermal management [4, 5]. Higher power demands higher discharge rates, which leads to higher heat generation in the batteries, which eventually takes their temperature off the limit [6]. The estimate the impact of higher discharge current modeling the battery becomes a crucial option.

It has been shown that high temperatures can affect the cycle life of the batteries [7]. They can cause an increase in the interface and SEI layer’s charge transfer resistance and at times, an increase in the electrode and electrolyte resistance or inhomogeneous distribution or diffusion of lithium ions, etc. The calendar life of the battery is also affected at high temperatures [4]. Thermal aging permanently reduces the electrode’s capacity to hold lithium ions due to intercalation [8]. High temperatures can lead to thermal runaway phenomena posing a fire hazard risk to the occupants [9]. Thus, a careful estimation of the effect of discharge rate of the thermal and electrical performance of the battery is essential considering the performance, life, safety and cost implications.

This paper demonstrates an empirical model to assess the impact of load on the thermal and electrical performance of 30Ah LiFePO₄ cell. The structure of the model is as follows.

- (i) Input parameters:
 - a. Operating parameters: Discharge profile
 - b. Electrochemical parameters: Overpotential resistance, open-circuit voltage
- (ii) Output performance parameters: Cell temperature, cell voltage

The model can optimize the battery thermal management system’s design. This study can act as a guideline for modeling any battery chemistry or shape variations.

2 Experimentation

This section details the experimental test setup and the procedure followed to obtain various thermal and electrical parameters of the battery used in this work.

Test setup The cell is cycled at different discharge rates on a charger-electronic load combination from ITECH. The charger configuration is 80 V, 40A and that for

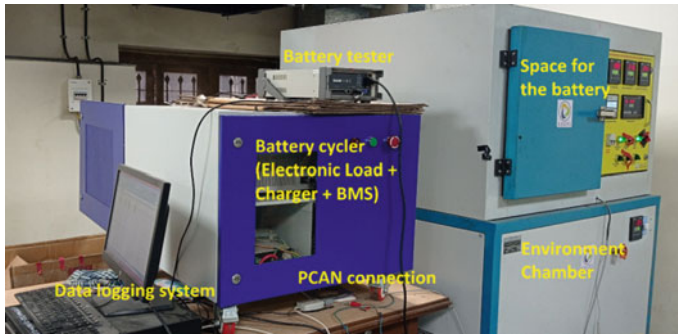


Fig. 1 Test facility for the investigation of battery thermal and electrical performance

an electronic load is 120 V, 240 A. The voltage sensors have an accuracy of ± 1 mV, and that for temperature sensors is ± 0.1 °C. This work utilizes LFP pouch geometry cell with a capacity of 30Ah, 3.2 V nominal. The cell's dimensions are 173 mm \times 138 mm \times 12 mm, and the cell's mass is 600 g. The environmental chamber is glycol cooled. It is provided with an internal air circulation fan to maintain spatial temperature uniformity. It is a calorimetric chamber with a volumetric capacity of 125 L and has a facility to maintain a constant temperature with an accuracy of ± 1 °C. It is used for maintaining an ambient for the cell to a reference temperature of 25 °C throughout the tests conducted. The environmental chamber and battery cycler are both connected to a data logging system (Fig. 1).

The setup is used to experimentally estimate the electrochemical characteristics of the LFP cell and output thermoelectric performance parameters. The procedure to obtain the input and output parameters experimentally is as follows.

Test procedure The intermittent discharge test: The electrochemical parameters corresponding to given cell chemistry are initially evaluated. The cell is maintained at an ambient of 25 °C. A galvanostatic discharge test [10] is carried out where the discharge current is kept very low (0.2C), and the discharge is stopped after time intervals. This process continues until the end of the discharge is reached, defined as the cell voltage reaching a lower cutoff of 2.7 V. A low discharge current ensures that the temperature of the cell stays very near to the ambient temperature. When the discharge is stopped, the chemical reactions inside the cell come to equilibrium after being given a sufficient time [11]. The voltage across the electrodes thus reaches a theoretical value called open-circuit voltage (OCV) [12]. Thus, a curve of OCV Vs. time can be obtained. This procedure also helps in evaluating the overpotential [13]. These electrochemical parameters will be explained in the results and discussion section. The electrochemical parameters are then supplied to the model that will be developed in the model establishment section. The outputs of the model are then validated against the experimental results. The cells are fully charged, and then, a continuous CC discharge test [14] is carried out at an ambient temperature of 25 °C with varying discharge rates. The voltage versus time and temperature versus time discharge profiles of the cell assist in evaluating the thermoelectric performance. A

comparison between experimental results and the model output parameters is made in the results and discussion section.

3 Model Establishment

This section elaborates on the relationship between output performance parameters and input parameters. The first output performance parameter is the cell voltage, which depends on electrochemical characteristics of the cell and the discharge current profile and hence can be linked to them through the following equation [15].

$$V = U - \frac{I}{Y} \quad (1)$$

The cell electrochemistry parameters, Y and U can be expressed as polynomial functions as below [16, 17],

$$Y = \left[\sum_{n=0}^5 b_n (\text{DoD})^n \right] \quad (2)$$

$$U = \left[\sum_{n=0}^5 a_n (\text{DoD})^n \right] \quad (3)$$

The coefficients used in these polynomials, namely a_1 to a_5 , b_1 to b_5 are specific to the cell chemistry as specified in Tables 1 and 2. DoD indicates the depleted fraction of the Q_T at T_{ref} [18].

$$\text{DoD} = \frac{\int_0^t I dt}{Q_T} \quad (4)$$

The cell temperature which can be given by heat balance equation considering lumped capacity analysis as [19]

Table 1 Coefficients of OCV polynomial (as per Eq. 3)

Coefficients	Values
a_0	3.367
a_1	-1.154
a_2	6.84
a_3	-17.97
a_4	20.756
a_5	-8.751

Table 2 Coefficients of Y polynomial (as per Eq. 2)

e	Value
b ₀	253.71
b ₁	-2315.02
b ₂	11,707.62
b ₃	-25,588.8
b ₄	25,024.93
b ₅	-9047.12

$$mC \frac{dT}{dt} = \dot{q}_{\text{gen}} - \dot{q}_{\text{sink}} \quad (5)$$

' mC ' denotes the lumped heat capacity of the cell. The rate of heat generation during discharge given as [20]

$$q_{\text{gen}} = I(U - V) = \frac{I^2}{Y} \quad (6)$$

For convection heat transfer mode, \dot{q}_{sink} can be given as

$$\dot{q}_{\text{sink}} = hA(T - T_{\text{surr}}) \quad (7)$$

With these model equations, the effect of discharge current on thermal and electrical performance can be estimated.

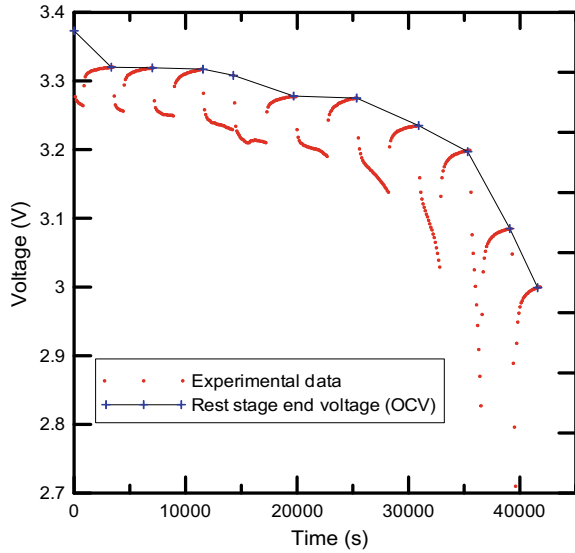
4 Results and Discussion

This section describes the dependence of thermal and electrical parameters on the discharge rate of the battery.

Discharge profile Discharge profile reflects the load profile of the application. Based on the power requirement, a particular discharge current is drawn from the battery. In current work, two types of tests have been carried out, viz. intermittent discharge test and a CC discharge test. The intermittent discharge test involved low current (0.2C) intermittent discharge for 10% decrease in DoD followed by 2700 s rest time and successive repetition until the cell voltage is 2.7 V. The CC discharge test involved a constant current of 1C, 1.5C and 2C until the cell voltage is 2.7 V.

Open-circuit voltage Open-circuit voltage (OCV) is defined as the theoretical maximum voltage across the cell's electrodes when the cell is open-circuited [21]. There are different methods of finding open-circuit voltage. One is the intermittent discharge method when the cell is discharged with a 0.2C rate intermittently. As explained in the experimentation section, the discharge is stopped after every 10% DoD level. A rest period is provided so that the chemical reactions inside the

Fig. 2 Open-circuit voltage from intermittent discharge test



cell stabilize, and the voltage across the electrodes reaches theoretical open-circuit voltage (Fig. 2).

The open-circuit voltage data is extracted from this curve, and the reference is changed from time to DoD using the current discharge profile.

A 2D regression analysis [12] performed on the open-circuit voltage Vs DoD curve gives the coefficients of OCV polynomial in Eq. (3) as specified in Table 1.

Overpotential Overpotential is the difference between the theoretical open-circuit voltage and actual voltage that appears across the battery terminals when in use [22]. The overpotential represents the loss of energy, which reflects the battery’s heat generation. Overpotential loss can be accounted for three primary reasons: activation overpotential, concentration overpotential and ohmic overpotential [23]. A curve of overpotential versus DoD can be obtained as follows.

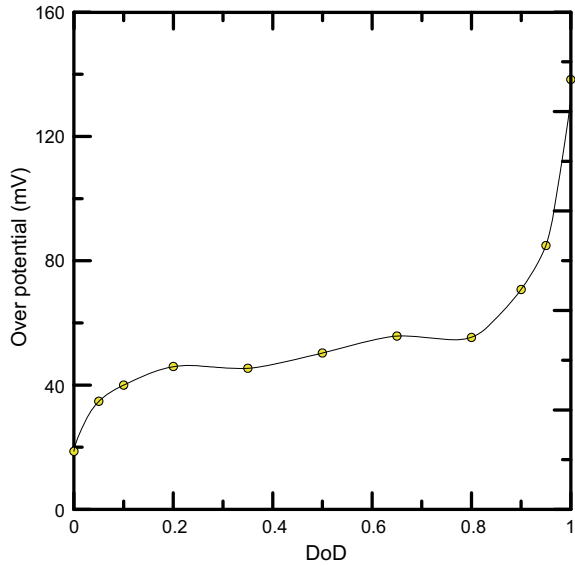
Regression analysis is then performed on the overpotential Versus DoD curve obtained. The relationship between overpotential and coefficient Y can be obtained by modifying Eq. (1) as (Fig. 3)

$$Y = \frac{I}{(U - V)} \tag{8}$$

The coefficients of Y so obtained can then be supplied to the model. Using these coefficients in the model, the thermal and electrical performance of the cell can be evaluated, as shown in the model establishment section.

Thermal behavior Thermal performance directly impacts electrical performance, battery life and safety [24]. Hence, it is essential to study the impact of the discharge current on the thermal profile of the battery. Sophisticated battery thermal management systems are in place to control the thermal fluctuations due to load and ambient

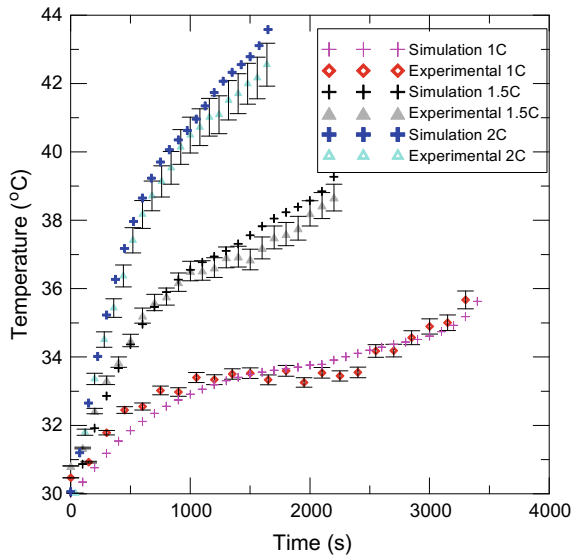
Fig. 3 Overpotential versus DoD obtained at a 0.2C rate



conditions. But the operation of these systems has associated costs and hence needs to be optimally designed, which can be possible through modeling the same.

Figure 4 shows a comparison of thermal profiles at varying discharge rates between the experimental and modeling results, which shows an error of about 5%.

Fig. 4 Temperature versus time at varying discharge rates



Electrical performance The difference of potential between the cathode and anode when the cell is in use is the cell’s voltage. It is an electrical parameter of fundamental importance, considering its role in determining the battery’s electrical performance. It can be utilized to estimate the power delivery, charge storage capacity, energy storage and battery efficiency [25, 26]. As can be seen from Eq. (1) that the voltage depends on the electrochemical parameters and discharge current rate. For the given electrochemistry of the cell, the voltage drops with increasing discharge current as shown in Fig. 4.

Figure 5 shows a comparison between experimental and simulation results. The error between the experimental and simulation results is found to be < 5%. The charge and energy delivered by the battery can be defined as (Table 3)

$$CapacityAh = \int_{V=V_{init}}^{V=V_{min}} Idt \tag{9}$$

$$Energydelivered = \int_{V=V_{init}}^{V=V_{min}} VIdt \tag{10}$$

Fig. 5 Voltage versus time discharge characteristics for varying discharge rate

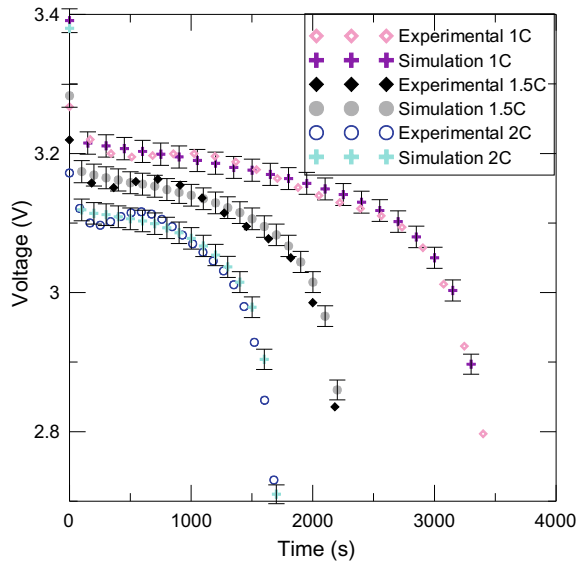


Table 3 Coefficients of Y polynomial

Discharge rate	Charge delivered (Ah)	Energy delivered (Wh)
1C	28.50	88.58
1.5C	28.43	87.42
2C	28.35	85.91

Thus, the discharge rate has an adverse impact on the charge and energy deliverable by the battery.

5 Conclusion

The discharge rate affects the thermoelectric behavior of the battery. Increasing the discharge rate decreases the battery voltage and thus affects the performance parameters such as battery charge capacity, energy storage and power delivery. Increasing the discharge rate increases the rate of temperature rise of the battery, which has proved to decrease battery life and hamper safety. Modeling the functional relationship between discharge rate and battery's thermoelectric performance has assisted in optimization and hence can significantly reduce the cost of operation of battery thermal management system. This work can thus serve as a guideline for a thermal management system's designer to optimize its performance and reduce its burden on overall EV economics.

Acknowledgements Funding This work was supported by the All India Council for Technical Education (AICTE), India. [Grant number: 8-23/RIFD/RPS-NDF/Policy-1/2018-19].

Conflicts of Interest/Competing Interests The authors declare that they have no known competing financial interests or personal relationships that could have appeared to influence the work reported in this paper.

References

1. Wang Q et al (2016) A critical review of thermal management models and solutions of lithium-ion batteries for the development of pure electric vehicles. *Renew Sustain Energy Rev.* 64:106–128. <https://doi.org/10.1016/J.RSER.2016.05.033>. Pergamon
2. Scrosati B, Garche J, Tillmetz W (2015) Advances in battery technologies for electric vehicles. *Advan Battery Technol Electric Veh.* <https://doi.org/10.1016/c2014-0-02665-2>
3. Diao W et al (2019) Algorithm to determine the knee point on capacity fade curves of lithium-ion cells. *Energies.* MDPI AG 12(15). <https://doi.org/10.3390/en12152910>.
4. Kim J, Oh J, Lee H (2019) Review on battery thermal management system for electric vehicles. *Appl Therm Eng* 192–212. <https://doi.org/10.1016/j.applthermaleng.2018.12.020>. Elsevier Ltd
5. Wu W et al (2019) A critical review of battery thermal performance and liquid based battery thermal management. *Energy Convers Manage.* <https://doi.org/10.1016/j.enconman.2018.12.051>
6. Siruvuri SDVSSV, Budarapu PR (2020) Studies on thermal management of Lithium-ion battery pack using water as the cooling fluid. *J Energy Storage.* 29:101377. <https://doi.org/10.1016/j.est.2020.101377> Elsevier Ltd
7. Wu W, Wu W, Wang S (2017) Thermal optimization of composite PCM based large-format lithium-ion battery modules under extreme operating conditions. *Energy Convers Manage.* 153:22–33. <https://doi.org/10.1016/j.enconman.2017.09.068>. Elsevier Ltd
8. Viswanathan VV et al (2010) Effect of entropy change of lithium intercalation in cathodes and anodes on Li-ion battery thermal management. *J Power Sources.* <https://doi.org/10.1016/j.jpowsour.2009.11.103>

9. Yunyun Z et al (2014) Heat dissipation structure research for rectangle LiFePO₄ power battery. *Heat Mass Transfer/Waerme- und Stoffuebertragung*. <https://doi.org/10.1007/s00231-013-1284-y>
10. Zhang J et al (2014) Comparison and validation of methods for estimating heat generation rate of large-format lithium-ion batteries. *J Therm Anal Calorim*. 447–461. <https://doi.org/10.1007/s10973-014-3672-z>. Kluwer Academic Publishers
11. Wang CH et al (2015) Temperature response of a high power lithium-ion battery subjected to high current discharge. *Mater Res Innovations*. S2156–S2160. <https://doi.org/10.1179/1432891715Z.0000000001318>. Maney Publishing
12. He H, Xiong R, Guo H (2012) Online estimation of model parameters and state-of-charge of LiFePO₄ batteries in electric vehicles. *Appl Energy*. <https://doi.org/10.1016/j.apenergy.2011.08.005>
13. Huang X et al (2018) A dynamic capacity fading model with thermal evolution considering variable electrode thickness for lithium-ion batteries, *Ionics*. *Institute Ionics* 24(11):3439–3450. <https://doi.org/10.1007/s11581-018-2476-8>
14. Lv H, Huang X, Liu Y (2020) Analysis on pulse charging–discharging strategies for improving capacity retention rates of lithium-ion batteries. *Ionics* 26(4):1749–1770. <https://doi.org/10.1007/s11581-019-03404-8>. Springer
15. Tang Y et al (2018) Study of the thermal properties during the cyclic process of lithium ion power batteries using the electrochemical-thermal coupling model. *Appl Thermal Eng*. 137(3):11–22. <https://doi.org/10.1016/j.applthermaleng.2018.03.067>. Elsevier
16. Samba A et al (2014) Development of an advanced two-dimensional thermal model for large size lithium-ion pouch cells. *Electrochimica Acta*. <https://doi.org/10.1016/j.electacta.2013.11.113>
17. Sheng L et al (2019) An improved calorimetric method for characterizations of the specific heat and the heat generation rate in a prismatic lithium ion battery cell. *Energy Convers Manag* 180:724–732. <https://doi.org/10.1016/J.ENCONMAN.2018.11.030>. Pergamon
18. Han X, Huang Y, Lai H (2019) Electrochemical-thermal coupled investigation of lithium iron phosphate cell performances under air-cooled conditions. *Appl Therm Eng*. 147(August 2018):908–916. <https://doi.org/10.1016/j.applthermaleng.2018.11.010>. Elsevier
19. Feng X et al (2015) Thermal runaway propagation model for designing a safer battery pack with 25 Ah LiNi_xCo_yMn_zO₂ large format lithium ion battery. *Appl Energy*. <https://doi.org/10.1016/j.apenergy.2015.04.118>
20. Panchal S et al (2016) Experimental and theoretical investigations of heat generation rates for a water cooled LiFePO₄ battery. *Int J Heat Mass Transf* 101:1093–1102. <https://doi.org/10.1016/j.ijheatmasstransfer.2016.05.126>
21. Özdemir T et al (2021) Experimental assessment of the lumped lithium ion battery model at different operating conditions. *Heat Transf Eng* 1–16. <https://doi.org/10.1080/01457632.2021.1874666>. Taylor and Francis Ltd
22. Sun J et al (2015) Online internal temperature estimation for lithium-ion batteries based on Kalman filter. *Energies* 8(5):4400–4415. <https://doi.org/10.3390/en8054400>. MDPI AG
23. Ovejas VJ, Cuadras A (2019) State of charge dependency of the overvoltage generated in commercial Li-ion cells. *J Power Sources*. 418:176–185. <https://doi.org/10.1016/j.jpowsour.2019.02.046>. Elsevier B.V.
24. Xu X et al (2020) Integrated energy management strategy of powertrain and cooling system for PHEV. *Int J Green Energy* 17(5):319–331. <https://doi.org/10.1080/15435075.2020.1731516>. Taylor and Francis Inc
25. Shabani B, Biju M (2015) Theoretical modelling methods for thermal management of batteries. *Energies*. MDPI AG 10153–10177. <https://doi.org/10.3390/en80910153>
26. Wang Q et al (2014) Experimental investigation on EV battery cooling and heating by heat pipes. *Appl Therm Eng*. <https://doi.org/10.1016/j.applthermaleng.2014.09.083>
27. Global EV outlook-2019, scaling up the transition to electric mobility, IEA technology report—May 2019 (2019) *Global EV Outlook 2019*. <https://doi.org/10.1787/35fb60bd-en>

Application of Artificial Neural Network to Predict Effective Thermal Conductivity of Porous Foam Structure



Vipul M. Patel, Harsh Kumar, and Kuldeep Singh

Abstract In the present work, a combined conduction-radiation-based numerical model is developed to investigate the effect of porosity, solid phase thermal conductivity, and average temperature of the medium on effective thermal conductivity of the idealized porous foam structure. A tetrakaidecahedra unit cell structure is considered as a representative cell for an open-cell porous foam. The voxel information of solid and fluid media is stored using blocked-off region approach. The results obtained for more than 240 simulations are used to train artificial neural network (ANN). The trained network is employed to predict the effective thermal conductivity (k_{eff}) and found to capture linear and nonlinear variation of k_{eff} with porosity, thermal conductivity of solid, temperature gradients, and solid wall temperature.

Keywords Open-cell foam · Combined heat transfer · Tetrakaidecahedra cell structure · Machine learning · ANN

Nomenclature

<i>ANN</i>	Artificial neural network
<i>BR</i>	Bayesian regularization
<i>G</i>	Incident radiation ($W = m^2$)
<i>I</i>	Radiation intensity ($W = m^2\text{sr}$)
<i>k</i>	Thermal conductivity ($W = mK$)

V. M. Patel (✉)

Department of Mechanical Engineering, Sardar Vallabhbhai National Institute of Technology
Surat, Surat, Gujarat, India

e-mail: vipul.mech140@gmail.com

H. Kumar

Centre for Automotive Research and Tribology (CART), IIT Delhi, New Delhi, India

K. Singh

Gas Turbine and Transmission Research Centre (G2TRC), University of Nottingham,
Nottingham, UK

L	Length of the computational domain (m)
q	Heat flux ($W = m^2$)
\vec{r}	Position vector (m)
\hat{s}	Direction vector for radiation intensity
T	Temperature (K)

Greek Symbols

ΔT	Temperature difference (K)
σ	Stefan Boltzmann constant ($5.67 \times 10^{-8} W/m^2K^4$)
Φ	Porosity
Ω	Solid angle, (sr)

Subscripts

avg	Average
b	Blackbody
cond	Conduction
eff	Effective
E	Pertaining to 'East' boundary
f	Fluid
face	Solid–fluid interface
R	Radiation
s	Solid

1 Introduction

The open-cell porous foam can be envisioned as a potential candidate for heat transfer applications due to its attractive properties such as high tortuous flow path, high surface area to volume ratio, and moderately high thermal conductivity. In literature, porous foams are tested for different applications such as compact heat exchanger, fire retardants, radiant burner, and porous media combustion. Convection to radiation converter is also one of the novel applications of porous foam. In order to meet the designed condition, beforehand knowledge of effective thermos-physical properties of porous media is essential. The evaluation of thermal characteristics of porous foam can be performed by either experimental or numerical investigation. Due to complex morphology of foam structure, the analytical solution is impossible to achieve. The numerical investigation can be broadly classified into (i) pore-level

simulation on actual structure obtained using CT scan images, (ii) pore-level simulation on representative unit cell structure, and (iii) homogeneous medium approach (HMA). Among these, the pore-level simulation on actual foam structure is computationally more expensive and demands dedicated computational resources. The pore-level simulation on representative foam structure is comparatively less expensive as compared to the previous one. However, reliability of the evaluated performance depends on the selection of representative unit cell structures. In open literature, the porous foam is idealized as cubic unit cell structure with and without lump [1], Viskanta's unit cell (spherically voided cubic cell) [1], tetrakaidecahedra cell [2], Voronoi cell [3], and Weaire–Phelan cell [4]. Among these, the last three structures are considered as most accurate representation of open foam structure. The HMA is comparatively least computationally expensive model and hence enjoys popularity in research community. The HMA-based models are categorized into local thermal equilibrium and local non-thermal equilibrium models. Although the HMA models are computationally less expensive, the accuracy of these models depends on the accurate values of effective properties involve in the standard volume averaged governing equations. Some of the important properties are effective thermal conductivity, tortuosity, dispersion coefficient, interfacial heat transfer coefficients, extinction coefficient, and scattering albedo. These properties can be estimated using experimental investigation or calculated using numerical simulations. In the present work, a pore-level numerical simulation with appropriate boundary conditions is performed to calculate effective thermal conductivity idealized porous structure subjected to combined conduction-radiation mode of heat transfer. The void space of the porous structure is filled with radiatively participating gas. The effects of porosity, solid phase thermal conductivity, average temperature of the domain, and temperature gradient in the dominant direction of heat transfer on ETC of the foam structure are investigated. The data obtained from more than 300 simulations are trained and tested using artificial neural network (ANN). ANN approach is a well-established approach which has been used in diverse areas to predict the performance. Kenanoğlu et al. [5] investigated cascade-forward networks with LM as learning algorithm to predict motor torque, power generated and NO_x emission in a diesel engine. In total, 176 data sets were developed by varying motor speed (1300–2500 rpm), fuel type, and fuel consumption to train ANN. The developed network predicted motor torque, motor power, and NO_x emission with 95.82%, 96.07%, and 92.35% accuracy. Nasser and Naser [6] modeled ANN with feed forward back propagation (FFBP) to predict the tumor category as an output, based on 17 input data from patient information like age, sex, histologic type (epidermoid, adedefalse, anaplastic), degree-of-diffe (well, fairly, poorly), bone, bone-marrow, lung, pleura, peritoneum, liver, brain, skin, neck, supraclavicular, axilla, mediastinum, and abdominal. ANN was successfully able to classify 76.67% of the data which showed that the possibility of the network to predict tumor type based on body test but with low accuracy. Qiu and Song [7] studied Japan's stock market and used ANN to predict its direction. In the study of Siregar and Wanto [8], ANN (FFBP) was used to predict the human development index (HDI). In total, 165 training data (33 different cities for five different year (2011–2015)) were used. Chae et al. [9] used ANN for short-term load forecasting (STLF)

of building electricity usage. Input variables used were outdoor relative humidity (%), outdoor dry-bulb temperature ($^{\circ}\text{C}$), day indicator (0: weekdays, 1: Saturday, 2: Sunday), HVAC operation schedule and interval stamp (0–95) along with energy consumption as the output variable.

2 Problem Description

2.1 Modeling of Geometry

The actual morphology of the open-cell foam structure is complex and difficult to generate for numerical simulations. Thanks to the advancement in CT scan imaging techniques because of which the actual foam structure can be replicated. However, this would inevitably involve many grids and hence the numerical investigation becomes computationally expensive. The afore-mentioned complexity can be reduced by considering idealized unit cell structures such as cubic unit cell, spherically voided cubic cell, tetrakaidecahedra cell, Weaire-Phelan cell, and Voronoi structure. Since the present work is intended to develop a numerical model to estimate effective thermal conductivity (ETC) of open-cell foam subjected to combine conductive-radiative heat transfer, the accuracy of the property of interest also depends on the accuracy of the foam structure considered. The tetrakaidecahedra structure, Weaire-Phelan cell, and Voronoi structures are considered as most accurate approximation of actual foam structure. Hence, in the present work, the tetrakaidecahedra cell structure, as shown in Fig. 1, is considered to ETC estimation.

In the present work, the voxel information of solid and void phase is stored using Cartesian coordinate-based blocked-off region approach. The solid phase is radiatively in-active and marked as '0' whereas the radiatively participating media stored in the void space is marked as '1'. Both phases are allowing conduction heat transfer to take place. The investigated parameters on the tetrakaidecahedra cell structure are given in Table 1.

Fig. 1 Tetrakaidecahedra unit cell structure

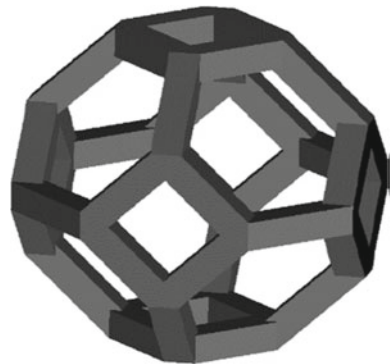


Table 1 Investigated conditions

Sr. No.	Parameter	Range
1	Porosity (Φ)	0.72–0.944
2	Average temperature of the computational domain (T_{avg})	750–1950 (K)
3	Thermal conductivity of solid (k_s)	0.5–200 (W/mK)
4	Temperature difference between wall and fluid (ΔT)	100–900 (K)

2.2 Numerical Modeling

In order to determine ETC of the tetrakaidecahedra unit cell structure, the numerical method, suggested by Patel et al. [2], is adopted. A brief description of the method is as follows. The tetrakaidecahedra unit cell structure is encompassed in a cubic enclosure filled with participating gas. The ‘East’ and ‘West’ walls are assumed to be black and subjected to different isothermal conditions. The remaining transverse boundaries parallel to applied temperature gradients are maintained at adiabatic conditions. Moreover, the emissivity of the transverse walls is assumed to be zero. In the present study, temperature of the ‘East’ wall (T_E) is greater than that of the ‘West’ wall (T_W), the dominant direction of heat transfer is from ‘East’ to the ‘West’. In such case, the ETC of the considered structure depends on (i) applied temperature gradient, (ii) porosity of the tetrakaidecahedra structure, (iii) emissivity (and hence reflectivity) of the opaque struts (i.e., solid walls), (iv) thermal conductivity of the solid and gas phases, (v) radiative properties of the participating gas, and (vi) geometry of the porous structure. Talukdar et al. [10] observed that the influence of radiative properties and thermal conductivity of the participating gas, and emissivity of the solid phase have negligible influence on ETC as compared to the other parameters. Hence, in the present study, the afore-mentioned parameters are considered constant. The porosity of the tetrakaidecahedra cell varies from 0.72 to 0.94. The solid phase thermal conductivity ranges from 0.5 W/mK to 200 W/mK. The temperature gradient across the ‘East’ and the ‘West’ walls is varied as 100, 300, and 500 K. In the present study, the entrapped participating gas is assumed to be stagnant. The overall heat transfer is taking place via combined conduction and radiation modes of heat transfer. For the considered steady-state case, the governing combined conduction-radiation-based energy equation can be written as

$$\nabla \cdot (k \nabla T) - \nabla \cdot \vec{q}_R = 0 \quad (1)$$

Here, k denotes the local thermal conductivity and takes the values of solid and fluid phase depending on the assigned voxel number, i.e., k_s for solid voxels, represented by ‘0’ and k_f for fluid voxels, denoted by ‘1’. The weighted harmonic mean of k_s and k_f [i.e., $2k_s k_f / (k_s + k_f)$] is considered at solid–fluid interphase. The first term on the left hand side of Eq. (1) represents the diffusive part of the heat transfer that can be solved using Dirichlet boundary conditions on the ‘East’ and the ‘West’ walls. All other faces which are parallel to the applied temperature gradient are subjected

to Neumann boundary conditions. The second term of Eq. (1) ($\nabla \cdot \vec{q}_R$) represents divergence of radiation heat flux and acts as a source term in the energy equation. In the present analysis, finite volume method developed by Chai and Patankar [11] is employed to solve the standard radiative transfer equation. The $\nabla \cdot \vec{q}_R$ can be obtained using the following expression:

$$\nabla \cdot \vec{q}_R = \kappa(\vec{r})[4\pi I_b(\vec{r}) - G(\vec{r})] \tag{2}$$

where I_b ($= \sigma T^4/\pi$) is the black body radiation intensity and κ is the absorption coefficient of the participating gas.

The irradiation term $G(\vec{r})$ is evaluated as

$$G(\vec{r}) = \int_{4\pi} I(\vec{r}, \hat{s}) d\Omega \tag{3}$$

Once the solution is converged, the ETC of the tetrakaidehedra unit cell structure can be calculated as

$$ETC = \frac{q_{avg,E}}{\Delta T/L} \tag{4}$$

where $q_{avg,E}$ is the resultant average radiation heat flux on the ‘East’ wall and $\Delta T/L$ is the temperature gradient imposed over ‘East’ and ‘West’ walls. The dimension of the surrounding cubic cell is denoted as ‘ L ’.

Artificial Neural Network (ANN) ANN is a processing system, design of which is inspired by the structure and functioning of the human brain that can be trained to analyze and model nonlinear, complex processes that are not well explored or understood. A schematic diagram showing signal processing by an artificial neuron is shown in Fig. 2.

An artificial neural receives signal as an input and multiply these inputs with the weights corresponding to each input signal. The cumulative signal is processed by an activation function to get an output. An artificial neural network is combination of several such neurons. The network consists of input layer, hidden layer, and output layer. The network is defined as the matrix of neurons and its topology or connections between them which is governed by its learning rule, Jones et al. [12]. Each output

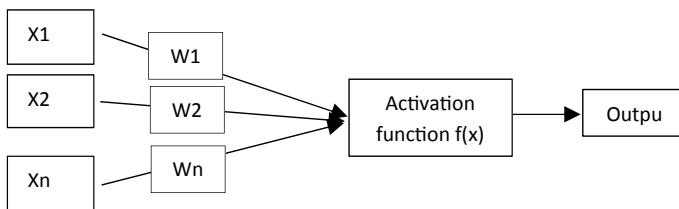


Fig. 2 Schematic diagram showing signal processing by an artificial neuron

of a neuron becomes the input to the next layer neuron. Complex relationships can be modeled with the help of multiple layers of neurons with different neurons in each layer. Until the desired target value is obtained, training is done by sequentially applying inputs and adjusting their corresponding weights according to a specified algorithm. While training, the weights for each input will end up to a specific value, till its output approximately reaches the desired target.

In the present study, MATLAB is used to create an ANN. MATLAB is a programming language and numeric computing environment developed by MathWorks [13]. Neural network tool (nntool) of MATLAB provides a platform to create an ANN, where the data set can be trained, and output can be predicted.

Data obtained from CFD analysis is segregated into input and target data. In total, 240 data sets were used to develop artificial neural network. Due to brevity, only a fraction of data is shown in Table 2 which was used as input data for ANN.

In this study, a supervised neural network is used that requires target data set. A sample target data set is shown in Table 3.

Feed forward back propagation (FFBP) neural network is developed in MATLAB feeding the data shown in Tables 1 and 2. The developed network is shown in Fig. 3. It consists of input layer that has five neurons. These neurons represent the five input variables. The network has one hidden layer with 35 neurons and output layer containing three neurons. Three neurons in the output layer represent the predicted variables, i.e., q_{cond} , q_{rad} , and k_{eff} .

A sigmoid function is used as an activation function in the present study, as given in equation (ref).

$$f(x) = \frac{1}{1 + \exp(-x(n))}$$

Table 2 Sample of input data for the network (5 × 240)

Data set	1	100	200	240
$T_{E,Wall}$ (K)	800	800	1000	600
$T_{W,Wall}$ (K)	700	700	900	300
ΔT (K)	100	100	100	300
k_s (W/mK)	0.5	5	7	50
Porosity (Φ)	0.944	0.919	0.87	0.83

Table 3 Sample of target data for the network (3 × 240)

Data set	1	100	200	240
q_{cond} (W)	0.9631	2.25323	5.136	89.353
q_{rad} (W)	3.3804	3.09506	5.318	2.236
k_{eff} (W/mK)	0.4343	0.534829	1.045	3.052

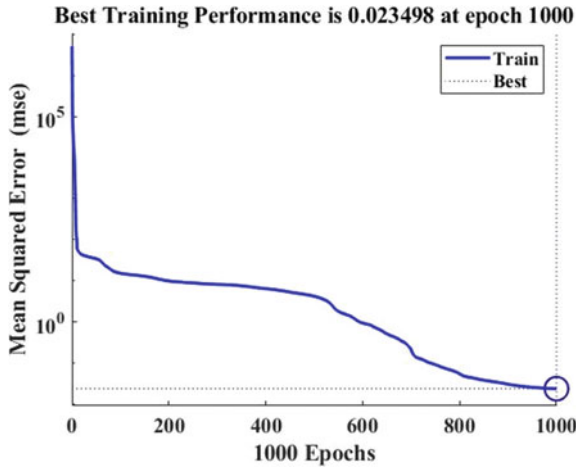


Fig. 3 Network diagram

Bayesian regularization (BR) method is used to train the network. This method is commonly used to get good generalization for difficult, small, or noisy data sets. Training of the network stops when adaptive weight is minimized for the given target value in the Bayesian regularization. The variation of mean square error (MSE) with the training iteration is shown in Fig. 4.

A lower value of MSE is an indication of good network training, and it can be expected that the network predictions would be reliable. Regression plot is another training performance parameter that is plotted in Fig. 5. The value of regression coefficient $R = 1$ indicates that the training is adequate and trained network can reliably be used to predict the output parameters.

The trained network was used to predict the q_{cond} , q_{rad} , and effective thermal conductivity.

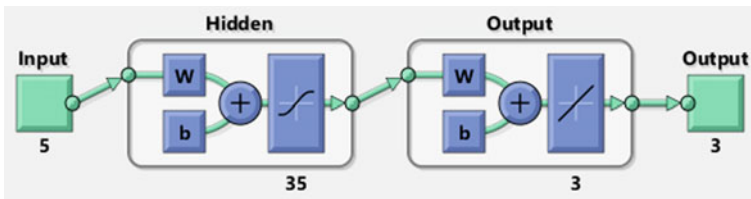
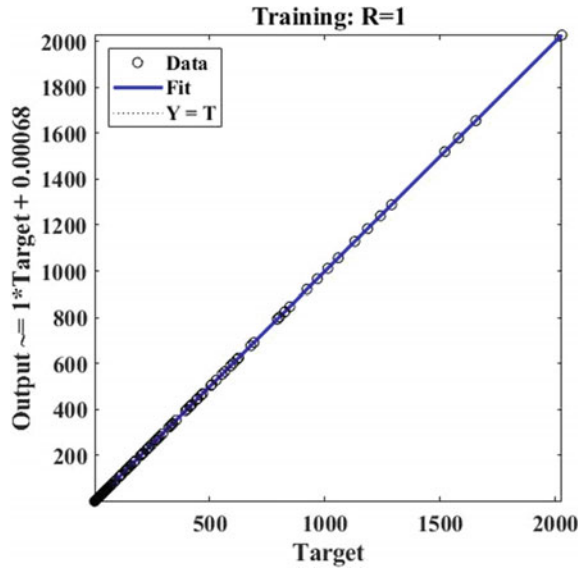


Fig. 4 Training performance of the network

Fig. 5 Regression plot of the trained network



3 Results and Discussion

Effect of porosity

Figure 6 shows the variation of effective thermal conductivity with porosity for two different solid phase thermal conductivity, i.e., $k_s = 0.5$ and 10 W/mK . The ‘East’ and the ‘West’ walls are maintained at temperature of 1000 and 900 K, respectively. Hence, the average temperature of the computational domain is 950 K. The variation of k_{eff} of the tetrakaidehedra unit cell with $k_s = 0.5 \text{ W/mK}$ shows increasing trend with porosity. On the other hand, the variation of k_{eff} with porosity shows declining curve. In the present study, combined conduction and radiation effect are investigated, the magnitude of k_{eff} depends on the averaged value of conduction heat flux q_{cond} and radiation heat flux q_{rad} evaluated at the ‘East’ wall. The conduction heat transfer is taking place in both solid and gaseous phase, whereas the radiation transfer is possible in the participating medium, i.e., gas. The tetrakaidehedra unit cell with $k_s = 10 \text{ W/mk}$ shows dominant mode of conduction heat transfer as compared to that with $k_s = 0.5 \text{ W/mk}$. As porosity increases, solid fraction present in the unit cell decreases. Hence, the contribution from the solid heat transfer also decreases. Although, the radiation heat transfer, and hence, the value of q_{rad} increases but the reduction in q_{cond} is more as compared to increase in q_{rad} . Hence, the overall trend of k_{eff} shows declining trend. The increasing nature of k_{eff} with porosity can be attributed to the fact that the increase in the value of q_{rad} is more as compared to decrease in q_{cond} . The trained ANN is implemented to predict this nonlinear behavior. Results of ANN predictions are shown in Fig. 6 along with the CFD results. It can be observed that the predictions of ANN are capable to capture the trend identified

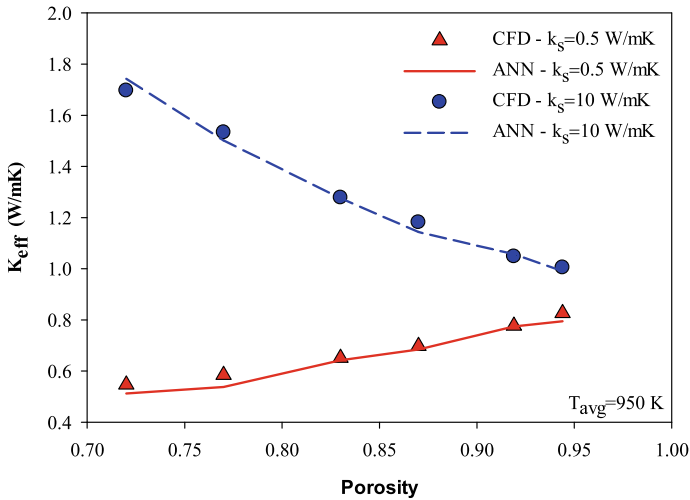


Fig. 6 Comparison of CFD and ANN predictions of effective thermal conductivity with varying porosity

by the CFD simulations. The maximum deviation in the ANN and CFD results are less than 0.5%.

Effect of thermal conductivity of solid

Figure 7 shows the variation of k_{eff} with solid phase thermal conductivity k_s at two different T_{avg} . The porosity of the unit cell for the present trend is kept 0.87.

The variation of k_{eff} for both average temperature of the computational domain $T_{\text{avg}} = 950$ K and 1150 K shows increasing trend with increase in k_s . This trend can be attributed to the fact that as k_s increases, the contribution from the conduction heat transfer increases, whereas the radiation heat transfer remains as it is. With increase in T_{avg} from 950 to 1150 K, both conduction and radiation heat transfer increase and hence, the resultant k_{eff} is higher than that obtained at 950 K.

The trained ANN model is used to predict the variation of the effective thermal conductivity with the conductivity of the solid material. ANN predictions along with the CFD results are presented in Fig. 7. Like the results presented in the previous section, ANN predictions are comparing well with the CFD results. ANN is identifying and predicting trends observed in the CFD simulations.

Effect of wall temperature

The effect of temperature gradient (ΔT) on k_{eff} is depicted in Fig. 8. The trends are shown for two different k_s , i.e., 50 and 200 W/mK. As described earlier, the ΔT ranges from 300 to 900 K. As expected, with increase in ΔT , both conduction and radiation heat transfer increase. However, its effect of k_{eff} is not significant as compared to the previously discussed parameters. Moreover, because of high thermal conductivity, the contribution from conduction heat transfer is higher as compared to

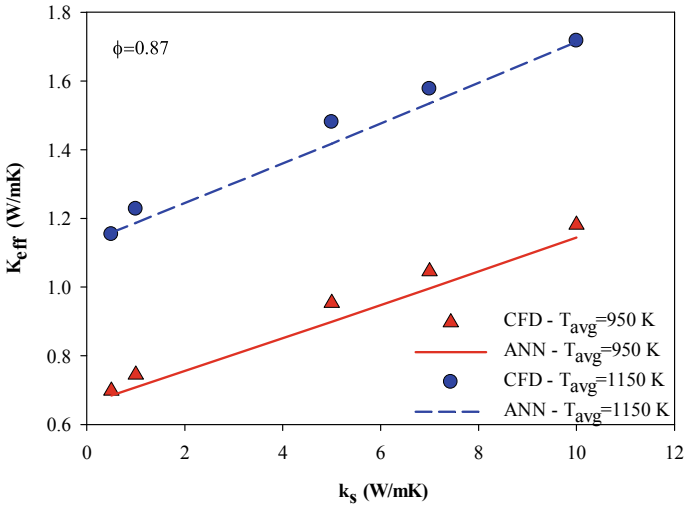


Fig. 7 Comparison of CFD and ANN predictions of effective thermal conductivity with varying thermal conductivity of the solid material

the radiation transport. This contribution further increases with increase in k_s which is reflected in Fig. 8.

Artificial neural network predictions of effective thermal conductivity variation with the temperature gradient also showed remarkable comparison with the CFD results as depicted in Fig. 8. It should be noticed that the effective thermal conductivity

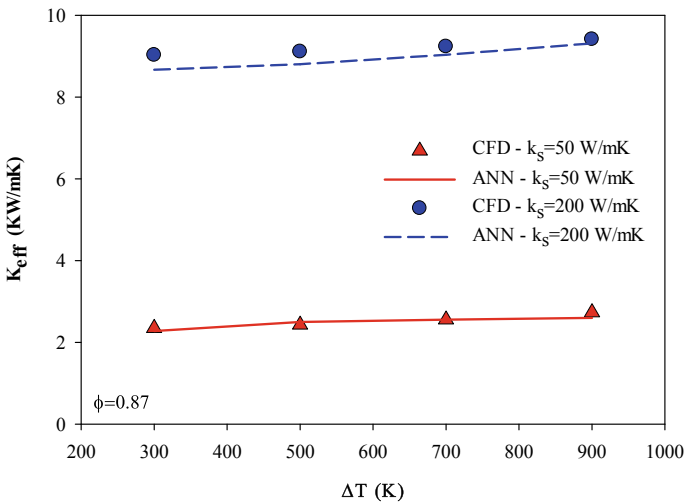


Fig. 8 Comparison of CFD and ANN predictions of effective thermal conductivity with varying temperature gradient

varies from 2 to 3 when temperature gradient is increased from 300 to 900 K, keeping solid material thermal conductivity $k_s = 50$ W/mK. The magnitude of effective thermal conductivity is much higher for $k_s = 200$ W/mK. Despite of a huge deviation in the effective thermal conductivity, ANN predictions are in well agreement with the CFD predictions.

Effect of mean temperature

The variation of k_{eff} against average temperature of the computational domain at two different porosities is shown in Fig. 9. As discussed earlier, the increase in average temperature results in to increase in both conduction and radiation heat transfer. Since thermal conductivity of the solid phase is 5 W/mK for the present case. Hence, the contribution from radiation transport is dominant as compared to that of the conduction heat transfer. With increase in porosity, the radiation transport and hence q_{rad} increases. This results into increase in k_{eff} as observed in Fig. 9. This increment in k_{eff} is almost identical to the exponential variation.

ANN predictions of k_{eff} at the investigated T_{avg} for two level of porosity are shown in Fig. 9. It can be observed that the ANN predictions are capturing trends observed in the CFD simulations.

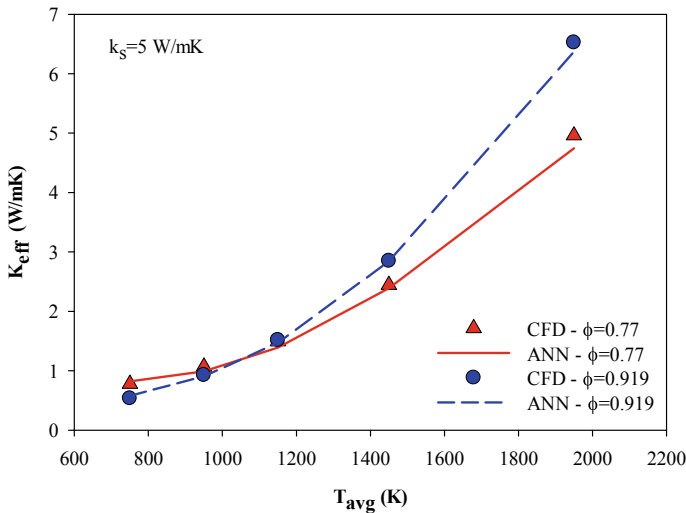


Fig. 9 Comparison of CFD and ANN predictions of effective thermal conductivity with varying average temperature of the domain

4 Conclusions

In the present work, a combined conduction-radiation-based numerical model is developed to calculate effective thermal conductivity of the idealized open-cell foam structure, represented by a tetrakaidecahedra unit cell. To investigate the effects of various parameters such as porosity of the unit cell, solid phase thermal conductivity, average temperature of the computational domain, and temperature gradient on k_{eff} , parametric studies is carried out. The important conclusions drawn from the present study are as follows:

- For unit cell structure with relatively high k_s , k_{eff} shows decreasing trend with porosity.
- At low k_s , k_{eff} shows increasing trend with porosity.
- Irrespective of any value of T_{avg} , k_{eff} increases with increase in k_s .
- Although, k_{eff} increases with increase in temperature gradient ΔT , this increment is small and hence k_{eff} can be considered constant for the considered ΔT range.
- The variation of k_{eff} with T_{avg} follows almost exponential trend.
- ANN predictions are capable to capture linear variation of k_{eff} with solid thermal conductivity and temperature gradients and nonlinear variation with the porosity and average temperature of the domain.

References

1. Patel VM, Talukdar P (2016) Evaluation of radiative properties of a representative foam structure using blocked-off region approach integrated with finite volume method. *Int J Therm Sci* 108:89–99
2. Patel VM, Mendes MA, Talukdar P, Ray S (2018) Development of correlations for effective thermal conductivity of a tetrakaidecahedra structure in presence of combined conduction and radiation heat transfer. *Int J Heat Mass Transf* 127:843–856
3. Xiao F, Yin X (2016) Geometry models of porous media based on Voronoi tessellations and their porosity–permeability relations. *Comput Math Appl* 72(2):328–348
4. Weaire D, Phelan R (1994) A counter-example to Kelvin’s conjecture on minimal surfaces. *Philos Mag Lett* 69(2):107–110
5. Kenanoğlu R, Baltacıoğlu MK, Demir MH, Erkinay Özdemir M (2020) Performance and emission analysis of HHO enriched dual-fuelled diesel engine with artificial neural network prediction approaches. *Int J Hydrogen Energy* 45(49):26357–26369
6. Nasser IM, Abu-Naser SS (2019) Predicting tumor category using artificial neural networks. *Int J Acad Heal Med Res* 3(2):1–7
7. Qiu M, Song Y (2016) Predicting the direction of stock market index movement using an optimized artificial neural network model. *PLoS ONE* 11(5):1–11
8. Siregar SP, Wanto A (2017) Analysis of artificial neural network accuracy using backpropagation algorithm in predicting process (Forecasting). *IJISTECH (Int J Inf Syst Technol)* 1(1):34
9. Chae YT, Horesh R, Hwang Y, Lee YM (2016) Artificial neural network model for forecasting sub-hourly electricity usage in commercial buildings. *Energy Build* 111:184–194
10. Talukdar P, Mendes MAA, Parida RK, Trimis D, Ray S (2013) Modelling of conduction-radiation in a porous medium with blocked-off region approach. *Int J Therm Sci* 72:102–114

11. Chai JC, Patankar SV (2000) Finite volume method for radiation heat transfer. CRC Press advances in numerical heat transfer, pp. 109–138 (Chapter 4)
12. Jones SP, Jansen R, Fusaro RL (1997) Preliminary investigation of neural network techniques to predict tribological properties. Tribol Trans 40(2):312–320
13. MATLAB (2018) 9.7.0.1190202 (R2019b), The MathWorks Inc., Natick, Massachusetts

Numerical Analysis of Heat Transfer Enhancement of Heat Sink Using Different Phase Changing Materials for Electronic Cooling Application



K. Naga Ramesh, M. Manoj Sai, K. Vineeth Goud, K. Raghavendra, S. Amruth, and T. Karthikeya Sharma

Abstract Heat sinks absorb thermal energy from devices which operates at higher temperatures and dissipates to surrounding medium. Overheating of electronic components can reduce the efficiency, reliability and life of energy systems. The focus of most of the researchers is on the improvement of the performance of the heat sinks. The performance of the heat sinks can be enhanced by incorporation of the phase change materials (PCM). In the present work, a novel design of PCM-based finned heat sink is modeled numerically using ANSYS FLUENT. Holes are drilled along the fins and filled with PCM to improve the heat storage capacity of the heat sink. PCM-based heat sinks with high heat dissipating qualities are well suitable for electronic cooling application. In this study, thermal resistance is calculated to analyze the performance of the heat sink. The performance of the PCM-based heat sink is evaluated for various PCM and composite PCMs and compared with the heat sink without PCM.

Keywords Heat sinks · Thermal energy devices · Finned heat sink · Performance enhancement · Ansys Fluent · Phase change material (PCM) · Composite PCM and PCM slurries

Nomenclature

A_b	Heat sink base area (m^2)
C_p	Specific heat ($J/kg\ K$)
H	Height of the heat sink base
H_e	Enthalpy of suspension (W)
k	Thermal conductivity ($W/m\ K$)

K. Naga Ramesh · M. Manoj Sai · K. Vineeth Goud · K. Raghavendra · S. Amruth · T. Karthikeya Sharma (✉)
Department of Mechanical Engineering, NIT Andhra Pradesh, Tadepalligudem, India

K. Naga Ramesh
e-mail: knramesh.sclr@nitandhra.ac.in

PCM	Phase change material
q	Heat flux entering (W/m^2)
R_T	Thermal resistance (K/W)
T	Temperature (K)
T_{in}	Inlet temperature (K)
\bar{T}_w	Average temperature at heat sink base (K)

Greek symbols

ρ	Density (kg/m^3)
μ	Dynamic viscosity (m^2/s)

1 Introduction

Nowadays, there is massive usage of electronic devices and continuous heat is generated by these devices, due to which the reliability and efficiency of device gets reduced. To improve the reliability, efficiency and reduce overheating, heat sinks are used which acts as a heat exchanger. Heat sinks remove the heat generated by the energy devices by various modes of heat transfer and rejects it to the surrounding medium, which is at lower temperature. By adding fins, the surface area increases due to which heat transfer is enhanced. Heat sinks are used in power plants, electronic systems like television, laptops and also in many industrial applications. Hung et al. [1] concluded the rise in the temperature of the heat sink is less when sandwich or trapezoidal distribution design because velocity of working fluid is higher in this case, so less time was available for working fluid to absorb the heat from walls. Park et al. [2] conducted experiments by giving partial heating position and thermal performance of heat sink was investigated for partial heating position and analysis on the parameters affecting the position are done. Heat sinks with air cooling is not that much effective, when there is more heat generation by the devices air alone as a cooling medium is not sufficient to cool the devices. To improve the performance of heat sinks, phase change materials (PCM) are incorporated into heat sink by drilling holes along the fins and holes are filled with phase change material.

Phase change materials undergoes cycling process, they melt when the heat is absorbed and solidifies upon releasing the heat to surrounding medium. In composite phase change material either phase change material reinforced into a metal or any other metal particles are reinforced into phase change material. Hybrid-nano particles inserted in PCM (HNCPCM) and PCM inserted in graphene oxide sheets (GOPCM) are the examples of composite PCMs. In microencapsulated PCM (MEPCM) slurry, encapsulated PCM is dispersed in water or any base fluid. Requirements for PCM are latent heat of the material must be high, the change in volume of the material must

be very less during the phase change and PCM must be non-poisonous. Mahmoud et al. [3] conducted experiments by adding the PCM to heat sink and observed the reduction in heating rate and maximum temperature of the heat sink and increase of life of electronic devices. Kandasamy et al. [4] examined the PCM-based heat sink and witnessed the improvement of cooling performance compared to heat sinks without PCM. Similar results were observed by Taghilou et al. [5] in their numerically study on ambient convective heat transfer effects of PCM-filled heat sink.

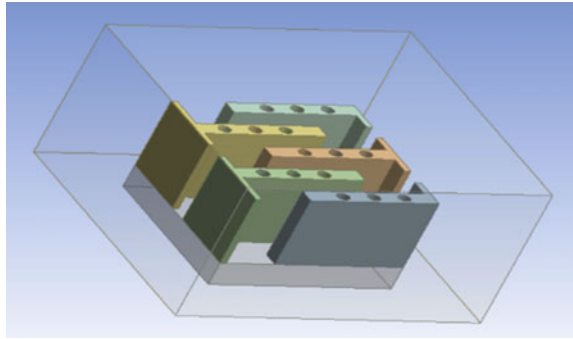
Kim et al. [6] conducted the numerical and experimental study on thermal performance of PCM-based cascade cooling system with constant heat flux. Anzar et al. [7] worked on PCM-filled finned heat sinks with PCM is fully filled in the fin, PCM is half filled in the fin, no PCM inside the fin are experimentally investigated and noticed the better performance in heat sink with fully filled fins. Deng et al. [8] investigated the heat transfer properties of microchannel heat sinks using microencapsulated PCM slurry as working fluid and microchannel heat sinks heat transfer process are explained with mathematical models.

Manoj Kumar et al. [9] conducted experiments on all-glass evacuated solar water heating system (AGSWH) by natural circulation using hybrid-nano composite PCM with different mass fraction of hybrid-nano particles and found 19.4% and 1.28% enhancement in energy and exergy efficiencies at 1% mass fraction. Wang et al. [10] concluded that copper foam can effectively enhance internal heat transfer of paraffin wax there by reduced the paraffin heat storage time by 40%. Yin et al. [11] have prepared graphite-paraffin composite PCM and found the 65.3% and 2.98% reduction in heat storage time and heat release time, respectively.

Ho and Gao [12] prepared PCM and nano particles emulsion using alumina nano particles in paraffin (n-Octadecane) and noticed a nonlinear increment in dynamic viscosity and thermal conductivity with the nano particle mass fraction of compared to pure paraffin. Heyhata et al. [13] studied the passive thermal management system and concluded that addition of nano particles to the PCM improve system performance was insignificant. Arora et al. [14] conducted experimental study on micro heat pipe using infra-red (IR) thermography and distilled water and Al_2O_3 /water nano fluid are used as the workings fluids. 5–10 °C reduction in surface temperature of heat pipe observed when nano fluid used as working fluid compared to distilled water. Shatikian, et al. [15] studied the PCM-based heat sink with internal fins numerically and expressed the unsteady phase change process in terms of volume melt fraction of the PCM.

Diaconu et al. [16] investigated heat transfer characteristics and phase change properties of microencapsulated PCM slurry to know its ability to use in air conditioning applications. Mehrali et al. [17] described about the composite PCM preparation, PCM characterization, PCM thermal properties and thermal stability and reliability. Zhang et al. [18] established the phase change temperature of composite phase change material and its latent heat by differential scanning calorimetry analysis. Lachheb et al. [19] paraffin PCM thermal conductivity enhanced by addition of graphites with paraffin. Dutkowski and Fiuk [20] conducted experiments on microencapsulated PCM slurry to find the rheological properties. The existing studies in

Fig. 1 Computational domain of heat sink



literature are evident that there is more scope for PCM to augment the performance of heat sinks for electronic cooling application.

In the present study, a novel PCM-based finned heat sink model developed and analyzed numerically. The enhancement in the thermal performance of the heat sink using various PCMs is evaluated and compared with heat sink without PCM. Thermal resistance, average temperature at the base of heat sink, outlet temperature of the fluid are studied for this analysis.

2 Physical Model

The computation domain of the present numerical analysis showed in Fig. 1. The geometry of heat sink presented in Fig. 1 includes the base, fins and rectangular enclosure. Air enters the heat sink from two openings provided at the right side and leaves the heat sink from the openings provide on the remaining three sides. W , L and H are width, length and height of the heat sink base. W_f , L_f and H_f are the width, length and height of the fins attached to the base. d is the diameter of the holes provided on the fins. For this study, the values of W , L and H values are considered as 30 mm, 30 mm and 5 mm, respectively. The values of W_f , L_f , H_f and d are 3 mm, 20 mm, 15 mm and 2 mm, respectively.

3 Mathematical Model

3.1 Governing Equations

The instantaneous continuity equation, momentum equation and energy equation for the fluid flow can be written as.

Continuity equation.

$$\nabla V = 0 \quad (1)$$

Momentum equation.

$$\rho(V \cdot \nabla V) = -\nabla P + \nabla \cdot (\mu \nabla V) \quad (2)$$

Energy equation.

$$\rho C_p (V \cdot \nabla H_e) = K \nabla^2 T \quad (3)$$

In the present work, thermal resistance was used as the parameter to estimate and compare the performance of the heat sink. It is a negative parameter, heat sink with high thermal resistance has the poor thermal performance. The thermal resistance is calculated as

$$R_T = \frac{\bar{T}_w - T_{in}}{q A_b} \text{ (W/K)} \quad (4)$$

3.2 Boundary Conditions

The present numerical problem is an external flow problem, so a rectangular enclosure is considered around the heat sink. Working fluid (air) enters from one face of enclosure and leaves from opposite face, they are considered as inlet and outlet respectively. Symmetry condition was applied for remain sides of the enclosure. Heat flux was applied on the bottom wall of the heat sink. Inlet temperature of the air set as 300 K. Two air inlet velocities, 1 m/sec and 5 m/sec are considered for this analysis.

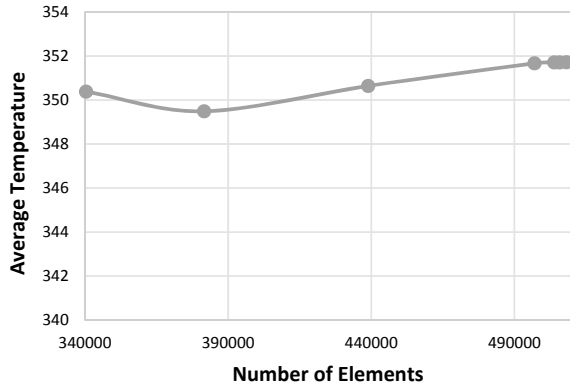
4 Validation

The results obtained from the present model was compared with the experimental results of Arularasan and Velraj [21]. Table 1 shows thermal resistance value obtained by present simulation method and experimental method. The outcomes of the present model have the good agreement with experimental values with the 1.25% deviation in the thermal resistance.

Table 1 Thermal resistance value obtained by present model and experimental method

Material	Thermal resistance (K/W)		Deviation (%)
	Present model	Experimental result [21]	
Aluminum	1.185	1.2	1.25

Fig. 2 Temperature variation with no of elements



4.1 Grid Sensitivity Study

Grid sensitivity study performed on the present simulation model by considering the heat sink base temperature at different grid size to find the solution which is independent of the grid size. The variation of temperature with grid size is presented in Fig. 2. The solution at the grid size of 504,000 elements (fifth point in Fig. 2) was considered as grid sensitive solution for the current problem.

5 Results and Discussion

Thermo-physical properties of PCMs considered for present study are listed in Table 2. Figure 3 shows temperature variation across the heat sink and the planes considered parallel to the heat sink base. The three planes considered are at the top, middle and bottom of the heat sink to analyze the heat sink temperature. Decrease of temperature of heat sink noticed from base to the top because of the working fluid (air) flowing over the heat sink absorbed the heat from fins fixed on the base. So, the temperature gradient was created in the vertical direction.

Figure 4 shows the temperature distribution on heat sink base in the direction perpendicular to the air flow at 1 mm, 7.5 mm, 15 mm, 22.5 mm and 29 mm distance from the inlet (Line 1 to 5, respectively). The lowest temperatures are observed at the edges because of more surface area available for heat transfer to the air by convection. Uniform distribution of temperature without any fluctuations was observed at the line

Table 2 Thermo-physical properties of PCMs [22, 23]

Material	Thermal conductivity (W/m K)	Specific heat (kj/kg K)	Solidus temp (°C)	Liquidus temp (°C)	Latent heat (kj/kg)
Paraffin wax	0.24 @300 K 0.22 @340 K	2.9	56	58	173.6
RT41	0.2	2	37.5	42.9	141.7
P116	0.21	2.1	50	50	190
n-eicosane	0.1505	17.31@311 K 17.18@325 K	36.5	36.5	237.4

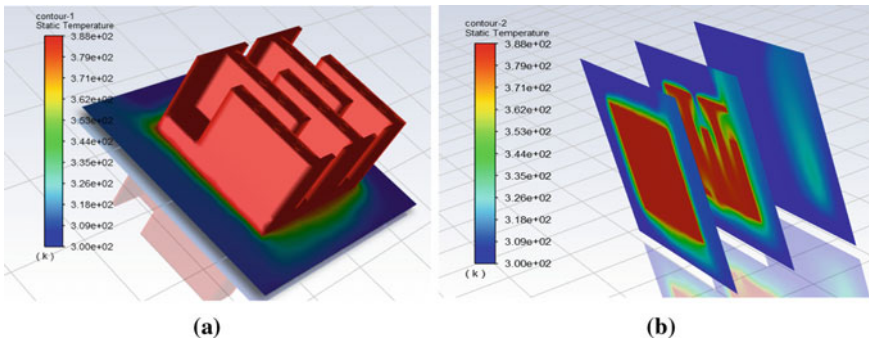


Fig. 3 Temperature contours of **a** heat sink **b** at different cut planes of the heat sink

3 (15 mm from inlet) because the working fluid had the contact with five fins at a time.

In the present study, thermal resistance was used to analyze and compare the performance of the heat sink. Thermal resistance obtained when different PCMs are incorporated in the heat sink at two heat flux values are presented in Table 3. Average temperature of heat sink bottom wall and outlet temperature of the air also showed in Table 3. The heat sink with PCMs show the better performance than heat sink without PCM. Maximum of 13.46% of reduction resistance of heat sink compared to the heat sink without PCM was noticed when N-Eicosane is incorporated at inlet velocity of 1 m/s. These results was measured at two values of heat flux. Thermal resistance of heat sink calculated at the inlet velocity of 5 m/s is presented in Table 4.

The improvement of the thermal performance of the heat sink was witnessed by inserting the PCMs in the heat sink even though PCM has the drawback of low thermal conductivity. The heat sink performance can be improved further by using composite PCMs. Thermal conductivity of composites was increased by adding the metal particles. Thermo-physical properties of different composite materials were presented in Table 5.

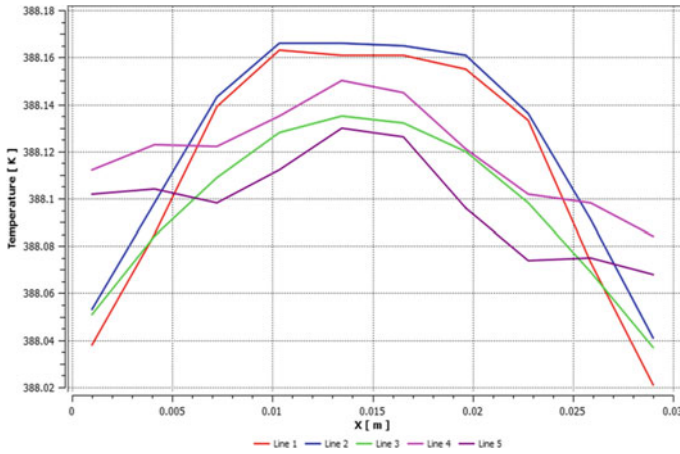


Fig. 4 Temperature distribution across the base of the heat sink with paraffin wax

Table 3 Thermal resistance of heat sink for different PCMs at air inlet velocity of 1 m/s

Material	Heat flux (W/m ²)	Outlet temp (K)	Average temp at base (K)	Thermal resistance (K/W)
Without PCM	25,000	303.39	397.65	4.34
Paraffin wax	25,000	302.9	387.85	3.90
RT 14	25,000	304.56	388.21	3.92
P 116	25,000	304.59	388.81	3.947
N-Eicosane	25,000	304.37	384.51	3.756
Without PCM	30,000	304.40	417.45	4.35
Paraffin wax	30,000	303.83	405.8	3.91
RT 14	30,000	305.48	406.04	3.93
P116	30,000	305.52	406.71	3.952
N-Eicosane	30,000	305.29	402.38	3.791

Table 4 Thermal resistance of heat sink for different PCMS at air inlet velocity of 5 m/s

Material	Heat flux (W/m ²)	Outlet temp (K)	Average temp at base (K)	Thermal resistance (K/W)
Paraffin wax	25,000	302.586	378.0787	3.47
RT 14	25,000	303.123	394.2232	3.48
P 116	25,000	302.648	379.8724	3.54
N-Eicosane	25,000	303.185	396.171	3.56
Paraffin wax	30,000	302.6245	379.1733	3.5188
RT 14	30,000	303.1649	395.4694	3.537
P116	30,000	302.52	376.2091	3.39
N-Eicosane	30,000	303.07	392.63	3.43

Table 5 Thermo-physical properties of composite PCMs [9, 17]

Material	Mass fraction	Thermal conductivity (W/m K)	Solidus temp (°C)	Liquidus temp (°C)	Latent heat (kJ/kg)
Paraffin wax	0%	0.18	57.01	63.74	140.2
HNCPCM 1	0.5%	0.231	57.06	63.27	136.1
HNCPCM 2	1%	0.26	58.79	62.81	133.7
HNCPCM 3	2%	0.298	58.21	63.09	111.2
GOPCM 1	47.80	1.04	51.48	44.78	63.11
GOPCM 2	47.39	1.19	52.33	45.76	62.53
GOPCM 3	48.30	0.985	44.59	53.57	63.76
MCPCM 1	0.07	0.597	28	28	10.2
MCPCM 1	0.15	0.566	28	28	21.8
MCPCM 1	0.30	0.483	28	28	43.6
MCPCM 2	0.05	0.568	14.3	14.3	7
MCPCM 2	0.158	0.506	14.3	14.3	22
MCPCM 2	0.28	0.446	14.3	14.3	38.6

Thermal resistance of heat sink obtained for various composite PCMs with different mass fraction was presented in Table 6. These results were considered at heat flux value of $40,000 \text{ W/m}^2$ and air inlet velocity of 1 m/s. Heat sink MCPCM2 with the mass fraction of 0.05 has the lowest thermal resistance among the various composite PCMs used for this study.

Table 6 Thermal resistance of heat sink for composite PCMs

Material	Heat flux (W/m^2)	Outlet temp (K)	Average temp of bottom wall (K)	Thermal resistance (K/W)
Paraffin wax	40,000	307.343	441.8	3.938
HNCPCM 1	40,000	307.3473	441.938	3.942
HNCPCM 2	40,000	307.3495	441.98	3.943
HNCPCM 3	40,000	307.36	442.344	3.95
GOPCM 1	40,000	307.47	444.34	4.009
GOPCM 2	40,000	307.709	449.09	4.141
GOPCM 3	40,000	307.404	443.002	3.972
MCPCM 1(0.07)	40,000	307.27	440.49	3.902
MCPCM 1(0.15)	40,000	307.28	440.73	3.909
MCPCM 1(0.30)	40,000	307.30	441.15	3.920
MCPCM 2(0.05)	40,000	307.26	440.42	3.900
MCPCM 2(0.158)	40,000	307.29	440.96	3.915
MCPCM 2(0.28)	40,000	307.32	441.51	3.930

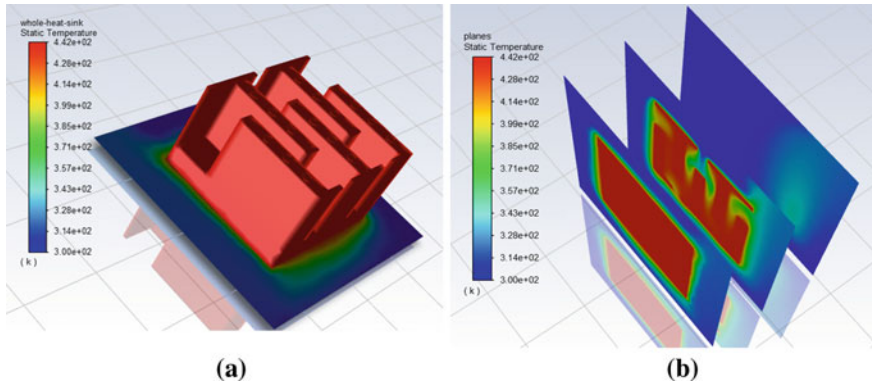


Fig. 5 Temperature contours of **a** heat sink **b** at different cut planes of the heat sink with composite PCM HNCPCM 1

Temperature contours of heat sink and at the different cut planes parallel to the heat sink base are showed in Fig. 5. The three planes were considered at the top, middle and bottom of the heat sink. Contours was obtained for the composite PCM of HNCPCM 1 at the heat flux of $40,000 \text{ W/m}^2$.

The temperature distribution on heat sink base in the direction perpendicular to the air flow for the MNCPCM1 with 0.07% mass fraction was showed in Fig. 6. These distribution are considered at five different positions at distance of 1, 7.5, 15, 22.5 and 29 mm from the inlet (line 1 to 5 in Fig. 6). The lowest temperature observed at the edges of the heat sink. More uniform distribution of temperature was noticed for line 3 because of heat dissipation by five fins at this position. The depressions in the line 4 and line 5 are because of more heat absorbed by fins presented at that position.

6 Conclusions

In the present numerical analysis, a PCM-based finned heat sink was modeled using ANSYS FLUENT. The results of the present model validated by comparing with experimental results in the literature and good agreement between the present model and experimental results was noticed. The main conclusions drawn from this study are as follows,

- The performance of the heat sink was improved significantly by placing the PCM in the heat sink.
- Maximum of 13.46% of reduction in resistance of heat sink compared to the heat sink without PCM was noticed when N-Eicosane is incorporated at inlet velocity of 1 m/s.

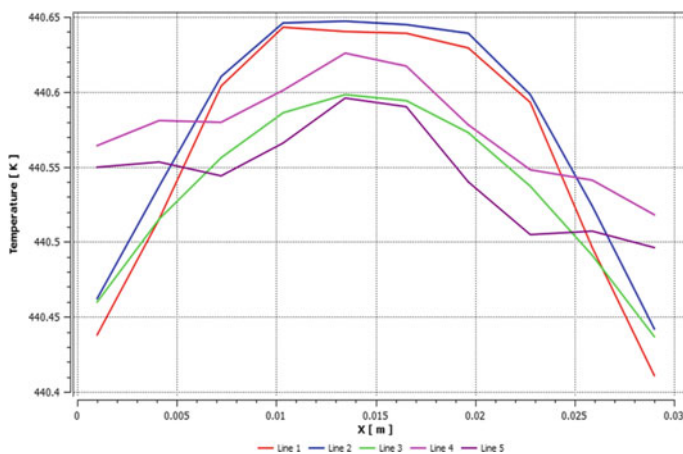


Fig. 6 Temperature distribution across the base of the heat sink of MNCPCM1 with 0.07% mass fraction

- Among all the phase change materials considered in this study paraffin wax shows the better thermal performance.
- Uniform distribution of the temperature was noticed at this middle position of heat sink because of heat dissipation by 5 fins.
- The performance of the heat sink with composite PCMs is better than the PCMs because of improved thermal conductivity in the composite PCMs.
- The PCM keeps the heat sink at almost constant and safe temperatures under the fluctuating heat load also.

References

1. Hung TC, Huang YX, Yan WM (2013) Thermal performance analysis of porous-microchannel heat sinks with different configuration designs. *Int J Heat Mass Transf.* <https://doi.org/10.1016/j.ijheatmasstransfer.2013.07.019>
2. Yoon Y, Park SJ, Kim DR, Lee KS (2018) Thermal performance improvement based on the partial heating position of a heat sink. *Int J Heat Mass Transf.* <https://doi.org/10.1016/j.ijheatmasstransfer.2018.03.080>
3. Mahmoud S, Tang A, Toh C, et al (2013) Experimental investigation of inserts configurations and PCM type on the thermal performance of PCM based heat sinks. *Appl Energy.* <https://doi.org/10.1016/j.apenergy.2013.04.059>
4. Kandasamy R, Wang XQ, Mujumdar AS (2008) Transient cooling of electronics using phase change material (PCM)-based heat sinks. *Appl Therm Eng.* <https://doi.org/10.1016/j.applthermaleng.2007.06.010>
5. Taghilou M, Khavasi E (2020) Thermal behavior of a PCM filled heat sink: The contrast between ambient heat convection and heat thermal storage. *Appl Therm Eng.* <https://doi.org/10.1016/j.applthermaleng.2020.115273>

6. Kim SH, Heu CS, Kim DR, Kang SW (2020) Numerical modeling and experimental validation of a phase change material-based compact cascade cooling system for enhanced thermal management. *Appl Therm Eng.* <https://doi.org/10.1016/j.applthermaleng.2019.114470>
7. Anzar A, Hafiz PA, Ashiq N, Shaheer M (2016) Heat transfer analysis on PCM based heat sink incorporated with air convection. 7:441–456
8. Deng X, Wang S, Wang J, Zhang T (2017) Analytical modeling of microchannel heat sinks using microencapsulated phase change material slurry for chip cooling. In: *Procedia engineering*
9. Manoj Kumar P, Mysamy K, Alagar K, Sudhakar K (2020) Investigations on an evacuated tube solar water heater using hybrid-nano based organic phase change material. *Int J Green Energy.* <https://doi.org/10.1080/15435075.2020.1809426>
10. Wang C, Lin T, Li N, Zheng H (2016) Heat transfer enhancement of phase change composite material: copper foam/paraffin. *Renew Energy.* <https://doi.org/10.1016/j.renene.2016.04.039>
11. Yin H, Gao X, Ding J, Zhang Z (2008) Experimental research on heat transfer mechanism of heat sink with composite phase change materials. *Energy Convers Manag.* <https://doi.org/10.1016/j.enconman.2007.10.022>
12. Ho CJ, Gao JY (2009) Preparation and thermophysical properties of nanoparticle-in-paraffin emulsion as phase change material. *Int Commun Heat Mass Transf.* <https://doi.org/10.1016/j.icheatmasstransfer.2009.01.015>
13. Heyhat MM, Mousavi S, Siavashi M (2020) Battery thermal management with thermal energy storage composites of PCM, metal foam, fin and nanoparticle. *J Energy Storage.* <https://doi.org/10.1016/j.est.2020.101235>
14. Cooling performance of micro heat pipe used for mobile. *J Eng Perform C* 7:331–341 (2018)
15. Shatikian V, Ziskind G, Letan R (2005) Numerical investigation of a PCM-based heat sink with internal fins. *Int J Heat Mass Transf.* <https://doi.org/10.1016/j.ijheatmasstransfer.2004.10.042>
16. Diaconu BM, Varga S, Oliveira AC (2010) Experimental assessment of heat storage properties and heat transfer characteristics of a phase change material slurry for air conditioning applications. *Appl Energy.* <https://doi.org/10.1016/j.apenergy.2009.05.002>
17. Mehrali M, Latibari ST, Mehrali M et al (2013) Shape-stabilized phase change materials with high thermal conductivity based on paraffin/graphene oxide composite. *Energy Convers Manag.* <https://doi.org/10.1016/j.enconman.2012.11.023>
18. Zhang Z, Zhang N, Peng J et al (2012) Preparation and thermal energy storage properties of paraffin/expanded graphite composite phase change material. *Appl Energy.* <https://doi.org/10.1016/j.apenergy.2011.10.014>
19. Lachheb M, Karkri M, Albouchi F et al (2014) Thermophysical properties estimation of paraffin/graphite composite phase change material using an inverse method. *Energy Convers Manag.* <https://doi.org/10.1016/j.enconman.2014.03.021>
20. Dutkowski K, Fiuk JJ (2018) Experimental investigation of the effects of mass fraction and temperature on the viscosity of microencapsulated PCM slurry. *Int J Heat Mass Transf.* <https://doi.org/10.1016/j.ijheatmasstransfer.2018.05.158>
21. Arularasan R, Velraj R (2010) Modeling and simulation of a parallel plate heat sink using computational fluid dynamics. *Int J Adv Manuf Technol.* <https://doi.org/10.1007/s00170-008-1867-9>
22. Yadav A, Soni S (2017) Simulation of melting process of a phase change material (PCM) using ANSYS (Fluent). *Int Res J Eng Technol* 2395–56
23. Hasan MI, Tvena HL (2018) Using of phase change materials to enhance the thermal performance of micro channel heat sink. *Eng Sci Technol an Int J* 21:517–526. <https://doi.org/10.1016/J.JESTCH.2018.03.017>

Performance Analysis of Active Cooling System in Lithium-Ion Batteries Using Dual Potential Multi-Scale Multi-Dimensional Battery Model Approach in Extreme Environment



Ashima Verma and Dibakar Rakshit

Abstract Efficacious thermal management of Lithium-ion (Li-ion) batteries is essential for the safety, longevity, and performance of the battery pack in electric vehicles (Evs). Li-ion batteries are sensitive to harsh ambient conditions and stressful thermal loading. This paper demonstrates the result of liquid cooling system through minichannels on Li-ion battery under stressful conditions. Newman, Tiedemann, Gu, and Kim (NTGK) semi-empirical electrochemical model, which is based on porous electrode theory, is used in the battery simulations. The reduced order model (ROM) or model order reduction (MOR) technique is used to speed up the simulation for long cyclic loading conditions. Thermal performance is evaluated based on the parameters like number of aluminium minichannel, liquid species, velocity of the fluid, and ambient temperature. Repeated cycles of charging and discharging persisted for 333.33 min and proved the competence of the cooling media.

Keywords Electric vehicle · Thermal management · Li-ion battery · NTGK · Minichannels

Nomenclature

a	Specific area of electrode sandwich sheet (m^2)
DOD	Depth of discharge
j	Current density (A/m^2)
q	Heat generation rate during battery operation (W/m^3)
Q_{Ah}	Battery's capacity (Ah)
T	Reference temperature (K)

A. Verma · D. Rakshit (✉)
Department of Energy Science and Engineering, IIT Delhi, New Delhi, India
e-mail: dibakar@iitd.ac.in

A. Verma
e-mail: esz198262@iitd.ac.in

Greek symbols

σ_+	Effective electric conductivity of positive electrode
σ_-	Effective electric conductivity of negative electrode
φ_+	Phase potential for positive electrode
φ_-	Phase potential for negative electrode

1 Introduction

The global crisis on climate change as observed by scientists today is a concern for human survival and existence. An upswing in the development of non-conventional methods to limit the rising global average temperature has led the way for electric vehicles (EVs) to ascent in the field. The recent times of global pandemic COVID-19 have seen improved AQI in India and across the world due to little or no traffic on roads. Current time calls for a solution to this issue which paves the way for research and development in the area of Lithium-ion (Li-ion) batteries which are power house of an EV. A battery is an electrochemical unit that consists of electrodes, a separator, and an electrolyte. Anode (negative electrode) is the electrode where oxidation takes place during the discharge cycle and cathode (positive electrode) where reduction takes place. The negative electrode is made from lithium-carbon material and the positive electrode is generally a lithium oxide. The role of anode and cathode gets reversed depending upon the direction of the current. The electrolyte is a mixture of organic carbonates or salts of lithium. Li-ion batteries are rechargeable batteries with high energy density (up to 705 Wh/L), power density (10,000 W/L), and low self-discharge rates [1]. The performance however has a strong dependence on the ambient. The working range is $-20\text{ }^\circ\text{C}$ to $60\text{ }^\circ\text{C}$ and the optimum range is $15\text{--}35\text{ }^\circ\text{C}$ [2]. At elevated temperatures, the capacity of the Li-ion battery fades and this is more predominant for high discharge rates [3]. At high temperatures (above $40\text{ }^\circ\text{C}$), the cells in the pack face capacity degrade, whereas with temperature below $20\text{ }^\circ\text{C}$, increase in internal resistance is observed. Temperature non-uniformity with in the cell is also a serious threat to Li-ion batteries [4]. Development of above-mentioned thermal stresses in the cell can lead to thermal runaway of the battery, and sometimes in extreme conditions, cells may burst causing fire hazards. The control of temperature especially in extreme ambient conditions is thus imperative. The effect of high discharge rates on the performance of Li-ion is also crucial. The abuse behaviour of high power rates on the performance and life cycle of Li-ion batteries has also been vividly explained by many researchers [5]. High C rates are more critical when combined with hyper-ambient conditions like that of deserts which calls for aggressive cooling of the battery pack. Air, liquid, and phase change material (PCM) cooling are recent techniques adopted by many leading manufacturers. PCM cooling falls under the passive cooling technique and is good for absorbing peak temperature in the cell at high C rates. Active cooling techniques absorb power from the battery

pack to operate and often require complex circuits and heavy pumps and compressors which decreases the EV's overall efficiency. Minichannels cooling technology is a promising technology that is being widely adopted by many researchers. Aluminium channels are mainly used in this cooling technique. References [6, 7] analysed the performance of minichannel cooling system and deduced that the pumping power required for this active cooling system is only 5 milliwatt. Presently, circular slots and zigzag channels are also being explored [8]. The present study is an attempt to develop a mathematical model of a Li-ion battery with liquid cooling system for hyper-ambient conditions for low and high discharge rates.

2 Problem Description

A 20 Ah LiFePO₄ battery with dimension 127 mm × 196 mm × 7 mm has been considered in the study [9]. The specifications are given in Table 1 [10].

A lot of simulations and experiments have been conducted to predict the performance of Li-ion batteries at different operating conditions. The physics, which covers the working of a Li-ion battery, is typical and computationally costly. There are two main approaches towards a holistic battery model. First is the simulation should not be time-consuming and costly, and second, it should be accurate. Battery models, which are based on electrochemical reactions, are accurate but are time-consuming. Porous electrode theory for battery model was first given by Newman and Tiedemann in 1975 [11]. The electrodes are assumed to be the superimposition of solid and electrolyte material matrix. Li-ion battery's complex physics has been captured by the dual potential multi-scale multi-dimensional battery model approach by ANSYS-Fluent.

Anode-separator-cathode sandwich layers hold the overall physics occurring inside the Li-ion battery, and electrical and thermal fields are solved in the CFD domain in the MSMD approach by the following equations:

$$\frac{\partial \rho C_p T}{\partial t} - \nabla \cdot (k \nabla T) = \dot{q} \quad (1)$$

Table 1 Battery specifications [10]

Properties	Positive electrode	Negative electrode	Cell
Material	Aluminium	Copper	Active zone material
Density (kg/m ³)	2719	8978	2092
Specific heat (J/kg-K)	871	381	678
Thermal conductivity (W/m K)	202	387.6	18.2

$$\nabla \cdot (\sigma_+ \nabla \varphi_+) = -j \quad (2)$$

$$\nabla \cdot (\sigma_- \nabla \varphi_-) = j \quad (3)$$

where

- σ_+ effective electric conductivity of positive electrode
- σ_- effective electric conductivity of negative electrode
- φ_+ phase potential for positive electrode
- φ_- phase potential for negative electrode
- j volumetric transfer for current density
- q heat generation rate during battery operation.

The present studies utilize Newman, Tiedemann, Gu, and Kim (NTGK) semi-empirical electrochemical model for the battery simulations. In this model, expression for volumetric transfer for current density in terms of phase potential is given as:

$$j = aY[U - (\varphi_+ - \varphi_-)] \quad (4)$$

where

a specific area of electrode sandwich sheet.

Y and U are model parameters, obtained through curve fitting of Voltage-current response curves of a certain reference battery and are functions of the depth of discharge (DOD).

$$Y = \left(\sum_{n=0}^5 a_n \text{DOD}^n \right) \exp \left[-C_1 \left(\frac{1}{T} - \frac{1}{T_{\text{ref}}} \right) \right] \quad (5)$$

$$U = \left(\sum_{n=0}^3 b_n \text{DOD}^n \right) - C_2 (T - T_{\text{ref}}) \quad (6)$$

$$\text{DOD} = \frac{\text{Vol}}{3600 Q_{\text{Ah}}} \left(\int_0^t j dt \right) \quad (7)$$

Here, Vol denotes battery's volume and Q_{Ah} stands for battery's capacity in ampere-hours, and C_1 and C_2 are NTGK model constants.

Heat is generated as a result of reversible and irreversible heat sources in the operation of the battery. Joule heating, electrochemical reaction heating, and entropic heating are the main causes of the generation of heat inside the battery. The heat source term is thus given as:

$$\dot{q} = \sigma_+ \nabla^2 \varphi_+ + \sigma_- \nabla^2 \varphi_- + j \left[U - (\varphi_+ - \varphi_-) - T \frac{dU}{dT} \right] \tag{8}$$

The study includes liquid cooling, and the governing equations of the process are defined by the following fundamental equations. [12]

1. Continuity equation:

$$\nabla \cdot \vec{V} = 0 \tag{9}$$

2. Momentum equation:

$$\rho_l \frac{\partial v}{\partial t} + \rho_l C_{pl} \nabla \cdot (vT) = \nabla \cdot (k_l \nabla T) \tag{10}$$

3. Energy equation:

$$\rho_l C_{pl} \frac{\partial(T)}{\partial x} = k_l \nabla^2 T \tag{11}$$

3 Meshing and Validation

The present study utilized the multizone method to generate a quality hexahedral mesh. The smooth transition from thicker boundaries to thinner boundaries was also ensured. The hexahedral elements generate fewer total elements and thus results in a faster and accurate solution. Figure 1 shows the meshed image of the battery model. There are 224,416 nodes and 194,249 elements in the generated mesh. The grid independence study showed that the model is stable.

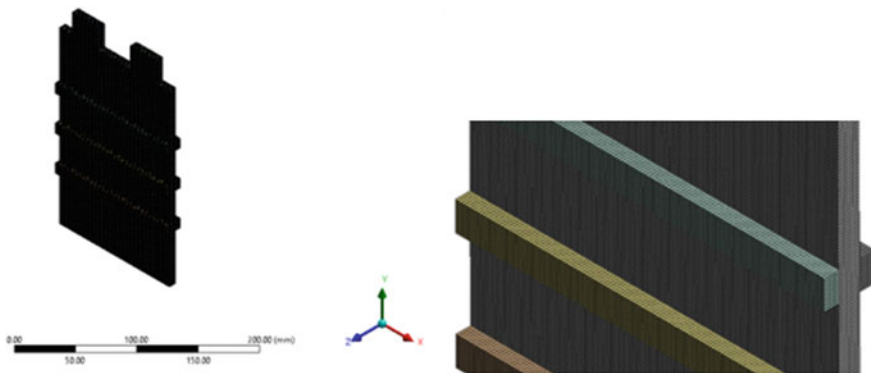
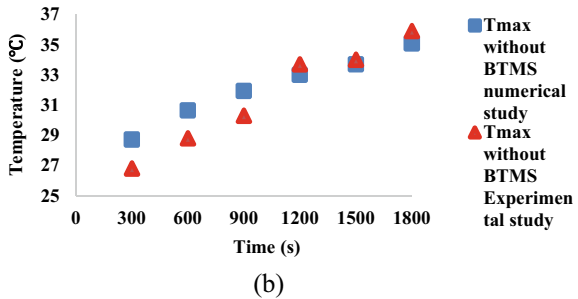
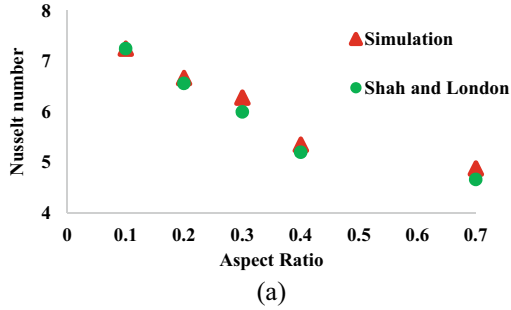


Fig. 1 Meshing

Fig. 2 a Validation for liquid cooling system **b** Validation for battery model without PCM



The validation of the battery model for aluminium minichannels has been done with Shah and London. Nusselt number was calculated for different aspect ratios of the minichannel. The calculated Nusselt number holds a strong agreement with the study done by Shah and London [13] on flow through rectangular minichannels. Figure 2a shows the validation study. The battery model was validated with the experimental study done by [14]. The error in the temperature values at initial time intervals is mainly due to: (i) design change restriction in the NTGK model and (ii) lack of the heat generation rate curves for the battery model in the experimental study. The results did not deviate from one another and hence the battery model is validated. Figure 2b shows the result of the validation study for the battery model.

4 Results and Discussions

The battery was simulated for 1800s at 298 K ambient condition using the battery model for 5 different C rates. The temperature–time trend is shown in Fig. 3. Lower discharge rates witnessed normal temperature value at the end of cycle, whereas for 5C discharge rate which lasted for 500 s, maximum temperature observed at the end of discharge cycle was 322.22 K.

The battery model was incorporated with rectangular minichannels of cross-sectional area 10 mm × 2 mm. An equal number of minichannels was incorporated on both faces of the battery. The liquid cooling system was tested with two liquids: (1)

Fig. 3 Without BTMS at 298 K

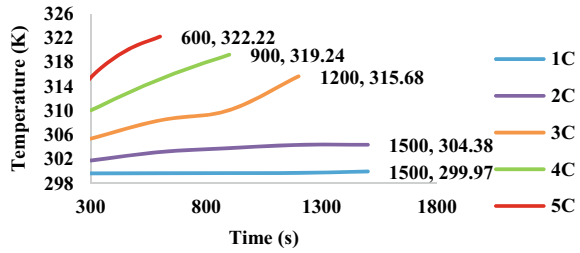


Table 2 Max–min temperature for 298 K, 15 m/s velocity

C Rates	Time (s)	T _{max} (K)	T _{min} (K)	Temp diff (K)
Ethylene glycol				
2C	1500	301.85	299.94	1.91
3C	1200	309.72	304.73	5
4C	900	310.43	304.51	5.9
5C	600	313.74	299.95	13.79
Water				
2C	1500	301.57	300.22	1.6
3C	1200	308.89	302.57	6.32
4C	900	309.18	302.29	6.89
5C	600	312.19	301.78	10.41

ethylene glycol and (2) water. The results proved that water is better cooling media than ethylene glycol when circulated at the same initial temperature, velocity, and C rates. Table 2 demonstrates the results of a comparative study between ethylene glycol and water.

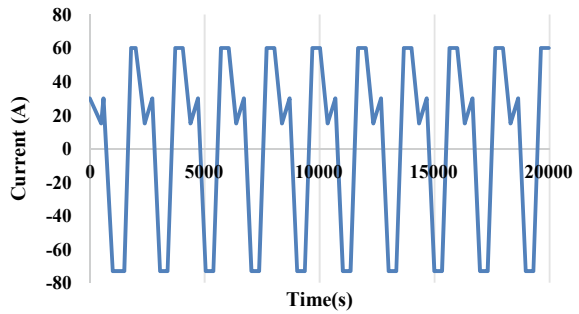
The thermal performance of the battery model was compared with different numbers of minichannels on each face of the battery. It was noticed that increasing the number of channels from 4 to 6 on each face improved the thermal performance of the battery for different C rates as given in Table 3. The study also noted that uniform temperature distribution in the battery is hard to achieve at high discharge rates. The temperature difference in the battery should be less than 5 K [15].

The thermal performance of the battery under liquid cooling system was further analysed by putting cyclic loading for a longer duration. The battery was simulated for a cyclic loading as shown in Fig. 4a. Water at the velocity of 0.15 m/s was circulated at an initial temperature of 308 K and ambient was maintained at 318 K. The charge–discharge cycles lasted for 20,000 s or 333.33 min. ROM technique was used to quicken the simulation [16]. It was observed that the battery’s maximum temperature was maintained at 318 K even after repeated charge–discharge cycles as shown in Fig. 4b. Figure 5 shows the variation of volume average temperature in the battery during the cyclic loading.

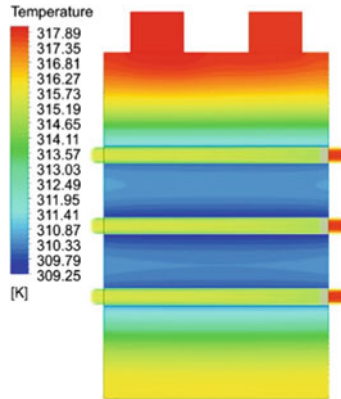
Table 3 Comparison between 6 and 4 mini channels at fluid velocity 0.02 m/s at ambient of 298 K

6 channels			
C rate	Time (s)	T _{max} (K)	T _{min} (K)
2C	1500	301.72	299.98
3C	1200	309.34	303.35
4C	900	309.86	303.09
5C	600	313.04	302.66
4 channels			
2C	1500	304.53	303.96
3C	1200	316	311.5
4C	900	319.63	316.55
5C	600	322.77	320.45

Fig. 4 a Cyclic loading on the battery b Temperature contour at the end of cyclic load

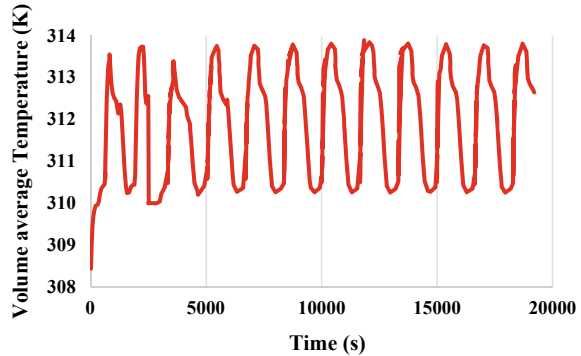


(a)



(b)

Fig. 5 Volume average temperature variation under cyclic loading



5 Conclusions

The study elucidates the idea of utilization of minichannels for battery thermal management in EVs. Parameters like the number of aluminium minichannel, liquid species, the velocity of fluid, and ambient temperature were found to have an ample effect on the thermal performance of the cooling system. Water was shown to have better performance than ethylene glycol. It was observed that the number of minichannels influences the maximum temperature in the battery, which decreases if the number of minichannels is increased. The temperature distribution in the battery gets disturbed when high discharging current is applied. This calls for application of a scattered pattern of minichannels rather than a concentrated one. The maximum temperature in the battery after the end of cyclic loading was 318 K. The limitation of the study is the demand for specific fluid inlet temperature especially when the battery is discharging in a hyper-ambient condition. Cyclic loading lasted for 333.33 min and proved that this cooling system has the potential to reduce the maximum temperature rise and temperature difference across the whole battery if incorporated appropriately.

Acknowledgements The authors would like to offer their sincere thanks to the Department of Science and Technology, Government of India funded project titled “Different Energy Vector Integration for Storage of Energy”, Grant number-TMD/CERI/MICAL19/2020/03(G) for providing the necessary sources for carrying out the research.

References

1. Ma S, Jiang M, Tao P, Song C, Wu J, Wang J, Deng T, Shang W (2018) Temperature effect and thermal impact in lithium-ion batteries: a review. *Progress Nat Sci: Mater Int* 28:653–666. <https://doi.org/10.1016/J.PNSC.2018.11.002>
2. Wright DR, Garcia-Araez N, Owen JR (2018) Review on high temperature secondary Li-ion batteries. *Energy Procedia* 174–181. <https://doi.org/10.1016/j.egypro.2018.09.044>. Elsevier Ltd

3. Ramadass P, Haran B, White R, Popov BN (2002) Capacity fade of Sony 18650 cells cycled at elevated temperatures: part I. Cycling performance. *J Power Sources* 112:606–613. [https://doi.org/10.1016/S0378-7753\(02\)00474-3](https://doi.org/10.1016/S0378-7753(02)00474-3)
4. Cho HM, Choi WS, Go JY, Bae SE, Shin HC (2012) A study on time-dependent low temperature power performance of a lithium-ion battery. *J Power Sources* 198:273–280. <https://doi.org/10.1016/J.JPOWSOUR.2011.09.111>
5. Chen Y, Kang Y, Zhao Y, Wang L, Liu J, Li Y, Liang Z, He X, Li X, Tavajohi N, Li B (2021) A review of lithium-ion battery safety concerns: the issues, strategies, and testing standards. *J Energy Chem* 59:83–99. <https://doi.org/10.1016/J.JECHEM.2020.10.017>
6. An Z, Shah K, Jia L, Ma Y (2019) A parametric study for optimization of minichannel based battery thermal management system. *Appl Therm Eng* 154:593–601. <https://doi.org/10.1016/J.APPLTHERMALENG.2019.02.088>
7. Lan C, Xu J, Qiao Y, Ma Y (2016) Thermal management for high power lithium-ion battery by minichannel aluminum tubes. *Appl Therm Eng* 101:284–292. <https://doi.org/10.1016/J.APPLTHERMALENG.2016.02.070>
8. Amalesh T, Narasimhan NL (2020) Introducing new designs of minichannel cold plates for the cooling of Lithium-ion batteries. *J Power Sources* 479:228775. <https://doi.org/10.1016/J.JPOWSOUR.2020.228775>
9. Panchal S, Dincer I, Agelin-Chaab M, Fraser R, Fowler M (2016) Experimental temperature distributions in a prismatic lithium-ion battery at varying conditions. *Int Commun Heat Mass Transfer* 71:35–43. <https://doi.org/10.1016/j.icheatmasstransfer.2015.12.004>
10. Verma A, Rakshit D (2022) Performance analysis of PCM-fin combination for heat abatement of Li-ion battery pack in electric vehicles at high ambient temperature. *Thermal Science and Engineering Progress* 32:101314. <https://doi.org/10.1016/J.TSEP.2022.101314>
11. Smith RB, Bazant MZ (2017) Multiphase porous electrode theory. *J Electrochem Soc* 164:E3291–E3310. <https://doi.org/10.1149/2.0171711JES/META>
12. Deng T, Zhang G, Ran Y, Liu P (2019) Thermal performance of lithium ion battery pack by using cold plate. *Appl Therm Eng* 160:114088. <https://doi.org/10.1016/J.APPLTHERMALENG.2019.114088>
13. Shah RK, London AL (1978) Rectangular ducts. *Laminar Flow Forced Convection Ducts* 196–222. <https://doi.org/10.1016/B978-0-12-020051-1.50012-7>
14. Talluri T, Kim TH, Shin KJ (2020) Analysis of a battery pack with a phase change material for the extreme temperature conditions of an electrical vehicle. *Energies* 13:507. <https://doi.org/10.3390/EN13030507>
15. Kim J, Oh J, Lee H (2019) Review on battery thermal management system for electric vehicles. *Appl Therm Eng*. <https://doi.org/10.1016/j.applthermaleng.2018.12.020>
16. Ghoreyshi M, Jirásek A, Cummings RM (2014) Reduced order unsteady aerodynamic modeling for stability and control analysis using computational fluid dynamics. *Prog Aerosp Sci* 71:167–217. <https://doi.org/10.1016/J.PAEROSCI.2014.09.001>

Numerical Investigation on Characteristics of Methane Combustion



Keyur Kadia, Nikhil A. Baraiya, and R. D. Shah

Abstract The fuel and oxidiser react as soon as they mix in a non-premixed flame, and the rate of combustion is restricted by the mixing. To improve mixing in such kinds of combustion, a high turbulence shear layer in the combustion system is preferred. By assisting in the fuel–air mixing process and providing a recirculation region that can act as flame holders and impact residence time, air swirling can control combustor performance. ANSYS will be used to do numerical analysis for the conditions mentioned above. The turbulence model used in this work is k-epsilon, which has been shown to be reliable in similar experiments. Fluent has a number of pressure-based algorithms. For velocity and pressure coupling, a SIMPLE method was used in this work. With two-equation turbulence models, the first-order upwind technique has been applied. The interaction between turbulence chemistry and non-premixed combustion was modelled using the (PDF). The thermal properties and flow velocity were displayed across the axial positions of the burner at varied regulating parameters.

Keywords Methane swirl combustion · Non-premixed model · Flow behaviour near swirler · Combustion flow physics

Nomenclature

AFR	Air–fuel ratio
CFD	Computational fluid dynamics
CTRZ	Central toroidal recirculation zone
PDF	Probability density function

K. Kadia (✉) · N. A. Baraiya · R. D. Shah
Mechanical Engineering Department SVNIT, Surat, India
e-mail: kadiakeyur982@gmail.com

Greek symbols

\emptyset	Equivalence ratio
f	Mixture fraction
R	Radius
S_N	Swirl number

1 Introduction

Combustion is the controlled release of heat and light when a substance burns in the presence of oxygen. Because it offers higher flame stability, safety, and operating range than premixed combustion, non-premixed combustion was used in most practical combustion systems, such as gas turbine engines, rocket combustion, and so on. Oxidiser and fuel are individually into the chamber in a non-premixed combustion process, depending on the distance between the fuel input and the oxidiser. The two types of diffusion flames are the normal and inverse diffusion flame (NDF) (IDF) swirl flows fascinate aeronautical and mechanical engineers in general, and they include an interaction of recirculation and turbulent flow mixing that assists flame stabilisation in CC systems. The development of a core toroidal recirculation zone is aided by this.

Karyeyen et al. [1] shown that the oxy-colourless distributed combustion approach produces a more homogeneous and regulated heat field, increases flame stability, and lowers pollutants, including combustion noise (CDC) conditions were achieved by controlled by hot reactive gaseous and species. Kumaran and Shet [2] has shown that using quantify the Using an annular premixed pilot flame, the effect of swirl level on the lean flame stability limits of swirled open premixed turbulent flames. A unique approach to the trials is to vary the swirl levels while keeping the Reynolds number and equivalency ratio constant. Low-swirl lean flame stability data from pilot testing may be utilised to build lean premixed (LP) low-emission burner systems. Huang and Yang [3] have shown that a vortex-breakdown-induced CTRZ occurs in the downstream area when the input S_N reaches a critical threshold. As the swirl number (S_N) grows, the recirculation zone (RZ) flows upstream and joins with the WRZ behind the centre body. If the central recirculating flow (CRF) penetrates in inlet annulus, excessive swirl can cause flame flashback. A greater S_N tends to enhance the turbulence's severity as a result, the flame's speed. Raj and Ganesan [4] have shown that the most critical geometric characteristics are hub-to-tip ratio, vane numbers, and vane angle. The flow parameter is influenced by characteristics of a proper turbulence prediction method. The study was unique in that it used appropriate turbulence models to determine the best vane angle for both weak and strong swirls. Kim [5] has shown that the flow and thermal characteristics in the effects of altering factors like the equivalency ratio and the inlet swirl angle on a three-dimensional combustor have been examined. The value of the equivalent

ratio grows as the equivalence ratio rises. Fuel is provided as a result of a higher inlet fuel velocity, the flame temperature rises, and the maximum temperature is shifted downstream. Because of the presence of inlet swirl velocity, the fuel and combustion air are more thoroughly mixed and burned over a shorter distance. As a result, as compared to the case where there was no swirl, the maximum reaction rate and temperature were shifted forward. Hashemi [6] has shown that pdf beta (beta-pdf) integration over a beta-pdf model for investigation of the turbulent non-premixed (NP) combustion flow. The characteristics of the species mole fraction, temperature, and density were obtained by utilising the flame holder to determine species concentrations and temperature in a burner, which are functions of the mixture fraction. Syred and Beer [7] have shown swirl flow improves stability by generating a toroidal recirculation zone and reduces combustion duration by causing high rates of fast mixing and entrainment of ambient fluids, especially near the recirculation zone borders. Swirl and cyclone burners are the two most common forms of swirl combustor. The swirling flow (SF) exhausts into a furnace or cavity in a swirl burner, and combustion takes place within slightly beyond the burner outlet. Air is forced tangentially into a huge, typically CC in the cyclone combustion chamber, where it exits centrally placed exit point on one point. The majority of the combustion occurs in the cyclone c. Hosseini [8] has shown that in this paper, using the ANSYS Fluent CFD simulation diffusion of methane into the air, the inlet air swirl number was used to investigate the radiation heat flux distribution flame's dynamic flow behaviour and temperatures. According to the findings, raising the swirl number of intake air 0 to 0.6 improves the furnace's IRZ, resulting in generation products of combustion in IRZ. As a result, fuel and air are mixed more effectively, eliminating high-temperature zones as a main source of nitrogen oxides to improve combustion efficiency (NO_x). Moreover, when the SN increases,, Wang [9] shown that in turbulent, 4 kW NP swirl flames of methane and air at three different air supply rates, the relationships among flow field, flame shape, and soot dispersion were examined experimentally. Two shear layers with maximal soot volume percentages were created at the interfaces of the central fuel jet (CFT) injection, RZ, and spinning jet. The reduction in soot towards the air side was linked to greater OH levels, suggesting that OH is involved in oxidation of soot. The studies revealed that encircling the jet with a greater recirculation rate increased the turbulent mixing between the jet and the surrounding air. Due to the recirculating fluid and fuel jet, the fuel jet penetration length was decreased. As a result, the increase in turbulent mixing and oxidation rate in the RZ is connected and decrease in soot volume % with air flow rate. Li [10] has shown that under various fuel-lean process parameters, under connected (V-shaped) swirl stabilised flames, a significant extension of the (IRZ) along the nozzle was observed to investigate the impact of flow velocity on heat release rate oscillation with a fixed global equivalence ratio for all tested conditions.

The literature reviewed above demonstrates a research gap in understanding the intricacies of the processes that influence methane combustion characteristics. Methane, as one of the most important components of natural gas, is regarded a very essential fuel, and detailed study is necessary to improve combustion efficiency. The

goal of this research is to better understand the thermal properties of swirl stabilised methane flames.

2 Numerical Set-Up

2.1 Geometry Modelling

The air channel, axial swirler, and unconfined test section make up the burner's geometry. Figure 1 depicts the model geometry of the unconfined burner under consideration in this study.

The axial swirler consists of radially inclined blades that impart a swirling motion to the axially entering air. The geometry consists of a 50 mm long, 53 mm outer surface, and 12.5 mm inner diameter intake air and fuel pipe. With 10 vanes at a 45° vane angle, the axial swirler has a 53 mm outer diameter and a 12.5 mm hub diameter. The axial swirler has been following by the test section.

To solve governing differential equations numerically, the CFD code fluent employs the control volume approach. Fluent solves turbulence equations and transport equations for conserved scalars (mean mixture fractions and variation) during the simulation in addition to continuity and momentum equations. Although the isotropic eddy viscosity hypothesis was utilised, a realisable k- ϵ type model was used for steady state simulations.

This RSM model was utilised for the subsequent computation of this numerical method for validation reasons. For whirling flow, the RSM model has proven to be the most effective. Fluent has a number of pressure-based algorithms. For velocity and pressure coupling, a SIMPLE method was used in this work. With two-equation turbulence models, the first-order upwind method was employed. The interaction between turbulence chemistry and non-premixed combustion has been studied using the probability density function (PDF).

Fig. 1 Geometry of burner
(all dimensions are in mm)

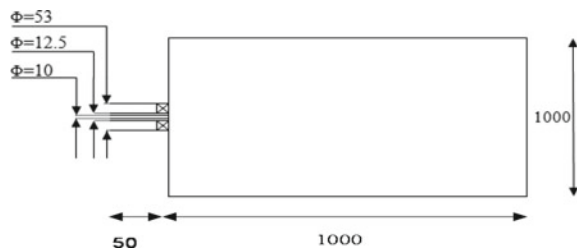


Table 1 Boundary conditions and parameter at different zones

Zone name	Zone type	Boundary condition
Air flow inlet	MFR inlet	0.025 kg/s
Fuel inlet	MFR inlet	0.000833 kg/s
Air exit from air passage	Interface	–
Air swirler inlet	Interface	–
Air swirler outlet	Interface	–
Air inlet to test section	Interface	–
Test section side walls	wall	–
Test section outlet	Pressure outlet	Zero pascal (Gauge)

3 Boundary Condition

For CFD analysis, precise boundary conditions must be implemented. The kind and character of the solution are determined by boundary conditions. In this work, a solver based on pressure is used. To find the solutions to the governing equations, the mass flow intake has been established as the inlet for air and fuel. At the test section's output, the atmospheric pressure condition was employed. Because the test portion is taken far away from the intake, its side faces are designated as walls. No-slip boundary criteria are applied to sidewalls. The interface is defined as the point where two neighbouring domains meet to allow fluid to flow. 0.025 kg/s was used as the air mass flow rate. 0.000833 kg/s is the appropriate fuel's mass flow rate (MFR). The fuel intake's mean mixture fraction has dropped from 1 to 0 (Table 1).

4 Numerical Simulation

Reactive analysis on combustor geometry is performed under burner case to understand the flame physics. For reactive analysis, methane had used as a fuel. The methane-air combination has a stoichiometric air–fuel ratio of 17.426. The analysis had carried out for different air–fuel ratios in the present case. Air mass flow rate has taken as a constant equal to 0.025 kg/s and according to the air–fuel ratio, mass of fuel varies from 0.00125 kg/s to 0.0005 kg/s. For numerical simulation, steady state two-equation realisable k-e turbulence and a non-premixed combustion model and steady state have used.

The equivalency ratio is calculated by dividing the stoichiometric fuel-to-air ratio which provides a ratio of fuel to air for combustion. The stoichiometric air–fuel ratio for methane-air combustion is 17.426. A different set of fuel mass flow rate values

Table 2 Fuel mass flow rate at different AFR

AFR	Fuel mass flow rate (kg/s)
20	0.00125
30	0.000833
40	0.000625
50	0.0005

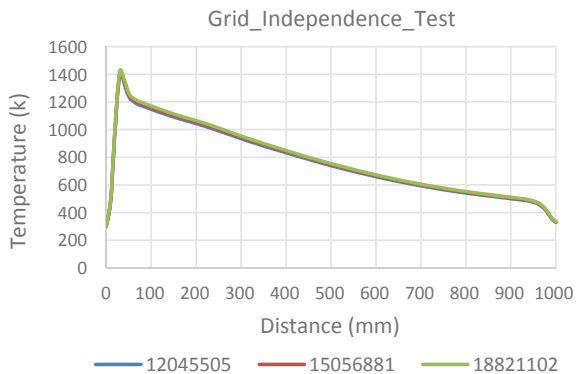
was used in the simulation analysis. Table 2 gives the MFR fuel values utilised with the various air–fuel ratios.

5 Grid Independence Test

The grid independence study has the most important aspect of CFD simulation. Grid independence has been carrying out. The simulation results are unaffected by the grid size refinement. Grid independence study starts with some initial less no. of elements then after next grid size (total number element) has taken as approximately 1.25 times the previous grid size (Total number elements). Three different grids size 12,045,505, 15,056,881, and 18,821,102 had the grid independence research which was chosen to be carried out.

In Fig. 2, the variation of temperature with centreline had taken at an axial distance has shown. Three different grid sizes had taken. Grid size one and grid size two both sizes temperature different has 3%. And for the grid size two and grid size three, temperature difference was only 1%. Grid size two had taken for analysis which is 150566881. So the difference negligible 1% variation in temperature. Grid size two had taken.

Fig. 2 Centre line variation of temperature at three different grid



6 Validation

The flame shape obtained from experimentally resembles a numerical simulation temperature contour. The maximum temperature in the above temperature contours is 2153 K, while the methane adiabatic flame temperature of is 2236 (k). Thus numerical work is validated by analytical theory and experimental work.

7 Result and Discussion

7.1 Velocity Contour

Velocity plays very important role in governing the thermal characteristics and flame stability which is analysed in this section.

Figure 4 shows the velocity contour for swirl number 0.70 (45^0). The mass flow rate of air is equal to 0.025 kg/s and it was fixed, however, the fuel flow rate was varied. Figures 1, 2, 3 and 4 show that the length of recirculation decreases as AFR increases at higher. This is due to the reduction in the dilation with the increase in the AFR due to decreasing temperatures with increase in AFR. To understand the vortical structures, the streamlines are plotted (Fig. 5). This analysis confirms the previous observation of variation in size of vortical structure with AFR. Also from the streamlines images, we can strength of recirculation zone is decreasing with decreasing fuel velocity flame. The observed behaviour is due to reduction in the shear with the deceasing velocity of the fuel. The reduction in the strength of the vortex reduces the mixing of fuel and mixing of air reduces which affects the flame stability drastically. But the strong turbulent structures may also trigger the fear of the instability which is need to be optimised for the stable flame.

The high swirl motion creates an (IRZ) in front of the swirler that fills the majority of the chamber cross section, and an outer recirculation zone (ORZ) towards chamber walls that finishes at zero axial velocity. The IRZ is crucial in stabilising the flame; hence, understanding swirling flow dynamics is important for understanding swirl flow dynamics with combustion.

8 Streamline Contour

Figure 5 illustrates streamline contour which has shown the swirler vigorous swirling flow creates significant velocity gradients in the swirler near area, resulting in rapid generation of high turbulence levels, as represented by the solid circles. The high swirl motion creates an IRZ in front of swirler that fills majority of the chamber cross section, and an ORZ towards chamber walls that finishes at zero axial velocity. The IRZ is crucial in stabilising the flame; hence, understanding swirling flow dynamics

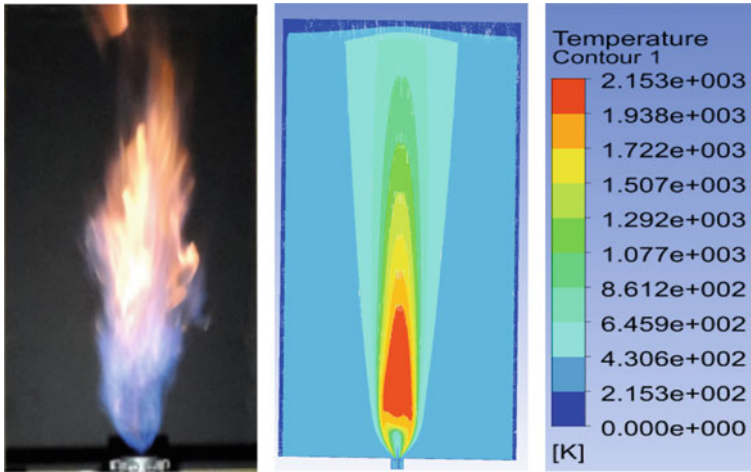


Fig. 3 Comparison of experiment and numerical simulation with variation of mass flow rate of fuel at $S_N = 0.70$ and $m_f = 0.00125$ kg/s

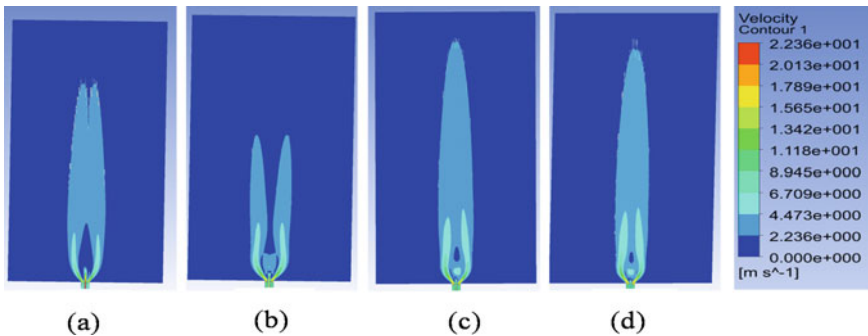


Fig. 4 Axial velocity for case $M_a = 0.025$ kg/s **a** AFR = 20; **b** AFR = 30; **c** AFR = 40; **d** AFR = 50

is important for understanding swirl flow dynamics with combustion. The ignition source is found in the recirculation region. Here, MFR of air kept same and decreased the MFR of fuel as AFR increased, and the length and strength of inner circulation zone decreased. That is the reason why the mass of fuel and mass of air did not get mix well. So the proper mixing did not happen for MFR of fuel and MFR of air maximum temperature of flame decreased along with flame length and width has changed like we will see in Fig. 6.

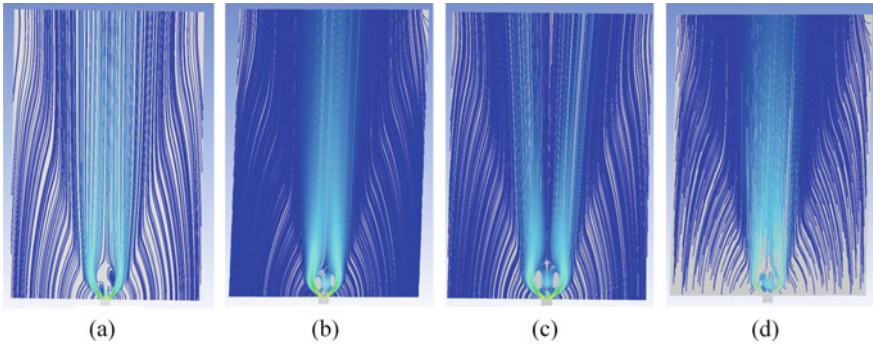


Fig. 5 Streamline for case and $Ma = 0.025$ kg/s **a** AFR = 20; **b** AFR = 30; **c** AFR = 40; **d** AFR = 50

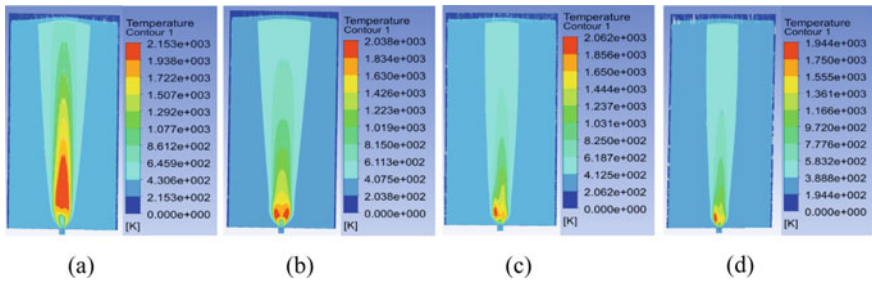


Fig. 6 Temperature for case and $Ma = 0.025$ kg/s **a** AFR = 20; **b** AFR = 30; **c** AFR = 40; **d** AFR = 50

9 Temperature Contour

Figure 6 shows the temperature contour for swirl vortex starts forming at the base of the burner. Comparison of Fig. 6 reveals that there is a large red region appears in flames captured with $S_N = 0.70$. The red flame region indicative of the maximum temperature zone is also seen to be reducing which is obvious due to aforementioned reason of the lower equivalence ratio and the quenching of the flame due to fuel deficiency. Swirl number 0.70 (45°) with the fix mass flow rate of air as 0.025 kg/s and varying AFR from 20 to 50 in a step of 10. With increase in the AFR, the flame temperature contours show the reduction in the overall temperature correspondingly the flame height is also expected to get reduced. With the higher AFR, the fuel flow rate reduces and hence the global equivalence ratio is reduced so the decreasing resulting into the reduction in the flame length. Though from the velocity and streamline contours from the previous section (4 and 5), the strength of the vorticity reduces with the increase the AFR but low fuel content results into quenching of the flame closer to the burner exit. Thus even at lower mixing, the flame length at lower equivalence ratios is lower. It can be observed that with an increase in

fuel flow rate, the flame length increases drastically. With an increase in airflow rate, the vortex starts forming at the base of the burner. Comparison of Figure 6 reveals that there is a large red region which appears in flames captured with $S_N = 0.70$. The red flame region indicative of the maximum temperature zone is also seen to be reducing which is obvious due to aforementioned reason of the lower equivalence ratio and the quenching of the flame due to fuel deficiency. The flame length is observed to be reducing with increase AFR shown in Figure 6; however, the width of the flame is seen to be independent and unaffected. This is due to the width dependency on the diffusion of the fuel into the fuel which dominant in the radial direction. However, the axial length is governed by the convection of the fuel. Hence, when the velocity of the fuel is decreasing, the flame length reduces, whereas the width of the flame is remaining constant.

In summary, the flame length reduces with increasing the air–fuel ratio due to lower equivalence ratios. The flame width did not alter because due to dominance of the diffusion in the radial direction compared to convection which is dominant in the axial direction. At a higher fuel flow rate, larger energy released due to combustion due higher equivalence ratios and also due to stronger vertical structure due to shear at higher fuel velocities. Also at lower equivalence ratio due to complete combustion, the yellow region, which is representative of soot formation, also reduces.

10 Conclusions

The swirled stabilised open flame combustor's flame stability is determined by the AFR and swirl intensity. Swirling flow is required for combustion to maintain high air velocity and adequate fuel and air mixing, as well as to ensure high flame stability in the combustor.

With increase in the AFR, the flame temperature contours show the reduction in the overall temperature; correspondingly, the flame height is also expected to get reduced. With the higher AFR, the fuel flow rate reduces and hence the global equivalence ratio is reduced so the decreasing resulting into the reduction in the flame length. Though from the velocity and streamline contours from the previous section Figs. 4 and 5, the strength of the vorticity reduces with the increase in the AFR but low fuel content results into quenching of the flame closer to the burner exit. Thus even at lower mixing, the flame length at lower equivalence ratios is lower.

Acknowledgements We are thankful to Mr. Piyuh Savaj, for his help during this work. This work was supported by the S. V. National Institute of Technology Surat [Grant Code No. 2020-21/Seed Money/13].

References

1. Karyeyen S, Feser JS, Gupta AK (2019) Swirl assisted distributed combustion behaviour using hydrogen-rich gaseous fuels. *Appl Energy* 251(5)
2. Kumaran K, Shet USP (2007) Effect of swirl on lean flame limits of pilot-stabilized open premixed turbulent flames. *Combust Flame* 151:391–395
3. Huang Y, Yang V (2005) Effect of swirl on combustion dynamics in a lean-premixed swirl-stabilized combustor. *Proc Combust Inst* 30:1775–1782
4. Raj RTK, Ganesan V (2008) Study on the effect of various parameters on flow development behind vane swirlers. *Int J Therm Sci* 47:1204–1225
5. Kim MY (2012) Effect of swirl on gas-fired combustion behaviour in a 3-D rectangular combustion chamber. *World Acad Sci, Eng Technol* 6
6. Hashemi SA, Fattahi A, Sheikhzadeh GA, Mehrabian MA (2011) Investigation of the effect of air turbulence intensity on Knox emission in non-premixed hydrogen and hydrogen-hydrocarbon composite fuel combustion. *Int J Hydrogen Energy* 36:10159–10168
7. Syred N, Beer JM (1974) Combustion in swirling flows: a review. *Combust Flame* 23:143–201
8. Hosseini AA, Ghodrat M, Moghiman M, Pourhoseini SH (2020) Numerical study of inlet air swirl intensity effect of a Methane-air diffusion flame on its combustion characteristics. *Case Stud Therm Eng* 18(2):100610
9. Wang LY, Chatterjee S, An Q, Steinberg AM, Gülder ÖL (2019) Soot formation and flame structure in swirl-stabilized turbulent non-premixed methane combustion. *Combust Flame* 209:303–312
10. Wang K, Li F, Zou P, Lin X, Mao R, Yu X (2019) Effect of the fuel-air flow velocity on heat release rate of swirling non-premixed methane flames. *Aerosp Sci Technol* 95:105465

Computational Heat Transfer Analysis of Perforated Annular Fin with Highly Conductive Insert Under Forced Convection



S. Lakshmanan and M. Venkatesan

Abstract Annular fins are commonly employed in industrial applications to cool cylindrical surfaces such as tube walls. In the present work, heat transfer characteristics of a perforated annular fin with insert are studied using commercial code COMSOL Multiphysics. The effect of perforation radius, position of perforation, insert radius, and insert conductance ratio on fin base temperature is studied. A constant boundary heat flux of 10 W, with air inlet velocity of 0.1 m/s is fixed. The annular fin and heating cylinder dimensions are kept constant. Heat transfer characteristics of various combinations of insert and fin materials are studied. When compared to solid annular fins, the perforated annular fin exhibits a substantial improvement in heat transfer and a significant weight reduction. The effect of the highly conductive insert on the fin base temperature is reported. The results demonstrate that when the conductance ratio rises, the base temperature falls.

Keywords Annular fin · Forced convection · Perforation · Highly conductive insert · Laminar flow

Nomenclature

N	Number of perforations
H_{fin}	Fin height, mm
R_o	Radius of heating cylinder, mm
R_{fin}	Radius of fin, mm
D	Radial distance of perforation, cm
R_{pe}	Radius of perforation, mm
W_i	Width of insert, mm
T	Temperature, °C

S. Lakshmanan · M. Venkatesan (✉)

School of Mechanical Engineering, SASTRA University, Tirumalaisamudram, Thanjavur, Tamil Nadu 613401, India

e-mail: mvenkat@mech.sastra.edu

1 Introduction

Fins are extended surfaces that are utilized to disperse heat and keep the device running efficiently by keeping the base temperature below a specified threshold. Different types of fins with various cross-sectional profiles are used to enhance the heat transfer based on the requirements. Annular fins are most commonly used in industrial applications and electronic systems, where heat is dissipated radially. Ullmann and Kalma [1] studied the fin efficiency and optimized dimensions of annular fins with four different profiles. Chen and Hsu [2] investigated the heat transfer characteristics of a vertical annular circular fin under forced convection through experiments. By subdividing the annular fins into six subdomains, the average heat transfer coefficient was calculated for various fin spacings and air velocity.

More heat is produced by modern engineering systems. The system's performance is largely influenced by the heat generated. These systems demand more effective fins with less weight. In electronic systems used for aerospace applications, reducing the weight of a system decreases the failure risk and increases its life. Balachandar et al. [3] studied the heat transfer characteristics of a hollow cylindrical pin fin on a vertical base plate. It was concluded that perforations decreased the weight as well as increased the heat transfer rate by increasing the airflow. The optimum pin fin dimensions were predicted using artificial neural network technique. Ibrahim et al. [4] studied the effect of various hole shapes on vertical heated fins in forced convection. Circular holes have the greatest temperature differential between the fin tip and the heat collector, followed by square and triangular perforations. By changing the number of holes in a rectangular fin on a flat surface, Shaeri and Yaghoubi [5] numerically investigated the effect of perforations on a flat surface. The efficacy of the perforated fin was predicted using a correlation. Karabacak and Yakar [6] experimentally studied the effect of the position of holes on a perforated horizontal circular fin under forced convection conditions. Jassem [7] experimentally studied the effect of different shapes of perforation in a rectangular perforated fin under natural convection. Triangular perforations had the highest heat transfer coefficient, followed by circular, square, hexagonal, and non-perforation perforations.

Adding high conductive materials ('inserts') is a method of improving the heat transfer rate of a fin without changing its dimension by reducing its conduction resistance. Chung [8] reviewed materials for enhancing thermal conduction using inserts. The properties of highly conductive materials, thermal interface materials, and the methods of preparation were reviewed. Bejan [9] proposed a constructal theory for increasing heat transfer by incorporating high conductivity materials into a tree-like structure within a heat transfer system. Hajmohammadi et al. [10] numerically studied the impact of inserts in a rectangular fin numerically and discovered an optimal insert aspect ratio that maximizes insert efficacy for a given insert volume fraction. Recently, Hajmohammadi et al. [11] numerically studied the effect of highly conductive inserts in an annular fin and geometrically optimized the insert dimensions to maximize the heat transfer.

In this study, the effect of perforation in an annular fin attached to a heating tube is studied; numerical simulations are used to investigate the parametric dependency of the fin on fin base temperature. Fins with holes of 4, 8, 12 are investigated individually. The effects of several parameters on base temperature are studied, including perforation radial distance and perforation radius. Numerical simulations with various combinations of insert materials are also used to study the influence of high conductivity inserts on a perforated annular fin. The impact of insert radius on various material combinations is analyzed.

2 Problem Description

In this study, a single annular fin made of aluminum is put around a vertical pipe with a radius of 1 cm and a height of 4 cm, as illustrated in Fig. 1. The fin assembly is held within a 15 × 15 × 15 cm air domain, with the top side serving as an inlet and the bottom serving as an outlet, and the ambient air temperature is 20 °C. Three distinct models with number of perforations (4, 8, 12) are analyzed by varying the perforation radius and the radial distance of the perforations from the center. Figures 3a–c show isometric views of 4 holes, 8 holes, and 12 holes, respectively. Insert metals are used as high conductive materials near the pipe. Effect of the insert metal on the base temperature is studied by varying its width. The model’s top perspective is shown in Fig. 2. The impact of perforation radius and its radial distance from the origin is investigated in depth using parametric analysis on the annular fin. The impact of insert material on the temperature of the fin base is also noted.

3 Governing Equations and Boundary Conditions

COMSOL Multiphysics (5.3a) is used to solve Eqs. (1), (2), and (3) in numerical analysis.

The continuity equation:

$$\frac{\partial \rho}{\partial t} + \nabla \cdot (\rho \mathbf{u}) = 0 \quad \frac{\partial \rho}{\partial t} + \nabla \cdot (\rho \mathbf{u}) = 0 \tag{1}$$

The momentum equation:

$$\frac{\partial \rho \mathbf{u}}{\partial t} + \nabla \cdot (\rho \mathbf{u} \mathbf{u}) = -\nabla p + \nabla \cdot \boldsymbol{\tau} + \mathbf{F} \quad \frac{\partial \rho \mathbf{u}}{\partial t} + \nabla \cdot (\rho \mathbf{u} \mathbf{u}) = -\nabla p + \nabla \cdot \boldsymbol{\tau} + \mathbf{F} \tag{2}$$

The energy equation:

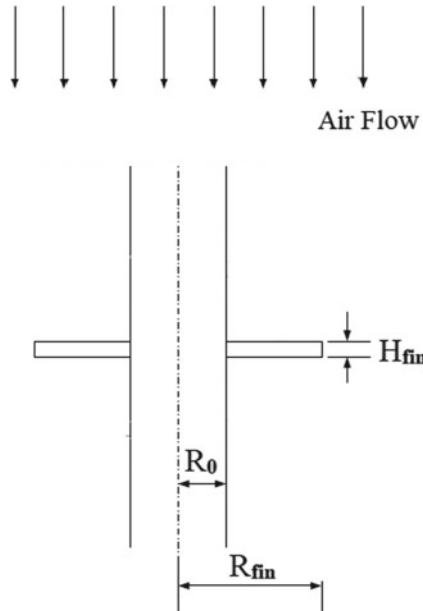


Fig. 1 Side view of the model

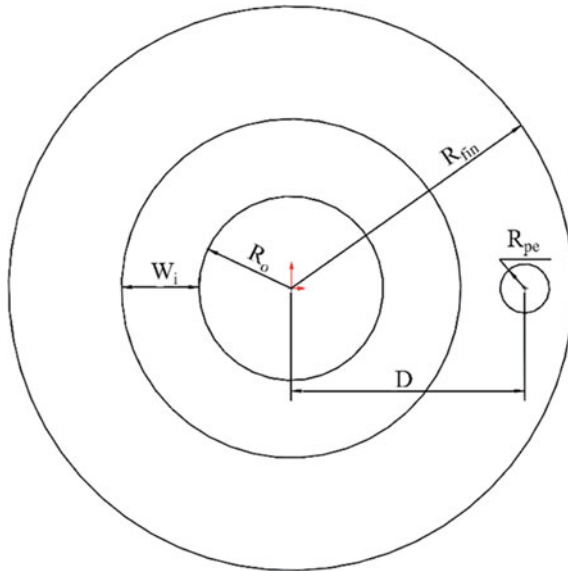


Fig. 2 Top view of the with model (details of a perforation)



Fig. 3 Types of model examined in the present study

$$\frac{\partial}{\partial t} \left[\rho \left(e + \frac{1}{2} u^2 \right) \right] + \nabla \cdot \left[\rho \mathbf{u} \left(e + \frac{1}{2} u^2 \right) \right] = \nabla \cdot (k \nabla T) + \nabla \cdot (-p \mathbf{u} + \boldsymbol{\tau} \cdot \mathbf{u}) + \mathbf{u} \cdot \mathbf{F} + Q \quad (3)$$

The heating cylinder is heated with a constant boundary heat supply of 10 W. Air flows from top to bottom with an inlet velocity of 0.1 m/s. Heat conduction governed by Fourier’s law governs the heat transfer from heating cylinder to the annular fin, while convection mode governed by mass momentum and energy equations takes place between the solid and fluid. Heat transmission from the fin surface to the surrounding fluid is implemented using a laminar flow model. Heat transmission from the fin surface to the surrounding fluid is implemented using a laminar flow model. A steady state is assumed where the heat transfer and laminar flow physics are coupled using non-isothermal flow Multiphysics. The effect of radiation on heat loss is negligible at low ambient temperatures. So, heat loss due to radiation is not taken into account in this analysis.

4 Grid Independence Study

The model is given a uniform normal meshing. According to the grid independence analysis presented in Fig. 4, the ideal mesh value is obtained by having a number of domain elements higher than 190,000. As a result, the minimum mesh quality is 0.009475.

5 Model Validation

The model validated in Balachandar et al. [3] is modified in the present work. As a further validating exercise, a cylinder in cross flow problem is taken from Cengel et al. [12]. A cylinder of diameter 10 cm is placed in an open area where an air of 10 m/s velocity and temperature of 10 °C is flowing across the cylinder. The average surface temperature of the cylinder is given as 110 °C. The heat loss from the cylinder and its heat transfer coefficient is calculated theoretically and numerically. Table 1

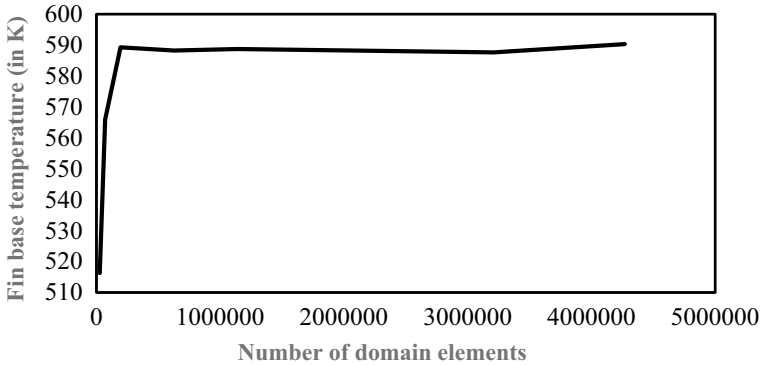


Fig. 4 Grid independent study (applied to a vertical cylinder powered by a 15 W power source)

Table 1 Comparison of results of analytical solution of Cengel et al. [12] and numerical method

Q (W) this work	Q (W) Cengel	h (W/m ² °C) present work	h (W/m ² °C) Cengel
1116.5	1093	35.5	34.8

gives the comparison of results between Cengel et al. [12] and the numerical method. The values obtained are very close to the results in Cengel et al. [12]. Hence, the numerical model is validated.

6 Results and Discussion

6.1 Heat Transfer Characteristics of an Annular Fin

The cases for which parametric studies are conducted in this study are listed in Table 2. It was found that the heat transfer characteristics of the fin depend on parameters such as number of perforations, perforation radius, and radial perforation distance from the center and the amount of insert material.

For a given boundary heat flux, the influence of fin geometry on heat transfer characteristics is investigated by changing the number of perforations, perforation

Table 2 Cases considered in the present analysis

Case no	Parameters	Range
–	Number of perforations (N)	4,8,12
1	Radius of perforation (R _p)	2–1.2 mm
2	Radial distance of perforation (D)	2.5–1 mm
3	Width of insert (W _i)	0–10 mm

radius, and perforation radial distance. To show their effects, graphs are plotted for 10 W heat supply in all cases. However, the results are found to be identical for other heat sources as well.

Case 1–Variation with perforation radius.

Figures 5 and 6 show the relationship between heat transfer characteristics and perforation radius. The analysis is done by varying perforation radius and keeping radial distance as 2.5 and 2 cm and all other parameters constant. It is clear from Figs. 5 and 6 that the fin base temperature decreases as the radius of perforation increases up to a certain point. In Fig. 5, the base temperature starts increasing when a part of perforation starts going out (after 0.5 cm radius) from the fin outer periphery. Fin breaks when the radius of perforation reaches a value of 0.68 cm in 12 holes at D = 2.5 cm.

In case of Fig. 6, base temperature starts increasing when the fin is about to break due to the enlargement of perforations. In both the cases, initial decrease in base temperature is due to an increase in convection heat transfer.

An increase in perforation radius increases airflow air area and increases the heat transfer. In Fig. 5, base temperature starts decreasing when the conduction heat transfer decreases. When the perforation starts disturbing the outer geometry of the fin, heat transfer decreases. Fin breaks when the radius of perforation reaches a value of 0.7 cm and 0.6 cm in 8 and 12 holes model, respectively, at D = 2 cm.

Case 2–Variation with radial distance of perforation.

Figures 7 and 8 depict the heat transfer variation with respect to the radial distance of perforations. The radius of perforation is 0.3 and 0.4 cm from origin, respectively. To study the dependency of radial distance alone, all other parameters are kept constant. Base temperature decreases slightly as the radial distance is decreased due to an

Fig. 5 Variation of fin base temperature with respect to perforation radius (at D = 2.5 cm)

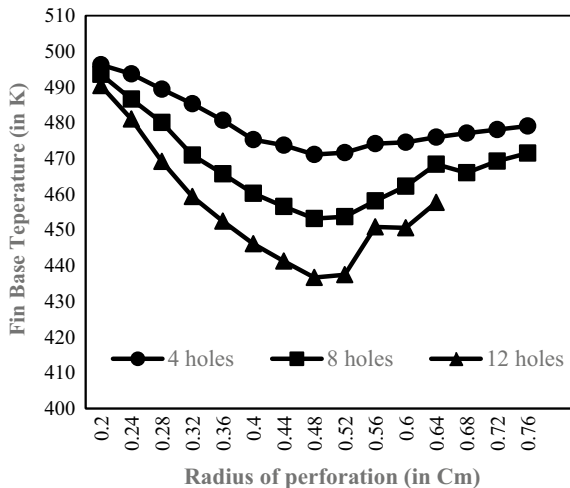
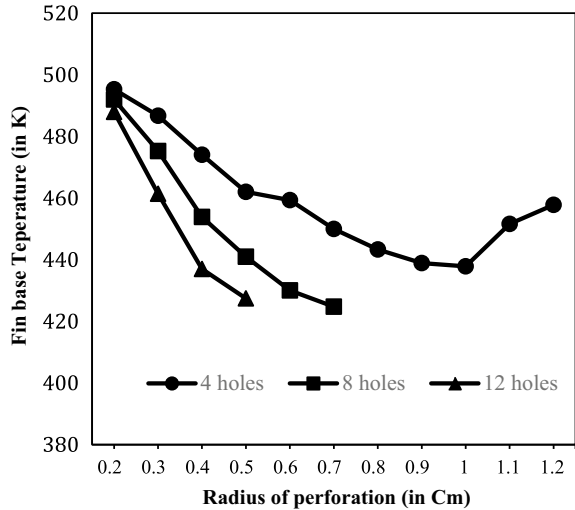


Fig. 6 Variation of base temperature with respect to perforation radius ($D = 2\text{ cm}$)



increase in temperature gradient, and after a particular distance, base temperature starts increasing due to an increase in conduction resistance.

In case of 4 holes model, the base temperature starts to increase when the hole comes near the source or fin base. In case of 8 holes and 12 holes model, base temperature starts to increase when the distance between two adjacent holes decreases and the fin is about to break. Figure 9a–c show the temperature distribution of perforated annular fin with 4, 8, 12 holes, respectively. The red color denotes the high temperature zone, which is the temperature of the heating cylinder, and the temperature decreases radially from there.

Case 3–Variation with insert width.

Fig. 7 Variation of fin base temperature with respect to the radial distance of perforation ($R_{pe} = 0.3\text{ cm}$)

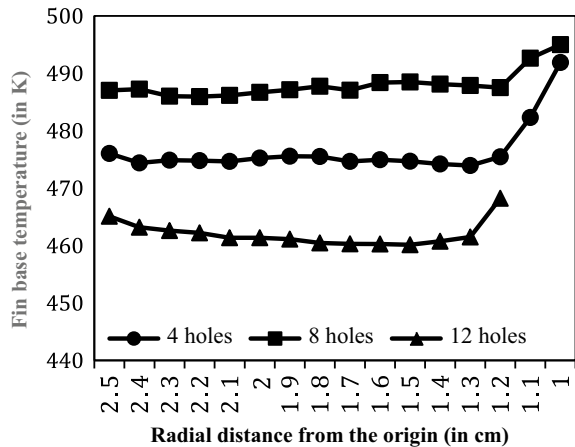
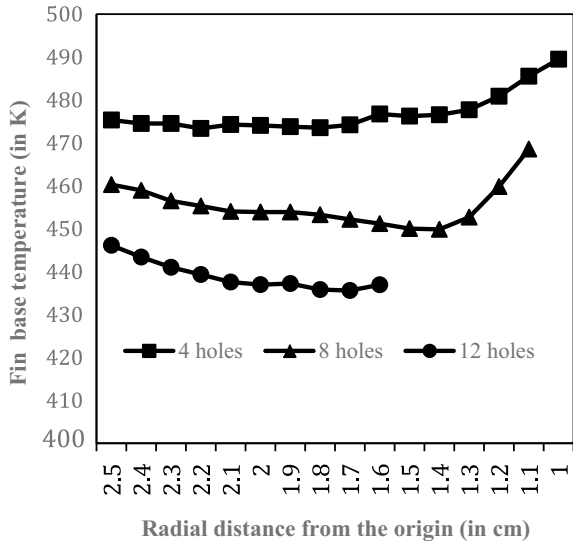


Fig. 8 Variation of base temperature with respect to the radial distance of perforation ($R_{pe} = 0.4$ cm)



High conductive insert metals are added to the fin material for enhancing the conduction heat transfer. Adding high conductive material near the heating tube will conduct more heat toward the perforations followed by increased heat dissipation through convection from perforation. When compared to a solid fin, adding high conductive material enhances heat transfer and lowers the base temperature.

Width of the insert material is varied and its effect on fin base temperature is shown in Figs. 10, 11, 12 for 4, 8, 12 holes models, respectively. When the insert radius is increased, volume fraction of high conductive material increases. This will result in enhanced heat transfer due to increased conduction reduction in base temperature. The combinations of fin-insert materials are Steel-Aluminum (Al), Steel-Copper (Cu), Steel-Silver (Ag), Aluminum-Copper, and Aluminum (Al)-Silver (Ag).

Insert conductance ratio is the ratio of thermal conductivity of insert material to fin material. In Figs. 10, 11, and 12, the models having more insert ratios have more variations in slope. The decreasing trend shows the decrease in base temperature. Less insert ratio produces almost a flat curve indicating no change in temperature. 12 holes models have more slope compared to that of 4 holes and 8 holes model with same combinations. The effect of insert in decreasing the base temperature is more in case of 12 holes models.

7 Conclusions

The present study used the commercial CFD code COMSOL Multiphysics (5.3a) to simulate forced convection heat transfer in a perforated annular fin with highly conductive inserts. The heat transfer characteristics of various fin parameters, such as

Fig. 9 Temperature distribution at $R_{pe} = 4$ mm and $D = 2.5$ cm. **a** for $N = 4$, Temperature distribution. **b** For $N = 8$. **c** For $N = 12$

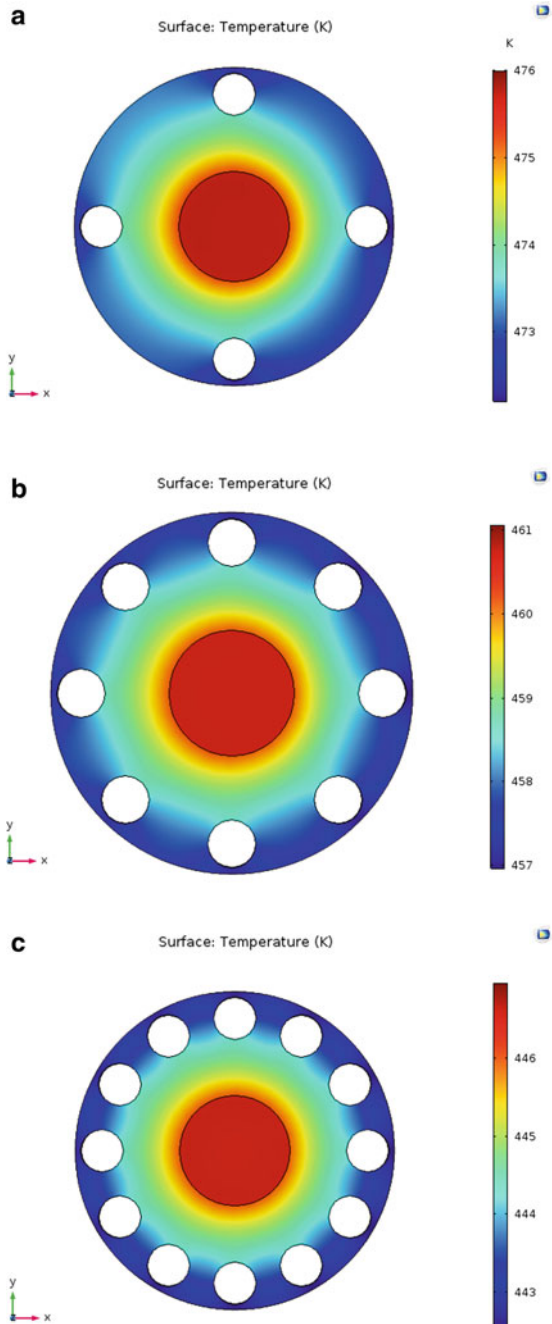


Fig. 10 Variation of base temperature with respect to insert width ($N = 4$, $R_{pe} = 4$ mm, $D = 2.5$ cm)

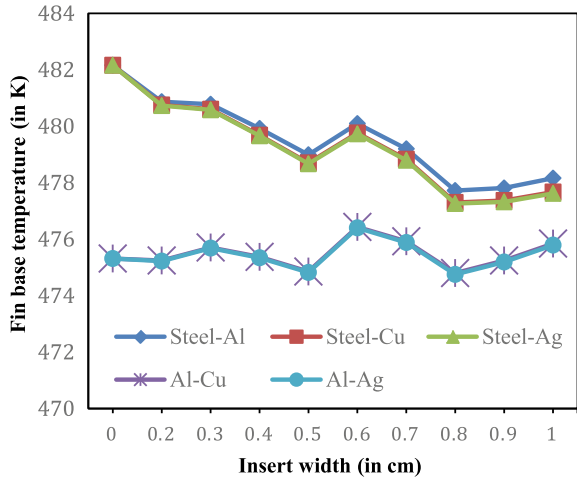
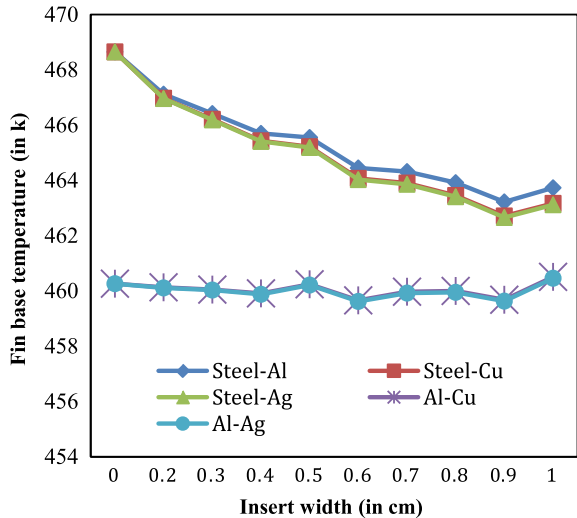
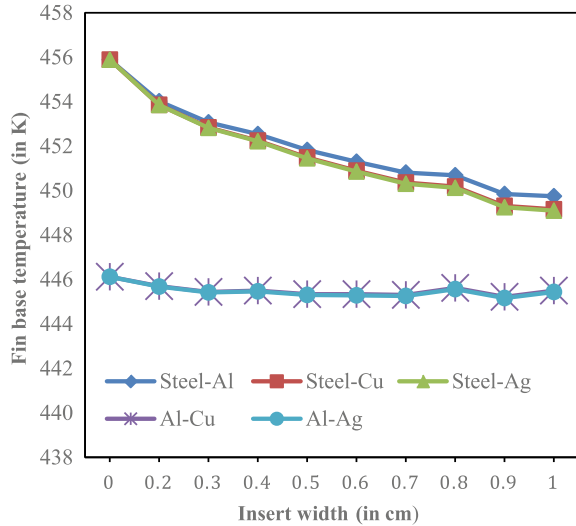


Fig. 11 Variation of base temperature with respect to insert width ($N = 8$, $R_{pe} = 4$ mm, $D = 2.5$ cm)



perforation radius and radial distance, were studied. The results show that a perforated annular fin increases heat transfer with a significant reduction in weight. Addition of a highly conductive insert in the perforated fin decreases the fin base temperature. Increasing the conductance ratio of the insert increases the heat transfer.

Fig. 12 Variation of base temperature with respect to insert width ($N = 12$, $R_{pe} = 4$ mm, $D = 2.5$ cm)



References

1. Ullmann A, Kalman H (1989) Efficiency and optimized dimensions of annular fins of different cross-section shapes. *Int J Heat Mass Transf* 32(6):1105–1110
2. Chen HT, Hsu WL (2008) Estimation of heat-transfer characteristics on a vertical annular circular fin of finned-tube heat exchangers in forced convection. *Int J Heat Mass Transf* 51(7–8):1920–1932
3. Balachandar C, Arunkumar S, Venkatesan M (2015) Computational heat transfer analysis and combined ANN–GA optimization of hollow cylindrical pin fin on a vertical base plate. *Sadhana* 40(6):1845–1863
4. Ibrahim TK, Mohammed MN, Mohammed MK, Najafi G, Sidik NAC, Basrawi F, Abdalla AN, Hoseini SS (2018) Experimental study on the effect of perforations shapes on vertical heated fins performance under forced convection heat transfer. *Int J Heat Mass Transf* 118:832–846
5. Shaeri MR, Yaghoubi M (2009) Thermal enhancement from heat sinks by using perforated fins. *Energy Convers Manage* 50(5):1264–1270
6. Karabacak R, Yakar G (2011) Forced convection heat transfer and pressure drop for a horizontal cylinder with vertically attached imperforate and perforated circular fins. *Energy Convers Manage* 52(8–9):2785–2793
7. Jassem RR (2013) Effect the form of perforation on the heat transfer in the perforated fins. *Acad Res Int* 4(3):198
8. Chung DD (2001) Materials for thermal conduction. *Appl Therm Eng* 21(16):1593–1605
9. Bejan A (1997) Constructal-theory network of conducting paths for cooling a heat generating volume. *Int J Heat Mass Transf* 40(4):799–816
10. Hajmohammadi MR, Ahmadian M, Nourazar SS (2019) Introducing highly conductive materials into a fin for heat transfer enhancement. *Int J Mech Sci* 150:420–426
11. Hajmohammadi MR, Rasouli E, Elmi MA (2020) Geometric optimization of a highly conductive insert intruding an annular fin. *Int J Heat Mass Transf* 146:118910
12. Cengel YA, Pérez H (2004) Heat transfer: a practical approach. *Transferencia de calor*

Membrane Electrode Assembly Material for DMFC-A Review



Seema S. Munjewar, Arunendra K. Tiwari, and Rohan Pande

Abstract Direct alcohol fuel cells (DAFCs) have recently attracted much attention. In all DAFCs, direct methanol fuel cells (DMFCs) are seen as reliable substitute to Li-ion batteries in movable application. At present, improvement in the DMFC performance has been observed. Material of DMFC component is the key factor for performance improvement DMFC. But within all component, membrane electrode assembly (MEA) is the shank of DMFC as it directly takes part in chemical reaction. This paper studied MEA material of DMFCs and also addresses the material evolution of DMFC. The improvement to be expected in the DMFC for the future energy potential resources.

Keywords Methanol · Methanol fuel cell · Direct alcohol fuel cell

1 Introduction

The movable electronic devices expending more power and also anticipated more in future. Li-ion batteries are unable to hold with movable electronic devices. Thus, the direct liquid fuel cell (DLFC) is best suited as substitute to movable electronic devices. DLFC is the polymer membrane fuel cell, where liquid fuel (alcohol family) is directly used. Easy handling, storage, transport of fuel, high theoretical energy density and eliminates fuel reformer are the several advantages of DLFC. Energy density of fuel is given in Table 1 [1].

With a tremendous literature survey, it has been noticed that methanol fuel cell is the best suited for movable application. DMFC has various merits over other type of fuel cell (like easy storage, high energy density, small and simple construction)

S. S. Munjewar (✉)
VNIT, Nagpur, India
e-mail: seemamunjewar@gmail.com

A. K. Tiwari
SPRERI, Anand, Gujarat, India

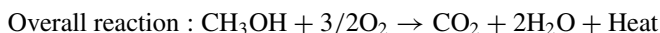
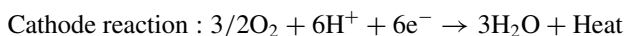
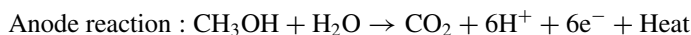
R. Pande
SVNIT, Surat, India

Table 1 Liquid fuel energy density [1]

Alcohol	ΔG° (KJ/mol)	E_{cell} (V)	W_e (KWh/Kg)
CH ₃ OH	-702	1.213	6.09
C ₂ H ₂ OH	-1325	1.145	8.00
C ₃ H ₃ OH	-1853	1.067	8.58

[1–4]. Portable electronics devices like laptop, mobile phones require few watts to a few hundred watts, thus DMFCs are suited for portable devices [4]. DMFC is subcategorized into passive DMFCs and active DMFCs based on the reactant feed. Aqueous methanol solution is used in passive DMFC. In active DMFC, pure methanol is circulated by small size pump at anode side [3–7]. Active supply of fuel and oxygen makes the fuel cell system more bulky and consumes the electricity which is generated by fuel cell, thus reducing the overall efficiency. In contrast, passive supply of DMFC is best suited in place of Li-ion battery for movable electronics gadgets because of low parasitic losses [3].

Oxidation and reduction flow diagram of DMFC is shown in Fig. 1. Membrane conducted positive ion from the anode side to the cathode side. Methanol at anode catalyst produces electron and supplies by some electrical cable to cathode. The oxidation and reduction reaction shown below generates six electrons, six protons, CO₂ and heat.



At present, research has been carried out on both active and passive DMFCs. Motorola lab developed micro-active DMFC system and also developed polymer vapour feed DMFC. Some other companies developed and optimized passive DMFC catalyst and membrane [6]. Although major development has been done in methanol fuel cell and some has to be developed in future.

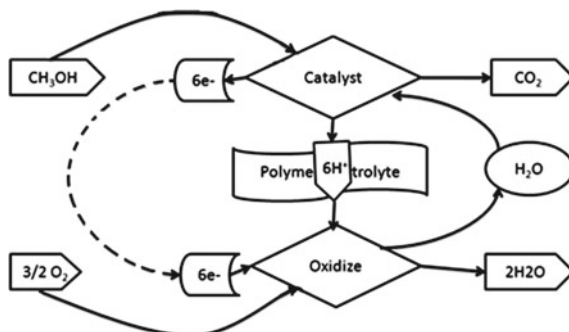
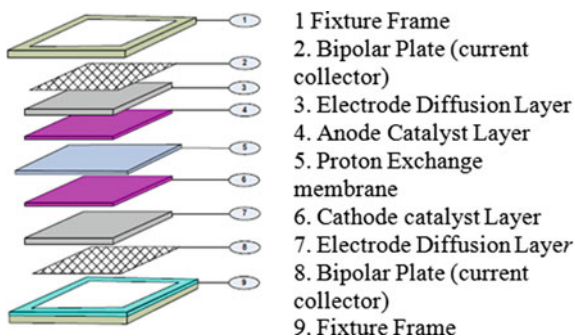
Fig. 1 Reaction flow chart of DMFC

Fig. 2 DMFC structure [2]

The aim of this paper is to review commercial material of membrane electrode assembly (MEA) of passive DMFC and simultaneously discuss the material evolution of MEA which make DMFC possible to be commercialized.

2 Passive DMFC

The main important component in DMFC is PEM, anode cathode catalyst, and current collector which is shown in Fig. 2. The membrane electrode assembly is sandwiched between the flow field plates [1].

3 Membrane Electrode Assembly (MEA)

Anode catalyst supported on diffusion layer, electrolyte membrane, cathode catalyst supported on diffusion layer are the five sequential part of membrane electrode assembly [3]. The electrode both anode and cathode are supported on carbon paper or carbon cloth. The carbon paper or carbon cloth gives the way to flow the reactant, oxidant and product of reaction. They also perform the role of conductor as well as current collector. The catalyst is used to increase the chemical reaction (oxidation and reduction) to harness electricity.

Generally, the two approaches used to produce MEA divided into (a) and (b) as depicted in Fig. 3. In the first method, catalyst directly applied onto the proton conductive membrane to form catalyst coated membrane (CCM) and CCM sandwiched in between electrically conductive supports (diffusion layer) by rolling or hot pressing as shown in Fig. 3a. In a second method called separate electrode method, catalyst spreads onto the diffusion layer formed electrode and then a polymer membrane assembled with electrode by hot pressing as shown in Fig. 3b [3]. The various methods for catalysts application either on the membrane or diffusion layer are given also in Fig. 3.

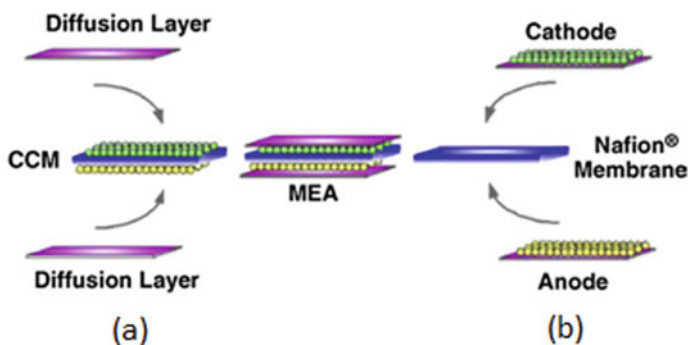


Fig. 3 Making of MEA **a** catalyst layer fixed onto the membrane **b** separate electrode method [3]

3.1 Polymer Electrolyte Membrane (PEM)

Electrolyte membrane development is the important and broad topic in DMFC. The essential separator and proton carrier in MEA are electrolyte membrane which sandwiches in between the anode and cathode electrode. Nafion® (Nafion® 112, Nafion® 115 and Nafion® 117) is most commonly used and readily available membrane in solid polymer electrolyte due to their high chemical stability and excellent proton conductivity. The limitation of direct methanol fuel cell is methanol permeation through Nafion® membrane and interfacial resistance of MEA layer. Teflon polymer is similar to Nafion® which provides mechanical strength. The problem with Nafion® membrane is high methanol permeation which reduces fuel utilization and performance of DMFC. Nafion® membrane is extremely costly and Nafion® membrane fuel cell requires noble metal catalyst. To solve mentioned issue, varieties of polymer have been suggested like non-fluorinated composite fluorinated, composite non-fluorinated and acid–base composite membrane [4, 5]. Figure 4 shows the complete classification of fluorinated membrane and non-fluorinated membrane [5]. Evaluation of membrane has been investigated on basis of methanol crossover (MCO), ion conductivity, life of membrane, maximum power density, thermal stability, temperature and manufacturing cost. In fuel cell market, hydrocarbon and composite fluorinated membrane suggest good potential with low methanol permeability, high durability and low cost [4]. Improvement in membrane is done by making composite membrane such as organic, non-organic and acid–base membrane. By comparing the cost of membrane, sulphonated poly (ether ether ketone) membrane (sPEEK) is less costly ($\$375 \text{ m}^{-2}$) than Nafion ($\$600\text{--}1200 \text{ m}^{-2}$) which also depends on the compactness [4]. The main issue of Nafion proton conductivity is increased by adding some additives like electronic conductor polyline. Other acid–base additives, molybdophosphoric acid [6], phosphortungstic [7] and silicotungstic acid [8] also increased proton conductivity. Zirconium phosphate (ZrP) is added for water retention enhancement. References [9, 10] and structure is modified by adding hydroxypatite [11] and zeolite [12]. MCO reduction without affecting proton conductivity

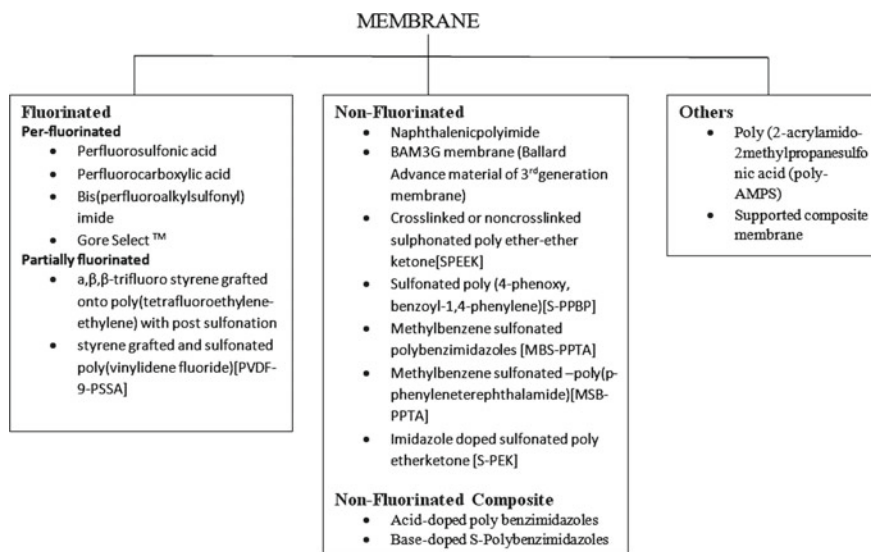


Fig. 4 Complete classification of electrolyte membrane [5]

is modification of fluorinated and non-fluorinated membranes such as SPEEK, PBI and AMPS [13]. Other problem with fluorinated membrane is its low operating temperature, which reduces the proton conductivity and slows kinetics of oxidation. Need of high temperature membrane developed from polymer and acidic basic such as polyether ketones (PEK), SPEEK sulfonated polysulfones (SPSU) [13, 14], poly (arylenethioethilenesulfone) [15], poly (phenyl quinoxaline) (PPQ) and polybenzimidazole (PBI) [16], polystyrene sulfonate (PSS) [17], styrene grafted and sulfonated poly (vinylidene fluoride) (PVDF-g-PSSA) [18]. Several hydrocarbon and modification of hydrocarbon increases the stability and durability with 5000 h lifetime, i.e. modified SPEEK membrane by silica poly (arylene ether benzonitrile) membrane (6FCN-35) [19]. New development has been noticed for better adhesion electrodes with lower resistance than SPEEK and BPSH [20].

3.2 Anode Catalyst

Electro-oxidation of methanol takes place at anode with many chemical intermediates. The main function of anode electrode is collecting the electrons and delivering/collecting reactants (Methanol) and product CO_2 .

Slow kinetics is unavoidable in DMFC which can suppress by some researcher by introducing new anode catalyst material. Carbon monoxide (CO) is the intermediate found in oxidation reaction which limits the oxidation reaction rate; woefully, CO is

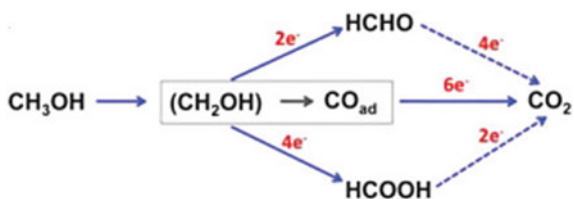
the most stable intermediate. Some anode catalyst material has been discussed below in details.

3.2.1 Platinum (Pt)

Two important functions of anode are to deliver the electrons and also to collect product species. Due to these additional requirements, anode catalyst must be highly porous, active and conductive. Platinum (Pt) is noble catalyst for hydrogen fuel cell. But Pt catalyst is not acceptable for methanol fuel cell due to formation CO as shown in Fig. 5. Thus, CO on Pt anode catalyst destructs the Pt catalyst; hence, reaction is suppressed. Thus, to avoid CO on anode catalyst, different alloy materials such as Ru, Sn, W, Pb, Mo, Os or Re are used with platinum as binary catalyst. Ruthenium (Ru) is the best alloying material for CO tolerance. Ru forms OH_{ads} and converts CO into CO₂ and H⁺ thus CO poison solved. With survey, it is observed that Pt/Ru gives the remarkable activities and stability. Some researcher has been improved the mechanism of methanol oxidation by adding second binary Pt-based alloy as PtRu, PtOs, PtSn, PtW, PtMo, PtCo, PtNi, etc. [21].

The activity of catalyst is depending on structure, particle size configuration and morphology. Recently, the research is focused on maintaining the optimum catalyst ratio with complete utilization. This issue focused on the nano-scale particle. By considering the life of fuel cell, 2–8 mg/Cm² catalyst loading is preferred. But, more noble metal loading will expend more in fuel cell thus restrict the use of DMFCs in day to day life. Binary system Pt/Mo has been described CO tolerance improvement but lower the potential. Pt–Ni and Co binary catalysts have been reported methanol tolerant cathode, improved anode oxidation reaction and low cost [22, 23]. But in terms of mass activity, Pt–Co/C and Pt–Ni/C found comparatively bad [23]. Some researcher investigated Pt–Ru-based ternary catalyst such as PtRuCo, PtRuFe, PtRuMo PtRuNi [23–25] and PtRuW [26] to improve active surface area and oxidation reaction. To avoid Ru dissolution in DMFC, the researcher confirmed Ru-free catalyst like Pt–Co, Pt–Ni, Pt–Fe, Pt–Pb, Pt–Ni–Cr [27, 28] and Pt–Co–Cr [29]. Pt₂₈Ni₇₂/C and Pt₂₈Cr₇₂/C suggested larger EAS values than that of PtRu/C [27]. PtRuMo/c presented new reaction path of direct CO₂ production without CO from CHO [30].

Fig. 5 Reaction flow chart of methanol fuel cell



3.2.2 Other Anode Catalysts

High cost of platinum raises DMFC cost, thus some researcher has been focused on non-platinum catalyst. Zhang et al [31] developed non-noble catalyst [31]. They observed improvement in catalyst activity by using supportive tactics. Few researchers developed platinum substitute like metal alloy carbide and oxide. Tungsten carbide (WC) was found more suitable for anode in DMFC. Tungsten carbide and molybdenum carbide (MoC) as anode catalyst have been published for PMFC and DMFC [32, 33]. Titanium oxide (TiO_2) and manganese oxide (MnO_2) were also found the preferable anode material for DMFC.

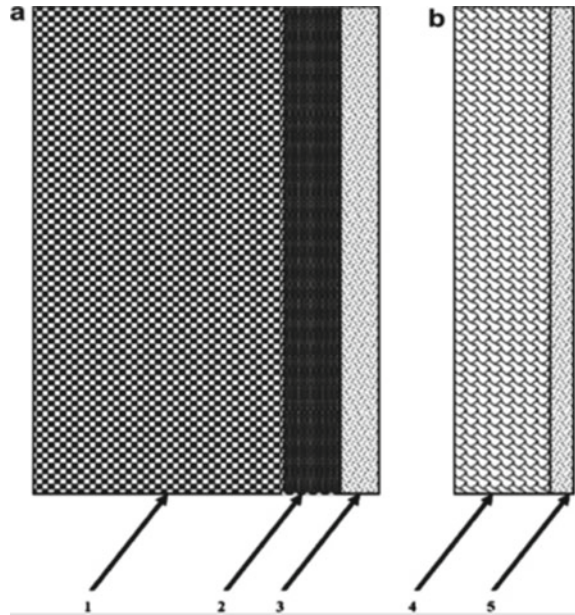
3.3 Cathode Catalyst

Oxygen reduction reactions (ORR) are a key factor in selection of cathode catalyst. Mostly, Pt or Pt/C has been used for DMFC. Unwanted Pt oxide formed at Pt surfaces due to the oxidation of crossover methanol. Thus, inactive cathode catalyst towards methanol oxidation is demanded. Feng et al. [34] reviewed several Ru-based binary and ternary catalyst and noticed ORR in acid solution [34]. Eradication of non-noble metal from Pt-alloy catalyst during reaction decreased stability and methanol tolerance. Some platinum alloy cathode catalyst such as Pt-Fe/C, Pt-Cr/C Pt-Co/C, Pt-Cr-Co/C and Pt-Ni/C exhibits remarkable performance in methanol fuel cell [34–39]. Li et al. [38] compared ORR of Pt/C with Pt-Fe/C [38]. They also noticed remarkable cathode activity for 1.2:1 Pt: Fe ratio. In terms of cost and stability, Pd or Pd/C found the best suited cathode catalyst, but in contrast reported low catalytic activity [39]. Pd-Pt catalyst tolerates the washing out problem because of high stability in acidic solution [39, 40]. Some researcher investigated improvement in catalytic activity of Pd with addition of Co, Ni, Cr, Fe and Ti. Wang et al. [35] observed nearly same performance of Pd-Co/C catalyst like Pt/C catalyst [35]. They further reported, Pd-Co/C is methanol tolerant with high ORR.

3.4 Catalyst Support

Catalyst needs backing support for easy removal of gas and water. Carbon paper or cloth used as back support called gas diffusion layer (GDL). For high stability and utility of catalyst, the use of GDL has been recommended to support catalyst. Carbon material tested for DMFC as the catalyst support called as micro porous layer (MPL), which increases the conductivity of GDL. Similarly, PTFE deposition increased the hydrophobicity of GDL. Hence, single MEA consists three layers at anode side (GDL, MPL catalyst layer) and three layer at cathode side (GDL, MPL catalyst layer) and PEM sandwiched between two electrodes. Some researcher directly applies catalyst on membrane. Shao Z. et al. developed Ti mesh electrode without polymer electrolyte

Fig. 6 a Anode electrode b mesh anode electrode
1-GDL, 2-MPL, 3-catalyst,
4- mesh, 5-catalyst [41]



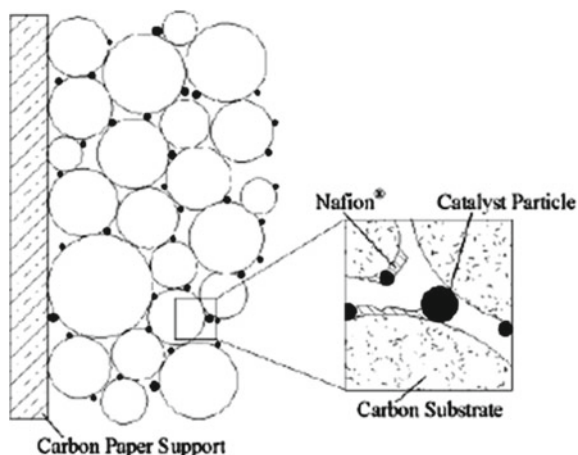
membrane (PEM) and mixing anode–cathode as one component as shown in Fig. 6 [41].

From last twenty years, several carbon materials showed the great influence to support noble metal catalyst in fuel cell and improved the properties of catalyst. Figure 7 shows three-phase morphology of catalyst, GDL and MPL. Three phase consists of photonic phase, electronic phase and space for reactant [42]. Tremendous work has been found on carbon as catalyst support material such as carbon black (CB), ketjen black, Vulcan Xc-72 and acetylene black. Ketjen black is known for high surface area which is not found in acetylene black [42, 43]. During the literature survey, the maximum use of Vulcan Xc-72 is found as anode catalyst ($\sim 250 \text{ m}^2/\text{g}^{-1}$).

The use of carbon black restricted due to crack formed on surfaces. Hence, need of the other alternatives catalyst support materials is demanded [43–45]. Other supporting material carbon nano-tubes (CNT) also used to disperse the catalyst, reported the increase in performance and also reported remarkable mechanical, thermal and electrical properties [46–48]. Lebert et al. [47] noticed benefit of CNTs for high performance and easy electrode design [47]. Soehn et al. [48] made electrode of nano-carbon mainly MWNTs, increasing surfaces significantly with floor structured surface [48].

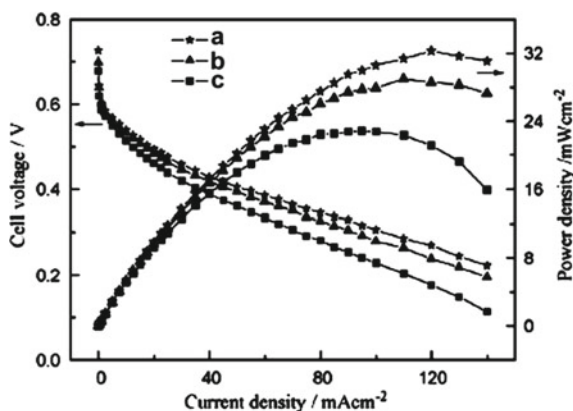
Figure 8 compares passive DMFCs for different anodic MPL [49]. DMFC with CNT as anode MPL improved the DMFC performance. Reshetyenko et al. reported high breathing cathode catalyst with filamentous CNTs as MPL [50]. Carbon nano-coil (CNC) is the nano-material reported increase in current density for DMFC (Vulcan XC-72–4 times and CB-20 times) [51]. A carbon nano-fiber (CNF) shows the greater activity in DMFC [52]. Bessel et al. [53] tested graphitic CNF (platelet,

Fig. 7 Catalyst morphology [42]



ribbon and herring bone supported Pt) [53]. They reported poor activity of herring-bone supported Pt, while platelet and ribbon show the good activity. Steigerwalt et al. [54] compared Pt-Ru/GCNF and Pt-Ru [54]. Pt-Ru/GCNF shows 50% higher performance than Pt-Ru. Mesoporous carbon (range 2–50 nm) dispersed and utilized the catalyst properly. Chai et al. [55] reported 43% increase in activity with mesoporous carbon on Pt–Ru [55]. They observed compared to commercial Pt–Ru/C. Recently, silica found as catalyst support ad tested for at high methanol immersion. Better performance of silica is observed with high methanol immersion than Pt–Ru/C [56]. Carbon catalyst support offered corrosion hence demanded non-carbonaceous catalyst support. Sharma and Pollet [57] reviewed the non-carbonaceous support material [57].

Fig. 8 Passive DMFC performance **a** carbon nano-tubes **b** mixture of carbon nano-tubes and Vulcan XC-72 **c** Vulcan XC-72 XC-72 as anode microporous layer [48]



4 Conclusions

To understand passive DMFC, its component and the material development to overcome the issues, various research papers have been reviewed and understood. As DMFCs is much closer to commercialization but some major challenges restrict which has been discussed. Following are some important conclusion.

As per the PEM study, composite fluorinated membrane and non-fluorinated (hydrocarbon) membrane are more advantageous over commercial available fluorinated (Nafion) membrane like low MCO and ruthenium crossover, better conductivity and stability, work for high temperature range (80–180 °C). Future work on hybrid membrane is expected to get low cost, low MCO with high cell performance than the commercial available Nafion membrane.

Low cost anode catalyst is desirable with high MOR. The poisonous Co deposition on reaction side demanded the platinum-free catalyst material but platinum-free catalyst offers low performance in DMFC. Non-noble catalyst with desirable catalytic activity is the future scope for passive DMFC.

The carbon material as catalyst support reported the poor catalytic activity and poor performance. The non-carbon material showed the improvement in performance with noble and commercial catalyst. Non-corrosive catalyst support material gives research direction to avoid corrosion.

References

1. Munjewar SS, Thombre SB, Mallick RK (2017) A comprehensive review on recent material development of passive direct methanol fuel cell. *Ionics* 23(1):1–18
2. Faghri A, Guo Z (2008) An innovative passive DMFC technology. *Appl Therm Eng* 28:1614–1622
3. Kamarudin MZF, Kamarudin SK, Masdar MS, Daud WRW (2013) Review: direct ethanol fuel cells. *Int J Hydrogen Energy* 38:9438–9453
4. Neburchilov V, Martin J, Wang H, Zhang J (2007) A review of polymer electrolyte membranes for direct methanol fuel cells. *J Power Sources* 169:221–238
5. Mehata V, Cooper JS (2003) Review and analysis of PEM fuel cell design and manufacturing. *J Power Sources* 114:32–53
6. Dimitrova P, Friedrich KA, Stimming U, Vogt B (2002) Modified Nafion-based membranes for use in direct methanol fuel cells. *Solid State Ionics* 150:115–122
7. Antonucci PL, Arico AS, Creti P, Ramunni E, Antonucci V (1999) Investigation of a direct methanol fuel cell based on a composite Nafion[®]-silica electrolyte for high temperature operation. *Solid State Ionics* 125:431–437
8. Tazi B, Savadogo O (2000) Parameters of PEM fuel-cells based on new membranes fabricated from Nafion[®], silicotungstic acid and thiophen. *Electrochim Acta* 45:4329–4339
9. Yang C, Srinivasan S, Arico AS, Creti P, Baglio V (2001) Composite Nafion/Zirconium phosphate membranes for direct methanol fuel cell operation at high temperature. *Electrochem Solid-State Lett* 4:A31–A34
10. Vaivars G, Maxakato NW, Mokrani T, Petrik L, Klavins J, Gericke G, Linkov V (2004) Zirconium phosphate based inorganic direct methanol fuel cell mater. *Sci* 10:162–165
11. Park YS, Yamazaki Y (2005) Novel Nafion/Hydroxyapatite composite membrane with high crystallinity and low methanol crossover for DMFCs. *Polym Bull* 53:181–192

12. Tricoli V, Nannetti F (2003) Zeolite/Nafion composites as ion conducting membrane materials. *Electrochim Acta* 48:2625–2633
13. Ahmad H, Kamarudina SK, Hasran UA, Dauda WRW (2011) A novel hybrid Nafion-PBI-ZP membrane for direct methanol fuel cells. *Int J Hydrogen Energy* 36:14668–14677
14. Lufrano F, Squadrito G, Patti A, Passalacqua E (2000) Sulfonated polysulfone as promising membranes for polymer electrolyte fuel cells. *J Appl Polym Sci* 77:1250–1256
15. Rodrigues S, Reitz T, Dang TD, Bai Z (2005 Aug) Proceedings of the third international energy conversion engineering conference and exhibit. San Francisco, California, pp 15–18
16. Staiti P, Lufrano F, Arico AS, Passalacqua E, Antonucci VJ (2001) Sulfonated polybenzimidazole membranes—preparation and physico-chemical characterization. *J Membr Sci* 188:71–78
17. Chen SL, Krishnan L, Srinivasan S, Benziger J, Bocarsly AB (2004) Ion exchange resin/polystyrene sulfonate composite membranes for PEM fuel cell. *J Membr Sci* 243:327–333
18. Lehtinen T, Sundholm G, Holmberg S, Sundholm F, Bjornbom P, Bursell M (1998) Electrochemical characterization of PVDF-based proton conducting membranes for fuel cell. *Electrochim Acta* 43:1881–1890
19. Kim YS, Summer MJ, Harrison WL, Siffle JS, McGrath JE, Pivovar BS (2004) Direct methanol fuel cell performance of disulfonated poly(arylene ether benzonitrile) copolymers. *J Electrochem Soc* 151:A2150–A2156
20. Kreuer KD (2001) On the development of proton conducting polymer membranes for hydrogen and methanol fuel cells. *J Membr Sci* 185:29–39
21. Liu H, Song C, Zhang L (2006) A reviews of anode catalysis in the direct methanol fuel cell. *J Power Sources* 155:95–110
22. Jeon MK, Won JY, Lee KR, Woo SI (2007) Highly active PtRuFe/C catalyst for methanol electro-oxidation. *Electrochem Commun* 9:2163–2166
23. Jeon MK, Lee KR, Daimon H, Nakahara A, Woo SI (2008) Pt₄₅Ru₄₅M₁₀/C (M = Fe Co, and Ni) catalysts for methanol electro-oxidation. *Catal Today* 132:123–126
24. Wang ZB, Yin GP, Shi PF, Sun YC (2006) Novel Pt–Ru–Ni/C catalysts for methanol electro-oxidation in acid medium. *Electrochem Solid State Lett* 9:A13–A15
25. Oliveira Neto A, Franco EG, Arico E, Linardi M, Gonzalez ER, Eur J (2003) Electro-oxidation of methanol and ethanol on Pt–Ru/C and Pt–Ru–Mo/C electrocatalysts prepared by Bönemann's method. *J Eur Ceram Soc* 23:2987–2992
26. Umeda M, Ojima H, Mohamedi M, Uchida I (2004) Methanol electrooxidation at Pt–Ru–W sputter deposited on Au substrate. *J Power Sources* 136:10–15
27. Jeon MK, Zhang Y, McGinn PJ (2009) Effect of reduction conditions on electrocatalytic activity of a ternary PtNiCr/C catalyst for methanol electro-oxidation. *Electrochim Acta* 54:2837–2842
28. Jeon MK, McGinn PJ (2009) Composition dependence of ternary Pt–Ni–Cr catalyst activity for the methanol electro-oxidation reaction. *J Power Sources* 194:737–745
29. Jeon MK, Cooper JS, McGinn PJ (2009) Investigation of PtCoCr/C catalysts for methanol electro-oxidation identified by a thin film combinatorial method. *J Power Sources* 192:391–395
30. Tsiouvaras N, Martínez-Huerta MV, Paschos O, Stimming U, Fierro JLG, Pen MA (2010) PtRuMo/C catalysts for direct methanol fuel cells: effect of the pretreatment on the structural characteristics and methanol Electrooxidation. *Int J Hydrogen Energy* 35:11478–11488
31. Zhang L, Zhang JJ, Wilkinson DP, Wang HJ (2006) Progress in preparation of non-noble electrocatalysts for PEM fuel cell reactions. *J Power Source* 156:171–182
32. Zellner MB, Chen JG (2005) Surface science and electrochemical studies of WC and W₂C PVD films as potential electrocatalysts. *Catal Today* 99:299–307
33. Christian JB, Smith SPE, St M, Whittingham HDA (2007) Tungsten based electrocatalyst for fuel cell applications. *Electrochem Commun* 9:2128–2132
34. Feng Y, Gago A, Timperman L, Alonso-Vante N (2011) Chalcogenide metal centers for oxygen reduction reaction: activity and tolerance. *Electrochim Acta* 56:1009–1022
35. Wang W, Zheng D, Dua C, Zou Z, Zhang X, Xia B, Yang H, Akins DL (2007) Carbon-supported Pd–Co bimetallic nanoparticles as electrocatalysts for the oxygen reduction reaction. *J Power Sources* 167:243–249

36. Yang H, Coutanceau C, Leger JM, Alonso-Vante N, Larmy C (2005) Methanol tolerant oxygen reduction on carbon-supported Pt–Ni alloy nanoparticles. *J Electroanal Chem* 576:305–313
37. Malheiro AR, Perez J, Villullas HM (2010) Surface structure and electronic properties of Pt₂Fe/C nanocatalysts and their relation with catalytic activity for oxygen reduction. *J Power Sources* 195:3111–3118
38. Li W, Xin Q, Yan Y (2010) Nanostructured Pt–Fe/C cathode catalysts for direct methanol fuel cell: the effect of catalyst composition. *Int J Hydrogen Energy* 35:2530–2538
39. He W, Liu J, Qiao Y, Zou Z, Zhang X, Akins DL, Yang H (2010) Simple preparation of Pd–Pt nanoalloy catalysts for methanol-tolerant oxygen reduction. *J Power Sources* 195:1046–1050
40. Li HQ, Sun GQ, Li N, Sun SG, Su DS, Xin Q (2007) Design and preparation of highly active Pt–Pd/C catalyst for the oxygen reduction reaction. *J Phys Chem* 111:5605–5617
41. Shao ZG, Lin WF, Christensen AP, Huamin Z (2006) Ti mesh anodes prepared by electrochemical deposition for the direct methanol fuel cell. *Int J Hydrogen Energy* 31:1914–1919
42. Zainoodin AM, Kamarudin SK, Daud WRW (2010) Review electrode in direct methanol fuel cells. *Int J Hydrogen Energy* 35:4606–4621
43. Zhang Y, Lu J, Zhou H, Itoh T, Maeda R (2009) Effects of the nanoimprint pattern on the performance of a MEMS-based micro direct methanol fuel cell. *J Micromech Microeng* 19:15003–15009
44. Liu H, Song C, Zhang L, Zhang J, Wang H, Wilkinson DP (2006) A review of anode catalysis in the direct methanol fuel cell. *J Power Sources* 155:95–110
45. Wu QX, Zhao TS, Chen R, Yang WW (2009) Effects of anode microporous layers made of carbon powder and nanotubes on water transport in direct methanol fuel cells. *J Power Sources* 191:304–311
46. Girishkumar G, Vinodgopal K, Kamat PV (2004) Carbon nanostructures in portable fuel cells: single-walled carbon nanotube electrodes for methanol oxidation and oxygen reduction. *J Phys Chem B* 108:19960–19966
47. Lebert M, Kaempgen M, Soehn M, Wirth T, Roth S, Nicoloso N (2009) Fuel cell electrodes using carbon nanostructures. *Catal Today* 143:64–68
48. Soehn M, Lebert M, Wirth T, Hofmann S, Nicoloso N (2008) Design of gas diffusion electrodes using nanocarbon. *J Power Sources* 176:494–498
49. Yuan T, Zou Z, Chen M, Li Z, Xia B, Yang H (2009) New anodic diffusive layer for passive micro-direct methanol fuel cell. *J Power Sources* 192:423–8.
50. Tatyana V, Reshetenko V, Kim HT, Kweon HJ (2008) Modification of cathode structure by introduction of CNT for air-breathing DMFC. *Electrochim Acta* 53:3043–3049
51. Hyeon T, Han S, Sung YE, Park KW, Kim YW (2003) High performance direct methanol fuel cell electrodes using solid-phase-synthesized carbon nanocoils. *Angew Chem Int Ed* 42:4352–4356
52. Yang W, Yang S, Guo J, Sun G, Xin Q (2007) Comparison of CNF and XC-72 carbon supported palladium electrocatalysts for magnesium air fuel cell. *Carbon* 45:397–403
53. Bessel CA, Laubernds K, Rodriguez NM, Baker RTK (2001) Graphite nanofibers as an electrode for fuel cell applications. *J Phys Chem* 105:1115–1118
54. Steigerwalt ES, Deluga GA, Lukehart CM (2002) Pt–Ru/carbon fiber nanocomposites: synthesis, characterization, and performance as anode catalysts of direct methanol fuel cells. a search for exceptional performance. *J Phys Chem* 106:760–766
55. Chai GS, Yoon SB, Yu JS, Choi JH, Sung YE (2007) Ordered porous carbons with tunable pore sizes as catalyst supports in direct methanol fuel cell. *J Phys Chem B* 108:7074–7079
56. Nama K, Jung S-K-H-H (2012) Application of silica as a catalyst support at high concentrations of methanol for direct methanol fuel cells. *Int J Hydrogen Energy* 37:4619–4626
57. Sharma S, Pollet BG (2012) Support materials for PEMFC and DMFC electrocatalysts—a review. *J Power Sources* 208:96–119

Thermal Management of Lithium-Ion Battery Pack with Liquid Cooling: A Computational Investigation



Shankar Durgam and Vikrant Mahesh Deshmukh

Abstract This study is done for the thermal management of battery cells by using liquid cooling to maintain equal temperature among all the cells in the battery pack. This study starts with thermal analysis of a single battery cell with numerical analysis and validates its results with experimental analysis. By using the symmetry condition of the battery pack, six cells in a row with the consideration of variable contact length of aluminium block with the battery cells. This variable contact length of aluminium block helps in uniform heat transfer. There are circular cooling channels which passes through the aluminium block, through which liquid coolant is passed. Numerical simulation has performed in ANSYS Fluent software to get temperature distribution graphs of all six cells to find the maximum temperature of cells. The numerical results are validated with previous literature followed by thermal analysis of battery pack with different channel sizes, their shape and changing coolant from water to ethylene glycol. Results of this study include a comparison of thermal performance of battery cells by using different cases of battery pack with varying channel size and number of channels in order to get the optimized design of battery pack with liquid cooling which gives better thermal performance.

Keywords ANSYS Fluent · Battery pack · Thermal analysis · Li-ion battery

1 Introduction

Management of the thermal behaviour of the battery deals with reducing the battery pack temperature as well as maintaining the uniform temperature value in all battery cells of the battery pack. In thermal management of a battery pack with liquid cooling, the concept of variable contact length is used to get uniform heat transfer and to maintain the temperature uniformity [1]. The optimum temperature range of Li-ion

S. Durgam · V. M. Deshmukh (✉)

Department of Mechanical Engineering, College of Engineering Pune, Pune 411005, India

e-mail: vikrantdeshmukh.1596@gmail.com

S. Durgam

e-mail: sodiitm@gmail.com

Table 1 Battery cell parameters

Chemistry	LiFePo4
Nominal rated voltage	3.3 V
Maximum voltage	3.7 V
Minimum voltage	2.1 V
Rechargeable	Yes
Nominal capacity	3000 mAh
Energy capacity	9.9 Wh
Life cycle	1000 Times (Approx.)
Weight (gm)	85

battery is 20 °C to 40 °C. And there should not be more than 5 °C of temperature difference between two cells in a battery pack [2]. Uniformity of temperature of battery pack is very important in order to avoid thermal issues of the battery. [3]. As more volume of air is required if used as coolant, an indirect liquid cooling gives better cooling with less volume of coolant and thus needed less energy [4]. A group of researchers and co-workers [5–12] presented liquid/water cooled, composite phase change materials, and metal foam based cylindrical or prismatic Li-ion batteries and showed thermal performance. This study is important for maintaining the battery pack temperature within optimum range and thus avoid thermal issues of battery pack. In this study, we have used active liquid cooling with indirect contact to the battery cells. Study starts with selection of Li-ion battery cell. Generally, there are two types of battery cells such as cylindrical cell and prismatic cell. This study is based on battery pack with cylindrical cells. The cylindrical cell has better heat radiation, heat capacity and control temperature more easily. The Sony 26,650 cylindrical cell is considered for this study. Parameters of selected cell are as given in Table 1.

1.1 Single Cell Analysis

The study starts with the analysis of thermal behaviour of single cell. For this, we have done experimental analysis firstly on Sony 26,650 battery cell is discharged with constant current at 3C rate by using a charge discharge apparatus, until battery voltage reaches to 2.1 V. There are three K type of thermocouples located at positive electrode, at middle of cell and at negative electrode of battery cell in order to measure temperature values. Ambient temperature was 22.7 °C. Data logger which is connected to computer is used to record the data. The average of temperature values of three positions are used as experimental data. Further thermal simulation of single battery cell is done by using ANSYS Fluent 16.2 and validated simulation results with the experimental results. The graph in Fig. 1 shows that simulated results matches closely with experimental results. This shows the accuracy of heat generation value used in simulation.

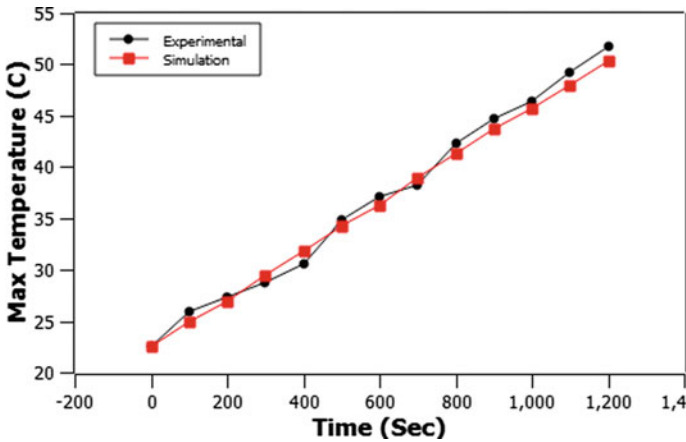


Fig. 1 Validation of single cell

1.2 Thermal Analysis of Battery Pack

A battery module of six cells along the flow channel on both sides was considered for this study. Variable contact length of aluminium block is kept in contact with battery cells in order to compensate the heat transfer through each cell. Circular cooling channels are passed horizontally through these aluminium blocks. High heat transfer rate of aluminium block helps in transferring more amount of heat which is taken away by coolant through cooling channels. Numerical simulation of the battery pack with six cells is done in order to reduce the complexity.

We have referred this from [1] and consider optimum design of variable contact area of aluminium with $K = 3$, at 3C rate and flow velocity is 0.1 m/s. Firstly validated our simulation results of maximum cell temperatures with the literature results by considering same boundary conditions. Further analysis is done by changing channel size and number of channels. A CFD software ANSYS Fluent 16.2 is used to get the simulation results.

2 Methodology

Simulation of battery pack with geometric variation of channel size and number of channels is done in five different cases. The thermal behaviour of battery pack is analysed using five cases of battery pack with geometric variation and find the best among these cases which gives better cooling.

2.1 Case 1

1. Design of battery pack:

By considering symmetry condition, we did study on six cells with variable contact aluminium block. In this case, battery pack with circular cooling channel of 2 mm diameter and total 10 cooling channels placed equidistance along the length of battery cell with 5 channels on each side of cells. The liquid coolant flow velocity is 0.1 m/s. 3D model of battery pack is shown in Fig. 2.

2. Meshing

Fine meshing is done with tetrahedron method having nodes 546,521 and elements 1,256,382 (Fig. 3).

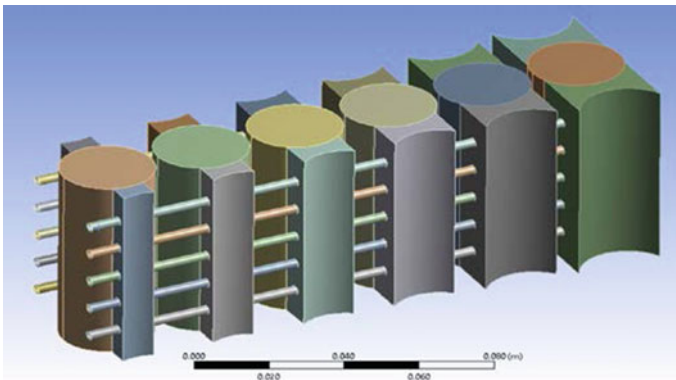


Fig. 2 Design model of case 1 battery pack

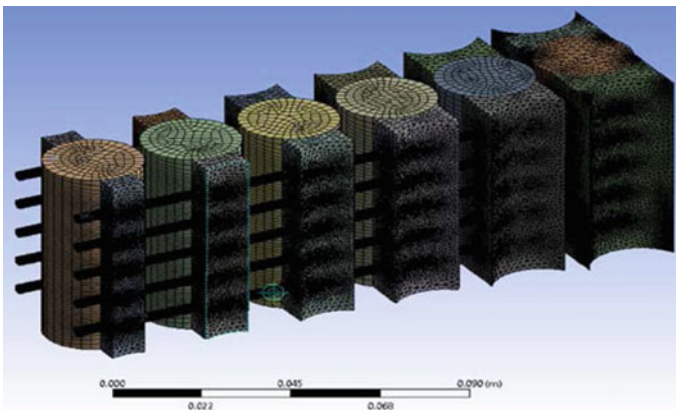


Fig. 3 Meshing of case 1 battery pack model

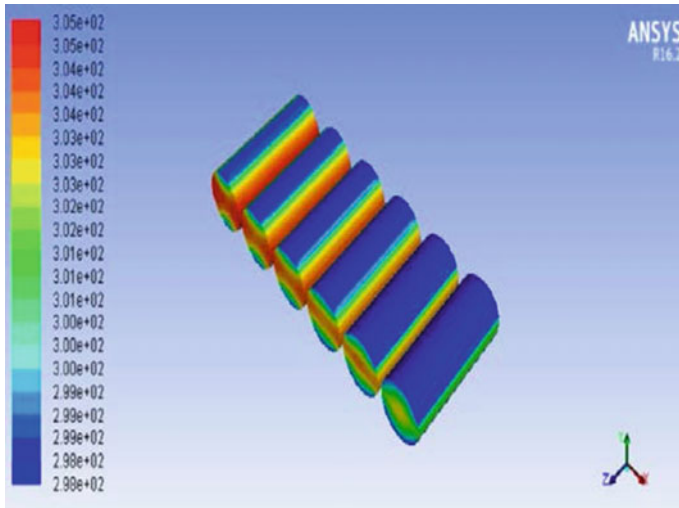


Fig. 4 Temperature contour of case 1 battery pack

3. Simulation results

Thermal simulation is done to find the maximum temperature value of each battery cell by using water and ethylene glycol as coolant. Validation of this battery pack design is done with literature work with water as coolant. Figure 4 shows the temperature contour of battery cells.

Figure 4 shows the maximum temperature value is 305.006 k and minimum temperature value is 303.30 k. Figure 5 shows the comparison graph of maximum temperature values of six cells between simulated result and previous literature work in order to validate our simulation work. This graph shows the simulated results matches closely with the literature results.

Further coolant is changed from water to ethylene glycol in order to compare thermal behaviour of maximum temperature of battery cells as shown in Fig. 6.

2.2 Case 2

1. Design of battery pack:

Battery pack with circular cooling channel of 2 mm diameter and total 12 cooling channels placed equidistance along the length of battery cell with 6 channels on each side of cells. The liquid coolant flow velocity is 0.1 m/s. 3D model of this battery pack is shown in Fig. 7.

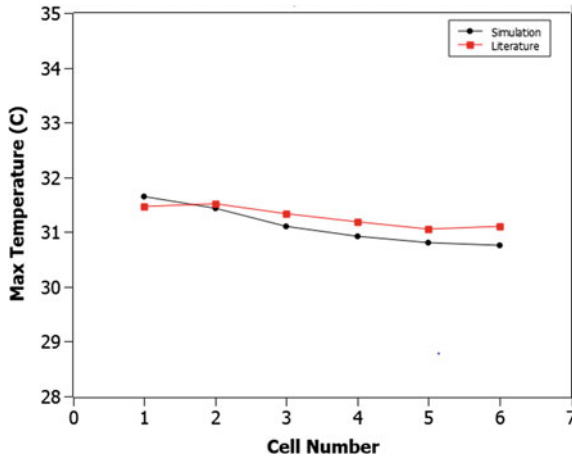


Fig. 5 Validation of maximum temperature values of battery pack

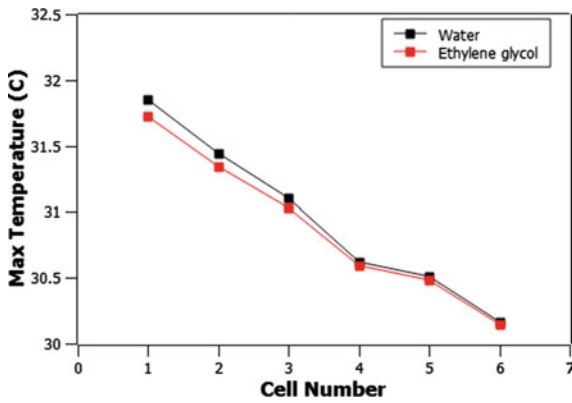


Fig. 6 Maximum temperature graph of water and ethylene glycol for case 1

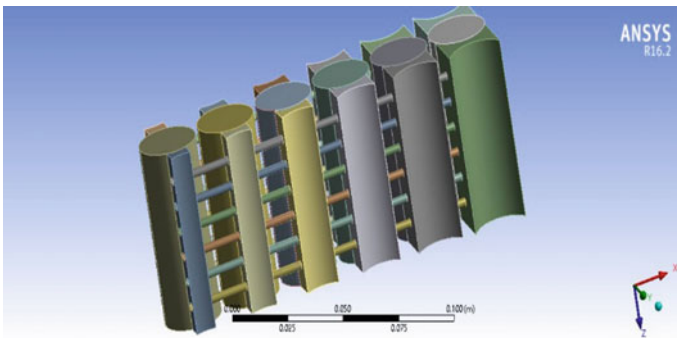


Fig. 7 Design model of case 2 battery pack

2. Meshing:

The mesh used for case 2 is shown in Fig. 8. The fine meshing is done with tetrahedron method. It has 552,521 nodes and 1,316,382 elements.

3. Simulated results:

Figure 9 shows temperature contour profile of battery pack cells. The comparative graph of maximum temperature values of battery pack cells between water and ethylene glycol as coolant used is shown in Fig. 10.

Above simulation results show that the maximum temperature value is 304.9 k and minimum temperature value is 303 k.

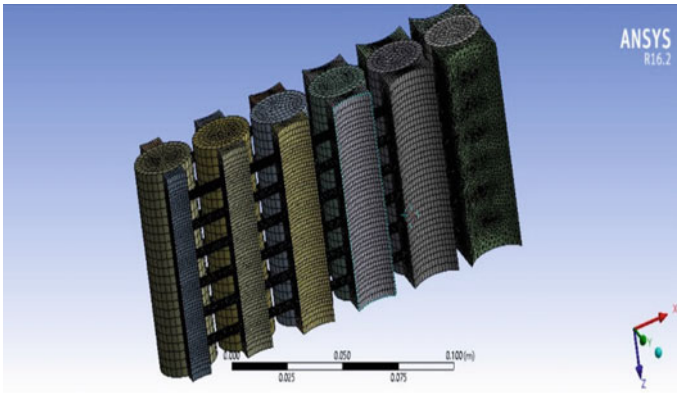


Fig. 8 Meshing of case 2 battery pack model

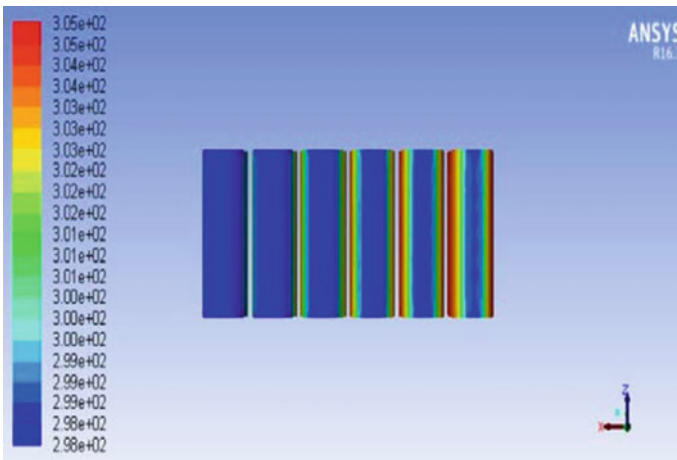
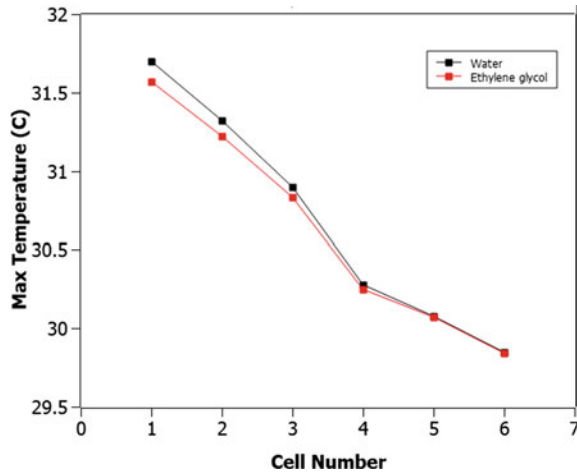


Fig. 9 Temperature contour of case 2 battery pack

Fig. 10 Variation of temperature in each cell using water and ethylene glycol for Case 2



2.3 Case 3:

1. Design of Battery pack:

Battery pack with circular cooling channel of 3 mm diameter and total 8 cooling channels placed equidistance along the length of battery cell with 4 channels on each side of cells. The liquid coolant flow velocity is 0.1 m/s. Three-dimensional model of this battery pack is shown in Fig. 11.

2. Meshing:

Fine meshing is done with tetrahedron method having 542,521 nodes and 1,216,382 elements. This mesh is selected for computations because it saves cost and time of simulations (Fig. 12).

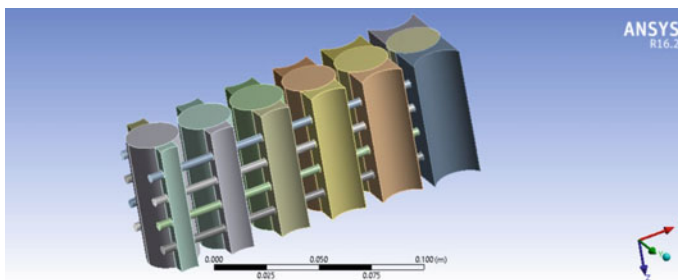


Fig. 11 Design model of case 3 battery pack

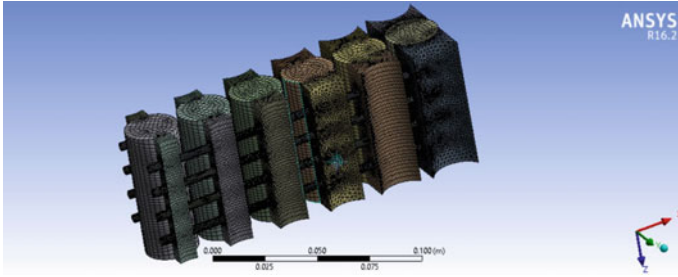


Fig. 12 Meshing of case 3 battery pack model

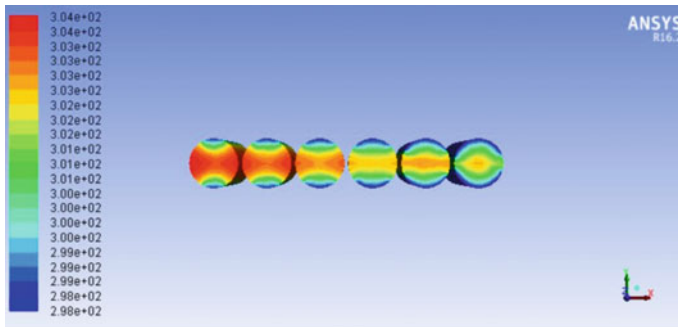


Fig. 13 Temperature contour of case 3 battery pack

3. Simulation results:

Figure 13 shows temperature contour profile of battery pack cells. The comparative graph of maximum temperature values of battery pack cells between water and ethylene glycol as coolant used is shown in Fig. 14. It is observed from the temperature contour profile that the temperature is reducing from cell 1 to cell 6. Simulation results show that the maximum temperature value is 304.17 k and minimum temperature value is 302.47 k.

2.4 Case 4:

1. Design of Battery pack:

Battery pack with circular cooling channel of 3 mm diameter and total 10 cooling channels placed equidistance along the length of battery cell with 5 channels on each side of cells. The liquid coolant flow velocity is 0.1 m/s. 3D model of this battery pack is shown in Fig. 15.

Fig.14 Maximum temperature graph of water and ethylene glycol for case 3

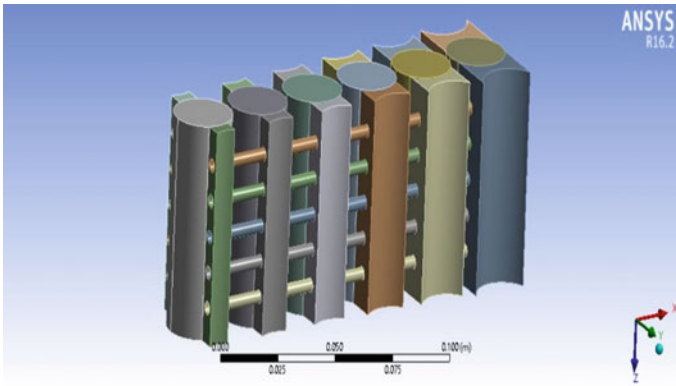
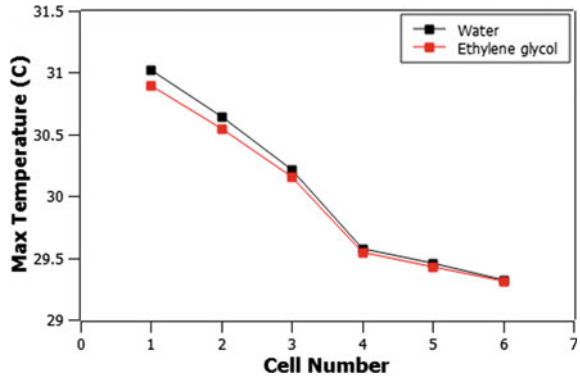


Fig. 15 Design model of case 4 battery pack

2. Meshing:

Fine meshing is done with tetrahedron method having 551,521 nodes and 12,306,382 elements (Fig. 16).

3. Simulation results

Figure 17 shows temperature contour profile of battery pack cells. Simulation results show that the maximum temperature value is 303.67 K and minimum temperature value is 302.2 K (Fig. 18).

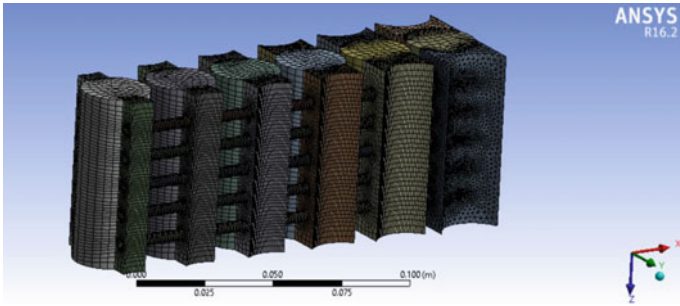


Fig. 16 Meshing of case 4 battery pack model

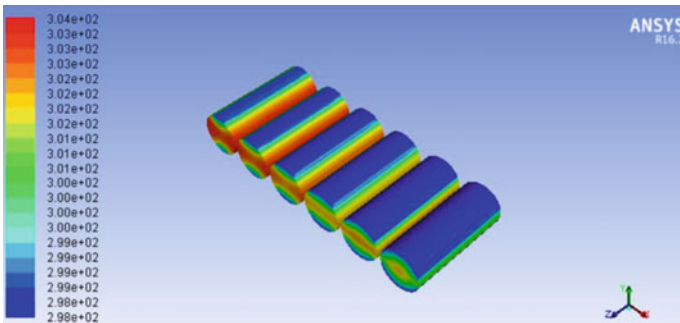
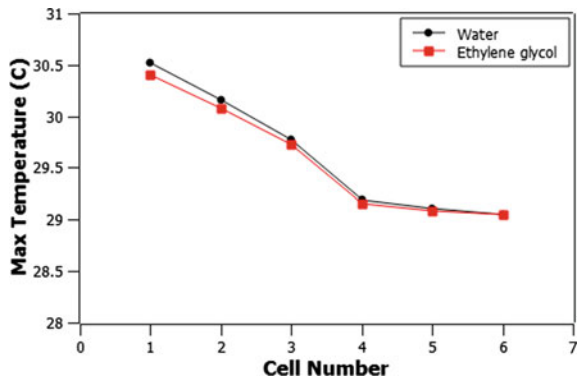


Fig. 17 Temperature contour of case 4 battery pack

Fig. 18 Maximum temperature graph of water and ethylene glycol for case 4



2.5 Case 5:

1. Design of Battery pack:

Battery pack with circular cooling channel of 3 mm diameter and total 12 cooling channels placed equidistance along the length of battery cell with 6 channels on each side of cells. The liquid coolant flow velocity is 0.1 m/s. 3D model of this battery pack is shown in Fig. 19. Fine meshing is done with tetrahedron method having 554,521 nodes and 1,336,382 elements.

2. Simulation results

Figure 20 shows temperature contour profile of battery pack cells. The comparative graph of maximum temperature values of battery pack cells between water and ethylene glycol as coolant used is shown in Fig. 21. Simulation results show that the maximum temperature value is 303.04 K and minimum temperature value is 301.61 K.

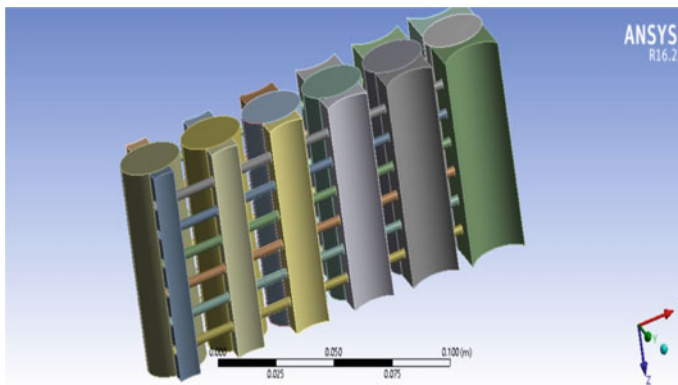


Fig. 19 Design model of case 5 battery pack

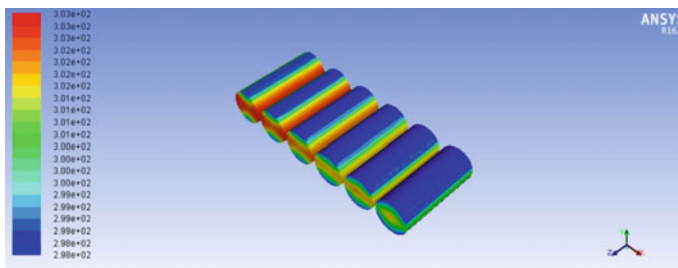
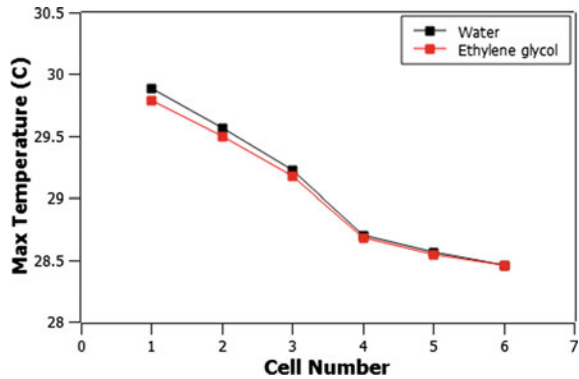


Fig. 20 Temperature contour of case 5 battery pack

Fig. 21 Maximum temperature graph of water and ethylene glycol for case 5



3 Conclusions

From the computational investigation of 5 different cases of lithium-ion battery pack with liquid cooling using water and ethylene glycol as coolant, following are the conclusions.

In the simulation results all 5 cases, it is observed that ethylene glycol as liquid coolant provides better cooling than water as liquid coolant. It is observed that the maximum temperature value of battery pack cells goes on reducing from cell 1 to cell 6. There is 6.15% of temperature reduction occurs in maximum temperature value of battery cells of case 5 battery pack compared to case 1 battery pack when water is used as liquid coolant. There is maximum temperature reduction of battery cell occurs in case 5 by 6.1% compared to case 1 of battery pack when ethylene glycol is liquid coolant. By comparing all the 5 cases of battery pack with water and ethylene glycol as coolant, it is concluded that case 5 of battery pack with ethylene glycol as liquid coolant provides effective cooling and maintain temperature uniformity compared to all other cases of battery pack considered in this computational investigation.

References

1. Rao Z, Qian Z, Kuang Y, Li Y (2017) Thermal performance of liquid cooling based thermal management system for cylindrical lithium-ion battery module with variable contact surface. *Appl Therm Eng* 123:1514–1522
2. Greco, Jiang X, Cao DP (2015) An investigation of lithium-ion battery thermal management using paraffin/porous-graphite-matrix composite. *J Power Sources* 278:50–68
3. Wilke S, Schweitzer B, Khateeb S, Al-Hallaj S (2017) Preventing thermal runaway propagation in lithium-ion battery packs using a phase change composite material: an experimental study. *J Power Sources* 1(340):51–9
4. Chen D, Jiang J, Kim G-H, Yang C, Pesaran A (2016) Comparison of different cooling methods for lithium-ion battery cells. *Appl Therm Eng* 94:846–854
5. Xie L, Huang Y, Lai H (2020) Coupled prediction model of liquid-cooling based thermal management system for cylindrical lithium-ion module. *Appl Therm Eng*

6. Qian Z, Li YM, Rao ZH (2016) Thermal performance of lithium-ion battery thermal management system by using mini-channel cooling. *Energy Convers Manage* 126:622–631
7. Lan C, Xu J, Qiao Y, Ma Y (2016) Thermal management for high power lithium-ion battery by minichannel aluminum tubes. *Appl Therm Eng* 101:284–292
8. Zhao JT, Rao ZH, Li YM (2015) Thermal performance of mini-channel liquid cooled cylinder-based battery thermal management for cylindrical lithium-ion power battery. *Energy Convers Manage* 103:157–165
9. Tong W, Somasundaram K, Birgersson E, Mujumdar AS, Yap C (2015) Numerical investigation of water cooling for a lithium-ion bipolar battery pack. *Int J Therm Sci* 94:259–269
10. Azizi Y, Sadrameli SM (2016) Thermal management of a LiFePO₄ battery pack at high temperature environment using a composite of phase change materials and aluminum wire mesh plates. *Energy Convers Manage* 128:294–302
11. Alipanah M, Li X (2016) Numerical studies of lithium-ion battery thermal management systems using phase change materials and metal foams. *Int J Heat Mass Transf* 102:1159–1168
12. Wang H, Xu W, Ma L (2016) Actively controlled thermal management of prismatic Li-ion cells under elevated temperatures. *Int J Heat Mass Transf* 102:315–322

Heat Transfer Characteristics of a Two-Phase Closed Vertical Thermosyphon: An Experimental Study



Aalekh Srivastava, Manish K. Rathod, and Naresh Yarramsetty

Abstract Thermal management is one of the most important research areas in thermal engineering. Due to higher heat transfer rate, use of thermosyphon has been advantageous for low and medium temperature ranges. This paper presents a report on experimental investigation on heat transfer characteristics of wickless heat pipe charged with water, ethylene glycol (EG) and binary fluid. Binary fluid used in this investigation is 1:1 ratio of water and EG. Thermosyphon of length 1200 mm and of copper material is used. The three sections of pipe, namely evaporator, adiabatic and condenser section of length 450 mm, 250 mm and 500 mm, respectively, and the thickness of pipe is 3.2 mm. The proportion of evaporator volume filled with liquid is called fill ratio. In this report, fill ratios of 25, 50, 75 and 100% are being used. Vertical thermosyphon is tested between heat inputs of 200–600 W. The thermal performance parameter of thermosyphon is thermal resistance, which mainly depends on the average evaporator temperature. Since ethylene glycol has been used as the suppressant in freezing point and elevates the boiling point of water. Therefore, the influence of ethylene glycol has been studied on the performance. For the vertical thermosyphon, effect of fill ratio and heat input is also analyzed on thermal resistance.

Keywords Thermosyphon · Water · Ethylene glycol · Fill ratio · Thermal resistance · Binary fluid

A. Srivastava (✉) · M. K. Rathod · N. Yarramsetty
S.V. National Institute of Technology, Surat, Gujarat, India
e-mail: aalekhsrivastav8381@gmail.com

M. K. Rathod
e-mail: mkr@med.svnit.ac.in

N. Yarramsetty
e-mail: naresh@med.svnit.ac.in

Nomenclature

T_{sat}	Saturation temperature
T_e	Average evaporator temperature
T_a	Average adiabatic temperature
T_c	Average condenser temperature
R_{th}	Thermal resistance
FR	Fill ratio

1 Introduction

Thermosyphon is a sealed container in which certain quantity of liquid as a working fluid is present which undergoes phase change makes enhances the heat transfer rate. It is used to transport heat from source to sink. Due to no moving components, the operation is noiseless. This also makes it more reliable for long-term service. The application of heat pipe is in thermal management, where high heat flux intensity is present. Applications can be from semiconductor industries where increasing number of transistor in unit area resulting increases in flux and hence need to be controlled to application in hyperloops, where the temperature of nose present in aerodynamic body is a stagnation point hence hotspot because of high heat can be produced and need to removed. Wickless heat pipe can also be used in permafrost where the ice present inside the surface needs to maintain and heat should be removed otherwise infrastructure can be collapsed [1, 2]. Thermosyphon has three parts, namely evaporator section, adiabatic section and condenser section. The heat extraction from source has been done by evaporator, transported by adiabatic part and rejected to sink through condenser. Outside of evaporator has been connected to source, while inside of evaporator, there is filling of working fluid that act as carrier to the heat flux. The heat flux provided in the evaporator would transfer it to the liquid pool through the walls. When the saturation temperature of liquid pool reaches, the vapor will start forming and due to buoyancy force, it starts rising. Leaving the interface, it will reach to the condenser section after flowing through adiabatic section. Condenser section is provided with condensing agent that will extract heat from the vapor. The agent may be blowing air, heat sink, fins to cooling water jacket depend on the amount of heat flux need to be extracted. Vapor on contacting with wall releases all the latent heat and condenses into liquid that will flow down along the wall by the gravity force. The liquid is now available for the next heat flux and this process goes in cycle. Due to assistance of gravity, it cannot be operated in horizontal position. The working fluid has been chosen depends on the operating temperature of evaporator. The boiling point should be in between range of temperature. The fluid with high merit number for that operating range should be chosen. The fluid also has compatible nature with the wall of thermosyphon. The material of thermosyphon should not have chemical

affinity with the working fluid, otherwise corrosive gases can damage the equipment as well as purpose.

1.1 Literature Survey

Maalej et al. [1] investigated thermal performance of finned heat pipe for central processing unit. They maintained the temperature below 90 °C even at heat input of 150 W when oriented in thermosyphon position.

Chen et al. [2] studied about the heat that has been rejected from warm oil pipeline and to remove the heat through thermosyphon in order to prevent permafrost. They maintained a daily extraction of 0.5 W/m² through thermosyphon.

Ong et al. [3] experimentally investigated a two-phase closed thermosyphon ($d_i = 32$ mm and $L = 760$ mm) using R410a and water as working fluids at various filling proportions (25–100%), inclination angles (30°–90°) and power input ranges between 100 and 830 W. The thermosyphon filled with R410a had also been better performed at all fill ratio vertically, and the thermosyphon filled with water had better performed at low fill.

Gregor et al. [4] experimentally investigated a two-phase closed thermosyphon of inner diameter $d_i = 16$ mm and length $L = 2200$ mm with a working temperature of 10–50 °C (cold side) and 60–80 °C on the warm side. They examined various liquids: water, methanol, ethylene glycol and R-134a. They proposed that a water and a 5% ethylene glycol mix is an appropriate substitute liquid although its output was, under certain circumstances, less than R134a.

Lataoui and Jemni [5] studied the heat transfer characteristics of a stainless steel two-phase closed thermosyphon experimentally. The tests were carried out in three compliant operating liquids: water, ethanol and acetone. There were also analyzed the impacts of heat flux at the evaporator section and of the cooling water temperature on the condenser. In multiple places along the thermosyphon, the stable wall temperature is then supervised. The findings have shown that a clear increase in temperature, particularly for the under filled situation, resulted in the dry out event at the base of evaporator,

Gedik [6] experimentally investigated with air, oxygen [6] and ethylene glycol as operating liquids for a two-phase closed thermosyphon. The investigation shall include various operational conditions, such as angles of inclination (30°, 60° and 90°), heat outputs (200,400 and 600 W) and cooling water stream rate (10, 20 l/h). The findings stated that when the heat inputs were 200 W and the cooling water rate of 10 l/h, water was the finest working fluid. When the heat outputs were 200 W and the cooling water flow rate of 30 l/h, ethylene glycol was the best working fluid. When the thermal inputs were 600 W and the cooling water flow rate of 10 l/h, ethanol was the best working flow.

Ashok and Anjankar [7] researched the impact of inclination, aspect ratios and bond number on the heat transfer efficiency of a two-phase closed high-density polyethylene thermosyphon under normal operating condition. The evaporator, adiabatic and condenser are of same length. R113 and R11 have been used as operating fluids with 50% filling ratio. The findings showed the angle of inclination ranging from 60 to 70 °C with peak heat transfer performance.

Naresh and Balaji [8] experimentally investigated effect of fin in condenser section. They used water and acetone as a working fluids. The optimum fill ratio they got was 50%. Induction of fin reduces the thermal resistance by 35.48% when tested between 50 and 275 W.

Nuntaphan et al. [9] studied enhancement of thermal performance of thermosyphon using binary fluid. They found out that for temperature less than 80 °C, water–ethanol mixture performs better than water and ethanol. However, the resistance is close to value of ethanol.

From the literature survey that has been carried out, detailed experimental studies and impact have been studied of fill ratios, inclination angle, heat input and working fluids over thermal resistance. However, considering binary fluid as working fluid, few researches have been carried using water–ethylene glycol (EG) binary fluid. In this paper, the thermal performance of thermosyphon has been carried out with water, EG and binary fluid. Impact of fill ratios has been studied in order to find the optimum fill ratio for the variation in heat input.

2 Problem Description

The performance of thermosyphon has been evaluated by thermal resistance. Thermal resistance is defined as the ratio of difference in average temperature of evaporator to condenser with the heat input. The thermal resistance depends on various parameters like inclination angle, fill ratios, heat input and working fluid. In this paper, effect of fill ratio and heat input is analyzed for vertical thermosyphon. The fill ratios that are used are 25%, 50%, 75% and 100% of evaporator volume. The heat input is varied from 200 W to 600 W. Working fluid has a great influence on performance of thermosyphon. As mentioned in literature, many works have been done on impact of performance considering the working fluid. However, few researches are available for ethylene glycol as a working fluid. This paper uses water as a working fluid and for comparison, ethylene glycol is used in thermosyphon. Binary fluid which is the mixture of ethylene glycol and water has been made with 1:1 ratio. The thermo-physical properties has been mentioned for all mentioned working fluid in Table 1. From merit number, the important properties are latent heat of vaporization, dynamic viscosity, density and surface tension. Comparison of these data for all the fluids are used along with their saturation temperature at 1 atm.

From Table 1, it can be concluded that water has highest latent heat of vaporization; however, the boiling point is 100 °C that is easily achieved at 200 W heat input.

Table 1 Thermo-physical properties of working fluids

Properties	Water [10]		EG [10]		50–50 [11]	
Temperature (°C)	40	100	40	100	40	100
Density (kg/m ³)	995	961	1101	1058	1060	1000
Viscosity (Ns/m ²) × 10 ⁻³	0.657	0.28	9.56	2.14	1.14	0.8
BP (°C) @ 1 atm	100		197.4		125	
Latent heat (kJ/kg)	2256		857.09		1556.5	
Surface tension (N/m) @ 25 °C	0.0697		0.047		0.056	

Taking EG as a working fluid, the latent heat of vaporization is less and boiling point is approximately double of water. High boiling of EG and high latent heat of vaporization of water is simultaneously needed; hence, binary fluid is taken that make all the properties in between, and performance is analyzed using it. A comparison is made using all the working fluids and effect of change in parameters is concluded.

2.1 Experimental Setup

The thermosyphon has three parts, namely evaporator section, adiabatic section and condenser section. There is heater wrapped around the evaporator, which is connected to power supply in order to get desired heat input. The condenser section has a cooling fluid supply in order to get the extracted heat out of the thermosyphon.

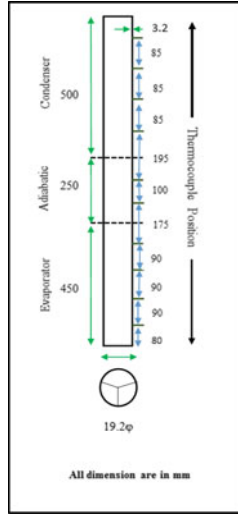
The thermosyphon has inside diameter to be 19.2 mm and thickens of pipe is 3.2 mm. The length of respective parts is 450 mm, 250 mm and 500 mm for evaporator, adiabatic part and condenser, respectively. Figure 1a represents the positioning of thermocouple around the thermosyphon. The thermocouple is tightened around the jacket provided outside the sections and it is made sure that thermocouple should contact the wall, and there should be no contact with heater. Figure 1b represents the actual photograph of experimental setup. The connections of thermocouples and insulation are also shown in Fig. 2 for all the three parts of thermosyphon.

The detailed description of setup and components has been made in Table 2.

2.2 Experimental Methodology

Impact of fill ratios, heat input and working fluid have been analyzed on thermal resistance of thermosyphon. The heat input is varied from 200 to 600 W. The fill ratios provided are 25, 50, 75 and 100%. The flow rate of coolant, i.e., water is maintained at 2.8 l/min. Working fluids are water, EG and binary fluid. When the rise in temperature of evaporator is less than 1 °C in 10 min, it is assumed that the steady state is achieved, and the heat input as well as the water supply should be

Fig. 1 View of experimental setup



(a) Schematic line diagram of positioning of thermocouple

(b) Photograph of experimental setup

Fig. 2 Components of setup



(a) Cerawool insulation around evaporator

(b) Condenser section

off. Initially, water is used as a working fluid. Effect of fill ratios and heat input is analyzed on thermal resistance of vertical thermosyphon. After that, ethylene glycol and binary fluid are examined as a working fluid inside it. Results for all the working fluids have been compared in results and discussion part.

Table 2 Description of experimental setup

S. No.	Equipment	Description
1	Experimental test rig	With angle structure Size: 1252 mm (l) × 402 mm (b) × 1920 mm (h)
2	Thermosyphon	Material: Cu Size: 19.2 mm (d) × 1200 mm (l) × 3.2 mm (t)
3	Heater	Make: sensewell Material: inconel Type: hot runner capacity: 0–800 W
4	Insulation	Material: cerawool Density: 64 kg/m ³
5	Condenser jacket	Material SS 304 Size: 25.5 mm (d_i) × 108 mm (d_o) × 500 mm (l)
6	Outer shell of evaporator section	Material SS 304 Size: 72 mm (d) × 450 mm (l) × 3 mm (t)
7	Outer shell of adiabatic section	Material SS 304 Size: 53.5 mm (d) × 250 mm (l) × 3.5 mm (t)
8	Outer cover over condenser section	Material: aluminum foil LM-4
9	Condenser section piping	Material: SS 304 Diameter: 0.5 in.
10	K-type thermocouples (Simplex, ungrounded)	Make: sensewell Material: inconel 600 Diameter: 1.5 mm Quantity: 28

3 Results and Discussion

The most important performance parameters of thermosyphon are thermal resistance which mainly depends on average temperature of evaporator. The thermal resistance is calculated as follow.

$$R_{th} = \frac{T_e - T_c}{Q_e} \quad (1)$$

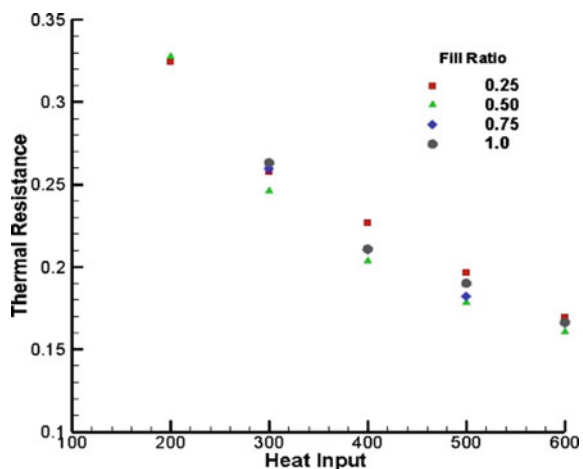
where T_e is the average temperature of evaporator section, T_c is the average temperature of condenser section and Q_e is the heat supplied by heater, i.e., heat input at evaporator section. There are mainly two things which will affect the thermal resistance of thermosyphon. First parameter is the height of liquid column inside the thermosyphon evaporator section. As bubbles form in the evaporator section, it will rise to the free surface. If the height of liquid pool is small, then the formed bubbles will rise to the free surface without colliding with each other. If the height of

liquid pool is more, then the small bubbles will collide and stuck in the liquid pool before they reach to the free surface. This large bubbles are having lower thermal conductivity. Hence, the rate of heat transfer will reduce, which will in turn increase the temperature of evaporator section. Thus, lower height of liquid pool is desirable according to this first parameter. When the evaporator is not fully filled with liquid, bare part of evaporator section is directly exposed to heat source. At this part, because of not availability of liquid, sudden rise in the evaporator temperature will occur. Hence, the height of the liquid pool should be higher according to this parameter. Too low fill ratio causes poor evaporation. High fill ratio causes weakening of condensation. Hence, optimum fill ratio (FR) would be there.

Figure 3 represents effect of heat input on thermal resistance when thermosyphon is charged with water at different fill ratios. It is observed that on increasing heat input, the thermal resistance decreases. This is because of increase in nucleation sites inside the evaporator pool interface. More amount of vapor combines to form bigger vapor pocket that would escape the interface and reach the condenser section. It can be concluded that at 200 W, due to low volume of working fluid, the thermal resistance of 0.25 FR is minimum. This is because of easy escape of small amount of vapor from small liquid pool. However, for all heat input, 0.50 FR performs better. Hence, it can be summarized that 50% fill ratio is optimum for all heat input. After the effect of heat input and fill ratios for thermosyphon charged with water has been analyzed, effect of changing of working fluids for above-mentioned parameters has been analyzed over thermal resistance.

Variation of thermal resistance on changing heat input at 0.25 FR for all working fluids has been shown in Fig. 4. It can be illustrated that binary fluid performs better than their individual constituents. It can also be concluded that after binary fluid, for low heat input, water performs better; however, at high heat input, EG performs better after binary fluid. Low fill ratio of low boiling point fluid can easily convert into vapor and because of low heat input dry out is not there that responsible for

Fig. 3 Effect of heat input on thermal resistance for all FR of Water



temperature rise. On increasing heat input, dry out of low boiling point fluid could be possible for low fill ratio. Because of high boiling point of EG, 0.25 FR volume can be sufficient even at high heat input. Irrespective of working fluid, the thermal resistance drops on increasing heat input.

Figure 5 represents variation of thermal resistance on heat input for all working fluids at 0.50 FR. In this case also binary fluid performs better than the individual. Because of sufficient volume of liquid inside pool, therefore, low boiling point water performs better than EG, for all heat input which is not the case for 0.25 FR. As the heat input increases, the difference in thermal resistance among individuals minimizes.

Figure 6 represents the variation of thermal resistance on heat input for all working fluids at 0.75 FR. Due to large volume of liquid inside evaporator that makes the

Fig. 4 Effect of heat input on thermal resistance at 0.25FR

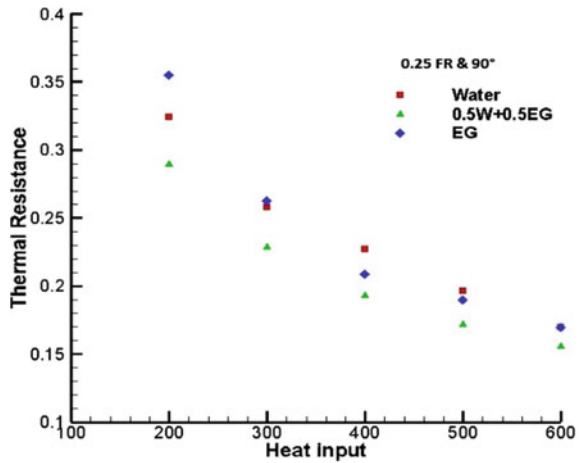


Fig. 5 Effect of heat input on thermal resistance at 0.50 FR

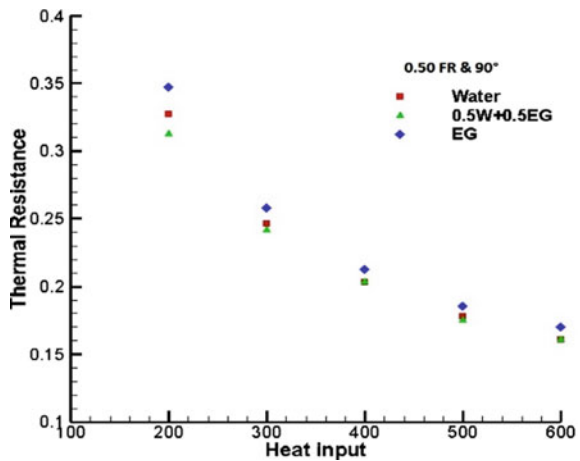
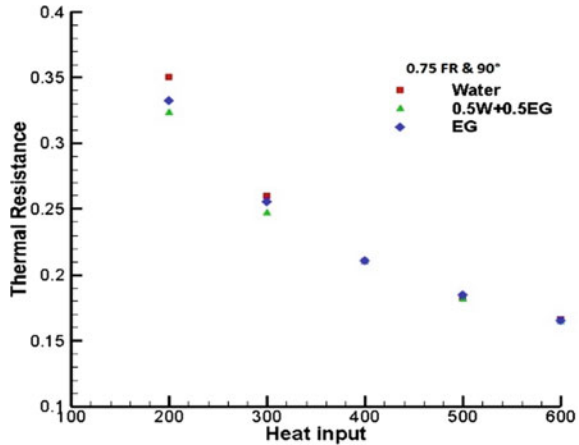


Fig. 6 Effect of heat input on thermal resistance at 0.75 FR



availability of liquid hence, difference in thermal resistance is not much significant. When all fluids are compared, binary fluid performs best with maximum enhance of 8 and 3% with water and EG.

Figure 7 represents the variation of thermal resistance on heat input for all working fluids at 1.0 FR. The trend is same as 0.75 FR. For all the cases, binary fluid performs best for all heat input. However, the differences tend to reduce when the fill ratio is increasing. The present of liquid in the pool makes the mass transfer to be a consistent phenomenon rather than depends on the returning of condensate. The increase in mass transfer also enhances the pressure that suppress the boiling, therefore, increase in thermal resistance is observed.

From the comparison, it has been concluded that binary fluid performs better than the individual constituents for all FR. Water has low boiling point, and high latent heat of vaporization. Rapid mass transfer makes the liquid availability less in the evaporator. EG has been seen that high boiling point only creates nucleate boiling, and due to less latent heat of vaporization, the temperature is high and therefore thermal resistance. However, for binary fluid, qualities and defects from the both the fluid make it average latent heat of vaporization and boiling point to be 127 °C, which is in the operating range of temperature.

When water is charged in thermosyphon, 0.50 fill ratio came as optimum. Now, for binary fluid, which has been obtained as best among all shows a different behavior when optimum is considered.

Figure 8 represents the variation of thermal resistance on increasing heat input for binary fluid. It can be seen that, for all heat input, 0.25 FR is optimum. It gives least thermal resistance. This can be explained from the fact that it has high boiling point compared to water, and hence, the temperature inside the evaporator wall has less fluid that can easily convert into vapor. On increasing the heat input, the difference in thermal resistance among all the fill ratios decreases. Hence, for water being low boiling point, optimum fill ratio is 0.50 FR, and for binary fluid due to high boiling point than former, optimum fill ratio would be 0.25.

Fig. 7 Effect of heat input on thermal resistance at 1.0 FR

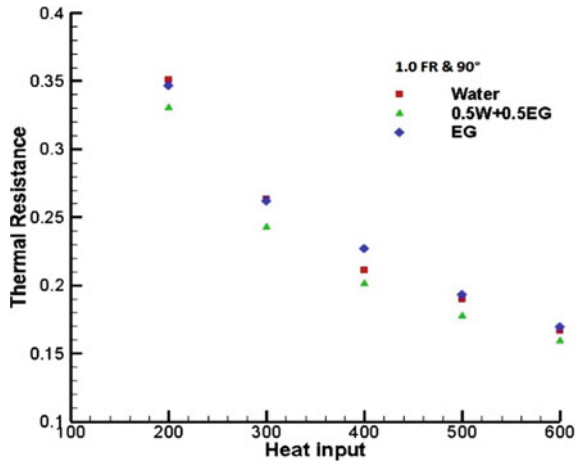
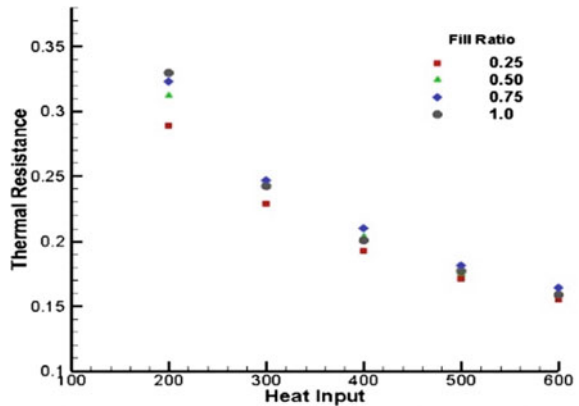


Fig. 8 Effect of heat input on thermal resistance for all FR of Binary fluid



4 Conclusion

Thermosyphon is one of the advance heat transfer devices used in the area of thermal management. Different working fluids are being tested to obtain the optimum working fluid and fill ratios. Heat input is varied from 200 to 600 W for fill ratios of 0.25, 0.50, 0.75 and 1.0. Working fluids used are water, ethylene glycol (EG) and binary fluid which is the mixture of water and EG in 1:1 ratio. Irrespective of working fluid, thermal resistance decreases on increasing heat input. Due to increase in nucleation sites, large amount of vapor combines to form vapor pocket that would easily escape from the pool and the interface. When thermosyphon is charged with water, 0.50 FR obtained as the optimum fill ratio for all heat input except for 200 W. However, difference is 1% which is insignificant. When all the working fluids are considered, it has been found that binary fluid performs best rather than individual constituents. Maximum enhancement in heat transfer characteristics when compared

Table 3 Uncertainties in thermal resistance for water at 0.50 FR

Heat input (W)	Uncertainty (%)
200	1.0035
300	0.677
400	0.5192
500	0.43004
600	0.44122

with water is 12.2% at 0.25 FR and 200 W heat input. If same has been done with ethylene glycol, the maximum rise has been found out to be 23% at 0.25 FR and 200 W heat input. It has been visualized that on increasing the heat input, the difference in thermal resistance among them shrinks. At 0.25 FR, when compared with water, the differences shrink from 12 to 9%; however for EG, it is 23–9%. The best working fluid, i.e., binary fluid when considered with all the fill ratios. It has been find out 0.25 FR gives optimum result. When normal hollow pipe of thermosyphon is used for heat transport, its thermal resistance is 52 times the thermosyphon. Hence, it can be concluded that boiling and condensation are 52 times rapid than when it is transferred from axial conduction.

Uncertainties

The term “uncertainty” is used to refer to “a possible value that an error may have” [12] and it still seems an appropriate and valuable concept. The term “uncertainty analysis” refers to the process of estimating how the uncertainties in the individual measurements have been propagated on the calculated results.

References

1. Maalej S, Zayoud A, Abdelaziz I, Saad I, Zaghoudi MC (2020) Thermal performance of finned heat pipe system for central processing unit cooling. *Energy Conv Manag* 218:112977
2. Chen L, Yu W, Lu Y, Wu P, Han F (2021) Characteristics of heat fluxes of an oil pipeline armed with thermosyphons in permafrost regions. *Appl Thermal Eng* 190:116694
3. Goh G, Tshai KH, Ong KS, Chin WM (2016) Thermal resistance of a thermosyphon filled with R410A operating at low evaporator temperature. *Appl Thermal Eng* 106:1345–1351
4. Reay DA, Kew PA, MacGregor RW (2013) Investigation of low global warming potential working fluids for a closed two-phase thermosyphon. *Appl Thermal Eng* 51:917–925
5. Jemmi A, Lataoui Z (2017) Experimental investigation of a stainless steel two-phase closed thermosyphon. *Appl Thermal Eng* 121:721–727
6. Gedik E (2016) Experimental investigation of the thermal performance of a two-phase closed thermosyphon at different operating conditions. *Energy Build* 127:1096–1107
7. Ashok FN, Anjankar PG (2015) Effect of filling ratio on thermal performance of thermosyphon heat pipe. *Int J Theoret Appl Res Mech Eng* 4(1):1–8
8. Naresh Y, Balaji C (2017) Experimental investigations of heat transfer from an internally finned two phase closed thermosyphon. *Appl Thermal Eng* 112:1658–1666

9. Shanbedi M, Zeinali Heris S, Baniadam M, Amiri A (2013) The Effect of multi-walled carbon nanotube/water nanofluid on thermal performance of a two-phase closed thermosyphon. *Experimental Heat Transfer* 26(1):26–40
10. Kothandaraman CP, Subramanyan S (2018) Heat and mass transfer data book. New age international publishers
11. Ethylene Glycol project guide (2013) ME Global
12. Mcclintock F, Kline S (1953) Describing uncertainties in single-sample experiments. *Mech Eng* 75:3–8

Application of Inverse Heat Transfer Technique in Thin Slab Continuous Casting for Estimating the Interfacial Boundary Heat Flux



Ananda S. Vaka, Pedduri Jayakrishna, Saurav Chakraborty, Suvankar Ganguly, and Prabal Talukdar

Abstract The funnel-shaped moulds used in thin slab continuous casting process does not permit the usage of conventional process such as thermal resistance networks for determining the interfacial boundary heat flux. Empirical heat flux correlations mentioned in the literature were not suitable to use for funnel-shaped moulds used in thin slab casting since they are developed for billet or thick slab casting processes. An efficient inverse algorithm, called salp swarm algorithm (SSA), is used in this study for determining 3D interfacial boundary heat flux profile on hot face of the funnel-shaped mould. This study also explored the minimum number of sensors to be placed inside the funnel-shaped mould for accurate estimation of the interfacial boundary heat flux.

Keywords Heat transfer · Continuous casting · Salp swarm algorithm · Inverse heat transfer

Nomenclature

cu	Copper plate
D	Diameter [m]
h	Hydraulic
h_w	Cooling water heat transfer coefficient [$\text{W}/\text{m}^2 \text{K}$]
k	Thermal conductivity [$\text{W}/\text{m K}$]
NF	Narrow face
Pr	Prandtl number
Re	Reynolds number

A. S. Vaka (✉) · P. Jayakrishna · S. Chakraborty · P. Talukdar
Department of Mechanical Engineering, Indian Institute of Technology, Delhi, New Delhi 110016, India
e-mail: srivaka@gmail.com

S. Ganguly
Research and Development, Tata Steel, Jamshedpur, Jharkhand 831001, India

T	Temperature [K]
T_a	Temperature of the surrounding above meniscus [K]
T_{act}	Actual temperature measured [K]
T_{dir}	Temperature calculated using direct method [K]
T_w	Average temperature of cooling water taken at inlet and outlet [K]
T_{∞}	Free stream temperature [K]
WF	Wide face
x, y, z	Co-ordinate axis in x, y, z directions [m]

1 Introduction

Solidification of steel in high casting speed continuous casting processes such as thin slab continuous casting process takes place in a specially designed funnel-shaped moulds. The design of these funnel-shaped moulds is complex due to its funnel shape and complicated arrangement of cooling water channels inside the mould. Due to these complexities, many aspects in thin slab continuous casting are not explored. One of the major contributing topics in thin slab casting is the estimation of interfacial boundary heat flux. In literature, several empirical correlations like Savage-Pritchard correlations [1, 2] and Power-law correlations [3] are available which are applicable mostly to billet casting. Because of having large aspect ratios, the traditional method of determining boundary heat flux using thermal resistance network [4, 5] fails in thin slab casting.

One of the most efficient methods for accurate estimation of unknown parameters in any process is “Inverse heat transfer technique”. Various inverse methods/algorithms such as least square adjustment method (LSAM) [6], conjugate gradient method (CGM) [7], and salp swarm algorithm (SSA) [8, 9] are also used in continuous casting processes but those methods/algorithms are applied only in thick slab or billet casting process. As per literature, research has not been done in the direction of exploring interfacial boundary heat flux in thin slab continuous casting by using complicated 3D funnel-shaped mould along with cooling water channel arrangement. This study adopted a novel approach for determining interfacial boundary heat flux in 3D funnel-shaped mould using SSA and also explored the minimum number of sensors to be placed inside the funnel-shaped mould for accurate estimation of the interfacial boundary heat flux.

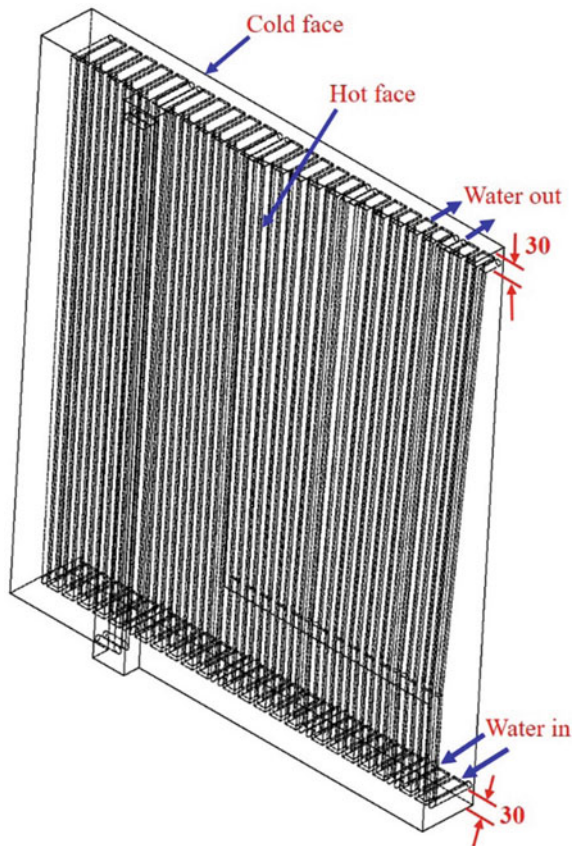
2 Methodology and Solution Procedure

Solidification of liquid metal in thin slab continuous casting takes place when liquid metal passes through the funnel-shaped mould. Cooling water arrangement and holes for incorporating thermocouples are at a constant distance away from the hot face of

the funnel-shaped mould. Hence, at any location in the mould, the shape of cooling water channels resembles the funnel shape of the mould. Figure 1 shows the funnel-shaped mould along with cooling water geometry. Cooling water geometry consists of circular-shaped holes and ‘U’-shaped cooling slots. They extends from 30 mm below mould top to a length of 1040 mm inside the mould. The dimensional details of these holes and slots are represented by taking a section at the meniscus region as shown in Fig. 2(a) and (b). A total of 15 thermocouples measurements are received from the industry in which ‘9’ thermocouples are located on wide face and ‘3’ thermocouples are located on narrow face and ‘3’ thermocouples are located close to corner region. The location and measurement of thermocouples inside the mould are shown in Fig. 3.

Inverse heat transfer technique estimates the 3D interfacial boundary heat flux profile on hot face of the funnel-shaped mould by solving direct and inverse problems. Equation (1) represents the 3D heat conduction equation that is solved in direct problem to obtain temperature distribution inside the mould. The empirical correlation mentioned in Eq. (2) calculates the cooling water heat transfer coefficient which

Fig. 1 Cooling channel geometry inside funnel-shaped mould



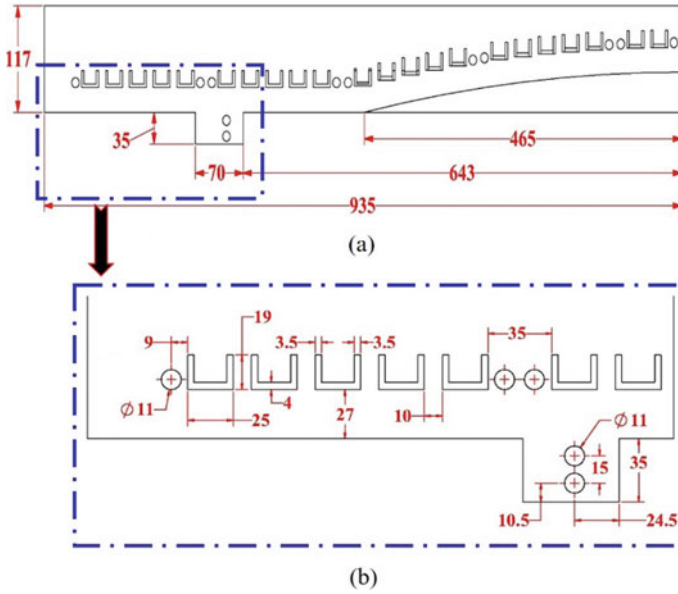


Fig. 2 Dimensions of cooling water channel holes and slots (a) Section at the meniscus region. (b) Channel dimensions

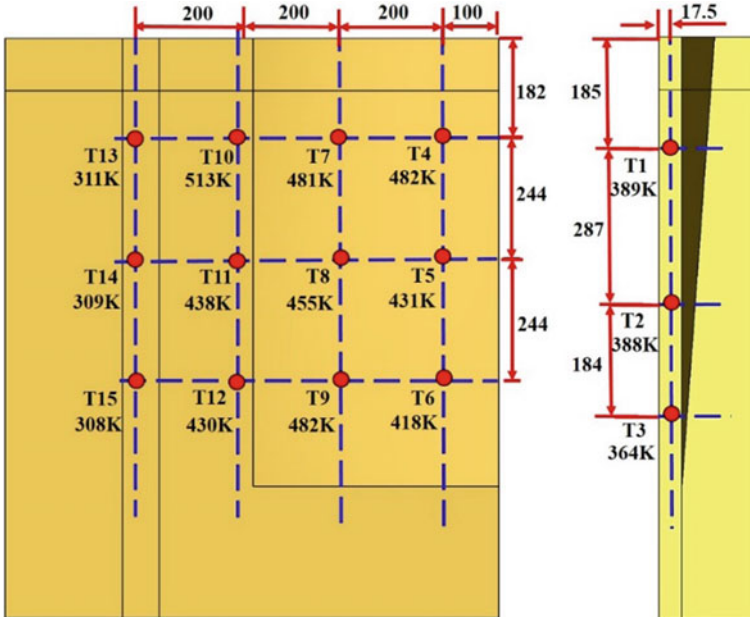


Fig. 3 Location of thermocouples on wide (left) and narrow (right) faces of the mould

in turn used to represent the heat carried away from the narrow and wide faces of the mould using Eqs. (3) and (4). The heat flux which acts at the interface of both wide and narrow faces of the mould is shown in Eq. (5). The heat loss at the meniscus is modelled as convective heat loss to atmosphere with suitable value of convective heat transfer coefficient.

The heat flux profile which captures the heat loss from hot face of the mould is taken in the form of a quadratic profile by incorporating all forms of non-linear terms is typically represented as $a_1 + a_2x + a_3y + a_4z + a_5xy + a_6yz + a_7zx + a_8x^2 + a_9y^2 + a_{10}z^2$. The SSA inverse algorithm used in the Inverse problem estimates the interfacial heat flux profile (\vec{Q}'') with the help of experimental values of measured temperatures (T_{act}) and temperature distribution found out using assumed heat flux at those locations where temperatures are measured (T). Based on (T_{act}) and T , an objective function (f) as shown in Eq. (6) is formulated and monitored at the end of every iteration till the convergence condition is satisfied. Detailed explanation of SSA is available in author's previous work [8].

$$\frac{\partial^2 T}{\partial x^2} + \frac{\partial^2 T}{\partial y^2} + \frac{\partial^2 T}{\partial z^2} = 0 \tag{1}$$

$$\frac{h_w D_h}{k_w} = 5 + 0.015 \text{Re}^{0.88 - 0.24/(4 + \text{Pr})} \text{Pr}^{0.333 + 0.5e^{-0.6\text{Pr}}} \tag{2}$$

$$\text{Narrowface} : -k_{cu} \frac{\partial T}{\partial x} = h_w [T - T_w] \tag{3}$$

$$\text{Wideface} : -k_{cu} \frac{\partial T}{\partial y} = h_w [T - T_w] \tag{4}$$

$$-k_{cu} \frac{\partial T}{\partial x} \hat{i} - k_{cu} \frac{\partial T}{\partial y} \hat{j} - k_{cu} \frac{\partial T}{\partial z} \hat{k} = \vec{Q}'' , 0.1 \leq z \leq 1.1 \tag{5}$$

$$f = \sqrt{\frac{1}{P} \sum_1^P \left[T_{act}(x_p, y_p, z_p) - T \left\{ x_p, y_p, z_p; \vec{Q}'' \right\} \right]^2} \tag{6}$$

3 Validation of the Inverse Code

For validating the SSA algorithm, a quadratic form of reference heat flux profile is considered. With the help of direct problem, thermal field inside the funnel-shaped mould shown in Fig. 1 is calculated by applying the assumed reference heat flux profiles on hot face of the mould. From the obtained temperature distribution, the temperatures at the thermocouple locations mentioned in Fig. 3 are extracted. Temperatures at the 15 locations are given as input to SSA, and inverse problem

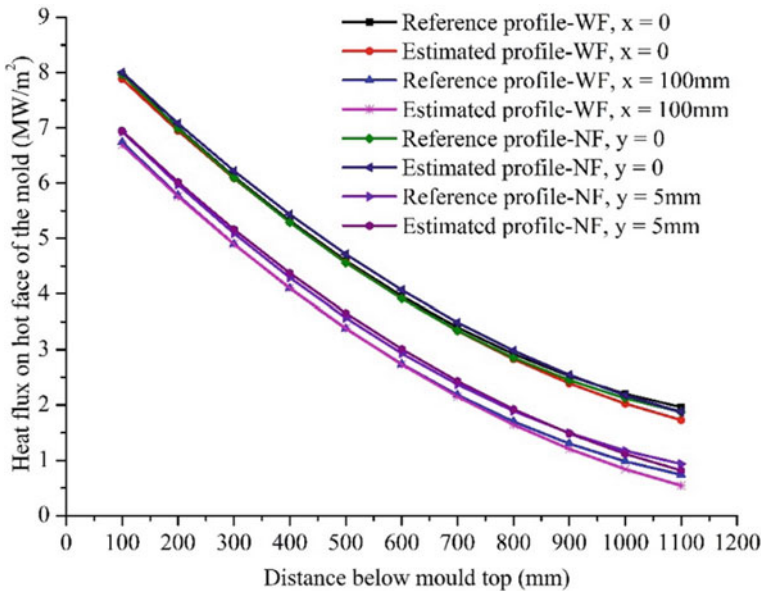


Fig. 4 Validation of quadratic heat flux profile on hot face of the mould

is solved to estimate the heat flux profiles. The assumed reference heat flux profile and estimated heat flux profiles are compared. Figures 4 and 5 show the deviation between both profiles at different locations in the mould is within the accepted tolerance limits. Hence, it is confirmed that the proposed inverse algorithm, salp swarm algorithm, is capable enough to estimate the interfacial boundary condition in thin slab continuous casting which uses funnel-shaped mould.

4 Results

4.1 Estimation of Interfacial Heat Flux Using Experimental Data

The spatially varying quadratic form of nonlinear heat flux profile obtained on hot face of the funnel mould using inverse heat transfer analysis for the experimental data is shown in Eq. (7). Figures 6 and 7 show the distribution of temperature and heat flux on hot faces of the mould, respectively. From the obtained results, it is observed that the maximum temperature and heat flux are located near the meniscus slightly away from the central region, and minimum temperature and heat flux are observed at the corner location at the mould exit [10]. The maximum and average heat flux values on wide face are 5.78 MW/m² and 3.3 MW/m², respectively. Figures 8 and

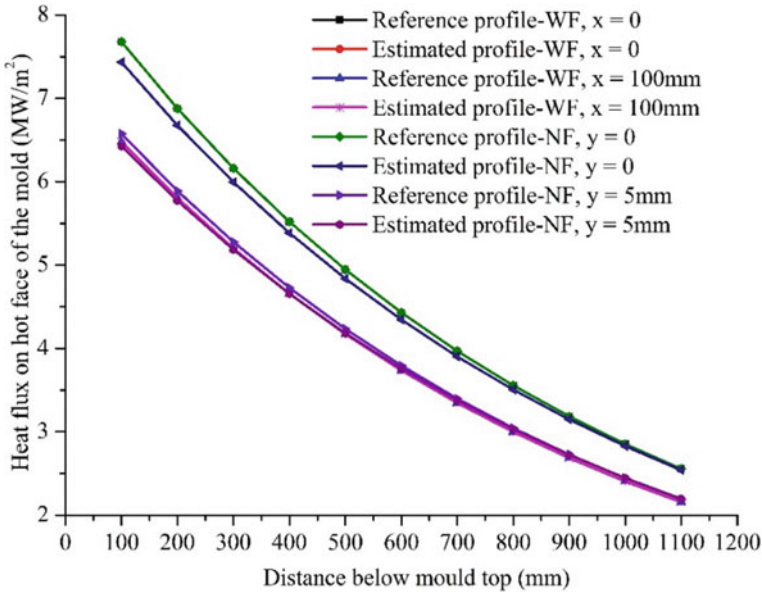


Fig. 5 Validation of exponential heat flux profile on hot face of the mould

9 show the 3D surface plots of interfacial heat flux profile on wide and narrow faces of the mould which show the non-linear variations along the length as well as width directions on hot face of the mould.

$$Q''(\text{MW/m}^2) = 6.2551 - 0.2617(y) - 2.5663(x) - 8.5907(xy) - 7.8276(y^2) - 11(x^2) + 7.0594(z) + 2.6198(xz) + 8.6211(yz) + 3.7493(z^2) \tag{7}$$

4.2 Effect of Number of Sensors on Estimated Heat Flux Profile

If the number of sensors is increased, the heat flux estimation will be more accurate. However, it is not practical to increase the number of sensors in an industrial mould. Hence, the number of sensors is to be optimized. To study the number of thermocouples required for the accurate heat flux estimation, the number of sensors on narrow face of the mould are doubled and tripled as shown in Fig. 10 to study the number of thermocouples required for the accurate estimation of heat flux profiles on wide and narrow faces of the mould. Sensor locations considered on the narrow face of the mould at distance of 5, 17.5, and 30 mm from the symmetric face.

Fig. 6 Temperature contour on hot face of the mould

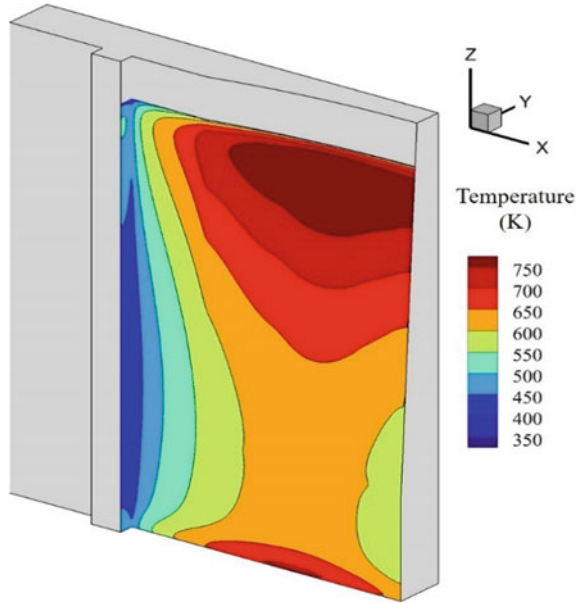
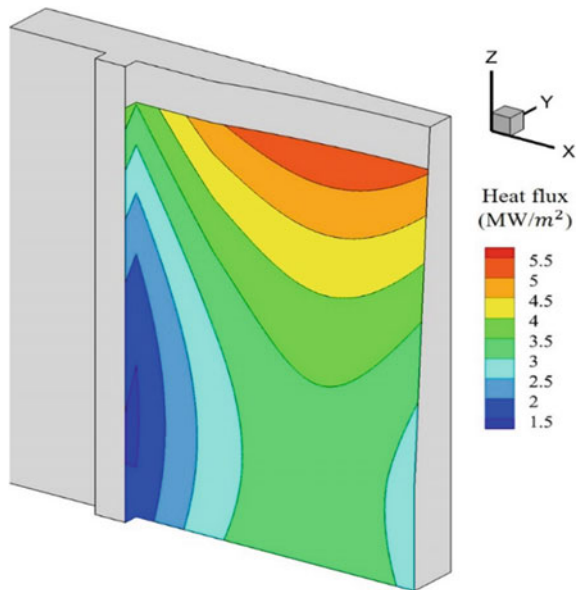


Fig. 7 Heat flux contour on hot face of the mould



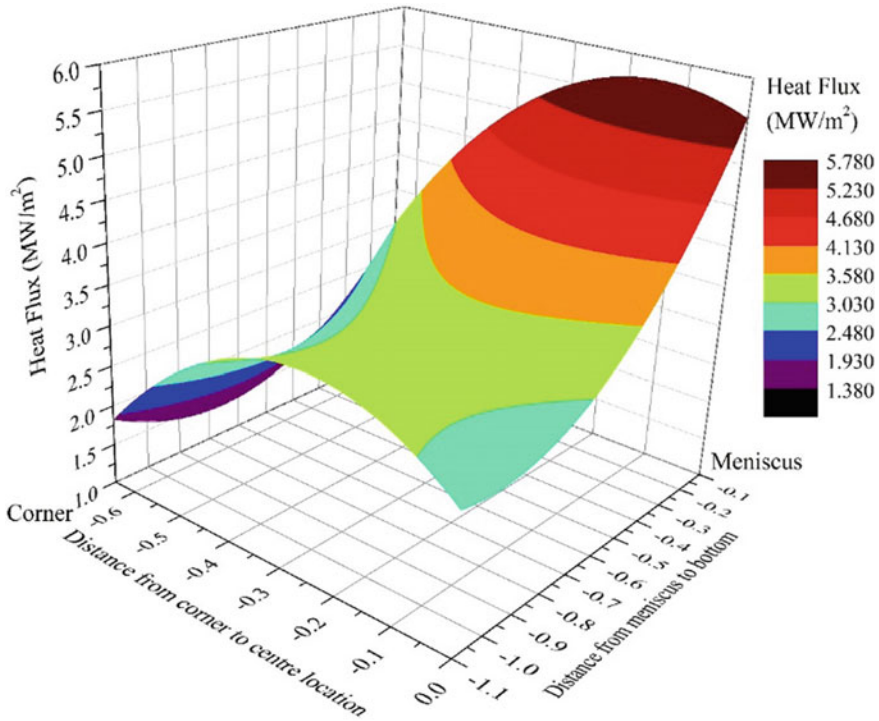


Fig. 8 Surface plot of interfacial heat flux profile on wide face

The quadratic heat flux profile (Reference profile) considered in the previous section is applied on hot face to produce the temperature distribution in the funnel mould using the direct code. Temperature readings obtained at 12 locations (‘9’ on WF and ‘3’ on NF (17.5 mm from symmetric face)), 15 locations (‘9’ on WF and ‘6’ on NF (5 mm and 17.5 mm from symmetric face)), and 18 locations (‘9’ on WF and ‘9’ on NF (5, 17.5, and 30 mm from symmetric face)) are considered for the heat flux estimation on hot face of the mould using the inverse code.

Figure 11 shows the comparison between the reference and estimated heat flux profiles with different number of sensors on hot face of the mould at symmetric location on wide face of the mould. Similarly, Fig. 12 show the heat flux profiles on the narrow face. The results confirmed that there is a significant deviations present when estimated heat flux profiles are estimated using 12 sensors. These deviations are almost nullified when the number of sensors are increased to 15 and 18. Hence, for the accurate estimation of heat flux on hot face of the mould at least ‘9’ thermocouples on wide face and ‘6’ thermocouples on narrow face are required.

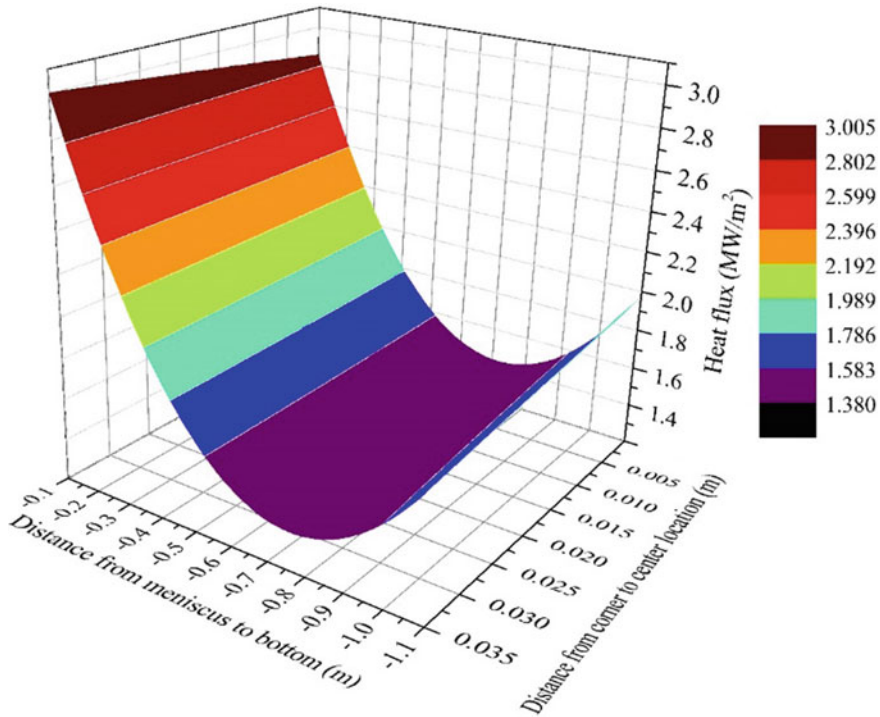


Fig. 9 Surface plot of interfacial heat flux profile on narrow face

4.3 Effect of Measurement Error

Measurements always have some amount of errors and hence, it is essential to analyse and quantify the effect of measurement error of the boundary heat flux estimation using inverse technique. In order to test that, artificial errors are created by modifying temperature data, T_{dir} found by the solution of direct problem using the relation:

$$T_{\text{act}} = T_{\text{dir}} + \omega\sigma \quad (8)$$

where ω is the random variable generated by assuming normal distribution within $[-2.576, 2.576]$ for the 99% confidence level and σ is the standard deviation of the measurement error. Standard deviation is related to the measurements and it depends on accuracy of the measuring instrument. T_{act} , thus, mimics the actual temperature data measured by a thermocouple with measurement errors.

The error analysis is done with three pre-defined σ values as was done in the literature [7]. The results obtained for these three different σ values are almost same as shown in the Fig. 13 for the wide face of the mould and in Fig. 14 for the narrow

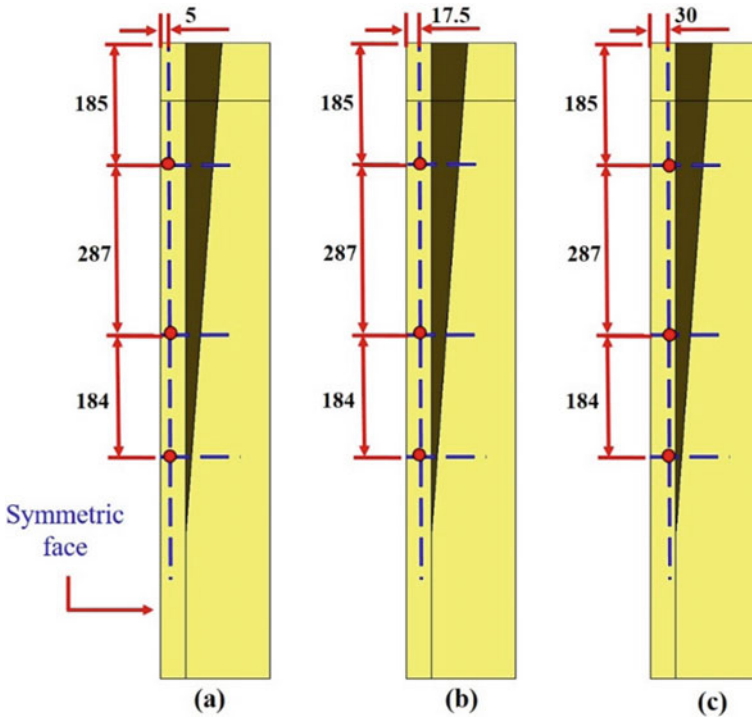


Fig. 10 Sensor locations considered on the narrow face of the mould at distance of (a) 5 mm, (b) 17.5 mm and (c) 30 mm from the symmetric face

face of the mould. Thus, it can be concluded that the results are stable for small changes in the input values of the problem.

5 Conclusions

An efficient inverse algorithm called salp swarm algorithm (SSA) is used in this study for determining the interfacial boundary heat flux on hot faces of the funnel-shaped mould using the actual 3D problem domain. The obtained heat flux profile has nonlinear variations both in longitudinal and transverse directions. The location of maximum and minimum heat flux locations and their values are consistent with the values observed in the literature. Heat flux variation as high as 77% relative to wide face centre and 85% relative to the maximum heat flux was observed in the corner region. The importance of having sufficient temperature data is reconfirmed. The effect of measurement errors is also investigated.

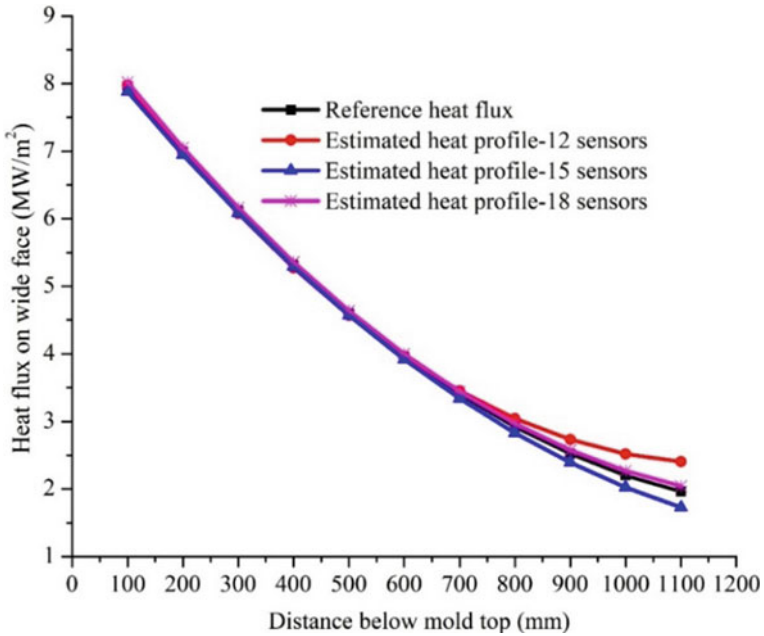


Fig. 11 Comparison of reference and estimated heat flux profiles on wide face at symmetric location

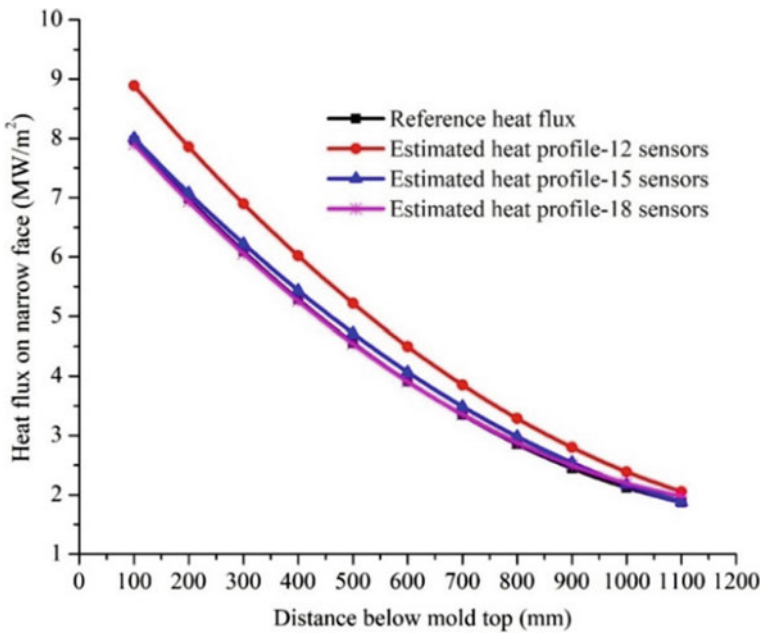


Fig. 12 Comparison of reference and estimated heat flux profiles on narrow face at symmetric location

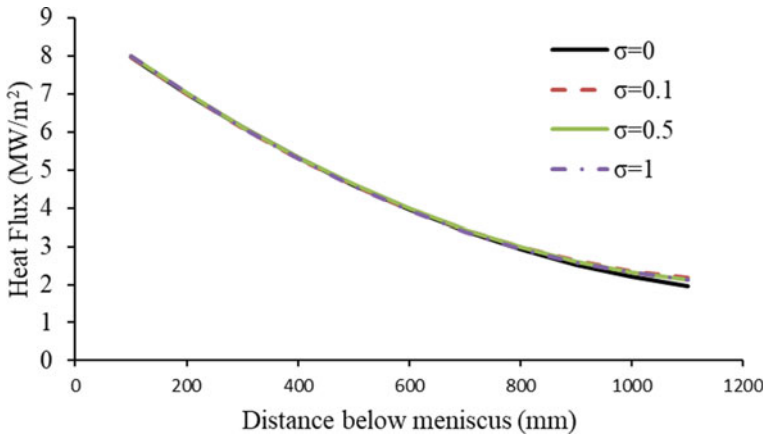


Fig. 13 Effect of measurement error at symmetric face on the wide face of the mould

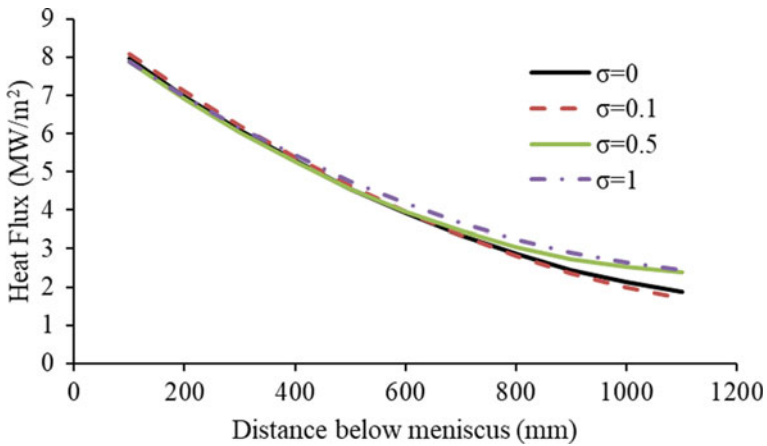


Fig. 14 Effect of measurement error at symmetric face on the narrow face of the mould

Acknowledgements The authors are thankful to the Council of Scientific and Industrial Research (CSIR), India, for providing financial assistance involved in carrying out the work.

References

1. Gonzalez M et al (2003) Modeling of the solidification process in a continuous casting installation for steel slabs. *Metall Mater Trans B* 34(4):455–473. <https://doi.org/10.1007/s11663-003-0072-3>
2. Savage J, Pritchard WH (1954) The problem of rupture of billet in the continuous casting of steel. *Tetsu-to-Hagane* 178(11):269–277
3. Gupta A et al (2018) Effect of mould geometry, coating, and plate thickness on the thermal profile of continuous casting moulds. *J South Afr Inst Min Metall* 118(5):505–513. <https://doi.org/10.17159/2411-9717/2018/v118n5a7>
4. Chakraborty S, Ganguly S, Talukdar P (2020) Determination of thermal resistance at mould-strand interface due to shrinkage in billet continuous casting—development and application of a novel integrated numerical model. *Int J Therm Sci* 152:106305. <https://doi.org/10.1016/j.ijthermalsci.2020.106305>
5. Jayakrishna P et al (2020) A novel method for determining the three dimensional variation of non-linear thermal resistance at the mold-strand interface in billet continuous casting process. *Int Commun Heat Mass Transfer* 119:104984. <https://doi.org/10.1016/j.icheatmasstransfer.2020.104984>
6. Nawrat A, Skorek J (2004) Inverse finite element technique for identification of thermal resistance of gas-gap between the ingot and mould in continuous casting of metals. *Inverse Problems Sci Eng* 12(2):141–155. <https://doi.org/10.1080/10682760310001598580>
7. Udayraj et al (2017) Estimation of surface heat flux in continuous casting mould with limited measurement of temperature. *Int J Therm Sci* 118:435–447. <https://doi.org/10.1016/j.ijthermalsci.2017.05.012>
8. Vaka AS, Ganguly S, Talukdar P (2021) Novel inverse heat transfer methodology for estimation of unknown interfacial heat flux of a continuous casting mould: a complete three-dimensional thermal analysis of an industrial slab mould. *Int J Thermal Sci* 160:106648. <https://doi.org/10.1016/j.ijthermalsci.2020.106648>
9. Vaka AS, Talukdar P (2020) Novel inverse heat transfer technique for estimation of properties and location-specific process parameters of roof-mounted solar PV plants. *Thermal Sci Eng Progress* 19. <https://doi.org/10.1016/j.tsep.2020.100657>
10. Jayakrishna P, Vaka AS, Chakraborty S, Ganguly S, Talukdar P (2021) Interfacial Heat Flux Estimation in a Funnel Shaped Mould and Analysis of Solidification Characteristics in Thin Slab Continuous Casting. *J Heat Transfer, ASME*, 143(12). <https://doi.org/10.1115/1.4052204>

Heat Transfer Enhancement of Fin and Tube Heat Exchanger Using Ribs



Vaidant Rathore, Atharva A. Lokhande, Yogesh G. Mane,
and Mandar M. Lele

Abstract The heat transfer can be done more efficiently with various methods. These methods are mostly used to save energy and materials and hence helping to make a financially effective method good enough to keep going long and fill its need. This paper enlists the various sorts of heat transfer enhancement techniques used. In recent times, there has been a considerable amount of research being carried out in the scope of improving the heat transfer. These methods can be broadly classified into three divisions: active, passive, and compound. The practises that require an outer wellspring of force are termed as the active methods, while the ones that don't need an outer wellspring of force are referred to as the passive methods. The compound methods are the ones that use complex designs which limits their use. The main aim is to deal with the various types of heat transfer techniques and get a desired detailed information about them. The paper goes into the details using ribs in fin and tube heat exchanger to make a more efficient heat transfer. It is observed that for the normal fin and tube heat exchanger the heat enhancement was around 30% which was increased to 34% with the help of eight ribs on each side of fins. There is a slight increase in the heat transfer with an increase in the number of ribs.

Keywords Active heat transfer · Passive heat transfer · Compound heat transfer · Heat exchangers

Nomenclature

Di Internal Diameter of Tube
Do External Diameter of Tube
L Length of Tube
t1 Thickness of Fin
t2 Thickness of Ribs

V. Rathore (✉) · A. A. Lokhande · Y. G. Mane · M. M. Lele
MIT WPU, Pune, India
e-mail: vsr3024@gmail.com

s	Side of square fin
Fp	Pitch of Fins
h	Height of Rib
w	Width of Rib

1 Introduction

A heat exchanger can be defined as a system that is used to transfer heat between two or more fluids. One can find the use of heat exchangers in various fields ranging from industries to domestic work for thermal recovery jobs. A few specific applications of heat exchangers can be listed out as space heating, air conditioning, refineries, chemical plants, etc. A heat exchanger can be used for both heating and cooling requirements [1–10].

1.1 Importance of Heat Transfer Enhancement

It is highly important to make heat exchangers more efficient and is the main reason for the development and use of techniques which are commonly called heat transfer improvement practises. The heat transfer can be done more efficiently with various methods. These methods are mostly used to save energy and materials and hence helping to make a financially effective method good enough to keep going long and fill its need. This paper enlists the different types of enhancement techniques used. These techniques mostly concentrate on reducing the thermal resistance faced by the heat exchangers [11–13].

2 Classification

These methods can be broadly classified into three divisions: active, passive, and compound. The active methods are the ones that require an outer wellspring of force. The passive methods are the ones that don't need an outer wellspring of force. And, the compound methods are the ones that involve complex designs [13–20].

2.1 Active Methods

The active methods are the ones that require an external source of power. The most common active techniques are: electrohydrodynamic, jets, sprays, etc.

2.2 Passive Methods

The methods that focus on geometrical modifications to enhance the heat transfer and do not include any external power source are known as the passive heat transfer enhancement techniques. These methods involve use of additional devices or joining inserts that help in changing the flow pattern and helping in the pressure drop to increase [20–29]. The most common passive techniques can be listed as:

1. Coiled Tubes
2. Fins
3. Winglets
4. Dimples
5. Ribs
6. Twisted tapes
7. Conical rings
8. Vortex rings
9. Coiled wire.

2.3 Compound Methods

It is notable that two of the above-mentioned methods can be used all the while to create an upgrade bigger than that delivered by just a single strategy. The blend of various procedures acting at the same time is known as compound enhancement techniques.

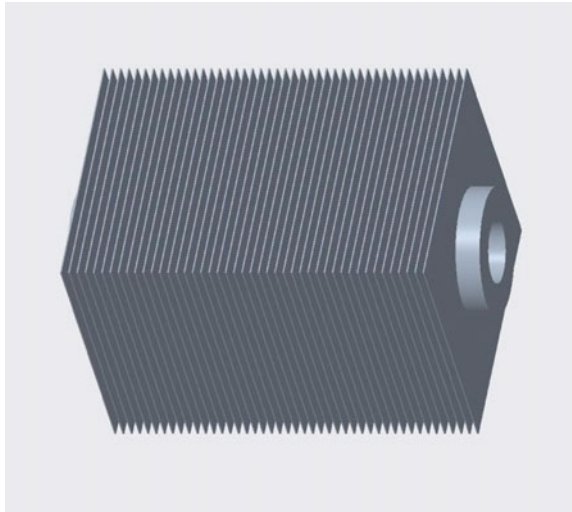
3 Methodology

The project was carried out in following stages:

3.1 Problem Description:

Setting ribs intermittently on the heat transfer surface increases the disturbance and since these ribs are little, they don't upset the centre stream thus a high heat transfer performing surface could be accomplished without causing the disadvantages of friction and pressing factor drop.

Fig. 1 Fin and tube heat exchanger



3.2 Geometry Construction and Pre-Analysis:

The geometry of the models was created in PTC CREO 4.0

Dimensions considered for the Heat Exchanger for Tubes,

$d_i = 15$ mm, $d_o = 30$ mm, $L = 150$ mm

For Fins, $T1 = 0.5$ mm, $Fp = 3$ mm, $s = 60$ mm

For Ribs, $h = 15$ mm, $t2 = 1.5$ mm, $w = 1.2$ mm.

The heat exchanger mentioned in the Fig. 1 is used to analyse the effect of ribs on the heat transfer. The ribs are attached to the fin surface on both its faces.

The rib number is varied from 0 to 8 and the heat transfer enhancement is analysed with the help of ANSYS 2020 R2 software.

3.3 Meshing

Mapped face meshing was done with mesh size of 0.002 m.

3.4 Numerical Analysis and Post Processing

The tube was subjected to a fluid of temperature 200 °C and convection coefficient that was calculated as 25 W/m² °C. The temperature variation and the total heat flux were calculated for all the models.

3.5 Validation

The mesh independency study was finished with three different meshes, which is for coarse, medium, and fine to see which test has the most magnificent outcome. Thus, the outcomes show the course has less pressing factor contrast with medium and fine. For the instance of fine mesh, results show predominant execution, yet the computational time is twice contrasted with the medium with less error in the outcomes. Subsequently, the medium mesh has been chosen for this examination to assess the results (Figs. 2, 3, 4, 5 and 6).

Fig. 2 Ribs alignment on fin surface

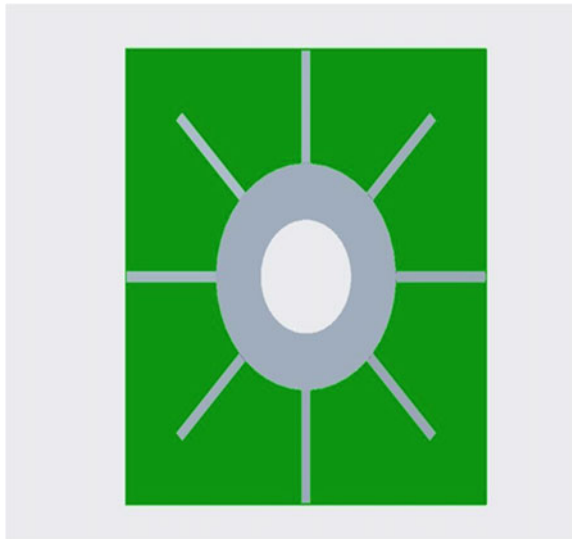
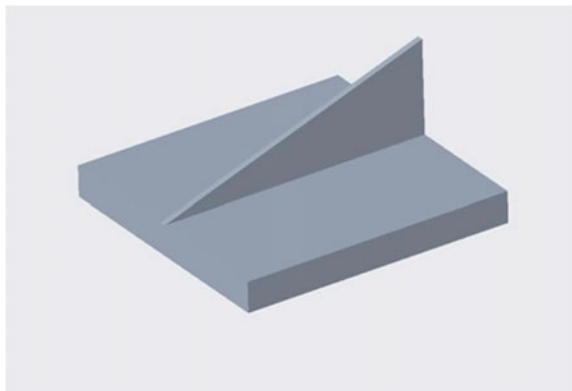


Fig. 3 Shape of rib created



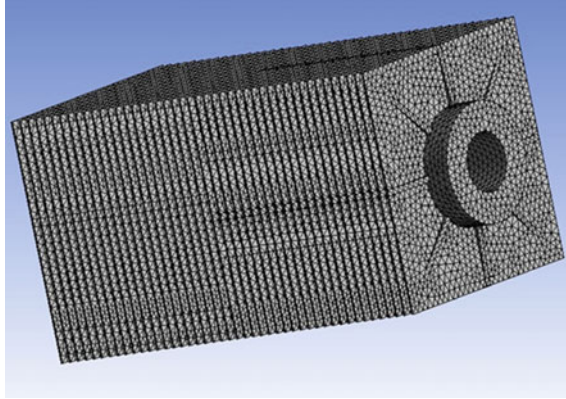
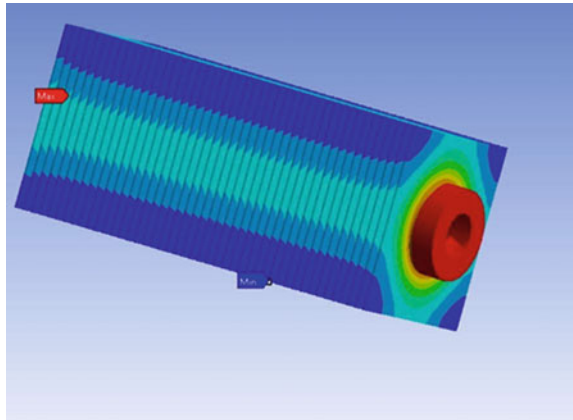


Fig. 4 Meshed 8 ribs heat exchanger

Fig. 5 Analysis of fin and tube heat exchanger with ribs (1)



4 Results

The maximum temperature was considered to be 200 °C and the minimum temperature achieved without the attachment of ribs was 140 °C.

After the use of ribs, the minimum temperatures achieved were 138, 137.6, 137, 136.36, 135.36, 132.8, and 132 °C with the subsequent increase of number of ribs (Fig. 7 and Table 1).

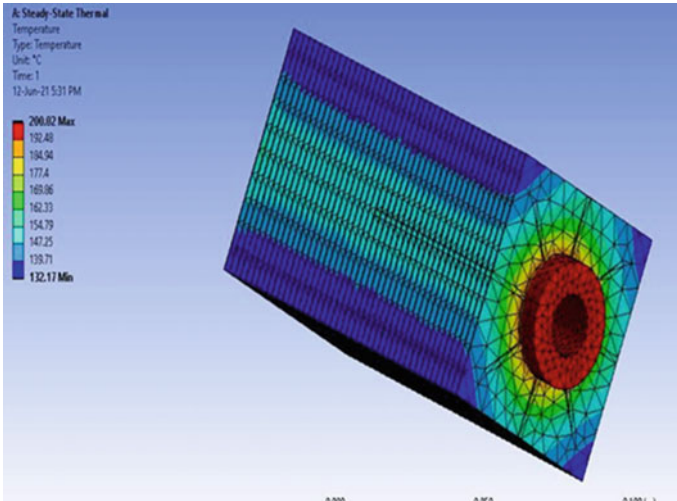


Fig. 6 Analysis of fin and tube heat exchanger with ribs (2)

Fig. 7 Variation of heat transfer enhancement with ribs

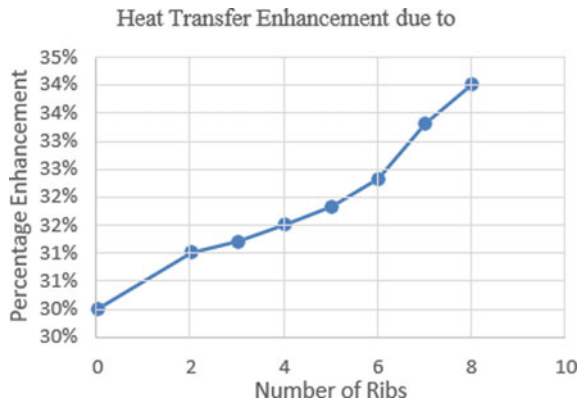


Table 1 Increase of heat transfer enhancement due to ribs

S. No.	No. of ribs on each face of fin	% of heat enhancement
1	0	30
2	2	31
3	3	31.2
4	4	31.5
5	5	31.82
6	6	32.32
7	7	33.6
8	8	34

5 Conclusion

This paper concludes that the use of passive heat transfer improvement practices, especially ribs, is highly fruitful. Heat transfer enhancement techniques are highly important for economical and energy-saving reasons. Heat transfer improvement methods diminish the heat resistance either by expanding the successful heat transfer surface area. The passive techniques are very crucial when the correct arrangement is used. The number of ribs influences the transfer of heat extensively.

It is observed that for the normal fin and tube heat exchanger, the heat enhancement was around 30% which was increased to 34% with the help of eight ribs on each side of fins. There is a slight increase in heat transfer with an increase in the number of ribs.

References

1. Sheikholeslami M, Bandpy M, DomiriGanji D (2015) Review of heat transfer enhancement methods: focus on passive methods using swirl flow devices. *Renew Sustain Energy Rev* 49:444–469
2. Gugulothua R, Vijaya Kumar Reddy K, Somanchi NS, Adithya EL (2017) A review on enhancement of heat transfer techniques. *Mater Today Proc* 4:1051–1056
3. Lal L, Miscevic M, Lavieille P, Amokrane M, Pigache F, Topin F, Nogarde B, Tadrist (2013) An overview of heat transfer enhancement methods and new perspectives: focus on active methods using electroactive materials. *Int J Heat Mass Transfer* 61:505–524
4. Siddique M, Khaled A-R-A, Abdulhafiz NI, Boukhary (2010) Recent advances in heat transfer enhancements: a review report. *Int J Chem Eng* 1–2
5. Mousa MH (2021) Review of heat transfer enhancement techniques for single phase flows. *Renew Sustain Energy Rev* 137:110566
6. Ji Z, Zhu X, Mondejar ME, Haglind F (2019) A review of heat transfer enhancement techniques in plate heat exchangers. *Renew Sustain Rev* 101:305–328
7. Niyas H, Muthukumar P (2018) A novel heat transfer enhancement technique for performance improvements in encapsulated latent heat storage systems. *Solar Energy* 164:276–286
8. Wen-Tao, Fan JJ-F, Zhao C-Y, Tao W-Q (2018) A revised performance evaluation method for energy saving effectiveness of heat transfer enhancement techniques. *Int J Heat Mass Transfer* 1381142–1381153
9. Rezaee M, Taheri AA, Jafari M (2020). Experimental study of natural heat transfer enhancement in a rectangular finned surface by EHD method. *Int Commun Heat Mass Transfer* 119104969
10. Kakaç S, Bergles AE, Mayinger F, Yüncü H (eds) (2013) Heat transfer enhancement of heat exchangers, vol 355, Springer Science & Business Media
11. Tada Y, Takimoto A, Hayashi Y (1997) Heat transfer enhancement in a convective field by applying ionic wind. *J Enhanced Heat Transfer* 4(2):71–86
12. Huang M, Lai FC, Oosthuizen PH, Molki M (2006) Effects of joule heating on electrohydrodynamics-enhanced natural convection in an enclosure. *J Thermophys Heat Transf* 20:939–945
13. Yan Y, Zhang H, Hull J (2004) Numerical modeling of electrohydrodynamic (EHD) effect on natural convection in an enclosure. *Numerical Heat Transfer A Appl* 46:453–471
14. Kasayapanand N, Kiatsiriroat T (2009) Enhanced heat transfer in partially open square cavities with thin fins by using electric field. *Energy Convers Manag* 50:287–296
15. Kasayapanand N (2008) Electrohydrodynamic enhancement of heat transfer in vertical fin array using computational fluid dynamics technique. *Int Commun Heat Mass Transfer* 35:762–770

16. Huang RT, Sheu WJ, Wang CC (2009) Heat transfer enhancement by needle-arrayed electrodes—an EHD integrated cooling system. *Energy Convers Manag* 50:1789–1796
17. Fazlollahi F, Alemrajabi AA (2018) Effect of fin and electrodes on electro-hydrodynamic enhanced heat transfer in enclosures. *Int J Therm Sci* 127:194–200
18. Fadaki ST, Amanifard N, Deylami HM, Dolati F (2017) Numerical analysis of the EHD driven flow with heat transfer in a smooth channel using multiple collectors. *Heat Mass Transf* 53(7):2445–2460
19. Deylami HM (2019) Effects of EHD on the flow and heat transfer characteristics in a rectangular corrugated channel. *Heat Mass Transf* 55(12):3711–3720
20. Laohalertdecha S, Naphon P, Wongwiset S (2007) A review of electrohydrodynamic enhancement of heat transfer. *Renew Sust Energy Rev* 11(5):858–876
21. Jasim HH (2020) Heat transfer enhancement from heat sources using optimal design of combined fins heat-sinks. *Propulsion Power Res* 9(4):372e382
22. Ibrahim TK (2020) The impact of square shape perforations on the enhanced heat transfer from fins: experimental and numerical study. *Int J Therm Sci* 149:106144
23. Mahdi JM (2019) Hybrid heat transfer enhancement for latent-heat thermal energy storage systems: a review. *Int J Heat Mass Transfer* 137; 630—eat transfer enhancement in microchannel heat sink using hybrid technique of ribs and secondary channels. *Int J Heat Mass Transfer* 114:640–655
24. Bahiraei M, Hanooni M (2021) Performance enhancement of a triple-tube heat exchanger through heat transfer intensification using novel crimped-spiral ribs and nanofluid: a two-phase analysis. *Chem Eng Process Process Intensification* 160:108289
25. Varun Kumar B (2021) Enhancement of heat transfer in SAH with polygonal and trapezoidal shape of the rib using CFD. *Energy* 121154
26. Yogendra Rathore KR, Aharwal (2020) Heat transfer enhancement due to a staggered element using liquid crystal thermography in an inclined discrete rib roughened solar air heater. *Int Commun Heat Mass Transfer* 118:104839
27. Mahmoodi Jezeh SV, Wang BC (2021) Direct numerical simulation of turbulent heat transfer in a square duct with transverse ribs mounted on one wall. *Int J Heat Fluid Flow* 89:108782
28. Suri ARS, Pun AK, Haque MSA (2020) Review of heat transfer augmentation methods and effect of using dimpled ribs and nanofluids
29. Gnanavel C, Saravanan R (2020) Heat transfer enhancement through nano-fluids and twisted tape insert with rectangular cut on its rib in a double pipe heat exchanger. *Mater Today Proc* 21, Part 1:865–869

Effect of Dilution on Lean Blow-Off Limit of Methane Combustion



Keyur Kadia, Nikhil A. Baraiya, and R. D. Shah

Abstract Gasification of the bio-mass has shown to be very fuel flexible depending upon the sources of extraction. The effect of the gases like carbon dioxide as diluents had studied for the thermal characteristics of natural gas. Such Gases are present in realistic conditions. Also, the addition of the fuels like hydrogen has proven to improve the thermal and stability characteristics of the flame. The numerical analysis did carry out for the above-discussed conditions with the help of ANSYS. The turbulence model chosen for this study is k- ϵ and RSM. It is proven to be reliable in this type of study. Further, the addition to numerical analysis did carry out at lean blow-off conditions. Further, it is extended for the lean blow-off limit at 5% with dilution of carbon dioxide and hydrogen. The thermal characteristics and flow velocity had plotted across the axial locations. Centre line temperature variation has plotted for lean blow-off limit and dilution of carbon and hydrogen 5% at different mass flow rate of fuel to find out lean blow-off limit for dilution case.

Keywords Methane combustion · Lean blow-off limit · Effect of dilution · Combustion flow physics

Nomenclature

AFR Air to Fuel Ratio
CTRZ Central Toroidal Recirculation Zone
PDF Probability Density Function

K. Kadia (✉) · N. A. Baraiya · R. D. Shah
Mechanical Engineering Department SVNIT, Surat, India
e-mail: keyurkadia1@gmail.com

© The Author(s), under exclusive license to Springer Nature Singapore Pte Ltd. 2023
H. B. Mehta et al. (eds.), *Recent Advances in Thermal Sciences and Engineering*,
Lecture Notes in Mechanical Engineering, https://doi.org/10.1007/978-981-19-7214-0_34

Greek Symbols

θ	Equivalence ratio
f	Mixture fraction
R	Radius
S_N	Swirl number

1 Introduction

The energy systems are generally designed to be operated near the stoichiometric condition. Operating condition near stoichiometric is preferred due to higher adiabatic flame temperature and maximum combustion efficiency. But, slight deviation towards fuel-rich condition results into incomplete combustion of the fuel along with the lower flame temperature. This is not the combustion efficient condition. Generally, fuel lean operation conditions are preferred as it ensures the complete combustion of the fuel. Many times to reduce the Knox emission the combustors are operated at the lowest possible equivalence ratios. At very low equivalence ratios (ER) the flame stability biggest challenge. Dilutions in inert gas or other fuels is found to be useful in complete combustion as well as flame stability. Present chapter is dedicated to the LBO limits of methane for pure condition and also along with the dilution of inert gas (CO_2) and fuel (H_2).

Lieuwen [1] has shown that The Effects of Fuel Composition on Flashback, and Effects of Fuel Composition on and Combustor Blowout Operability of Lean Premixed (LP) Combustors It's a synopsis. Sansui [2] has shown that Using an ultra-lean combination of methane, hydrogen, and air, effect of fuel flexibility on the flame stability and emission of a swirl stabilized non-premixed (NP) combustor was investigated experimentally. To see how adding hydrogen to methane affects it. Cheng Tung [3] has shown that to It's important to understand the in order to keep current facilities safe, diluents must have an impact on natural gas combustion. Using a swirl flame burner, the current study analyses diluent-containing natural gas flame stability and spectroscopic properties. To create stable and continuous swirl flames, a variety of gas compositions were utilized, including those diluted with nitrogen and carbon dioxide. When compared to the pure methane sample, diluting the simulated gas with CO_2 and N_2 resulted in a larger blowout limit. Despite the fact that CO_2 has a greater influence on flame blowout than N_2 due to preheating the burner and mixes can assist to extend the flame blowout limits because to its increased heat capacity. Akhtar [4] has shown that the goal of this research is to develop an industrial tool that can anticipate the behaviour of lean flames approaching extinction and compute lean blowout limits at high temperatures and pressures. (RANS) turbulence model (TM) is utilized in conjunction with a tabular chemistry method to do comprehensive validation. Jackson [5] has shown that computational analysis examined and experimental In extremely strained counter flow, the consequences of adding H_2 to

lean-premixed CH_4 flames fields employing warmed flows indicates considerable Extinction strain rates and lean combustibility limits for extremely small amounts of H_2 have been improved. H_2 raises the maximum allowable strain rate before extinction temperatures are reached, allowing CH_4 combustion to occur under normally extinction-prone circumstances. Strakey [6] has shown effects of adding H_2 to a LP swirl-stabilized combustor burns natural gas and air were investigated. The equivalency ratio during blowout dropped from 0.46 to 0.30 when the hydrogen content of the fuel was raised from 0 to 80% by raising the nozzle velocity from 40 to 80 m/s, and the blowout was increased by 0.05. Shen [7] has shown that On The combustion characteristics of ignition processes were investigated in natural gas-fuelled microgas turbine CC with varied ignition fuel ratios. The equivalency ratio fluctuated from 0.024 to 0.994 when the air mass flow changed, but the fuel mass flow stayed constant. At the combustion chamber exit, flue gas compositions were tracked and utilized to calculate combustion efficiency. Optical measurements and digital image processing technologies were used to determine relative flame stability. The findings show that the combustor can ignite effectively at 10, 15, and 20% ignition fuel ratios, but that the combustion efficiency decreases as the ER decreases. As the equivalency ratio dropped, the amount of CO and unburned CH_4 in the combustion products rose. Day [8] has shown that the presence of hydrogen alters the chemistry of methane, which we study further. We found that when enough when hydrogen is introduced to the mixture, the local methane burning speed and local flame curvature have a significant positive connection. Furthermore, at higher $\text{H}_2\%$, the mixes have cellular burning processes, which are common in thermally diffusively combustible fuel combinations. Different methane oxidation routes are discovered, and they are shown to be substantially enhanced when H_2 combustion occurs. Hawkes [9] has shown that with the influence of H_2 blending on LP methane-air flames is explored using a simplified chemical mechanism and a (DNS) technique. Two flames were tested for stability and pollutant formation: one is a pure methane flame near the lean limit, and the other is a hydrogen-supplemented methane flame near the lean limit. The turbulent flame speed determines the flame's stability. The hydrogen-enriched flame has a faster rate, which is consistent with the experimentally observed extended blow-off stability limits. Greater laminar flame speed (LFS), improved area production, and increased burning rate per unit of fuel have all contributed to the increased flame speed.

The literature shows the operation of the engines near leaner condition gives maximum combustion efficiency. The present work is dedicated towards the numerical analysis of the lean blow-off limits for swirl stabilized methane flames. Additionally the effect of H_2 and CO dilution on the blow-off limit is studied.

2 Numerical Set Up

2.1 Geometry Modelling

The air channel, axial swirler, and unconfined test section make up the burner's geometry. Figure 1 depicts the model geometry of the unconfined burner under consideration in this study.

The axial swirler is made up of radially inclined blades that provide the axially entering air a swirling motion. The geometry consists of a 50 mm long, 53 mm OD, and 12.5 mm ID inlet air and fuel pipe. With 10 vanes at a 45° vane angle, the axial swirler has a 53 mm outer diameter and a 12.5 mm hub diameter. The test segment has been following the axial swirler.

To solve governing differential equations numerically, the CFD code fluent employs the control volume method. Fluent solves turbulence equations and transport equations for conserved scalars (mean mixture fractions and variation) during the simulation in addition to continuity and momentum equations. Although the isotropic eddy viscosity hypothesis was adopted, a realizable k- ϵ type model was used for steady-state simulations. This RSM model was used for the further calculation of this numerical technique for validation reasons. For swirling flow, the RSM model has proven to be the most effective. Fluent has a number of pressure-based algorithms. For velocity and pressure coupling, a SIMPLE method was used in this work. With two-equation turbulence models, the first-order upwind technique was applied. The interaction between turbulence chemistry and non-premixed combustion was studied using the probability density function (PDF).

Fig. 1 Geometry of burner
(all dimensions are in mm)

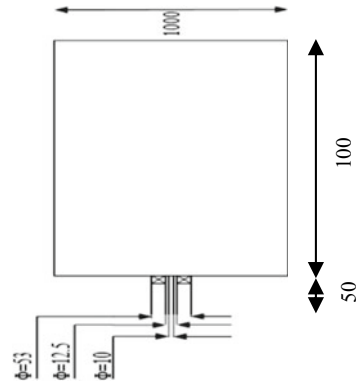


Table 1 Boundary conditions and parameter at different zones

Zone name	Zone type	Boundary condition
Air flow inlet	MFR inlet	0.025 kg/s
Fuel inlet	MFR inlet	0.0005 kg/s
Air exit from air passage	Interface	–
Air swirler inlet	Interface	–
Air swirler outlet	Interface	–
Air inlet to test section	Interface	–
Test section side walls	Wall	–
Test section outlet	Pressure outlet	Zero Pascal (Gauge)

2.2 Boundary Condition

For CFD analysis, precise boundary conditions must be implemented. The kind and nature of the solution are determined by boundary conditions. The governing equations are solved using a pressure-based solver. The mass flow inlet had been established as the inlet for air and fuel. At the test section's exit, the atmospheric pressure condition was used. Because the test portion is taken far away from the intake, its side faces are characterized as walls. Sidewalls are given no-slip boundary requirements. The interface is defined as the point where two adjacent domains meet to allow fluid to flow. About 0.025 kg/s was used as the MFR air and 0.0005 kg/s is the MFR of the fuel. The mean mixture fraction for the fuel input had gone from 1 to 0 (Table 1).

2.3 Numerical Simulation

To further understand the flame physics, a reactive analysis of the combustor shape is carried out in the burner case. Methane was employed as a fuel for reactive analysis. The stoichiometric air–fuel ratio of the methane-air combination is 17.426. The analysis was carried out for various air–fuel ratios. The air mass flow rate has been set to 0.025 kg/s as a constant. Two-equation realizable k- ϵ turbulence and a non-premixed combustion model were employed for numerical simulation. This problem's numerical simulation continues until it reaches the lean blow-off limit. Following that, the mass flow rate has been steadily decreasing till it reaches the lean blow-off limit. To obtain the blow-off state, the mass flow of fuel is reduced from 0.0005 to 0.0000078125 kg/s. For this numerical analysis, the RSM model was utilized since it is more reliable and accurate for whirling flow in particular.

Table 2 Fuel mass flow rate at different AFR

50	0.0005 kg/s
100	0.00025 kg/s
200	0.000125 kg/s
400	0.0000625 kg/s
800	0.00003125 kg/s
1600	0.000015625 kg/s
3200	0.0000078125 kg/s

After that, the numerical simulation was expanded for carbon dioxide and hydrogen dilution on methane for a 5% lean blow-off limit (Table 2).

2.4 Grid Independence Test

The most significant part of CFD simulation is the grid independence study. Grid independence is being implemented. The simulation results are unaffected by the grid size refinement. The study on grid independence starts with a small number of components, and the grid size after that (number of elements) is about 1.25 times the grid size before (number elements). Grid independence investigation was carried out on three distinct grid sizes: 12,045,505, 15,056,881, and 18,821,102. Figure 2 depicts the temperature variation with the centreline taken at an axial distance Three distinct grid sizes was utilized. The temperature difference between grid size one and grid size two is 3%. The variation in temperature between grid size two and grid size three is only 1%. Grid size two was used for the analysis, which is 150566881, resulting in a temperature difference of less than 1%. Grid size two had been selected.

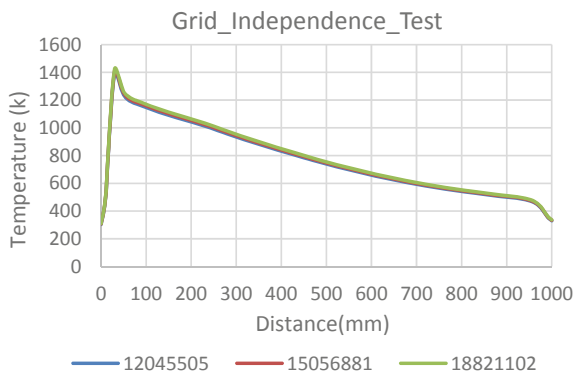


Fig. 2 Centre line variation of temperature at three different grid

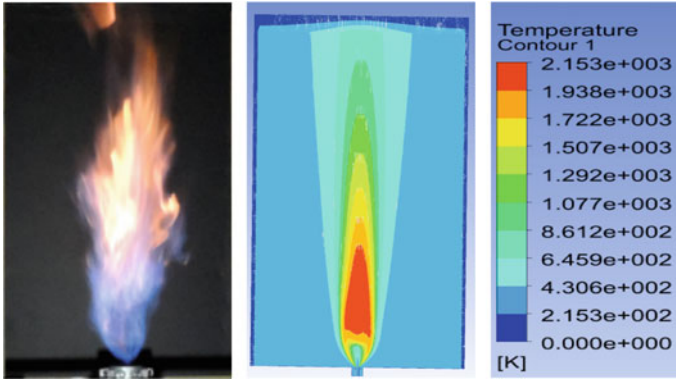


Fig. 3 Comparison of experiment and numerical simulation with variation of mass flow rate of fuel at $S_N = 0.70$ for $m_f = 0.00125$ kg/s

2.5 Validation

The experimentally determined flame form resembles a numerical simulation temperature contour. The maximum temperature in the above temperature contours is 2153 K, while the adiabatic flame temperature of methane is 2236 K. As a result, both analytical theory and experimental investigation validate the numerical work (Fig. 3).

2.6 Result and Discussion

A. Temperature Profile

Figure 4 depicts the temperature contours at fixed of air and reducing the MFR of the air till LBO limit. It is observed that across reducing MFR of the fuel maximum Temperature reduces and also the length of the flame is seen to be reduced. It is because of the lower equivalence ratios at lower mass flow rates. Another interesting facet which can be observed across lower mass flow rate is the transformation of a V-flame into an M-flame which are commonly observed flames in swirl stabilized combustion. This is mainly due to the competing shear layer between fuel and air streams.

The flame retreats towards the inner shear zone (IRZ) and interacts more with the inner shear layer, which has greater turbulence and vorticity. As a result, the flame fronts' hydrodynamic stretch rate rises, causing local extinction and breaks along the flame root. When the unburned fuel–air mixture passes through the shear layer, these breaks entrain it into the IRZ. When the unburned fuel air combination travels through the shear layer with the local vortex effect, it entrains into the IRZ, triggering reaction inside the IRZ. The span of the IRZ narrows in methane flames leading flames to

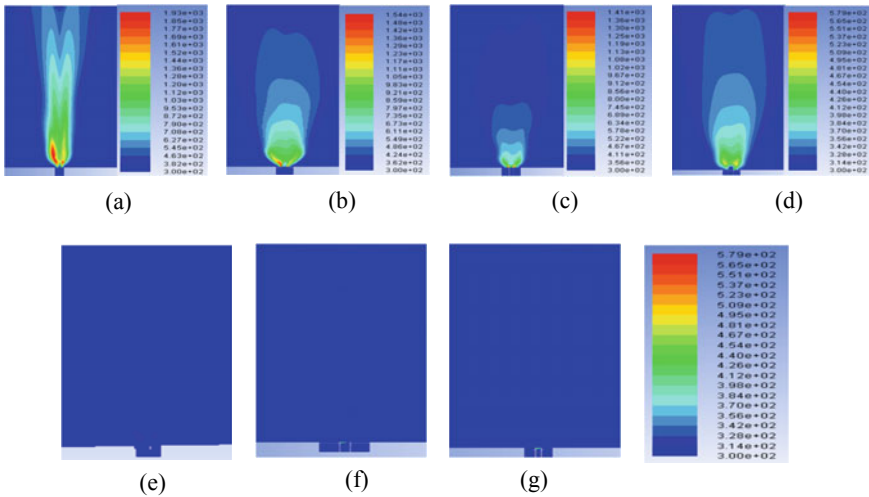


Fig. 4 Temperature contour $m_a = 0.025$ kg/s **a** $m_f = 0.0005$ kg/s; **b** $m_f = 0.00025$ kg/s; **c** $m_f = 0.000125$ kg/s; **d** $m_f = 0.0000625$ kg/s; **e** $m_f = 0.00003125$ kg/s; **f** $m_f = 0.000015625$ kg/s; **g** $m_f = 0.0000078125$ kg/s

straddle the IRZ’s barrier and become unstable The flame is physically blown-off in the combustor when the rates of heat release and chemical radicals created by the combustion reaction are insufficient to sustain the favourable reaction state for a given flow velocity in lean premixed combustion. This is referred to as a lean blow-off (LBO). Because I set 320 k for the LBO contours (e) and (f), the centre line temperature was greater than the LBO limit temperature higher than lean blow-off limit temperature so I had to choose another mass flow rate, which was the lean blow-off limit.

B. Comparison of Temperature with Different Mass Flow Rate at Centre Line for Lean blow-off Limit

Fluctuation at centreline temperature at the flow parameters shown in Fig. 4 is depicted in Fig. 5, where the MFR air is maintained while the MFR of fuel is reduced until a LBO state is reached. This figure highlights three significant points: (a) the maximum temperature drops when the FFR is reduced from 0.0005 kg/s to the LBO limit, and (b) length of flame diminishes. (c) The temperature peak is relocated away from the fuel outflow. The first two observations are related to the lower heating values associated with the reduced equivalent ration. With the reduction in the (FFR) fuel flow rate, the shift the peak is connected with changes in the flow fields and recirculation position. With a reinforced inner recirculation zone, the compact flames had generally been achieved (IRZ). In comparison to the flame holder, such flames are short. The IRZ flame is more amenable to flame stabilization. The cooling of the IRZ flame was commonly attributed to the blow-off of the compact and brief flames. The cooling is caused by large amounts of cold backflow in the downstream region.

As a result, the cold, unburned mixture leaks into the IRZ. Flame blow-off was also detected surrounding the flame root, which was thought to be the cause of flame detachment and blow-off.

C. Effect of Carbon Dioxide dilution on Blow-off Limit of Methane Combustion

The temperature contour for varied mass flow rates with a 5% carbon dioxide dilution is shown in the figure. With 5% carbon dioxide dilution, we want to discover a lean blow-off limit for this combustion system. As a result, we fixed the air mass flow rate and the carbon dioxide dilution percentage. The temperature contour depicts the decrease in maximum temperature as the MFR of fuel decreases with fixed dilution and MFR of air. The nitrogen oxide synthesis process is weakened by the fall in temperature caused by CO₂ dilution, which is frequently utilized for more uniformly distributed heat release.

Increases in CO₂ dilution lower flame temperatures by lowering radical species concentrations in the flame, but increases in the heat capacity of the unburned mixture have a similar effect on flame temperatures. CO₂ is an excellent diluent for lowering flame temperature and Knox concentration while also limiting the production of soot. At 0.00001171875 kg/s, there is a lean blow-off for a 5% carbon dioxide dilution (Fig. 6).

D. Effect of Hydrogen in dilution on Blow-off Limit of Methane Combustion

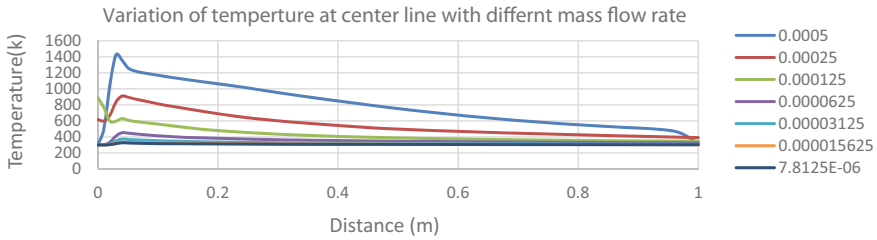


Fig. 5 Variation of temperature at centre line with different mass flow rate

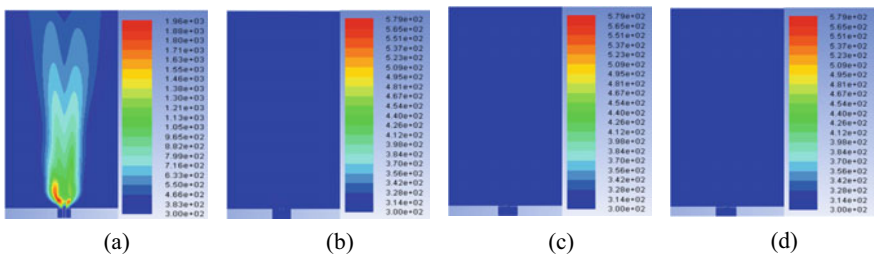


Fig. 6 Temperature contour for 5% CO₂ $m_a = 0.025$ kg/s **a** $m_f = 0.0005$ kg/s; **b** $m_f = 0.00003125$ kg/s; **c** $m_f = 0.000015625$ kg/s; **d** $m_f = 0.00001171875$ kg/s

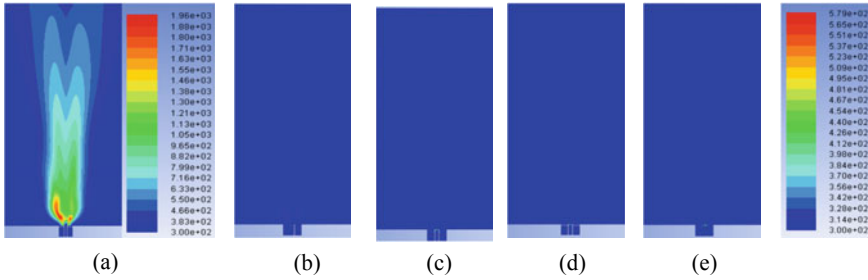


Fig. 7 Temperature contour for 5% H_2 $m_a = 0.025$ kg/s **a** $m_f = 0.0005$ kg/s; **b** $m_f = 0.00003125$ kg/s; **c** $m_f = 0.000015625$ kg/s; **d** $m_f = 0.00001171875$ kg/s; **e** $m_f = 0.000009765625$ kg/s

Figure 7 depicts the contour for various mass flow rates at a fixed 5 per cent hydrogen dilution and air mass flow rate. With 5% hydrogen dilution, we want to discover a lean blow-off limit for this combustion system. As a result, we fixed the air MFR and the hydrogen dilution percentage. Temperature contour demonstrated that as the MFR of fuel was decreased. With fixed dilution, the temperature continued to drop.

Hydrogen has particularly special transport qualities, such as the highest diffusivity and reactivity of any substance. As the IRZ approaches the LBO limit, its breadth widens, allowing the flame region to be contained within it, allowing reactions to continue in this low-temperature region. Furthermore, as the LBO limit approaches, the surplus reactant in the shear layer, which has a high mass diffusivity hydrogen, diffuses quicker into the IRZ, which has a favourable combustion environment. Longer residence times allow reactions to take place inside the IRZ, This flame also acts as a pilot flame, re-igniting reactants in the shear layer. As a result, the lean blow-off limit for hydrogen is somewhat greater than that of carbon dioxide. As we can see in Fig. 7b–e are very similar in terms of colour contour. For a 5% hydrogen dilution, the lean blow-off occurs at 0.00001171875 kg/s.

3 Conclusions

The flame characteristics, flame stability, blow-off limitations, and emission are all affected by the dilution of the reactive gases and inert gases.

The length of the flame diminishes when the fuel flow rate is reduced to 0.0005 kg/s to the lean blow off limit centre line maximum temperature. The temperature peak is relocated downstream from the fuel outflow. The first two findings are connected to the lower heating values that come with a lower equivalent ration. The shift in the peak is linked to changes in the flow fields and recirculation location when the fuel flow rate is reduced. With a reinforced inner recirculation zone, the compact flames

had generally been reached (IRZ). In comparison to the flame holder, such flames are short.

Acknowledgements We thank Mr. Piyush Savaj for his help during this work. This work was supported by the S. V. National Institute of Technology Surat [Grant Code No. 2020-21/Seed Money/13].

References

1. Lieuwen T, Mcdonell V, Santavicca EPD Fuel flexibility influences on premixed combustor blowout, flashback, auto ignition, and stability
2. Sanusi YS, Habib MA, Mokheimer EMA (2015) Experimental study on the effect of hydrogen enrichment of methane on the stability and emission of nonpremixed stabilized combustor
3. Chong CT, Ng JH, Aris MS, Mong GR, Shahril N, Ting ST, Zulkifli MF (2019) Impact of gas composition variations on flame blowout and spectroscopic characteristics of lean premixed swirl flames. *Process Saf Environ Prot* 128:1–13
4. Akhtar S, Piffaretti S, Shamim T (2018) Numerical investigation of flame structure and blowout limit for lean premixed turbulent methane-air flames under high pressure conditions. *Appl Energy* 228(June):21–32
5. Jackson GS, Sai R, Plaia JM, Boggs CM, Kiger KT (2003) Influence of H₂ on the response of lean premixed CH₄ flames to high strained flows. *Combust Flame* 132(3):503–511
6. Strakey P, Sidwell T, Ontko J (2007) Investigation of the effects of hydrogen addition on lean extinction in a swirl stabilized combustor. *Proc Combustion Inst* 31(2):3173–3180
7. Shen W, Liu L, Hu Q, Liu G, Wang J, Zhang N, Wu S, Qiu P, Song S (2021) Combustion characteristics of ignition processes for lean premixed swirling combustor under visual conditions. *Energy* 218:119521
8. Day MS, Gao X, Bell JB (2011) Properties of lean turbulent methane-air flames with significant hydrogen addition. *Proc Combust Inst* 33(1):1601–1608
9. Hawkes ER, Chen JH (2004) Direct numerical simulation of hydrogen-enriched lean premixed methane-air flames. *Combust Flame* 138(3):242–258

Experimental Investigation on the Performance of Solar Stills with Vent Holes and Hybrid Nano PCM



M. Padmanaban, S. Suresh, and P. Kalidoss

Abstract In this experimental study, a conventional solar still is designed and developed by two-layer transparent glass with provided vent hole and integrated with PCM (paraffin) added to high thermal conductivity nano hybrid materials like titanium dioxide and graphene nanoplatelets at the ratio 1:1 in the bottom basin of the solar still. This Hybrid Nano PCM materials used in this experimental is more effective sensible storage materials. This experimental output express that the regular production of modified solar still with Hybrid Nano PCM is more than that of ordinary solar still. Using Hybrid Nano PCM in a single basin the daily production was recorded up to 342 ml/day, while ordinary single basin still value was recorded 202 ml/day. The modified single basin still with Hybrid Nano PCM as an energy storage material is greater in daily production than a conventional single basin. These experimental results disclose that the modified solar still increases 69.3% distilled water productivity compared with the conventional solar system causes by the presence of double-layer transparent glass solar still with vent holes and Hybrid Nano PCM materials.

Keywords Solar desalination · Hybrid nano PCM · Vent holes · Thermal conductivity

1 Introduction

The main global problem today is the insufficiency of potable water. The drinking-water shortage is increasing due to the increasing growth rate of population, as the maximum available water is unfit for drinking like saline water, which is the main water sources in the world. There are many processes used for water purification like decontamination, filtration, refining, and distillation. Here, the solar distillation is one of the famous and most important method of water purification.

M. Padmanaban (✉) · S. Suresh · P. Kalidoss

Department of Mechanical Engineering, National Institute of Technology, Tiruchirappalli 620015, India

e-mail: padhu.best@gmail.com

For solar desalination solar still needs the advantages of simple structure and implementation with low maintenance that do not require high skill to work. Also, it gives low performance and low production.

Several research works are being carried out to enhance the solar basin behaviour by design modifications of the conventional solar still. In addition to that, several researchers has also shown that using phase change materials (PCMs) as the latent heat storage medium has the potential to improve the temperature difference between the basin water and cover.

The productivity improvement due to the impact of PCM on the a solar still coupled with a solar collector was studied by Al-harabsheh et al. [1] in which they have identified that 40% of the products i.e. a distillate production about 4300 ml/day m^2 were formed during the sunset. An experimental investigation on the effects of PCM on the thermal performance of a single basin solar still was done by Shalabyet al. [2]. In this study, they have identified that using a v-corrugated absorber with PCM can improve the productivity by 12 A theoretical study by Dashtban and Tabrizi [3] on the effect of PCM on distillate production has shown that the daily production of distillate was 6700 ml/ m^2 with PCM and 5100 ml/ m^2 without PCM. A study on the thermal behavior of the solar still that contained PCM under the basin by Ansariet al. [4] has shown that there occurred 40% improvement in productivity when PCM is used. Venkitraj et al. [5] studied Neopentyl glycol with CuO of 0.1 wt. was used for the application of building cooling. The thermal cycling was carried out for the samples up to 100 cycles, and its thermal and chemical properties were reported. The time taken for charging and discharging was reduced after the addition of CuO. The thermo physical properties of nano-pcm (D-manitol-CuO) was investigated by Salyan et al. [6] by varying the mass fraction by 0.1, 0.2, and 0.5 wt.%. In this study, the DSC result showed that there was no abnormal changes in the melting point although the thermal conductivity was increased by 25% for maximum mass fraction. Thermal and chemical stability of Pentaerythritol (PE) with LMA (Zn, Sn, Bi, and In) was studied by Venkitaraj et al. [7]. In this study, 0.1 and 0.5 wt.% of PE—LMA are prepared and thermal cycling was done up to 100 cycles, heating rate of 10°/min, respectively. Here, 3.77 and 17.27% thermal conductivity were increased and decreased by 3.21, 4.55, and 10.08% after 100 cycles for PE and increasing LMA concentrations.

Long et al. [8] studied the DSC of paraffin mixture up to 10,000 cycles. Every 800 cycles, the melting temperature of the paraffin mixture was analyzed, The result shows that there are negligible changes in the melting point even after ten thousand cycles, but there is a reduction in the heat of fusion which is about 9.1%, respectively. The enhancement in the thermal conductivity of the PCM by the addition of nanoparticles was studied by Li et al. [9]. He proposed that increasing the concentration of nanographite (NG) to paraffin will enhance the thermal conductivity of the paraffin composites. The mass fraction of 1 and 10 wt.% shows the increment of thermal conductivity was 2.89 and 7.49 times compared to paraffin.

Enhancement in the thermal conductivity of the PW by adding CuO nanoparticles in concentrations of 0.25–1% in the PCM was studied by Mandal et al. [10]. The

result shows due the addition of nanoparticles, there are changes in melting and solidification temperature of the CuO-PW nanocomposites.

Numerous works have been carried out with an objective to improve the solar still performance. One approach is by experimentally improving the performance of the conventional solar still by implementing modifications. One such modification is by improving the design and development using two-layer transparent glass provided with vent holes. Another type of modification is by using energy storage materials in order to enhance the temperature difference between the basin water and the cover.

In the current experimental work, Hybrid Nano PCM with high thermal conductivity and latent heat was kept under the basin to improve the performance of the single basin solar still. Investigation was done on the nano hybrid PCM, which is found to have high thermal conductivity and sensible heat storage properties. Therefore, it was used as the energy source to the basin when the solar intensity was low, particularly after sunset.

2 Materials and Methods

2.1 Construction of Solar Still

Two geometrically similar prototypes were used, the outer box made up of wood and water basin made up of thin copper plate length 110 cm, width 50 cm, and height 9 cm which is placed inside the wood part 120 cm length, 60 cm width. The outside of the wooden part insulated with the help of glass wool so that heat loss from inside to outside be reduced. Inside wooden parts are painted silver color paint for reflectivity, and water basin was coated with black paint so that high absorption of solar radiation had been possible, shown in Table 1. Two transparent glass covers were installed above the wooden part which was tilted at 10^0 angles of latitude.

In our study, we were used two glass covers for transferring more solar radiation into the system if we go with single glass cover, there is temperature loss from the outer glass cover due to outer wind velocity so such kind of problems were encountered by incorporating two glass cover. Also, we had provided a vent hole at the outer glass cover so that the cold air is passed through this hole and remove some heat from the surface due to this reduction in the temperature of the top surface of the bottom glass. This reduction in temperature is driving force for condensation so

Table 1 Dimension of solar still

Dimension	Wood material (cm)	Water basin (cm)
Length	120	110
Width	60	50
Height (back end)	60	9
Height (front end)	20	9

that we will get maximum yield. By comparing with the conventional solar still, this modified solar still gave better yield.

K type thermocouples were placed at four different places: bottom glass cover, water basin, and PCM basin. Water depth of 5 cm is kept in both solar stills.

The titanium dioxide and graphene nanoplatelets added to phase change material (PCM) paraffin used in modified solar still for further increase in liquid yield. About 1.5 kg of PCM used for our experiment which is placed bottom of the water basin. During day time, PCM takes excess energy from the system and release it whenever it's needed.

2.2 Materials Properties

In this study, raw paraffin wax is used as a base material that is available at very low cost, and paraffin wax thermal properties is given in Table 2. Our aim of this study has to prepare the nano hybrid paraffin wax sample which was obtained by nano dipping of high conductive particle into paraffin material and find out the effect of nanoparticle in PCM.

Two samples were prepared one was pure paraffin wax, and the second sample was 1 wt.% of nanoparticle with paraffin wax in this study we have taken TiO₂ and graphene as our nanoparticles. The samples were prepared by melting-mixing procedure, and the first sample was 0% nanoparticle which was pure paraffin wax that was melting at a constant temperature around 30 min and cooled that solution (Tables 3 and 4).

The second sample was prepared by adding nanoparticle (TiO₂ and Graphene) with 1% weight which was measured by the weighing machine. First, the paraffin wax was melting at the above melting point and then added nanoparticle (TiO₂ and Graphene) into melted paraffin wax solution with 1 wt.% and mixed well with a mechanical stirrer for 20 min and leave it for 1 hour. for uniform dispersion of nanoparticle into paraffin wax structure. Then the materials were poured into the square shape component and then it was solidified with atmospheric temperature for 45 min after solidification now the material is ready for testing or thermal measurements (Fig. 1).

Table 2 Paraffin wax

Material properties of paraffin wax (PCM)	
Melting temperature (°C)	44
Latent heat of fusion (kJ/kg)	190
Thermal conductivity (W/m °C)	0.21
Solid density (kg/m ³)	930
Liquid density (kg/m ³)	830

Table 3 Titanium dioxide

Material properties of TiO ₂ hybrid nano PCM	
Melting temperature (°C)	1843
Latent heat of fusion (kJ/kg)	820
Thermal conductivity (W/m k)	11.8
Maximum density (Mg/m ³)	4.05
Minimum density (Mg/m ³)	3.97
Maximum specific heat (J/kg K)	697
Minimum specific heat (J/kg K)	683

Table 4 Graphene nano platelets

Material properties of graphene nano platelets hybrid nano PCM	
Specific density (g/cm ³)	2.26
Latent heat of fusion	1 TPa
Thermal conductivity (W/m K)	0.97
Thermal expansion	$-1 \times 10^{-6} \text{ k}^{-1}$
Thermal stability	450–650 °C

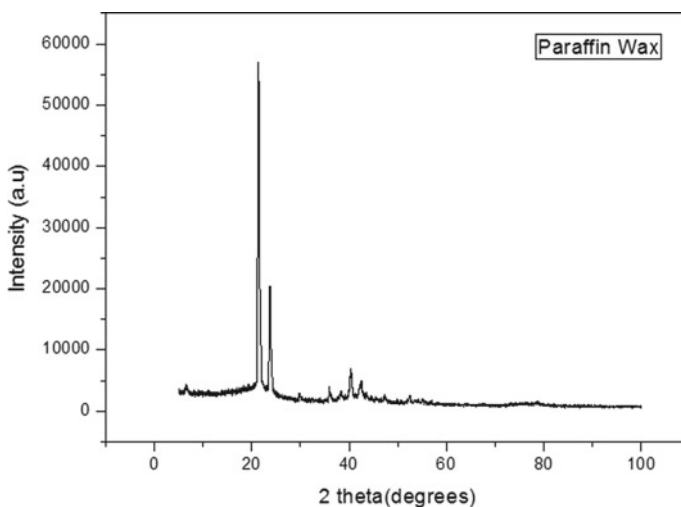


Fig. 1 Crystalline structure of paraffin wax

2.3 XRD Analysis

The XRD pattern of the prepared Nano TiO₂ and graphene paraffin wax was shown in Fig. 2. XRD is used to find out the crystalline structure of nanoparticle on paraffin

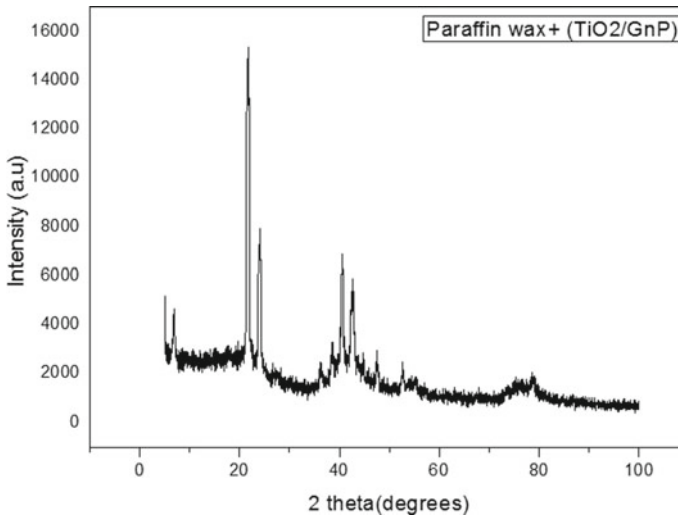


Fig. 2 Crystalline structure of paraffin wax + (TiO₂/GnP)

structure, and the results carried out at the temperature range of 5–100 °C. The diffraction peaks were found at 2 θ value of 25 and 45 °C. The prepared nanocomposite PCM peaks were matched with standard TiO₂ and graphene peaks, and they have good agreement with the standard nanoparticle peaks at 25 °C. This will indicate that there was no impurity present in the paraffin structure and the dispersion of nanomaterial TiO₂, and graphene is well mixed with base paraffin structure. The standard XRD pattern of TiO₂-graphene was found from the literature which has the maximum peak of titanium oxide were found at Fig. 4 plane and the corresponding 2 θ value around 25 °C which is good agreement with our result of nanocomposite paraffin wax. This was indicating that the titanium oxide particles were equal distribution on paraffin wax. Similarly, the maximum peak of graphene crystal occurred at (002), and (100) plane and corresponding 2 θ values were found at 11, and 45 °C which is good agreement with our XRD result of nanocomposite paraffin wax. This was indicated that the graphene particles were equal distribution on the paraffin wax structure (Figs. 2 and 3).

3 Experimental Setup

3.1 First Experimental Set Up

The conventional solar desalination system is shown in Fig. 5. Solar still consists saline water tank as a water source, outer box, saline water basin with insulator, transparent glass, and distilled water collector. As the water tank was placed at a

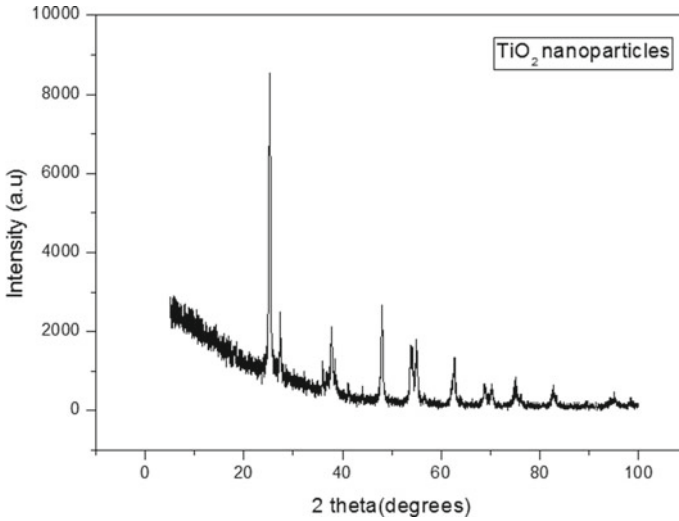


Fig. 3 Crystalline structure of TiO₂ nanoparticles

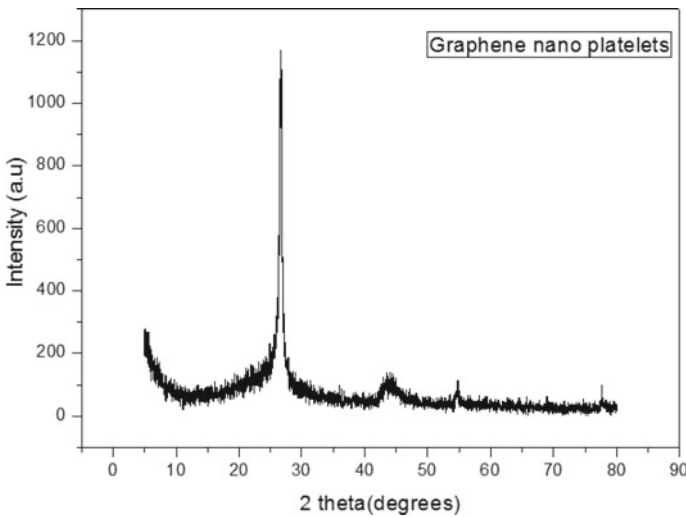


Fig. 4 Crystalline structure of Graphene nano platelets

higher elevation than the basin that contains the saline water, the elevation difference causes the flow of the saline water through its outer hole via a hand valve that facilitates different flow rates. A water depth of 5 cm is kept in solar still. The solar desalination system works on the principle of causing complete evaporation of the water and collecting the distilled water using a collector.

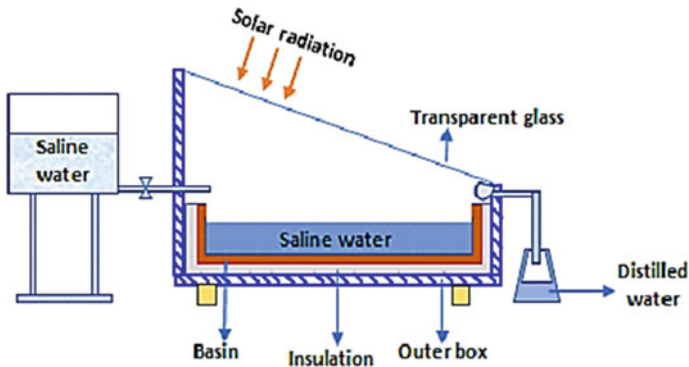


Fig. 5 Schematic diagram of conventional solar still

3.2 Second Experimental Set Up

For the second setup, similar geometry has been taken with some small modification shown in Fig. 6. In experimental set up we provide two transparent glass covers were installed above the wooden part which was tilted at 10° angles of latitude. We had provided a vent hole at the outer glass cover so that the cold air is passed through this hole and remove some heat from the surface due to this reduction in the temperature of the top surface of the bottom glass. This reduction in temperature is driving force for condensation so that we will get maximum yield.

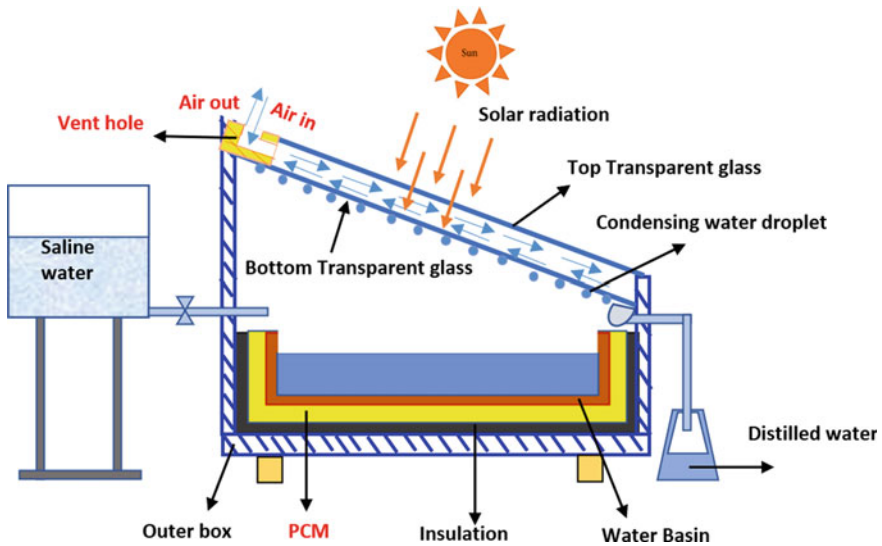


Fig. 6 Modified solar still with vent hole and PCM (hybrid nano materials)

Further enhance the performance of modified solar still by adding Nano hybrid PCM on the bottom of the basin shown in Fig. 6. For our experiment we choose the titanium dioxide and Graphene Nano platelets as Phase change material, the titanium dioxide and Graphene Nano platelets have a high latent heat of fusion and low cost, PCM placed between saline water basin and below the PCM tray insulation is done using low thermal conductivity material. For increase the yield of the solar still by adding PCM to the bottom of the water basin that gave there result of yield even after 5 pm.

In this modified still, we provided screws on top of the wooden frame for periodical cleaning and remove salt formation at the bottom of the water basin.

4 Experimental Procedure

The experiments were conducted from 9 am to 7 pm through the period of September 2020 to November 2020 at National Institute of Technology, Trichy, India for both conventional and modified solar stills. In our study, data logger was used for temperature measurements, so thermocouple wire was connected to the data logger.

To compare the conventional and modified solar still, we measured the temperature of two glass surfaces, ambient temperature, water basin temperature, and distillate water productivity. The readings were taken for every 1 hour once for both solar stills, and also solar insolation and liquid yield were measured (Figs. 7 and 8).

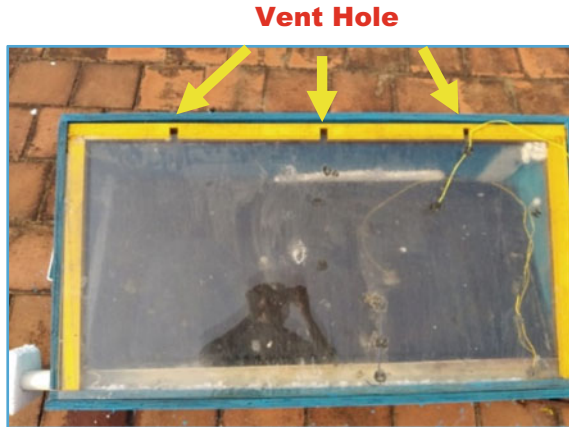
The basin temperature was measured by placing the K type thermocouples inside the still. Temperatures of bottom surface of the glass and top surface of glass were measured by placing the K type thermocouples.

Modified still glass cover is placed toward on the direction of south–east. Measuring cylinder has a resolution of 1 ml is used to measure the distillate output. During each experiment, PET bottle is used to collect the distillate.

Fig. 7 Conventional solar still



Fig. 8 Modified solar still with vent hole and PCM



5 Result and Discussion

In second experimental setup we provide vent hole with double glass and Nano hybrid PCM. The various temperatures and distilled output were measured by this experimental method. A comparison study was also carried out for both conventional and modified solar still, and results were tabulated (Tables 5 and 6).

From Table 5, we found a maximum vapor temperature of 49.6 °C and the basin temperature is around 46.8 °C at 2 pm from conventional solar still shown in Graph 1. The maximum temperature difference between Inner glass bottom and top surface temperature is 1.9 °C at 2 pm from conventional solar still shown in Graph 2.

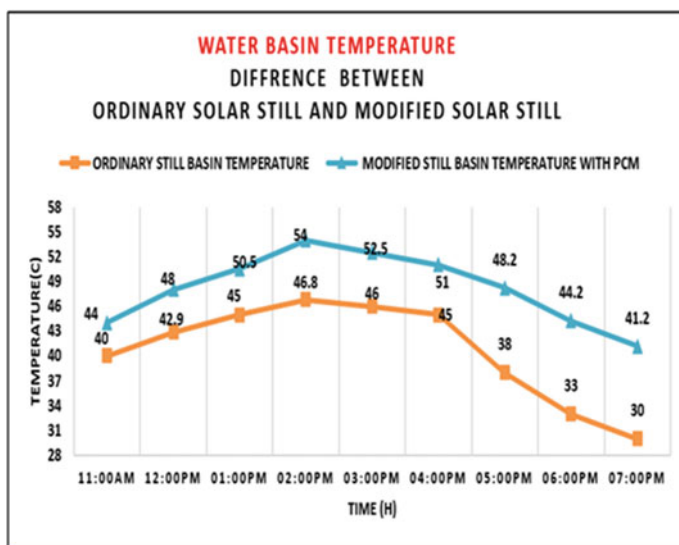
Table 5 Temperature of ordinary solar still

Time	Water basin temp (T1)	Inner glass 1 temp (T2)	Outer glass 1 temp (T3)	Temp difference (T2 – T3)
11:00 AM	40	43.3	42.4	0.9
12:00 AM	42.9	45.5	44	1.4
01:00 PM	45	47.2	45.6	1.6
02:00 PM	46.8	49.6	47.7	1.9
03:00 PM	46	48.1	46.5	1.6
04:00 PM	45	44	43.2	0.8
05:00 PM	38	38	37.4	0.6
06:00 PM	33	33	32.7	0.3
07:00 PM	30	30	29.8	0.2

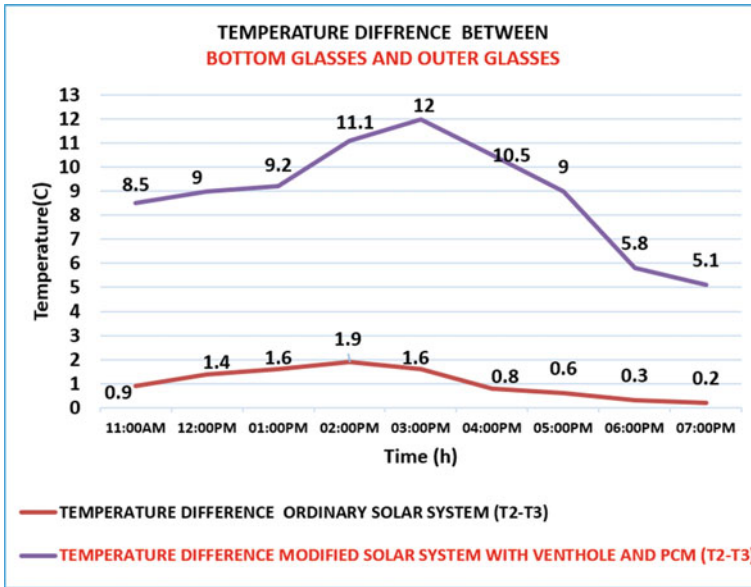
Table 6 Temperature of modified solar still with vent hole and PCM

Time	Water basin temp (T1)	Inner glass 1 temp (T2)	Outer glass 1 temp (T3)	Temp difference (T2 – T3)
11:00 AM	44	50.5	42.4	8.5
12:00 AM	48	52.5	43.5	9
01:00 PM	50.5	54	44.8	9.2
02:00 PM	54	56.8	45.7	11.1
03:00 PM	52.5	55.5	43.5	12
04:00 PM	51	52	41.5	10.5
05:00 PM	48.2	49	40	9
06:00 PM	44.2	41	35.2	5.8
07:00 PM	41.2	34.3	29.2	5.1

Graph 1



Graph 2



From table 6 modified still water basin temperature found maximum 54 °C at 2pm. The maximum temperature difference between inner glass bottom and top glass surface temperature is 12 °C at 3 pm from ordinary solar still shown in Graph 2.

The onset, transition, and melting temperatures of the NANOPCM are obtained by the DSC test using PerkinElmer DSC 6000. The test is carried out in the temperature range of 30–70 °C with a heating rate of 5 °C in the nitrogen atmosphere. The maximum peak temperature and enthalpy of 55.01 °C and 102.85 J/g. The pure paraffin wax enthalpy is 124.62 J/g, which shows its suitability for solar desalination applications.

Based on XRD results and DSC result analysis, in modified still, we using hybrid Nano PCM at bottom of basin, so basin temperature increases by 15.38% compared to ordinary still (Graph 1). If basin temperature is increased, vapor efficiency also increases. So, it gives increased productivity when compared to ordinary still up to 7 pm. From the experimental result Tables 5 and 6, we found the maximum temperature difference between the glasses is 1.9 °C only in ordinary still. But in the case of modified solar still, we found maximum temperature difference is 12 °C (Graph 2). This indicates that the modified one has higher effectiveness than ordinary one.

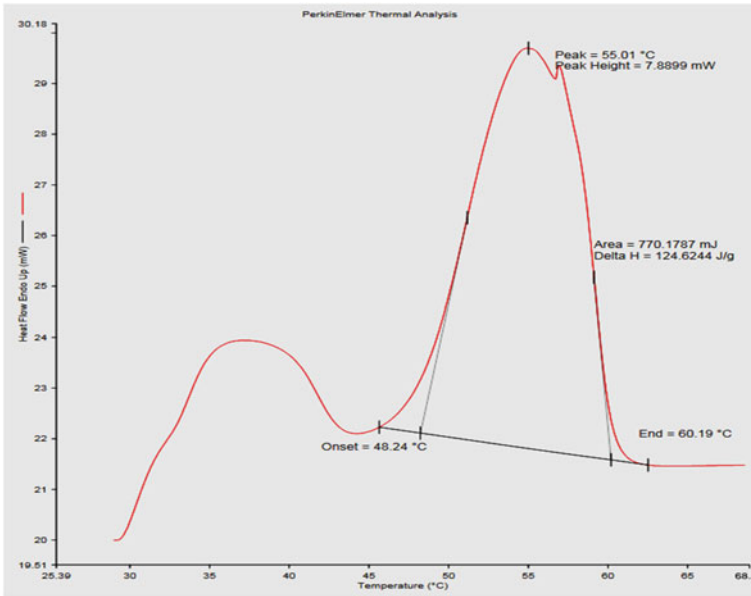


Fig. 9 Express the DSC result of hybrid nano PCM,

From Table 7, Modified still with vent hole and PCM gave liquid yield as 342 ml/day up to 7 pm and conventional solar still gave 202 ml/day.

We can observe that maximum yield is obtained in between 12 and 3 pm in modified solar still. As a result, modified still has better storage of heat energy and the basin temperature increased by 15.38% compared to ordinary still, it leads to increase in the vapor formation efficiency and increase the productivity.

Table 7 Liquid yield

Time	Ordinary solar still	Modified still—vent hole with hybrid nano PCM
11:00 AM	30	37
12:00 AM	33	46
01:00 PM	37	48
02:00 PM	40	45
03:00 PM	35	45
04:00 PM	27	36
05:00 PM	–	35
06:00 PM	–	30
07:00 PM	–	20
Total	202 ml/day	342 ml/day

6 Conclusion

The demand for freshwater is increasing year by year, so we need an alternative solution for producing freshwater from a considerable quantity of available saline water on earth.

Many desalination methods are available, but the solar-based desalination method exhibits enormous economic advantages over other methods. Minimum material and less operating costs, and free energy availability through the sun are the things that showed that solar desalination is one of the best methods for producing freshwater.

The following were the conclusions made by comparing the two types of solar still, on the aspects of temperature of the glasses and the desalination output.

In modified solar still, due to air circulation through the vent hole, the temperature difference between inside glass cover and top glass has higher than existing conventional solar still. The difference between the temperature is the driving force for producing condensate water. In case of modified solar still, we found maximum temperature difference is 12 °C but in conventional still temperature difference is 1.9 °C only. This indicates that the modified still has higher effectiveness than ordinary still.

The titanium dioxide and graphene nanoplatelets added to phase change material (PCM) paraffin used in modified solar still for increase the temperature of the water basin. Thus, result is basin temperature increases by 15.38% compared to ordinary still.

From the experimental result, modified one gave liquid yield as 342 ml/day and conventional solar still gave yield as 202 ml/day. These results show better performance of modified solar still up to 7 pm after sunset in this study. The daily productivity of modified solar still obtained is 69.3% more than ordinary still.

References

1. Al-harash M et al (2018) Solar desalination using solar still enhanced by external solar collector and CM. *Appl Thermal Eng* 128:1030–1040
2. Shalaby SM, El-Bialy E, El-Sebaai AA (2016) An experimental investigation of a v-corrugated absorber single-basin solar still using PCM. *Desalination* 398:247–255
3. Dashtban M, Tabrizi FF (2011) Thermal analysis of a weir-type cascade solar still integrated with PCM storage. *Desalination* 279(1–3):415–422
4. Ansari O et al (2013) Desalination of the brackish water using a passive solar still with a heat energy storage system. *Desalination* 324:10–20
5. Praveen B, Suresh S (2018) Experimental study on heat transfer performance of neopentyl glycol/CuO composite solid-solid PCM in TES based heat sink. *Eng Sci Technol Int J* 21(5):1086–1094
6. Salyan S, Suresh S (2018) Study of thermo-physical properties and cycling stability of D-Mannitol-copper oxide nanocomposites as phase change materials. *J Energy Storage* 15:245–255
7. Venkataraj KP, Suresh S (2017) Experimental study on thermal and chemical stability of pentaerythritol blended with low melting alloy as possible PCM for latent heat storage. *Exp Thermal Fluid Sci* 88:73–87

8. Zhang L, Dong J (2017) Experimental study on the thermal stability of a paraffin mixture with up to 10,000 thermal cycles. *Thermal Sci Eng Progress* 1:78–87
9. Li M (2013) A nano-graphite/paraffin phase change material with high thermal conductivity. *Appl Energy* 106:25–30
10. Mandal SK et al (2020) Performance investigation of nanocomposite based solar water heater. *Energy* 198:117295

Performance Characterization of Domestic Liquefied Petroleum Gas Cookstove



Kishan Dash and Sikata Samantaray

Abstract Liquefied petroleum gas (LPG) is a popular fuel for domestic cooking purposes in India as it is easy to utilize and gives clean and efficient cooking. This paper aims to investigate the thermal efficiency of the LPG cookstove available in India for different fuel injector (nozzle) sizes for the thermal load of 0.5–1.5 kW. The impact of thermal load and heating height on LPG cookstove's thermal efficiency are discussed. The LPG cookstove's thermal efficiency decreases with the increase in thermal load. The ideal heating height is found to be 50 mm for obtaining the highest thermal efficiency. Above the heating height of 50 mm, the thermal efficiency decreases with the increases in heating height. Similarly, the ideal nozzle size is found to be 0.77 mm for obtaining the highest thermal efficiency for the thermal load of 0.5–1.5 kW. Above or below the nozzle size of 0.77 mm, the thermal efficiency is found to decrease. The LPG cookstove's thermal efficiency is found to be a maximum of 64% for the thermal load of 0.5 kW at the nozzle size of 0.77 mm and heating height of 50 mm.

Keywords Liquefied petroleum gas cookstove · Nozzle · Thermal load · Heating height · Thermal efficiency

1 Introduction

Liquefied petroleum gas (LPG) is treated as a common fuel for domestic cooking purposes in most developing countries because it is easy to utilize and gives clean and efficient cooking. In India, LPG as a primary cooking fuel was used four times higher in urban areas than in rural areas [1]. The National Sample Survey Office (NSSO) report on energy utilized in domestic cooking, India 2011–12, is shown in Fig. 1.

Since 2011–12, the Government of India (GOI) has promoted LPG for rural areas by subsidizing the distribution of LPG to minimize the indoor air pollution from

K. Dash (✉) · S. Samantaray
Mechanical Engineering Department, ITER, SOA Deemed to Be University,
Bhubaneswar 751030, India
e-mail: kishandash90@gmail.com

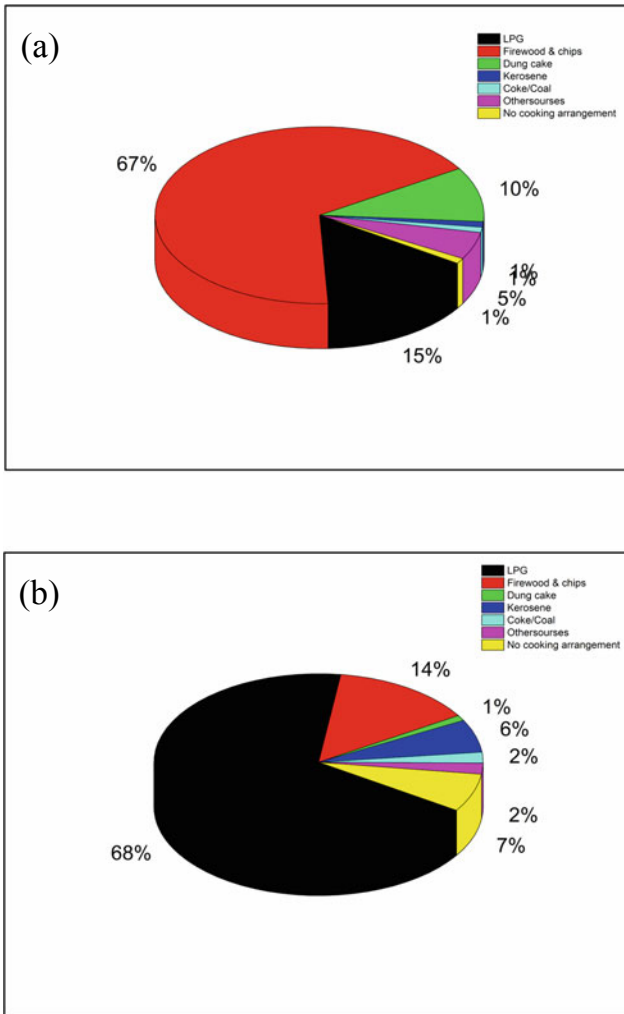


Fig. 1 Energy utilized in domestic cooking **a** rural, **b** urban India, 2011–12 [1]

wood and cow dung, etc. The GOI has introduced many initiatives such as Pratyaksh Hanstantrit Labh (PAHAL), Pradhan Mantri Ujjwala Yojana (PMUY), and “#Give It Up” schemes to better ease subsidies and minimize profitable use of LPG [2].

The performance of the LPG cookstove is determined by the water boiling test. The conventional gas cookstove burner’s thermal efficiency can be improved by optimizing parameters like thermal load, load height, load height to flame length ratio, oblique angle (θ), nozzle-to-plate distance (H/d), jet-to-jet spacing to nozzle diameter ratio (S/d), equivalence ratio (ϕ), primary aeration, inlet gas pressure, burner cap material, etc. The natural gas cooktop burner’s thermal efficiency decreased due

to the increase in the thermal load and the load height to flame length ratio [3]. It was observed that the cooktop burner's thermal efficiency decrease due to the increase in load height for the thermal load of 0.49, 0.82, and 1.65 kW. The maximum thermal efficiency was found for the minimum load height of 48 mm. The thermal efficiency increased due to the decrease in the thermal load at a constant low load height [4]. Ko and Lin [5] found that the thermal efficiency of the natural gas burner is less for the higher heating value ($41,741.48 \text{ kJ/m}^3$) than the lesser heating value ($36,236.46 \text{ kJ/m}^3$) of natural gas. The single natural gas burner's thermal efficiency decreased with the increase in the gas flow rate (thermal load) for both the lesser and higher natural gas heating value. It was found that the burner's thermal efficiency increased for the reduction of gas pressure from 150 to 100 mm H₂O for medium and maximum fuel flow rates at the higher heating value of natural gas. Hou et al. [6] observed that the laminar fuel-rich dual-flame Bunsen burner's thermal efficiency increased due to the increase in heating height (H) from 5 to 15 mm. The maximum thermal efficiency was obtained at $H = 15 \text{ mm}$. But at $H > 15 \text{ mm}$, the thermal efficiency decreased with the increase in heating height. Hou et al. [7] experimented on a laminar fuel-rich dual-flame (premixed and diffused flame) in the Bunsen burner for three different oblique angles (θ) of 30° , 60° , and 90° as well as three different heating heights (H) of 12, 23, 38 mm at injection velocity (U_i) of 0.41 m/s and methane concentration (Ω_{CH_4}) of 16.7%. The thermal efficiency increased with the increase in θ except for $H \leq 12 \text{ mm}$. The thermal efficiency of the burner increased first to a maximum value and then decreased slowly for a fixed θ and $H > 8 \text{ mm}$. In another study, researchers found that the LPG-air premixed flame jet cooktop burner's thermal efficiency decreased at a constant rate with the increase in Reynold number (Re) from 200 to 500. The thermal efficiency first decreased to a minimum value, then increased slightly with the increase in the value of ϕ from 1.4 to 2.0. The thermal efficiency also decreased due to the increase in the H/d from 3 to 21 mm but increased due to the increase in the S/d from 5.2 to 15.6 [8]. Some researchers found that the swirl burner is a preferable one to the conventional radial flow burner in LPG cookstoves because of 15% more thermal efficiency. The thermal efficiency of the swirl burner was further increased to 3% by using lightweight support (mass < a factor of 3.7) instead of conventional support. The thermal efficiency in the swirl burner again improved to 3% for preheated secondary air instead of lightweight support [9]. In another study, it was reported that the swirl flow burner (SB) produced more thermal efficiency than the radial flow burner (RB) operating at the same thermal load and load height. For both burners, the thermal efficiency increased with the reduction of gas pressure from 330 to 230 mm H₂O at a fixed fuel flow rate. The primary aeration did not affect the thermal efficiency of both the burner [10].

2 Problem Description

Based on the above literature review, one can conclude that there is a lack of performance analysis of LPG cookstove available in India. This paper aims to analyze the

LPG cookstove's thermal efficiency by taking the different sizes of the fuel injector (nozzle) for the thermal load of 0.5–1.5 kW. The effects of thermal load and heating height (gap between the top surface of the burner and pot) on the LPG cookstove's thermal efficiency are also analyzed.

3 Methodology

3.1 Experimental Setup and Procedure

The schematic diagram of the experimental arrangement for the thermal efficiency test of the LPG domestic cookstove is shown in Fig. 2. Coriolis mass flow meter with appropriate valve is used to monitor the LPG flow rate. For primary aeration, three distinct fuel injection nozzles sizes are considered for the study is shown in Fig. 3. The nozzle sizes (diameter) are measured by profile projector (Model: Metzger M, 806 A, horizontal floor type) with an accuracy of $\pm 0.1\%$.

The water boiling test is used in India to measure the LPG cookstove thermal efficiency, according to Indian standards (IS) 4246:2002 [11]. The technique that was followed is briefly given below. LPG from a 14.2 kg cylinder reaches the cookstove via a Coriolis mass flow meter (accuracy ± 0.01 g). The Coriolis mass flow meter with an appropriate control valve is used to measure the fuel flow rate. An aluminum pot of 5 kg water, with a lid and stirrer, is used for the experiment. A weighing balance

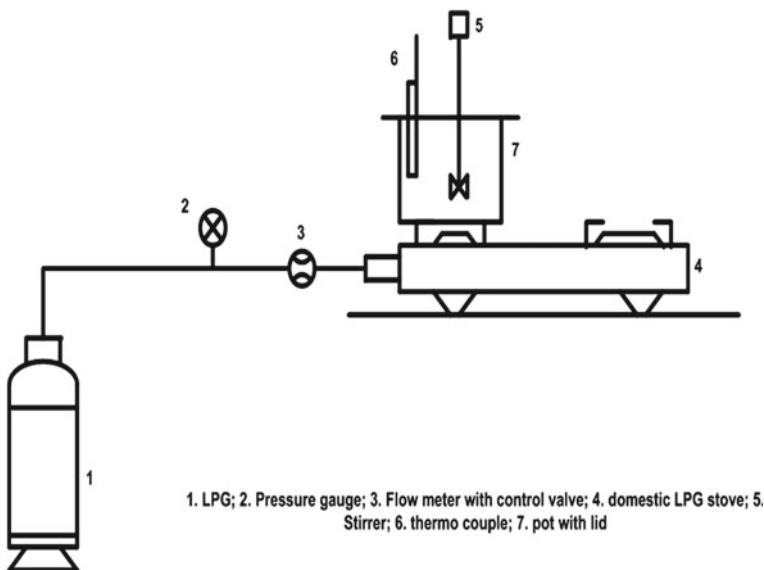


Fig. 2 Schematic diagram of the experimental arrangement

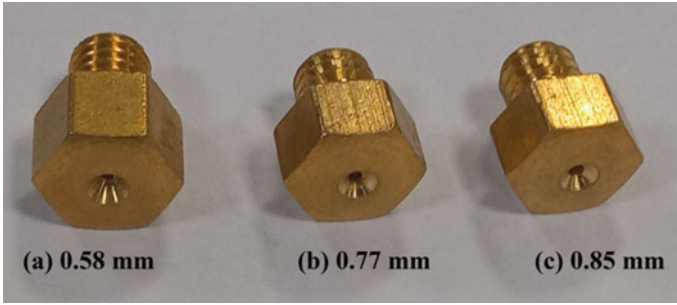


Fig. 3 Different nozzle sizes of 0.58, 0.77, and 0.85 mm

(accuracy ± 0.5 g) is used to measure the amount of water in the pot. A mercury thermometer (accuracy ± 0.5 °C) is used to measure the initial temperature (T_1) of water. After the stabilization of flame, the pot is kept over the burner. First, the water temperature is increased to 80 °C, after that stirring is initiated and maintained until the temperature of water (T_2) reaches 90 ± 0.5 °C. At this stage, the cookstove is switched off. The time needed for increasing the initial temperature of water (T_1) to 90 °C is recorded. In each case, experiments were repeated three times with an average of three taken for investigation. The LPG cookstove’s thermal efficiency is calculated using Eq. 1 [11].

$$\eta_{th} = \frac{(m_w \cdot c_w + m_p \cdot c_p)(T_2 - T_1)}{m_f \cdot \Delta t \cdot CV} \tag{1}$$

where m_w = mass of water, c_w = specific heat of water, m_p = mass of aluminum-based pan with lid and stirrer, c_p = specific heat of aluminum, m_f = mass flow rate of LPG, Δt = time taken to increase the water temperature from its initial temperature to 90 °C, CV = lower calorific value (45,780 kJ/kg) of LPG.

Experimental uncertainty

The uncertainty analysis in thermal efficiency of the LPG cookstove is calculated by using the method suggested by Klein and McClintock [12]. The maximum value of uncertainty is given by Eq. 2.

$$W_R = \left[\left(\frac{\partial x_1}{x_1} \right)^2 + \left(\frac{\partial x_2}{x_2} \right)^2 + \left(\frac{\partial x_3}{x_3} \right)^2 \dots + \left(\frac{\partial x_n}{x_n} \right)^2 \right]^{\frac{1}{2}} \tag{2}$$

The maximum value of uncertainty in thermal efficiency of LPG cookstove is found to be around $\pm 1.4\%$.

4 Results and Discussions:

In the following section, the results of the LPG cookstove’s thermal efficiency for different nozzle sizes at the thermal load of 0.5–1.5 kW are presented. The impacts of thermal load and heating height on LPG cookstove’s thermal efficiency are also discussed.

4.1 Thermal Efficiency

The LPG domestic cookstove’s thermal efficiency depends on nozzle size. The deviation in thermal efficiency of domestic cookstove for different nozzle sizes at the thermal load of 0.5–1.5 kW is shown in Fig. 4.

It is clear from the graph that the LPG cookstove’s thermal efficiency is found to be a maximum of 64% for the nozzle size of 0.77 mm at the thermal load of 0.5 kW and heating height of 50 mm. The thermal efficiency is found to be varied at a particular thermal load because of variation in nozzle size. The nozzle size helps in getting the necessary air (primary aeration) for the cookstove which is necessary for complete combustion of the air–fuel mixture. But, it has been observed that for a smaller nozzle size of 0.58 mm, the LPG cookstove thermal efficiency is less because the primary aeration is more than the fuel flow rate resulting incomplete combustion.

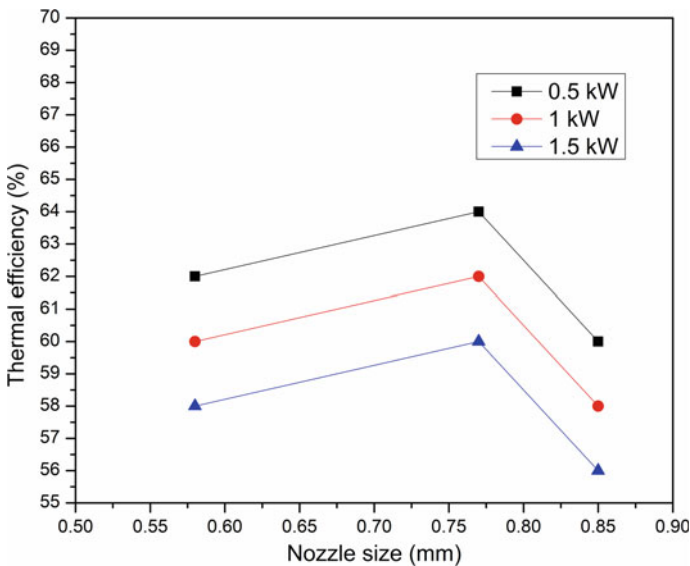


Fig. 4 Thermal efficiency of LPGcookstove for three different nozzle sizes; heating height = 50 mm, thermal load = 0.5–1.5 kW

On the other hand, for a larger nozzle size of 0.85 mm, the fuel flow rate is more compared to the primary aeration resulting in more amount of heat loss, lowers the LPG cookstove's thermal efficiency.

The LPG cookstove thermal efficiency is found to be in the range of 60–64% for the thermal load of 0.5–1.5 kW at the nozzle size of 0.77 mm and heating height of 50 mm. The effect of thermal load on the thermal efficiency of the LPG cookstove is shown in Fig. 5.

From the graph, it is clear that the LPG cookstove's thermal efficiency decreases due to the increase in thermal load. It is because the flame height is found to increase due to the increase in thermal load resulting in maximum heat loss from the LPG cookstove.

The thermal efficiency of the LPG cookstove also depends on heating height. For the thermal load of 0.5 kW, and nozzle size of 0.77 mm, the variation in thermal efficiency of LPG cookstove with heating height is shown in Fig. 6.

The thermal efficiency of the LPG cookstove is 60% when the heating height is 30 mm. The highest thermal efficiency of 64% is found when the heating height is maintained at 50 mm. With the further increase in the heating height to 70 mm, thermal efficiency decreased. The reason for the above observation is that when the heating height is 30 mm, the amount of diffusion air required for combustion is partially reduced. The complete combustion happens at a heating height of 50 mm, resulting in the highest thermal efficiency. Above this heating height (distance of heating height more than 50 mm), the radiation and convection heat losses through

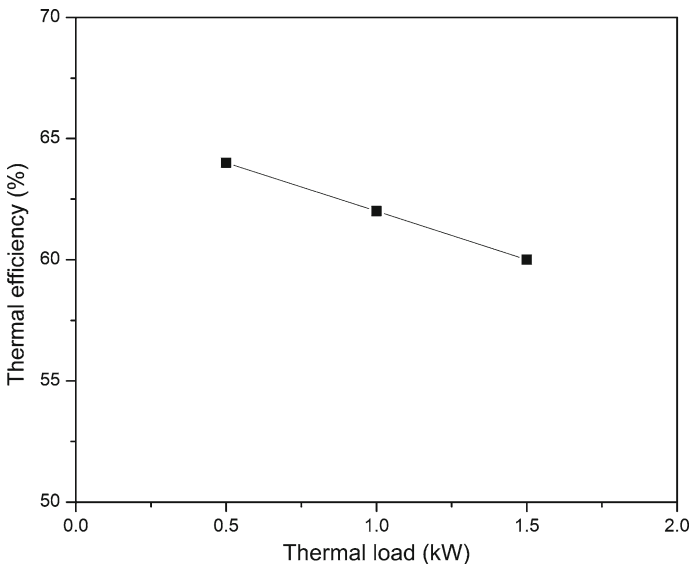


Fig. 5 Effect of thermal load on the thermal efficiency of LPG cookstove; nozzle size = 0.77 mm, heating height = 50 mm

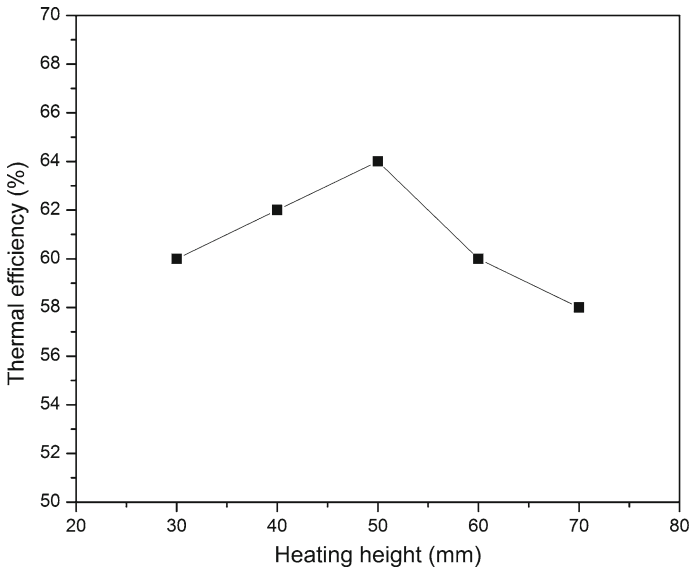


Fig. 6 Effect of heating height on thermal efficiency for LPG cookstove; thermal load = 0.5 Kw, nozzle size = 0.77 mm

the gap between the bottom surface of the pot and the top surface of the burner increase, resulting in a decrease in thermal efficiency.

5 Conclusions

The performance of an LPG cookstove can be improved by optimizing the nozzle size to 0.77 mm for the thermal load of 0.5–1.5 kW. The nozzle size helped to get the necessary air (primary aeration) for the cookstove for the complete combustion of the air–fuel mixture. The LPG cookstove’s thermal efficiency decreases with the increase in thermal load. The ideal heating height is found to be 50 mm for obtaining the highest thermal efficiency. Above the heating height of 50 mm, the thermal efficiency decreases with the increases in heating height. The maximum thermal efficiency of the LPG cookstove is found to be 64% for a thermal load of 0.5 kW at the nozzle size of 0.77 mm and heating height of 50 mm.

References

1. Energy sources of Indian households for cooking and lighting, 2011–12. <http://www.indiaenvironmentportal.org.in/content/367060/energy-sources-of-indianhouseholds-for-cooking-and-lighting>
2. Niti Aayog. https://niti.gov.in/sites/default/files/2020-01/IEA-India%202020-In-depth-Energy-Policy_0.pdf. Accessed on 04 July 2021
3. Stubington JF, Ashman PJ, Sergeant GD (1994) Emissions and efficiency from production cooktop burners firing natural-gas. *J Inst Energy* 67(473):143–155
4. Ashman PJ, Junus R, Stubington JF, Sergeant GD (1994) The effects of load height on the emissions from a natural gas-fired domestic cooktop burner. *Combust Sci Technol* 103(1–6):283–298
5. Ko YC, Lin TH (2003) Emissions and efficiency of a domestic gas stove burning natural gases with various compositions. *Energy Convers Manage* 44(19):3001–3014
6. Hou SS, Ko YC (2004) Effects of heating height on flame appearance, temperature field and efficiency of an impinging laminar jet flame used in domestic gas stoves. *Energy Convers Manage* 45(9–10):1583–1595
7. Hou SS, Ko YC (2005) Influence of oblique angle and heating height on flame structure, temperature field and efficiency of an impinging laminar jet flame. *Energy Convers Manage* 46(6):941–958
8. Li HB, Wong TT, Leung CW, Probert SD (2006) Thermal performances and CO emissions of gas-fired cooker-top burners. *Appl Energy* 83(12):1326–1338
9. Jugjai S, Tia S, Trewetaskorn W (2001) Thermal efficiency improvement of an LPG gas cooker by a swirling central flame. *Int J Energy Res* 25(8):657–674
10. Hou SS, Lee CY, Lin TH (2007) Efficiency and emissions of a new domestic gas burner with a swirling flame. *Energy Convers Manage* 48(5):1401–1410
11. Indian Standard, IS 4246: domestic gas stoves for use with liquid petroleum gases (LPG) specification (fifth revision) (2002)
12. Kline SJ (1953) Describing uncertainty in single sample experiments. *Mech Eng* 75:3–8

Improvement in the Electric Vehicle Battery Performance Using Phase Change Material



Jay R. Patel and Manish K. Rathod

Abstract The electric vehicle lithium-ion battery is extremely influenced by temperature. The high temperature affects the performance, lifespan, and safety of the battery. Therefore, it is essential to add some system that can maintain battery temperature in desired range. These types of systems are known as battery thermal management system (BTMS). Among the different cooling techniques such as air, liquid, phase change material (PCM), and heat pipe cooled battery pack, PCM is highly effective due to its high latent heat and can also be used without any power consumption. The objective of the present work is to study the influence of PCM in the battery pack. The numerical model of a 5×5 battery pack is developed and simulated with and without PCM. The results show 31.9 and 76.1% reduction in the maximum battery temperature (T_{\max}) and maximum battery temperature difference (ΔT_{\max}). The improved results justifies the utilization of PCM for better thermal performance of battery pack.

Keywords Electric vehicle · Lithium-ion battery · Battery thermal management system · Phase change material

Nomenclature

\vec{V}	Velocity (m/s)
\vec{s}	Momentum source term
A_{mush}	Mushy zone constant ($\text{kg/m}^3 \text{ s}$)
C_p	Specific heat (J/kg K)
g	Gravitational acceleration (m/s^2)

J. R. Patel (✉) · M. K. Rathod
Mechanical Engineering Department, Sardar Vallabhbhai National Institute of Technology,
Surat 395007, India
e-mail: jay.patel7693@gmail.com

M. K. Rathod
e-mail: mkr@med.svnit.ac.in

H	Latent enthalpy (J/kg)
h	Sensible enthalpy (J/kg)
k	Thermal conductivity (W/m K)
L	Latent heat (J/kg)
T	Temperature ($^{\circ}\text{C}$)
T_0	Ambient temperature ($^{\circ}\text{C}$)
T_{\max}	Maximum battery temperature ($^{\circ}\text{C}$)
ΔT_{\max}	Maximum battery temperature difference ($^{\circ}\text{C}$)

Greek Symbols

μ	Dynamic viscosity (kg/m s)
β	Thermal expansion coefficient ($1/^{\circ}\text{C}$)
λ	Liquid fraction
ρ	Density (kg/m^3)

1 Introduction

World is facing two major crisis of energy scarcity and environmental pollution in the last decade. The automotive sector of combustion vehicle is directly interconnected with these two issues. The majority of car vehicles run on fossil fuels, and the availability of fossil fuels is diminishing by the day. Traditional gasoline/diesel cars emit a considerable amount of greenhouse gases, as well as solid dispersed particles. As a result, the car industry is being compelled to focus on electric vehicles (EVs) to replace conventional vehicles. Over the last 10 years, EV adoption has accelerated, with the worldwide stock of passenger EVs surpassing 5 million in 2018, with an increment of 63% from the year 2017. The government of India has devised a two-pronged approach aimed at both customers and producers in order to promote the growth of the electric vehicle (EV) sector in the country. The massive \$1.4 billion in subsidies will be provided, followed by an increase in import taxes next year to encourage domestic businesses to produce the vehicles.

In India, only 1–2% of vehicles are EVs out of total vehicles sold in the year [1]. However, it is aimed to reach a 30% market using electric mobility by the end of 2030. For that purpose, the government of India has also taken some excellent decisions. The government of India has approved Rs. 10,000-crore program under the FAME-II scheme for the promotion of electric and hybrid vehicles in February [1]. The GST on EV was also reduced from 12 to 5%, which helped a lot in improving the sentiments. Hence, India is also moving rapidly toward electric mobility, however, it requires the solution of challenges against the battery problems.

Reversible entropy, resistive dissipation, relaxation of the cell's concentration gradient, and chemical reaction create heat in rechargeable Li-ion cells [1]. This generated heat increases the temperature of battery cells. The performance of battery cells declines as the temperature rises, and the risk of fire/explosion rises as well. According to the research, the battery temperature should be kept between 15 and 40 °C to get the most out of it [12]. The temperature differential between cells inside the battery pack has an impact on the battery's performance [3, 4], and hence it is also required to reduce the temperature difference. Therefore, it is required to reduce battery temperature and temperature difference for better performance and safety purposes.

In recent times, air and liquid-based BTMS are widely used in EVs [5, 11]. In such types of systems, air or liquid is made to flow around the heated battery cells. This type of BTMS has the disadvantage of a complex structure. Even using power consumption, these BTMS are not sufficient in achieving battery temperature in the optimal range.

The passive BTMS using phase change material (PCM) is currently in trend due to its less complex structure and zero power consumption [1, 6]. PCM is a material that stores energy through a phase shift at almost isothermal temperatures. When it melts, it absorbs a huge quantity of energy from the local surroundings and releases the same amount of energy when it freezes. PCM is stored around the battery cells in PCM-based BTMS. The temperature of the battery begins to rise when the charging/discharging process begins. Because of the temperature difference between them, the heat produced by the battery cells is absorbed by PCM. When PCM is heated, it begins to melt by absorbing latent heat, and natural convection occurs, which boosts heat absorption from the battery cells even more. During the heat storage in form of latent heat, PCM temperature almost remains constant, hence, PCM restricts the temperature increment of battery pack. The objective of present study is to check whether PCM inclusion inside battery pack is beneficial or not. The improvement in thermal parameters of battery pack is studied with PCM.

2 Problem Description

In this study, the performance of battery thermal management system of air cooling (natural convective), and passive cooling using PCM is compared and investigated. For that purpose, cylindrical lithium-ion batteries (Panasonic, NCR18650PF, and 2.4 Ah) are selected [2].

The battery pack of 25 battery cells with a 5×5 configuration is modeled as shown in Fig. 1. In the present study, commercially available PCM, paraffin wax (RT42) is used as PCM, and aluminum is used as container material. The properties of PCM, battery cells, and aluminum are given in Table 1.

Fig. 1 Design of 5×5 battery pack

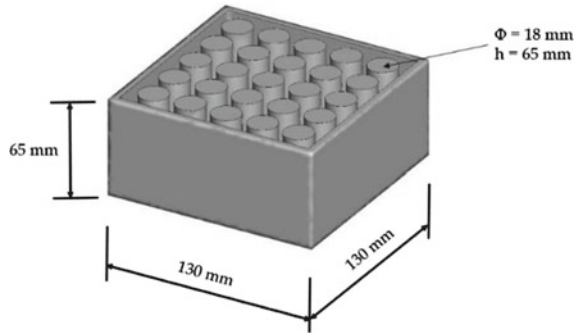


Table 1 Properties of materials [2, 10]

	PCM (RT42)	Battery	Aluminum
Density (kg/m^3)	760	2720	2719
Specific heat (J/kg K)	2000	300	871
Thermal conductivity (W/m K)	0.2	3	202.4
Melting temperature ($^{\circ}\text{C}$)	38–43	–	–
Latent heat (J/kg)	165,000	–	–
Thermal expansion coefficient ($1/^{\circ}\text{C}$)	0.000125	–	–
Dynamic viscosity (kg/m s)	0.02	–	–

3 Numerical Modeling

The phase change process of PCM is mainly controlled by convection–diffusion processes. The PCM changes from one phase to another with varying liquid fraction levels overtime temperature distribution is nonlinear in nature. To tackle conduction-controlled phase change issues, the finite volume method (FVM) has been frequently used. Patankar [7] had presented the finite volume method for conduction, which assists the formation of a melting and solidification model based on combined conduction convection.

An enthalpy-porosity method is widely employed for tracking a semi solid–liquid (moving) boundary between solid and liquid PCM. For mathematical modeling of melting and solidification process assumptions are [8]:

- PCM is homogeneous and isotropic.
- Thermo-physical properties of the PCM are constant.
- The flow of the liquid PCM is considered to be laminar and incompressible Newtonian fluid flow.
- The viscous dissipation term is considered negligible.

- During the phase change process, a Boussinesq approximation is used to examine the effects of natural convection. This approximation considers density fluctuations with buoyancy force only.

Governing equations

For transient 3D melting and solidification problems, three governing equations—continuity, momentum—and energy, are used, which are expressed as follows:

Continuity equation

$$\nabla \cdot (\rho \vec{V}) = 0 \quad (1)$$

Momentum equation

$$\frac{\partial \vec{V}}{\partial t} + \vec{V} \cdot \nabla \vec{V} = \frac{1}{\rho} \left\{ -\nabla P + \mu \nabla^2 \vec{V} + \rho \beta \vec{g} (T - T_{ref}) \right\} + \vec{S} \quad (2)$$

Energy equation

$$\frac{\partial H}{\partial t} + \nabla \cdot (\vec{V} h) = \nabla \cdot \left(\frac{k}{\rho c_p} \nabla h \right) \quad (3)$$

The sum of the sensible enthalpy (h) and the latent heat (H) in PCM may be calculated as follows:

$$H^1 = h + \Delta H \quad (4)$$

where

$$h = h_{ref} + \int_{T_{ref}}^T c_p dT \quad (5)$$

The latent heat content can be expressed in terms of the material's latent heat, L :

$$\Delta H = \lambda L \quad (6)$$

where H may range from 0 (solid) to L (liquid). As a result, the liquid fraction may be defined as follows:

$$\lambda = \begin{cases} 0, & \text{if } T < T_{solidus} \\ 1, & \text{if } T > T_{liquidus} \\ \frac{T - T_{solidus}}{T_{liquidus} - T_{solidus}}, & \text{if } T_{solidus} < T < T_{liquidus} \end{cases} \quad (7)$$

Here, \vec{S} used in momentum Eq. 2, which is the source term known as Darcy's law damping terms, which is used for convection consideration with the phase change process and defined as:

$$\vec{S} = \frac{(1 - \lambda)^2}{\lambda^3 + \varepsilon} A_{\text{mush}} \vec{V} \quad (8)$$

where ε is a small computational constant, and just used to avoid division by zero. The coefficient A_{mush} is known as the mushy zone constant, which has a large value, mostly 10^4 – 10^7 .

The battery performance is studied at 1C charging rate. The constant heat generation rate of $10,447 \text{ W/m}^3$ is taken as heat source of battery cells. The common boundary between PCM and battery cells, and PCM and container are given coupled wall boundary conditions. While, other boundaries with direct contact to atmosphere are given natural convective boundary conditions. The initial condition is taken as ambient condition, and ambient temperature is taken as 30°C .

The commercial computational software ANSYS 16.2 is used to simulate the battery thermal management using PCM. The 3D Cartesian geometry is created using ANSYS DESIGN MODELER and meshed using ANSYS MESH. All parts of the models are developed with proper dimensions. The geometry is meshed using tetrahedral types of cells. After modelling and meshing, FLUENT 16.2 software is used to simulate the problem. For pressure–velocity coupling, the PISO scheme is selected, as it is highly preferable for transient solutions. The second order upwind method is used to discretize momentum and energy equations, while Pressure Staggering Option (PRESTO) scheme is used for pressure equation. The pressure, velocity, energy, and liquid fraction under-relaxation parameters utilized in this investigation are 0.3, 0.7, 1, and 0.9, respectively. The energy equation's convergence requirements are set to 10^{-6} , whereas the other controlling equations are set to 10^{-4} .

Figure 2 shows the comparison of battery surface temperature obtained using the developed model with the result by Sun et al. [9]. The battery surface temperature was measured at the middle plan using thermocouples in the experiments. The battery surface temperature at the similar location is obtained from the simulation and compared. It can be observed that the transient variation of temperature is well matched with 6–7% difference between the experimental and numerical results. Hence, the developed model can be used for the further study of PCM-based BTMS.

4 Results and Discussion

The objective of present study is to check the improvement in battery thermal performance using PCM. The thermal performance of any battery pack is derived from two parameters: (i) maximum battery temperature (T_{max}) and (ii) maximum battery temperature difference (ΔT_{max}). The higher value of T_{max} degrades the battery capacity in terms of cyclic life. While, higher value of ΔT_{max} creates non-uniform

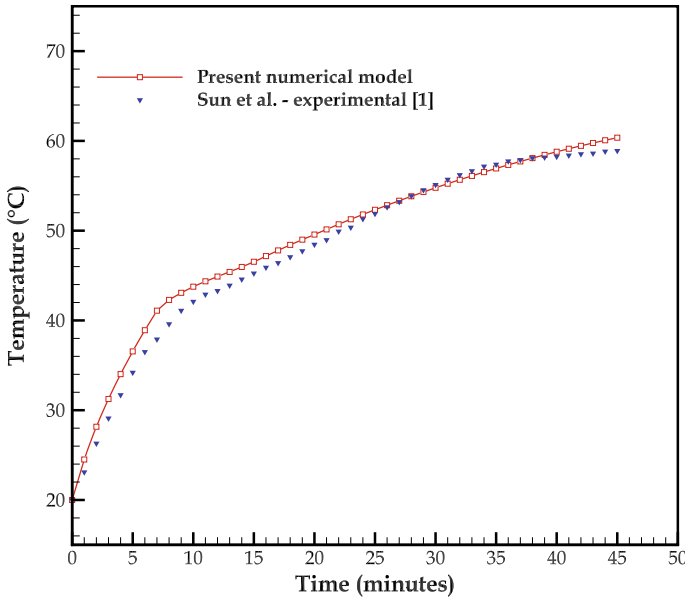


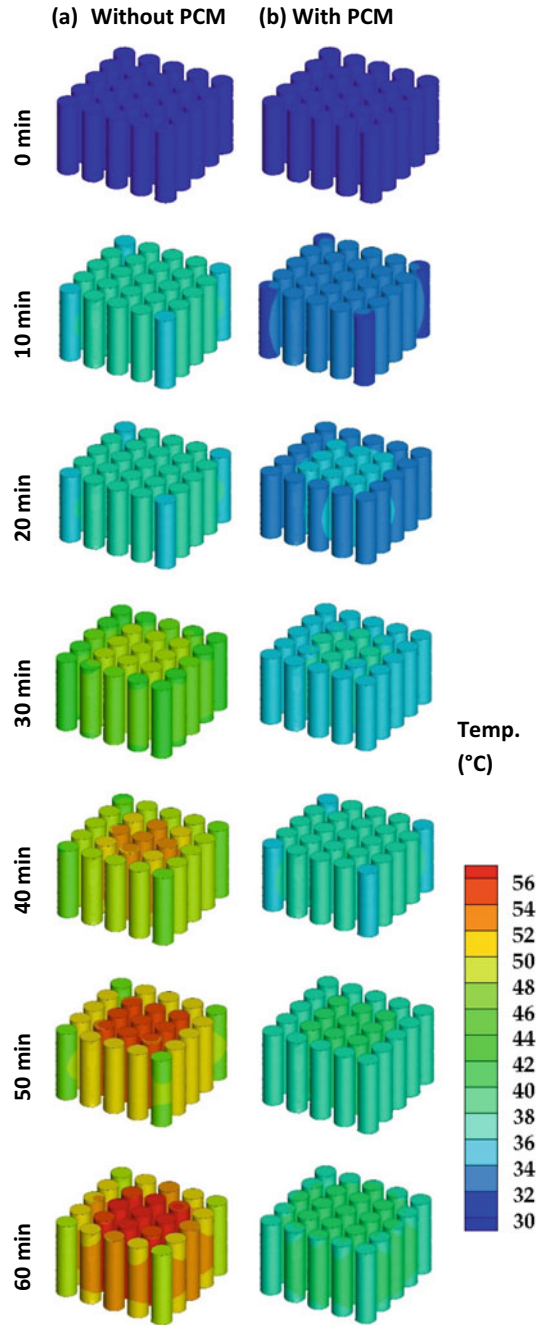
Fig. 2 Validation of the developed numerical model

temperature distribution inside battery pack. The capacity of high temperature battery cell becomes lesser than other cells. The whole battery pack gives output according to that weakened cell, and hence whole battery pack degrades due to non-uniform temperature. Thus, both T_{\max} and ΔT_{\max} should be minimum for better battery performance.

Figure 3 shows the temperature contours of the battery surface with and without PCM. The ambient temperature is taken as 30 °C, and the charging rate of the battery pack is taken as 1C. As the battery takes 60 min for complete charging at a 1C rate, temperature contours till 60 min are shown with the interval of 10 min. It can be observed, without PCM, battery temperature increases with time and reaches around 56 °C after 60 min. Similarly, battery temperature also increases with PCM, but it reaches around 40 °C after 60 min. These contours show the significant influence of PCM on battery temperature. In the case of without PCM, central cells can be seen at high temperatures compared to the peripheral cell, creating a significant temperature difference. The peripheral cells are in direct contact with the atmosphere, while central cells are surrounded by neighboring battery cells. Hence, peripheral and corner cells are cooled more by atmospheric air compared to central cells. That is the reason due to which central cells have higher temperatures compared to peripheral cells. Similarly, less temperature discrepancy can be found with the use of PCM.

Figure 4 shows the transient variation of the maximum battery temperature (T_{\max}) with and without PCM and liquid fraction variation of PCM. The battery temperature increases with time due to continuous heat generation and reaches to the maximum at the end of charging process. Without PCM, battery temperature starts to increase from

Fig. 3 Temperature contours of the battery pack with and without PCM



30 °C and reaches 56.77 °C after completing the charging process; hence, temperature almost doubles after the charging of battery. While by using PCM inside the battery pack, this maximum temperature after complete charging is restricted to 38.66 °C. So, the inclusion of PCM inside the battery reduces the maximum temperature by 31.9%. From the liquid fraction plot, PCM can be seen in solid form till 40 min and that means it only absorbs battery heat in sensible heat form. Nevertheless, once PCM temperature reaches its melting point temperature, it starts to melt and absorb heat in the form of latent heat. PCM with melting temperature 38–43 °C is used, so when PCM temperature reaches 38 °C, it absorbs heat with phase change. It can be seen that after 40 min, battery temperature reaches around 38 °C, and after that, PCM starts to melt. So, after 40 min, PCM absorbs heat by changing its phase from solid to liquid at an almost constant temperature. So, after that, the battery temperature almost becomes constant.

Figure 5 shows the transient variation of the maximum temperature difference (ΔT_{max}) inside the battery pack. The value of ΔT_{max} continuously increases with time and almost reaches to 10 °C after 60 min. This temperature difference is quite higher than desired ΔT_{max} (less than 5 °C). Hence, battery pack may fail after several cycles of charging and discharging without any thermal management system. However, with PCM filling inside the battery pack, this temperature difference ΔT_{max} increases till 40 min, and then reduces till completion of charging process. The value of ΔT_{max}

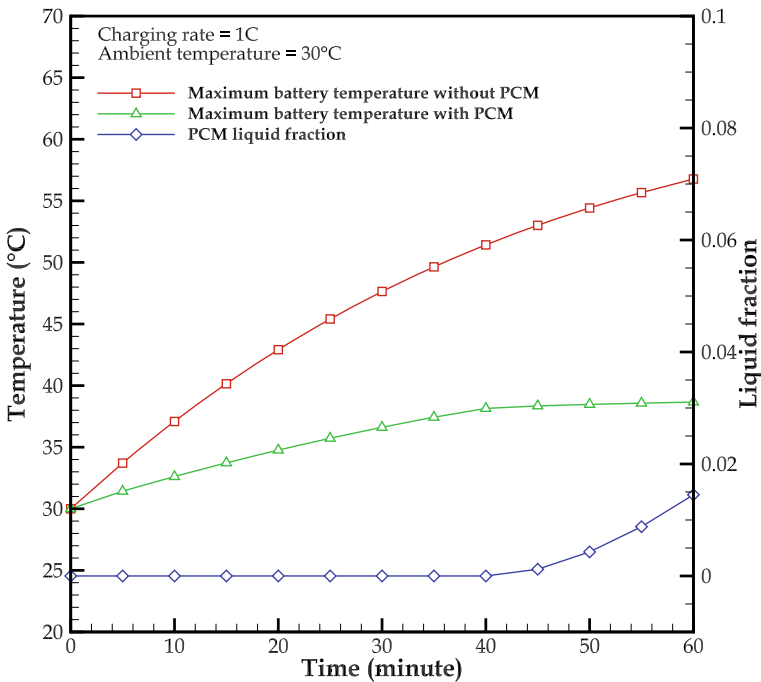


Fig. 4 Comparison of maximum battery temperature (T_{max}) with and without PCM

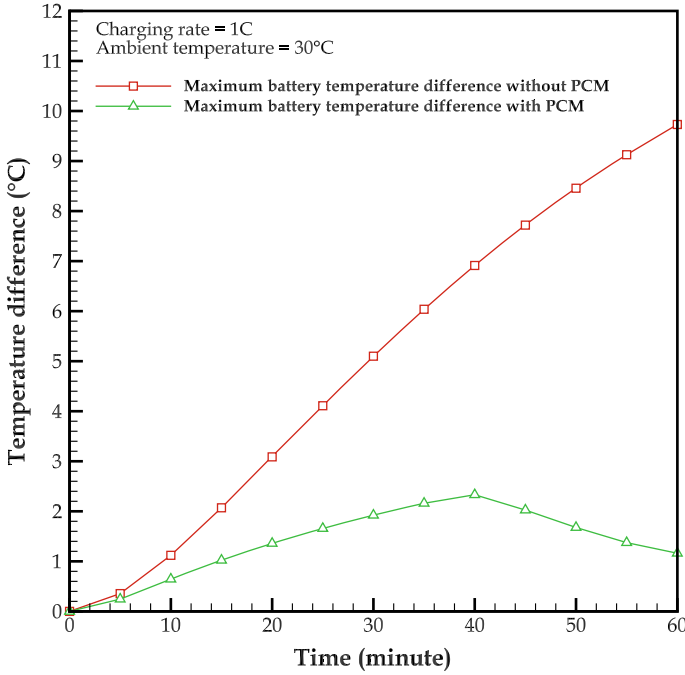


Fig. 5 Comparison of maximum battery temperature difference (ΔT_{\max}) with and without PCM

reaches the maximum of 2.33 °C, after 40 min. This maximum ΔT_{\max} at the mid-charging is due to start of PCM melting. After 40 min, PCM temperature reaches to its solidus temperature (38 °C) and starts to melt. Due to melting, most of the battery heat is utilized in phase change and temperature doesn't increase. As PCM temperature remains almost constant, PCM creates uniform temperature distribution. At the end of charging, ΔT_{\max} around 1 °C can be observed. The maximum battery temperature difference is reduced by 76.1% with using PCM inside the battery pack.

5 Conclusions

To check the importance of PCM inside the battery pack, battery pack with 5×5 arrangement with 18,650 battery cells is studied in the present study. Initially, a comparison of battery pack thermal performance with and without PCM is carried out. The importance of PCM inside the battery pack is studied. The maximum battery temperature, T_{\max} is found as 56.77 °C and 38.66 °C without and with PCM, respectively. The significant reduction in T_{\max} of 31.9% is achieved using PCM. The maximum battery temperature difference, ΔT_{\max} is found as 9.77 °C and 2.33 °C without and with PCM, respectively. Around 76% reduction in ΔT_{\max}

is achieved using PCM. PCM can reduce T_{\max} significantly, but it is excellent in achieving uniform temperature distribution.

References

1. Chen J et al (2019) Effects of different phase change material thermal management strategies on the cooling performance of the power lithium ion batteries: a review. *J Power Sources*. Elsevier B.V., 442:227228. <https://doi.org/10.1016/j.jpowsour.2019.227228>
2. Choudhari VG, Dhoble AS, Panchal S (2020) Numerical analysis of different fin structures in phase change material module for battery thermal management system and its optimization. *Int J Heat Mass Transfer Elsevier Ltd* 163. <https://doi.org/10.1016/j.ijheatmasstransfer.2020.120434>
3. Ianniciello L, Biwolé PH, Achard P (2018) Electric vehicles batteries thermal management systems employing phase change materials. *J Power Sources Elsevier* 378:383–403. <https://doi.org/10.1016/j.jpowsour.2017.12.071>
4. Jouhara H et al (2019) Applications and thermal management of rechargeable batteries for industrial applications. *Energy Elsevier Ltd* 170:849–861. <https://doi.org/10.1016/j.energy.2018.12.218>
5. Lan C et al (2016) Thermal management for high power lithium-ion battery by minichannel aluminum tubes. *Appl Thermal Eng Elsevier Ltd* 101:284–292. <https://doi.org/10.1016/j.applthermaleng.2016.02.070>
6. Murali G et al (2021) A review on hybrid thermal management of battery packs and its cooling performance by enhanced PCM. *Renew Sustain Energy Rev Elsevier Ltd* 150:111513. <https://doi.org/10.1016/j.rser.2021.111513>
7. Patankar S (1980) Numerical heat transfer and fluid flow. Taylor & Francis (Series in computational methods in mechanics and thermal sciences). Available at: <https://books.google.co.in/books?id=5JMYZMX3OVcC>
8. Patel JR, Joshi V, Rathod MK (2020) Thermal performance investigations of the melting and solidification in differently shaped macro-capsules saturated with phase change material. *J Energy Storage* 31. <https://doi.org/10.1016/j.est.2020.101635>
9. Sun Z et al (2019) Thermal management of the lithium-ion battery by the composite PCM-Fin structures. *Int J Heat Mass Transfer Elsevier Ltd* 145:118739. <https://doi.org/10.1016/j.ijheatmasstransfer.2019.118739>
10. Wang Q et al (2018) Parametric analysis of using PCM walls for heating loads reduction. *Energy Build* 172:328–336. <https://doi.org/10.1016/j.enbuild.2018.05.012>
11. Xie J et al (2017) Structural optimization of lithium-ion battery pack with forced air cooling system. *Appl Therm Eng* 126:583–593. <https://doi.org/10.1016/j.applthermaleng.2017.07.143>
12. Yan J et al (2016) Numerical study on the thermal performance of a composite board in battery thermal management system. *Appl Therm Eng* 106:131–140. <https://doi.org/10.1016/j.applthermaleng.2016.05.187>

Effect of Dilution on Emission from Methane Combustion



Keyur Kadia, Nikhil A. Baraiya, and R. D. Shah

Abstract In a non-premixed flame mode of combustion, the fuel and oxidizer react. It began to mix very immediately. The flow rate had slowed due to the mixing. For such modes of combustion, the combustion system's high turbulence shear layer has been chosen to encourage mixing. ANSYS was used to do the numerical analysis for the parameters mentioned above. By aiding in the air whirling can impact combustor performance by affecting the fuel–air mixing process and creating a recirculation zone that can function as a flame holder. RSM turbulence models were employed in this study. It has been proven to be reliable in this type of study. The numerical data had been backed up by the available experimental results. Carbon dioxide can impact Hydrogen has unique combustion characteristics as compared to hydrocarbons, such as well as a broad flammability range, a low minimum ignition energy, and a fast flame speed. At AFR 50, hydrogen and carbon dioxide were diluted from 0 to 50% hydrogen and carbon dioxide. Investigate thermal emission with this numerical set-up. It has been expanded to include thermal emission at AFR 50 for carbon dioxide and hydrogen dilution, as well as a PPM emission contour.

Keywords Effect of dilution on emission · Thermal emission · Swirl combustor · Combustion flow physics

Nomenclature

AFR Air to Fuel Ratio
CTRZ Central Toroidal Recirculation Zone
PDF Probability Density Function

K. Kadia (✉) · N. A. Baraiya · R. D. Shah
Mechanical Engineering Department SVNIT, Surat, India
e-mail: keyurkadia1@gmail.com

Greek Symbols

θ	Equivalence ratio
f	Mixture fraction
R	Radius
S_N	Swirl number

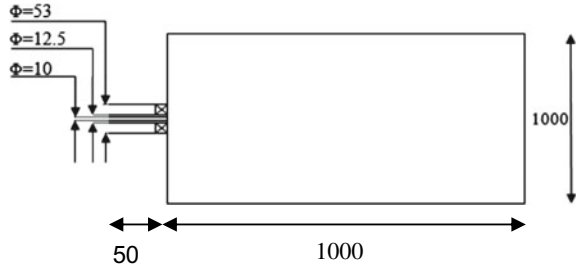
1 Introduction

Due to the stringent rules imposed on emission from combustion, meeting the growing need of energy is a big challenge. It is proven that the dilution of other gases can reduce the emission either by lowering the adiabatic flame temperature or by enhancing the combustion by high reaction rates or by replacing the carbon content from the hydrocarbon fuel itself. This chapter is devoted to recognise the impact of dilutions like hydrogen and carbon dioxide on the emission characteristics of methane. Zhen [1] has shown that experimentally; the emission and thermal properties of swirl-stabilized turbulence IDF with liquefied petroleum gas were investigated. They looked at how the equivalence ratio and Reynolds number affect CO and Knox emissions, as well as the temperature at the centre line. They discovered that the Internal Recirculation Zone (IRZ) is crucial in stabilizing and shortening IDFs. Because a high swirling flame produces a low maximum temperature, Knox production is reduced while CO emissions rise. Barakat [2] has shown that the heat transfer and combustion characteristics of two alternative IDF burner configurations were investigated. Flame length, high temperature zone CO, and Knox emissions from a single airport and several airports with a distributed fuel port were investigated experimentally. CO emissions drop as the diameter of the airport is reduced in a single airport configuration. Cheng [3] has shown that to maintain present facilities safe, it's important to understand how diluents affect natural gas combustion. In this paper, a swirl flame burner is used to examine the diluent-containing fossil fuel flame stability and photometric characteristics. A range of gas compositions, including those diluted with nitrogen and carbon dioxide, were successfully used to produce stable and continuous swirl flames. When compared to the pure methane example, diluting the simulated natural gas with CO₂ and N₂ raises the blowout limit. Although CO₂ has a greater influence on flame blowout than N₂ because of its higher heat capacity, preheating the burner and mixtures can help to prolong the flame blowout limits. Kumaran [4] has shown that Using Quantify the impact of swirl level on the lean flame stability limits of swirled open premixed turbulent flames using an annular premixed pilot flame. The experiments are conducted out using a novel approach that involves altering the swirl levels while keeping the Reynolds number and equivalency ratio constant. Pilot-stabilized low-swirl lean flame stability data can be utilised to create lean premixed low-emission burner systems. Chang [5] has shown that with increased CO₂ dilution, the CH₄/air laminar

flame speed reduced. As CO_2 concentrations climbed, the concentrations of the reactants dropped, lowering the rate of net reaction (and thus the flame speed). CO_2 is also a heat sink. Lowering reaction temperatures and, as a result contributes to our understanding of how inert gas affects methane's flammability characteristics. Rajpara [6] has shown that temperature and emissions at the combustor's output are monitored and recorded, and the flame is visible. Flames grow longer and wider for the same energy input when H_2 concentrations are higher. Adding hydrogen to a flame improves its velocity, temperature, rate of chemical reactions, and CO emissions. Higher flame temperature favours Knox emissions with higher hydrogen concentrations. Chemical kinetic effects are decreased, and the decline at a fixed volumetric fuel flow, hydrocarbon substitution occurs in carbon-generated species. With just a little increase in Knox emissions, hydrogen increases flame temperature, reduces flame durations, and lowers CO emissions. Nasiri [7] has shown that when the quantity of CO_2 diluent in the fuel increases, in contrast to the temperature at the combustion chamber's input, the total lift-off height and flame length drop linearly, and the maximum temperature in the combustion chamber falls. As the CO_2 level in the fuel grows, temperature differences at the combustion chamber's entry become negligible. With the CO_2 shorter combustion, chambers with diluents can be utilised. Increasing the length of the combustion chamber while the diluent is in operation will have no effect on the Knox emissions reduction. Rete [8] has shown that to create dilution-induced extinction; the carbon dioxide mole percentage was varied from 0 to 0.22 while maintaining a constant jet velocity. In the post-flame region, variations in the length of the flame, the lift-off height, the temperature of the flame, and the constitution of the flame and emission indices of the species were examined. At various degrees of carbon dioxide dilution in the fuel, they exhibited an increase in the flame's lift-off height, a reduction in the overall flame duration, a drop in the flame temperature, and a drop in the Knox concentration. Ashwani [9] has shown that in stationary gas turbine applications, colourless distributed combustion (CDC) has been shown to enhance combustor performance, resulting thermal field with near-zero emissions, efficiency and high combustion intensity homogeneity, and increased stability. This article compares the results of approach for in a partly premixed combustion; air dilution is used, to premixed and non-premixed air and fuel injection. A part of the fuel is injected into the air stream, and a part of the atmosphere is introduced into the fuel stream, to ensure that the local equivalency ratios for each stream are considerably over the limit of combustibility. Tripathi [10] has shown that the research looked at the pollution and efficiency of a when the methane energy share (MES) increases, the brake thermal efficiency (BTE) and relative air fuel ratio (RAFR) decrease, but unexplained heat loss increases.

The previous work shows the importance of the requirements in emission reducing techniques. The present work is aimed towards reduction in NO , CO_2 , and CO emission makes the findings of this research will help in achieving the strict emission norms.

Fig. 1 Experimental geometry



1.1 Numerical Set up

Geometry Modelling

The air channel, axial swirler, and unconfined test section make up the burner's geometry. Figure 1 depicts the model geometry of the unconfined burner under consideration in this study.

The axial swirler is made up of radially inclined blades that provide the axially entering air a swirling motion. The geometry consists of a 50 mm long, 53 mm OD, and 12.5 mm ID inlet air and fuel pipe. With 10 vanes at a 450 vane angle, the axial swirler has a 53 mm outer diameter and a 12.5 mm hub diameter. The test segment has been following the axial swirler.

To solve governing differential equations numerically, the CFD code fluent employs the control volume method. Fluent solves turbulence equations and transport equations for conserved scalars (mean mixture fractions and variation) during the simulation in addition to continuity and momentum equations. Although the isotropic eddy viscosity hypothesis was adopted, a realisable k- ϵ type model was used for steady-state simulations. This RSM model was used for the further calculation of this numerical technique for validation reasons.

For swirling flow, the RSM model has proven to be the most effective. Fluent has a number of pressure-based algorithms. For velocity and pressure coupling, a SIMPLE method was used in this work. With two-equation turbulence models, the first-order upwind technique was applied. The interaction between turbulence chemistry and non-premixed combustion was studied using the Probability Density Function (PDF), and the Knox formation model was utilised to determine the thermal emission of this problem.

1.2 Boundary Condition

For CFD analysis, precise boundary conditions are required. The type and nature of the solution are determined by the boundary conditions. The governing equations are solved using a pressure-based solver. Mass flow inlet had been defined as air and fuel

Table 1 Boundary conditions and parameter at different zones

Zone name	Zone type	Boundary condition
Air flow inlet	MFR inlet	0.025 kg/s
Fuel inlet	MFR inlet	0.0005 kg/s
Air exit from air passage	Interface	–
Air swirler inlet	Interface	–
Air swirler outlet	Interface	–
Air inlet to test section	Interface	–
Test section side walls	Wall	–
Test section outlet	Pressure outlet	Zero Pascal (Gauge)

inlet. At the test section's output, atmospheric pressure was used. Because the test portion is taken far away from the intake, the side faces are defined as walls. Similar meeting faces between two adjacent domains are known as the interface, which allows fluid to flow. 0.025 kg/s was used as the air mass flow rate. The MFR of the relevant fuel is 0.0005 kg/s. The fuel input's mean mixture fraction has decreased from 1 to 0 (Table 1).

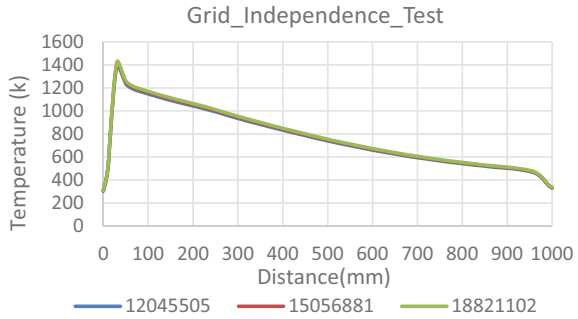
1.3 Numerical Simulation

To better understand flame physics, combustor shape is analysed in the context of a burner. Methane was employed as a fuel for reactive analysis. The methane–air mixture has a stoichiometric air–fuel ratio of 17.426. In this example, the analysis was carried out to set the air–fuel ratios. The MFR of air has been set at 0.025 kg/s, and the mass flow rate of fuel has been set at 0.0005 kg/s based on the air–fuel ratio. Two-equation realisable k-e turbulence and a non-premixed combustion model were employed for numerical simulation. And for this numerical analysis, the RSM model was utilised since it is more reliable and accurate for whirling flow in particular. After that, the numerical simulation was extended to include carbon dioxide and hydrogen dilution on methane. Dilution of methane from 0 to 50% carbon dioxide and hydrogen at 0.0005 kg/s was done, and thermal emission was investigated in this study.

1.4 Grid Independence Test

The most significant part of CFD simulation is the grid independence study. Grid independence is being implemented. The simulation results are unaffected by the grid size refinement. The study on grid independence starts with a small number of

Fig. 2 Centre line variation of temperature at three different grid



components, and the of elements) is about 1.25 times size of the preceding grid (total number elements). The grid independence investigation was carried out on three distinct grid sizes: 12,045,505, 15,056,881, and 18,821,102. Figure 2 depicts the temperature variation with the centre line taken at an axial distance. Three distinct grid sizes were utilised. The difference in temperature between grid size one and grid size two is 3%. The variation in temperature between grid size two and grid size three is only 1%. Grid distinction: temperature variation is less than 1%. Grid size two had been selected.

1.5 Validation

The experimentally determined flame form resembles a numerical simulation temperature contour. The maximum temperature in the above temperature contours is 2153 K, while the adiabatic flame temperature of methane is 2236 K. As a result, both analytical theory and experimental investigation validate the numerical work (Fig. 3).

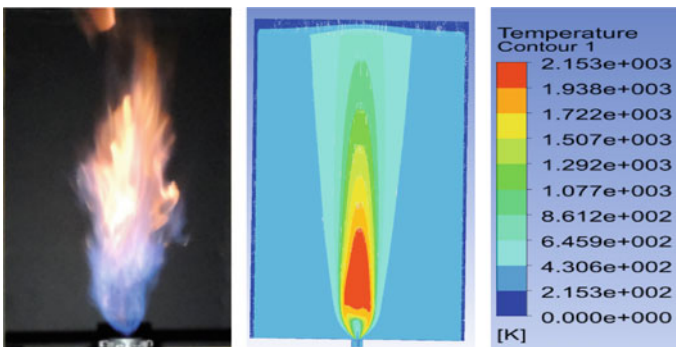


Fig. 3 Comparison of experiment and numerical simulation with variation of mass flow rate of fuel at $S_N = 0.70$ for $m_f = 0.00125$ kg/s

2 Result and Discussion

A. Emission Characteristics with Carbon Dioxide Dilution

Figure 4a–h shows the adiabatic flame temperature reduced with a dilution of carbon dioxide increase up to 50%. In summary, fuel dilution with CO₂ lowers flame temperature, lowering thermal Knox emissions. Carbon dioxide has the ability to change the characteristics of burning. Such temperature of the flame, flame speeds (laminar and turbulent), heat transmission, NO and CO emissions, as well as flame duration and combustion efficiency are all factors to consider. When the dilution rate is raised, the flame temperature drops, resulting in a reduction in thermal Knox missions. We could see that NO PPM reducing in the above shown Fig. 4a–h and from the Table 2 because of adiabatic flame temperature decreased with dilution.

NO Emission

See Fig. 4.

CO Emission

Figure 5a–h shows how the adiabatic flame temperature may be lowered by up to 50% by increasing the carbon dioxide dilution. In conclusion, CO₂ dilution reduces thermal Knox emissions by lowering flame temperature. Carbon dioxide affects temperature of the flame, laminar and turbulent flame speeds, heat transmission, flame length, combustion efficiency, and NO and CO emissions which are all factors to consider. With dilution, the temperature of the adiabatic flame dropped. Using data changes in the flame structure at in mixture fraction space, various amounts of diluent CO₂ mole fraction may be observed for species mass fractions. The flame’s luminance decreases as the diluent concentration increases, and the lift-off height of the flame has increased significantly, although the overall visible flame duration has decreased. The above contour shows that CO PPM is also decreasing.

CO₂ Emission

Figure 6a–h shows how the adiabatic flame temperature is lowered by up to 50% when the carbon dioxide in the atmosphere is diluted. In conclusion, CO₂ dilution

Table 2 Variation of emission with dilution of CO₂ with different percentage

Dilution (%)	0% CO ₂	5% CO ₂	10% CO ₂	15% CO ₂	20% CO ₂	30% CO ₂	40% CO ₂	50% CO ₂
Max. NO PPM	33.96	35	13	2.24	11.78	0.089	7.79e-05	1.75e-07
Max. Co PPM	38,588	11,238	2077	375	6158	1.33	0.0144	0.0144
Max. CO ₂ PPM	78,966	100,188	107,888	150,000	200,000	300,000	400,000	500,000

NO Emission

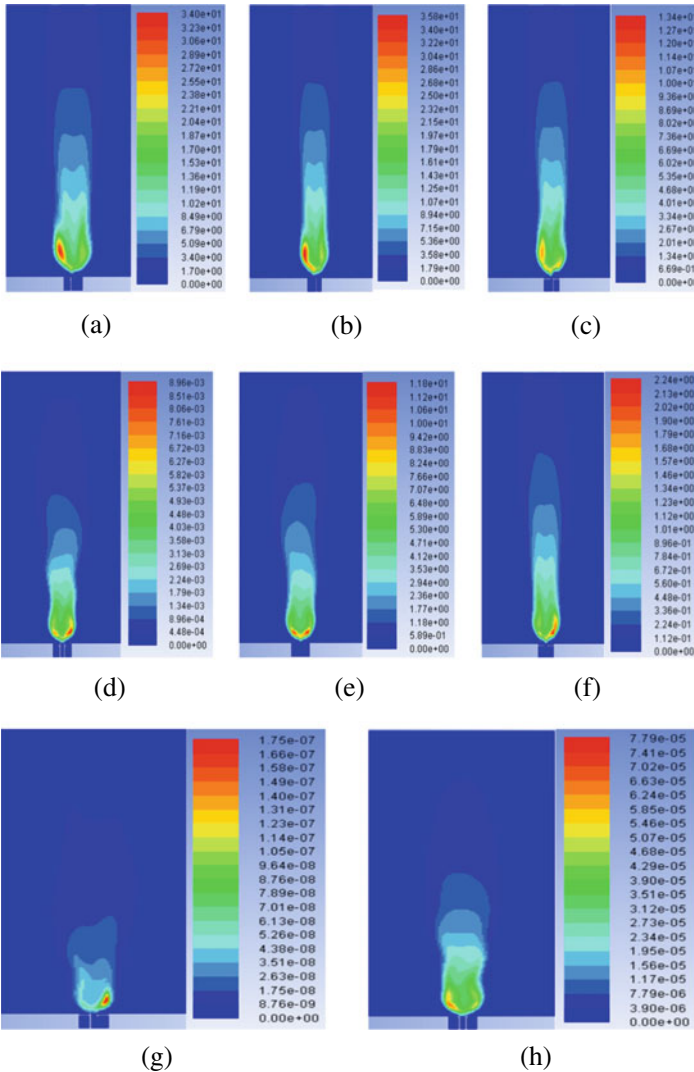


Fig. 4 Emission contour for NO PPM **a** without dilution; dilution of CO₂. **b** 5%; **c** 10%; **d** 15%; **e** 20%; **f** 30%; **g** 40%; **h** 50%

reduces flame temperature, resulting in decreased thermal Knox emissions. Combustion properties flame temperature, laminar and turbulent flame speed, to name a few. Emissions can all be affected by carbon dioxide. As the dilution rate is raised, the temperature of the flame decreases. As the population grows, CO₂ dilution levels, the flame’s brightness decreases as the diluent content increases. Fuel containment has

CO Emission

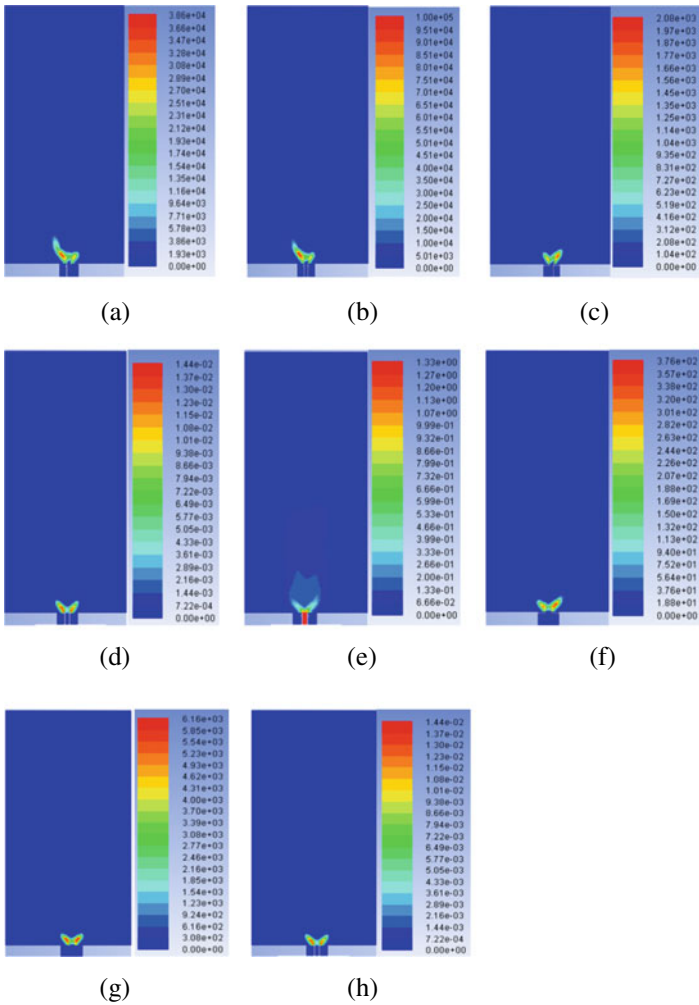


Fig. 5 Emission contour for CO PPM a without dilution; dilution of CO₂, b 5%, c 10%, d 15%, e 20%, f 30%, g 40%, h 50%

decreased as the methane mass percentage has decreased, resulting in less complete combustion. The CO₂ PPM has obviously grown when the CO₂ dilution has been raised.

CO₂ Emission

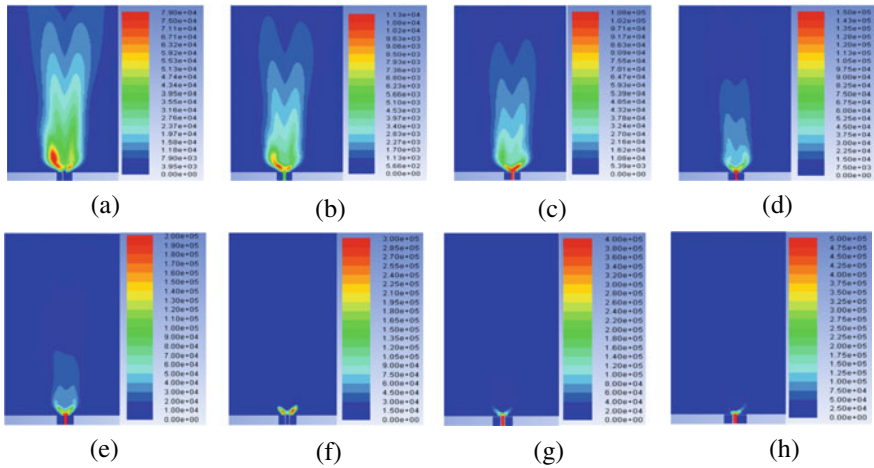


Fig. 6 Emission contour for CO₂ PPM **a** without dilution; dilution of CO₂, **b** 5%, **c** 10%, **d** 15%, **e** 20%, **f** 30%, **g** 40%, **h** 50%

B. Emission Characteristics with Hydrogen Dilution

NO Emission

In the shown Fig. 7a–h, the adiabatic flame temperature increased with a dilution of hydrogen increase up to 50%. We could see that NO PPM increasing in the above shown Fig. 7 (a) to (h) because of adiabatic flame temperature increased with dilution the decrease in hydrocarbon species gives rise to the reduction of N₂ and rise to NO emission.

CO Emission

Shown by Fig. 8a–h, the adiabatic flame temperature increased with a dilution of hydrogen increase up to 50%. We could see that NO PPM increasing in the above shown Fig. 8a–g because of adiabatic flame temperature increased with dilution the decrease in hydrocarbon species gives rise to CO PPM. As the methane mass fraction has reduced fuel contain reduced complete combustion of fuel has happened. We could not see drastically change in CO PPM.

CO₂ Emission

Figure 9a–h illustrates, the adiabatic flame temperature increased with a dilution of hydrogen increase up to 50%. We could see that NO PPM increasing in the shown Fig. 9a–h because of adiabatic flame temperature increased with dilution the decrease in hydrocarbon species gives rise to As the methane mass fraction has reduced fuel contain reduced complete combustion of fuel has happened. As we increasing the H₂ dilution it is but obvious the CO₂ PPM has also decreased because hydrogen did not contain the hydrocarbon particle. CO₂ PPM decreased (Table 3).

NO Emission

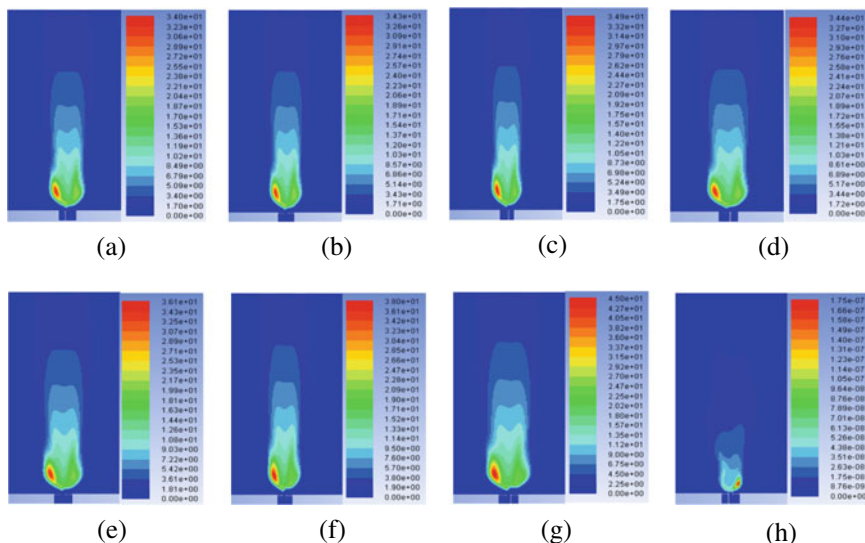


Fig. 7 Emission contour for NO PPM **a** without dilution; dilution of H₂ **b** 5%; **c** 10%; **d** 15%; **e** 20%; **f** 30%; **g** 40%; **h** 50%

CO Emission

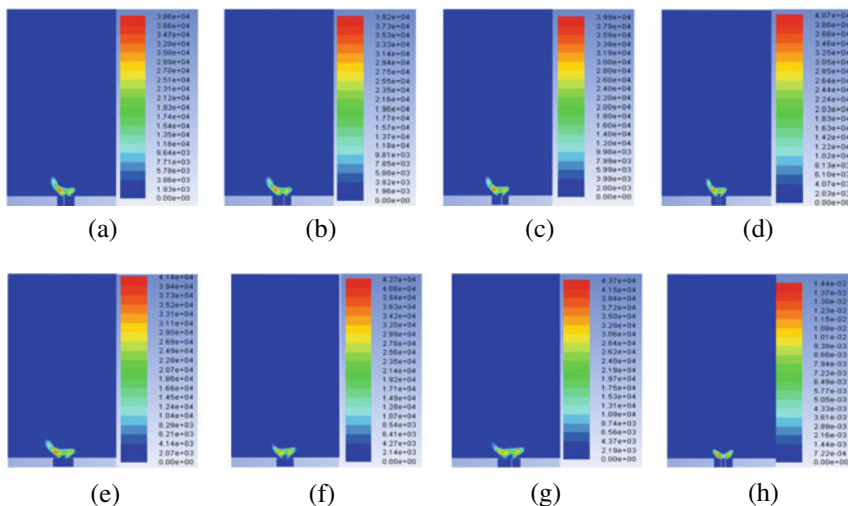


Fig. 8 Emission contour for CO PPM **a** without dilution; dilution of H₂ **b** 5%; **c** 10%; **d** 15%; **e** 20%; **f** 30%; **g** 40%; **h** 50%

CO₂ Emission

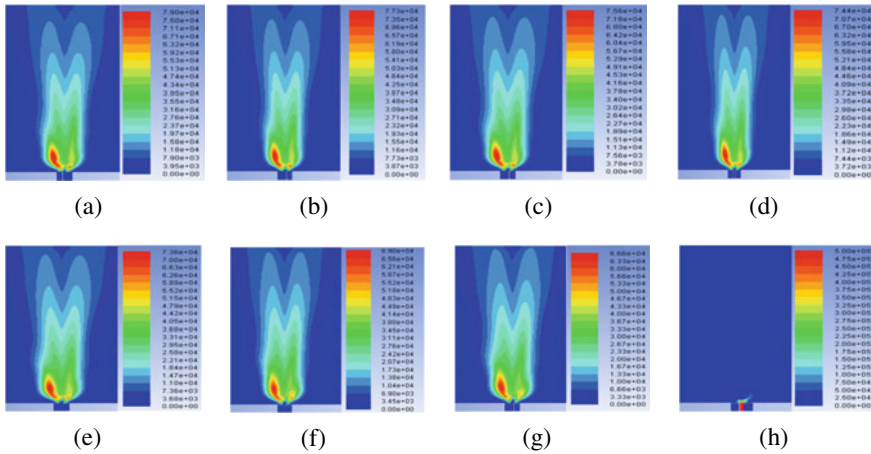


Fig. 9 Emission contour for CO₂ PPM **a** without dilution; dilution of H₂, **b** 5%; **c** 10%; **d** 15%; **e** 20%; **f** 30%; **g** 40%; **h** 50%

Table 3 Variation of emission with dilution of H₂ with different percentage

Dilution (%)	0% H ₂	5% H ₂	10% H ₂	15% H ₂	20% H ₂	30% H ₂	40% H ₂	50% H ₂
Max. NO PPM	33.96	34	34	34	36	38	44	62
Max. CO PPM	38,588	39,230	39,935	40,654	41,432	42,700	43,722	44,610
Max. CO ₂ PPM	78,966	77,236	75,561	74,394	73,635	69,205	66,646	66,178

3 Conclusions

When the hydrogen content increases, the flammability limit increases also the centre line maximum temperature increases, whereas with the CO₂ dilution overall temperature reduces due to lower equivalence ratios and heat capacity of CO₂. Knox emission is dependent upon the adiabatic flame temperature, adiabatic flame temperature decreased Knox emission decreased as adiabatic flame temperature increased the Knox emission increased. CO₂ emission increased for CO₂ dilution due to increasing concentration of carbon dioxide in the mixture and complete combustion of fuel fraction. CO emission has decreased with carbon dioxide dilution case due to complete combustion of the fuel. For hydrogen concentration, CO emission increases but not drastically.

Acknowledgements We thank Mr. Piyush Savaj for his help during this work. This work was supported by the S. V. National Institute of Technology Surat [Grant Code No. 2020-21/Seed Money/13].

References

1. Zhen HS, Leung CW, Cheung CS (2010) Thermal and emission characteristics of a turbulent swirling inverse diffusion flame. *Int J Heat Mass Transf* 53(5–6):902–909
2. Barakat H, Kamal M, Saad H, Eldeeb W (2015) Performance enhancement of inverse diffusion flame burners with distributed ports. *Proc Inst Mech Eng Part J Power Energy* 229(2):160–175
3. Chong CT, Ng JH, Aris MS, Mong GR, Shahril N, Ting ST, Zulkifli MF (2019) Impact of gas composition variations on flame blowout and spectroscopic characteristics of lean premixed swirl flames. *Process Saf Environ Prot* 128:1–13
4. Kumaran K, Shet USP (2007) Effect of swirl on lean flame limits of pilot-stabilized open premixed turbulent flames. *Combust Flame* 151:391–395
5. Chan YL, Zhu MM, Zhang ZZ, Liu PF, Zhang DK (2015) The effect of CO₂ dilution on the laminar burning velocity of premixed methane/air flames. *Energy Procedia* 75:3048–3053
6. Rajpara P, Shah R, Banerjee J (2018) Effect of hydrogen addition on combustion and emission characteristics of methane fuelled upward swirl can combustor. *Int J Hydrogen Energy* 43(36):17505–17519
7. Soloklou MN, Golneshan AA (2020) Effect of CO₂ diluent on the formation of pollutant Knox in the laminar non-premixed methane-air flame. *Int J Heat Mass Transfer* 148:119071
8. Erete JI, Hughes KJ, Ma L, Fairweather M, Pourkashanian M, Williams A (2017) Effect of CO₂ dilution on the structure and emissions from turbulent, non-premixed methane–air jet flames. *J Energy Inst* 90(2):191–200
9. Khalil AEE, Gupta AK (2015) Toward ultra-low emission distributed combustion with fuel air dilution. *Appl Energy* 148(x):187–195
10. Tripathi G, Sharma P, Dhar A (2020) Effect of methane augmentations on engine performance and emissions. *Alex Eng J* 59(1):429–439

Energy and Exergetic Analysis of Thermal Transport in Latent Heat Thermal Energy Storage Systems Impregnated with Metal Foam



Varun Joshi, Jay R. Patel, and Manish K. Rathod

Abstract A thermal performance of the metal foam impregnated phase change material (PCM) is widely evaluated based on the first law of thermodynamics. It is, however, rare to avail literature that report energetic, as well as exergetic analysis of metal foam-PCM composite (MFPC) infused latent heat thermal energy storage (LHTES) systems. The thermal performance of such system is, therefore, investigated using the first and second law of thermodynamics during the melting process in a present study. The influence of metal foam porosity on thermal transport is analysed. A numerical code is developed to realize the enhancement in thermal performance. Results show that phase change thermal transport can be improved substantially by infusion of a metal foam. The conduction as mode of heat transport dominates the melting process, while the natural convective transport is observed to be hindered with a decrease in the metal foam porosity. The metal foam with porosity of 0.97 and 0.90 improves the overall melting rate by 40% and 66.67%, respectively, compared to the pure PCM. It is observed that the reduction in the porosity eliminates the high temperature difference and, hence, an entropy generation rate/irreversibility. Subsequently, the steady state exergetic efficiency is found to be 89.20% and 97.87% using pure PCM and MFPC, respectively.

Keywords Metal foam-PCM composite · Entropy generation number · Exergy efficiency · Latent heat thermal energy storage system

V. Joshi

Department of Energy Science and Engineering, Indian Institute of Technology, Bombay 400076, India

e-mail: here.varunjoshi@gmail.com

J. R. Patel (✉) · M. K. Rathod

Mechanical Engineering Department, Sardar Vallabhbhai National Institute of Technology, Surat 395007, India

e-mail: jay.patel7693@gmail.com

M. K. Rathod

e-mail: mkr@med.svnit.ac.in

1 Introduction

Latent heat thermal energy storage (LHTES) systems with phase change materials (PCMs) have gain significant attention for the energy conservation due to its large storage density and latent heat of fusion at nearly isothermal melting temperature. These PCMs are categorized as inorganic, organic, and eutectic combination. However, the low thermal conductivity of these PCMs affects energy storage and release rate and leads to constrained applicability. Therefore, many researchers have proposed various thermal conductivity enhancers (TCE) to enhance the thermal transport rate [4]. These TCE can be extended surfaces, nanoparticles, encapsulation, heat pipes, and metallic foams. An open cellular high porosity (above 90%) metal foam has promising attributes such as excellent thermal conductivity and more heat transfer area among PCM and metal foam. A numerous investigation has been carried out, which often deal with the influence of metal foam structural characteristics including porosity, pore diameter, effective thermal conductivity, etc., on the performance characteristics of metal foam infused PCM, called metal foam-PCM composite (MFPC). A melting performance of such MFPC was analysed by Zheng et al. [12], where the copper foam is saturated with paraffins. It was noted that with the addition of metal foam, the total melting rate could be increased by 20.5% in comparison with pure paraffin. The total melting was found to be identical when heated from side and bottom walls; it was increased by 10% while heating from the top portion. Yang et al. [10] examined the impact of metal foam porosity and its location on melting process in shell and tube LHTES system. They reported that the variation in porosity did not show linear relationship with an improvement in thermal transport. A high porosity metal foam showed better natural convective transport (lower flow resistance to fluid flow). It was also said that the metal foam should be employed at the both sides (shell and tube) of the LHTES system, which reduces the total melting time by 88.54%. Al-Jethelah et al. [1] investigated the melting performance of nanoparticle enhanced MFPC experimentally. The result showed that the charging process could be accelerated by 2.61 and 28.81% with the addition of nanoparticles and metal foam in compared to a PCM without any addition.

The thermal performance of these systems was studied using an energy balance, where the first law of thermodynamics is commonly used to predict quantitative ways to increase the amount of thermal energy stored and released. However, the study becomes inadequate when the quality with which it is stored and released with TES potential is concerned. Bejan [2] quoted that the main motive of any thermal system is to store useful work, not the storage of energy. Thus, the qualitative analysis is required to perform using the second law of thermodynamics, which brings insight to degradation of energy stored and released using the concept of entropy generation, and second law efficiency. Jagdishwaran et al. [6] presented a lucid review on second law-based thermal performance study of LHTES. A second law analysis of the shell and tube LHTES was performed by Erekan and Dincer [3], which showed that the second law efficiency was significantly lesser than the energy efficiency during melting process due to external and internal irreversibilities associated with it.

Rathod and Banerjee [9] employed the concept of entropy generation minimization to study the effect of inlet temperature of heat transfer fluid, mass flow rate, and initial temperature on the entropy generation number. It was reported that the selection of melting temperature is crucial task and should be near to the optimum melting temperature. The entropy generation number was found to be minimized with a higher PCM initial temperature. Furthermore, the inlet temperature of the heat transfer fluid has a significant impact on entropy production. Similarly, the entropy generation and its distribution in such system were estimated by Guelpa et al. [5] and showed that distribution of entropy generation could assist in the fin arrangement in order to increase second law efficiency. In addition, although extensive research has been carried out on energy analysis of metal foam infused LHTES systems using the first law of thermodynamics, however, literature lacks a second law performance investigation of metal foam infused LHTES system.

Based on the above discussion, an objective is defined to present a comprehensive analysis of metal foam characteristic, porosity, which influences the melting performance, using the first and second law of thermodynamics. An in-house numerical code is developed using a local thermal non-equilibrium (LTNE) coupled enthalpy porosity method to establish the performance characteristics. The results are evaluated using a liquid–solid interface evolution, a melt volume fraction with the thermal energy storage rate, entropy generation number, and exergy efficiency. The outcome of the study depicts that the reduction in metal foam porosity enhances the phase change thermal transport with reduction in temperature gradients, hence, total melting time. In addition, the estimation of dependence of metal foam parameters on energetic and exergetic performance can assist in the qualitative selection of optimum MFPC configuration for efficient performance of LHTES system.

2 Physical System and Numerical Method

2.1 Domain Description

An experimental investigation of Zhang et al. [11], which consist of a rectangular enclosure comprising copper foam saturated paraffin, is taken into consideration. The MFPC has a height (H), length (L), and width (W) of 0.1 m, 0.1 m, and 0.01 m, respectively. The heat flux as $6207.51-0.0108t$ W/m² is given to the left side wall, while other walls are kept adiabatic. The material properties of paraffin and copper foam are adopted from their study [11].

2.2 Governing Equations

The LTNE supplemented enthalpy porosity method is solicited owing to non-ignorable attributes, where copper foam and paraffin are at thermal non-equilibrium temperature. The transport equations are as follows:

(a) Continuity equation:

$$\frac{\partial(\rho u)_p}{\partial x} + \frac{\partial(\rho v)_p}{\partial y} = 0 \quad (1)$$

(b) X momentum transport equation:

$$\begin{aligned} \rho_p \left(\frac{\partial u_p}{\partial t} \right) + \frac{\partial(\rho u u)_p}{\partial x} + \frac{\partial(\rho v u)_p}{\partial y} &= - \frac{\partial p}{\partial x} + \frac{\partial}{\partial x} \left(\mu_p \frac{\partial u_p}{\partial x} \right) \\ + \frac{\partial}{\partial y} \left(\mu_p \frac{\partial u_p}{\partial y} \right) - A_{mushy} \left(\frac{(1-f)^2}{f^3+z} \right) u_p & \\ - \frac{\mu_p}{K} u_p - \frac{1}{\sqrt{K}} C_i \rho_p u_p \sqrt{u_p^2 + v_p^2} & \end{aligned} \quad (2)$$

(c) Y momentum transport equation:

$$\begin{aligned} \rho_p \left(\frac{\partial v_p}{\partial t} \right) + \frac{\partial(\rho u v)_p}{\partial x} + \frac{\partial(\rho v v)_p}{\partial y} &= - \frac{\partial p}{\partial x} + \frac{\partial}{\partial x} \left(\mu_p \frac{\partial v_p}{\partial x} \right) \\ + \frac{\partial}{\partial y} \left(\mu_p \frac{\partial v_p}{\partial y} \right) - A_{mushy} \left(\frac{(1-f)^2}{f^3+z} \right) v_p & \\ - \frac{\mu_p}{K} v_p - \frac{1}{\sqrt{K}} C_i \rho_p v_p \sqrt{u_p^2 + v_p^2} + \rho_p g \beta (T_p - T_{ref}) & \end{aligned} \quad (3)$$

(d) Thermal energy transport equation: paraffins

$$\begin{aligned} \varepsilon(\rho C_p)_p \left(\frac{\partial T_p}{\partial t} \right) + \frac{\partial(\varepsilon \rho C_p u T)_p}{\partial x} + \frac{\partial(\varepsilon \rho C_p v T)_p}{\partial y} & \\ = \frac{\partial}{\partial x} \left((k_{pe} + k_{td}) \frac{\partial T_p}{\partial x} \right) + \frac{\partial}{\partial y} \left((k_{pe} + k_{td}) \frac{\partial T_p}{\partial y} \right) & \\ - \varepsilon L_h \rho_p \frac{\partial f}{\partial t} + h_{cup} A_{cup} (T_{cu} - T_p) & \end{aligned} \quad (4)$$

(e) Thermal energy transport equation: copper foam

$$(1 - \varepsilon)(\rho C_p)_{cu} \left(\frac{\partial T_{cu}}{\partial t} \right) = \frac{\partial}{\partial x} \left(k_{cue} \frac{\partial T_{cu}}{\partial x} \right) + \frac{\partial}{\partial y} \left(k_{cue} \frac{\partial T_{cu}}{\partial y} \right) + h_{cul} A_{cul} (T_p - T_{cu}) \quad (5)$$

Here, p is pressure, and u and v are velocity components. The independent variable, t is time, μ is dynamic viscosity, ρ is density, K is permeability, β is a volumetric thermal expansion coefficient, C_i is inertia coefficient, and T_{ref} is a reference temperature. f is liquid fraction and T_p is paraffin temperature. T_{cu} is temperature of the metal foam. ε is the metal foam porosity, L_h is latent heat of fusion, and k_{pe} and k_{cu} are an effective thermal conductivity of PCM and metal foam, respectively, C_p is specific heat, k_{td} is thermal conductivity due to dispersion, A_{cup} is interfacial surface area, and h_{cup} is an interstitial heat transfer coefficient. The detailed description of these parameters are available in a reference [7]. The subscript cu denotes copper foam. The subscript p denotes paraffin.

The volume rate of local entropy generation ($S''_{gen,local}$) can be expressed as follows:

$$S''_{gen,local} = \frac{k_{pe}}{T_0^2} \left[\left(\frac{\partial T_p}{\partial x} \right)^2 + \left(\frac{\partial T_p}{\partial y} \right)^2 \right] + \frac{\mu_p}{T_0} \left(2 \left[\left(\frac{\partial u_p}{\partial x} \right)^2 + \left(\frac{\partial v_p}{\partial y} \right)^2 \right] + \left(\frac{\partial u_p}{\partial y} + \frac{\partial v_p}{\partial x} \right)^2 \right) \quad (6)$$

The global entropy generation rate can be evaluated by integrating over a volume (V),

$$S'''_{global} = \int S''_{gen,local} dV \quad (7)$$

Thereby, the entropy generation number (N_s) and second law efficiency (η_{II}) can be estimated as,

$$N_s = \left(\frac{T_0 S'''_{global}}{Ex_{in}} \right) \quad (8)$$

$$\eta_{II} = 1 - N_s \quad (9)$$

A 2D rectangular domain with 0.1 m height and 0.1 m width is discretized using finite volume method. The SIMPLE [8] algorithm is employed to obtain the velocity and pressure field. The temperature and liquid fraction of PCM are derived by an enthalpy porosity. While, and thermal energy transport equation for metal foam are addressed separately. The fully implicit numerical code is developed, and convective terms are handled by QUICK scheme. Discretized algebraic equations are solved with the help of Gauss–Seidel successive over-relaxation via an iterative procedure.

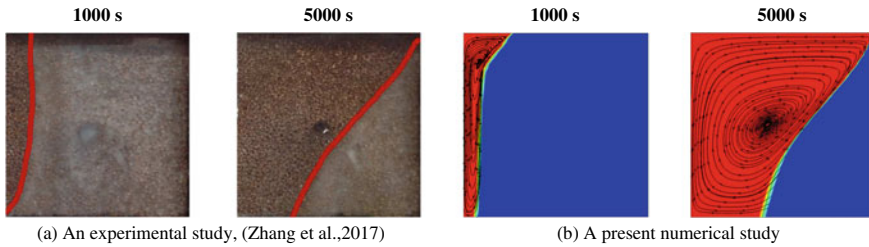


Fig. 1 Comparison of liquid–solid contours using numerical study with the experimental observations

The residual 10^{-6} is selected as the convergence criteria of governing equations. Due to the attainment of satisfactory specified convergence, the optimal grid size and time step of 10,000 cell with 0.001 s are utilized, respectively.

2.3 Validation

Figure 1 shows a comparison of the liquid–solid interface contours evolution after 1000 and 5000 s during the melting process using numerical study with the experimental observations [11]. The relative positions and morphology of the liquid–solid interfaces are found well matched with the experimental observations, and therefore developed code can be used for further study.

3 Results and Discussion

A numerical method mentioned above is used to study the influence of the variation in the porosity (from 0.97 to 0.90) on the melting performance. The temporal evolution of the liquid–solid interface for the configuration with $\varepsilon = 1$ (Configuration 0, pure PCM), $\varepsilon = 0.97$ (Configuration 1), for the configuration with $\varepsilon = 0.95$ (Configuration 2), for the configuration with $\varepsilon = 0.92$ (Configuration 3), and for the configuration with $\varepsilon = 0.90$ (Configuration 4) are shown in Fig. 2. The value 0.5 indicates the half range of mushy zone, a semi-liquid–solid region. Using a conductive method of thermal transport, the MFPC collects thermal energy from a high temperature thermal energy wall at the start of the melting process and transmits it to the surrounding solid PCM layer at a low temperature. The melting procedure begins once PCM reaches to its melting temperature. A thin line of liquid may be seen between the liquid–solid boundary and the thermal energy source wall. As the melting process proceeds, liquid PCM builds in the container's top part, which can be seen after 10 min for all designs. This ensures the naturally induced convective current. Further, a liquid PCM accumulation at the top portion decreases with the decrease in the porosity from 97

to 0.90% during the entire melting process in comparison with Configuration 0. It demonstrates that natural convective transport has been suppressed. This reduction in buoyancy-caused convective transport can be explained by the metal foam structure's limited permeability compared to pure PCM's infinite permeability. High porosity along with high permeability allows the flow of liquid PCM, and creates channelling phenomenon, and reduces the inertia force. The considerable improvement in the bottom section of the enclosure, on the other hand, can be attributed to the PCM's enhanced effective thermal conductivity. The high thermal conductivity ligaments assist to overcome thermal resistance due to poor conductive thermal transport, which results into significant improvement in the melting rate. Therefore, the conductive transport is found to be dominant as driving mechanism of phase change process over convective transport. In addition, it is to note that the increase in the metal mass concentration (decrease in a porosity) increases the melting rate.

To compare the melting rate in each configuration, the melt volume fraction is presented in Fig. 3. Due of its low thermal conductivity, pure PCM has the slowest melting rate of all the arrangements. The total time requires to melt a pure PCM is 15000 s. A profound influence of metal foam on the melting process can be seen in Configuration 1 to 4 when compared to Configuration 0 due to high effective thermal conductivity ligaments. The linearity of the curves explains the intense conductive transport that decreases thermal resistance and hence, the high temperature gradients. The overall melting time required, therefore, in Configuration 1, 2, 3, and 4 to melt paraffins is 9000 s, 7000 s, 6000 s, and 5000 s, respectively. Further, it is important to note that while decreasing the porosity of the metal foam increases the rate of fusion; it reduces a mass of the PCM and hence, the total thermal energy stored with increases the cost substantially. The overall thermal energy stored in the configuration 0, 1, 2, 3, and 4 is 417.49 kJ/kg, 404.18 kJ/kg, 396.58 kJ/kg, 384.12 kJ/kg, and 375.70 kJ/kg, respectively.

The temporal variation in the volumetric entropy generation ($S_{\text{gen,local}}''$) in different configurations has been shown in Fig. 4. The maximum $S_{\text{gen,local}}''$ can be seen during early melting period of pure PCM. This is because pure PCM has huge temperature gradients at low temperatures. After 1000 s, the temporal variation of entropy generation begins to gradually increase due to a reduction in local temperature gradients and a rise in the temperature of the PCM. Furthermore, as compared to the pure PCM, the entropy production rate of the MFPC is lower with a value of 0.97. This is due to the high metal foam thermal conductivity, which enhances the effective thermal conductivity. The low entropy generation rates indicate uniform temperature distribution hence, the lower temperature gradients/thermal resistances and more rapid the melting process. Furthermore, it is possible to see that the increase in the mass of metal (decrease in porosity) attenuates entropy generation rate/irreversibility of LHTES system. The trend of $S_{\text{gen,local}}''$ for all the MFPC configurations can be observed to be almost identical up to 3000 s. Until this period, liquid–solid interface is found in the top portion of enclosure. The significant reduction in $S_{\text{gen,local}}''$ rate in the Configurations 3 and 4 can be observed post to 3000 s when the liquid–solid interface extends to middle part of enclosure. Further reduction in $S_{\text{gen,local}}''$ rate can be observed when

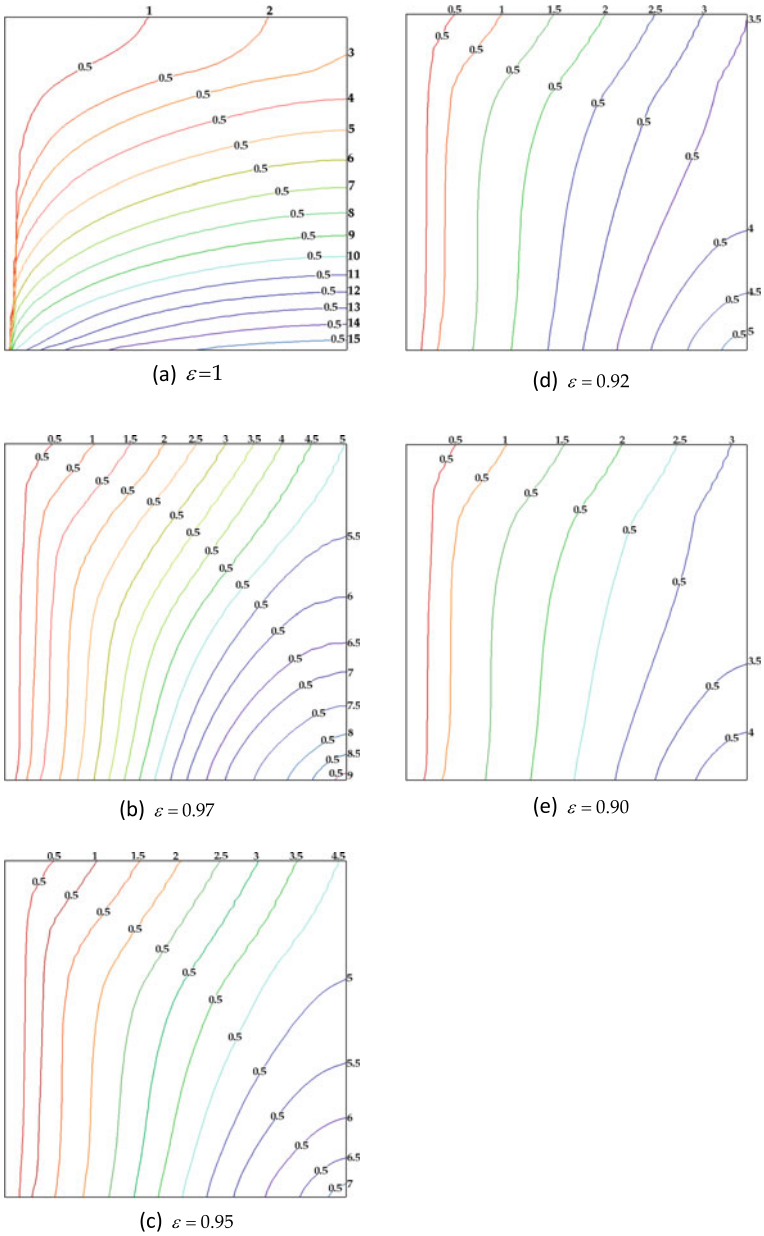


Fig. 2 Evolution of the Liquid–solid interface for the various porosities at the different time intervals ($\times 10^3$ s)

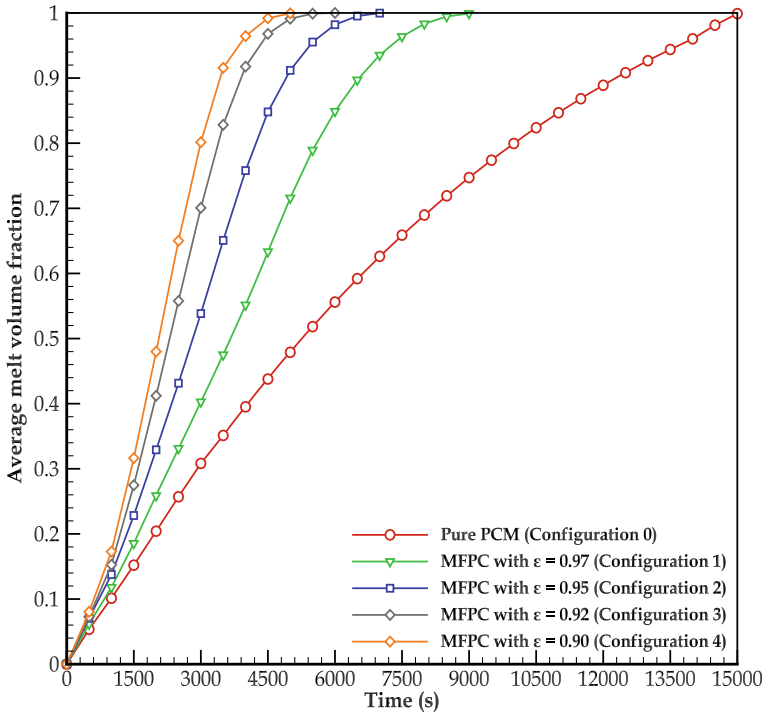


Fig. 3 History of the average melt volume fractions

the interface in the lower portion of the enclosure, especially at a final stage of the melting process. Hence, it can be concluded that the thermal transport in the MFPC can be improved by decreasing the metal foam porosity, which increases exergy of a system and results in the decrease in irreversibilities.

The entropy generation number, N_s , aids in the calculation of exergy destruction, and therefore the loss of the accessible usable part of energy, which is computed using a first law of thermodynamics. The exergy input (Ex_{in}) remains equal to flux ($6207.51-0.0108t$ W/m²) supplied at a left wall of the enclosure. As Ex_{in} is identical, no change in the trajectory of curve can be observed in Fig. 5 when compared to Fig. 4. It has been observed that the N_s is maximum for the pure PCM due to the poor conductive transport and the high temperature gradients. In addition, the decrement in the porosity metal gradually decreases N_s . The N_s for pure PCM is found to be 0.108 at steady state. The lower N_s can be observed in Configuration 4 (i.e. 0.0071), while Configuration 3 (i.e. 0.014), 2 (i.e. 0.0177), and 1 (0.0211) stand next to it. A corresponding η_{II} for Configuration 0, 1, 2, 3, and 4 are found to be 89.20%, 97.87%, 98.23%, 98.6%, and 99.29%, respectively.

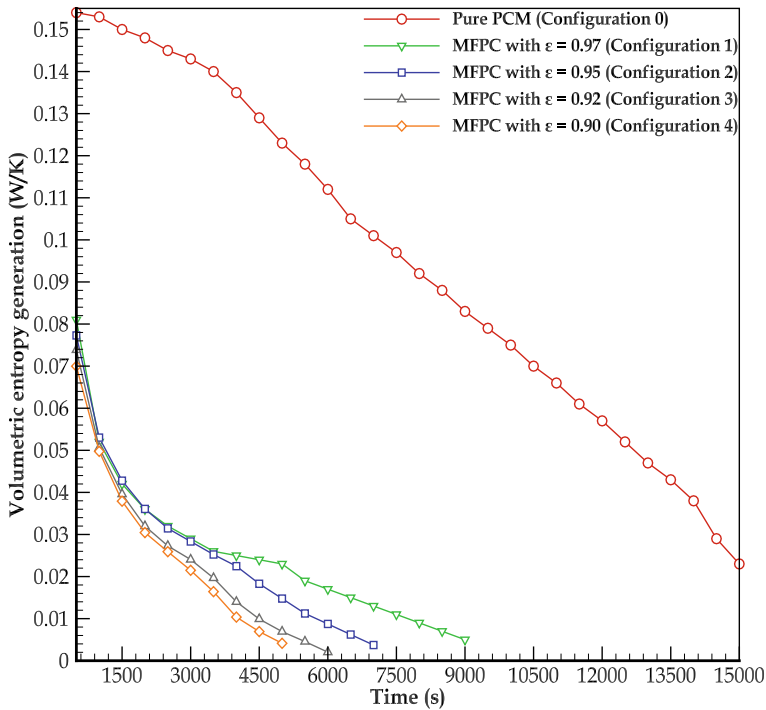


Fig. 4 History of the volumetric entropy generation

4 Conclusions

An energetic and exergetic analysis of metal foam impregnated LHTES system is carried out. The effects of metal foam porosity on the melting rate, total melting time, storage capacity, entropy generation, and exergy efficiency are estimated and compared with that of pure PCM. The results show that the decrease in porosity significantly improves the conductive thermal transport and hence, the total melting rate. The PCM melting time is reduced by 40% and 66.67% with 97% and 90% porosities of the metal foam in comparison with PCM without any addition. However, it suppresses the natural convective transport and reduces the total thermal storage capacity. Furthermore, it is seen that the incorporation of metal foam attenuates the entropy generation rate and overall second law performance. The exergy efficiency is found to be increased (with a reduction in entropy generation) with a decrease in the metal foam porosity. The maximum exergetic efficiency is observed to be 99.29% for 90% metal foam porosity among given configurations. This is owing to increased effective thermal conductivity and thermal resistance attenuation due to significant temperature gradients.

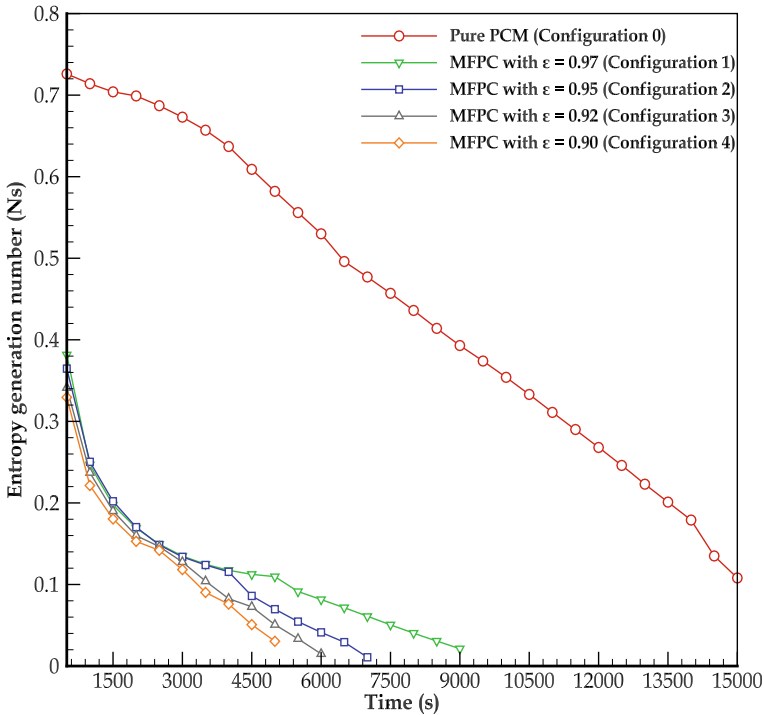


Fig. 5 Time series of the entropy generation number

References

1. Al-Jethelah M, Ebadi S, Venkateshwar K, Tasnim SH, Mahmud S, Dutta A (2019) Charging nanoparticle enhanced bio-based PCM in open cell metallic foams: an experimental investigation. *Appl Therm Eng* 148:1029–1042
2. Bejan A (2013) Entropy generation minimization: the method of thermodynamic optimization of finite-size systems and finite-time processes. CRC Press
3. Ereker A, Dincer I (2009) A new approach to energy and exergy analyses of latent heat storage unit. *Heat Transf Eng* 30(6):506–515
4. Fan L, Khodadadi JM (2011) Thermal conductivity enhancement of phase change materials for thermal energy storage: a review. *Renew Sustain Energy Rev* 15(1):24–46
5. Guelpa E, Sciacovelli A, Verda V (2013) Entropy generation analysis for the design improvement of a latent heat storage system. *Energy* 53:128–138
6. Jegadheeswaran S, Pohekar SD, Kousksou T (2010) Exergy based performance evaluation of latent heat thermal storage system: a review. *Renew Sustain Energy Rev* 14(9):2580–2595
7. Joshi V, Rathod MK (2019) Thermal performance augmentation of metal foam infused phase change material using a partial filling strategy: An evaluation for fill height ratio and porosity. *Appl Energ* 253:113621
8. Patankar SV, Spalding DB (1983) A calculation procedure for heat, mass and momentum transfer in three-dimensional parabolic flows. In: Numerical prediction of flow, heat transfer, turbulence and combustion, pp 54–73. Pergamon
9. Rathod MK, Banerjee J (2015) Entropy generation assessment of shell and tube latent heat storage unit. *Int J Exergy* 16(1):97–108

10. Yang X, Yu J, Guo Z, Jin L, He YL (2019) Role of porous metal foam on the heat transfer enhancement for a thermal energy storage tube. *Appl Energy* 239:142–156
11. Zhang P, Meng ZN, Zhu H, Wang YL, Peng SP (2017) Melting heat transfer characteristics of a composite phase change material fabricated by paraffin and metal foam. *Appl Energy* 185:1971–1983
12. Zheng H, Wang C, Liu Q, Tian Z, Fan X (2018) Thermal performance of copper foam/paraffin composite phase change material. *Energy Convers Manage* 157:372–381

Numerical Investigation on Finned Latent Heat Storage Unit



Nitish Gupta and Manish K. Rathod

Abstract Due to its high thermal energy storage density, the latent heat thermal energy storage (LHTES) system using Phase Change Material (PCM) is an outstanding choice. But the lower thermal conductivity of PCM restricts its widespread utilization. In this present report, innovative design of fins is proposed to maximize the performance of LHTES. The impact of fin form on the PCM melting process is quantified in a rectangular enclosure with a constant heat source wall temperature. The PCM substance used in the analysis is lauric acid. The temperature of the heated wall is set to 343 K. Three different configurations are considered with different shapes of fins. The results show that configuration 2 saves up to 720 s of the whole melting process. It is concluded that the shape of the fins plays a major role in the augmentation of the heat transfer process in PCM.

Keywords Phase change material · Fin shape · Melt fraction · Latent heat thermal energy storage

Nomenclature

A_{mushy}	Mushy coefficient
K	Thermal conductivity (W/m.K)
T	Temperature (K)
L	Latent heat (J/kg)
g	Gravity (m/s^2)
h	Specific enthalpy (kJ/kg)
p	Pressure (N/m^2)

N. Gupta (✉) · M. K. Rathod
Department of Mechanical Engineering, Sardar Vallabhbhai National Institute of Technology,
Surat, Gujarat, India
e-mail: gnitish93@gmail.com

M. K. Rathod
e-mail: mkr@med.svnit.ac.in

u	Velocity
t	Time (s)

Greek Symbols

ρ	Density (kg/m^3)
μ	Dynamic viscosity ($\text{kg}/\text{m}\cdot\text{s}$)
β	Thermal expansion coefficient ($1/\text{K}$)
ϕ	Liquid fraction
E	Correction number

Abbreviations

LHTES	Latent heat thermal energy storage
TES	Thermal energy storage
PCM	Phase change materials

1 Introduction

Energy storage in a form that can be turned into the required useable form is a significant difficulty. Energy storage not only decreases supply and demand mismatches, but also enhances energy performance and reliability [1]. Thermal energy storage (TES) is a form of energy storage in which a substance collects energy as its temperature rises and releases it as it cools. It works in 3 steps: charging, storing, and discharging. Latent heat thermal storage (LHTES) with PCM has become a favoured technology for thermal energy applications due to advantages such as high energy storage density and low temperature change during melting and solidification [2]. Organic, inorganic, and eutectic PCMs are the three types of PCMs. The PCM used in the design of a latent heat storage system must possess appropriate thermo physical, kinetics, and chemical properties. Various applications of LHTES with PCM are solar water heater, electronics, solar cooker, building for human comfort, solar greenhouse gas, refrigerator and AC, cold storage, and defence [3]. But the main problem associated with PCM is their low conductivity; due to this reason, heat storage and retrieval rate of PCM are very low which limit their practical application. As a result, several thermal enhancement techniques should be used to improve PCM's thermal conductivity [4]. Many researchers proposed different enhancement techniques like adding of high conductivity fin [5–7], adding single or hybrid nanoparticles to the PCM, microencapsulation [8], multiple PCM used in the study, and porous media.

Several recent advancements in thermal enhancement techniques, such as adding fins and nanoparticles [9], combine two of the preceding methodologies to improve the heat transfer performance of the system.

In comparison with other enhancing procedures, insertion of metal fins into the PCM is simple, quick, and inexpensive and results in a uniform temperature field. As a result, numerous researchers have been drawn to this method to explore and improve fin design. Qin et al. [2] quantitatively investigated the effect of fin placement on the PCM melting process in a rectangular enclosure and discovered that the bottom fin location provides the best heat transfer enhancement performance and reduces melting time by 3.6% when compared to the top fin location. According to Kamkari and Shokouhmand [10] experimental study of PCM melting in a rectangular enclosure with horizontal partial fins, increasing the number of fins decreased the melting time while increasing total heat transmission, and their results show that the total melting time for 1 fin and 3 fins is 18 and 37% less than an unfinned enclosure, respectively. Sinaga et al. [11] used the shape and position of fins to quantitatively analyse the melting performance of a thermal storage system, finding that fins in the lower half of the enclosure may achieve 1800s less melting time than fins in the upper half of the enclosure. Furthermore, when it comes to the effect of fin shape, triangular fins have accomplished 1000 s less melting time than rectangular-shaped fins. The melting performance of PCM thermal energy storage with unique stepped fins was quantitatively explored by Nakhchi and Esfahani [12]. To improve the melting process, they looked at several upward- and downward-stepped fins with varying stepped ratios, and their findings revealed that the melting process in all stepped fins is faster than in typical horizontal fins. For all types of the stepped fin, downward-stepped fin could enhance the melting up to 56.3% at 800 s as compared to conventional horizontal fin. The constructal amplification of thermal transport in a fin-assisted latent heat storage system was numerically analysed by Joshi and Rathod [13]. The study's main goals were to reduce fin size and reposition fins in high heat potential zones to reduce melting time. According to the findings, halving the fin-to-PCM volume ratio increased melting fraction by 6.34 per cent and total absorbed energy by PCM by 4.38 per cent when the fin-to-PCM volume ratio was reduced by half. In a rectangular enclosure, Tian et al. [14] studied the influence of fin materials such as copper, aluminium, carbon steel, and steel302 on PCM melting. Their findings showed that by inserting copper fins melting time was reduced by 41.6% as compared to no fin scheme.

Based on the aforementioned literature research, it is discovered that while the use of fins improves heat transfer, the rate of natural convection is impeded. It creates obstruction to the natural convection current. Thus, in the present study, the innovative shape of the fins is proposed that enhances the natural convection that results in higher melting rate of PCM. As a result, in this research, a 2D rectangular model is used to mimic the melting of PCM. Natural convection is taken into account while creating a transient, phase change numerical model. Different parameters including liquid fraction, temperature distribution, total melting time, and absorbed heat during the charging process are investigated.

Table 1 Physical properties of PCM and fin [10]

PCM	Lauric acid
Melting temperature range(°C)	43.5–48.2
Latent heat of Fusion (J/kg)	187,210
Density (kg/m^3)	940(solid)/885(liquid)
Heat capacity (J/kg.K)	2180(solid)/2390(liquid)
Conductivity (W/m.K)	0.14(solid)/0.16(liquid)
Kinematic viscosity (m^2/s)	6.7×10^{-6}
Thermal expansion coefficient (1/K)	0.00005
Fins	Aluminium alloy
Conductivity thermal (W/m K)	130

2 Model Construction

2.1 Problem Descriptions

A two-dimensional rectangular body with a width of 50 mm and a height of 120 mm makes up the geometric model. On the right side of the enclosure, a triple fin constructed of aluminium alloy (aluminium silumin) is joined to the source wall. The right wall of the heater is isothermally heated to a constant temperature of 70 °C, and the heater plate is 5 mm thick. The container's surface, as well as the top and bottom walls of the heater, is adiathermic. The fin area is taken as 300 mm², and the area of PCM remains constant in all the cases. The fins are installed in such a way that there is no heat resistance between the contact surface and the fin base. Lauric acid is selected as a PCM material, and its properties are shown in Table 1. PCM's starting temperature is set to 25 °C (Table 1).

It should be emphasized that the area of the PCM and the fin stay constant in order to make the results comparable. Because the arithmetic field is two-dimensional, the length of the model plane's third dimension is assumed to be unity. The dimensions and configurations of different case studies are shown in Fig. 1.

2.2 Governing Equations

To model the melting of PCM in the rectangular container, an enthalpy porosity approach is applied [15]. In this way, the mushy zone is viewed as a porous medium, with the volumetric component of each cell representing the porosity of each cell. Solid regions are given a porosity of 0 in this method, while melted parts are given a porosity of 1. Numerical model is based on the following assumption.

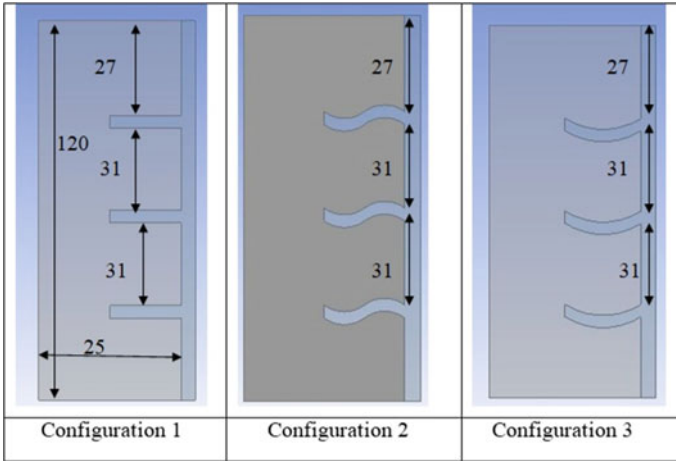


Fig. 1 Configuration of different shapes of fins

- Two-dimensional, unsteady state and laminar
- PCM is incompressible and Newtonian in its liquid
- Constant thermal physical properties
- PCM volumetric expansion after melting is not considered
- Viscous dissipation and thermal radiation are also neglected.

To account for the buoyancy-driven convective flow, the Boussinesq approximation is applied. The term density is determined in the momentum equation as follows using this method.

$$\rho = \frac{\rho_l}{\beta(T - T_l) + 1} \tag{1}$$

where T_l is the PCM melting temperature and β is the thermal expansion coefficient.

Based on the assumptions made, the governing equations, which comprise the continuity, momentum, and energy equations, can be stated as follows:

$$\frac{\partial \rho}{\partial t} + \nabla \cdot (\rho \vec{u}) = 0 \tag{2}$$

$$\frac{\partial(\rho \vec{u})}{\partial t} + \nabla \cdot (\rho \vec{u} \vec{u}) = \mu \nabla^2 \vec{u} - \nabla p + \rho \vec{g} + \vec{S} \tag{3}$$

$$\frac{\partial(\rho H)}{\partial t} + \nabla \cdot (\rho \vec{u} H) = \nabla \cdot (K \nabla T) \tag{4}$$

Here, the time is t , the velocity vector is \vec{u} , the gravitational acceleration is \vec{g} , and the pressure is p .

In the momentum Eq. (3), the source term \vec{S} is given by

$$S = -A_{\text{mushy}} \left\{ \frac{(1 - \emptyset)^2}{\emptyset^3 + \epsilon} \right\} V \quad (5)$$

On the right side of momentum transport equations, the peripheral velocity source term appears (3) and is employed in the computational continuum to distinguish the liquid–solid area of PCM. The ‘pseudo’ flow motion of PCM through porous material is used to investigate the transport mechanism of PCM. The mushy zone constant is represented by the parameter A_{mushy} , and a greater value for this parameter accelerates the velocity decrease to zero during the solidification process. It varies between 10^4 and 10^7 and sets at 10^5 in the present study. \emptyset is the fluid volume fraction of the cell. When the substance in the cell is a solid, ϵ is a modest number on the order of 0.001 to avoid division by zero.

The enthalpy of PCM is the sum of the sensible enthalpy h and the latent enthalpy H and is calculated as

$$H = h + \Delta H \quad (6)$$

Considering no variation in c_p , h is the sensible heat and is calculated as

$$h = h_{\text{ref}} + \int_{T_{\text{ref}}}^T c_p \Delta T \quad (7)$$

h_{ref} is the reference enthalpy at T_{ref} , and ΔH is the latent heat and is calculated as

$$\Delta H = L\emptyset \quad (8)$$

The liquid fraction \emptyset used in the above equation can be found out by the following relation

$$\begin{aligned} \emptyset &= 0 \quad \text{if } T < T_{\text{solidus}} \\ \emptyset &= \frac{T - T_s}{T_l - T} \quad \text{if } T_{\text{solidus}} < T < T_{\text{liquids}} \\ \emptyset &= 1 \quad \text{if } T_{\text{liquids}} < T \end{aligned} \quad (9)$$

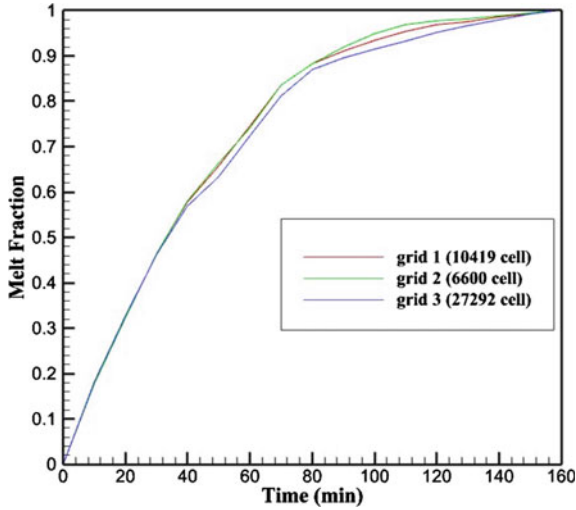


Fig. 2 Mesh independency checking of cell 10,419, 6600, and 27,292

2.3 Numerical Method and Grid Independency Test

Simulations are performed using ANSYS FLUENT 2020 R2 software. Pressure-based couple algorithm is adopted to solve the continuity and momentum equation. To calculate the connection between pressure and velocity, the SIMPLE algorithm is used. The gravitational vector was set to be $-9.81 \text{ m}^2/\text{s}$ in the downward direction for the effect of natural convection. The velocity, energy, pressure, and liquid fraction under relaxation value factors are set to 0.2, 1.0, 0.3, and 0.9, respectively. For the continuity equation, the residuals are less than 10^{-9} , and for the momentum and energy equations, they are less than 10^{-6} . For better consistency of the simulation, grid study is employed for the simulation. Three alternative cell numbers of 6600, 10,419, and 27,292 are used to validate the mesh independency analysis (refer Fig. 2). The melt fraction values linked with three cell counts do not differ significantly, according to the data. For the following simulations, the cell number 10,419 is used. Three-time increments of 0.05 s, 0.1 s, and 0.2 s are also used for time independency analysis. Thus, time step of 0.1 s is taken for the subsequent simulation.

2.4 Model Validation

The precision with which the data collected in this investigation for the fin-configured test section is validated with the experimental result of Joshi and Rathod [16]. In the experimental study, a LHTES system which consists of rectangular enclosure whose size is $150 \times 100 \times 200$ was developed. The left side is maintained at a temperature

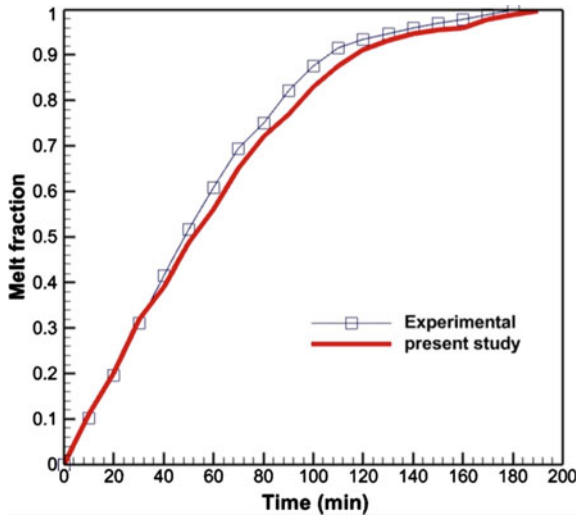


Fig. 3 Validation results with Joshi and Rathod [16]

of 85 °C, and other walls are well adiabatic insulated. The melt fraction and contours against time are compared in Fig. 3.

There is little deviation (approx. 6%) between the contours of the present study and study carried out by Joshi and Rathod [16] in the initial stage, but in the later stage this deviation is increased up to 13%. This is due to the reason that in experimental setup, the heated left wall transfers the heat to the bottom and top plate (that is considered as fin). Further, there is a heat loss to the environment though there is appropriate insulation provided. However, on the other hand perfectly insulation is considered in the numeric analysis. A set of contours is also shown in Fig. 4 to help with comparisons between numerical and experimental data.

3 Results and Discussions

3.1 Analysis of Melt Fractions

The impact of fin position and form on melting process enhancement is examined in this section. The melt fraction (M_f) is one of the most critical characteristics that might affect the position and shape of the fin during the charging and discharging process. Melt fraction is represented by Eq. (5)

$$M_f = \iint \frac{S(T > 321.2K)}{S(\text{initial})} dx dy \quad (10)$$

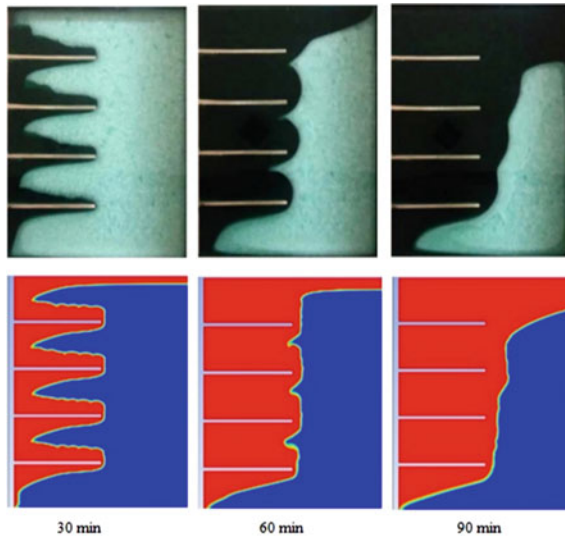


Fig. 4 Comparison of contours with Joshi and Rathod [16]

The $S (T > 321.35 \text{ K})$ is the zone that has reached melting point and is liquid. The S (initial) represents the process’s first solid surface.

3.2 Melting Process is Influenced by the Shape of the Fins

Figure 5 represents variations of melt fraction with time for 3 configurations that have been compared in this study. All fin designs feature a straight melt fraction shape with a steep slope up to 30 min. After 30 min, the melt fraction takes on a curved shape with a downward slope in all situations. Between 30 and 80 min, the declining slopes of the configurations 2 and 3 almost remain constant. The configuration 1 with rectangular fins has the highest rate of decline. In configuration 2, melting fraction of 1 is reached faster than others. Configuration 1 takes 160 min to complete the full melting of PCM, configuration 2 takes 148 min to complete the melting, and similarly, configuration 3 takes 155 min. As a result of this investigation, it can be concluded that configuration 2 takes 7.5 per cent less time to melt than configuration 1. When compared to configuration 1, configuration 3 takes 3.125 per cent less time. The same can also be reflected in Fig. 6. It shows the contour of melt fraction with time.

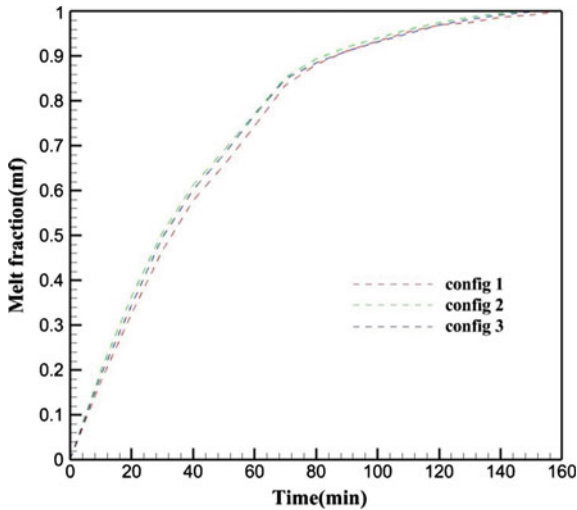


Fig. 5 Comparison of melt fraction for three configurations 1, 2, and 3

Looking at Fig. 6, it could be observed that configuration 2 melts more quickly than configurations 1 and 3. The temperature contours at different time intervals, as illustrated in Fig. 7, are a great explanation for this occurrence. Looking at Fig. 7, at 80 min. configuration 2 reaches the maximum temperature as compared to configurations 1 and 3. This is due to the design of new type of fin that promotes natural convection quickly as compared to the simple type of fin. The new design of fins assists the natural current to move upward direction due to density difference.

4 Conclusions

The effect of fin form on the PCM melting process in a rectangular geometric body with a constant heat source wall temperature was quantified in this work. The model validation inquiry is complete, and the numerical findings were reasonably accurate in matching the experiment data from the literature. The PCM substance used in the analysis is lauric acid. The melting process is simulated using the enthalpy porosity approach. Three different configurations are considered. For the effect of fin shape, configuration 2 shows better results. It was found that configuration 2 saves up to 720 s of the whole melting process as compared to configuration 1.

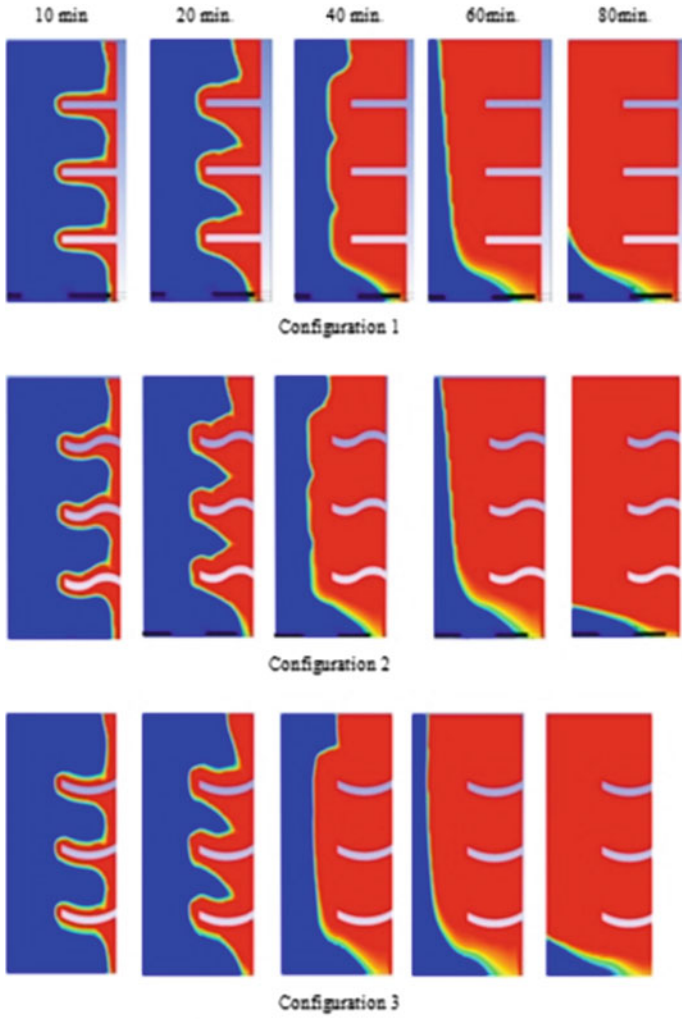


Fig. 6 Contour of melt fraction on the basis of shape of fin

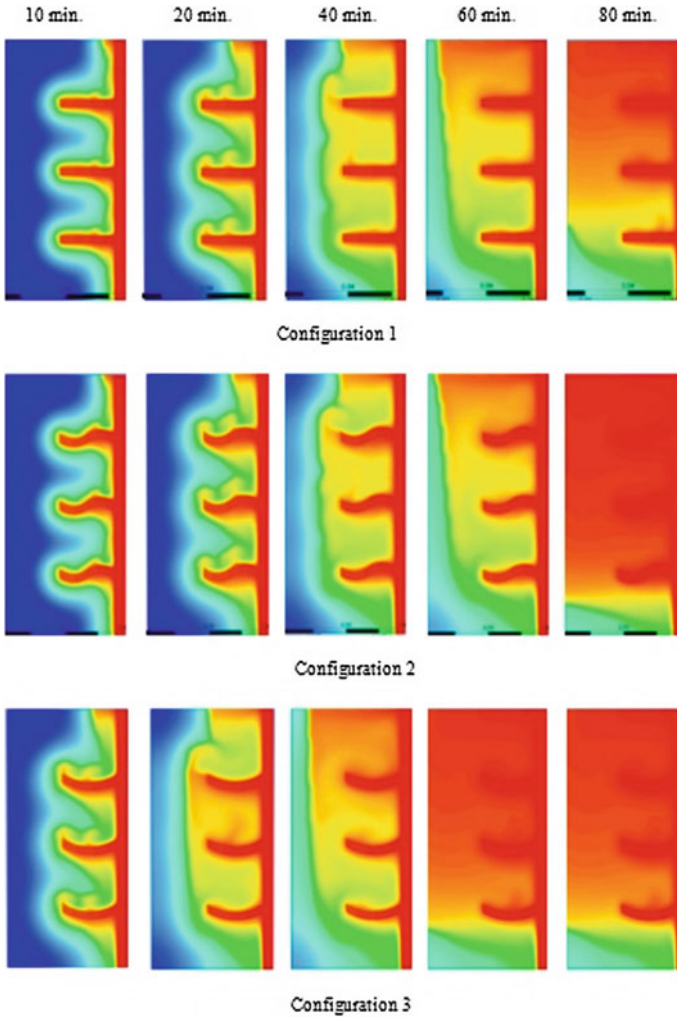


Fig. 7 Contours of temperature for three configurations

References

1. Gawande AM, Wasokar AP (2016) Thermal energy storage by phase change material. *Int Res J Eng Technol* 03:149–152
2. Qin Z, Ji C, Low Z, Dubey S, Choo FH, Duan F (2017) Effect of fin location on the latent heat storage: a numerical study. *Energy Procedia* 143:320–326
3. Ali S, Deshmukh SP (2020) An overview: applications of thermal energy storage using phase change materials. *Mater Today: Proc* 26:1231–1237
4. Watanabe T, Kanzawa A (1992) Enhancement of charging and discharging rates in latent heat storage system by use of PCM. *Heat Recovery Syst* 13:57–66

5. Ding P, Liu Z (2021) Numerical investigation of natural convection enhancement in latent heat energy storage units with punched-fin and slit-fin. *Int J Therm Sci* 163:106834
6. Duan J, Xiong Y, Yang D (2020) Study on the effect of multiple spiral fins for improved phase change process. *Appl Therm Eng* 169:114966
7. Mehta DS, Vaghela B, Rathod MK, Banerjee J (2020) Enrichment of heat transfer in a latent heat storage unit using longitudinal fins. *Heat Transf*, 1–27
8. Irani F, Ranjbar Z, Moradian S, Jannesari A (2017) Microencapsulation of n-heptadecane pcm with starch shell. *Prog Org Coat* 113:31–38
9. Sheikholeslami M, Haq R, Shafee A, Li Z, Elaraki YG, Tlili I (2019) Heat transfer simulation of heat storage unit with nanoparticles and fins through a heat exchanger. *Int J Heat Mass Transf* 135:470–478
10. Kamkari B, Shokouhmand H (2014) Experimental investigation of phase change material melting in rectangular enclosures with horizontal partial fins. *Int J Heat Mass Transf* 78:839–851
11. Sinaga N, Moria H, Heidarshenas B (2021) Melting performance enhancement of thermal storage system by utilizing shape and position of double fin. *Case Studies Thermal Eng* 23:100813
12. Nakhchi ME, Esfahani JA (2020) Improving the melting performance of PCM thermal energy storage with novel stepped fins. *J Energy Storage* 30:101424
13. Joshi V, Rathod MK (2019) Thermal performance augmentation of metal foam infused phase change material using a partial filling strategy: an evaluation for fill height ratio and porosity. *Appl Energy* 253:113621
14. Tian L, Liua X, Chenc S, Shena Z (2020) Effect of fin material on PCM melting in a rectangular enclosure. *Appl Therm Eng* 167:114764
15. Voller VR, Prakash C (1987) A fixed grid numerical modelling methodology for convection-diffusion mushy region phase-change problems. *Int J Heat Mass Transf* 30:1709–1719
16. Joshi V, Rathod MK (2020) Experimentation and numerical assessments of thermal transport in fins and metal foam infused latent heat thermal energy storage system: review. *Appl Therm Eng* 178:115518

Material Recovery from End-of-Life Solar Photovoltaic Module Through Thermal and Chemical Processes



Aparna Singh, Ahmed Ali Kabir, Sachin Gupta, Jyotsna Singh,
and R. B. Singh

Abstract The expected life of photovoltaic (PV) modules is 10–20 years as solar modules degrades over the course of time. This degradation is mainly due to the water ingress, ultra violet (UV) rays exposure and temperature stress. The module failure indicators include delamination of the module encapsulation, anti-reflection coating deterioration, discolouration of Ethylene Vinyl Acetate (EVA), glass breakage, open/short circuit failure, hot spot failure and bypass diode failure. The most valuable element utilized in terms of economics is pure silicon, which can be recycled from PV cells. Pure silicon may be recovered from broken or end-of-life PV modules, which can have both financial and environmental advantages. Because of the high purity required of the recovered silicon, chemical treatment is the most critical stage in the recycling process. This work used a variety of etching techniques to etch electric connections, anti-reflective coating and the *p-n* junction in crystalline-Si(c-Si)-based PV systems which require nitric acid, potassium hydroxide and hydrofluoric acid. Also, the study contains the comparison between thermal and chemical processes availed for the removal of EVA. The thermal process has been performed using a muffle furnace where the samples have been heated at different temperatures 250, 350, 375 and 400 °C at a rate of 15 °C/min. The intact solar cells have been gathered after the heating process and then chemical processes to remove coatings have been performed. Whereas the chemical process for EVA removal required the use of chemical solvents like acetone, ethanol, trichloroethylene and nitric acid in which cells have been immersed. An oven and heat gun has been used to remove the Tedlar sheet. Lastly, the bare silicon wafers obtained from the processes have been collected and tested to confirm the removal.

A. Singh · J. Singh · R. B. Singh

Centre of Excellence in Renewable Energy Education and Research, University of Lucknow (New Campus), Lucknow 226021, India

A. A. Kabir

Département de Physique, Faculté des Sciences Exactes et Appliquée, Université de N'Djaména, N'Djaména, Tchad

S. Gupta (✉)

Sardar Patel Renewable Research Institute, V V Nagar, Gujarat, India

e-mail: sachin.energy123@gmail.com

Keywords Ethylene vinyl acetate disposal of photovoltaic cell · Degradation of modules · Pure silicon · Recycle

1 Introduction

The energy demand of the world is increasing at an alarming rate, causing the fast depletion of conventional energy sources. India has a 4.8% global share in electricity generation making it the world's third-largest producer of electricity in 2013. 80% of the coal produced in the country is consumed by the electricity sector. Renewable energy sources serve as an alternative to meet up the escalating energy demands and also significantly reduce carbon dioxide emissions. The Government of India aims to generate 175 GW energy capacity from renewable energy sources by 2022. Generation of 100 GW energy capacity from solar power, 60 GW from the energy of the wind, 10 GW energy capacity from biomass and 5 GW from small hydropower are the set objectives.

PV generating percentages in the entire power generation mix has increased significantly over the previous decade, from 0.2% in 2010 to 2% in 2018, with a 94 GW annual rate. As a result, installation costs have decreased from 4621 USD per kW in 2010 to 1210 USD per kW in 2018 [1]. The total installed PV capacity was 500 GW at the end of 2018, and it is anticipated to quadruple by 2022–2023, reaching 10 TW in 2030 and 30–70 TW by 2050 [2–4]. Solar photovoltaic module (SPV) energy has the potential to not only satisfy the rising global need for power but also to do it without the enormous environmental costs associated with burning fossil fuels. When compared to coal, each gigawatt-hour of PV-generated electricity avoids up to 10 tonnes of SO₂, 4 tonnes of NO₂, 0.7 tonnes of particulates (including Cd and As) and up to 1000 tonnes of CO₂ emissions (NREL [5]). Apart from the numerous benefits of the SPV, it has one issue. SPV module has an expected life of 10–20 years and then will have to dispose of or reused in some way. SPV modules have some toxic materials (like Cd, Pb and Se). So, disposing of SPV modules in a landfill may create environmental issues. Recycling end-of-life SPV modules is one of the solutions to such an issue. However, the damaged and end-of-life modules contradict being the green technology as it is considered in Waste Electrical and Electronic Equipment (WEEE). The best solution to handle them is the recycling method. The recycling method not only prevents toxic metals from contaminating the environment but also saves energy and cost used in the manufacture.

Furthermore, in 2012, the European Commission (EC) published the WEEE Directive (2012/19/EU, EU 2012), which state at least 85 per cent material must be recovered and 80 per cent must be recycled, it also includes PV waste [6].

Nowadays, crystalline PV base technology is most popular [7, 8]. A schematic of solar cell fabrication has been shown in Fig. 1. Crystalline-Si PV cells are fabricated in the form of silicon wafers. Firstly, a *p-n* junction is created on the front surface of these wafers and this layer is afterwards coated with an anti-reflective coating. The next stage involves forming two conductors made of silver paste and aluminium on the

front and back surfaces of the wafer, respectively. Further the process of lamination of solar cells after forming the $p-n$ junction layer is involved. Solar cell and electric connectors generally composed of c-Si, Ag and Al are sandwiched among two layers of encapsulation, which are generally formed of ethyl vinyl acetate. The layers in the front and rear are generally constructed of glass and polyvinyl fluoride (Tedlar), respectively [9, 10]. An aluminium frame holds the layers together. Commonly, SPV modules contain 75–80% glass, 10% encapsulant and back sheet, 10% aluminium, 3–5% Si, 1% connectors, less than 0.1% silver and others metals [11].

Some of the PV recycling technologies studied worldwide has been discussed below with their advantages and disadvantages (Table 1).

In order of mass, PV modules of crystalline-Si solar cells are made up of the elements hereinafter: junction box, aluminium frame, glass, Tedlar protective sheet,

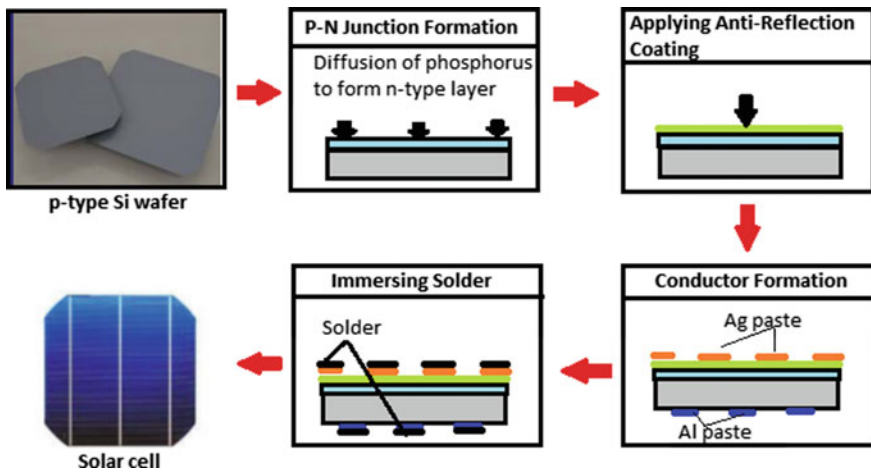


Fig. 1 Conventional procedures of Si solar cell fabrication

Table 1 Developed silicon solar modules recycling processes

Process	Status	References
Organic solvent dissolution	Research	[13]
Organic solvent and ultrasonic irradiation	Research	[14]
Electro-thermal heating	Research	[15]
Mechanical separation by hotwire cutting	Research	[16]
Pyrolysis (conveyor belt furnace and fluidized bed reactor)	Research (pilot)	[17]
Solvent (nitric acid) dissolution	Research (pilot)	[18]
Physical disintegration	Commercial	[19]
Two-step thermal heating	Commercial	[20]
Chemical etching	Commercial	[21]

EVA transparent layer, photovoltaic cells and assembly bolts. Disassembling of PV modules in the recovery process is done according to the flowchart presented in Fig. 1. The thermal process to remove the Tedlar sheet is subsequently carried out after separating the junction box and aluminium frame mechanically. The next step is the delamination of EVA which can be done thermally as well as chemically. Then, the silicon solar cells are etched to get wafers in the chemical process in which the silicon and the silver have also recovered. The recovered silicon from processes mentioned might be used as a raw material in the PV modules again, or as a supplement to change mechanical properties of steel by amalgamating it, and as a ceramic material, depends on the purity of silicon in non-metal powders manufactured. The profitability analysis [12] of solar cell recycling has been performed. It showed that the recycling cost and total profit for recycling of 1 kg of solar cell is \$68.9 and \$185.428, respectively.

In this study, we focused on the feasibility of the process of recycling Si wafer and glass. To reduce the hazardous waste generation during Si wafer recycling a process has also been developed.

2 Experimental

Here, a broken multi-crystalline solar module (p-type) of dimensions 225 mm × 175 mm ($L \times W$) containing 20 solar cells have been used for the recovery process where mechanical, thermal and chemical processes have been performed subsequently to obtain high purity of recovered Si wafer. The aluminium frame and junction box have been removed mechanically. The different layers (Tedlar sheet and EVA) of solar panels have been separated by thermal and chemical treatment.

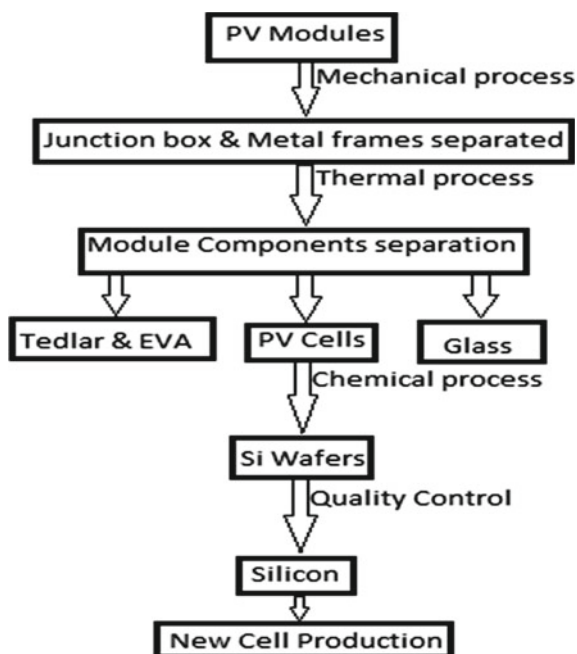
2.1 Thermal Treatment

The electrical oven and heat gun were used for the thermal treatment of the Tedlar sheet. The module was heated in the oven which has an on-off temperature controller. After heating in the oven or with the heat gun the Tedlar was peeled off from the module. Then the module was placed in the muffle furnace with the backside of the panel facing up. After heating at 400 °C for 30 min, the intact solar cells were gathered.

2.2 Chemical Treatment

The above-mentioned process was repeated till the removal of the Tedlar sheet. Then the module was immersed in nitric acid at room temperature for 7 days before intact cells with completely removed EVA were collected. The alternate method taken was

Fig. 2 Processes to recycle Si wafer from solar PV module



placing the module immersed in nitric acid in the oven which gave the required result in 24 h at 80 °C. The collected solar cells were chemically treated to obtain Si wafers. The conductors of silver (Ag) and aluminium (Al) have been etched out with nitric acid (HNO_3) and potassium hydroxide (KOH), respectively. Also, the anti-reflective coating of silane was removed by hydrofluoric acid (HF). The HNO_3 and KOH treated solutions have been analysed by atomic absorption spectroscopy (AAS) using a 3300 Spectrometer (Biotech Park, Lucknow, Uttar Pradesh) to evaluate the amount of Ag and Al extracted from the cells. By comparing the results, the amount of silicon and silver recovered can be known. This also confirms that coatings have been etched out.

We have used different processes to remove the different layers of the solar module as in Fig. 2. Various instruments and chemicals have been used in these processes as listed in Tables 2 and 3.

2.3 Separation Process of Junction Box and Metal Frames

The junction box, aluminium frame and cables have been separated mechanically which are attached with the help of adhesive glue (Silica gel). Mechanical separation is the only method to remove them without damage. The advantages of this method are the glass can be recovered, the aluminium frame recovered is intact and could

Table 2 Specification of instruments used in experimentation

S. No.	Instrument	Model	Make	Specification
1	Oven	SSI-111	U-Tech	Temperature range: 50–200 °C Rated input power: 1500 W Temperature controller:
2	Heat gun	GHG 180	Bosch	Temperature range: 60–550 °C Rated input power: 1800 W Temperature controller: on–off
3	Muffle furnace	STXMF1128	Stericox	Temperature range: 250–1100 °C Rated input power: 2000 W Temperature controller: programmable

Table 3 Specification of chemicals used in experimentation

S. No.	Chemical	Make	Specification
1	Acetone	Merck	Purity: 95% Density: 0.79 (gm/cm ³) Boiling point: 56 °C
2	Ethanol	Generic	Purity: 99.9% Density: 0.79 (gm/cm ³) Boiling point: 78.2 °C
3	Trichloroethylene	Laballey	Purity: 99.9% Density: 1.46 (gm/cm ³) Boiling point: 87.2 °C
4	Nitric acid	Merck	Purity: 65% Density: 1.39 (gm/cm ³) Boiling point: 121 °C
5	Potassium hydroxide	Merck	Purity: 30% Density: 1.51 (gm/cm ³) Boiling point: 145 °C
6	Hydrofluoric acid	Merck	Purity: 40% Density: 1.13 (gm/cm ³) Boiling point: 111 °C

be used again, and also the junction box could be used again. The whole process of recycling could be mechanical but the disadvantage is it could cause breakage of solar cells, no removal of dissolved solids and incomplete removal of EVA. For the complete removal of EVA, other separation processes are required. Therefore,

thermal and chemical processes foster the recycling of waste photovoltaic modules along with the mechanical process.

2.4 Separation Processes of Solar Cell and Glass

To separate the glass and solar cells from each other removal of Tedlar and EVA is essential. In this study to remove the Tedlar and EVA thermal and chemical methods has been used.

2.4.1 Amputation of Tedlar Sheet

Tedlar is a thermoplastic fluoropolymer material with great weather resistance and inherent strength, low moisture, vapour and oil permeability and can operate at temperatures ranging from $-70\text{ }^{\circ}\text{C}$ to $+110\text{ }^{\circ}\text{C}$. Tedlar is laminated in the PV module at a temperature of $120\text{ }^{\circ}\text{C}$. To remove the Tedlar sheet, we need to heat it at medium temperature. This heat can be provided by using a heat gun or Oven.

- In the oven at $150\text{ }^{\circ}\text{C}$ for 3 h.
- Heat gun.

After getting heated, the Tedlar sheet is easily peeled off and separated from the solar cells.

2.4.2 Amputation of Ethylene Vinyl Acetate (EVA)

EVA sheet works as an adhesive that attaches the solar cell with glass and a Tedlar sheet. It becomes transparent and allows for a high degree of light spectrum permeability after heating it at $120\text{ }^{\circ}\text{C}$ in a vacuum. To isolate solar cells from glass, removal of EVA sheet is essential which can be removed by using thermal as well as chemical processes. In this study, both of the processes have been studied to remove the EVA.

(i) Thermal Process

A small piece of a broken solar module has been put in the muffle furnace facing glass downwards and back sheet facing upward. The samples have been heated at different temperatures 250, 350, 375 and $400\text{ }^{\circ}\text{C}$ at a rate of $15\text{ }^{\circ}\text{C}/\text{min}$. The intact solar cells have been gathered after the heating process.

(ii) Chemical Process

The thermal process emits high toxic gases so the chemical dissolution of the EVA sheet has been carried out. Effect of various chemicals such as acetone, ethanol and trichloroethylene has been used to dissolve the EVA sheet in different conditions has been studied.

2.5 Recovery of Silicon Wafer

A solar cell consists Si wafer, conductors made of Ag and Al and an anti-reflective coating (SiN_x). Ag and Al must be retrieved from the electrodes and SiN_x layers must be removed to recover the Si wafer from a solar cell. To remove different metal coatings, chemical etching has been opted. 65% Nitric acid (HNO_3) has been used to etch out silver (Ag) coatings, 30% potassium hydroxide (KOH) etches out aluminium (Al) coatings from the rear and back surface, respectively, and 40% hydrofluoric acid (HF) etches anti-reflective coating (SiN_x) layer.

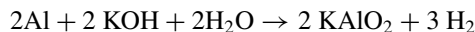
2.5.1 Removal of Silver Coatings

When the damaged solar cells are treated with nitric acid, the silver present in solar cells reacts with nitric acid and forms silver nitrate. Further, it is possible to extract the silver from silver nitrate through electrolysis.



2.5.2 Removal of Aluminium Coatings

Solar cells are treated with potassium hydroxide to etch out aluminium from the back surface of the solar cell. Aluminium is soluble in potassium hydroxide. It forms potassium aluminate and hydrogen gas. Aluminium contact is removed from the back surface.



2.5.3 Removal of Silane Layer

After the above reactions, the product is treated with hydrofluoric acid. The result is a bare silicon cell with a removed anti-reflective coating.

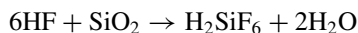
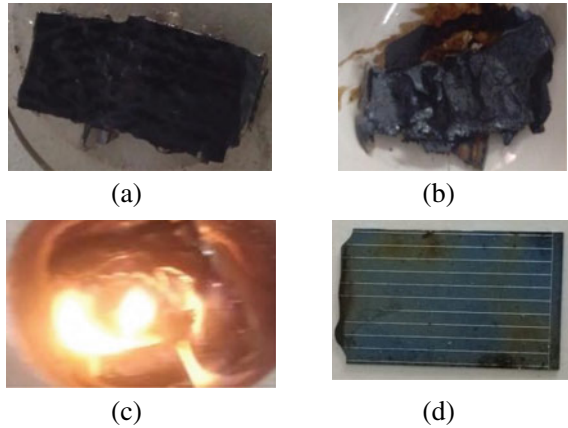


Fig. 3 Solar modules in a furnace to remove EVA via thermal process: **a** at 250 °C; **b** at 350 °C; **c** at 375 °C and **d** 400 °C after the thermal process



3 Results and Discussions

3.1 Amputation of Tedlar Sheet

After removal of frame and junction box through mechanical process, Tedlar sheet has been removed using heat. It became soft after heating in the oven at 150 °C for 3 h and then easily peeled off.

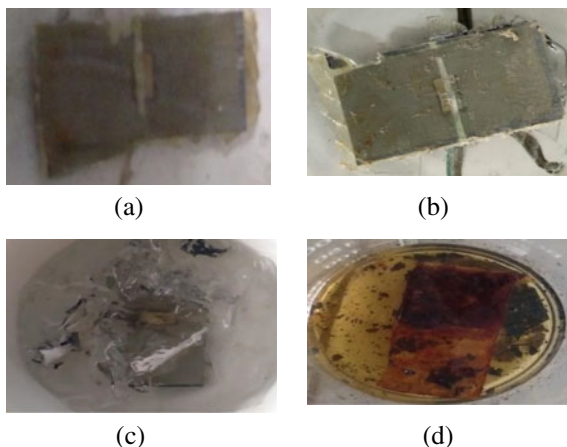
3.2 Amputation of Ethylene Vinyl Acetate (EVA) Through the Thermal Process

The solar cells are heated in the furnace at different temperatures and results have been assessed to find the optimum one. Figure 3 shows the condition of the solar module after the thermal process at different temperatures. At 250 °C, there is no change in the state of solar cells. By 350 °C, smoke started rising which reflects incomplete combustion and at 375 °C, the solar cell caught fire. By heating at 400 °C for 30 min, no traces of EVA were left. So, the inference has been drawn to get the best results, a module should be heated for 30 min at 400 °C in the muffle furnace.

3.3 Amputation of Ethylene Vinyl Acetate (EVA) Through a Chemical Process

To chemically remove the EVA layer, tests have been conducted with different chemical solvents which are nitric acid, acetone, ethanol and trichloroethylene. With nitric

Fig. 4 Solar modules in different chemicals to remove EVA via chemical process: **a** with acetone; **b** with ethanol; **c** with trichloroethylene and **d** with nitric acid after chemical process



acid, the EVA layer is separated in 7 days at room temperature while it takes 24 h at 80 °C for separation. Acetone and ethanol show no effect on EVA. Trichloroethylene causes EVA to turn into gel at 80 °C in 5 h (Fig. 4).

EVA is separated by a thermal process, i.e. in the muffle furnace at 400 °C for 30 min and chemical process, i.e. by immersing the module in HNO₃ either at room temperature for 7 days or 24 h in the oven. The inference is made from the results that thermal separation is the more favourable alternative for the removal of EVA economically and ecologically in comparison with chemical processes involving expensive and toxic reagents. The only disadvantage of thermal separation is that the glass gets cracked. Chemical processes can be opted to get an intact glass.

3.4 Recovery of Silicon Wafer

After chemical treatment, an isolated bare silicon wafer has been procured. To quantify the presence of Si and Ag, the different samples prepared have been analysed through atomic absorption spectroscopy (AAS). Three different sample S1, S2 and S3 has been described in Table 4.

Figure 5 shows the presence of Si in crystalline form in the prepared sample. After each chemical treatment, an increase of Si concentration has shown in the

Table 4 Description of three samples prepared for AAS

Sample	Definition
S1	Initial sample after thermal process
S2	Sample after treatment with HNO ₃
S3	Sample after treatment with HNO ₃ and KOH

Fig. 5 Si results of AAS three samples

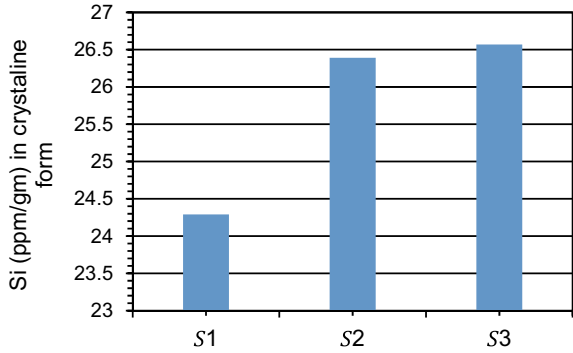
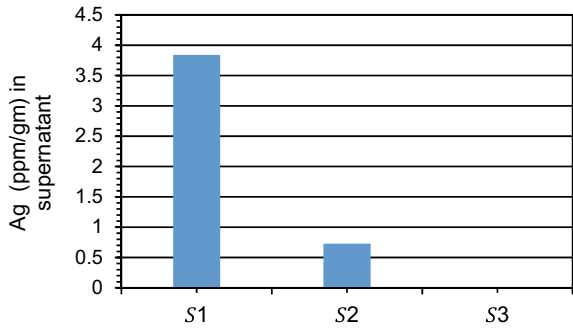


Fig. 6 Ag results of AAS of three samples



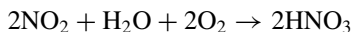
figure, therefore confirming the removal of the coatings applied on the surface of the silicon wafers with the help of the chemicals used in the above-mentioned processes.

Figure 6 shows the absence of Ag in sample S3. Ag is coated on the grid of the silicon wafers to enhance the electron collection efficiency of solar cells and is the costly component of solar panels. Its recovery is essential and therefore in the above-mentioned process, it is etched out from the wafers which can be seen in Fig. 6 that shows the reduction in the concentration of Ag in different samples.

This recovered c-Si is *p*-type wafer which have *p*-type doping impurities to confirm the impurities the further study will be carried out.

3.5 Waste Treatment After Si Wafer Recovery

- i. During the removal of silver coating, NO₂ gas is released which is toxic and causes many harmful effects such as smog, acid rain, etc. This chemical process should be done inside the incinerator which is connected with the container of water through a passing tube; the NO₂ released directly goes into the water container and gets dissolved in water.



- ii. Hydrofluoric Acid (HF) is used for its ability to etch silicon compounds. Disposal of HF after use is a major concern. The neutralization of HF can be done with caustic soda (NaOH) or lime.

4 Conclusion

The study presented that recycling the waste PV module to recover Si and Ag is technically feasible as they are costly components of the solar PV module and also environmentally and economically important. Apart from the metals of great value and toxicity, the aluminium frame, junction box, glass, EVA and Tedlar sheet has also been recycled. Though these components are not as valuable as Si and Ag in terms of raw materials from the prospect of the environment it is important to recycle them. Analysing different processes of recycling helped to make inferences of the advantages and disadvantages of these different methods. The junction box and aluminium frame have been removed mechanically. To remove Tedlar, a thermal process has been opted. For EVA, thermal and chemical both the processes have been performed and it can be concluded from the experiments the thermal process is the best solution from an economic and ecological point of view but to get intact glass, the chemical process can opt. Then using chemical solvents, i.e. nitric acid, potassium hydroxide and hydrofluoric acid, electrodes and coatings of Ag, Al and silane has been removed which could be even seen with the naked eye, to get bare silicon wafers. The increase in the presence of silicon and reduction of silver has been analysed and confirmed by atomic absorption spectroscopy from the prepared samples. Silver has been extracted from silver nitrate formed in the process of removal of Ag coating through electrolysis.

The recovered silicon from processes mentioned can be used as a raw material in the industrial application of PV modules again, or as a supplement to change mechanical properties of steel by amalgamating it, and as a ceramic material, depending on the purity of silicon in non-metal powders manufactured. Also, the components other than silicon wafers and Ag retained from the processes performed in the study can be used again further reducing the photovoltaic wastes. To reduce the environmental hazards, chemical solvents have been treated properly after their use.

References

1. IRENA (2019) Future of solar photovoltaic: deployment, investment, technology, grid integration and socio-economic aspects (a global energy transformation: paper), Int Renew Energy Agency. Available at: https://www.irena.org/-/media/Files/IRENA/Agency/Publication/2019/Oct/IRENA_Future_of_wind_2019.pdf

2. Gupta S et al (2021) Comparative performance analysis of flat plate solar collectors with and without aluminium oxide-based nano-fluid. *Mater Today Proc* 46:5378–5383. <https://doi.org/10.1016/j.matpr.2020.08.797>
3. Haegel NM et al (2019) Terawatt-scale photovoltaics: transform global energy. *Science* 364(6443):836–838. <https://doi.org/10.1126/science.aaw1845>
4. Tiwari AK et al (2021) TRNSYS simulation of flat plate solar collector based water heating system in Indian climatic condition. *Mater Today Proc* 46:5360–5365. <https://doi.org/10.1016/j.matpr.2020.08.794>
5. NREL (1990) The potential of renewable energy, an interlaboratory white paper. National Renewable Energy Laboratory, Golden, CO, SERI/TP260-3674
6. Ansanelli G et al (2021) A life cycle assessment of a recovery process from end-of-life photovoltaic panels. *Appl Energy* 290:116727. <https://doi.org/10.1016/j.apenergy.2021.116727>
7. Tao J, Yu S (2015) Review on feasible recycling pathways and technologies of solar photovoltaic modules. *Sol Energy Mater Sol Cells* 141:108–124. <https://doi.org/10.1016/j.solmat.2015.05.005>
8. Dias PR, Benevit MG, Veit HM (2016) Photovoltaic solar panels of crystalline silicon: characterization and separation. *Waste Manage Res* 34(3):235–245. <https://doi.org/10.1177/0734242X15622812>
9. Farrell C et al (2019) Assessment of the energy recovery potential of waste photovoltaic (PV) modules. *Sci Rep* 9(1):1–13. <https://doi.org/10.1038/s41598-019-41762-5>
10. Pern J (2008) Module encapsulation materials, processing and testing. In: APP international PV reliability workshop, 4–5 Dec 2008. Shanghai, China, pp 1–33. Available at: <http://www.nrel.gov/docs/fy09osti/44666.pdf>
11. Weckend S, Wade A, Heath G (2016) End of life management solar PV panels, international renewable energy agency (IRENA) and the international energy agency (IEA)
12. Punathil L et al (2021) Recovery of pure silicon and other materials from disposed solar cells. *Int J Photoenergy* 2021. <https://doi.org/10.1155/2021/5530213>
13. Schlummer M et al (2006) Report: recycling of flame-retarded plastics from waste electric and electronic equipment (WEEE). *Waste Manage Res* 24(6):573–583. <https://doi.org/10.1177/0734242X06068520>
14. Kim Y, Lee J (2012) Dissolution of ethylene vinyl acetate in crystalline silicon PV modules using ultrasonic irradiation and organic solvent. *Solar Energy Mater Solar Cells* 98:317–322. <https://doi.org/10.1016/j.solmat.2011.11.022>
15. Doni A, Dughiero F (2012) Electrothermal heating process applied to c-Si PV recycling. In: Conference record of the IEEE photovoltaic specialists conference, pp 757–762. <https://doi.org/10.1109/PVSC.2012.6317715>
16. SR Y (2013) Improvement on recycling process and life cycle assessment of photovoltaic panel. In: Proceedings of the EcoDesign 2013 international symposium. Jeju, Korea
17. Bogacka M et al (2019) Thermal decomposition of the silicon photovoltaic cells covered with EVA and ETFE foil. In: Heraklion 2019 7th international conference on sustainable solid waste management, pp 1–9
18. Shin J, Park J, Park N (2017) A method to recycle silicon wafer from end-of-life photovoltaic module and solar panels by using recycled silicon wafers. *Sol Energy Mater Sol Cells* 162:1–6. <https://doi.org/10.1016/j.solmat.2016.12.038>
19. Berger W et al (2010) A novel approach for the recycling of thin film photovoltaic modules. *Resour Conserv Recycl* 54(10):711–718. <https://doi.org/10.1016/j.resconrec.2009.12.001>
20. Wang TY, Hsiao JC, Du CH (2012) Recycling of materials from silicon base solar cell module. In: Conference record of the IEEE photovoltaic specialists conference, pp 2355–2358. <https://doi.org/10.1109/PVSC.2012.6318071>
21. Kang S et al (2012) Experimental investigations for recycling of silicon and glass from waste photovoltaic modules. *Renew Energy* 47:152–159. <https://doi.org/10.1016/j.renene.2012.04.030>

Effect Analysis of Heat Extraction on the Performance of the TAE



S. R. Solanki, A. B. Desai, and H. B. Mehta

Abstract The experimental investigations are performed in a half-wavelength standing type thermoacoustic engine that is also known as TAE. The aim of this study is to analyse the effect of variation in heat extraction across the stack on the performance of TAE while using Nitrogen gas as a working material. In present work, the variation in heat extraction at cold end of stack is obtained by passing different water flow rate through Cold Heat Exchange (CHX), while same at the hot end side of stack is obtained by placing air cooling fan at outside the hot end of heater assembly. The effect of these two variation in heat extraction from stack of TAE is examined in terms of on-set time/temperature, pressure amplitude and die-out time/temperature. The effects of variation in heat extraction on the parameters, on-set time and die-out time give the study of transient behaviour of the system. This paper shows that heat extraction at hot end side of stack affect adversely on the pressure amplitude produced by TAE and on-set temperature, while this variation decreases the on-set time so acoustic vibration output generate within short time. The effects of variation in heat extraction at cold end side are decrease in on-set temperature as water flow rate through CHX increases but shows no effect on the on-set time, no effect on pressure amplitude for higher and lower charging pressure but at intermediate pressure it will affect pressure amplitude. The study of die-out behaviour of system can be useful for automatic control inside the thermoacoustically driven cooling system.

Keywords Cold heat exchanger · Pressure amplitude · On-set time/temperature · Die-out time/temperature · Transient analysis

1 Introduction

The word “Thermoacoustics” is the combination of the two words, “Thermo” means Heat and “Acoustics” means Sound. Thermoacoustics is the science that studies

S. R. Solanki (✉) · A. B. Desai · H. B. Mehta
Department of Mechanical Engineering, Sardar Vallabhbhai National Institute of Technology,
Surat, India
e-mail: solankisagar2020@gmail.com

the interaction between heat and acoustic. In thermoacoustic devices, temperature gradient is imposed on porous solid to generate acoustic wave or an acoustic wave interact with porous solid material to generate temperature gradient across the solid. The devices working on principle of thermoacoustics mainly divided into two types, 1) thermoacoustic engine (TAE) and 2) thermoacoustics refrigerator (TAR). Thermoacoustic engines (TAE) are the devices that generate acoustic work by taking heat as an input. TAE can use industrial waste heat, automobile exhaust waste heat, solar heat, as their heat input resources. The construction of TAE is very simple due to the fewer number of components. The main advantage of thermoacoustic devices is they have no moving or rotating component. TAR devices the acoustic power is supplied to produce cooling effect across the TAR stack. According to physical construction these devices can be of different configuration as such as quarter wavelength type or half-wavelength type, etc.

The working fluid in these thermoacoustic devices is Air, Nitrogen, Helium and other noble gases which are environmentally harmless which make this thermoacoustics technology environment friendly. This acoustic work produced by TAE can be used to drive thermoacoustic refrigerators (TAR) [1], producing electricity [2], gas separation [3], etc. So, that thermoacoustics has become an area of interest for many researchers for several decades. The history of thermoacoustics is long but sparsely populated. Bayron Higgins [4] made the first observation of thermoacoustic oscillation generated by placing a hydrogen flame inside a both side open large pipe at particular position in 1777. Sondhauss [5] performed an experimental investigation in 1850, on Sondhauss tube, which is open at one end and terminated in the bulb on the other end which is the earliest thermoacoustic engine and also quantitatively investigated the relationship between the pitch of the sound and the dimensions of the apparatus. Carter et al. [6] in 1962 the important improvement in soundhauss tube was done by placing a new structure inside the tube known as “Stack”, they enhance the sound generated from the tube. Lord Rayleigh [7] quantitatively explained the soundhauss tube in 1896. In his book “The Theory of Sound”, he stated that, “At the moment of the greatest condensation heat is received by the air and at the moment of the greatest rarefaction heat is given up from the air, so this will have the tendency to maintain vibration”. Swift [8] in 1988, derived the basic mathematical equation for single plate, and explain working principle of heat transfer mechanism inside the stack used in thermoacoustic devices. Hao et. al. [9] in 2011 studied the influence of the working fluid on the performance of the standing wave type thermoacoustic prime mover using helium-argon gas mixture. Karla et. al. [10] studied the effect of charging pressure on the performance of the system is studied in terms of resonating frequency, on-set temperature, pressure amplitude, acoustic power and efficiency. Desai et. al. [11–13] studied the effect of hot end temperature, charging pressure, stack length, heater housing hot buffer on the pressure amplitude and on-set temperature of the thermoacoustic engine for helium and nitrogen considered as working gas.

The most of the experimental investigations are carried out for improvement in TAE performance by keeping variation in lots of parameters like stack length, working gas or gas mixture, hot buffer length, charging pressure, etc. On-set

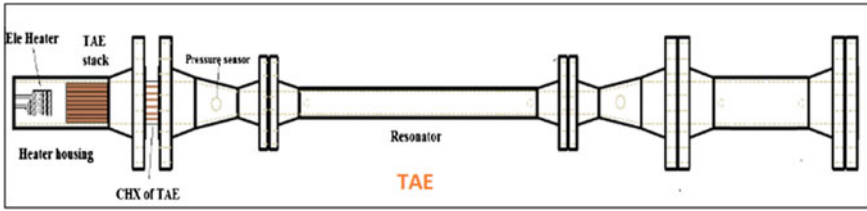


Fig. 1 The schematic of TAE

behaviour and pressure amplitude are the most important parameters to analyse the performance of TAE. The present study reports the experimental investigation on the performance of half-wavelength standing wave type TAE in terms of on-set time and temperature, pressure amplitude and die-out temperature and time by keep variation in heat extraction from hot and cold end of stack of TAE. Figure 1 Shows the schematic of TAE.

2 Experimental Setup

Present work is done on a half-wavelength standing wave type thermoacoustic engine. Thermoacoustic devices generally consist of four components: (1) Hot heat exchanger, (2) Cold Heat Exchanger, (3) Resonator tube and (4) Stack. The stack is placed between heater coil (Hot Heat Exchanger) and Cold Heat Exchange, inside the heater housing. A steep temperature gradient is maintained across the stack to generate acoustic power. Stack is only the work producing component inside the TAE, other components like resonator tube, heat exchangers are the work consuming components.

Figure 2 shows the experimental setup on which current experimental analysis was performed. 1. Main Component of Experiment Setup contains: TAE components, heater housing, CHX, resonator tube, experimental test skid, 2. Data Acquisition System, 3. Auxiliary system: water chiller and air cooling fan and 4. Instrumentation: pressure measurement system, temperature control system and rota-meter.

3 Results and Discussion

The experiments are carried out on TAE with Nitrogen gas as a working medium to analyse the influence of heat extraction on the performance of TAE. There are very large number of parameters by changing them we can study the different results and effect on the output of the system. The effect of variation in heat extraction at hot and cold end of stack of TAE is assessed on the performance of the TAE. The variation in heat extraction at cold end of stack of TAE is achieved by changing the water

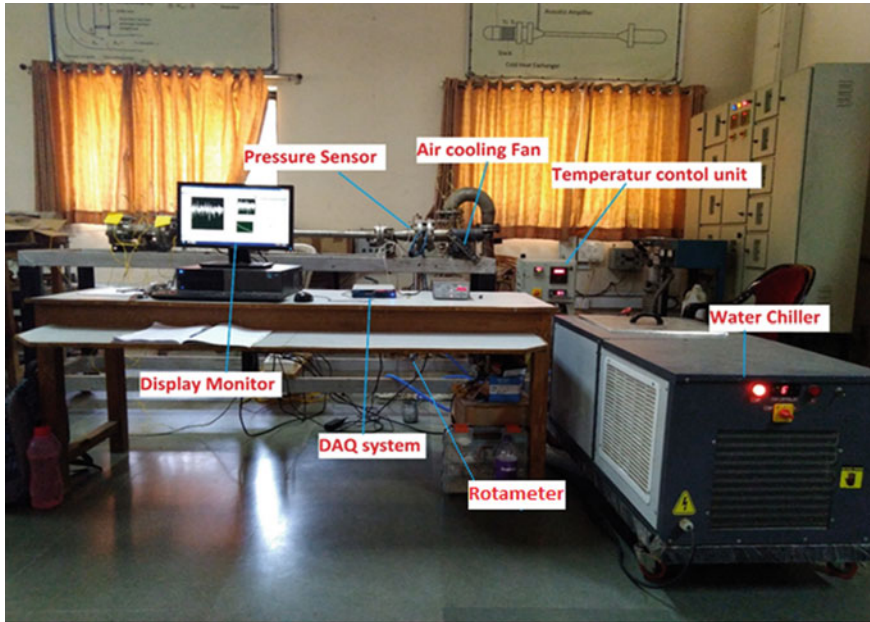


Fig. 2 Experimental setup

flow rate through the CHX with the help of Sensewell flow-metre and similarly the additional air cooling fan is placed at hot end of stack of TAE to vary heat extraction at hot end.

In TAE system, main output is the acoustic power generated due to temperature gradient imposed on it. This acoustic power is mainly depend on the pressure amplitude of oscillating wave. So here the results are mainly discussed in the form of pressure amplitude, on-set time and temperature and die-out time and temperature (Table 1).

3.1 Effect on the On-Set Temperature

Figure 3 shows the effect of different water flow rate through CHX, normal and fan cooling working conditions with respect to pressure on the on-set temperature. As the charging pressure increases the on-set temperature increases. At 21 bar charging pressure water flow rate of 4 LPM through CHX shows highest on-set temperature as compared to 3 LPM and 5 LPM water flow rate. By changing water flow rate through CHX from 3 to 4 LPM and 4 LPM to 5 LPM at 21 bar charging pressure the on-set temperature raised by 4.8 °C (+2.64%) and decreased by 12 °C (−6.43%), respectively, for normal working condition. While for air cooling fan on condition changing water flow rate through CHX from 3 to 4 LPM and 4 LPM to 5 LPM at 21 bar

Table 1 Parametric choice for TAE with experiment analysis

	Parameter	Parameter details
Fixed	TAE stack	$L = 80$ mm, $OD = 60$ mm, Parallel plate placed in horizontal orientation
	TAE housing	$L = 200$ mm, $ID = 62.5$ mm
	Working gas	Nitrogen
	Stack position	40 mm away from inner edge of CHX
	Air cooling fan position	Heater end to Fan Centre distance = 120 mm
	Chiller temp	5 °C
Variation	Water flow rate	CHX water flow rate variation 3LPM, 4LPM and 5LPM
	Charging pressure	From 14 to 35 bar with step of 7 bar

charging pressure the on-set temperature raised by 4.9 °C (+2.70%) and decreased by 13.7 °C (-7.23%), respectively. At higher pressure of 35 bar the maximum variation in on-set temperature is found 4.4 °C (0.91%) for normal operating condition and 3.9 °C (0.81%) for air cooling fan on operating condition.

The on-set temperature raised when keep air cooling fan on at hot end side of stack of TAE, more this effect is significant at lower charging pressure, as the charging pressure increasing effect of heat extraction as hot end of stack of TAE will decreased. At 4 LPM water flow rate through CHX the difference in on-set temperature found maximum between normal and air cooling fan on working condition. At 4 LPM

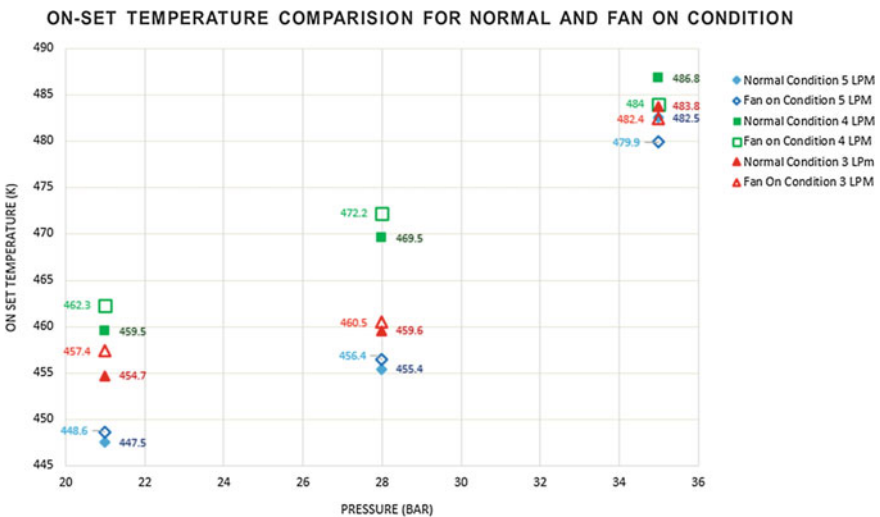


Fig. 3 On-set temperature comparison for normal and cooling fan on condition

water flow rate through CHX, the on-set temperature at 21 bar increased by 2.8 °C (+1.5%) and at 35 bar decreased by 2.8 °C (−1.31%).

3.2 Effect on On-Set Timing

Figure 4 shows the variation of on-set timing for different water flow rate through CHX and different working condition at different charging pressures. From most common observation, it is found that on-set timing almost reduced by 33% to 50% or remains same for air cooling fan on working condition as compared to normal operating condition. At 21 bar charging pressure on-set time reduced by almost 50% for air cooling fan on working condition as compared to normal working condition. As increased charging pressure at 28 bar the on-set time reduced by 33.33% for 4 LPM and 5 LPM water flow rate through CHX for air cooling fan on working condition as compared to normal working condition. Air cooling fan on working condition reduced on-set timing at lower charging pressure, as the charging pressure increases on-set time almost become same for both working condition and at very high pressure on-set timing will be greater for air cooling fan on working condition as compared to normal working condition.

On-set time variation with respect to different water flow rate through CHX is not significant. Even from common observation it is found that on-set time for 3 LPM water flow rate through CHX will be slightly greater than or equal to on-set time for 4 LPM and 5 LPM water flow rate through CHX for every charging pressure and for both working conditions.

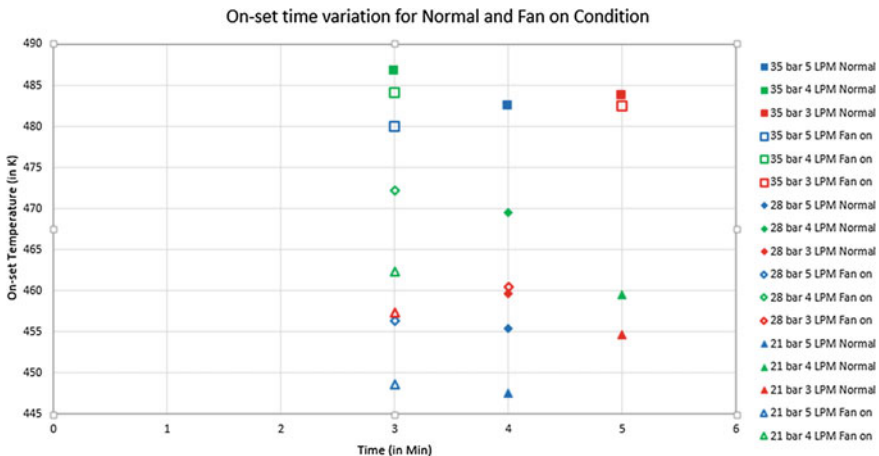


Fig. 4 On-set time variation for normal and fan on operating condition

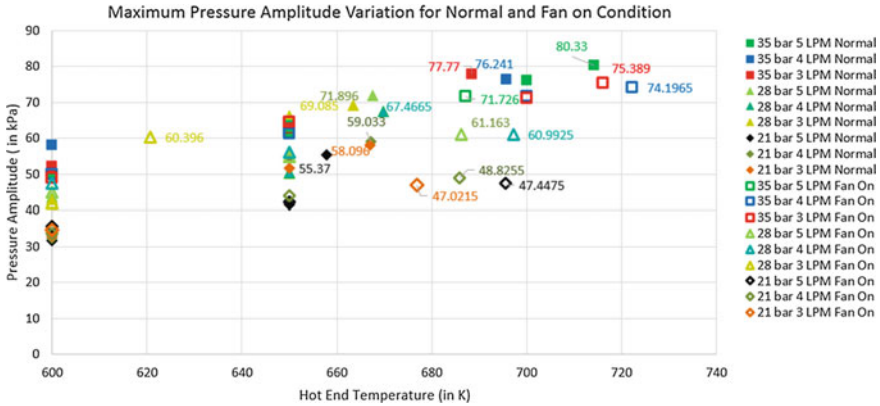


Fig. 5 Variation in maximum pressure amplitude for different charging pressure for different working condition

3.3 Effect on Pressure Amplitude

In Fig. 5, the filled shape shows normal working condition while empty shape shows air cooling fan on working condition. The variation in maximum pressure amplitude achieved for different water flow rate through CHX for 35 bar, 28 bar and 21 bar charging pressure is respectively 3.67 kPa (4.80%), 4.43 kPa (6.56%) and 3.24 kPa (5.82%) for normal operating condition and 2.72 kPa (3.77%), 0.77 kPa (1.27%) and 1.46 kPa (3.09%) for air cooling fan on working condition. So effect of different water flow rate through CHX on pressure amplitude is reduced while working with air cooling fan on working condition as compare to normal working condition.

The maximum pressure amplitude for any fixed charging pressure and water flow rate through CHX is lower in air cooling fan on operating condition as compared to normal operating condition. The reduction in pressure amplitude for air cooling fan on working condition as compared to normal operating condition for 35 bar, 28 bar and 21 bar charging pressure is 7.58 kPa (9.44%), 10.73 kPa (14.93%) and 7.92 kPa (14.31%) for 5 LPM water flow rate, 2.05 kPa (2.69%), 6.48 kPa (9.59%) and 10.2075 kPa (17.29%) for 4 LPM water flow rate and 2.38 kPa (3.06%), 8.69 kPa (12.58%) and 11.074 kPa (19.06%) for 3 LPM water flow rate through CHX, respectively. From above observation, the effect of air cooling fan on operating condition on reduction in pressure amplitude is more at lower charging pressure as compared to high charging pressure.

3.4 Effect on Die-Out Temperature

Figure 6 shows the effect of different water flow rate through CHX, normal and fan cooling working conditions with respect to pressure on the die-out temperature. As

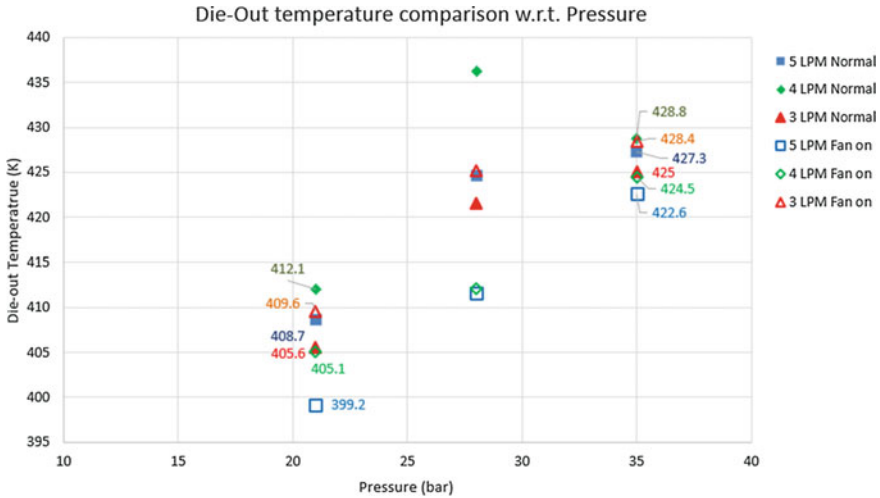


Fig. 6 Die-out temperature comparison for normal and cooling fan on condition

the charging pressure increases the die-out temperature increases. At 21 bar charging pressure water flow rate of 4 LPM through CHX shows highest die-out temperature as compared to 3 LPM and 5 LPM water flow rate. By changing water flow rate through CHX from 3 to 4 LPM and 4 LPM to 5 LPM the die-out temperature raised by 6.5 °C (+4.90%) and decreased by 3.4 °C (−2.44%), respectively, for normal working condition at 21 bar. While for air cooling fan on working condition at 21 bar changing water flow rate through CHX from 3 to 4 LPM and 4 LPM to 5 LPM the die-out temperature decreased by 4.5 °C (−3.29%) and 5.9 °C (−4.47%), respectively.

The die-out temperature raised when keep air cooling fan on at hot end side of stack of TAE, more this effect is significant at lower charging pressure, as the charging pressure increasing effect of heat extraction as hot end of stack of TAE will decreased. At 21 bar charging pressure the difference in die-out temperature for different working conditions is found 4 °C (3.02%) for 3 LPM water flow rate, 7 °C (5.30%) for 4 LPM water flow rate and 9.5 °C (7.53%) for 5 LPM water flow rate through CHX. While at 35 bar charging pressure the difference in die-out temperature for different working conditions are found 3.4 °C (2.24%) for 3 LPM water flow rate, 4.3 °C (2.84%) for 4 LPM water flow rate and 2.4 °C (1.60%) for 5 LPM water flow rate through CHX.

3.5 Effect on Die-Out Time

Figures 7, 8 and 9 show the variation of die-out timing for different charging pressure and different working condition at different water flow rate through CHX. At 21 bar

pressure with normal operating condition shows no variation in die-out time with respect to different water flow rate through CHX. As the pressure increases the variation in die-out time for normal operating condition found 1 min (6.67%) at 28 bar, and 3 min (23.08%) at 35 bar charging pressure. As the charging pressure increases the die-out time decreases for both operating conditions.

The die-out temperature decreases for air cooling fan on working condition as compared to normal operating condition. For 21 bar maximum variation in die-out time is found 3 min (17.65%) for 3 LPM water flow rate through CHX for normal and air cooling on operating condition. Similarly, for 28 bar and 35 bar charging pressure

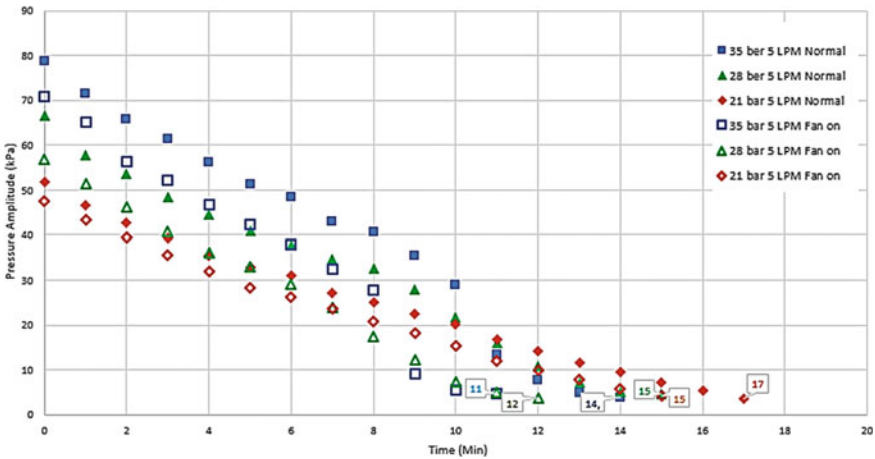


Fig. 7 Die-out time variation at 5 LPM water flow rate

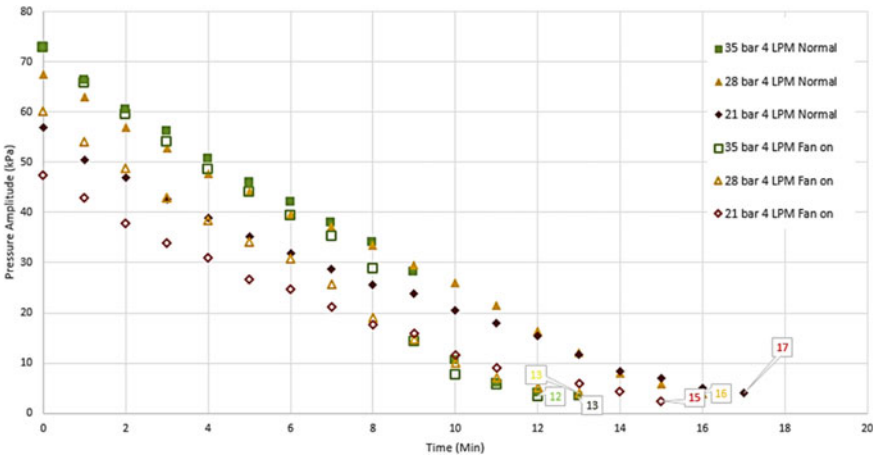


Fig. 8 Die-out time variation at 4 LPM water flow rate

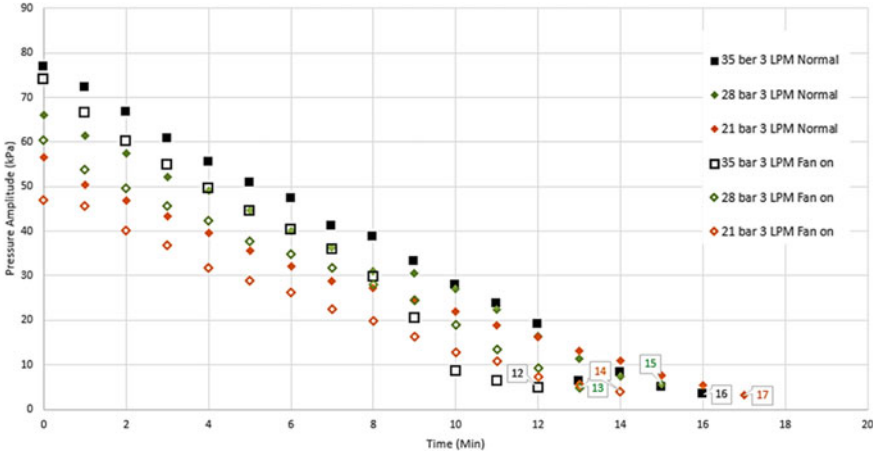


Fig. 9 Die-out time variation at 3 LPM water flow rate

the maximum variation in die-out time is found 3 min (20%) for 5 LPM water flow rate and 4 min (25%) for 3 LPM water flow rate through CHX for different working conditions, respectively.

4 Conclusions

The conclusion outcomes from experimental investigation for system operating under normal conditions and air cooling fan on operating conditions are mentioned here under:

On-set temperature decreases with increasing water flow rate through CHX. While keeping air cooling fan on operating condition, on-set temperature increases at lower pressure and shows no variation at higher pressure compared to normal operating condition.

On-set time shows no variation w.r.t water rate through CHX, while keeping air cooling fan on operating condition, the on-set time is reduced.

Pressure amplitude decreases for air cooling fan on operating working condition as compared to normal operating condition.

Die-out temperature decrease with decrease in water flow rate through CHX. For air cooling fan on operating condition die-out temperature reduced as compared to normal operating condition.

Die-out time decrease for air cooling fan on operating working condition as compared to normal operating condition.

References

1. Tijani MEH, Zeegers JCH, Waele ATAM de (2002) Design of thermoacoustic refrigerators. *Cryogenics* 42:49–57
2. Hamood A, Jarwoski AJ, Mao X (1970) Development and assessment of two-stage thermoacoustic electricity generator. *Energies* 12
3. Remiorz L, Wiciak G, Grzywnowicz K (2019) Novel concept of supporting the membrane separation of CO₂ in power plants by thermoacoustic dehumidification. *Energy* 185:116191
4. Higgins B (1802) *Nicholson's J* 1:130
5. Sondhauss C (1850) Ueber die Schallschwingungen der Luft in erhitzten Glasröhren und in gedeckten Pfeifen von ungleicher Weite. *Ann Phys* 155:1–34
6. Carter RL, White M, Steele AM (1962) Private communication of Atomic International Division of North American Aviation, Inc.
7. Rayleigh JWS (1945) 1886 *The theory of sound*, vol 2, Sec 322, 2nd edn. Dover, New York
8. Swift GW (1995) Thermoacoustic engines and refrigerators. *Phys Today* 48:22–28
9. Hao XH, Ju YL, Behera U, Kasthuriangan S (2011) Influence of working fluid on the performance of a standing-wave thermoacoustic prime mover. *Cryogenics* 21
10. Karla S, Desai KP, Naik HB, Atrey MD (2012) Theoretical study on standing wave thermoacoustic engine. ICEC 25—ICMC 2014
11. Desai AB, Desai KP, Naik HB, Atrey MD (2016) Design and analysis of standing wave quarter wavelength thermoacoustic engine. *Indian J Cryogen* 41:69–74
12. Desai AB, Desai KP, Naik HB, Atrey MD (2020) Experimental investigation on high frequency thermoacoustic engine. *Indian J Cryogen* 45
13. Desai AB, Desai KP, Naik HB, Atrey MD (2020) Experimental study and analysis of a thermoacoustically driven thermoacoustic refrigerator. *Sādhanā* 45:213